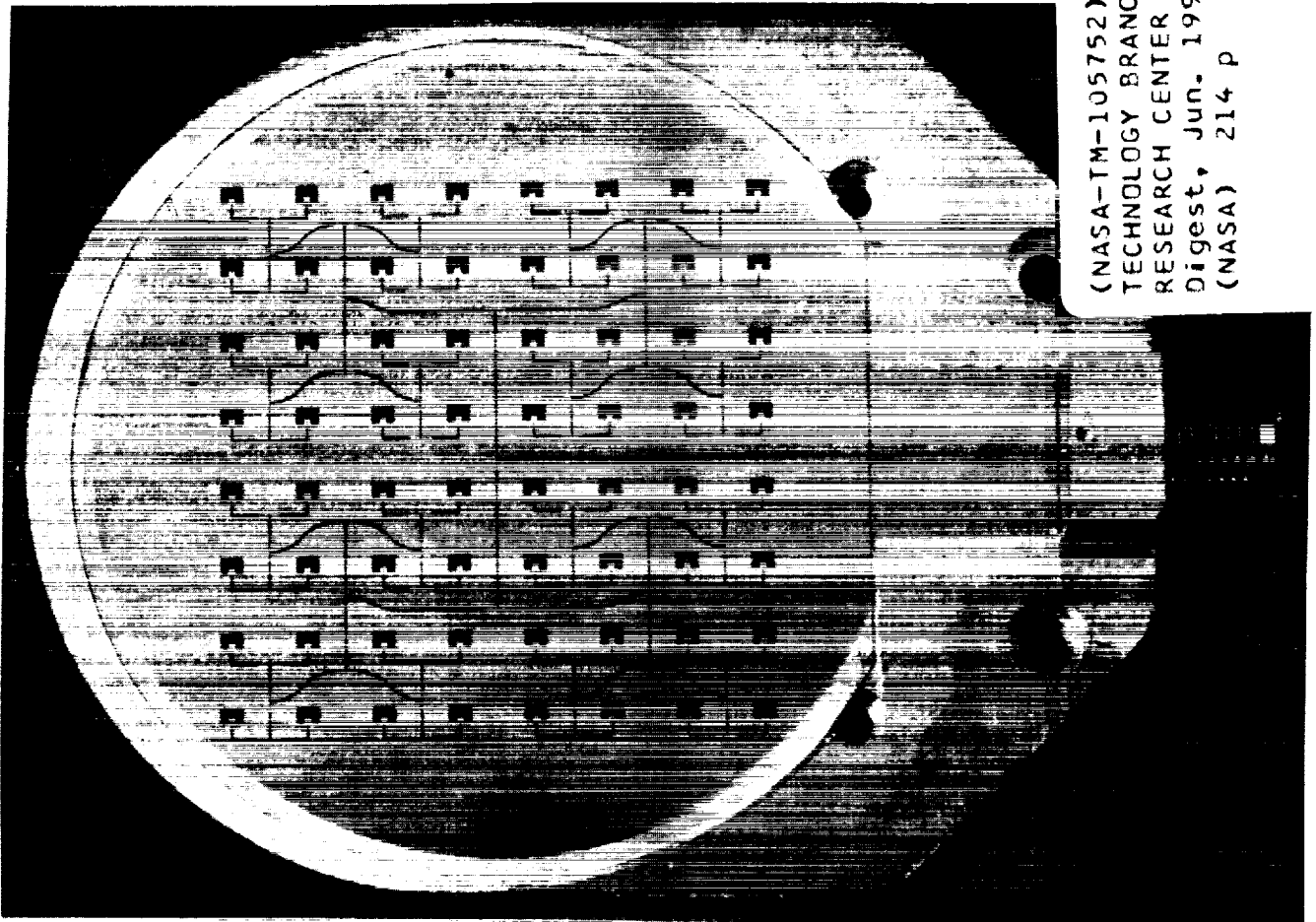


N92-32965  
--THRU--  
N92-32984  
Unclas

G3/32 0116609

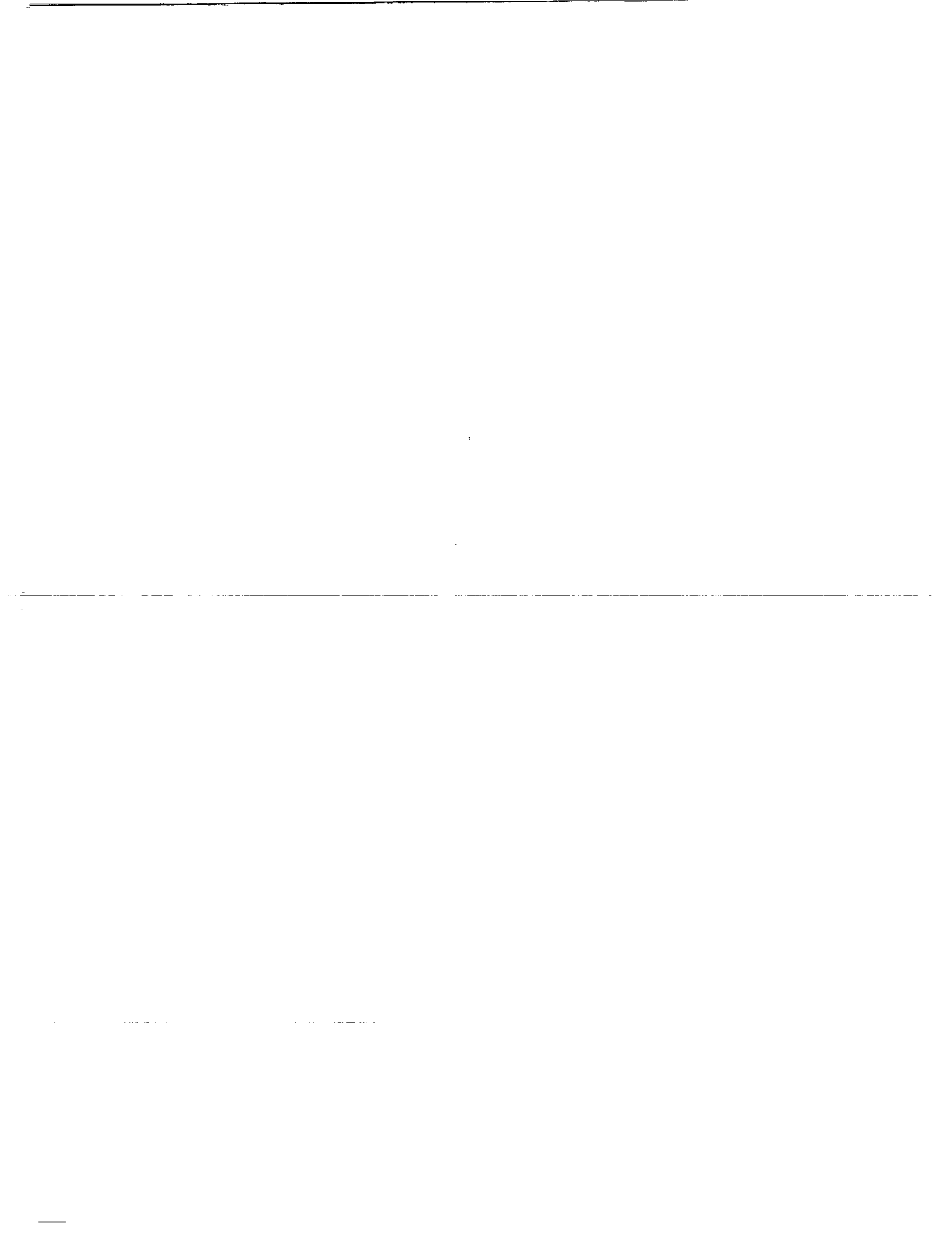
# Solid State Technology Branch of NASA Lewis Research Center Fourth Annual Digest

(NASA-TM-105752) SOLID STATE  
TECHNOLOGY BRANCH OF NASA LEWIS  
RESEARCH CENTER Fourth Annual  
Digest, Jun. 1991 - Jun. 1992  
(NASA) 214 p



**NASA**

June 1991 - June 1992  
Lewis Research Center



## Preface

As with previous volumes of this digest, the present edition represents 1 year (June 1991 to June 1992) of publications by the Solid State Technology Branch of NASA Lewis Research Center. The digest does not include a number of oral presentations or symposia for which no proceedings were published. Nevertheless, the present volume clearly indicates the areas of solid-state research where branch efforts are focused, and provides the reader with the names of people who can be contacted for more detailed information.

As usual, the digest is organized into three sections: MMIC and Hybrid Microwave Circuits, Development of Heterojunction Materials and Devices, and High Temperature Superconductivity. The topics in the MMIC and Hybrid Microwave Circuits section contain papers on V-band and W-band work and are indicative of the general move to higher frequencies. The paper describing a 1-W, Ka-band amplifier is representative of continuing efforts to insert our research into NASA missions. In the present case, the 1-W amplifier uses monolithic power amplifiers produced under contract by Texas Instruments in combination with in-house-designed coplanar waveguide power dividers and combiners. The resulting amplifier is intended to be used as a transmitter for a number of ACTS experimental ground terminals. In addition, the branch still maintains a significant effort in the design, fabrication, and testing of novel schemes for feeding array antennas.

In-house work in materials and devices research continues to feature a strong collaboration with the University of Michigan and a strong interest in InGaAs heterojunction materials, both on GaAs and InP. One of the most significant achievements in the last year was the production of a "decal" HEMT from which all of the GaAs substrate was removed. Deposition of the remaining active layers on a sapphire substrate yielded a device that outperformed the original GaAs substrate.

In the area of superconductivity, significant effort was maintained in determining microwave properties of thin films. However, because our film deposition facility was undergoing major modification, the principal sources for films was outside Lewis. The largest part of our effort in superconductivity this year was directed to the design, fabrication, and testing of an X-band oscillator stabilized by a superconducting resonator and a cryogenic mixer. These will serve as the local oscillator and down converter for a receiver, developed jointly with the Jet Propulsion Laboratory, to be submitted to the Naval Research Laboratory for their Superconducting Space Experiment (HTSSE-II).

New facilities this year reflected branch research interests. A W-band test set was added to permit ANA work on monolithic 90-GHz parts that will be delivered by TRW. An addition to our Hall measurement facility, which will permit optically modulated measurements, became fully operational this year. Finally, a major modification in the laser ablation system will provide cleaner vacuums while permitting sequential ablation of multiple targets. The primary objective of the modification was to allow the in situ deposition of multilayer structures.

Regis F. Leonard  
Branch Chief, Solid State Technology Branch  
NASA Lewis Research Center  
August 1992



**SOLID STATE TECHNOLOGY BRANCH OF  
NASA LEWIS RESEARCH CENTER  
FOURTH ANNUAL DIGEST  
June 1991 – June 1992**

*Contents*

**Section One  
MMIC And Hybrid Microwave Circuits**

|  |    |
|--|----|
| Advances in MMIC Technology for Communications Satellites<br>by Regis F. Leonard .....   | 3  |
| Low Noise InP-Based MMIC Receiver for W-Band<br>by Regis F. Leonard .....  | 9  |
| V-Band Pseudomorphic HEMT MMIC Phased Array<br>Components for Space Communications<br>by G.L. Lan, C.K. Pao, C.S. Wu, M. Hu, and Alan N. Downey .....        | 15 |
| Planar Dielectric Resonator Stabilized HEMT Oscillator Integrated<br>With CPW/Aperture Coupled Patch Antenna<br>by Rainee N. Simons and Richard Q. Lee ..... | 21 |
| A Vertically Integrated Ka-Band Phased Array Antenna<br>by R.R. Kunath, R.Q. Lee, K.S. Martzaklis, K.A. Shalkhauser,<br>A.N. Downey, and R. Simons .....     | 25 |
| An Optically Controlled Ka-Band Phased Array Antenna<br>by R.R. Kunath, R.Q. Lee, K.S. Martzaklis, K.A. Shalkhauser,<br>A.N. Downey, and R. Simons .....     | 35 |
| Coplanar Waveguide Aperture-Coupled Microstrip<br>Patch Antenna<br>by Richard Q. Lee and Rainee N. Simons .....  | 45 |
| Coplanar Waveguide Aperture Coupled Patch Antennas<br>With Ground Plane/Substrate of Finite Extent<br>by R.N. Simons and R.Q. Lee .....                      | 47 |
| Electromagnetic Coupling Between Coplanar Waveguide<br>and Microstrip Antennas<br>by Rainee N. Simons, Richard Q. Lee, and Glenn R. Lindamood .....          | 49 |

|  |    |
|--|----|
| New Techniques for Exciting Linearly Tapered Slot Antennas<br>With Coplanar Waveguide<br>by R.N. Simons, R.Q. Lee, and T.D. Perl .....   | 53 |
| Ka-Band Dual Frequency Array Feed for a Low<br>Cost ACTS Ground Terminal<br>by Richard Q. Lee, Rainee N. Simons, and Ajit K. Sil .....   | 55 |
| Coplanar Waveguide Feeds for Phased Array Antennas<br>by Rainee N. Simons and Richard Q. Lee .....   | 61 |
| New Coplanar Waveguide to Rectangular Waveguide End Launcher<br>by R.N. Simons and S.R. Taub .....   | 69 |
| Analysis of Shielded CPW Discontinuities With Air-Bridges<br>by N.I. Dib, P.B. Katehi, and G.E. Ponchak .....  | 71 |
| A Flexible CPW Package for a 30 GHz MMIC Amplifier<br>by Rainee N. Simons and Susan R. Taub .....  | 75 |
| A 1W, 30-GHz, CPW Amplifier for ACTS Small Terminal Uplink<br>by Susan R. Taub and Rainee N. Simons .....  | 79 |
| Comparative Evaluation of Optical Waveguides as Alternative<br>Interconnections for High Performance Packaging<br>by S.E. Schacham, Henri Merkelo, L.-T. Hwang,<br>Bradley D. McCredie, Mark S. Veatch, and I.Turlik ..... | 83 |

## **Section Two**

### **Development Of Heterojunction Materials And Devices**

|  |     |
|--|-----|
| New Materials and Techniques for Improved mm Wave Devices<br>by Samuel A. Alterovitz .....   | 95  |
| Intermodulation in the Oscillatory Magnetoresistance<br>of a Two-Dimensional Electron Gas<br>by S.E. Schacham, E.J. Haugland, and S.A. Alterovitz .....  | 105 |
| Reduced Mobility and PPC in $\text{In}_{.20}\text{Ga}_{.80}\text{As}/\text{Al}_{.23}\text{Ga}_{.77}\text{As}$<br>HEMT Structure<br>by S.E. Schacham, R.A. Mena, E.J. Haugland, and S.A. Alterovitz ..... | 111 |

|  |     |
|--|-----|
| Study of InGaAs-Based Modulation Doped Field Effect Transistor Structures Using Variable-Angle Spectroscopic Ellipsometry<br>by S.A. Alterovitz, R.M. Sieg, H.D. Yao, P.G. Snyder, J.A. Woollam<br>J. Pamulapati, P.K. Bhattacharya, and P.A. Sekula-Moise ..... | 117 |
| Microwave Properties of “Peeled” HEMT Devices<br>Sapphire Substrates<br>by Paul G. Young, Samuel A. Alterovitz,<br>Rafael A. Mena, and Edwyn D. Smith .....  | 123 |
| A Model for the Trap-Assisted Tunneling Mechanism in Diffused n–p and Implanted n <sup>+</sup> –p HgCdTe Photodiodes<br>by David Rosenfeld and Gad Bahir .....   | 127 |

### Section Three

## High Temperature Superconductivity

|   |     |
|---|-----|
| High Temperature Superconductor Analog Electronics for Millimeter-Wavelength Communications<br>by R.R. Romanofsky and K.B. Bhasin .....   | 137 |
| NASA Space Applications of High-Temperature Superconductors<br>by Vernon O. Heinen, Martin M. Sokoloski, Paul R. Aron,<br>Kul B. Bhasin, Edwin G. Wintucky, and Denis J. Connolly ..... | 143 |
| Measurement Techniques for Cryogenic Ka-Band Microstrip Antennas<br>by M.A. Richard, K.B. Bhasin, C. Gilbert, S. Metzler, and P.C. Claspy .....   | 151 |
| Performance of a Four-Element Ka-Band High-Temperature Superconducting Microstrip Antenna<br>by M.A. Richard, K.B. Bhasin, C. Gilbert, S. Metzler,<br>G. Koepf, and P.C. Claspy .....   | 159 |
| Performance of a Y–Ba–Cu–O Superconducting Filter/GaAs Low Noise Amplifier Hybrid Circuit<br>by K.B. Bhasin, S.S. Toncich, C.M. Chorey,<br>R. R. Bonetti, and A.E. Williams .....       | 163 |
| YBCO Superconducting Ring Resonators at Millimeter-Wave Frequencies<br>by Christopher M. Chorey, Keon-Shik Kong, Kul B. Bhasin,<br>J.D. Warner, and Tatsuo Itoh .....                   | 167 |

|  |     |
|--|-----|
| Performance of a K-Band Superconducting<br>Annular Ring Antenna<br>by M.A. Richard, K.B. Bhasin, R.Q. Lee, and P.C. Claspy .....   | 175 |
| Laser Ablated $\text{YBa}_2\text{Cu}_3\text{O}_{7-x}$ High Temperature Superconductor<br>Coplanar Waveguide Resonator<br>by G.J. Valco, A.R. Blemker, and K.B. Bhasin .....  | 179 |
| Coaxial Line Configuration for Microwave Power<br>Transmission Study of $\text{YBa}_2\text{Cu}_3\text{O}_{7-\delta}$ Thin Films<br>by C.M. Chorey, F.A. Miranda, and K.B. Bhasin .....   | 183 |
| Microwave Properties of $\text{YBa}_2\text{Cu}_3\text{O}_{7-\delta}$ High-Transition-Temperature<br>Superconducting Thin Films Measured by the Power<br>Transmission Method<br>by F.A. Miranda, W.L. Gordon, K.B. Bhasin, V.O. Heinen, and J.D. Warner ..... | 187 |
| Magnetic Penetration Depth of $\text{YBa}_2\text{Cu}_3\text{O}_{7-\delta}$ Thin Films<br>Determined by the Power Transmission Method<br>by Vernon O. Heinen, Felix A. Miranda, and Kul B. Bhasin .....   | 201 |
| Magnetic Flux Relaxation in $\text{YBa}_2\text{Cu}_3\text{O}_{7-x}$ Thin Film:<br>Thermal or Athermal<br>by Satish Vitta, M.A. Stan, J.D. Warner, and S.A. Alterovitz .....  | 205 |

## Biographies

|                             |     |
|-----------------------------|-----|
| Samuel A. Alterovitz .....  | 213 |
| Christopher M. Chorey ..... | 213 |
| Alan N. Downey .....        | 214 |
| Edward J. Haugland .....    | 214 |
| Thomas J. Kascak .....      | 215 |
| Regis F. Leonard .....      | 215 |
| Rafael A. Mena .....        | 216 |
| Felix A. Miranda .....      | 216 |
| Carlos R. Morrison .....    | 217 |
| George E. Ponchak .....     | 217 |
| John J. Pouch .....         | 218 |
| Robert R. Romanofsky .....  | 218 |

|                                       |     |
|---------------------------------------|-----|
| David Rosenfeld                       | 219 |
| Samuel E. Schacham                    | 219 |
| Ajit K. Sil                           | 220 |
| Rainee N. Simons                      | 220 |
| Mark A. Stan                          | 221 |
| Stephan Stecura                       | 221 |
| Susan R. Taub                         | 222 |
| Joseph D. Warner                      | 222 |
| Paul G. Young                         | 223 |
| Solid State Technology Branch Members | 224 |



***SECTION  
ONE***

***MMIC AND HYBRID  
MICROWAVE CIRCUITS***



# ADVANCES IN MMIC TECHNOLOGY FOR COMMUNICATIONS SATELLITES

Regis F. Leonard  
NASA Lewis Research Center  
Cleveland, Ohio

## Abstract

This paper discusses NASA Lewis Research Center's program for development of monolithic microwave integrated circuits (MMIC) for application in space communications. Emphasis will be on the improved performance in power amplifiers and low noise receivers which has been made possible by the development of new semiconductor materials and devices. Possible applications of high temperature superconductivity for space communications will also be presented.

## I. Background

Advanced satellite communications systems, with ever increasing data rates, multiple beams, higher frequencies, on-board processing, and complex interconnects, place an ever increasing demand on the spacecraft resources, most specifically the prime power and weight budgets. One solution to these requirements is the use of phased array antennas, which can provide multiple beams and electronically steerable beams without the complications required by mechanical steering. A practical system, however, will usually require the availability of components utilizing a high degree of monolithic integration (MMICs), inasmuch as discrete components and hybrid technology are prohibited by the volume and weight constraints of space missions.

Over the last ten years, NASA Lewis Research Center has undertaken a program aimed at demonstrating the feasibility of a variety of state-of-the-art MMIC modules with application in satellite communications systems. Primary goals of that work have been to increase the available power output from a MMIC module, to increase the efficiency of MMIC amplifiers, and to reduce the noise figure of MMIC receivers. Over that period, dramatic improvements in all of these parameters have been made possible by revolutionary advances in materials technology. Most of these have been enabled through the routine use of molecular beam epitaxy (MBE), which has made a variety of materials feasible. Most significant of these are lattice-matched and strained-lattice

(pseudomorphic) heterojunction structures. Combined with electron-beam lithography, which makes 0.1 micron features possible, frequencies and efficiencies are now possible which would have been unthinkable five years ago.

## II. Power Amplifiers

Over the last 5 to 7 years, new materials have been responsible for tremendous improvements in the power-added efficiency which can be achieved at either the device or circuit level. Typically, a conventional GaAs MESFET, the standard device 5 years ago, can achieve efficiencies near 20% at Ka-band, which in turn resulted in amplifier efficiencies of 10 to 15% over approximately the last five years. Since that time, however, structures such as the pseudomorphic HEMT, shown in Figure 1, have permitted record values of  $F_{max}$ , and subsequently, record values of gain and efficiency at frequencies up to near 100 GHz.

**PSEUDOMORPHIC HEMT STRUCTURE**

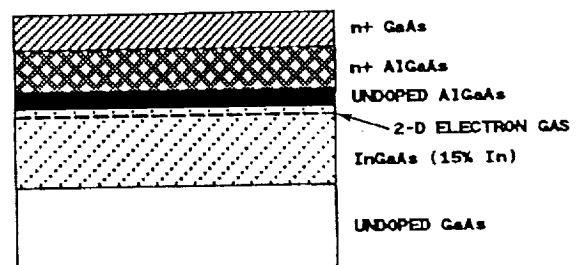


**Figure 1. Pseudomorphic HEMT Structure**

The pseudomorphic HEMT utilizes an active channel consisting of approximately 150 Angstroms of MBE-grown InGaAs, with approximately 15% indium. Using this percentage of indium results in a structure which is not lattice-matched to the GaAs substrate. However, the lower band gap of the InGaAs provides much improved charge confinement, significantly higher mobility, and higher saturation velocity. Combined with doped donor layers of AlGaAs, or even with doping within the channel, pseudomorphic HEMT devices have demonstrated a clear superiority to either conventional GaAs MESFETs or AlGaAs HEMT devices. This is illustrated by the results of development

contracts which NASA Lewis has sponsored at Texas Instruments and at Hughes Aircraft.

**Ka-Band Power Amplifiers**

Anticipating the possible conversion of NASA's deep space communications network to Ka-band, NASA Lewis commissioned Texas Instruments to develop a set of monolithic power amplifier chips at 32 GHz. This effort has established or equalled state-of-the-art performance in such devices. The characteristics of four of these chips are shown in Table 1.

| Stages | Gate widths (μm) | Output Power (mwatt) | Gain (dB) | Efficiency (%) | Frequency (GHz) |
|--------|------------------|----------------------|-----------|----------------|-----------------|
| 3      | 50-100-250       | 190                  | 23        | 30             | 31              |
| 3      | 100-300-800      | 390                  | 16        | 25             | 29              |
| 1      | 100              | 63                   | 6.5       | 40             | 31              |
| 1      | 800              | 710                  | 4.2       | 25             | 31              |

**Table I.** Performance Characteristics of Texas Instruments Monolithic Power Amplifiers.

The first two chips listed in Table 1 are 3-stage amplifiers, and represent a significant advance in the design of such circuits. Specifically, the design of interstage matching networks requires extremely accurate models for the devices being utilized at power levels well beyond the usual small signal approximations. The power output, efficiency, and gain represent an apparent record in performance of a multistage amplifier at this frequency. Details of the design of these amplifiers are reported elsewhere.<sup>1</sup>

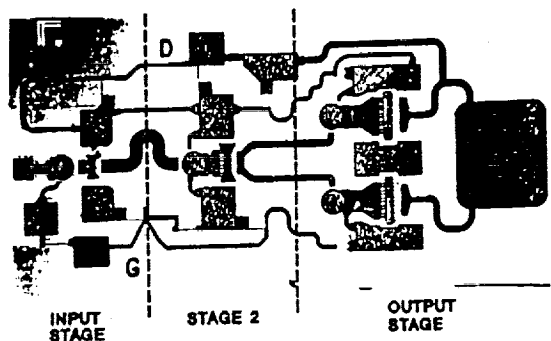


**Figure 2.** TI's Three Stage 32 GHz Monolithic Power Amplifier

The third and fourth chips listed in Table 1 are single stage pseudomorphic HEMT amplifiers. The 700 mW power output of the larger of these combined with its 25% efficiency represents a significant advancement in the state-of-the-art performance for such a module.

In a follow-on to this work, using a modified version of the pseudomorphic device and improved circuit designs, TI has accepted the performance goals given in Table 2. If achieved, these will again represent significant performance improvements for a 32 GHz multistage power amplifier.

| Power | Gain | Power-added efficiency |
|-------|------|------------------------|
| 250mW | 15dB | 50%                    |
| 1W    | 10dB | 35%                    |

**Table 2.** Performance Goals for Modified TI Amplifiers

**V-Band Power Amplifiers**

As NASA's science missions become more complex they require ever increasing capacity for data relay. To ensure that technology exists which can satisfy the requirements of anticipated intersatellite links, Lewis initiated a power amplifier development at 60 GHz at Hughes aircraft approximately 3 years ago. Again, the only device which appeared to have the potential for achieving the required gain, power and efficiency was the pseudomorphic HEMT. At the present time, the contract has not been completed. However, the contract goals, as well as Hughes' results to date for a pseudomorphic device, a single stage amplifier, and a 3-stage amplifier are shown in Table 3.

|            | GOAL  | PERFORMANCE |         |
|------------|-------|-------------|---------|
|            |       | ONE-stage   | 3-stage |
| POWER OUT  | 100mW | 112mW       | 100mW   |
| GAIN       | 15dB  | 6dB         | 17dB    |
| EFFICIENCY | 30%   | 26%         | -       |

**Table 3.** Goals and Performance for Hughes' 60 GHz Power Amplifier

### III. Low Noise Components

Materials developments similar to those reported in power amplifier applications have also taken place over the last ten years in low noise devices and circuits. These improvements are illustrated by the results which have been achieved first with AlGaAs/GaAs HEMTs, which produced device noise figures of 1.8 dB and amplifier noise figures of 3.2 dB at 60 GHz.<sup>2</sup> More recently, the use of InGaAs/InP HEMTs<sup>3,4,5,6</sup> became feasible, resulting in amplifier noise figures near 1.0 dB at 60 GHz. Such greatly reduced noise figures make low noise amplifiers a viable alternative to a mixer at frequencies up to nearly 100 GHz. In addition, a number of systems which could not afford the relatively small penalty imposed by monolithic circuit implementation, now become feasible.

#### W-Band Low Noise Amplifier and Mixer

The most recent work undertaken by NASA Lewis is the development of a 94 GHz monolithic low noise amplifier and a monolithic mixer. Although NASA has not identified a mission requiring a 94 GHz communications system at this time, the advantages in terms of reduced antenna size (or equivalently increased data rate or reduced RF power) should make it attractive if the technology were available.

The development, being carried out at TRW in Redondo Beach, will utilize lattice-matched InGaAs/InP technology, will include the design, fabrication and test of both hybrid and monolithic versions of low noise amplifiers and mixers at W-band. The performance goals for the required modules are shown in Table 4.

|                        |           |
|------------------------|-----------|
| Low Noise Amplifier    |           |
| RF Band:               | 90-98 GHz |
| Noise Figure           | 3 dB max  |
| Gain:                  | 18 dB min |
| W-Band Mixer           |           |
| Conversion Loss:       | 6 dB max  |
| LO Power:              | 5 dBm max |
| Noise Figure:          | 4 dB max  |
| Integrateable with LNA |           |

Table 4. Performance Goals for TRW's MMIC Receiver Modules

If successful, the work will result in a record noise performance for a monolithic amplifier at this frequency, and will demonstrate the feasibility of monolithic circuitry in InGaAs/InP, the clear choice for systems requiring the best possible noise performance. TRW's approach to the work is based on a lattice-matched InGaAs/InP device, which has demonstrated a noise figure of less than 2 dB. Such devices, incorporated into circuit designs which eliminate many sources of parasitics by utilizing coplanar waveguide as a transmission media, appear to provide an excellent chance of achieving the program goals.

The W-band mixer design, utilizes the same InGaAs/InP HEMT as does the LNA. This approach is expected not only to achieve the noise figure goals, but also to minimize conversion loss by incorporating gain within the mixer, to require reduced LO power, and to be integrateable with the low noise amplifier to allow a monolithic receiver.

### IV. High Temperature Superconductivity

Another technology which exhibits long term potential for significantly improving the performance of space communications systems is superconductivity. Since the discovery in 1987 of materials which become superconducting at 90K (and perhaps more significantly for space applications 120K) a number of superconducting microwave circuits have been explored by NASA Lewis. One of the most promising of these appear to be ultra-low noise receivers, such as might be required on an earth-orbiting relay satellite communicating with a power-limited planetary mission.

#### Low Noise Applications of Superconductivity

NASA Lewis, in collaboration with NASA's Jet Propulsion Laboratory is working on the design and fabrication of a low noise receiver module which would be a candidate for testing in NRL's High Temperature Superconducting Space Experiment (HTSSE). A block diagram of the X-band system is shown in Figure 3. The system will utilize "conventional" semiconductor devices (discrete or MMIC) as active elements in the low noise amplifier, mixer, and local oscillator, with superconducting interconnects used for passive portions of the circuitry. For example, the input filters and matching circuits for the LNA will employ HTS materials, thereby reducing

significantly the losses at the front end of the system, since at X-band, surface resistance of HTS transmission lines is only 1/50 that of gold. Similarly, the local oscillator will use FETs as active devices, but will employ a superconducting ring resonator as a stabilizing element. Such a circuit will produce a lower "Q" than a dielectric resonator, however, it should be approximately 20 times higher than any other planar implementation, and therefore advantageous for systems where size and weight are severe constraints.

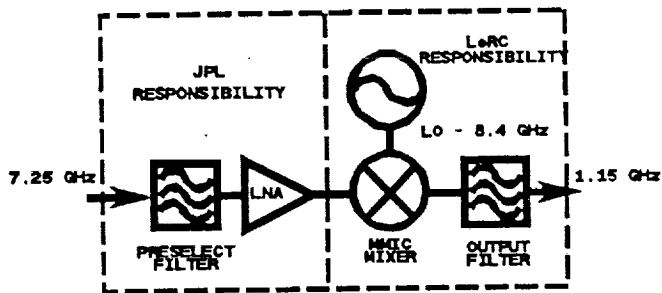


Figure 3. Schematic of HTSSE Experiment

Applications of HTS to Array Antennas

Superconductors could also offer significant advantages if used as interconnections in a large phased array antenna. In this case reducing the feed network losses effectively increases the gain of the antenna. This concept has been quantified by Dinger7, who showed that for a 100 cm<sup>2</sup> array, at 35 GHz, the effective gain would be increased by 3 dB by using superconducting interconnects. At the present time, work is ongoing to demonstrate this advantage experimentally. As an initial demonstration, a 2x2 patch array with microstrip feed, based on a design supplied by Ball Aerospace, has been fabricated and tested. A diagram of the antenna is shown in Figure 4.

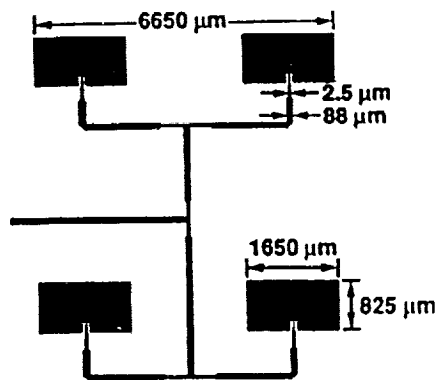


Figure 4. Layout of a 2x2 32 GHz Superconducting Array

Preliminary results of radiation pattern measurements on this antenna, compared with an identical gold antenna are shown in Figure 5.

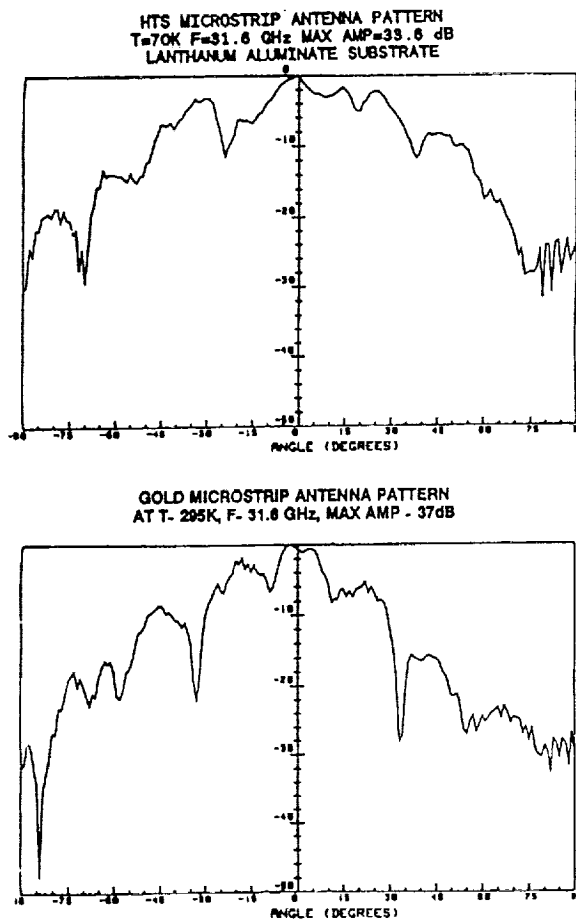


Figure 5. Radiation Patterns from a 2x2 Superconducting Array

A second array, similar in design to the 2x2 has been successfully fabricated by Ball, has passed preliminary RF testing, and has been delivered to NASA Lewis for measurement of radiation patterns and gain. Work is ongoing, in cooperation with Ball Aerospace, under NASA contract, to refine the basic antenna design by utilizing other feed concepts, such as capacitive coupling. In addition, Ball is investigating architectures which will minimize heat loads associated with a large array.

Superconducting Antenna Shuttle/Airborne Experiment

Figure 6 shows schematically an experiment which would use a superconducting, steerable array antenna as part of a ground-to-ACTS-to-shuttle-to-ground communications experiment. The uplink to ACTS would be at 30 GHz. The ACTS to shuttle link would be at 20 GHz, with the shuttle tracking the ACTS spacecraft electronically in one plane and mechanically in the other.

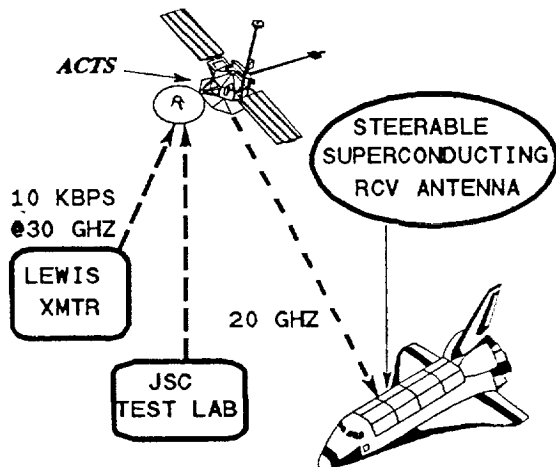


Figure 6. Superconducting Space Shuttle Experiment

A schematic diagram of the antenna portion of the proposed system is shown in Figure 7.

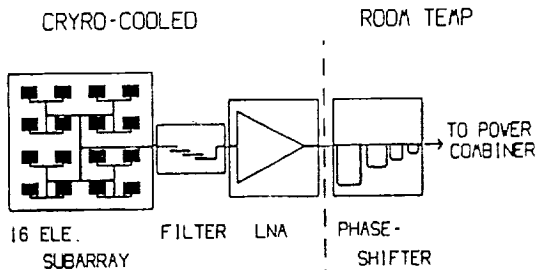


Figure 7. Schematic Diagram of Superconducting Array Antenna

As the diagram illustrates, the antenna would consist of a 1x9 array of 4x4 subarrays. Such a system would be large enough to demonstrate the advantages of superconductivity in the interconnects but small enough to realistically consider fabricating at this time. In addition, the low noise receivers associated with each antenna element would be cooled, thereby improving noise performance. The remainder of the system (a phase shifter for each 16-element subarray, a power combiner, and the IF amplifiers) would operate at ambient temperature.

V. References

1. P. Saunier, H.Q. Tserng, and Y.C. Kao, "A High Efficiency Ka-band Monolithic Pseudomorphic HEMT Amplifier", Monolithic Microwave Integrated Circuits for Sensors, Radar, and Communications Systems, Proc. SPIE1475, pp. 86-90, 1991.
2. K.H.G. Duh, P.C. Chao, P.M. Smith, L.F. Lester, B.R. Lee, J.M. Ballingall, and Y.M. Kao. "Millimeter Wave Low Noise Amplifiers", IEEE MTT-S International Microwave Symposium Digest, pp. 923-926, (1988).
3. S. Vaughn, K. White, U.K. Mishra, M.J. Delaney, P. Greiling, and S. Rosenbaum, "High Performance V-Band Low Noise Amplifiers", IEEE MTT-S International Microwave Symposium Digest, pp. 801-804 (1989).
4. K.H.G. Duh, P.C. Chao, M.Y. Kao, P.M. Smith, J.M. Ballingall, and A.A. Jabra, "High Performance InP-based Hemt Millimeter-wave Low Noise Amplifiers", IEEE MTT-S International Microwave Symposium Digest, pp. 805-808, (1989).
5. D.C. Streit, K.L. Tan, R.M. Dia, A.C. Han, P.H. Liu, H.C. Yen, and P.D. Chow, "High Performance W-band InAlAs-InGaAs-InP HEMTs", Electronics Letters, vol. 27, no. 13, June 1991.
6. P.D. Chow, K. Tan, D. Streit, D. Garske, P. Liu, and H.C. Han, "Ultra Low Noise High Gain W-Band InP-based HEMT Downconverter", IEEE MTT-S International Symposium Digest, pp. 1041-1044, (1991).
7. R.J. Dinger, "Some Potential Antenna Applications of High Temperature Superconductors", Journal of Superconductivity, vol. 3, No. 3, pp. 287-296, (1990).



## LOW NOISE InP-BASED MMIC RECEIVER FOR W-BAND

Regis F. Leonard  
NASA Lewis Research Center  
Cleveland, Ohio

### Abstract

This paper will describe a program, currently being carried out by TRW under LeRC sponsorship, to develop a monolithic W-band low noise amplifier, a critical element in any W-band communications, sensors, or radar application. Goals of the program include a fully monolithic low noise amplifier with a noise figure of  $<3.5$  dB, and a monolithic mixer suitable for integration with the LNA. The contractor has chosen lattice-matched InGaAs/InP as the baseline device for the program. The paper also briefly describes some potential applications of W-band technology, including communications, where the higher frequency would provide greater bandwidth and would make possible significant reductions in antenna size, or, for fixed antenna size, reductions in transmitter power.

### Potential W-Band Applications

A variety of potential space applications of W-band technology have been suggested. Most of these take advantage of the shorter wavelength of millimeter wave beamwidths, greater spatial resolution, and greater immunity to interference. At the same time, the higher frequency provides greater bandwidth and therefore greater information-carrying capability. In addition, there occurs a relative window in atmospheric absorption near 90 GHz, which gives W-band technologies another unique advantage.

Specific applications which NASA has examined include passive imaging radiometry and active radar sensors for earth observations, such as a geostationary rain radar system. Both of these would take advantage of increased spatial resolution of W-band as well as the reduced size of components and the possibility of monolithic implementation, which would make electronically scanned systems feasible.

Another candidate mission for the use of W-band radar would be a debris-tracking radar system for space station, where the 3-mm wavelength would permit the system to meet the requirement that it must detect and track particles as small as approximately 1 cm.

Finally, W-band technology, when applied to deep space communications, again offers the advantages of narrow beamwidths and large bandwidth. As with radar applications, these may be utilized either for the reduction of transmitter power, or for the reduction of antenna size, or an improvement in signal quality, depending on specific system requirements. In either case, however, some technology development is required before W-band can be considered a viable candidate for use in a space mission. The most critical elements of this technology are low noise receivers, preferably in a monolithic implementation, and power sources based on both solid state and vacuum electronics. The present paper describes developments in low noise/monolithic technology.

### State-of-the Art of Millimeter Wave Low Noise Technology

In the last four years advances in materials and device technology have had a revolutionary effect on the noise performance of both microwave and millimeter wave systems. As recently as 1986 Sholley and Nichols reported a noise figure of 4.6 dB for a one stage, 56 GHz amplifier using a 0.25 micron gate and AlGaAs/GaAs HEMT devices. At the time this represented some of the highest frequencies for which the HEMT technology had been demonstrated, and was considered excellent noise performance.

By 1988, Duh et al. reported 0.25 micron AlGaAs/GaAs HEMT devices with noise figures of 1.8 dB at 60 GHz.<sup>2</sup> Using these devices in a two stage V-band amplifier, they achieved 3.2 dB

noise figure and 12.7 dB gain at 61 GHz.

The current state of the art, however, appears to be based on the use of devices which utilize an active channel of InGaAs lattice-matched (53% indium) to an InP substrate. In 1989 Vaughn et.al. of Hughes and Duh et.al. of GE reported record performance for low noise amplifiers using InAlAs/InGaAs/InP devices with a gate length of approximately 0.25 microns.<sup>3,4</sup>

At 60 GHz the Hughes group reported single stage amplifiers with noise figures of typically 1.5 dB, and some as low as 0.8 dB without corrections for losses. GE fabricated devices with noise figures of 1.2 dB and 15 dB of small signal gain, and a three-stage 60 GHz amplifier with a noise figure of 3.0 dB and 22 dB gain. The Hughes three-stage amplifier exhibited a 2.6 dB noise figure and 19.5 dB gain. At 90 GHz, using this same technology, GE reported a 2.1 dB noise figure for the deembedded HEMT device, and a 4.5 dB noise figure for a two-stage amplifier. Most recently, TRW reported an InAlAs/InGaAs/InP device with a gate length of 0.15 microns with a minimum noise figure of 1.7 dB and 7 dB gain at 83 GHz.<sup>5</sup>

Performance Goals of the Present Effort

In view of these rapid advances in low noise technology, a contract was awarded to TRW, Redondo Beach, CA approximately 6 months ago for the development of two monolithic chips (a low noise amplifier and a mixer) as components of a low noise receiver. As intermediate steps in the program, the contract calls for the fabrication and test of critical submodules, as well as a hybrid version of each monolithic chip. The performance goals for each of these items are given in Table 1.

|              |                                    |
|--------------|------------------------------------|
| <u>LNA</u>   |                                    |
| RF FREQUENCY | 90 TO 98 GHz                       |
| GAIN         | 18 dB MIN                          |
| NOISE FIGURE | <3.5 dB (MMIC)<br><3.0 dB (HYBRID) |
| <u>MIXER</u> |                                    |
| RF FREQUENCY | 90 TO 98 GHz                       |
| LO FREQUENCY | 88 GHz                             |
| LO POWER     | <4 dBm                             |
| NOISE FIGURE | <4 dB DOUBLE-SIDE BAND             |

Table 1. Performance Goals for 90 GHz Receiver Modules

Deliverables from the contract will include three hybrid LNAs, 20 MMIC LNAs, and 20 MMIC mixers, as well as three sets of critical components and submodules, and one set of test fixtures.

Technical Approach of the Present Effort

Device Selection

TRW has studied three device types to determine the most appropriate approach to the present contract. These were the GaAs/AlGaAs HEMT, the pseudomorphic (InGaAs/GaAs) HEMT, and the lattice-matched InGaAs/InP HEMT. A comparison of the characteristics of the three devices is shown in Table 2.

| Parameter  | Device Technology                       |   |   |
|--|---|---|---|
|  | GaAs HEMT                               | Pseudomorphic InGaAs-HEMT (GaAs-Based)  | Lattice-Matched InGaAs HEMT (InP-Based) |
| Device NF/gain at 64 GHz                                 | Projected 3.0 dB/5.0 dB                 | TRW (1989) 2.1 dB/4.3 dB                | TRW (1990) 1.7 dB/7.7 dB                |
| Process maturity   | Excellent                               | Excellent                               | Good                                    |
| Reliability  | Excellent<br>MTTF > 10 <sup>7</sup> hrs | Excellent<br>MTTF > 10 <sup>7</sup> hrs | TBD                                     |
| 2-dcg density (cm <sup>-2</sup> )                        | 1.3 x 10 <sup>11</sup>                  | 2.7 x 10 <sup>12</sup>                  | 3.5 x 10 <sup>12</sup>                  |
| Mobility<br>μ <sub>n</sub> (cm <sup>2</sup> /V-sec) 77K  | 30,000                                  | >35,000                                 | >35,000                                 |
| Mobility<br>μ <sub>p</sub> (cm <sup>2</sup> /V-sec) 300K | >8000                                   | >6700                                   | >10,000                                 |
| Saturation velocity (cm/s)                               | -1.5 x 10 <sup>7</sup>                  | -2.0 x 10 <sup>7</sup>                  | -2.7 x 10 <sup>7</sup>                  |

Table 2. Comparison of HEMT Devices

Based on these data, the InP-based device, reported in reference 5, appeared to be the only approach capable of satisfying the contract

requirements. The basic structure of the TRW device is shown in Figure 1.

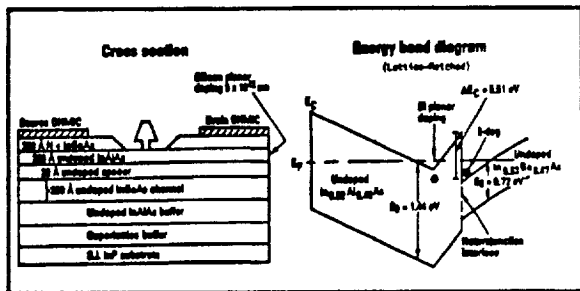


Figure 1. Structure of InGaAs/InP HEMT

Further performance improvement should result from shortening the gate length to 0.1 micron, which is well within the capability of state-of-the-art E-beam lithography. Therefore, in the present program, a 0.1x40 micron InP HEMT was selected as the baseline device for both the low noise amplifier module and for the mixer module.

Circuit Implementation

Following a study of the relative advantages of microstrip, coplanar and grounded coplanar transmission lines, grounded coplanar waveguide has been chosen as the baseline for the monolithic versions of both the LNA and the mixer. A comparison of the characteristics which led to this decision is shown in Table 3.

| ASPECT  | MICROSTRIP LINE                | COPLANAR WAVEGUIDE (CPW) | GROUNDING COPLANAR WAVEGUIDE (GCPW) |
|---|--------------------------------|--------------------------|-------------------------------------|
| SUBSTRATE THICKNESS   | 4 TO 8 MILS                    | 4 TO 35 MILS             | 4 TO 8 MILS                         |
| CHARACTERISTIC IMPEDANCE                                    | 25 TO 85 Ω                     | 30 TO 140 Ω              | 30 TO 140 Ω                         |
| EFFECTIVE DIELECTRIC CONSTANT, $\epsilon_{eff} = 12.8$      | -7                             | -8                       | -8                                  |
| SPURIOUS MODES  | LOW                            | LOW                      | MEDIUM                              |
| DISPERSION  | SMALL                          | MEDIUM                   | MEDIUM                              |
| RADIATION   | LOW                            | MEDIUM                   | MEDIUM                              |
| INTEGRATION LEVEL   | HIGH                           | HIGH                     | HIGH                                |
| ADJACENT LINE-COUPLED EFFECT                                | HIGHER                         | LOWER                    | LOW                                 |
| PROCESSING  | SMALL VIA-HOLES REQUIRED       | NO VIA-HOLES REQUIRED    | VIA-HOLES REQUIRED                  |
| SERIES COMPONENTS   | EASY                           | EASY                     | EASY                                |
| PARALLEL COMPONENTS   | DIFFICULT DUE TO USE VIA HOLES | EASY                     | EASY                                |
| DESIGN INFORMATION  | EXTENSIVE                      | FAMILY WELL              | FAMILY WELL                         |
| - DISCONTINUITY STRUCTURES, <math>\pm 0.5 \text{ dB}</math> | FAMILY WELL                    | SOME                     | SOME                                |
| - DISCONTINUITY STRUCTURES, <math>\pm 0.5 \text{ dB}</math> | MAJORAL                        | SOME                     | SOME                                |

Table 3. Comparison of Microstrip, CPW, and Grounded CPW Media

The most important considerations were the ease of integrating and grounding active components, the reduced sensitivity to substrate thickness, smaller parasitics, and ease of transition to slotline or notch antenna elements which seem most appropriate at W-band frequencies. In addition, the absence of a requirement for small dry-etched via holes facilitates the transition from the more mature pseudomorphic HEMT MMIC processes to the developmental InP.

Monolithic Low Noise Amplifier

Preliminary designs have been carried out for the monolithic low noise amplifier. It is anticipated that the chip will use three stages of amplification. The simulated performance of this design, based on a 0.1x40 micron InP HEMT device is shown in Figure 2.

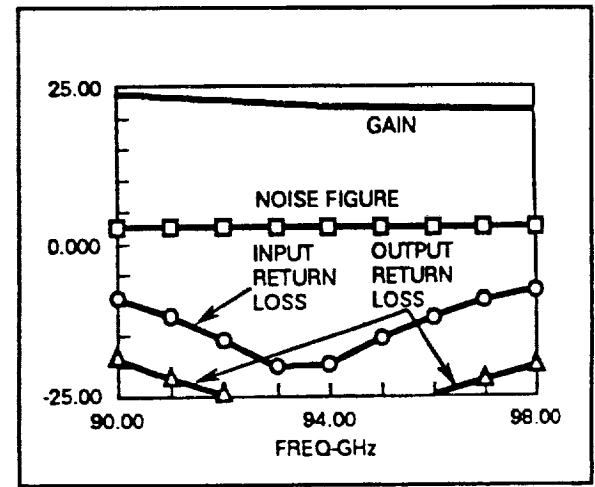


Figure 2. Simulated Noise and Gain of a Three-Stage W-Band LNA

As indicated, the gain is expected to be greater than 22 dB across the required band, while the noise figure should be less than 2.5 dB, both of which exceed performance goals by a sizeable margin.

Monolithic Mixer

Preliminary designs for the monolithic mixer module are based on a single-balanced active HEMT mixer, which would use the same 0.1x40 micron InGaAs/InP HEMT device which was chosen for the LNA. This

approach has the advantages of minimizing conversion loss (or even producing conversion gain), requiring a minimum of LO power (<4dBm), and being compatible with LNA technology should another level of monolithic integration be required. The measured performance of such a mixer in hybrid implementation with a 0.15 micron InP device was reported by Chow, et.al. of TRW.<sup>6</sup> In that work, with an 85 GHz, 3 dBm local oscillator, they observed a conversion gain of 2.4 dB and a single-sideband noise figure of 7.3 dB.

#### Program Status

At the present time TRW has been under contract for approximately six months (of a 36 month effort). In addition to the preliminary amplifier and mixer architectures which have been selected, some critical components and submodules have been tentatively identified. These include the low noise devices for which accurate models must be derived before detailed amplifier and mixer designs can be carried out, and a number of passive elements, such as MIM capacitors, nichrome resistors, coupled line sections, open stubs, Lange couplers, tee-junctions, crosses, and bends which have been used at lower frequencies, but require refined models at W-band. Submodules to be studied include bias networks, the input matching network, and single stage amplifier chips. For the monolithic mixer, critical components include a rat race coupler, matching networks for the mixing device, and the IF filter. At the present time detailed design and fabrication of these critical components and submodules is about to begin.

#### Program Challenges

Although considerable work has been carried out on InP devices, as well as on the design of low noise amplifiers, even to W-band frequencies, major challenges must still be met if the goals of the program are to be met. These include the development of an InP MMIC process. Although this activity will build on previous experience in pseudomorphic HEMT fabrication, the demonstration of a fully monolithic

circuit in InGaAs/InP will represent a significant advance.

The use of coplanar waveguide as a transmission medium at W-band requires the development of accurate models of such structures. This is made doubly challenging by the frequencies involved and by the paucity of work in CPW at any frequency. This difficulty will be overcome by using some of the newly developed electromagnetic simulations in conjunction with experimental studies of selected discontinuities.

Test procedures, particularly extremely low noise measurements at 90 GHz present many unique and difficult problems. Again, the frequencies involved preclude the use of commercially available "off-the-shelf" test equipment. One of the most significant needs is for on-wafer test equipment, which will significantly enhance the accuracy of the results, inasmuch as de-embedding procedures no longer need to take into account uncertainties such as bond wire characteristics. On-wafer probing of course also reduces the time and money spent in RF testing, as low quality chips can be screened and eliminated early.

#### References

- 1.M. Sholley and A. Nichols, "60 and 70 GHz HEMT Amplifiers", IEEE MTT-S International Microwave Symposium Digest, p.463 (1986).
- 2.K. H. G. Duh, P. C. Chao, P. M. Smith, L. F. Lester, B. R. Lee, J. M. Ballingall, and M. Y. Kao. "Millimeter Wave Low Noise Amplifiers", IEEE MTT-S International Microwave Symposium Digest, pp. 923-926, (1988).
3. S. Vaughn, K. White, U. K. Mishra, M. J. Delaney, P. Greiling, and S. Rosenbaum, "High Performance V-Band Low Noise Amplifiers", IEEE MTT-S International Microwave Symposium Digest, pp. 801-804, (1989).
4. K. H. G. Duh, P. C. Chao, M. Y. Kao, P. M. Smith, J. M. Ballingall, and A. A. Jabra, "High Performance InP-based Hemt Millimeter-wave Low Noise Amplifiers", IEEE MTT-S International Microwave Symposium

Digest, pp. 805-808, (1989).

5. D. C. Streit, K. L. Tan, R. M. Dia, A. C. Han, P. H. Liu, H. C. Yen, and P. D. Chow, "High Performance W-Band InAlAs-InGaAs-InP HEMTs", *Electronics Letters*, vol. 27, no. 13, June 1991.

6. P. D. Chow, K. Tan, D. Streit, D. Garske, P. Liu, and H. C. Han, "Ultra Low Noise High Gain W-Band InP-Based HEMT Downconverter", *IEEE MTT-S International Microwave Symposium Digest*, pp. 1041-1044, (1991).



V-BAND PSEUDOMORPHIC HEMT MMIC PHASED ARRAY COMPONENTS FOR  
SPACE COMMUNICATIONS<sup>1</sup>

G. L. Lan, C. K. Pao, C. S. Wu and M. Hu

Microelectronic Circuits Division  
Hughes Aircraft Company  
Torrance, CA 90509

Alan N. Downey

NASA Lewis Research Center  
Cleveland, OH 44135ABSTRACT

Recent advances in pseudomorphic HEMT MMIC (PMHEMT/MMIC) technology have made it the preferred candidate for high performance millimeter-wave components for phased array applications. This paper will describe the development of V-band PMHEMT/MMIC components including power amplifiers and phase shifters.

For the single-stage MMIC power amplifier employing a 200  $\mu\text{m}$  PMHEMT, we achieved 151.4 mW output power (757.0 mW/mm) with 1.8 dB associated gain and 26.4 % power-added efficiency at 60 GHz. A two-stage MMIC amplifier utilizing the same devices demonstrated small-signal gain as high as 15 dB at 58 GHz. And, for the phase shifter, a four-bit phase shifter with less than 8 dB insertion loss from 61 to 63 GHz has been measured.

1. INTRODUCTION

The need to develop V-band transmitter/receiver (T/R) components for use in radar, communication, and surveillance systems is rapidly increasing. At the same time, the approach employed must reduce the cost, size and weight of the system; therefore, monolithic techniques are essential.

Until recently, the development of millimeter-wave (MMW) monolithic T/R components has been limited to operation below 30 GHz primarily due to the low cutoff frequency of MESFETs, which have been the workhorse for MMICs. The increased use of MMW T/Rs has prompted extensive research in the field of high electron mobility transistors (HEMTs). After they were first successfully developed in 1980<sup>1</sup>, HEMTs have demonstrated their superior gain and noise figure performance over MESFETs because of their higher electron mobility and

---

<sup>1</sup> This work supported by the NASA Lewis Research Center, under Contract Number NAS3-25088.

velocity. The pseudomorphic HEMT, first demonstrated at MMW frequency in 1986<sup>2</sup>, overcomes many of the limitations of the conventional HEMTs, allowing significantly improved power performance and made the development of low cost, small size, light weight, and high performance MMW monolithic T/R components possible.

In this paper, we describe the development of state-of-the-art V-band monolithic components using pseudomorphic HEMT technology. These include monolithic single and two-stage power amplifiers, and four-bit monolithic phase shifters.

## 2. MONOLITHIC V-BAND POWER AMPLIFIERS

Advances in pseudomorphic HEMT technology have led to the recent progress in the development of MMW monolithic power amplifiers. The performance of MMW power amplifiers is primarily determined by three factors: (a) device and material properties, (b) device topology, and (c) matching circuits. High drain-gate breakdown voltage, large channel current density and high transconductances are the necessary device properties for high power amplification. Device topology determines the cutoff frequency, source-drain current, device impedance level, and parasitic losses. Proper gate length, gate width, and source-drain spacing are essential to high performance MMW HEMT amplifiers. The matching network determines gain, bandwidth, gain flatness, maximum output power and efficiency of the amplifier.

Figure 1 shows the photograph for a single-stage MMIC amplifier employing a 200  $\mu\text{m}$  PMHEMT. The amplifier chip was mounted on a V-band test fixture for power test. The fixture utilized E-plane probe transitions to couple the RF power from microstrip lines to waveguides. Figure 2 shows the power performance for the amplifier. We achieved 130 mW output power (650 mW/mm), 3.1 dB gain, 30.6 % power-added efficiency; 141.3 mW output power (706.5 mW/mm), 2.5 dB gain, 30.6 % power-added efficiency and 151.4 mW output power (757 mW/mm), 1.8 dB gain, 26.4 % power-added efficiency at 60 GHz. The same amplifier when biased for power achieved 182 mW output power (910 mW/mm). This result, to our knowledge, set the state-of-the-art for V-band MMIC amplifiers.

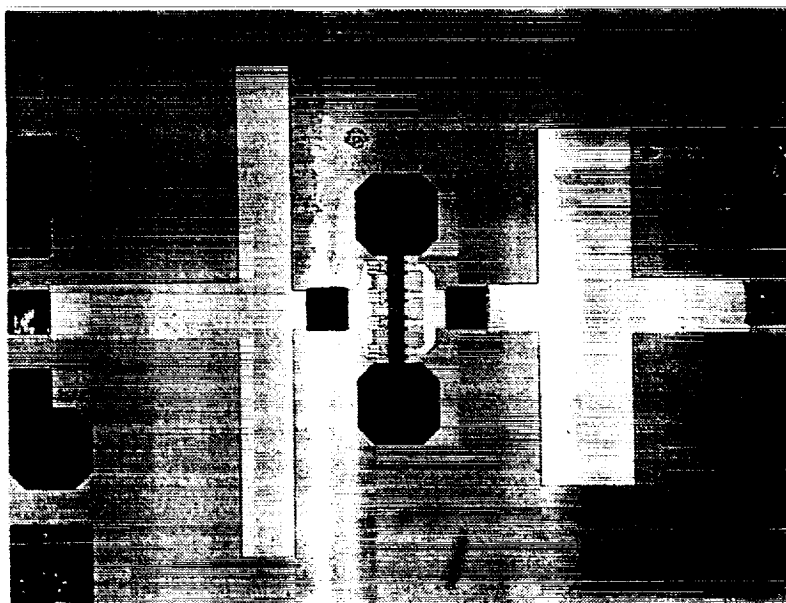


Figure 1 V-band Single-stage MMIC Power Amplifier.

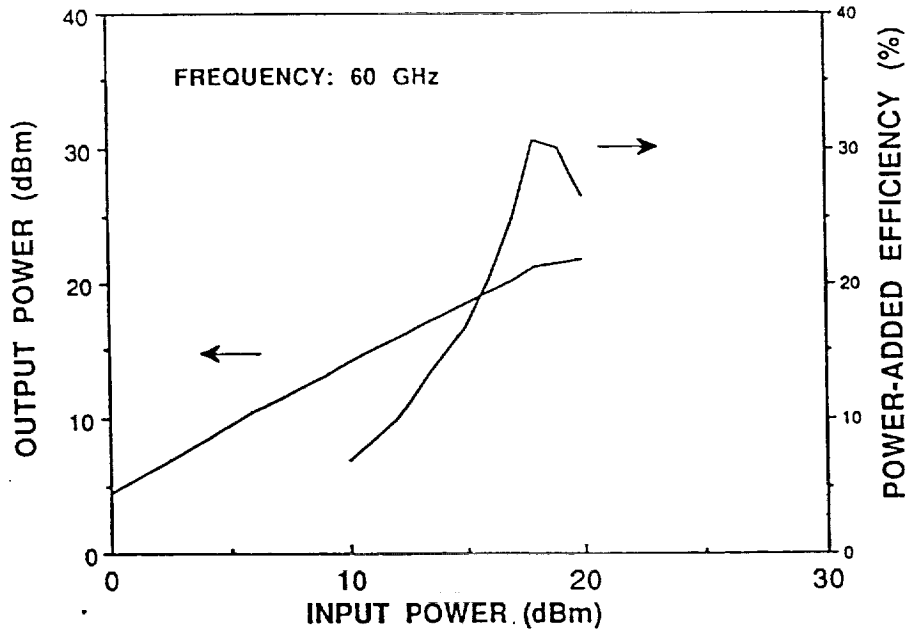


Figure 2 Power Performance for a V-band Single-Stage MMIC Amplifier.

After successfully demonstrating single-stage amplifier performance, we designed and fabricated a two-stage MMIC amplifier by cascading two single-stage amplifiers, as shown in

Figure 3. The amplifier's small-signal performance was measured on-wafer using an Automated Network Analyzer for the frequency range from 30 to 60 GHz. Figure 4 shows the small-signal performance for the two-stage power amplifier. A small-signal gain of more than 10 dB from 52 to 60 GHz with a peak gain of 15 dB at 58 GHz was achieved. Under higher power operation, we achieved 80 mW output power, 20.4 % power-added efficiency and 12 dB gain at 58 GHz.

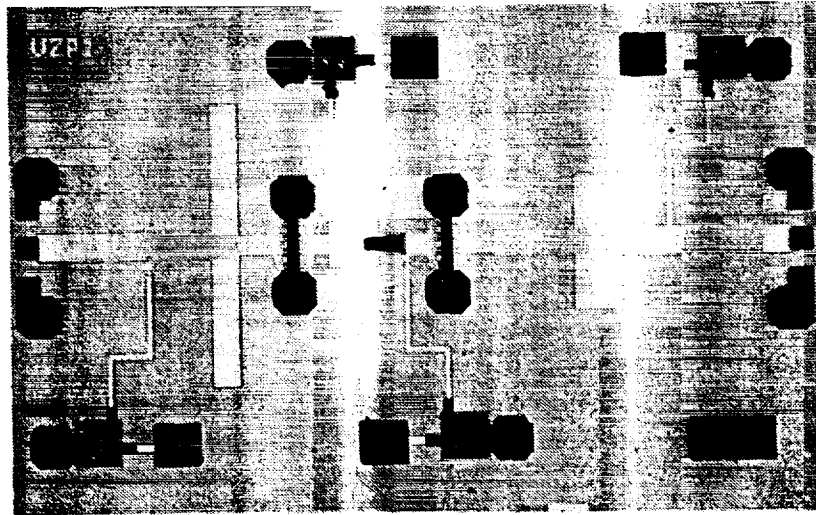


Figure 3 V-band Two-Stage MMIC Power Amplifier.

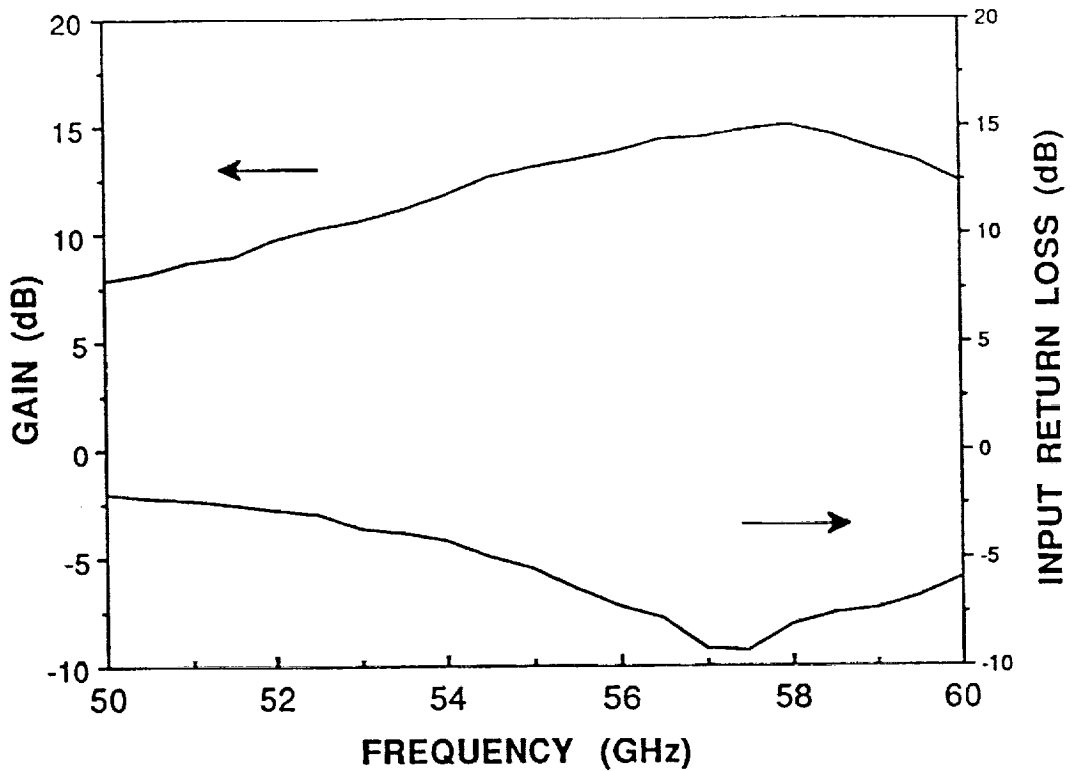


Figure 4 Small-Signal Performance for a V-band Two-Stage MMIC Amplifier.

### 3. MONOLITHIC PSEUDOMORPHIC HEMT PHASE SHIFTERS

With the development of a PMHEMT power amplifier, it is desirable to have PMHEMT phase shifters for MMIC process compatibility. Figure 5 shows the photograph of a PMHEMT MMIC four-bit phase shifter with a dimension of 75 x 260 mils. The process for this phase shifter is fully compatible with the PMHEMT power amplifier and other T/R MMIC components which allows future integration of the complete T/R module.

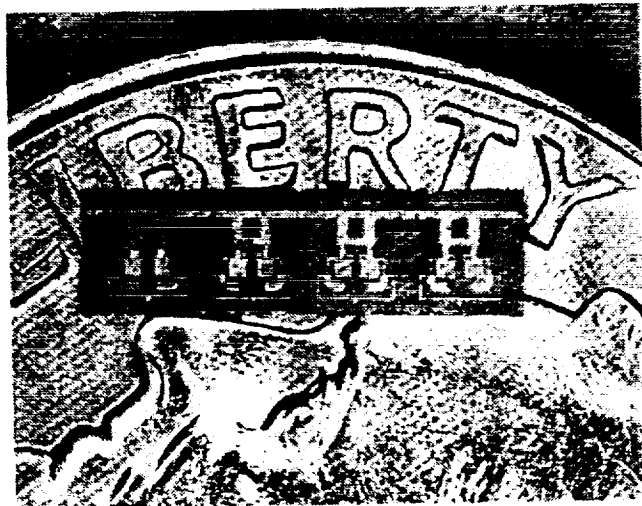


Figure 5 V-band Four-Bit Monolithic Pseudomorphic HEMT Phase Shifter.

The MMIC four-bit phase shifter consists of four single

branchline phase shifters: three with 200  $\mu\text{m}$  gate periphery PMHEMTs and one with 500  $\mu\text{m}$  gate periphery PMHEMTs. For each branchline phase shifter, the PMHEMTs are connected from the two output ports of the coupler to via hole grounds. The input signals are reflected at the device drain ports and recombined at the isolation port of the coupler. Phase shifts are achieved by controlling the gate bias of the device to vary the device channel impedance. We have achieved a 0 to 360 degree phase shift in 22.5 degree steps with less than 8 dB insertion loss from 61 to 63 GHz. The performance characteristics of the phase shifter is shown in Figure 6.

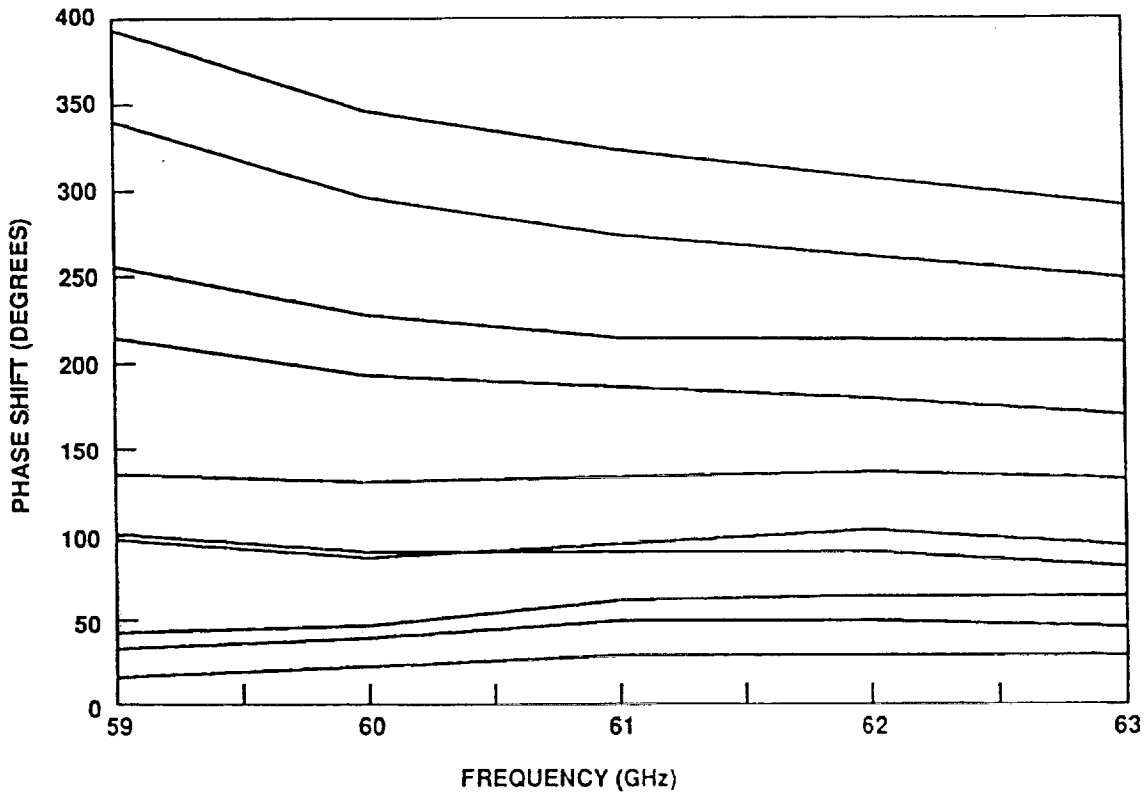


Figure 6 Phase Shift Performance for a V-Band Monolithic Four-bit Pseudomorphic HEMT Phase Shifter.

#### 4. CONCLUSION

We have developed state-of-the-art V-band monolithic components using PMHEMT technology. These components are critical to future space communications systems which require high performance, small size, light weight, and low cost modules.

## 5. REFERENCES

1. T. Mimura, S. Hiyamizu, T. Fujii, and K. Nanbu, "A New Field Effect Transistor with Selectively Doped GaAs n-Al(x)Ga(1-x)As Hetrostructures," Jpn. J. Appl. Phys., Vol. 19, pp. L225-L227, 1980.
2. T. Henderson, M. Aksun, C. Peng, H. Morkoc, P. C. Chao, P. M. Smith, K. H. G. Duh and L. F. Lester, "Microwave Performance of a Quarter-Micrometer Gate Low-Noise Pseudomorphic InGaAs/AlGaAs MODFET," IEEE Electron Device Letters, Vol. EDL-7, pp 645-661, 1986.

PLANAR DIELECTRIC RESONATOR STABILIZED HEMT OSCILLATOR  
 INTEGRATED WITH CPW/APERTURE COUPLED PATCH ANTENNA

Rainee N. Simons and Richard Q. Lee

National Aeronautics and Space Administration  
 Lewis Research Center  
 Cleveland, Ohio 44135

Abstract

A new design of an active antenna with a dielectric resonator stabilized HEMT oscillator (DRO) and an aperture-coupled patch antenna is reported. The circuit is fabricated using coplanar waveguide (CPW) with the oscillator and the antenna on opposite sides of the substrate. The active antenna was demonstrated at 7.6 GHz; however, the design can be scaled to higher frequencies. Excellent oscillator characteristics and radiation pattern have been obtained.

I. Introduction

As the frequency of operation of Earth observation systems (EOS) shifts into the millimeter wave and submillimeter wave regions of the spectrum, there is a need to develop efficient power combining techniques which can eliminate circuit losses, minimize expensive machining of mounts and housing for diodes, reduce thermal problems, provide graceful degradation and combine large number of active devices. Conventional low frequency power combining techniques are unable to meet the above requirements, and hence quasi-optical or spatial power combining have to be employed. In the past, a quasi-optical integrated antenna and receiver front end was demonstrated using MESFET oscillator coupled to a slotline-coplanar waveguide antenna.<sup>1</sup> A wideband tunable active antenna and power combiner was also demonstrated using a Gunn diode mounted in a slotline-coplanar waveguide resonator.<sup>2</sup>

In this paper, we demonstrate a new design of an active antenna module with a dielectric resonator stabilized HEMT oscillator (DRO) which is aperture-coupled to a patch. Several of these modular antennas can be combined to form a spatial power combiner. The circuit is fabricated using coplanar waveguide (CPW) with the oscillator and the patch antenna on opposite sides of a two-layer dielectric substrate. By fabricating the antenna and the oscillator on two substrates of different permittivity and thickness, both of these components can be independently optimized for best performance.

II. Design Description and Fabrication

Oscillator

Figure 1 shows the schematic of a DRO with series feedback. In this circuit  $\Gamma_g$  and  $\Gamma_r$  are the reflection coefficient looking into the gate terminal of the HEMT and the input terminal of

the transmission line coupled to the dielectric resonator respectively.  $\Gamma_g$  is written as<sup>3</sup>

$$\Gamma_g = S_{11} + S_{12}S_{21}\Gamma_L \times (1 - S_{22}\Gamma_L)^{-1}. \quad (1)$$

Where  $S_{11}$ ,  $S_{12}$ ,  $S_{21}$ , and  $S_{22}$  are the scattering parameters of the HEMT with a transmission line of length  $d_s$  connected in series with the source to provide feedback, and  $\Gamma_L$  is the reflection coefficient of the load connected to the drain.  $\Gamma_r$  is written as

$$\Gamma_r = \Gamma_c \exp\left(-j \frac{2\pi d_k}{\lambda_g}\right). \quad (2)$$

Where  $\Gamma_c$  is the reflection coefficient at the reference plane of the resonator which is at a distance  $d_k$  from the gate.  $\Gamma_c$  takes into account the coupling coefficient  $\beta$  and the termination  $Z_0$ . The condition for steady state oscillation to occur in the circuit can be written as<sup>3</sup>

$$\Gamma_g \Gamma_r = 1. \quad (3)$$

To fabricate the oscillator, the length  $d_s$  which provides the series feedback is adjusted so that the HEMT is unstable, that is,  $|\Gamma_g|$  should be greater than unity. The location  $d_k$  of the dielectric resonator with respect to the gate is adjusted so as to satisfy Eq. (3). The CPW circuit layout for the oscillator part of the active antenna is shown in Fig. 2. The circuit is fabricated on 0.635 mm thick RT/Duroid 6010.5. The active device is a low noise HEMT (Model S8902) manufactured by Toshiba. The dielectric resonator (Part no. TC-8500-x-001) is manufactured by Trans-Tech, Inc.

Antenna

Figure 3 illustrates the CPW aperture-coupled patch antenna part of the active antenna. The coupling takes place through an aperture in the common ground plane separating the CPW and the patch. The aperture width  $W_2$  of 0.254 mm is chosen for ease of fabrication. A good initial guess for the aperture length  $L_2$  is  $\lambda_{g(\text{slotline})}/2$ , where  $\lambda_g$  is the wavelength of an uniform slotline. This starting value of  $L_2$  is then slightly reduced to account for the slot end effects. To improve coupling a notch of width  $W_1$  (0.75 mm) and length  $L_1$  is cut out from the CPW ground plane located right above the aperture. The longitudinal distance between the extreme ends of the notches is slightly less than the aperture length  $L_2$ . The CPW is terminated in a short circuit at a

distance of approximately  $\lambda_{g(\text{CPW})}/2$  from the center of the notch. The length A of the patch is less than half wavelength after correcting for end effects. The width B of the patch is 1.5 times A. To improve coupling the aperture is offset by about 5.5 mm from the center of the patch. The feed and the patch are fabricated on 0.508 and 0.254 mm thick RT/Duroid 5880 respectively.

### III. Experimental Results and Discussions

The measured frequency spectrum at 7.6 GHz of the active antenna is shown in Fig. 4. The stability of oscillations is excellent. The measured H-plane radiation pattern of the active antenna is shown in Fig. 5 and is observed to be typical of a patch. The measured cross-polarization is less than -20 dB. By substituting the measured power and gain into the Friis transmission formula the absolute power radiated by the patch antenna is determined to be 1.1 mW. This is small since the HEMT is a low-noise low-power device.

### IV. Conclusions

An active antenna with a dielectric resonator stabilized HEMT oscillator and a CPW/aperture coupled patch antenna is

presented. Although the active antenna is demonstrated at 7.6 GHz, the design can be easily scaled to higher frequencies. Excellent oscillator characteristics and radiation pattern have been obtained.

### References

1. V.D. Hwang, T. Umano, and T. Itoh, "Quasi-optical integrated antenna and receiver front end," *IEEE Trans. Microwave Theory Tech.*, vol. 36, pp. 80-85, 1988.
2. J.A. Navarro, Y.H. Shu, and K. Chang, "Wideband integrated varactor-tunable active notch antennas and power combiners," *IEEE MTT-S International Microwave Symposium Digest*, New York: IEEE, 1991, vol. 3, pp. 1257-1260.
3. G.D. Vendelin, A.M. Pavio, and U.L. Rohde, *Microwave Circuit Design Using Linear and Nonlinear Techniques*. New York: John Wiley & Sons, 1990, Chap. 6.

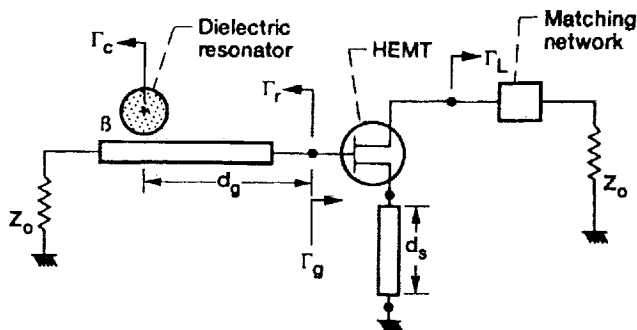


Figure 1.—Schematic of a dielectric resonator stabilized HEMT oscillator with series feedback.

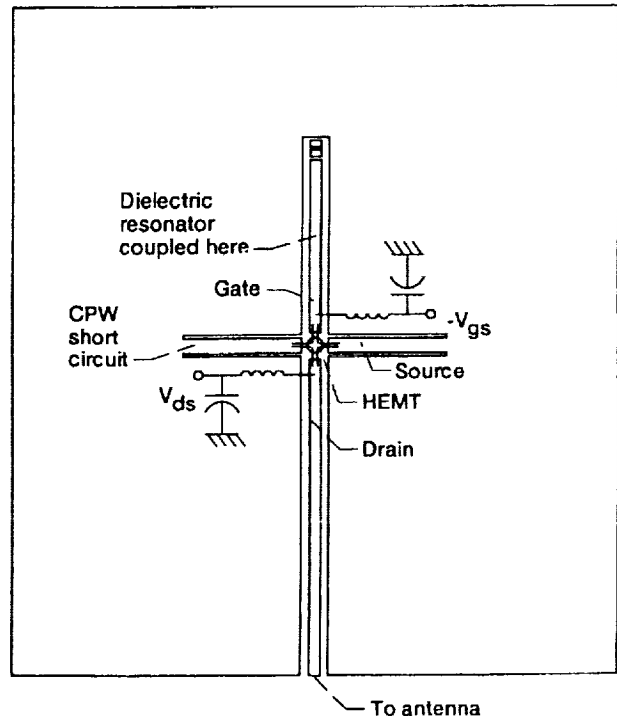


Figure 2.—CPW circuit for the oscillator part of the active antenna.

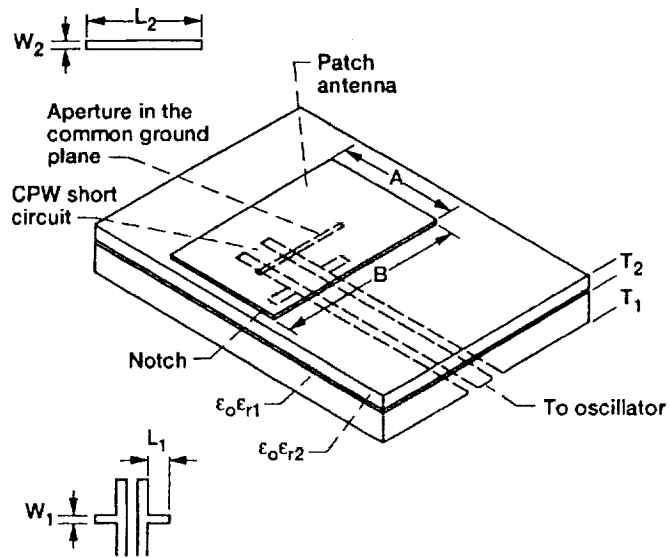


Figure 3.—Schematic illustrating the CPW aperture-coupled patch antenna part of the active antenna.

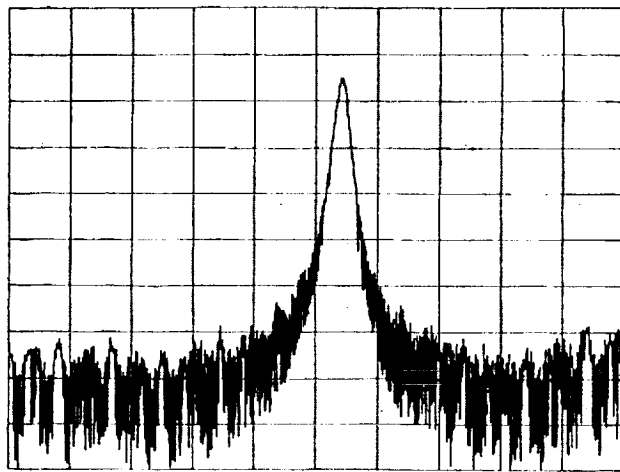


Figure 4.—Measured frequency spectrum of the oscillator. Center frequency is 7.6 GHz, Res. BW = 100 kHz, Hor. div = 1 MHz, Ver. div = 10 dB.

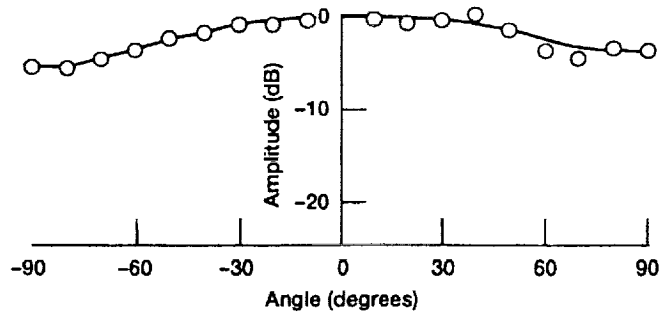


Figure 5.—Measured far field H-plane radiation pattern of the active antenna.



# A VERTICALLY INTEGRATED KA-BAND PHASED ARRAY ANTENNA

R. R. Kunath, R. Q. Lee, K. S. Martzaklis, K. A. Shalkhauser,  
and A. N. Downey

NASA Lewis Research Center  
Cleveland, Ohio

and

R. Simons

Sverdrup Technology, Incorporated  
Middleburg Heights, Ohio

## Abstract

Future communications satellites applications are considering phased array antennas as an integral part of the overall communications system. Monolithic Microwave Integrated Circuit (MMIC) based phased array antenna systems enable multi-functional system attributes such as electronic beam steering, multiple beams, system reconfigurability, and graceful system degradation. NASA Lewis Research Center's Space Electronics Division has been actively pursuing the development of MMIC-based phased array antennas for communication satellite applications in the Ka-band. This research has been focussed on the insertion of MMICs into functional phased array antenna designs.

This paper will discuss the design, development, and experimental demonstration of a small phased array antenna suitable for communications satellites applications. A vertical integration architecture is used which minimizes the size of the array with its associated beamforming network (BFN). The antenna features a 4-element linear microstrip array that uses aperture coupling of the

antenna elements to the BFN; a modified Wilkinson power divider BFN; and 32 GHz, 4-bit MMIC phase shifters on customized alumina carriers. Performance data is shown for all components and far field antenna radiation patterns are given.

## I. Introduction

As a result of the successful development of Monolithic Microwave Integrated Circuits (MMICs), phased array antennas have become an attractive option to meet communications systems antenna requirements. The inherent multi-functionality of phased array antennas (i.e. electronic steering, agile reconfigurability, graceful performance degradation, sidelobe control, etc.) makes them ideal candidates to meet the varied antenna needs of the communications system. The advantages of the phased array antenna are gained through the independent phase and amplitude adjustability of the individual antenna elements. Unfortunately, the discrete nature of the elements in the phased array antenna also gives rise to grating lobes, which, if not controlled, can lead to less than optimum performance. However, due to their small size, MMICs have enabled the antenna

\*Copyright © 1992 by the American Institute of Aeronautics and Astronautics, Inc. No copyright is asserted in the United States under Title 17, U.S. Code. The U.S. Government has a royalty-free license to exercise all rights under the copyright claimed herein for Governmental purposes. All other rights are reserved by the copyright owner.\*

designer to choose element spacings such that the impacts of grating lobes can be minimized.

At Ka-band frequencies and higher, the MMIC is approximately the size of the radiation wavelength. This creates a problem achieving optimum phased array antenna element spacing, and more importantly, minimizes the space available to distribute RF and control signals to the MMICs. One possible solution to this problem is the vertical integration or layering of the antenna. In vertical integration, the antenna is separated into layers, and each layer is specialized for a particular function. In this way, the vertical dimension of the antenna is exploited rather than the horizontal dimensions, and the space required per antenna element is minimized. The following is a description of the design and performance of a vertically integrated, 1X4, 32 GHz subarray.

## II. Antenna Layer

Figure 1 shows the 1X4 rectangular patch array used. The dimensions of the patch antennas, which are etched on a 10 mil PTFE substrate ( $\epsilon=2.2$ ), are 0.239 cm by 0.417 cm. The patch antennas are aperture coupled to a microstrip line through a slot in the ground plane. The ground plane on the antenna layer is common between the RF and antenna layers. The slot dimensions are 0.407 cm in length by 0.0254 cm in width, and are oriented along the H field line. The slot is placed at the location where the H field is a maximum. The exact slot position is determined by computing the input impedance of the  $TM_{10}$  mode of the patch antennas. For an antenna with a thin substrate, the patch antenna can be modelled as a cavity bounded by the patch, the ground plane, and a magnetic wall around its perimeter.<sup>1</sup> The input impedance computed from the cavity model approach has been found to be in good agreement with the measured results. For efficient coupling, the microstrip line is terminated in an open circuit which is approximately a quarter of a waveguide wavelength from the center of the slot. The patch antennas are designed to operate at approximately 30 GHz. Prior to fabricating the 1X4 phased array, a single aperture coupled patch was fabricated and tested to ensure good coupling efficiency and symmetrical radiation patterns. Based on the 90% coupling efficiency measured, a 1X4 phased array was fabricated and tested. An E-

plane radiation pattern of the 1X4 phased array without the MMICs is shown in Figure 2.

## III. RF Layer

### 1. 32 Ghz MMIC Phase Shifters

The MMIC phase shifters that were used were developed by Honeywell through a contract with NASA Lewis. The four-bit design consisted of three switched-line bits ( $180^\circ, 90^\circ, 45^\circ$ ) and one loaded-line (reactive) bit ( $22.5^\circ$ ). The MMICs were designed for a center frequency of 32 GHz and a bandwidth from 31-33 GHz. The targeted insertion loss was designed to be 2 dB/bit with an S11 and S22 of greater than 10 dB.<sup>2</sup>

The devices were fabricated in two iterations. In the first iteration Honeywell had three designs (Type I, II, and III). In the second iteration only two designs (Type II and III) were fabricated. The second iteration yielded 52 Type II devices from which 24 were packaged.

The device size was 6.41mm X 2.65 mm. Each switched-line bit is controlled by two pairs of FETs as shown in Figure 3. At any given time, the RF signal propagating through the bit is directed to either a delay path or a reference path by differentially biasing the pairs of FETs with zero and minus five volts. The loaded-line is controlled by applying a variable zero to minus five volt signal to it. While the loaded-line phase response is not linear, it does provide some trimming capability to accommodate the in-exact settings of the switched-line bits.

### 2. MMIC Carriers

Each phase shifter MMIC was mounted to an individual chip carrier to facilitate its RF characterization prior to use in the array. This approach not only adapted the MMIC for connection to the test fixturing, but also provided a stable mounting platform for the MMIC to help protect it from damage during handling. Furthermore, the use of a carrier meant that the MMIC would be mounted and wirebonded in one cycle, and would not be subjected to additional soldering, bonding, or probing steps. All electrical connections used in the characterization were made to the carrier

using non-destructive, temporary contacts to metalization patterns near the periphery of the carrier.

The carriers were fabricated from a simple design using a one-piece, 0.010" thick, alumina ( $Al_2O_3$ ) substrate mounted to a gold-plated kovar base (Figure 4). The central portion of the alumina was laser machined to remove ceramic material and allow the MMIC to be mounted with its top surface flush with the RF microstrip metalization of the carrier. To compensate for the differences in thickness between the 0.010" alumina and the 0.004" GaAs MMIC substrate, an elevated platform, or pedestal, was machined into the kovar base. Thus, when fully assembled, the MMIC mounts flush with the microstrip input and output lines, thereby minimizing bondwire lengths to improve RF performance. The mounting of the MMIC directly to the metal base had the additional benefit of improved heat removal. The alumina substrate was soldered to the kovar base using a solder preform. The MMIC was mounted into the carrier recess using a thermally and electrically conductive epoxy.

The carriers were originally designed with integral mounting tabs extending from opposite corners of the metal base to permit fastening of the carriers into the array structure. These tabs were later removed from the design to reduce the carrier size to achieve a tighter inter-element spacing. The resulting rectangular footprint of the carriers was 0.25" by 0.5". The carriers were designed with the intent of eventual hermetic sealing of the MMIC in a package. This would be accomplished through the addition of vertical walls (a seal ring) and a lid to the carrier and slight modification to the microstrip metalization designs. The lid of the package was also considered as a mounting location for phase shifter control circuits such as an application specific integrated circuit (ASIC) or opto-electronic interface circuit (OEIC).

### 3. MMIC Characterization and Performance

Characterization of the packaged MMIC's was accomplished using a Hewlett Packard (HP) 8510B Automatic Network Analyzer (ANA) and two HP 6626A system DC power supplies (MMIC bias and control), controlled by an HP 236 computer/controller. Package insertion was facilitated

using an ICM semi-custom TF-2001-C test fixture configured with OS-50 coaxial to microstrip launchers. The test fixture was inserted between the two ports of an Reflection/Transmission test set enabling measurements from 26.5 to 40 GHz. The characterization bandwidth was 30 to 34 GHz.

The main objective of the MMIC testing was the determination of the relative insertion phase as a function of phase shifter state setting. A 50 ohm, 500 mil long through line on a 10 mil thick Alumina substrate served as the thru standard. Multiple insertion of the thru standard demonstrated good test fixture repeatability (Figure 5). Calibration verification with regard to insertion phase was achieved via a 527.68 mil line resulting in a 527.72 mil measurement.

A total of 24 packaged MMIC's were characterized. For each of the 16 phase states, measurements were conducted for insertion loss and relative insertion phase. The variable loaded line bit was also characterized. Typical insertion loss values ranged from 10 to 12 dB for the test assembly (carrier, MMIC & bondwires) over the 16 phase states (Figure 6). To measure relative insertion phase, the MMIC was set to its reference state ( $0^\circ$ ) and this measurement was stored to memory. Since a division of two complex numbers in polar form is equivalent to the ratio of the magnitudes and the difference of the angles, the (S21/memory) display feature of the ANA was utilized to show the additional insertion phase as each state was switched in (Figure 7). The curves were generally linear at the frequencies of interest. Performance of the loaded line bit is shown in Figure 8. Eight of the 24 MMIC's were chosen for array integration.

### 4. 1X4 Power Divider

A 1X4 power divider was designed to split the signal from the RF source into four equal amplitude and equal phase signals to present to the MMIC phase shifters. Three modified Wilkinson<sup>3</sup> equal-split (3 dB) power dividers were formed on copper clad, 10 mil PTFE substrate material, with a copper/resistive metal composite layer from which shunt resistors were formed (Figure 9). In the transmit mode, a signal is applied to the input (port 1) and is split into two signals each having equal phase and amplitude. These two signals are

then each fed into a second power divider, yielding four signals (at ports 2,3,4, and 5) of equal amplitude and phase at a power level of about one-fourth (-6 dB) that of the original signal power. This signal is then applied to the MMIC phase shifter.

When the antenna is operated in the receive mode, the process is reversed. Signals processed by the MMIC phased shifters are presented to the four legs of the power divider (ports 2,3,4, and 5), which now act as a power combiner. Components of the signals from the MMIC phase shifters at ports 2 and 3, for example, which are in-phase, will add constructively, and out of phase components will be absorbed by the shunt resistors. Likewise, the other two signals from the remaining MMIC phase shifters at ports 4 and 5 combine into a common signal. The two new signals are then combined in the final Wilkinson power divider (combiner) to form the composite signal. If the signals from the phase shifters are all equal in amplitude and phase, the resulting signal will be approximately four times (6 dB) greater than the original signal for any individual phased shifter.

#### IV. Bias/Control Layer

The final layer of the antenna provides both structural support and bias/control signal distribution. Each of the MMIC phase shifters requires seven control signals, which are routed on this layer. This layer is fabricated from 62.5 mil PTFE material. The bias/control layer must lay directly on top of the microstrip lines of the 1x4 power divider as shown in Figure 1. The low dielectric constant of this board minimizes its impact on the 1X4 microstrip power divider. Additionally, four "windows" are cut into this board to provide wire bonding access to the MMIC phase shifters. Wire bonds are made between the MMIC carrier pads to their respective control lines on the bias/control board. Because the signal distribution lines on the board are copper, a gold mesh is first welded to the line, which facilitates a gold to gold wire bond. Finally, ribbon cable is used to bring the bias/control signals into the distribution lines.

Mechanically, this board acts as a stiffener for the overall structure. All other layers are mounted to this layer, including the MMIC aluminum mounting/heat sink plate. Tapped stand-offs are fas-

tened to the bias/control board to provide mounting points when the subarray is tested on the antenna range.

#### V. Antenna Subarray Performance

Figure 10 illustrates the antenna performance of the subarray. Figure 10 is a plot of relative gain versus angle for all elements set to relative phase difference of zero (boresite). This pattern agrees favorably with Figure 2; however, the mainlobe is not as well defined due to a phase imbalance between the elements. The cause of the phase imbalance is believed to be the close spacing between radiating elements ( $0.4 \lambda$ ), and therefore strong mutual coupling, and the lack of isolation between the radiating element and the phase shifter. The noise seen in the pattern is the result of the low RF level available during testing. A second iteration of this design provides for the insertion of an MMIC amplifier for each element which will provide the necessary isolation between elements.

#### VI. Conclusions

A vertically integrated 1X4, 32 GHz subarray antenna was designed, fabricated and tested. Each of the vertical layers was optimized for performance, and MMICs on custom carriers were characterized prior to insertion. Measurements indicate that the overall antenna performance is acceptable, but not ideal. Further modifications must be made to accommodate the impact of mutual coupling between radiating elements. To fully optimize the inter-element spacing at Ka-band and higher frequencies, still requires a distribution media that minimizes the space required for routing RF and control signals.

#### 7. References

1. Keith R. Carver and James W. Mink, "Microstrip Antenna Technology", IEEE Transactions on Antennas and Propagation, Volume AP-29, No. 1, January 1981.
2. J. Mondal, J. Geddes, T. Contolatis, P. Bauhahn, and V. Sokolov, "30 GHz Monolithic

**Receive Module Final Report\*, NASA Contrator  
Report No. CR 187085, October 1990.**

**3. Pozar, David M.: Microwave Engineering, Ad-  
dison-Wesley, 1990.**

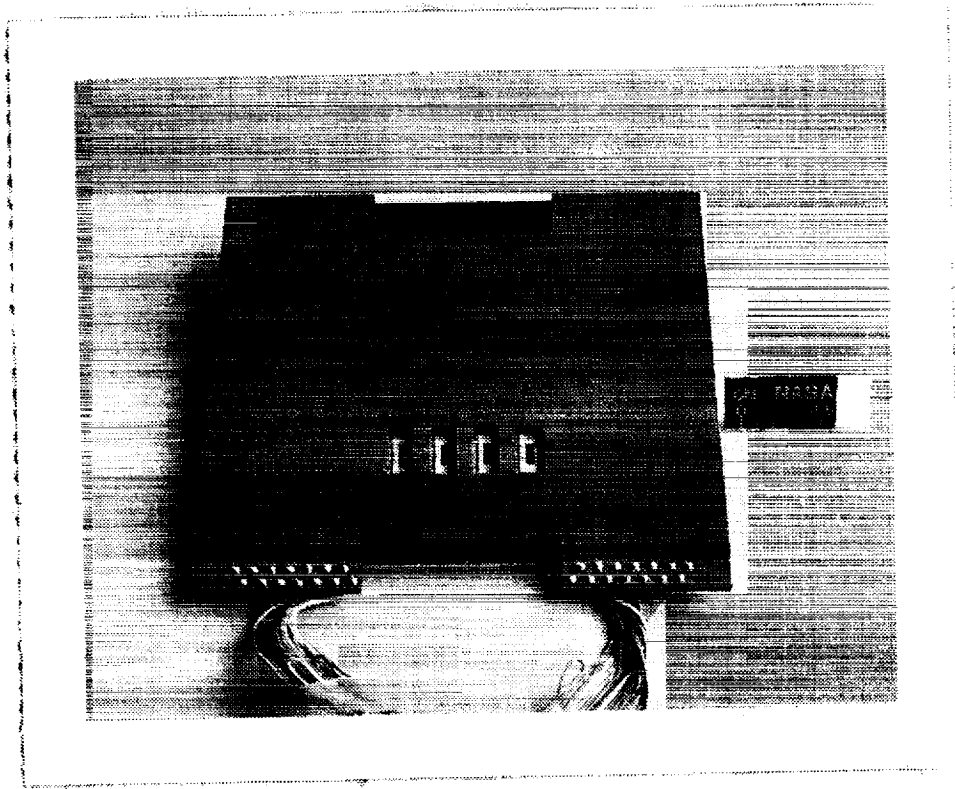


Figure 1. 1X4 Vertically Integrated Ka-Band Phased Array

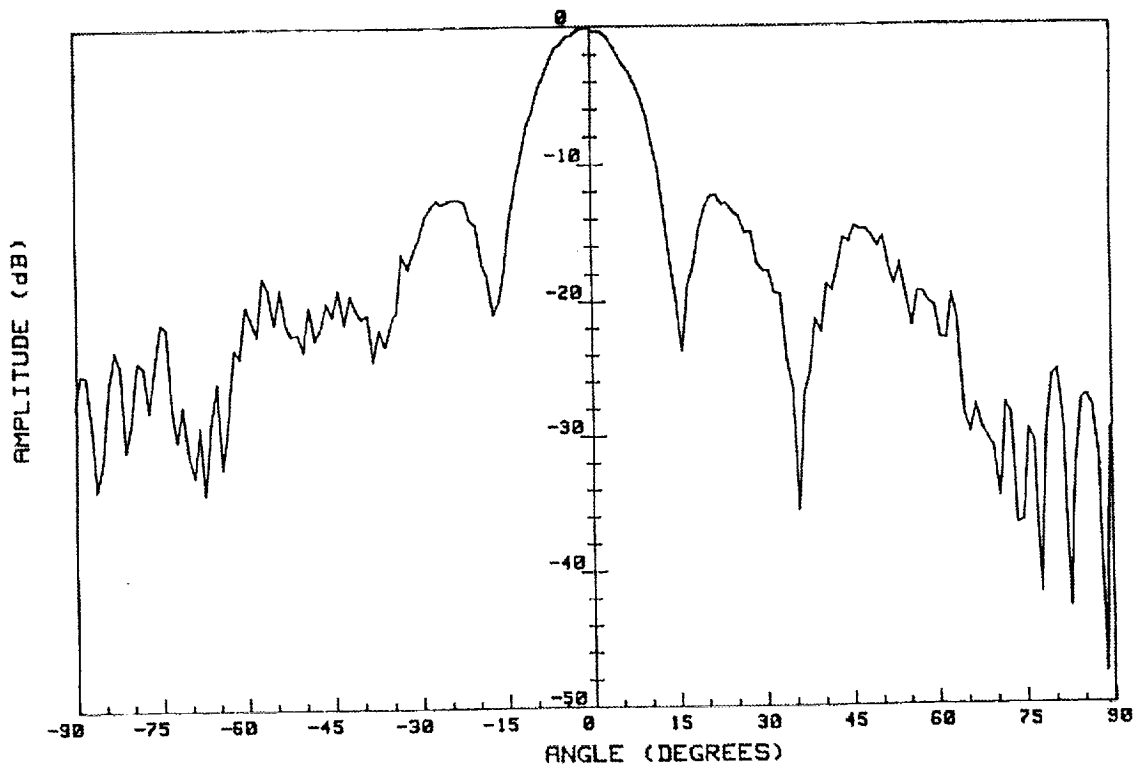


Figure 2. Far-Field Pattern of 1X4 Array without MMICs

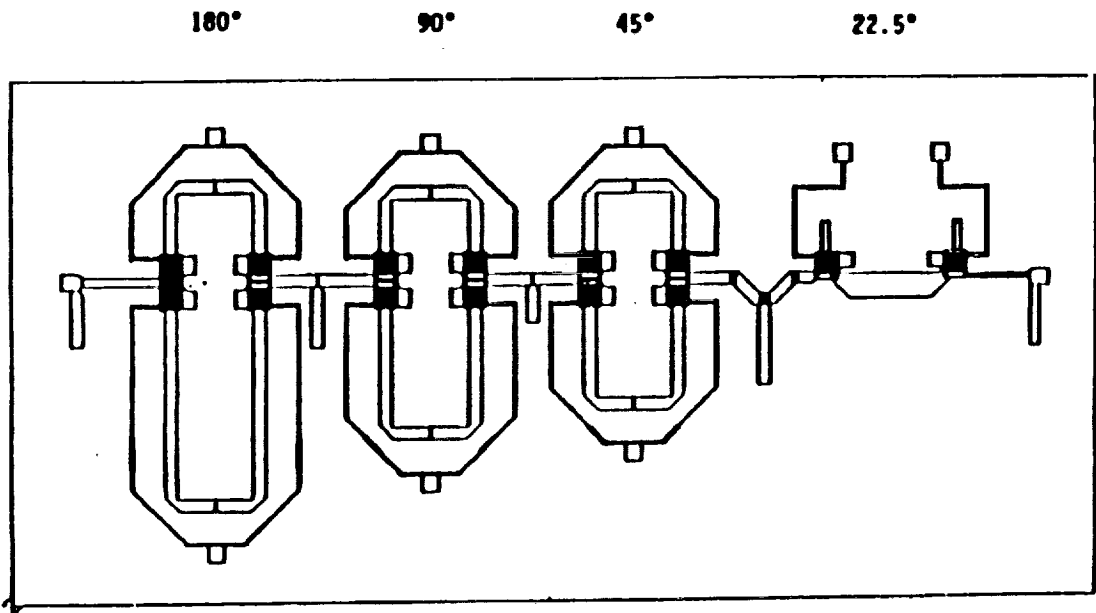


Figure 3. 32 GHz, 4-bit Honeywell Phase Shifter

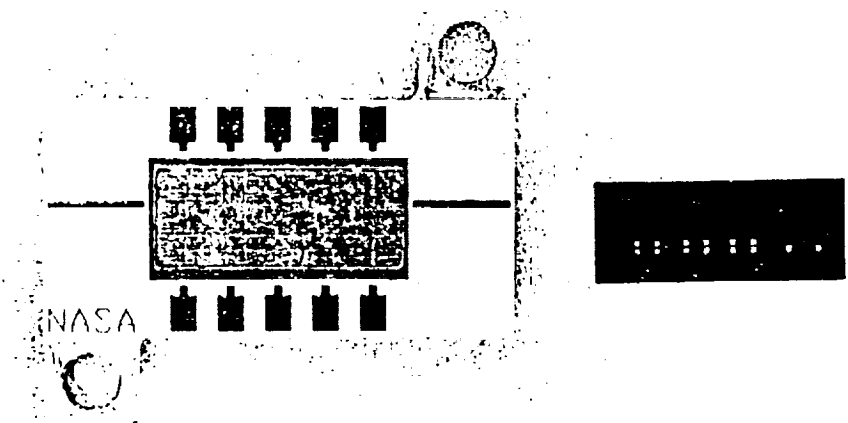


Figure 4. Holz Phase Shifter Carrier

S21 log MAG  
 REF 0.0 dB  
 2.0 dB/

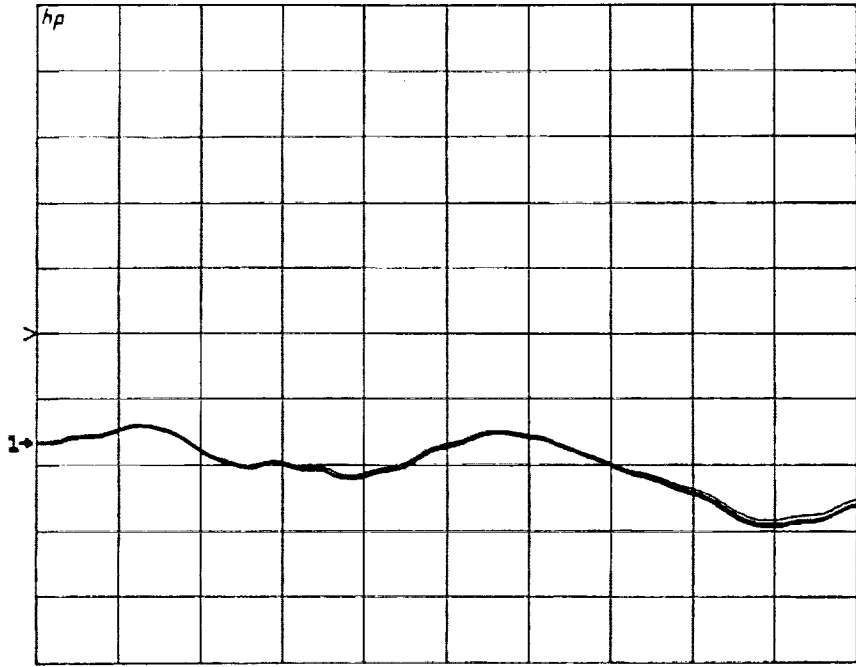


Figure 5. S21 of Test Fixture START 30.000000000 GHz STOP 34.000000000 GHz

S21 log MAG  
 REF 0.0 dB  
 10.0 dB/  
 -13.32 dB

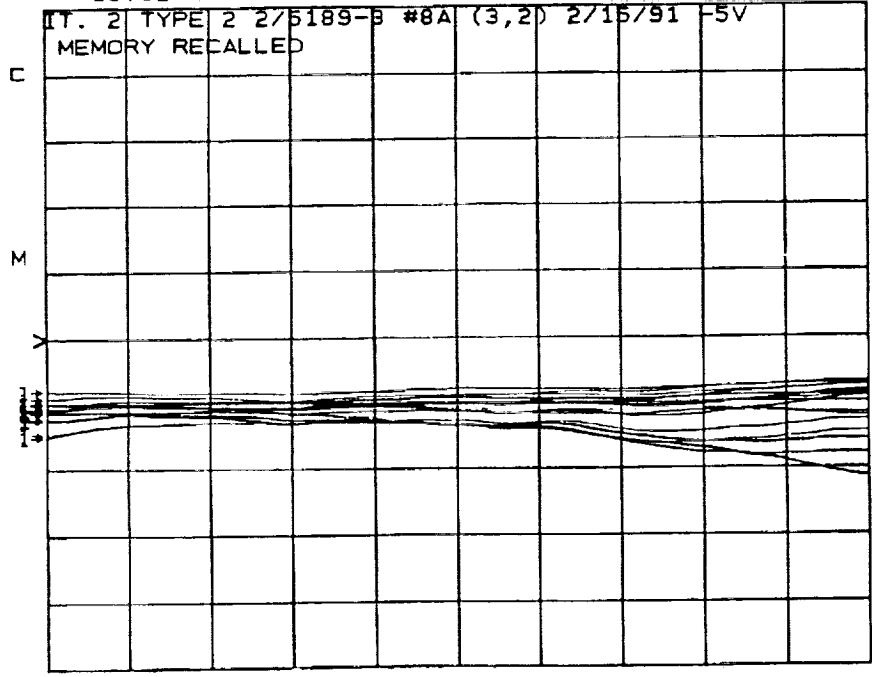


Figure 6. Phase Shifter Insertion Loss START 30.000000000 GHz STOP 34.000000000 GHz

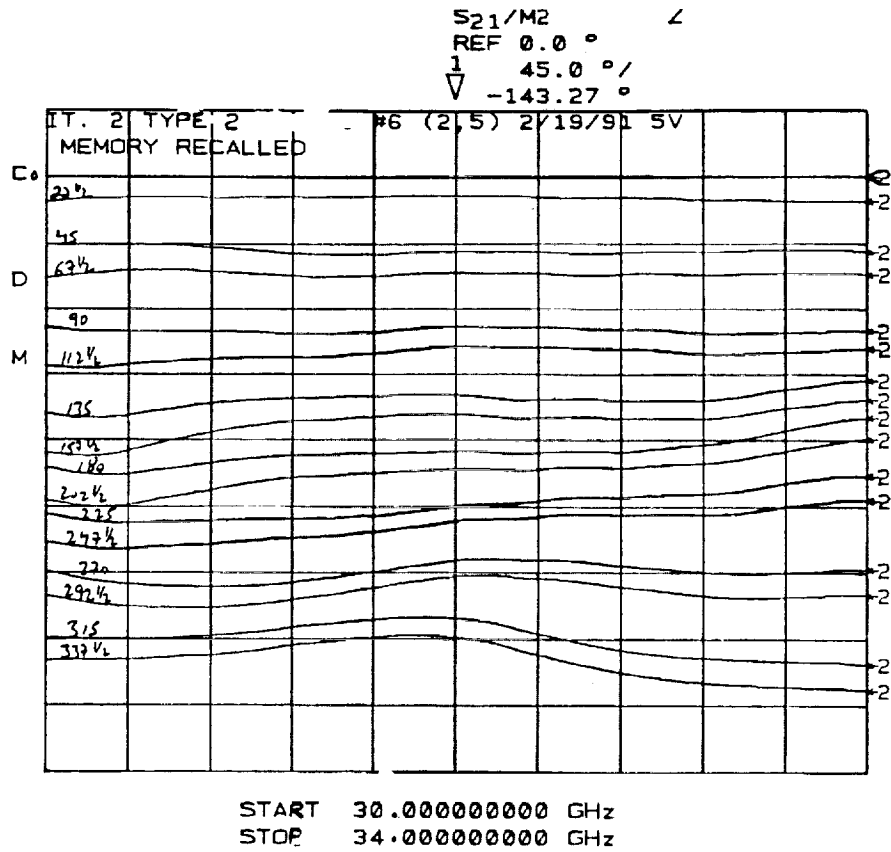


Figure 7. S<sub>21</sub> of Phase Shifter in all 16 Phase states

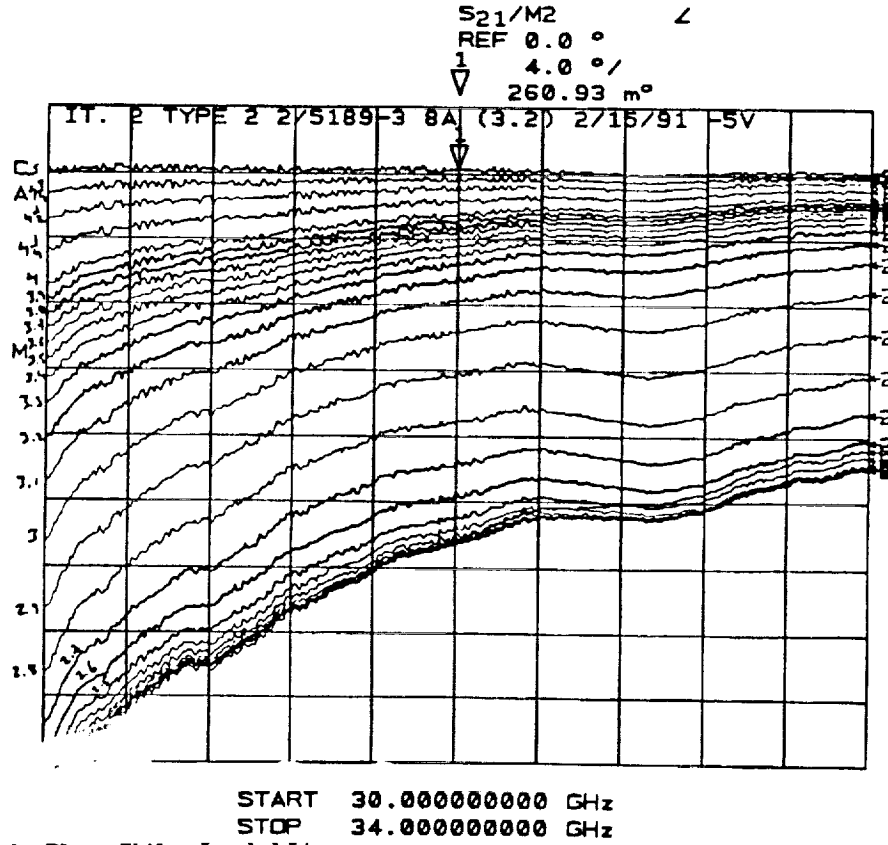
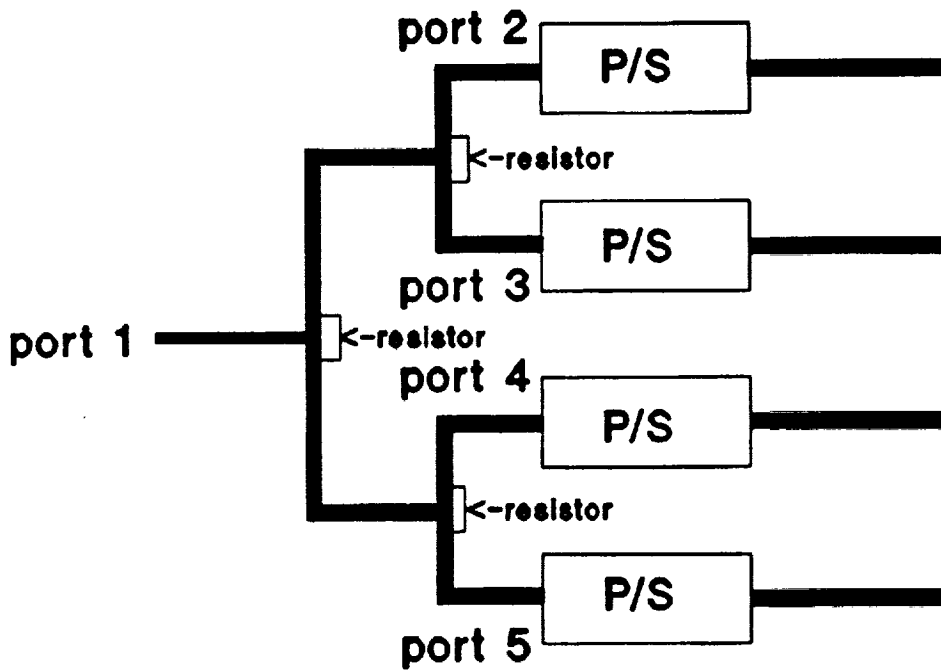


Figure 8. S<sub>21</sub> of the Phase Shifter Loaded Line



### 4-way modified Wilkinson divider/combiner

Figure 9. 1-to-4 Modified Wilkinson Power Divider

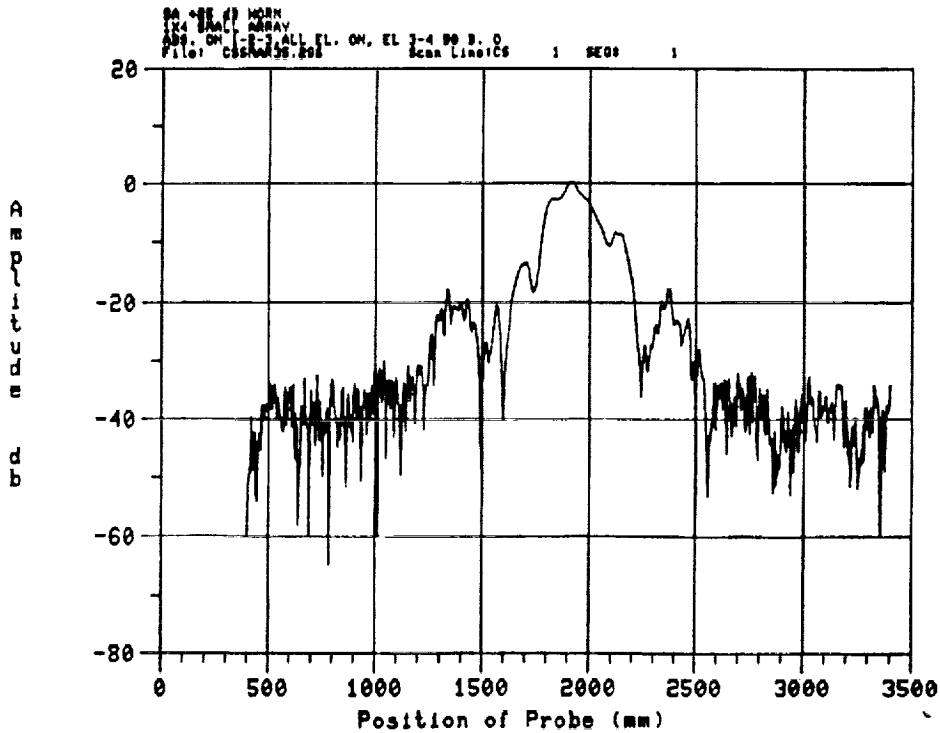


Figure 10. Far-Field Pattern of Array with MMICs

## AN OPTICALLY CONTROLLED KA-BAND PHASED ARRAY ANTENNA

R. R. Kunath  
R. Q. Lee  
K. S. Martzaklis  
K. A. Shalkhauser  
A. N. Downey

NASA Lewis Research Center  
Cleveland, Ohio

and

R. Simons

Sverdrup Technology, Incorporated  
Middleburg Heights, Ohio

Abstract

Future communications satellites applications are considering phased array antennas as an integral part of the overall communications system. Monolithic Microwave Integrated Circuit (MMIC) based phased array antenna systems enable multi-functional system attributes such as electronic beam steering, multiple beams, system reconfigurability, and graceful system degradation. NASA Lewis Research Center's Space Electronics Division has been actively pursuing the development of MMIC-based phased array antennas for communication satellite applications in the Ka-band. However, due to the compact spacing of these arrays, methods of reducing the number of control signals to each element of the phased array are being investigated. NASA Lewis has developed an OptoElectronic Interface Circuit (OEIC) which enables the distribution of control signals to each antenna element through a single fiber optic cable. With the application of this technology, the number of phased array interconnections has been minimized with a corresponding decrease in system weight.

This paper will discuss the design and development of a small, optically controlled phased array antenna suitable for communications satellites applications. A vertical integration architecture is used which minimizes the size of the array with its associated beamforming network (BFN). The antenna features a 4-element linear microstrip array that uses aperture coupling of the antenna elements to the BFN; a modified Wilkinson power divider BFN; and 32 Ghz, 4-bit MMIC phase shifters in customized quartz packages with corresponding OEICs for control signal reception.

## I. Introduction

Phased-array antennas have long been investigated to support the agile, multibeam radiating apertures with rapid reconfigurability needs of radar and communications. With the development of the Monolithic Microwave Integrated Circuit (MMIC), phased array antennas having the stated characteristics are becoming realizable. However, at K-band frequencies (20-40 GHz) and higher, the problem of controlling the MMICs using conventional techniques either severely limits the array size or becomes insurmountable due to the close spacing of the radiating elements necessary to achieve the desired antenna performance.

Investigations have been made that indicate using fiber optics as a transmission line for control information for the MMICs provides a potential solution<sup>1</sup>. By adding an optical interface circuit to pre-existing MMIC designs, it is possible to take advantage of the small size, lightweight, mechanical flexibility and RFI/EMI resistant characteristics of fiber optics to distribute MMIC control signals. Additionally, vertical integration, separating the antenna into discrete functional layers, further minimizes the space required to implement the antenna. This paper will describe the architecture, circuit development, testing and integration of an optically controlled K-band MMIC phased-array antenna.

## II. Vertically Integrated Antenna Architecture

Figure 1 shows an optically controlled, vertically integrated 1X4 rectangular patch array architecture. The dimensions of the patch antennas, which are etched on a 10 mil PTFE substrate ( $\epsilon=2.2$ ), are 0.239 cm by 0.417 cm. The patch antennas are aperture coupled to a microstrip line through a slot in the ground plane. The ground plane on the antenna layer is common between the RF and antenna layers. The slot dimensions are 0.407 cm in length by 0.0254 cm in width, and are oriented along the H field line. It was experimentally determined that a 90% coupling efficiency is achieved with this method.

The MMIC phase shifters were developed by Honeywell through a contract with NASA Lewis. The four-bit design consists of three switched-line bits ( $180^\circ, 90^\circ, 45^\circ$ ) and one loaded-line (reactive) bit ( $22.5^\circ$ ). The MMICs were designed for a center frequency of 32 GHz and a bandwidth from 31-33 GHz. The targeted insertion loss was designed to be 2 dB/bit with an S11 and S22 of greater than 10 dB.<sup>2</sup> The device size is 6.41mm X 2.65 mm. Each switched-line bit is controlled by two pairs of FETs as shown in Figure 2. At any given time, the RF signal propagating through the bit is directed to either a delay path or a reference path by differentially biasing the pairs of FETs with zero and minus five volts. The loaded-line is controlled by applying a variable zero to minus five volt signal to it. While the loaded-line phase response is not linear, it does provide some trimming capability to accommodate the in-exact settings of the switched-line bits.

The OEICs were also developed by Honeywell through a contract with NASA Lewis. These devices are follow-ons to a successful proof-of-feasibility, hybrid OEIC development. The current OEIC features a fully monolithic receiver which includes an integrated photodetector, LNA, link status monitor, clock recovery circuit, and a 1:10 demultiplexer with a 4B/5B decoder. Additional features include: operation from 10 to greater than 400 Mbps, burst and continuous mode operation, on-chip addressability and diagnostics, and a mil-spec, foundry compatible process. The die size is 0.215" by 0.109", and the device operates at wavelength between 780 and 820 nanometers (Figure 3). A specialized, two-layer carrier was fabricated on which to mount the devices. The two-layer design was designed to conform to the dimensions of the MMIC package lid, and to enable the bias connections to the OEIC to be limited to two.

Each phase shifter MMIC is packaged in an individual fused silica package fabricated by Hughes Aircraft Company to facilitate its RF characterization prior to use in the array. This approach not only adapts the MMIC for connection to the test fixturing, but also provides a stable mounting platform for the MMIC to help protect it from damage during handling. Fused silica was chosen because its electrical properties enable its use at high frequencies with the lowest known loss. Furthermore, because the OEIC requires no ground plane, the lid of the package provides a surface upon which it can be mounted. Figure 4 illustrates the package design, while Figure 5 details the "piggy-back" OEIC mounting.

A 1X4 power divider was designed to split the signal from the RF source into four equal amplitude and equal phase signals to present to the MMIC phase shifters. Three modified Wilkinson<sup>3</sup> equal-split (3 dB) power dividers are formed on copper clad, 10 mil PTFE substrate material, with a copper/resistive metal composite layer from which shunt resistors were formed (Figure 6). The shunt resistors provide isolation between the legs of the power divider by absorbing signals reflected from the MMIC phase shifters that propagate back through the divider network.

The final layer of the antenna provides both structural support and bias signal distribution. Each of the MMIC phase shifters requires seven control signals, which are provided by the OEIC, but the bias of zero and minus five volts is routed on this layer. This layer is fabricated from 62.5 mil PTFE material. The bias/control layer must lay directly on top of the microstrip lines of the 1x4 power divider as shown in Figure 1. The low dielectric constant of this board minimizes its impact on the 1X4 microstrip power divider. Additionally, four "windows" are cut into this board to provide wire bonding access to the MMIC phase shifters.

### III. MMIC and OEIC Characterization and Performance

The main objective of the MMIC testing was the determination of the relative insertion phase as a function of phase shifter state setting. The MMICs were characterized using a specially designed alumina carrier and an test fixture. A 50 ohm, 500 mil long through line on a 10

mil thick Alumina substrate served as the thru standard. Multiple insertion of the thru standard demonstrated good test fixture repeatability (Figure 7). Calibration verification with regard to insertion phase was achieved via a 527.68 mil line resulting in a 527.72 mil measurement. The characterization of the MMICs in the package has not yet been accomplished.

A total of 24 packaged MMIC's were characterized. For each of the 16 phase states, measurements were conducted for insertion loss and relative insertion phase. The variable loaded line bit was also characterized. Typical insertion loss values ranged from 10 to 12 dB for the test assembly (carrier, MMIC & bondwires) over the 16 phase states (Figure 8). To measure relative insertion phase, the MMIC was set to its reference state (0 °) and this measurement was stored to memory. Since a division of two complex numbers in polar form is equivalent to the ratio of the magnitudes and the difference of the angles, the (S21-/memory) display feature of the ANA was utilized to show the additional insertion phase as each state was switched in (Figure 9). The curves were generally linear at the frequencies of interest. Performance of the loaded line bit is shown in Figure 10. Eight of the 24 MMIC's were chosen for array integration.

The OEICs were tested by Honeywell in both bursted and continuous modes. Figure 11 shows the results of the OEIC being tested in bursted mode. The device was tested up to data rates in excess of 400 Mbps with no signs of degradation in performance. Testing instrumentation limitations prevented characterization beyond these data rates.

#### IV. Conclusions

An optically controlled 1X4, 32 GHz subarray antenna has been presented. The antenna features a vertically integrated architecture that uses MMIC phase shifters with "piggy-backed" OEIC control devices. Experimental results of the testing and characterization of the devices and components have been discussed. This type of architecture minimizes the space of the antenna, and the use of fiber optic control signal distribution minimizes the number of control signal lines to the devices, with an associated mitigation of weight.

#### 7. References

1. Richard R. Kunath and Kul B. Bhasin, "Optically Controlled Phased-Array Antenna Technology for Space Communication Systems", Proceedings of the SPIE Optoelectronics and Laser Applications in Science and Engineering Symposium (O/E LASE '88), January 1988.
2. J. Mondal, J. Geddes, T. Contolatis, P. Bauhahn, and V. Sokolov, "30 GHz Monolithic Receive Module Final Report", NASA Contractor Report No. CR 187085, October 1990.
3. Pozar, David M.: Microwave Engineering, Addison-Wesley, 1990.

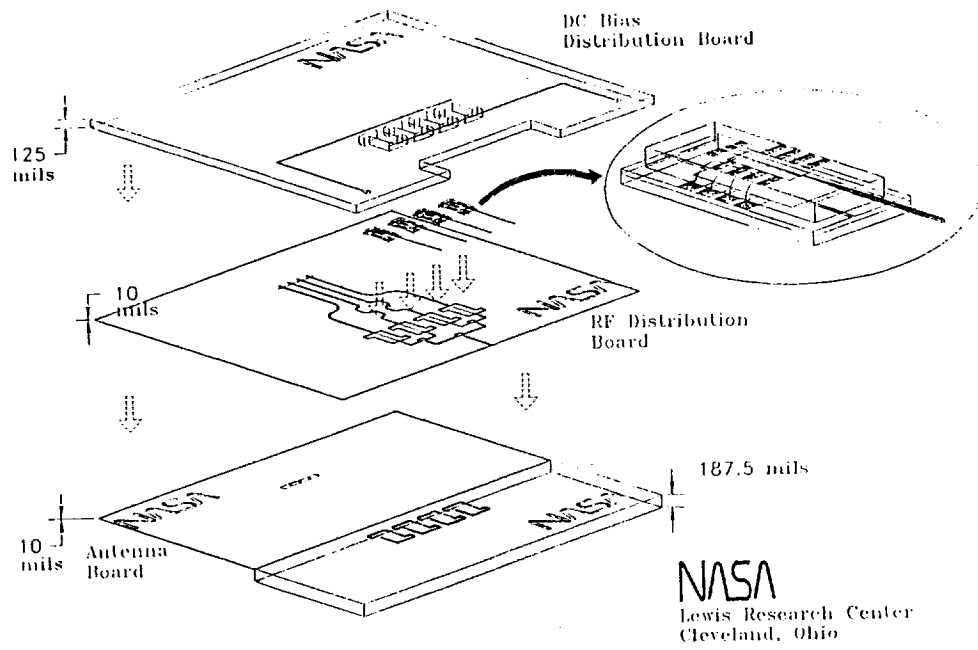


**Figure 1. 1X4 Optically Controlled Ka-Band Phased Array**

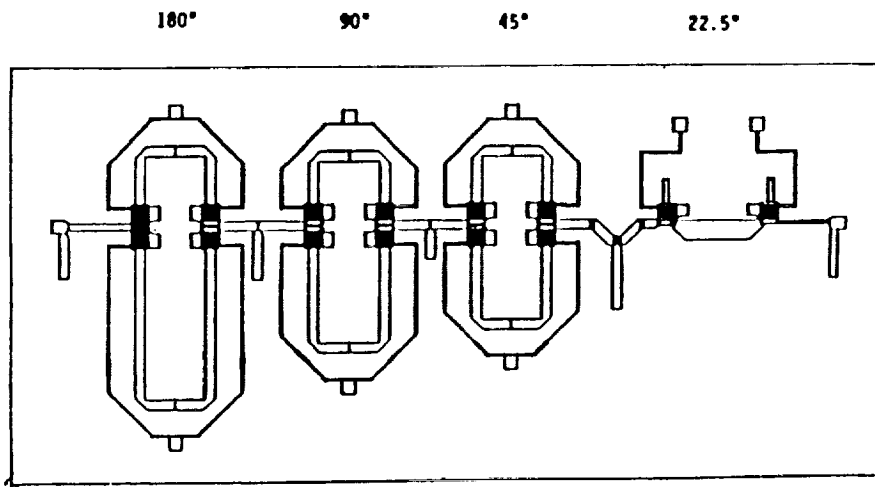


**Figure 2. 32 GHz, 4-bit Honeywell Phase Shifter**



Honeywell OEIC with Fiber Optic Pigtail

**Objective**  
Develop an optoelectronic interface circuit (OEIC) capable of interfacing MMICs in a phased array antenna controller using a fiber optic distribution network

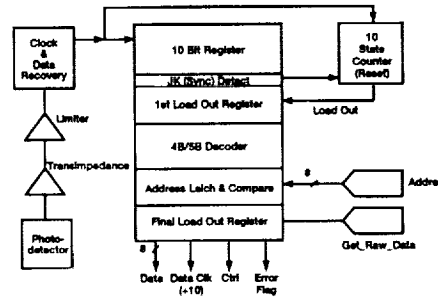
**Current Focus**  
Fabricate OEICs for an experimental optically controlled phased array antenna demonstration

**Rationale**  
MMIC-based phased array antennas require multi-bit control signal distribution

OEICs enable fiber optic signal distribution to MMICs in antenna arrays

OEICs enable lightweight, low loss signal distribution networks that feature high EMI suppression and mechanical flexibility

Highly Integrated Monolithic Optical Receiver



CD-91-56392

Figure 3. Honeywell OptoElectronic Interface Circuit

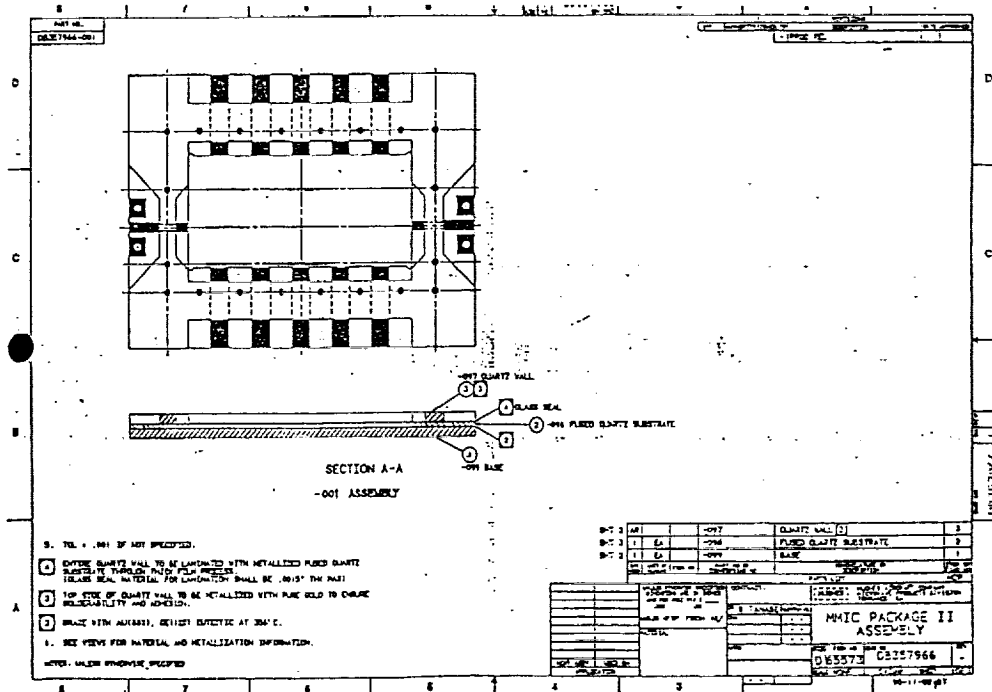


Figure 4. Hughes Fused Silica MMIC Package

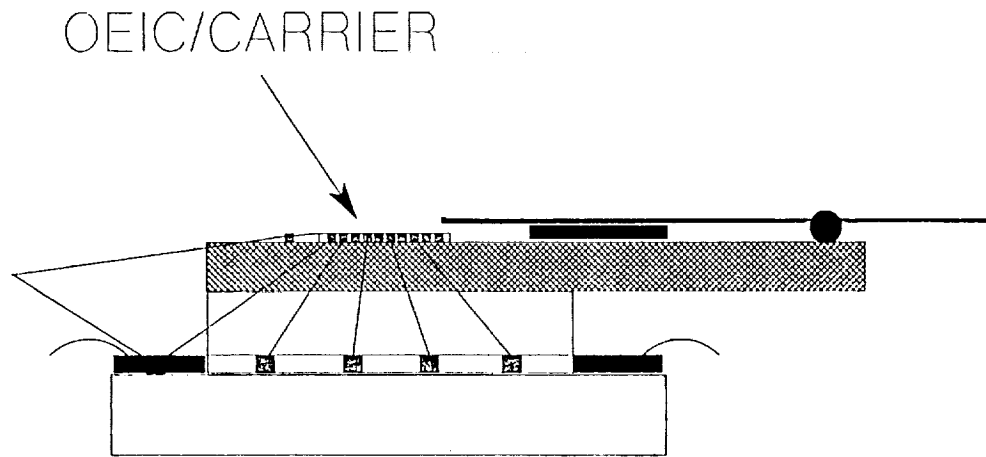
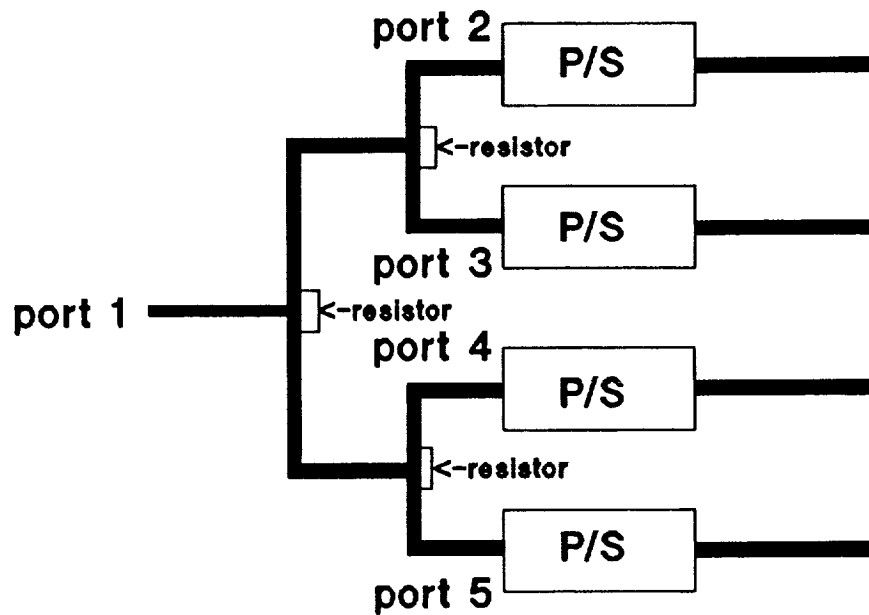


Figure 5. OEIC "Piggy-Back" Mounting



4-way modified Wilkinson divider/combiner

Figure 6. 1-to-4 Modified Wilkinson Power Divider

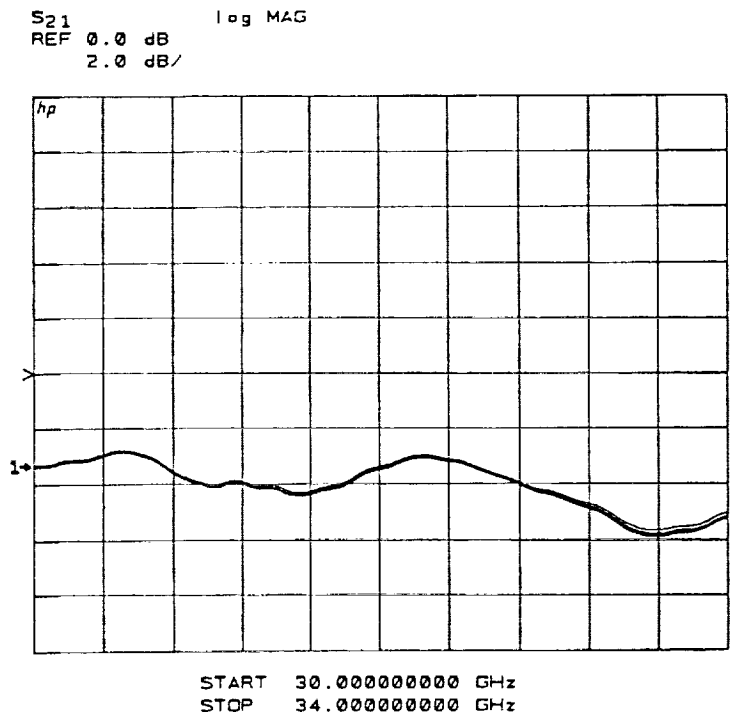


Figure 7. S<sub>21</sub> of Test Fixture

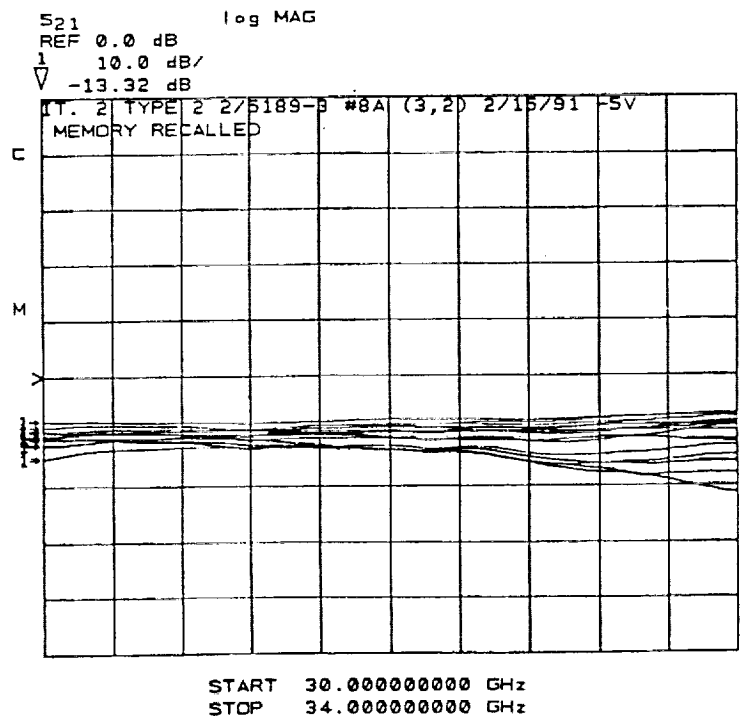


Figure 8. Phase Shifter Insertion Loss

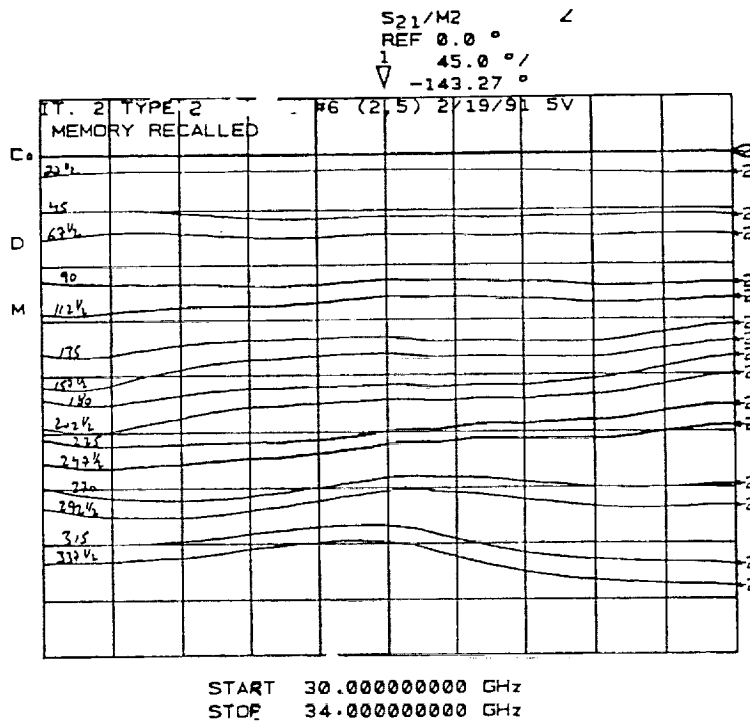


Figure 9. S<sub>21</sub> of Phase Shifter in all 16 Phase States

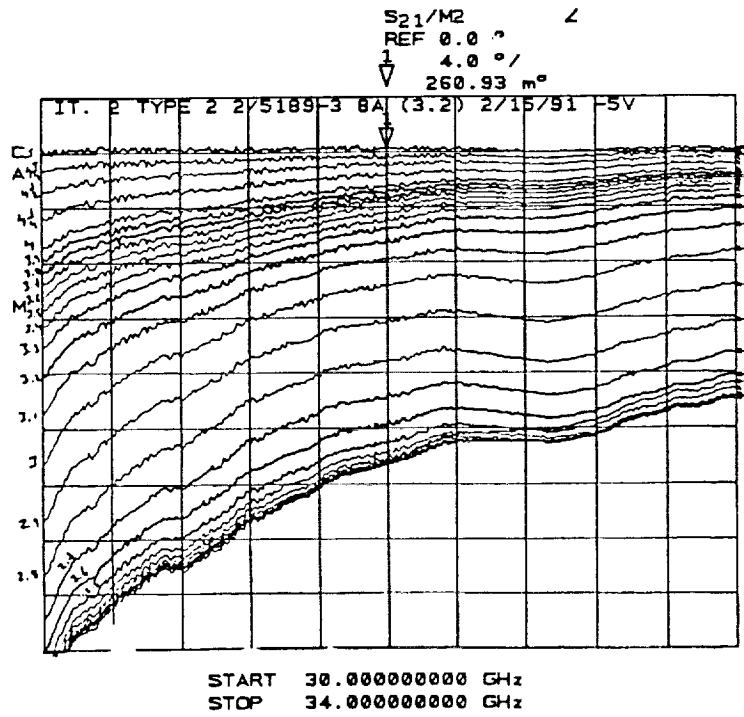
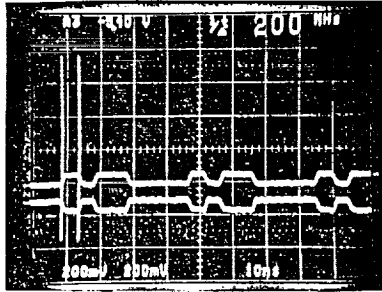
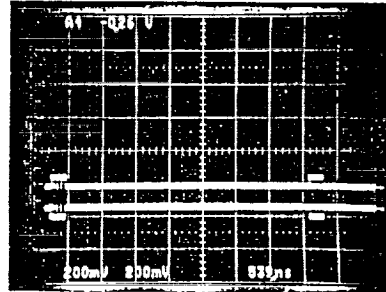


Figure 10. S<sub>21</sub> of Phase Shifter Loaded Line



Tested from 7-480 Mbps  
(Test System Limited)



Tested in Burst Mode to 130 Mbps  
(Test System Limited)

Contains the analog and digital circuits required to recover data and clock without the need for external components or a phase-locked loop.

- Additional Advantages:
- No preamble or set-up time required
  - Robust to jitter and amplitude variation
  - Broadband
  - Low cost

**Figure 11. OEIC Bursted Test Demonstration**

# Coplanar Waveguide Aperture-Coupled Microstrip Patch Antenna

Richard Q. Lee, *Member, IEEE*, and Rainee N. Simons, *Member, IEEE*

Permission to copy without fee all or part of this material is granted provided that the copies are not made or distributed for direct commercial advantage. Copying is by permission of the Institute of Electrical and Electronics Engineers. To copy otherwise, or to republish, requires a fee and specific permission.

**Abstract**—The performance characteristics of a coplanar waveguide (CPW) aperture-coupled microstrip patch antenna was investigated experimentally. A grounded CPW with a series gap in the center strip conductor was used to couple microwave power to the antenna through an aperture in the common ground plane. Results indicate good coupling efficiency and confirms the feasibility of this feeding technique.

## I. INTRODUCTION

APERTURE-COUPLED feeding is attractive because of advantages such as no physical contact between the feed and radiator, wider bandwidths, and better isolation between antennas and the feed network. The use of coplanar waveguide (CPW) as transmission media can also provide lower radiation losses and ease of monolithic microwave integrated circuit (MMIC) device integration in MMIC phase arrays [1]. Furthermore, aperture-coupled feeding allows independent optimization of antennas and feed networks by using substrates of different thickness or permittivity. Recently, it has been demonstrated that using a “dogbone” aperture can greatly improve the coupling efficiency [2]. CPW feed structures using probes as well as apertures to couple microwave power to the antenna have also been reported to have excellent coupling efficiency and antenna patterns [3], [4].

This letter reports an experimental investigation of a new aperture-coupled feeding technique where a grounded CPW with a series gap in the center strip conductor is used to couple microwave power to a microstrip patch antenna through an aperture in the common ground plane. This design permits the insertion of solid state devices in the series gap of the CPW feed and thus, is suitable for use in active antenna or quasi-optical combiner/mixer designs. To optimize the coupling efficiency three different feed configurations have been designed and tested.

## II. DESIGN DESCRIPTION

Fig. 1 shows the CPW aperture-coupled microstrip patch antenna configuration used in the experiment. In the experimental antenna, the patch and the CPW feed structure, with a series gap in the center strip conductor, are fabricated on separate substrates, and the aperture is etched on the common ground plane. The aperture is located directly above the series gap. Thus, microwave power is coupled from the ground CPW

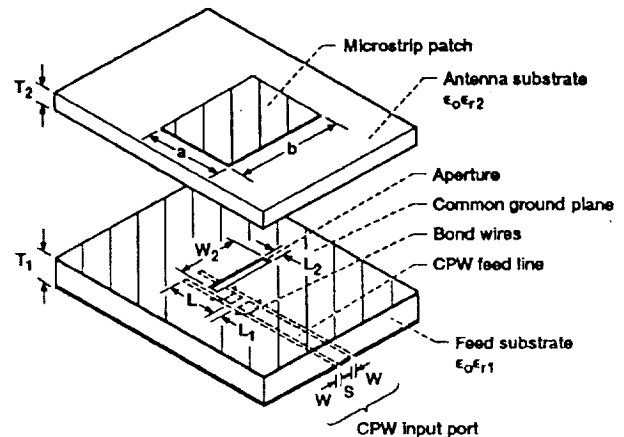


Fig. 1. Schematic of the CPW aperture-coupled microstrip patch antenna:  $S = 0.076$  cm,  $W = 0.025$  cm,  $L = 0.711$  cm,  $L_2 = 0.205$  cm,  $W_2 = 0.69$  cm,  $a = 0.76$  cm,  $b = 1.14$  cm,  $T_1 = 0.051$  cm,  $\epsilon_{r1} = 2.2$ ,  $T_2 = 0.025$  cm,  $\epsilon_{r2} = 2.2$ .

feed line to the patch through the aperture. The aperture is displaced by about 0.32 cm from the center of the patch to provide a proper impedance match. The inset in Fig. 2 shows the three different feed configuration designs reported here. In the first design, the length and width of the series gap and the aperture are  $L_1$  and  $S$ , and  $L_2$  and  $W_2$ , respectively. In the second design, the width of the series gap is increased from  $S$  to  $S_1$  by flaring the center strip conductor of the CPW feed line near the gap location. In the third design, the rectangular aperture is replaced by a dumbbell aperture of identical length and width. The design parameters for the antennas tested can be found in the figure caption.

## III. RESULTS AND DISCUSSIONS

The measured return losses for the three different feed configurations are shown in Fig. 2. As indicated in the composite curves, the return losses are improved from  $-8.2$  dB for (a) to  $-13.2$  dB for (b) to  $-16.9$  dB for (c). In the experiment, the short circuited CPW stub length,  $L$ , was set at about one third of a wavelength initially, and by reducing the stub length with an adhesive 3M copper tape, the coupling efficiency was improved by about 1 dB. Results also indicate that the coupling efficiency was improved by more than 3 dB each by using an enlarged series gap or a dumbbell aperture. However, the geometrical change in the series gap and aperture of the feed structure produced a slight change in the resonance frequency.

Manuscript received November 21, 1991.

The authors are with NASA Lewis Research Center, MS 54-8, 21000 Brookpark Road, Cleveland, OH 44135.

IEEE Log Number 9107672.

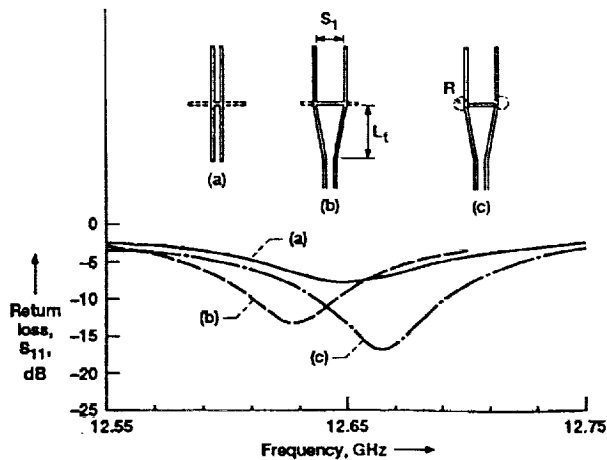


Fig. 2. Measured return vs. frequency for feed structures with (a) a series gap and a rectangular aperture; (b) an enlarged series gap and a rectangular aperture; (c) an enlarged series gap and a dumbbell aperture ( $S_1 = 0.355$  cm; taper length,  $L_t = 0.711$  cm; and radius,  $R = 0.0843$  cm).

Typical measured E- and H-plane patterns for the CPW aperture-coupled microstrip patch antenna are displayed in Figs. 3(a) and 3(b), respectively. The patterns look fairly symmetrical and exhibit a 3-dB beamwidth of about 61 degrees for the E-plane and 50 degrees for the H-plane. The measured front-to-back ratio is about 14 dB, which is typical for an aperture fed antenna configuration.

#### IV. CONCLUSION

A new type of microstrip patch antenna utilizing a series gap in the center strip conductor of the CPW feed line for coupling power to the antenna has been demonstrated. This design allows easy insertion of solid state devices in the CPW feed line, and therefore, has advantages over other CPW aperture coupled microstrip antenna designs in realization of active antennas. Techniques for improving coupling efficiency are described and discussed. Measured results indicate excellent radiation patterns and coupling efficiency.

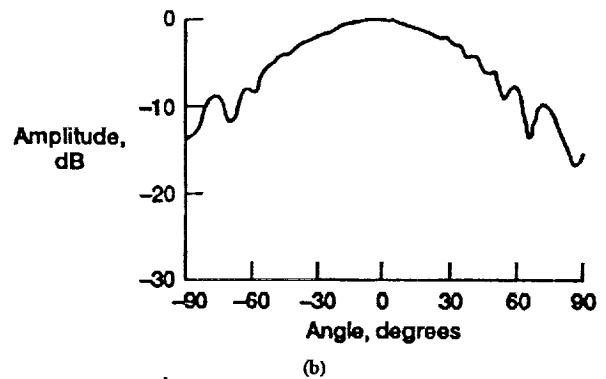
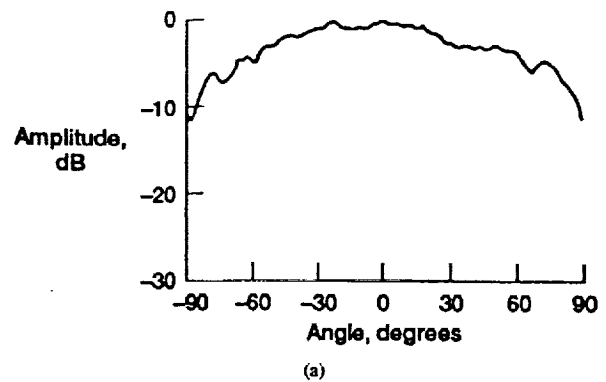


Fig. 3. Measured radiation patterns for the CPW aperture-coupled microstrip patch antenna: (a) E-plane, (b) H-plane.

#### REFERENCES

- [1] W. P. Harokopos, Jr. and P. B. Katchi, "Microstrip antenna fed by a coplanar waveguide feeding structure," *PIERS Proc.*, 1991, p. 360.
- [2] D. M. Pozar and S. D. Targonski, "Improved coupling for aperture coupled microstrip antennas," *Electron. Lett.*, vol. 27, no. 13, pp. 127-129, June 1991.
- [3] R. N. Simons, R. Q. Lee, and G. R. Lindamood, "New coplanar waveguide/stripline feed network for seven patch hexagonal CP subarray," *Electron. Lett.*, vol. 27, no. 6, pp. 533-535, Mar. 1991.
- [4] R. N. Simons, R. Q. Lee, and G. R. Lindamood, "Electromagnetic coupling between coplanar waveguide and microstrip antennas," accepted for publication in the *Microwave Optical Technol. Lett.*, vol. 5, Feb. 1992.

# COPLANAR WAVEGUIDE APERTURE COUPLED PATCH ANTENNAS WITH GROUND PLANE/SUBSTRATE OF FINITE EXTENT

R. N. Simons and R. Q. Lee

*Indexing terms: Antennas, Microstrip, Aperture coupled antennas*

Coplanar waveguide (CPW)/aperture coupled microstrip patch antennas constructed with ground coplanar waveguide (GCPW), finite coplanar waveguide (FCPW) and channelised coplanar waveguide (CCPW) are demonstrated. The measured characteristics show that the CCPW/aperture coupled microstrip patch antenna has the largest bandwidth, whereas the GCPW/aperture coupled microstrip patch antenna has the best front-to-back ratio.

**Introduction:** Coplanar waveguide/aperture coupled microstrip patch antennas have attracted much attention because of their suitable geometry for monolithic integration and their broader bandwidth characteristics. Recently, a coplanar waveguide/aperture coupled microstrip patch antenna has been demonstrated and found to have excellent performance characteristics [1]. In this Letter the relative performance of three CPW/aperture coupled patch antenna configurations are compared. The configurations are constructed using a grounded coplanar waveguide (GCPW), a finite ground plane coplanar waveguide (FCPW) [2] and a channelised coplanar waveguide (CCPW) [3]. The performance parameters investigated include modes supported by the CPW feed structure, coupling efficiency, radiation pattern, front-to-back ratio, and bandwidth.

**Feed design, fabrication and patch integration:** The cross-section view of a GCPW feed is shown in Fig. 1a. The semi-width  $G$  of the upper ground plane of the GCPW is chosen to

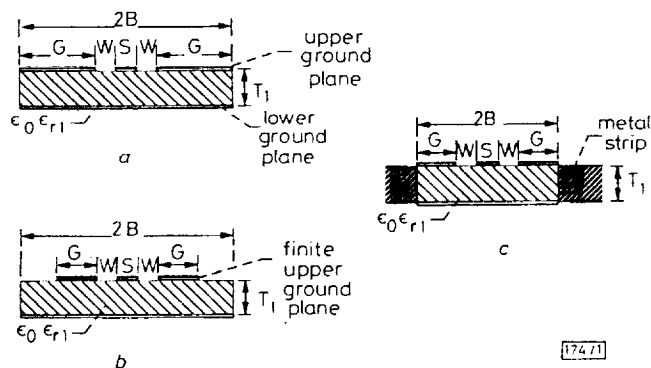


Fig. 1 Cross-section view of coplanar waveguide (CPW)

Feeds:

a Grounded CPW:

$S = 0.762$  mm,  $W = 0.254$  mm,  $G = 24.765$  mm,  $\epsilon_{r1} = 2.2$ ,  $T_1 = 0.508$  mm,  $2B = 50.8$  mm

b Finite CPW:

$G = 3.937$  mm

c Channelised CPW:

$G = 3.937$  mm,  $2B = 9.144$  mm

be greater than the coplanar waveguide wavelength  $\lambda_g$  at the patch resonance frequency. Consequently, the width  $2B$  of the GCPW is greater than  $2\lambda_g$ . The widths of the centre strip conductor and the slot, denoted as  $S$  and  $W$  respectively, are chosen to provide a good impedance match to a coaxial connector.

The cross-section view of a FCPW feed is shown in Fig. 1b. Unlike the GCPW, the upper ground plane of the FCPW is smaller than its lower ground plane. The semi-width  $G$  of the FCPW tested is less than  $0.25\lambda_g$ . The other parameters such as the total width  $2B$ ,  $S$  and  $W$  are the same as for the GCPW.

Fig. 1c shows the cross-section view of the CCPW feed. The entire feed structure is very small, and in this example,  $G$  and  $2B$  are less than  $0.25\lambda_g$  and  $0.5\lambda_g$ , respectively. The widths  $S$  and  $W$  are the same as for the GCPW. Further, along the vertical sides of the substrates, metal strips are placed. These metal strips not only provide mechanical support and heat sinking but form a channel with the lower ground plane that provides additional isolation between feed lines in an array.

The integration of the GCPW feed with a patch antenna is shown in Fig. 2a. The patch is electromagnetically coupled to the feed through an aperture as explained in Reference 1. Integration for the two other feed structures is realised by replacing the GCPW feed substrate with an FCPW or a CCPW feed substrate as shown in Fig. 2b and c, respectively.

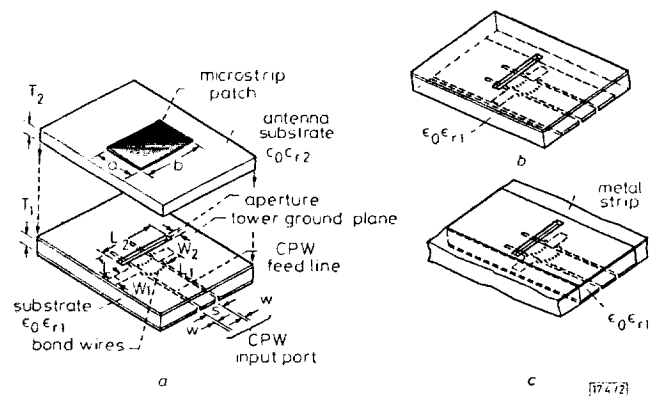


Fig. 2 Schematic diagram showing integration of CPW feeds with microstrip patch antenna

a Grounded CPW:

$W_1 = 0.762$  mm,  $L_1 = 2.794$  mm,  $L = 6.858$  mm

$W_2 = 0.254$  mm,  $L_2 = 6.91$  mm,  $\epsilon_{r2} = 2.2$

$T_2 = 0.254$  mm,  $a = 7.6$  mm,  $b = 11.4$  mm

b Finite CPW

c Channelised CPW

**Experimental antenna performance and discussions:** The measured performance of the antenna in Fig. 2 over the frequency range of 13.0–14.0 GHz is summarised in Table 1. Because the extent of the ground planes in a GCPW feed is several wavelengths, the feed supports parallel plate modes guided between the CPW plane and the lower conducting plane [4]. These spurious modes are manifest as resonance spikes in a  $S_{11}$  measurement made without the patch in place. By reducing the ground plane dimensions as in an FCPW or CCPW feed, the spurious modes are suppressed and give rise to fewer resonance spikes. In all three examples, the measurements show that the magnitude of  $S_{11}$  with the patch in place is better

**Table 1** RELATIVE PERFORMANCE OF CPW/APERTURE COUPLED MICROSTRIP PATCH ANTENNA CONFIGURATIONS

| Transmission line        | GCPW      | FCPW      | CCPW      |
|--------------------------|-----------|-----------|-----------|
| Spurious modes           | Several   | Few       | Few       |
| Coupling to patch        | Excellent | Excellent | Excellent |
| Radiation pattern        | Excellent | Excellent | Excellent |
| Front-to-back ratio (dB) |           |           |           |
| E plane                  | 10.8      | 10.2      | 10.3      |
| H plane                  | 14.0      | 11.1      | 12.4      |
| 2:1 VSWR bandwidth (%)   | 2.3       | 3.6       | 4.2       |
| Fabrication              | Simple    | Simple    | Complex   |
| Cost                     | Low       | Low       | High      |

than  $-20$  dB and therefore the coupling is excellent. The measured radiation patterns at 13.9 GHz for the three examples are shown in Fig. 3. The patterns are observed to be very good. The asymmetry in the E-plane pattern is caused by the proximity of the fixture that is used to support the coaxial connector which brings in the microwave signal. The front-to-back (F/B) ratio, which is defined as the magnitude of the peak radiation in the forward direction to the peak radiation in the backward direction, is observed to be higher for the antenna with the CCPW feed than with the FCPW feed. However, the antenna with the GCPW feed has the highest F/B ratio. This is expected due to higher shielding by the large ground planes of the GCPW feed. Further, the F/B ratios in

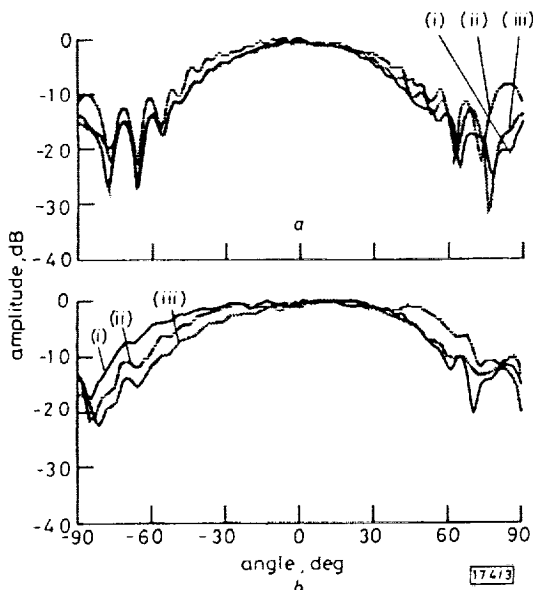


**Fig. 3** Measured radiation pattern of CPW/aperture coupled microstrip patch antenna

- (i) GCPW feed
- (ii) CCPW feed
- (iii) FCPW feed
- a H-plane
- b E-plane

the E and H planes are not equal. This is because the peak backward radiation has different amplitude and occurs at a different angle in the two planes. When compared with a microstrip aperture coupled patch antenna and a probe feed patch antenna, the above feeds have lower F/B ratios as indicated in Table 2.

The measured VSWR bandwidth is higher for the antenna with the FCPW feed than that with the GCPW feed. However, the antenna with the CCPW feed has the highest bandwidth. When compared with other feeding techniques the above feeds have higher bandwidth as indicated in Table 2. Lastly, the fabrications of the GCPW and FCPW feeds are simpler and lower in cost compared to the CCPW feed.

**Table 2** COMPARISON OF CCPW/APERTURE COUPLED PATCH ANTENNA WITH MICROSTRIP/APERTURE COUPLED PATCH ANTENNA AND PROBE FEED PATCH ANTENNA

|                          | CCPW | Microstrip | Probe |
|--------------------------|------|------------|-------|
| Front-to-back ratio (dB) |      |            |       |
| E plane                  | 10.3 | 5.5        | 10.9  |
| H plane                  | 12.4 | 15.1       | 18.8  |
| 2:1 VSWR bandwidth* (%)  | 4.2  | 2.4        | 1.2   |

\* Antenna substrate thickness is 0.254 mm

**Conclusions:** CPW/aperture coupled microstrip patch antennas constructed with GCPW, FCPW and CCPW feeds are demonstrated. The measured characteristics include the radiation pattern, coupling efficiency, bandwidth, and front-to-back ratio. Measurements show that the three examples have excellent radiation pattern and coupling efficiency. Finally, it is observed that the CCPW/aperture coupled microstrip patch antenna has the largest bandwidth while the GCPW/aperture coupled microstrip patch antenna has the best front-to-back ratio.

29th October 1991

R. N. Simons and R. Q. Lee (Mail Stop 54-5, NASA Lewis Research Center, 21000 Brookpark Road, Cleveland, OH 44135, USA)

#### References

- 1 SIMONS, R. N., LEE, R. Q., and LINDAMOOD, G. R.: 'Electromagnetic coupling between coplanar waveguide and microstrip antennas', to be published in *Microwave and Opt. Technol. Lett.*, February 1992, 5
- 2 JANICZAK, B. J.: 'Analysis of coplanar waveguide with finite ground planes', *Arch. Elek. Übertragung. (AEÜ)*, 1984, 38, (5), pp. 341-342
- 3 SIMONS, R. N., PONCHAK, G. E., MARTZAKLIS, K. S., and ROMANOFSKY, R. R.: 'Channelized CPW: discontinuities, junctions, and propagation characteristics'. 1989 IEEE MTT-S Int. Microwave Symp. Dig., Vol. III, pp. 915-918
- 4 JACKSON, R. W.: 'Mode conversion at discontinuities in finite-width conductor-backed coplanar waveguide', *IEEE Trans.*, 1989, MTT-37, (10), pp. 1582-1589

# ELECTROMAGNETIC COUPLING BETWEEN COPLANAR WAVEGUIDE AND MICROSTRIP ANTENNAS

Rainee N. Simons, Richard Q. Lee, and Glenn R. Lindamood  
 NASA Lewis Research Center  
 Cleveland, Ohio 44135

## ABSTRACT

Electromagnetic coupling between coplanar waveguides (CPW) and microstrip patch antennas has been investigated for two feed configurations: (1) direct aperture-coupled feeding of a patch antenna by a CPW feed, and (2) proximity-coupled feeding of a patch antenna by a microstrip line which is aperture coupled to a CPW feed. Results indicate that both feeding approaches are feasible and yield high coupling efficiency.

## KEY TERMS

Coplanar waveguide, aperture-coupled microstrip patch antennas, proximity-coupled microstrip patch antennas

## INTRODUCTION

Electromagnetic coupling is an attractive feeding technique, particularly for large microstrip array antennas. This tech-

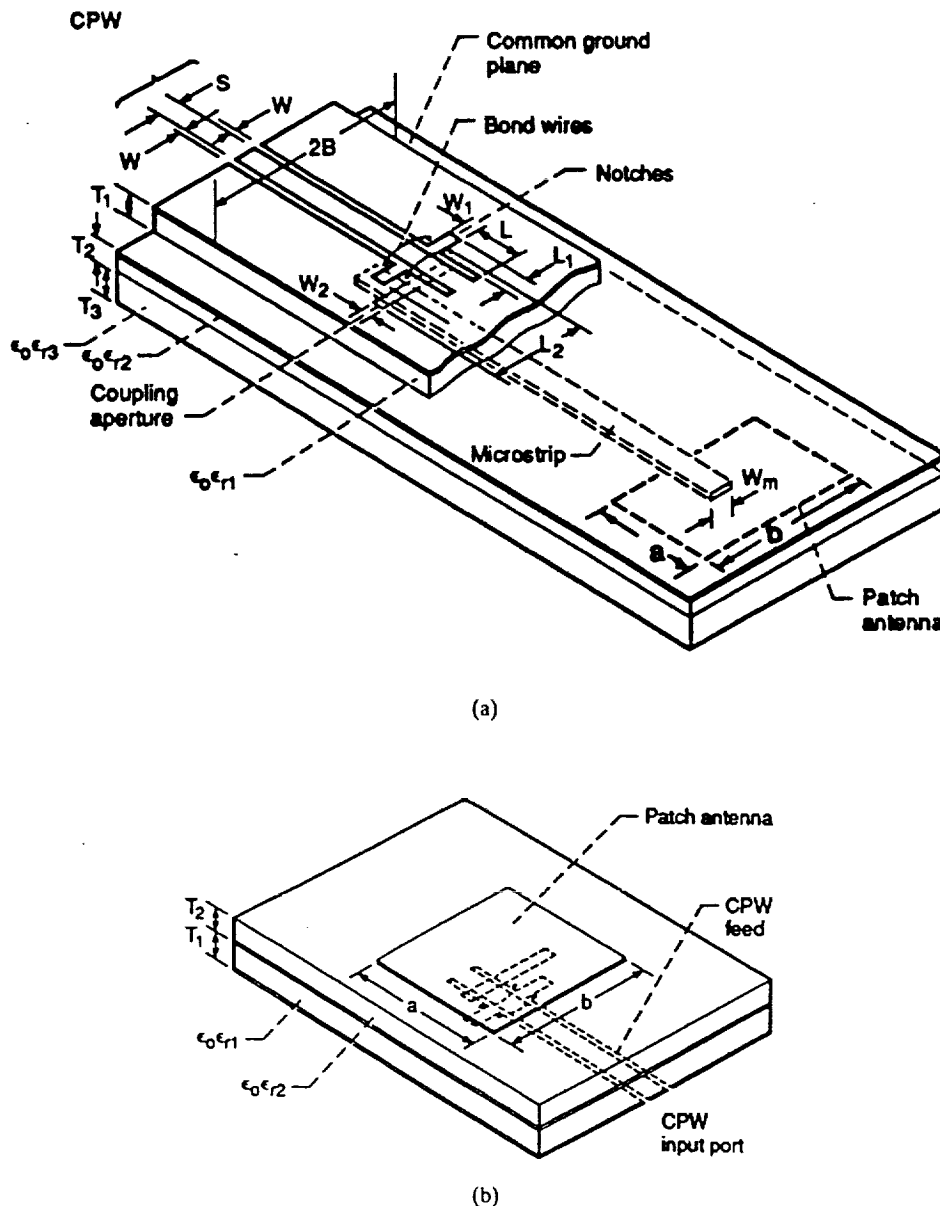


**Figure 1** Schematic illustrating (a) CPW proximity-coupled microstrip patch antenna:  $S = 0.762$  mm,  $W = 0.254$  mm,  $W_1 = 0.762$  mm,  $L_1 = 2.794$  mm,  $L = 6.858$  mm,  $T_1 = 0.508$  mm,  $\epsilon_{r1} = 2.2$ ,  $W_m = 0.77$  mm,  $W_2 = 0.254$  mm,  $L_2 = 6.91$  mm,  $\epsilon_{r2} = 2.2$ ,  $T_2 = 0.508$  mm,  $2B = 10.0$  mm,  $T_3 = 0.254$  mm,  $\epsilon_{r3} = 2.2$ ,  $a = 7.6$  mm,  $b = 11.4$  mm; (b) CPW aperture-coupled microstrip patch antenna:  $\epsilon_{r2} = 2.2$ ,  $T_2 = 0.254$  mm

nique requires no soldering, has wide bandwidths, and allows independent optimization of the antennas and the feed network. Also, since the feed and the antennas are on separate substrates, better isolation between the antennas and the feed network can be obtained. Electromagnetic coupling where the antenna is proximity or aperture coupled to a microstrip line has been demonstrated [1, 2]. Yet electromagnetic coupling between microstrip antennas and coplanar waveguides has received little attention in the literature. As a transmission line, coplanar waveguide offers many advantages over the microstrip line, such as easy shunt or series mounting of active or passive device, and low radiation loss. The use of CPW would greatly facilitate device integration in MMIC phased arrays [3]. This article is concerned with electromagnetic coupling between coplanar waveguide and microstrip patch antennas. In the article, the designs and performance characteristics of a CPW proximity-coupled and a CPW aperture-coupled microstrip patch antenna will be presented and discussed.

### CPW APERTURE COUPLED ANTENNA DESIGN

A CPW proximity-coupled microstrip patch antenna is shown in Figure 1(a). The coupling takes place through an aperture in the common ground plane separating the two transmission lines. The aperture width  $W_2$  of 0.254 mm is chosen for ease of fabrication. A good initial guess for the aperture length  $L_2$  is  $\lambda_{g(\text{slot line})}/2$ , where  $\lambda_g$  is the wavelength of a uniform slot line [4]. This starting value of  $L_2$  is then slightly reduced to account for the slot end effects. The microstrip line is terminated in an open circuit which is approximately  $\lambda_{g(\text{microstrip})}/4$  from the center of the aperture after correcting for the end effects. The other end of the microstrip line is proximity coupled to a rectangular patch antenna with the line extended about half-way into the patch. To improve coupling, a notch of width  $W_1$  and length  $L_1$  is cut out from the CPW ground plane located right above the aperture. The longitudinal distance between the extreme ends of the notches is approximately equal to the aperture length  $L_2$ . The CPW can be terminated in a short circuit or an open circuit at a distance of approximately  $\lambda_{g(\text{CPW})}/2$  or  $\lambda_{g(\text{CPW})}/4$ , respectively, from the center of the notch. A pair of bond wires on either side of the notch is used to suppress any spurious slot modes generated at the discontinuity.

A CPW aperture-coupled microstrip patch antenna is shown in Figure 1(b). The layout and design parameters are identical to the proximity-coupled case except that the patch is directly aperture-coupled to the CPW instead of proximity coupled through a microstrip line. To improve coupling, the aperture is offset by about 3 mm from the center of the patch.

### RESULTS AND DISCUSSIONS

In order to demonstrate good coupling efficiency for the CPW proximity-coupled microstrip patch antenna, the insertion loss ( $S_{21}$ ) between the CPW and the microstrip line, and the return

loss ( $S_{22}$ ) at the CPW port were measured and are shown in Figure 2(a) and 2(b), respectively. The insertion loss, including losses of the coaxial connectors at both ends, is less than 2 dB, and the return loss is better than 12 dB. For the CPW aperture-coupled microstrip patch antenna, the measured input impedance is shown in Figure 3, which also indicates good

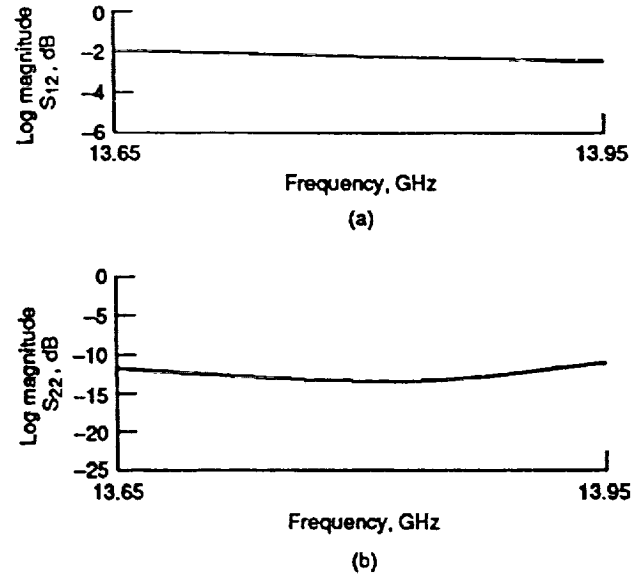
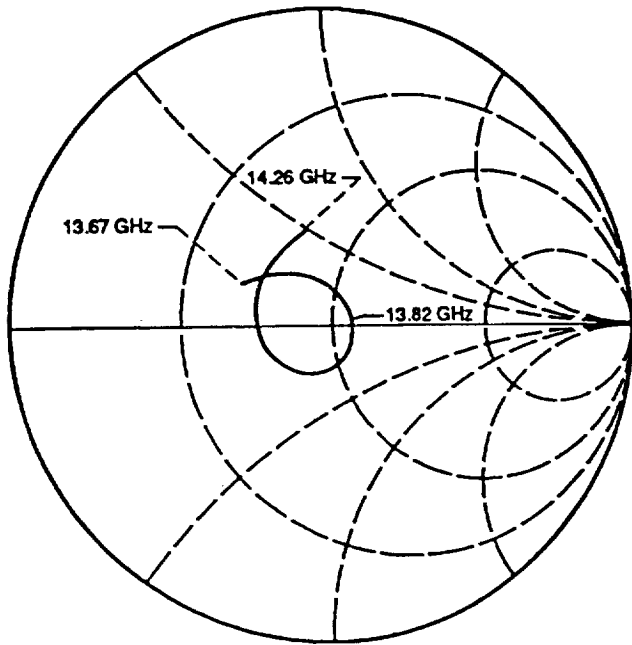
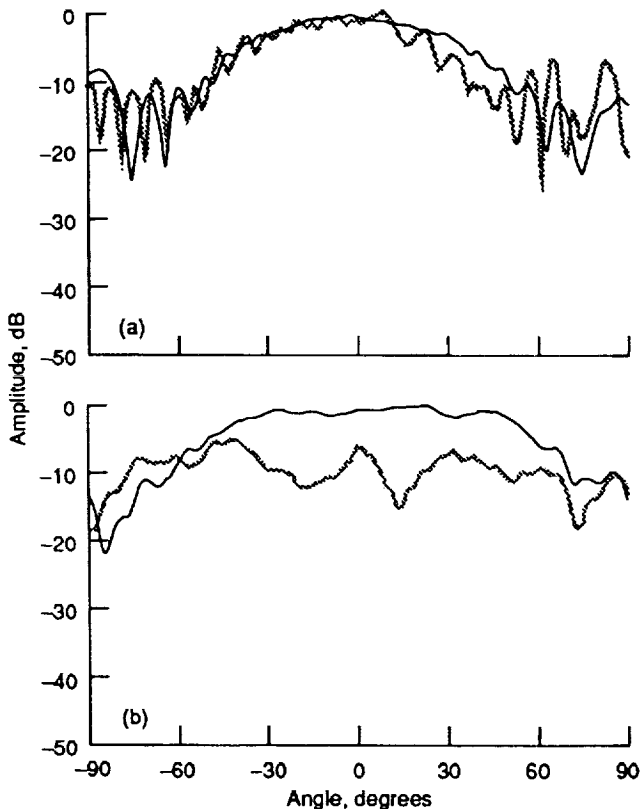


Figure 2 Measured characteristics of the aperture transition between the CPW and the microstrip line: (a) insertion loss and (b) return loss at the CPW port

coupling efficiency. At the best impedance match frequency of 14 GHz, the return loss is greater than 20 dB and the 2:1 VSWR bandwidth is 4.2%. The measured  $H$ - and  $E$ -plane patterns for the CPW aperture-coupled and the CPW proximity-coupled microstrip patch antennas are displayed in Figure 4(a) and 4(b), respectively. The degradation in the radiation patterns of the CPW proximity-coupled patch is due partly to radiation from the aperture adjacent to the patch.



**Figure 3** Measured input impedance of the CPW aperture-coupled microstrip patch antenna



**Figure 4** Measured radiation patterns for the aperture-coupled (solid lines) and proximity-coupled (dashed line) microstrip patch antennas: (a) *H* plane and (b) *E* plane

The measured front-to-back ratios for both antennas are about 14 dB, which is typical for an aperture-fed geometry.

## CONCLUSIONS

Aperture-coupled and proximity-coupled feeding techniques have been demonstrated for coupling microwave power from a CPW to a patch antenna. Both feeding techniques have shown excellent coupling efficiency, and have potential applications for MMIC phased array antennas.

## REFERENCES

1. K. Chang, Ed., *Handbook of Microwave and Optical Components*, Wiley Interscience, New York, 1989, Vol. 1, Chap. 13, p. 789.
2. J. A. Navarro, K. Chang, J. Tolleson, S. Sanzgiri, and R. Q. Lee, "A 29.3 GHz Cavity-Enclosed Aperture-Coupled Circular Patch Antenna for Microstrip Circuit Integration," *IEEE Microwave Guide Wave Lett.*, Vol. 1, No. 7, July 1991, pp. 170-171.
3. C. P. Wen, "Coplanar Waveguide: A Surface Strip Transmission Line Suitable for Nonreciprocal Gyromagnetic Device Applications," *IEEE Trans. Microwave Theory Tech.*, Vol. MTT-17, No. 12, Dec. 1969, pp. 1087-1090.
4. R. N. Simons, "Suspended Slot Line Using Double Layer Dielectric," *IEEE Trans. Microwave Theory Tech.*, Vol. MTT-29, No. 10, Oct. 1981, pp. 1102-1107.

Received 9-19-91

Microwave and Optical Technology Letters, 5/2, 60-62  
 © 1992 John Wiley & Sons, Inc.  
 CCC 0895-2477/92/\$4.00



# NEW TECHNIQUES FOR EXCITING LINEARLY TAPERED SLOT ANTENNAS WITH COPLANAR WAVEGUIDE

R. N. Simons, R. Q. Lee and T. D. Perl

*Indexing terms: Waveguides, Slot antennas, Antenna feeders*

Two new techniques for exciting a linearly tapered slot antenna (LTSA) with coplanar waveguide (CPW) are introduced. In the first approach, an air bridge is used to couple power from a CPW to an LTSA. In the second approach, power is electromagnetically coupled from a finite CPW (FCPW) to an LTSA. Measured results at 18 GHz show excellent return loss and radiation patterns.

**Introduction:** Linear tapered slotline antennas (LTSA) are useful in applications which require high element gain, narrow beam width and wide bandwidth [1]. Recently an LTSA excited by a CPW has been reported [2]. In this feed, the centre strip conductor of the CPW extends across the slotline orthogonally and meets the opposite slot edge. LTSA with a coplanar waveguide feed (CPW) have the advantages of reduced feed radiation loss, ease of monolithic microwave integrated circuit (MMIC) integration and fast an inexpensive on-wafer characterisation using CPW wafer probing equipment.

This letter demonstrates two new techniques for exciting LTSA with CPW feeds. The first is to directly couple a CPW to the LTSA through an air bridge (Fig. 1). Direct coupling requires the feed and antenna to be on the top side of the board, which makes fabrication simple. The second method is to electromagnetically couple a finite CPW (FCPW) to the LTSA (Fig. 2). Electromagnetic coupling does not require a direct solder connection and is therefore more reliable. Furthermore, the use of FCPW suppresses spurious modes

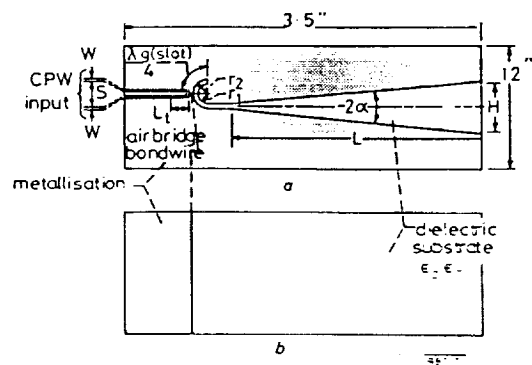


Fig. 1 Schematic diagram illustrating CPW feed directly coupled by air bridge to LTSA

- a Top metallisation,  $S = 0.0762$  cm  
 $W = 0.0254$  cm
- b Bottom metallisation

excited between the CPW plane and the lower conducting plane [3].

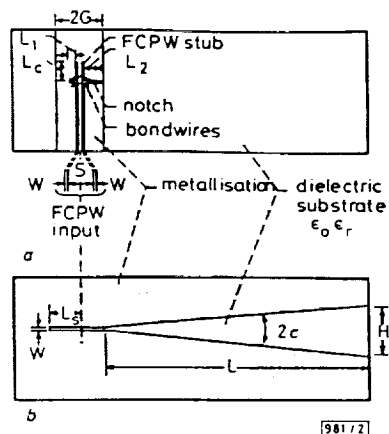


Fig. 2 Schematic diagram illustrating FCPW feed electromagnetically coupled to LTSA which is on opposite side of substrate

- a Top metallisation,  $S = 0.0762$  cm  
 $W = 0.0254$  cm
- b Bottom metallisation

### Feed design and fabrication

(a) **Air bridge feed:** A CPW directly coupled to an LTSA by an air bridge is shown in Fig. 1. A 0.00508 cm wide gold ribbon bridges over the slotline connecting the open end of the CPW to the opposite edge of the slotline. In this feed the CPW is terminated in a tapered open circuit of length  $L_1$ , which is about  $\lambda_{g(cpw)}/2$ , where  $\lambda_g$  is the guide wavelength at the centre frequency  $f_0$  of 18 GHz. The width  $S$  of the CPW centre strip conductor at the open end is 0.031 cm. The slotline of the LTSA is terminated in a curved short circuit of length  $\lambda_{g(slot)}/4$  beyond the bridge. The width of the slotline is the same as that of the CPW which is indicated as  $W$ . The radii of curvature  $r_1$  and  $r_2$  of the slotline are approximately  $\lambda_{g(slot)}/6$ .

(b) **Electromagnetically coupled feed:** In this feed network the FCPW feed and the LTSA are fabricated on opposite sides of a substrate as illustrated in Fig. 2a and b, respectively. The FCPW and the slotline cross each other at right angles. To improve coupling two notches of width  $W$  and lengths  $L_1$  and  $L_2$  are cut out from the FCPW ground plane located right above the slotline of the LTSA. The ratio of the lengths  $L_2/L_1$  is about 3 and  $L_2$  is approximately  $0.25\lambda_{g(slot)}$ . The width  $2G$  of the ground planes is about  $0.65\lambda_{g(cpw)}$ . The FCPW is terminated in a short circuit at a distance of  $L_c$  which is approximately  $0.4\lambda_{g(cpw)}$  from the centre of the notch. A pair of bondwires on either side of the notch is used to suppress any spurious slot modes generated at the discontinuity. The slotline is terminated in a short circuit at a distance  $L$ , which is  $\lambda_{g(slot)}/4$  from the notch.

**LTSA design and fabrication:** The LTSA is formed by gradually flaring the width of the slotline by an angle  $2\alpha$ . In general, a symmetric beam is required to illuminate a reflector for maximum aperture efficiency; this is achieved by choosing  $2\alpha$  equal to  $10.6^\circ$  [1]. Similarly, to optimise the radiation efficiency of the LTSA,  $H$  is chosen to be  $0.75\lambda_0$ , where  $\lambda_0$  is the free space wavelength at  $f_0$ . The length  $L$  of the antenna as determined by  $\alpha$  and  $H$  is  $4.1\lambda_0$ . The circuits are fabricated on 0.0508 cm thick RT, Duroid 5880 ( $\epsilon_r = 2.2$ ) substrates.

**Experimental results:** The measured return loss for the directly coupled and the electromagnetically coupled feed are shown in Fig. 3a and b, respectively. These measurements show that the return loss is better than  $-10$  dB (2:1 VSWR) and the bandwidths are 3.7 and 6.0 GHz for the two feeds, respectively. As expected, the electromagnetically coupled antenna exhibits the greater bandwidth. The measured E- and H-plane radiation patterns for the LTSA with the two feed networks are shown in Fig. 4a and b, respectively. The patterns are nearly identical because identical antenna designs are used for both feed networks.

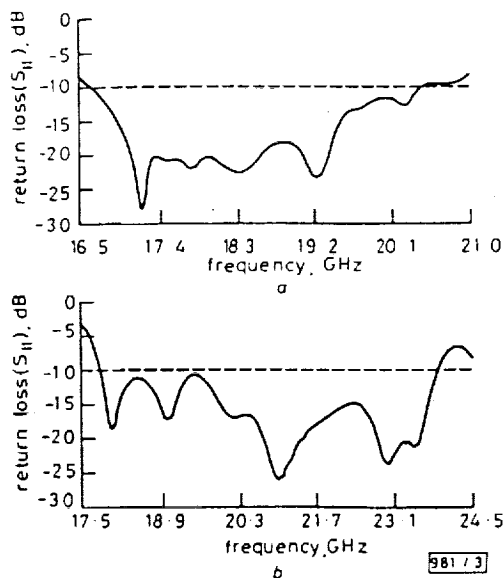


**Fig. 3** Measured return loss at CPW port  
 a Air bridge feed  
 b Electromagnetically coupled feed

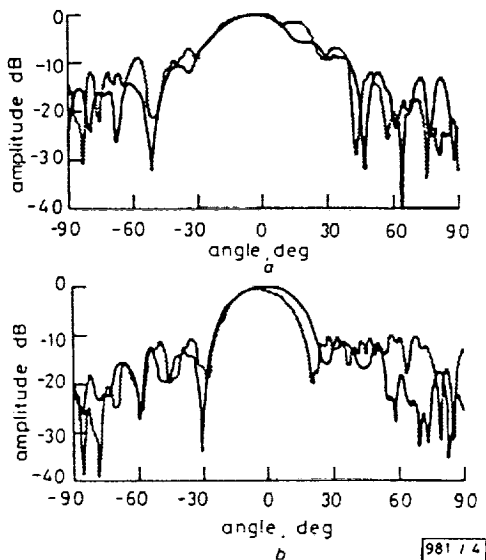


**Fig. 4** Measured radiation pattern of LTSA with air bridge and electromagnetically coupled feed  
 a E Plane  
 b H Plane  
 — air bridge  
 - - - electromagnetically coupled

**Conclusions and discussions:** Two new feeding techniques for the LTSA have been presented. Both yield excellent radiation patterns over their bandwidths. The return loss shows, however, that the CPW electromagnetically coupled LTSA has broader bandwidth than the CPW directly coupled LTSA.

31st January 1992

R. N. Simons, R. Q. Lee and T. D. Perl (Mail Stop 54-5 NASA Lewis Research Center, 21000 Brookpark Road, Cleveland, OH 44135, USA)

**References**

- 1 YNGVESSON, K. S., *et al.*: 'The tapered slot antenna—a new integrated element for millimeter-wave applications', *IEEE Trans.*, 1989, MTT-37, (2), pp. 365–374
- 2 NESIC, A.: 'Endfire slot line antennas excited by a coplanar waveguide', *IEEE AP-S Int. Symp. Dig.*, 1991, pp. 700–702
- 3 SIMONS, R. N., and LEE, R. Q.: 'Coplanar waveguide aperture coupled patch antennas with ground plane/substrate of finite extent', *Electron. Lett.*, 1992, 28, (1), pp. 75–76

Ka-BAND DUAL FREQUENCY ARRAY FEED FOR A LOW COST  
ACTS GROUND TERMINAL

Richard Q. Lee\*, Rainee N. Simons and Ajit K. Sil  
NASA Lewis Research Center  
21000 Brookpark Road  
Cleveland, OH 44135

ABSTRACT:

Because of low cost and ease of fabrication, microstrip arrays are attractive as feeds for reflector antenna systems. This paper describes the development of a 4x4 microstrip array which will be used as a feed for a low cost ACTS ground terminal. The array feed consisted of four 2x2 subarrays is fed with coplanar waveguide power dividing networks. The patch radiator is designed to excite two orthogonal, linearly polarized wave at Ka-band frequencies (around 20 and 30 GHz). In the paper, test results for the developed array will be presented and discussed.

I. INTRODUCTION:

The launching of NASA's Advanced Communication Technology Satellite (ACTS) in 1992 will provide a unique opportunity for the industry and government to experiment with and validate the new technologies to be flown onboard the ACTS spacecraft. One of the experiments currently contemplated by NASA is to demonstrate a low cost ground terminal (less than \$500) for establishing a communication link with ACTS. A voice link of 4.8 Kbs will connect the low cost ground terminal to the ACTS ground-based link evaluation terminal (LET) via one of the fixed beam from ACTS. The antenna for the proposed ground terminal consists of a prime focus offset-fed 0.6 m reflector and a 4x4 microstrip array feed. This antenna provides simultaneous operation across the receive (19.38-20.28 GHz) and transmit (29.1-30.0 GHz) frequency bands with linear

polarization. Mechanical scan and manual adjustment is used for beam and polarization alignment. Of the antenna system, the 0.6 m reflector can be purchased for about \$100, and the 4x4 array feed will be developed by NASA. This paper will describe the baseline design of the Ka-band 4x4 array feed. Results for the array performance will also be presented and discussed.

II. SYSTEM REQUIREMENTS:

For uplink at 29.6 GHz and downlink at 19.9 GHz, the 0.6 m reflector with 55% efficiency has a gain of 42.8 dB and 39.3 dB respectively. To complete the link with adequate margin, the required EIRP per carrier for uplink is 40.2 dBW and the required G/T for downlink is 12.0 dB/K. These results are obtained based on a feed loss of -2.5 dB and rain attenuation of -23.0 dB. The surface tolerance for the 0.6 m reflector is 0.01 in. rms which could result in a loss of 0.5 dB in antenna gain.

III. ARRAY DESIGN:

The proposed 4x4 array has rectangular microstrip patch elements which are arranged in rectangular lattice with  $\lambda/2$  element spacing (free-space wavelength). Coplanar waveguide (CPW) power dividers are used to distribute RF power to the array. All elements in the array are fed in phase and with equal amplitude to produce a beam in the broadside direction.

The microstrip patch used in the

experiment is shown in Figure 1(a). The patch with dimensions (a,b) is etched on 0.508 cm RT/Duroid substrate. The patch is designed for dual frequency (20-30 GHz) operation with a single feed at  $(a_0, b_0)$  to excite both the  $TM_{01}$  and  $TM_{10}$  modes. These modes generate two orthogonal, linearly polarized (LP) waves. The single feed approach requires only one RF power distribution network for both receive and transmit operations.

The feed position chosen for best impedance match with the feeding network is determined by computing the input impedance of each resonance mode at the specified feed position. For thin substrates, the patch antenna can be modelled as a cavity which consists of the patch, the ground plane and a magnetic wall along the perimeter [1]. The interior fields of the antenna are characterized in terms of a discrete set of modes, and can be replaced by a radiating magnetic current source along the perimeter as shown in Figure 1(b). The input impedance can then be computed in terms of the electromagnetic energy stored in the antenna, power dissipated in copper and dielectric, and losses due to surface wave and radiation. The input impedance computed by the cavity model approach are found to be in good agreement with measured results [1].

Using the cavity model approach, the input impedance can be computed for any given feed position and patch geometry. In general, the input impedance can be varied over a wide range by changing the feed positions along the edge of the excited mode (x-axis for  $TM_{10}$  mode), but very little along the radiating edge (y-axis) [1]. Thus, in determining the feed position for dual mode operation, the feed position for the  $TM_{10}$  mode is optimized first by varying the feed position along the x-axis. Then, the feed position is varied along the y-axis to optimize the impedance match for the  $TM_{01}$

mode. Since the input impedance at any given feed position is mode dependent, it is very difficult to achieve impedance match for both the  $TM_{01}$  and  $TM_{10}$  modes with a single feed point. Therefore, a compromised feed position where both modes can be strongly excited must be used. To validate the design approach, a dual frequency rectangular patch of dimensions  $a=.48\text{cm}$  and  $b=.3\text{ cm}$  has been designed, fabricated and tested at ka-band frequencies.

#### IV. POWER DIVIDER DESIGN ARCHITECTURE:

Figure 2 shows the cross sectional view of the 4x4 microstrip patch array constructed on a multilayer Duroid substrate. The 4x4 array is made up of four 2x2 subarray with each subarray fed by a 1:4 CPW power divider as shown in Figure 3. The power divider circuits and the patches are fabricated on opposite sides of a 20 mil thick Duroid substrate. The detailed layout of the 1:4 CPW power divider used in the experiment is shown in Figure 4. As indicated, the patches are electrically connected to the output ports of the power divider by probe couplers. To provide proper impedance match, the center conductor strips of the CPW lines are tapered toward the intersection. Furthermore, the output ports of the power divider are terminated in short tuning stubs.

The four subarrays are then excited by another 1:4 CPW power divider constructed on a second Duroid substrate. This substrate rests on top of the antenna substrate to form a multilayer feeding network. A novel coax-to-CPW nonplanar transition will be used to couple RF power to and from the array. The coaxial-to-CPW junction is formed by the intersection of four CPW lines with a coaxial cable whose outer conductor is slotted to form four coupled transmission lines. The

center pin of the coaxial line meets the intersecting CPW center conductor and the four outer conductors meet the CPW ground planes. A circulator is used to separate the transmit and receive signals. Isolation between the transmit and receive ports is better than 20 dB. Details for the design of the coax-to-CPW transition, CPW power dividers and the post coupler are described in [2], [3].

## V. RESULTS AND DISCUSSION:

The impedance and the return loss characteristics of the patch were measured using a HP8510 automatic network analyzer. Figure 5 shows the measured return loss which indicates resonances at 19.8 and 29.4 GHz. The return losses are 11.6 dB at 19.8 GHz and 6.9 dB at 29.4 GHz indicating good coupling efficiency. Figure 6 shows the measured impedance vs. frequency on a Smith chart. As indicated by the curves, the resistive parts of the impedance is 30.9 ohms at 19.8 GHz and 23.1 ohms at 29.2 GHz. Better impedance match for both frequency can be achieved with a proper choice of feed position. The measured E- and H-plane patterns at 19.80 and 29.98 GHz are shown in Figure 7. The patterns are symmetrical at both frequencies.

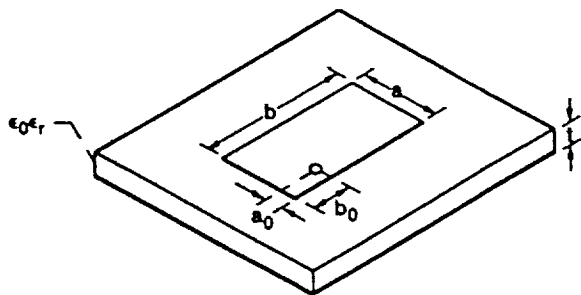
Figure 8 shows the measured return loss of a 2x2 microstrip subarray which was constructed based on the designs of the patch and power divider described above. The return losses are 15.38 dB at 19.48 GHz and 25.7 dB at 30.02 GHz. The H-plane patterns for the 2x2 subarray are display in Fig. 9. The patterns measured at 19.70 and 29.98 GHz are generally symmetrical and in agreement with computed patterns for a 2x2 subarray. Additional efforts are required to optimize the subarray performance. This modular subarray will be used as building block for the 4x4 dual frequency array feed. Results for the finished array will be reported at the conference.

## VI. CONCLUSION:

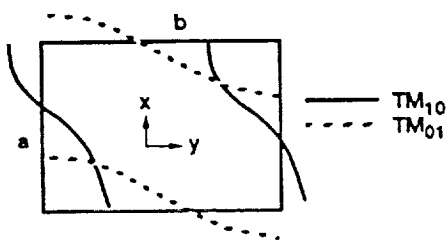
This paper reports the development of a Ka-band dual frequency array feed for a low cost ACTS ground terminal. The array has patch elements with a single feed to excite both the  $TM_{01}$  and  $TM_{10}$  modes. The patch antennas are fed by a multilayer coplanar waveguide power dividing network. A modular 2x2 subarray has been breadboarded and tested. Measured impedance and radiation patterns demonstrate good array performance indicating the validity of such an approach.

## REFERENCE

- [1] W. F. Richards, Y. T. Lo and D. D. Harrison, "An Improved Theory for Microstrip Antennas and Applications," IEEE Trans. Antennas & Propagation, Vol. AP-29, No.1, Jan. 1981, p.38
- [2] R. N. Simons and G. E. Ponchak, "Coax-to-Channelized Coplanar Waveguide In-Phase, N-Way, Radial Power Divider," Elect.Lett., Vol. 26, No.11, May 1990, pp.754-756.
- [3] R. N. Simons, R. Q. Lee and G. R. Lindamood, "A New Coplanar Waveguide/Stripline Feed Network for a Seven Patch Hexagonal CP Subarray," Elect. Lett., Vol. 27, No. 6, March 1991, pp.533-535.



(a)  $a = .30$  cm,  $b = .48$  cm,  $a_0 = .085$  cm,  $b_0 = .185$  cm,  $\epsilon_r = 2.2$ ,  $t = .508$  cm.



(b) Magnetic current distribution.

Figure 1.—Microstrip patch used in the experiment.

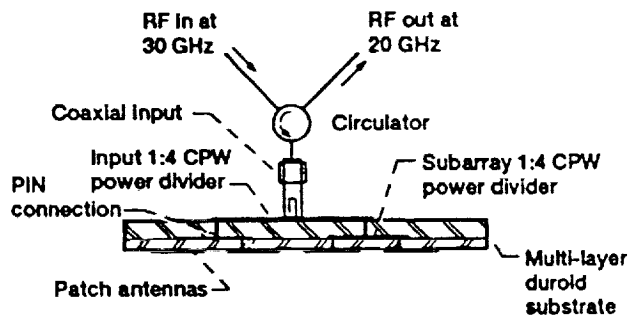


Figure 2.—Cross sectional view of the 4 x 4 microstrip patch array constructed on a multilayer dielectric substrate.

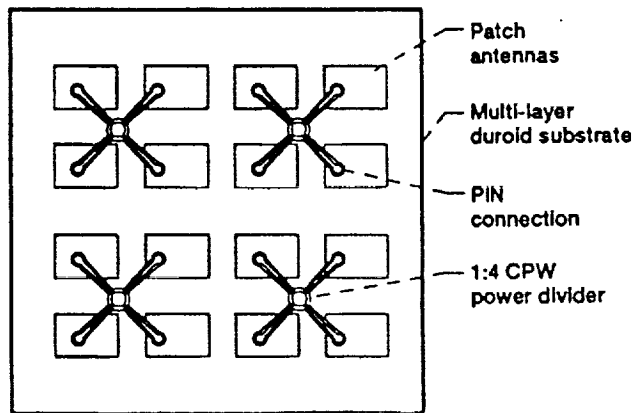


Figure 3.—Plan view illustrating the CPW 1:4 power divider for each of the four 2 x 2 subarrays.

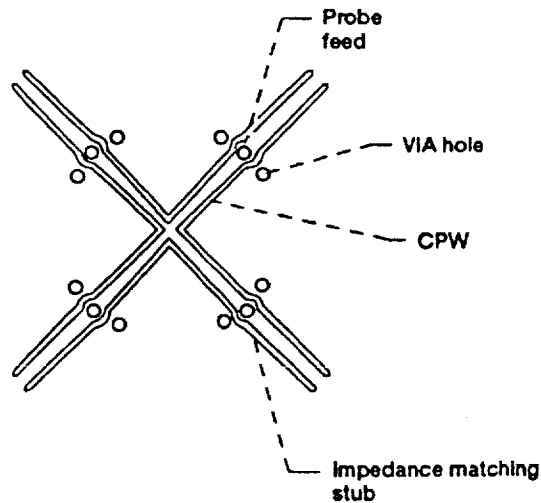


Figure 4.—Detailed layout of the CPW 1:4 power divider.

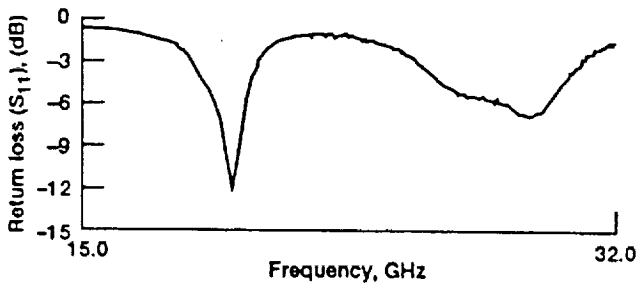


Figure 5.—Measured return loss ( $S_{11}$ ) at the coaxial input port which indicates the  $TM_{01}$  and  $TM_{10}$  resonances.

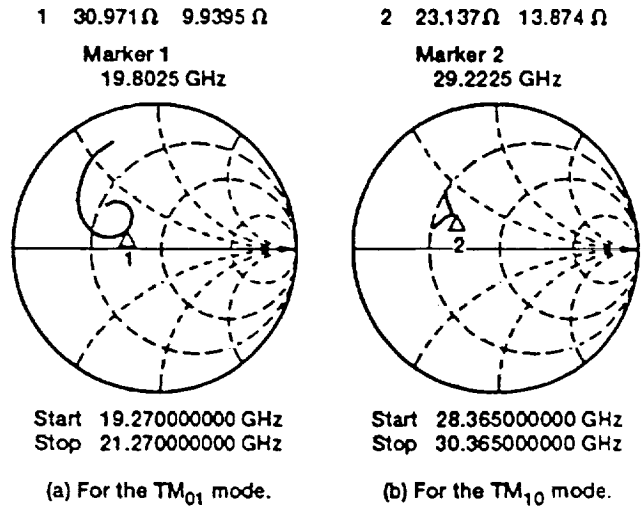


Figure 6.—Measured input impedance of the antenna as seen at the coaxial port.

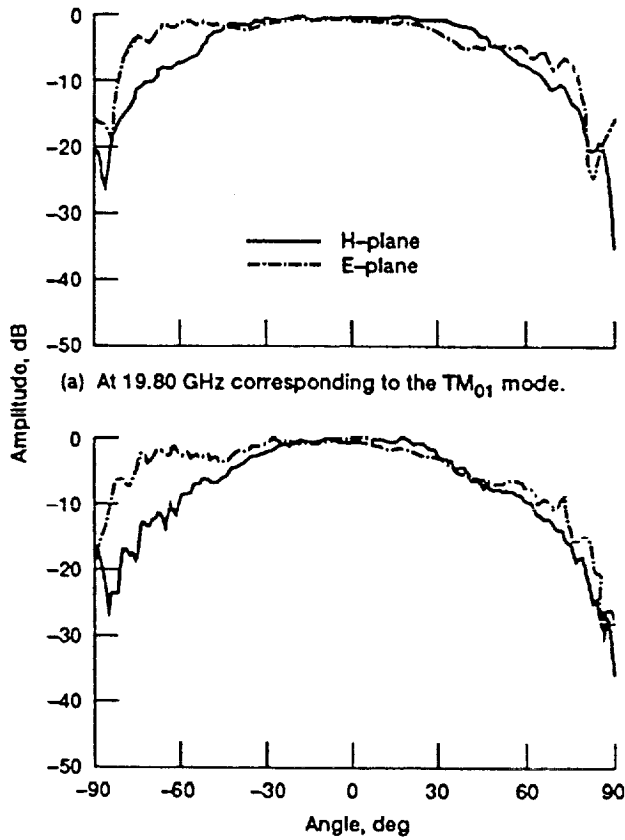


Figure 7.—Measured patch far field patterns.

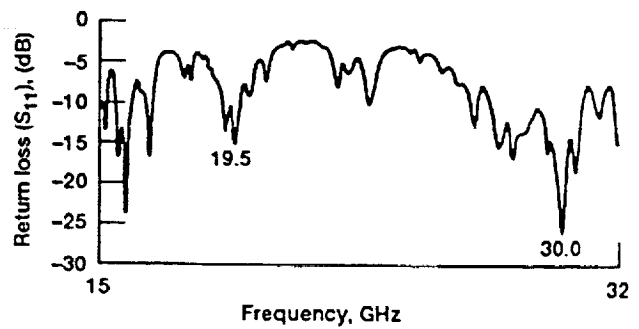


Figure 8.—Measured return loss ( $S_{11}$ ) for the 2 x 2 subarray.

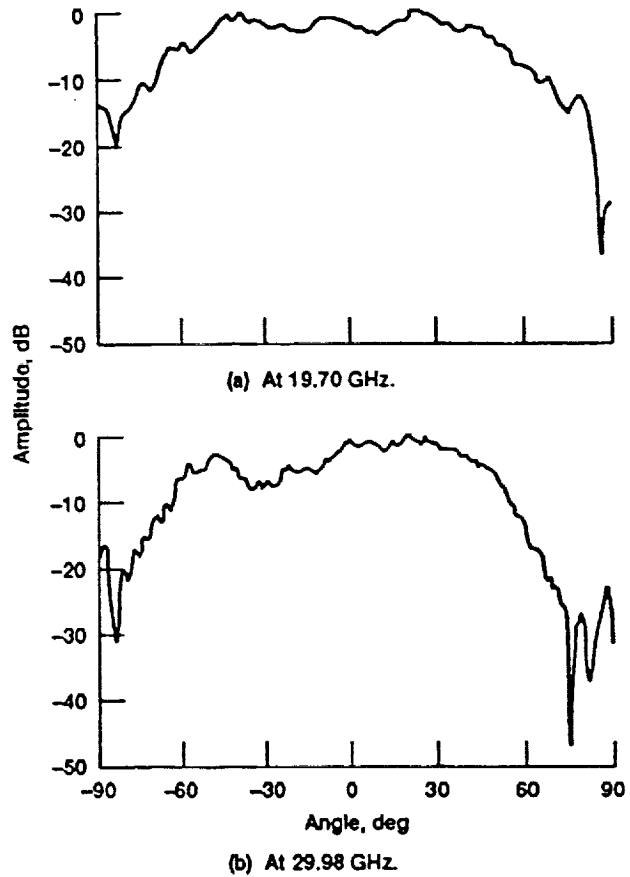


Figure 9.—Measured 2 x 2 subarray H-plane radiation.

## COPLANAR WAVEGUIDE FEEDS FOR PHASED ARRAY ANTENNAS

Rainee N. Simons  
Sverdrup Technology, Inc.  
Lewis Research Center Group  
Brook Park, Ohio 44142

and

Richard Q. Lee  
National Aeronautics and Space Administration  
Lewis Research Center  
Cleveland, Ohio 44135

### Abstract

This paper presents the design and performance of the following CPW microwave distribution networks for linear as well as circularly polarized microstrip patches and printed dipole arrays: (1) CPW/Microstrip Line feed, (2) CPW/Balanced Stripline feed, (3) CPW/Slotline feed, (4) GCPW/Balanced coplanar stripline feed, and (5) CPW/Slot coupled feed. Typical measured radiation patterns are presented, and their relative advantages and disadvantages are compared.

### Introduction

Coplanar waveguide (CPW) is a transmission line which consists of a center strip and a semi-infinite ground plane on either side of it<sup>1</sup> as shown in Fig. 1. This type of waveguide offers several advantages over conventional microstrip line, namely, it facilitates easy shunt as well as series mounting of active and passive devices; it eliminates the need for wraparound and via holes, and it has a low radiation loss. Another important advantage of CPW which has recently emerged is that CPW circuits render themselves to fast and inexpensive on-wafer characterization at frequencies as high as 50 GHz.<sup>2</sup> Lastly, since the RF magnetic fields in the CPW are elliptically polarized,<sup>3</sup> nonreciprocal components such as ferrite circulators and isolators<sup>4</sup> can be efficiently integrated with the feed network. These as well as other advantages make CPW useful for a MMIC based microwave distribution network. Grounded CPW (GCPW) is a variant of CPW which incorporates an additional ground plane on the back side of the substrate<sup>5</sup> as shown in Fig. 1. This additional ground plane can serve as a heat sink and provide mechanical strength. In addition, the ground plane serves as a shield between stacked antenna boards to improve isolation.

Several CPW fed antennas have been reported in the literature. A GCPW fed coplanar stripline antenna constructed by widening the center strip of the GCPW to form a rectangular patch (Fig. 2(a)) has been reported.<sup>6</sup> This antenna produces a linearly polarized far field radiation pattern in a direction normal to the plane of the substrate.

CPW fed slot antennas which are the complement to printed dipole antennas (Fig. 2(b)) have also been reported.<sup>7</sup> This antenna also radiates in a direction normal to the plane of the substrate.

This paper presents the design and performance of the following CPW microwave distribution networks for linear as well as circularly polarized microstrip patches and printed dipole arrays: (1) CPW/Microstrip Line feed, (2) CPW/Balanced Stripline feed, (3) CPW/Slotline feed, (4) GCPW/Balanced coplanar stripline feed, and (5) CPW/Slot coupled feed. Typical measured radiation patterns are presented, and their relative advantages and disadvantages are compared.

### CPW Microwave Distribution Network Design

#### Coplanar Waveguide/Microstrip Line Feed

A CPW to microstrip line feed with post coupler<sup>8</sup> is shown in Fig. 3. The CPW and the microstrip line share a common ground plane that has an aperture. The coupler is formed by a metal post which passes through the aperture connecting the strip conductors of the CPW and the microstrip line. A pair of wire bonds located adjacent to the post tie the CPW ground planes and the microstrip ground planes to a common potential. The diameters of the aperture and the metal post were experimentally optimized to obtain the best insertion loss characteristics. The advantage of this type of feed is that the thickness and relative permittivity of the dielectric substrates for the feed network and the antenna can be independently chosen. This allows the individual components to be optimized for the best performance.

#### Coplanar Waveguide/Balanced Stripline Feed

A CPW to balanced stripline feed also makes use of a post coupler<sup>9</sup> as illustrated in Fig. 4. The mechanical features of the coupler is similar to that described above. This coupler in addition uses a tapered stub to improve the bandwidth of the device. The advantage of this feed is similar to that of the previous example.

### Coplanar Waveguide/Slotline Feed

A CPW to slotline feed<sup>10</sup> which uses a nonplanar CPW T-junction is illustrated in Fig. 5. The circuit is formed when a CPW on a separate substrate is placed perpendicular on the CPW of the CPW/Slotline feed network. The advantage of this type of feed is that it eliminates the need for direct connection between the feed line and the feed network of the array module.

### Grounded Coplanar Waveguide/Balanced Coplanar Stripline Feed

Figure 6 shows a GCPW to balanced coplanar stripline feed.<sup>11</sup> Since the GCPW is an unbalanced structure, the transition to a balanced coplanar stripline requires a balun.<sup>12</sup> At the unbalanced end, currents of equal magnitudes but opposite direction flow in the center strip conductor 2 and in the ground planes 1 and 3 of the GCPW. At the balanced end, currents of equal magnitude but opposite in direction flow in the strip conductors 2 and 3 of the coplanar stripline. The short circuit placed between conductors 1 and 2 at the balanced end results in an open circuit between the conductors a quarter wavelength away at the unbalanced end forcing all currents to flow between conductors 2 and 3.

In addition, the balun also provides impedance transformation. This transformation ratio is determined by the characteristic impedance of the coplanar stripline formed by conductors 2 and 3. This is because all of the microwave energy propagates through this section of the transmission line. The advantage of this type of feed is that it allows construction of end fire arrays which are necessary for building large two-dimensional phased arrays. The disadvantage is that it requires a bond wire to tie conductors 1 and 3 at equal potential which might impact reliability.

### Coplanar Waveguide/Slot Coupled Feed

This circuit is formed by etching a narrow resonant slot in the bottom ground plane of a GCPW. The slot is oriented symmetrically and transverse to the center strip conductor of the GCPW. The advantage of this type of feed is that the microstrip patch antennas can be electromagnetically coupled to the feed through the aperture thus making integration easy.

### Coplanar Waveguide Feed System Performance and Antenna Integration

The measured return loss ( $S_{11}$ ) and insertion loss ( $S_{21}$ ) of the CPW/Microstrip line post coupler is shown in Fig. 7. The return loss and insertion loss are better than 10 and 1 dB, respectively, over a wide band of frequencies extending from 0.045 to 6.5 GHz. Figure 8 schematically illus-

trates the integration of a rectangular patch antenna with the feed.

The measured return loss ( $S_{11}$ ) and insertion loss ( $S_{21}$ ) of the CPW/Balanced stripline post coupler is shown in Fig. 9. The return loss and insertion loss are better than 17 and 0.25 dB at the design frequency of 2.2875 GHz. Figures 10(a) and (b) present the proof-of-concept model of a seven patch hexagonal circularly polarized (CP) subarray with the above feed system.

The above are typical characteristics of the feeds discussed in the previous section and the characteristics of the other feeds will be presented at the conference.

### Far Field Radiation Patterns of the Antennas

The measured far field radiation pattern of the microstrip patch antennas shown in Fig. 8 are presented in Fig. 11. The radiation is linearly polarized and is parallel to the plane of the antenna.

The measured far field radiation patterns of the CP subarray shown in Fig. 10 is presented in Fig. 12. These patterns were measured at 2.325 GHz. The on-axis axial ratio for the LHCP is 1.5 and 3 dB beam widths are 36° in both planes of the subarray. The gain of the subarray as determined from the beam widths is 13 dB. The measured return loss at the coaxial input port of the subarray is better than 10 dB at 2.325 GHz.

The above are typical measured radiation patterns of the antennas investigated and more results will be presented at the conference.

### Conclusions and Discussions

The paper presents the design and performance of several CPW microwave distribution networks which have potential applications in phased arrays. Typical measured far field radiation patterns of several antennas with the above feeds have been presented and discussed.

### References

1. Wen, C.P., "Coplanar Waveguide: A Surface Strip Transmission Line Suitable for Nonreciprocal Gyromagnetic Device Applications," *IEEE Transactions on Microwave Theory and Techniques*, Vol. MTT-17, No. 12, Dec. 1969, pp. 1087-1090.
2. Jones, K.E., Strid, E.W., and Gleason, K.R., "mm-Wave Wafer Probes Span 0 to 50 GHz," *Microwave Journal*, Vol. 30, No. 4, Apr. 1987, pp. 177-183.
3. Simons, R.N. and Arora, R.K., "Coupled Slot Line Field Components," *IEEE Transactions on Microwave Theory and Techniques*, Vol. MTT-30, No. 7, July 1982, pp. 1094-1099.

4. Koshiji, K. and Shu, E., "Circulators Using Coplanar Waveguide," *Electronics Letters*, Vol. 22, No. 19, Sept. 11, 1986, pp. 1000-1002.
5. Shih, Y.C. and Itoh, T., "Analysis of Conductor-Backed Coplanar Waveguide," *Electronics Letters*, Vol. 18, No. 12, June 10, 1982, pp. 538-540.
6. Greiser, J.W., "Coplanar Stripline Antenna," *Microwave Journal*, Vol. 19, No. 10, Oct. 1976, pp. 47-49.
7. Nestic, A., "Printed Slotted Array Excited by a Coplanar Waveguide," *12th European Microwave Conference Digest*, Microwave Exhibitions and Publishers, Kent, England, Sept. 1982, pp. 478-482.
8. Simons, R.N. and Lee, R.Q., "Coplanar Waveguide/Microstrip Probe Coupler and Applications to Antennas," *Electronics Letters*, Vol. 26, No. 24, Nov. 22, 1990, pp. 1998-2000.
9. Simons, R.N., Lee, R.Q., and Lindamood, G.R., "A New Coplanar Waveguide/Stripline Feed Network for a Seven Patch Hexagonal CP Subarray," *Electronics Letters*, Vol. 27, No. 6, March 1991, pp. 533-535.
10. Lee, R.Q. and Simons, R.N., "Electromagnetically Coupled Feed Network for an Array Module of Four Microstrip Elements," *1988 IEEE International Symposium on Antennas and Propagation Symposium Digest*, Vol. III, IEEE, 1988, pp. 1018-1021.
11. Simons, R.N., Ponchak, G.E., Lee, R.Q., and Fernandez, N.S., "Coplanar Waveguide Fed Phased Array Antenna," *1990 IEEE International Symposium on Antennas and Propagation Symposium Digest*, Vol. IV, IEEE, 1990, pp. 1778-1781.
12. DeBrecht, R.E., "Coplanar Balun Circuits for GaAs FET High-Power Push-Pull Amplifiers," *1973 IEEE G-MTT International Microwave Symposium Digest*, IEEE, 1973, pp. 309-311.

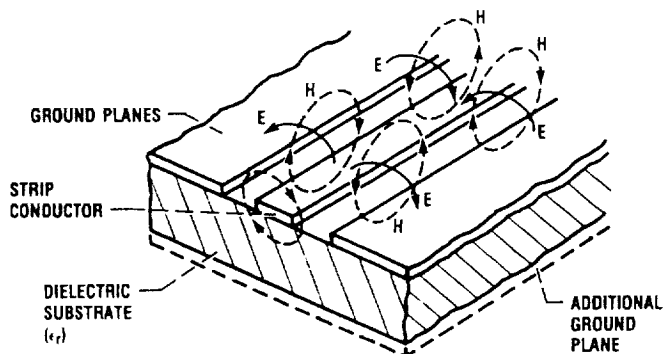
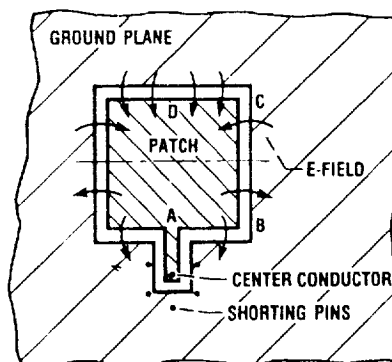
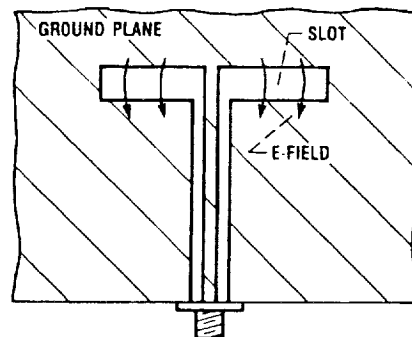


Figure 1.—Schematic illustrating the fields along the coplanar waveguide and the optional lower ground plane.



(a) CPW patch antenna.



(b) CPW slot antenna.

Figure 2.—Coplanar wave guide antenna.

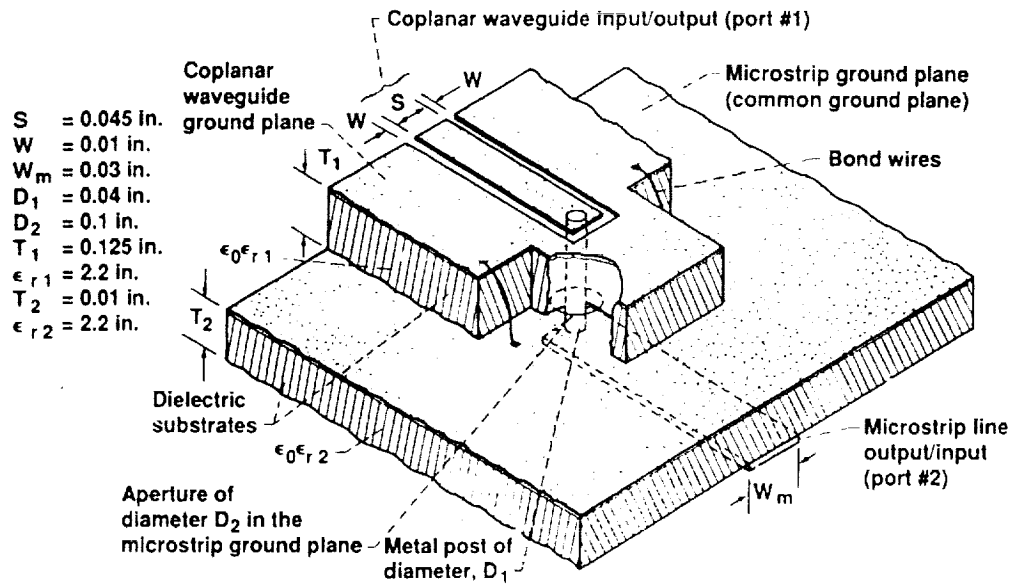


Figure 3.—Schematic of a CPW/microstrip line post coupler feed.

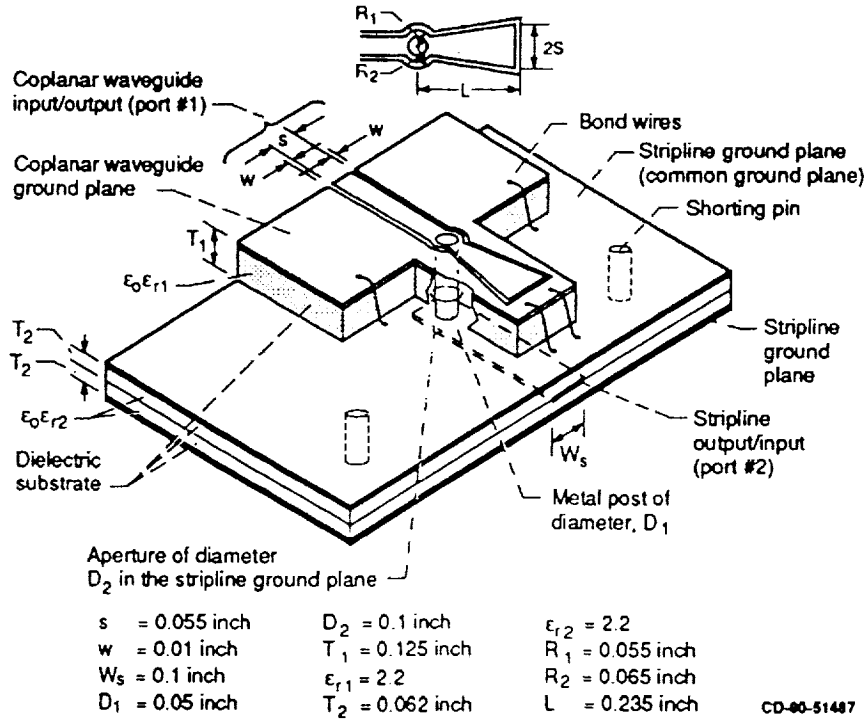


Figure 4.—Schematic of a CPW/balanced stripline post coupler.

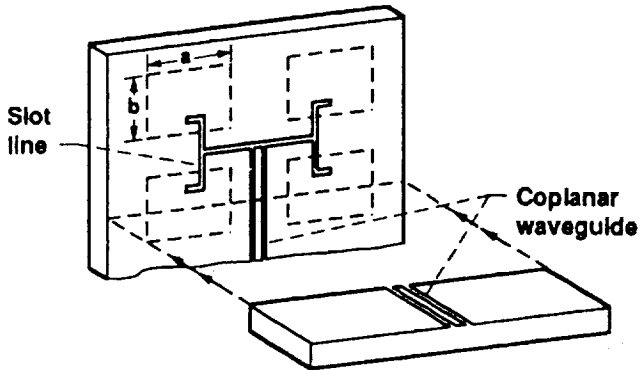


Figure 5.—Schematic of a CPW/slot line feed.

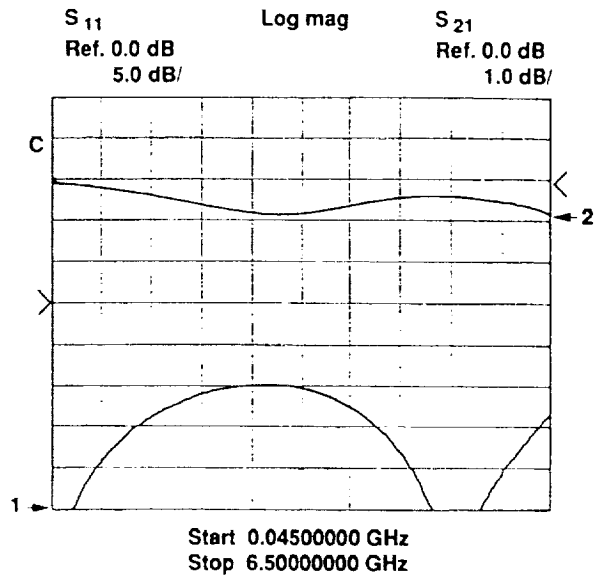


Figure 7.—Measured return loss ( $S_{11}$ ) and insertion loss ( $S_{21}$ ) of a CPW/microstrip line post coupler feed.

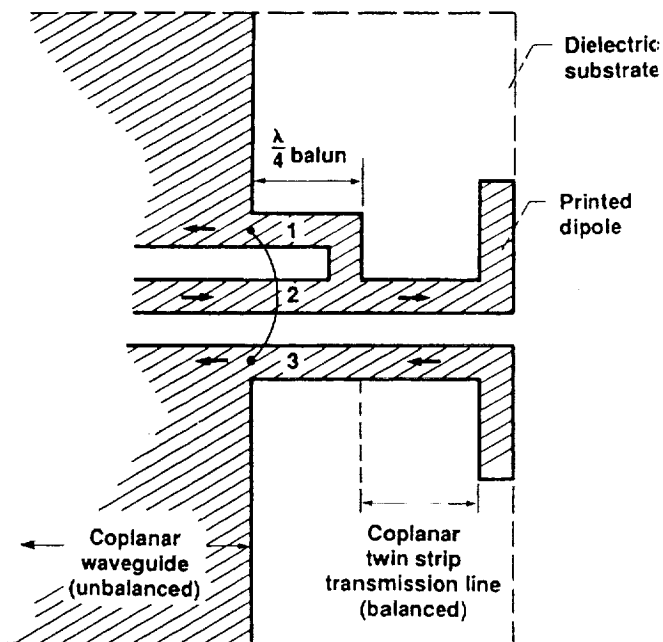


Figure 6.—Schematic of a CPW/balanced coplanar stripline feed.

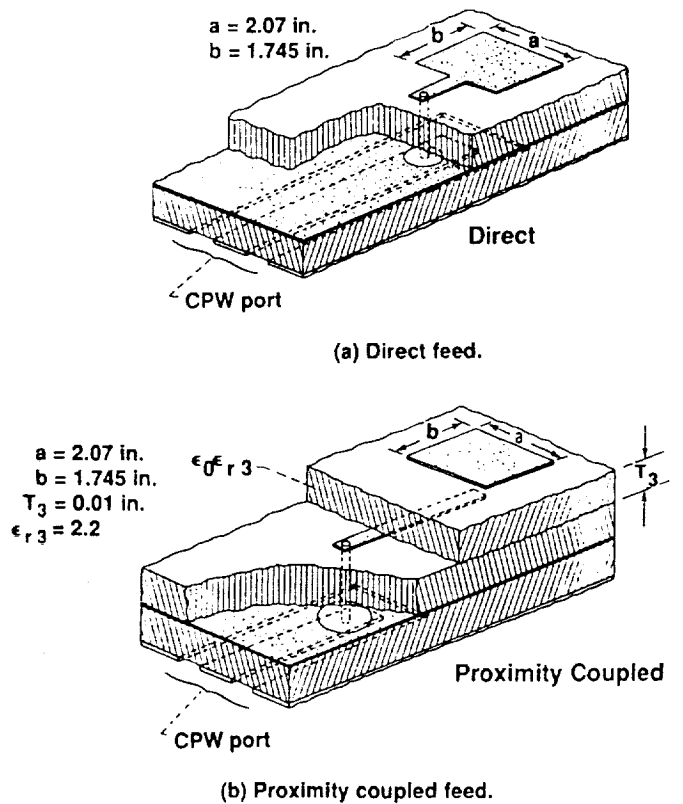


Figure 8.—Schematic illustrating the integration of a patch antenna with CPW/microstrip feed.

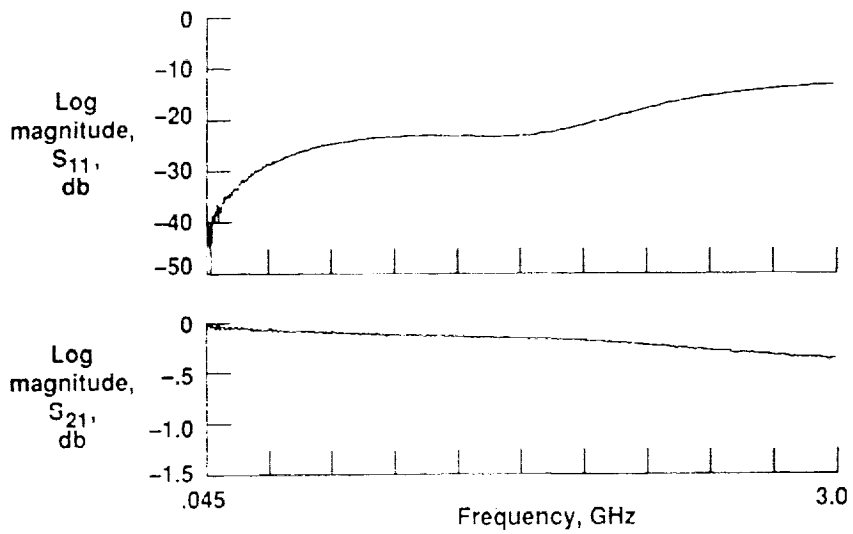
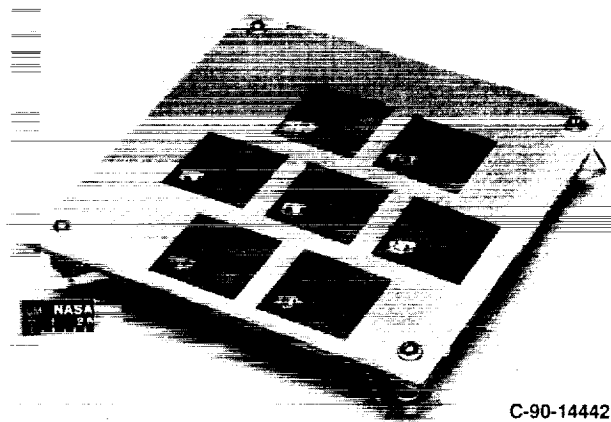
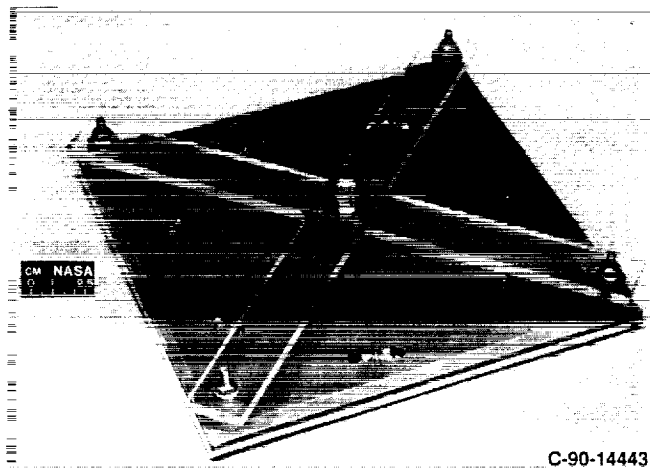


Figure 9.—Measured return loss ( $S_{11}$ ) and insertion loss ( $S_{21}$ ) of a CPW/balanced stripline coupler feed.



(a) Antenna layer.



(b) CPW power divider layer.

Figure 10.—Proof-of-concept model of a seven patch hexagonal CP subarray.





# NEW COPLANAR WAVEGUIDE TO RECTANGULAR WAVEGUIDE END LAUNCHER

R. N. Simons and S. R. Taub

*Indexing term: Waveguide couplers*

A new coplanar waveguide to rectangular waveguide end launcher is experimentally demonstrated. The end launcher operates over the  $K_u$ -band frequencies that are designated for the NASA Advanced Communication Technology Satellite (ACTS) uplink. The measured insertion loss and return loss are better than 0.5 and  $-10$  dB, respectively.

**Introduction:** Coplanar waveguide (CPW) is a very useful transmission line for microwave integrated circuits and has several advantages over conventional microstrip line [1]. CPW monolithic microwave integrated circuit (MMIC) components such as amplifiers and mixers have been demonstrated [2]. There are several applications where a CPW to rectangular waveguide coupler or transition is necessary. These include: direct injection of signals from a CPW MMIC into a waveguide, a feed network for waveguide radiating elements in a two-dimensional phased array antenna, and as a transition in a CPW wafer probe for on-wafer characterisation of solid state devices. The transition is important particularly at millimetre-wave frequencies where the small dimensions make coaxial connectors difficult to fabricate. Recently, CPW to rectangular waveguide post and slot couplers were demonstrated [3]. In the post and slot couplers, coupling is through an aperture in the broad wall and in the narrow wall of the rectangular waveguide, respectively.

This Letter presents the design and experimental characterisation of a new CPW to rectangular waveguide end launcher. In the end launcher, coupling is through an L-shaped loop that enters the waveguide through an aperture in the end wall.

**End launcher design and fabrication:** A CPW to rectangular waveguide end launcher is schematically illustrated in Fig. 1.

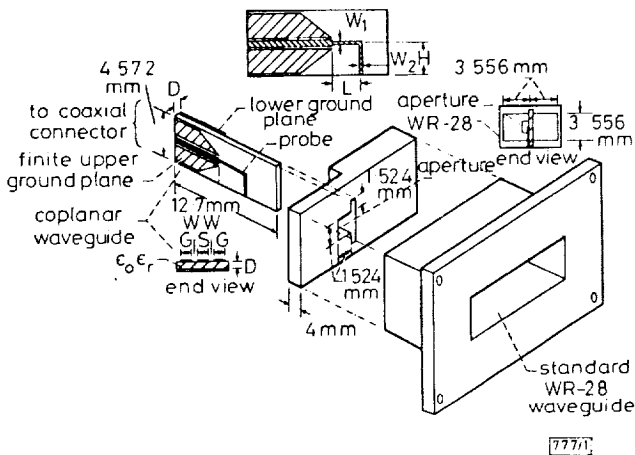


**Fig. 1** Schematic diagram of CPW to rectangular waveguide end launcher

$D = 0.254$  mm,  $\epsilon_r = 2.2$ ,  $S = 0.554$  mm  
 $W = 0.254$  mm,  $G = 1.25$  mm

The end launcher consists of a dielectric substrate carrying the CPW that enters the waveguide through an aperture in the centre of the end wall. The dielectric substrate is centred in the waveguide. Further, the CPW centre strip conductor extends into the waveguide and forms an L-shaped loop. The loop couples power from the quasi-TEM CPW mode to the  $TE_{10}$  waveguide mode. The centre strip conductor width  $S$  and slot width  $W$  of the CPW for a given substrate thickness  $D$  are determined so as to provide a good impedance match to a  $50 \Omega$  coaxial connector. The waveguide height and width are standard for a given frequency band. The length, height and widths of the probe extending into the waveguide are denoted as  $L$ ,  $H$ ,  $W_1$  and  $W_2$ , respectively.

**End launcher performance and discussions:** The length  $L$  is approximately  $\lambda_{g(\text{waveguide})}/6$  at the centre frequency  $f_0$  of 30.75 GHz. The height  $H$  is half the substrate height. The widths  $W_1$  and  $W_2$  are 0.4 and 0.508 mm, respectively. The above parameters, obtained through experimentation, resulted in excellent insertion and return loss characteristics. The measured return loss at the CPW port and the insertion loss between the CPW and the waveguide ports of the end launcher are presented in Figs 2 and 3, respectively. The end

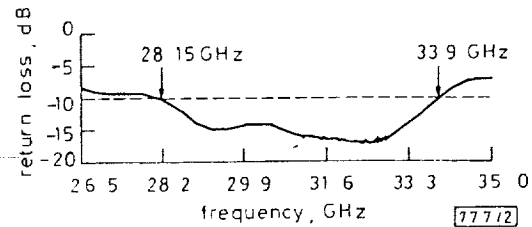


**Fig. 2** Measured return loss at CPW port

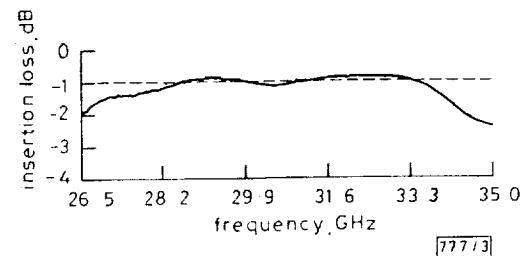


**Fig. 3** Measured insertion loss of end launcher

launcher operates with a return loss of better than  $-10$  dB over approximately 20% bandwidth centred at  $f_0$ . This bandwidth includes the NASA Advanced Communication Technology Satellite (ACTS) uplink frequencies (29–30 GHz). The insertion loss of the end launcher is  $\sim 1$  dB and includes the losses in the coaxial connector and in the coax-to-waveguide adapter of the test setup which were not practical to calibrate out. Hence, the net insertion loss of the launcher is very small and is of the order of 0.5 dB.

*Conclusions:* A new CPW to rectangular waveguide end launcher realised using printed circuit technology and having very small dimensions is experimentally demonstrated. The measurements show that the launcher has excellent insertion loss and return loss characteristics. Thus the launcher is inexpensive to fabricate, compact and efficient.

21st April 1992

R. N. Simons and S. R. Taub (*Mail Stop 54-5, NASA Lewis Research Centre, 21000 Brookpark Road, Cleveland, Ohio 44135, USA*)

### References

- 1 GUPTA, K. C., GARG, R., and BAHL, I. J.: 'Microstrip lines and slot-lines' (Norwood: Artech House, Inc., 1979), Chap. 7
- 2 KUMAR, M. (Ed.): IEEE 1991 Microwave and Millimeter-Wave Monolithic Circuits Symp. Dig. of Papers (91CH3016-3)
- 3 SIMONS, R. N.: 'New channelised coplanar waveguide to rectangular waveguide post and slot couplers', *Electron. Lett.*, 1991, **27**, (10), pp. 856-857

# ANALYSIS OF SHIELDED CPW DISCONTINUITIES WITH AIR-BRIDGES

N. I. Dib, P. B. Katehi

*Radiation Lab., University of Michigan, Ann Arbor, MI*

G. E. Ponchak

*NASA, Lewis Research Center, Cleveland, OH  
Presently with Radiation Lab, University of Michigan*

Permission to copy without fee all or part of this material is granted provided that the copies are not made or distributed for direct commercial advantage. Copying is by permission of the Institute of Electrical and Electronics Engineers. To copy otherwise, or to republish, requires a fee and specific permission.

## ABSTRACT

The effect of air-bridges on the performance of various coplanar waveguide (CPW) discontinuities is studied. Specifically, the coupled open-end CPWs and the short-end shunt CPW stub discontinuities are considered. The high frequency effect of the air-bridge is evaluated using a hybrid technique. At first, the frequency dependent equivalent circuit of the planar discontinuity without the air-bridge is derived using the Space Domain Integral Equation (SDIE) method. Then, the circuit is modified by incorporating the air-bridge's parasitic inductance and capacitance which are evaluated using a simple quasi-static model. The frequency response of each discontinuity with and without the air-bridge is studied and the scattering parameters are plotted in the frequency range 30-50 GHz for typical CPW dimensions.

## 1 INTRODUCTION

Recently, researchers have shown a great deal of interest in coplanar waveguides (CPW) for (M)MICs design due to several advantages such as design flexibility, potential for low dispersion and low radiation, and less dependency on the substrate thickness [1-3]. While there is no need for via holes in CPW circuits, air-bridges are fundamental components mainly used to connect the ground planes in order to suppress the propagation of coupled slotline mode [4]. In addition, they are used to connect CPWs with slotlines or coupled slotlines in uniplanar (M)MICs [5]. Unfortunately, air-bridges represent discontinuities which may cause parasitic effects depending on their electrical size and location. It has been found experimentally that the parasitic effect of a typical air-bridge along a uniform line is negligible. The size of a typical air-bridge is very small; the height is 3  $\mu\text{m}$  and length ranges from 10  $\mu\text{m}$  to 50  $\mu\text{m}$  [4, 5]. However, a 5% change in the resonant frequency of a CPW line resonator including ten air-bridges has been reported in [4].

In this paper, the two CPW discontinuities shown in Fig.1 are studied. In Fig.1a, the air-bridge is used to connect the center conductors of two coupled open-end CPWs, while in Fig.1b it connects the two ground planes of the shunt CPW stub in order to suppress coupled slotline mode. Since the size of a typical air-bridge is very small, a hybrid technique can be used to analyze these discontinuities. First, the frequency dependent equivalent circuit of the discontinuity, without the air-bridge, is derived using the Space Domain

Integral Equation (SDIE) method [6-8]. Then, this equivalent circuit is modified by incorporating the air-bridge's parasitic effects. These effects, a series inductance and a shunt capacitance, are evaluated using a quasi-static model. The theoretical method is discussed briefly in section 2, and numerical results for symmetric discontinuities are presented in section 3. Results for non-symmetric CPW discontinuities will be shown in the symposium. Moreover, experiments will be performed to validate the obtained theoretical results.

## 2 THEORY

The CPW under consideration is shown in Fig.2 where it is assumed to be inside a rectangular cavity of perfectly conducting walls. The cavity dimensions are chosen such that the CPW fundamental mode is not affected by higher order cavity resonances. The theoretical method used to study CPW discontinuities, in the absence of air-bridges, is based on a space domain integral equation which is solved using the method of moments. The SDIE approach has been previously applied to study several CPW discontinuities and has shown very good accuracy, efficiency and versatility in terms of the geometries it can solve [6-8]. Since the theoretical method is presented in detail in [7, 8], a brief summary will be given here.

The boundary problem pertinent to any CPW discontinuity may be split into two simpler ones by introducing an equivalent magnetic current  $\vec{M}_s$  on the slot apertures. This surface magnetic current radiates an electromagnetic field in the two waveguide regions (above and below the slots) so that the continuity of the tangential electric field on the surface of the slots is satisfied. The remaining boundary condition to be applied is the continuity of the tangential magnetic field on the surface of the slot apertures which leads to the following integral equation

$$\hat{x} \times \int_S \int [\vec{G}_0^h(\vec{r}/\vec{r}') + \vec{G}_1^h(\vec{r}/\vec{r}')] \cdot \vec{M}_s(\vec{r}') ds' = \vec{J}, \quad (1)$$

where  $\vec{G}_{0,1}^h$  are the magnetic field dyadic Green's functions in the two waveguide regions [7, 8] and  $\vec{J}$  denotes an assumed ideal electric current source exciting the coplanar waveguide mode (gap generator model).

The integral equation (1) is solved using the method of moments where the unknown magnetic current is expanded in terms of rooftop basis functions. Then, Galerkin's method is applied to reduce the above equation to a linear

system of equations

$$\begin{pmatrix} Y_{yy} & Y_{yz} \\ Y_{zy} & Y_{zz} \end{pmatrix} \begin{pmatrix} V_y \\ V_z \end{pmatrix} = \begin{pmatrix} I_x \\ I_y \end{pmatrix} \quad (2)$$

where  $Y_{ij}$  ( $i = y, z; j = y, z$ ) represent blocks of the admittance matrix,  $V_i$  is the vector of unknown  $y$  and  $z$  magnetic current amplitudes, and  $I_j$  is the excitation vector which is identically zero everywhere except at the position of the sources. Finally, the equivalent magnetic current distribution and consequently the electric field in the slots are obtained by matrix inversion.

In case of symmetric CPW structures, the aperture fields form standing waves of the fundamental coplanar waveguide mode away from the discontinuity. Consequently, using the derived electric field, an ideal transmission line method [9] is applied to determine the scattering parameters and evaluate the elements of the equivalent circuit.

Fig.3a shows the equivalent circuit ( $\pi$ -model) for the CPW discontinuities shown in Fig.1 in the absence of the air-bridges. For the structure of Fig.1a,  $X_1$  and  $X_2$  represent the fringing and coupling effects respectively between the two coupled open-ends. However, for the CPW stub discontinuity of Fig.1b,  $X_1$  and  $X_2$  represent the reactances due to the coplanar waveguide and the coupled slotline modes respectively which are excited in the CPW stub. It is the purpose of the air-bridges to short the series reactance in both discontinuities. Fig.3b shows the new equivalent circuit after taking the air-bridge into consideration. The air-bridge can be modeled as an air-filled microstrip line [4, 5], and the design formulas in [10] are used to evaluate its parasitic capacitance  $C_a$  and inductance  $L_a$ . A parallel plate waveguide model can be also used since the air-bridge height is very small (typically  $3 \mu\text{m}$ ). Both models give a capacitance  $C_a$  in the order of 1-10 pF and an inductance  $L_a$  in the order of 1-10 nH. Finally, new scattering parameters are evaluated from the modified equivalent circuit.

### 3 NUMERICAL RESULTS

In the numerical results shown here, the considered CPW discontinuities are printed on a  $300 \mu\text{m}$  GaAs substrate ( $\epsilon_r = 13$ ) with an inner conductor width of  $75 \mu\text{m}$  and slot width of  $50 \mu\text{m}$ . The characteristic impedance of such line is approximately  $50 \Omega$ . The slot width of the open-end and the CPW stub are both  $25 \mu\text{m}$ .

#### 3.1 Coupled open-end CPWs

Fig.4 shows  $\text{mag}(S_{12})$  for the coupled open-end CPW discontinuity (without air-bridge) as a function of frequency for different separation distances. It can be seen that the coupling between the two lines is small even with a separation distance of  $20 \mu\text{m}$ . It is worth mentioning that such structure is widely used as a test fixture for making precise scattering parameters measurements of a wide variety of active and passive circuit elements. This is performed by mounting the element (or (M)MIC) on the center area (called ground plane mounting island) and connecting it to the CPW lines using bondwires. Fig.5 shows the fringing

and coupling reactances of the equivalent  $\pi$ -model of the discontinuity with reference planes chosen to coincide with the end of the center conductors. It has been found numerically that  $X_1$  varies approximately as  $1/f$  and it is always capacitive for any separation distance depending mainly on the center conductor and slot widths. This behavior is not clear in Fig.5 because of the large vertical scale. On the other hand, the value and nature of  $X_2$  depends on the separation distance besides the center conductor and slot widths.

Fig.6 shows  $\text{mag}(S_{12})$  for the same discontinuity with an air-bridge connecting the center conductors (with a height of  $3 \mu\text{m}$ ). It can be noticed that the insertion loss in this case is very small compared to the case without the air-bridge shown in Fig.4. The variation of  $\text{mag}(S_{12})$  with respect to frequency and length of air-bridge is analogous to the one found experimentally in [4]. Thus, it is indeed reasonable to model the air-bridge quasi-statically as long as it is adequately small.

#### 3.2 A shorted-end shunt CPW stub

Fig.7 shows the scattering parameters of a shorted-end shunt CPW stub discontinuity (without the air-bridges) with a stub length of  $550 \mu\text{m}$ . It can be noticed that such structure behaves as a series stub (instead of a shunt stub) with a resonant frequency  $46.5 \text{ GHz}$ . Fig.8 clarifies this by showing that the series reactance  $X_2$  resonates at this frequency while the shunt reactance  $X_1$  resonates at  $49.5 \text{ GHz}$  (at which the length of the stub is approximately a quarter of a coplanar mode wavelength). However, the effect of this latter resonance does not appear in Fig.7 because of the existence of the series reactance  $X_2$ . It has been found that these two resonant frequencies are approximately independent of the separation distance between the two coplanar lines (ranging from  $20\text{-}80 \mu\text{m}$ ) depending mainly on the stub length. A similar equivalent circuit of this discontinuity is proposed in [10] where the reactances are assumed to be inductive, which is not always true as shown in Fig.8.

Fig.9 shows the scattering parameters of the same discontinuity with air-bridges connecting the ground planes of the CPW stub. The air-bridges are chosen with width of  $10 \mu\text{m}$  and height of  $3 \mu\text{m}$ . These air-bridges ensure that the two ground planes of the CPW stub are at the same potential and suppress the coupled slotline mode. This results in shorting the series reactance and thus reducing the equivalent circuit to a shunt reactance (with air-bridge parasitic effects). Fig.9 shows that this structure is indeed a shunt stub not a series one.

### 4 CONCLUSIONS

Two different CPW discontinuities involving air-bridges (coupled open-end CPWs and shorted-end shunt CPW stub) have been analyzed using a hybrid technique. In this approach, the planar structure without the air-bridge is analyzed with the SDIE method and a frequency-dependent equivalent circuit is derived. Then, the effect of the air-bridge is taken into account quasi-statically by modifying the equivalent circuit appropriately and the new scatter-

ing parameters are computed. It has been found that the coupling is very small between two open-end CPWs, when they are not connected with an air-bridge, even with small separation distances. In addition, it has been found that a shorted-end shunt CPW stub behaves as a series stub if the two ground planes of the CPW stub are not connected together due to the presence of the coupled slotline mode. It is the air-bridge, whose parasitic effects are typically negligible, that makes these structures behave as required. Experiments will be performed for both discontinuities with and without air-bridges to validate the theoretically derived data. In addition, results for non-symmetric CPW discontinuities will be shown in the symposium.

## 5 ACKNOWLEDGMENT

This work was supported by the National Science Foundation under contract ECS-8657951.

## References

- [1] P. A. Holder, "X-Band Microwave Integrated Circuits Using Slotlines and Coplanar Waveguide," *Radio Electronics Engineering*, Vol. 48, pp. 38-42, January/February 1978.
- [2] M. Riaziat, E. Par, G. Zdziuk, S. Bandy and M. Glenn, "Monolithic Millimeter Wave CPW Circuits," in *1989 IEEE MTT-S International Microwave Symposium Digest*, Long Beach, CA, pp. 525-528.
- [3] D. Leistner, W. Schmid and G. Eggers, "Application of Coplanar Waveguide Microwave Integrated Circuits at C- and Ku-Band Frequencies," *Proc. of 20th European Microwave Conference*, pp. 1021-1026, Sep. 1990.
- [4] N. H. Koster, S. Koblowski, R. Bertenburg, S. Heinen and I. Wolff, "Investigation of Air Bridges Used for MMICs in CPW Technique," *Proc. of 19th European Microwave Conference*, pp. 666-671, Sep. 1989.
- [5] T. Hirota, Y. Tarusawa, and H. Ogawa, "Uniplanar MMIC Hybrids-A Propose of a New MMIC Structure", *IEEE Trans. on Microwave Theory and Techniques*, Vol. MTT-35, pp. 576-581, June 1987.
- [6] N. I. Dib, P. B. Katehi, G. E. Ponchak, and R. N. Simons, "Coplanar Waveguide Discontinuities for P-i-n Diode Switches and Filter Applications," in *1990 IEEE MTT-S International Microwave Symposium Digest*, Dallas, TX, pp. 399-402.
- [7] N. I. Dib and P. B. Katehi, "Modeling of Shielded CPW Discontinuities Using the Space Domain Integral Equation Method (SDIE)," *Journal of Electromagnetic Waves and Applications*, April 1991.
- [8] N. I. Dib, P. B. Katehi, G. E. Ponchak, and R. N. Simons, "Theoretical and Experimental Characterization of Coplanar Waveguide Discontinuities for Filter Applications," *IEEE Trans. on Microwave Theory and Techniques*, May 1991.
- [9] L. P. Dunleavy and P. B. Katehi, "Generalized Method for Analyzing Shielded Thin Microstrip Discontinuities," *IEEE Trans. on Microwave Theory and Techniques*, Vol. MTT-36, pp. 1758-1766, Dec. 1988.
- [10] K. C. Gupta, R. Garg and I. J. Bahl, *Microstrip Lines and Slotlines*, Dedham, MA : Artech House, 1979.

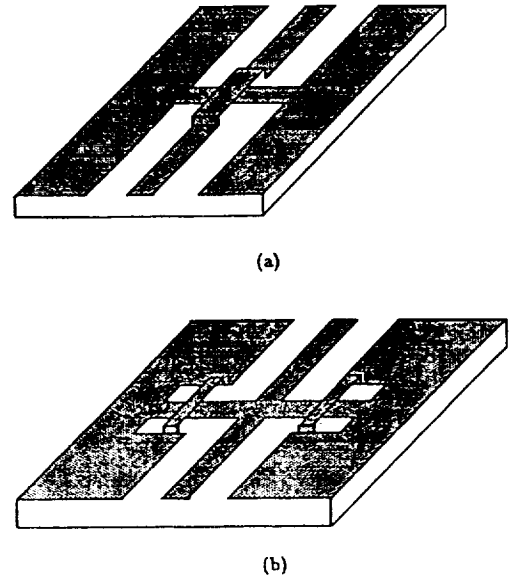


Figure 1: (a) Coupled open-end coplanar waveguides with an air-bridge. (b) A coplanar waveguide shorted-end shunt stub.

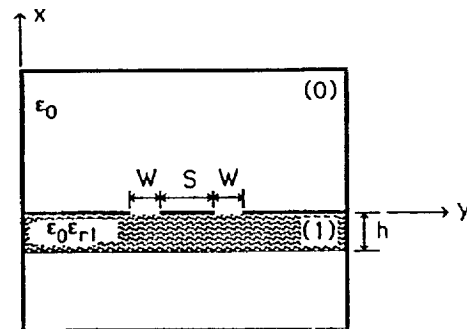


Figure 2: A cross section of a coplanar waveguide inside a cavity.

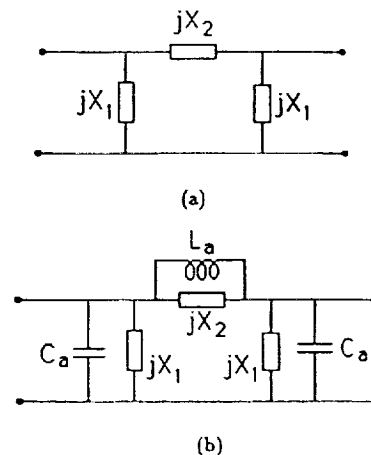


Figure 3: (a) Equivalent circuit of the CPW discontinuities shown in Fig.1 without the air-bridges. (b) Equivalent circuit of the CPW discontinuities shown in Fig.1 with the air-bridges taken into account.

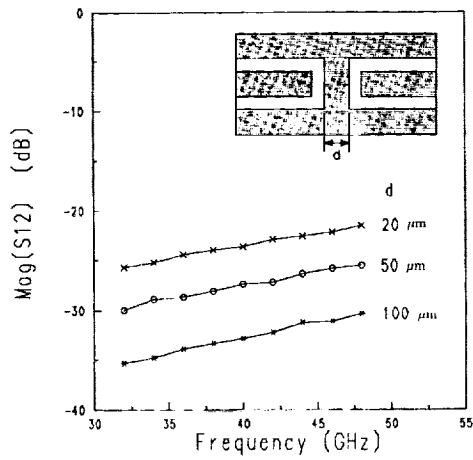


Figure 4:  $\text{Mag}(S_{12})$  for the coupled open-end CPWs discontinuity without the air-bridge for different separation distances. (Dimensions are stated in the text)

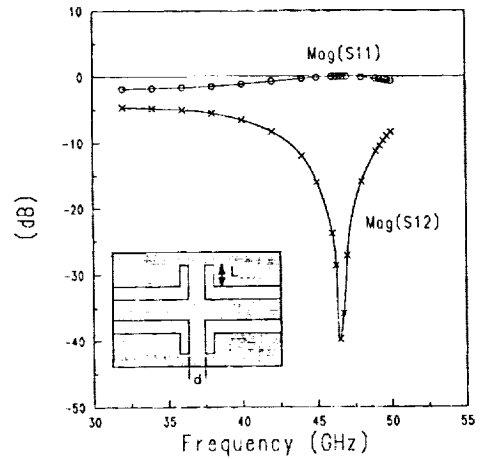


Figure 7: Scattering parameters of a shorted-end shunt CPW stub without air-bridges,  $L=550 \mu\text{m}$ ,  $d=20 \mu\text{m}$ .

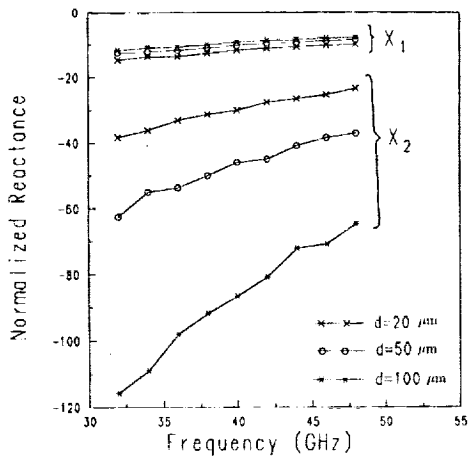


Figure 5: Coupling and fringing reactances for the coupled open-end CPWs discontinuity without the air-bridge for different separation distances.

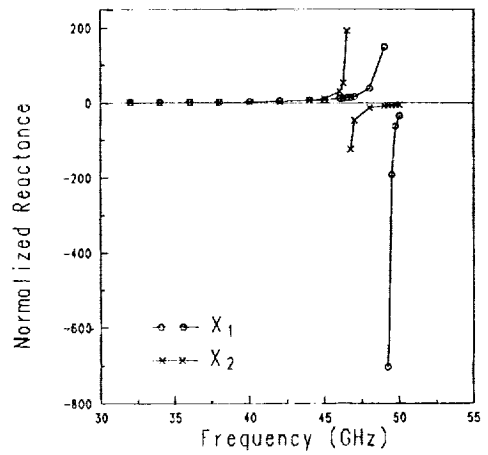


Figure 8: Series and shunt reactances for a shorted-end shunt CPW stub without air-bridges,  $L=550 \mu\text{m}$ ,  $d=20 \mu\text{m}$ .

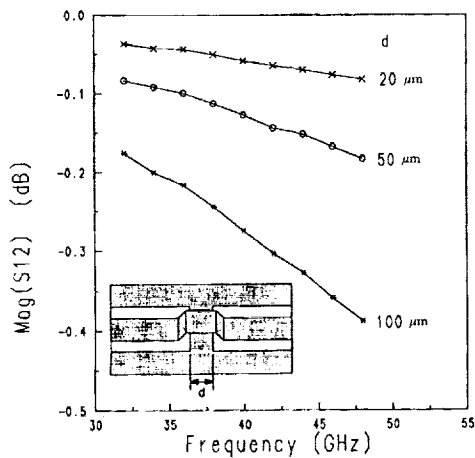


Figure 6:  $\text{Mag}(S_{12})$  for the coupled open-end CPWs discontinuity with an air-bridge of height  $3 \mu\text{m}$ .

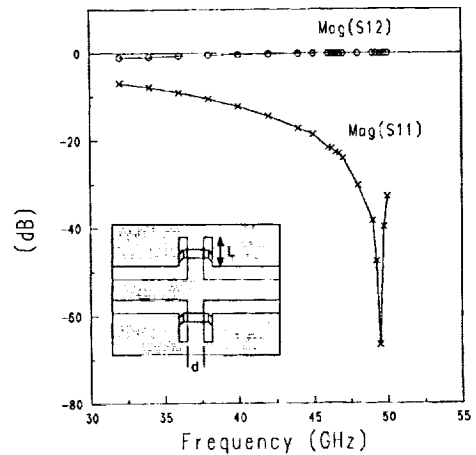


Figure 9: Scattering parameters of a shorted-end shunt CPW stub with air-bridges,  $L=550 \mu\text{m}$ ,  $d=20 \mu\text{m}$ .

## A FLEXIBLE CPW PACKAGE FOR A 30 GHz MMIC AMPLIFIER

Rainee N. Simons and Susan R. Taub  
National Aeronautics and Space Administration  
Lewis Research Center  
Cleveland, OH 44135

## SUMMARY

A novel package, which consists of a carrier and housing, has been developed for monolithic-millimeter wave Integrated Circuit amplifiers which operate at 30 GHz. The carrier has coplanar waveguide (CPW) interconnects and provides heat-sinking, tuning, and cascading capabilities. The housing provides electrical isolation, mechanical protection, and a feed-thru for biasing.

## INTRODUCTION

MMICs (monolithic-millimeter integrated circuits) are currently available for satellite communication applications at millimeter wave frequencies (ref. 1). However, very little has been done in the development of carriers and housings that enable these circuits to be inserted into actual systems. In this paper we present the design and characteristics of a CPW (coplanar waveguide) carrier and a housing for MMIC amplifiers operating at 30 GHz. CPW circuits have the advantage of providing easy series as well as shunt mounting of microwave devices. Furthermore, since the ground planes are on the same side as the strip conductor, via holes and wraparounds are eliminated; therefore, parasitics are small. Radiation loss, when compared to microstrip, is low; hence CPW circuits are less prone to interaction with the package and EM interference. Another advantage is that CPW circuits lend themselves to fast and inexpensive characterization using wafer probing equipment.

## CARRIER DESIGN

The carrier assembly is shown in figure 1. The carrier consists of a finite width conductor backed CPW (CBCPW) circuit on a dielectric substrate. The CBCPW circuit consists of a pair of tapered open circuits which face each other, and are separated by the surrounding ground plane. The ground plane also serves as an island for mounting MMIC devices and facilitates low inductance ground connections from any point on the perimeter of the MMIC. The length of separation between the open circuits is chosen to accommodate a particular MMIC chip. By tapering the CPW open circuit the electric field lines are concentrated at the open end and therefore are coupled efficiently to the short wire bonds between the CPW input/output lines and the MMIC. A copper post (diameter 0.031 in.) inserted in the center of the carrier serves as a heat sink for the MMIC. A brass backing plate provides heat dissipation and mechanical support. The MMIC and brass backing plate are attached to the dielectric substrate using silver conductive epoxy.

This carrier provides advantages in the following areas: Tuning, cascading and calibration. MMIC tuning is accomplished by sliding small lengths of metal strips over the CPW circuit until the desired S-parameters are obtained. The metal strips are then glued in place. Two or more of the above carriers can be cascaded, as shown in figure 1, by use of a novel plastic clip. The clip slides over and grips the two brass backing plates. This ensures excellent alignment for wire bonding. LRL calibration can be performed to the plane of the MMIC.

## HOUSING

A single carrier with the housing is shown in figure 2. The housing provides mechanical protection, electrical isolation, and a coaxial feed-thru for bias lines.

## EXPERIMENTAL RESULTS

A single carrier was tested by fixing a  $50\ \Omega$  GaAs microstrip line, 700 mils long, in place of an MMIC, wire-bonding it to the CPW lines and measuring the S-parameters over the frequency range of 29 to 30 GHz with an HP 8510B Network Analyzer. The measured insertion loss,  $S_{21} = 1.9\ \text{dB}$  and the return loss,  $S_{11} < -15\ \text{dB}$ , as shown in figure 3. This includes the losses of the Wiltron Universal Test Fixture and the carrier. These losses were found to be 0.9 dB by measuring the insertion loss of an identical CPW thru-line on an identical substrate. The insertion loss and return loss measured with and without the housing is shown in figure 4. The  $S_{21}$  measured, without the microstrip line, is a measure of the isolation between the input and output ports. The carrier and the housing were tested. An isolation of greater than 16 dB was measured, which is an improvement of 10 dB over the isolation of the carrier without the housing. The measured characteristics are shown in figure 5. Figure 6 shows the carrier, carrier with housing and cascaded carriers.

## REFERENCE

1. Saunier, P.; and Tserng, H.Q.: AlGaAs/InGaAs Heterostructures with Doped Channels for Discrete Devices and Monolithic Amplifiers. IEEE Trans. Electron Devices, vol. 36, Oct. 1989, pp. 2231-2235.

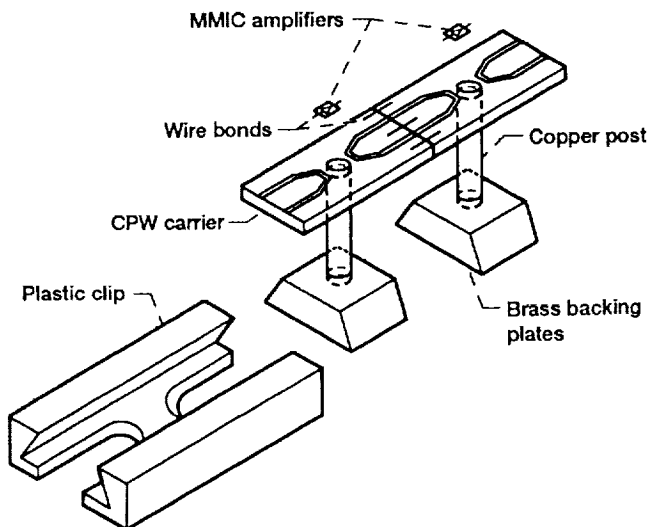


Figure 1.—Schematic for cascading CBCPW carriers using a plastic clip.

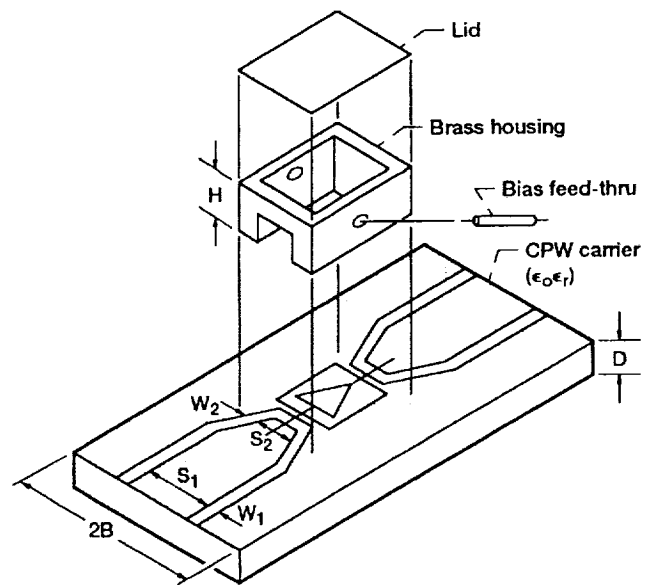
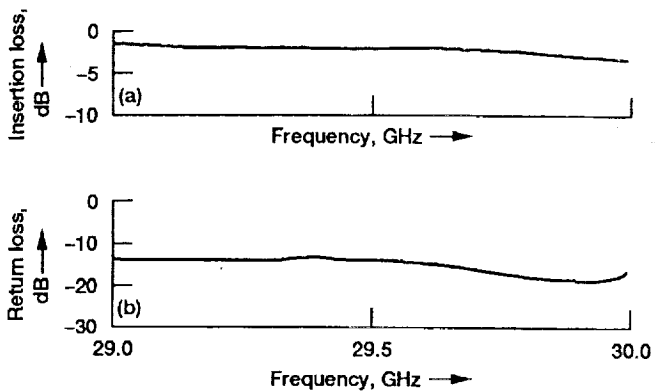
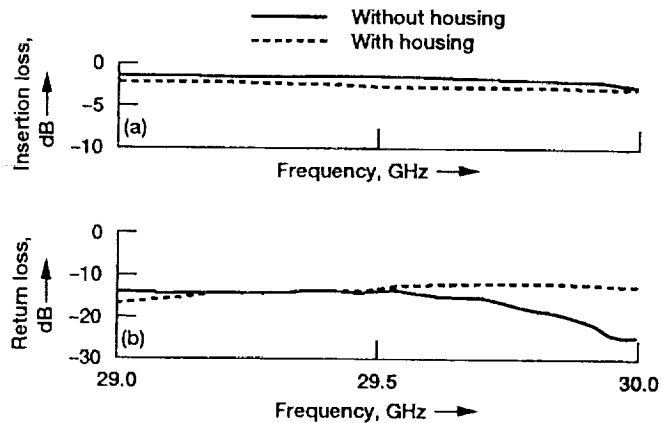


Figure 2.—Schematic of carrier with housing. Finite width conductor backed coplanar waveguide;  $S_1 = 0.013\ \text{in.}$ ,  $W_1 = 0.010\ \text{in.}$ ,  $S_2 = 0.010\ \text{in.}$ ,  $W_2 = 0.008\ \text{in.}$ ,  $D = 0.025\ \text{in.}$ ,  $\epsilon_r = 10.5$ ,  $2B = 0.2\ \text{in.}$ ,  $H = 0.135\ \text{in.}$



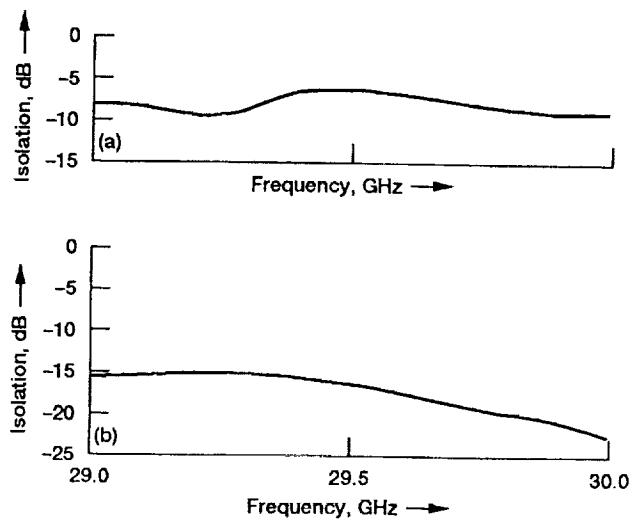
(a) Insertion loss.  
(b) Return loss.

Figure 3.—Measured characteristics of the carrier.



(a) Insertion loss.  
(b) Return loss.

Figure 4.—Effect of housing on the measured characteristics of the carrier.



(a) Without housing.  
(b) With housing.

Figure 5.—Measured isolation.

ORIGINAL PAGE  
BLACK AND WHITE PHOTOGRAPH

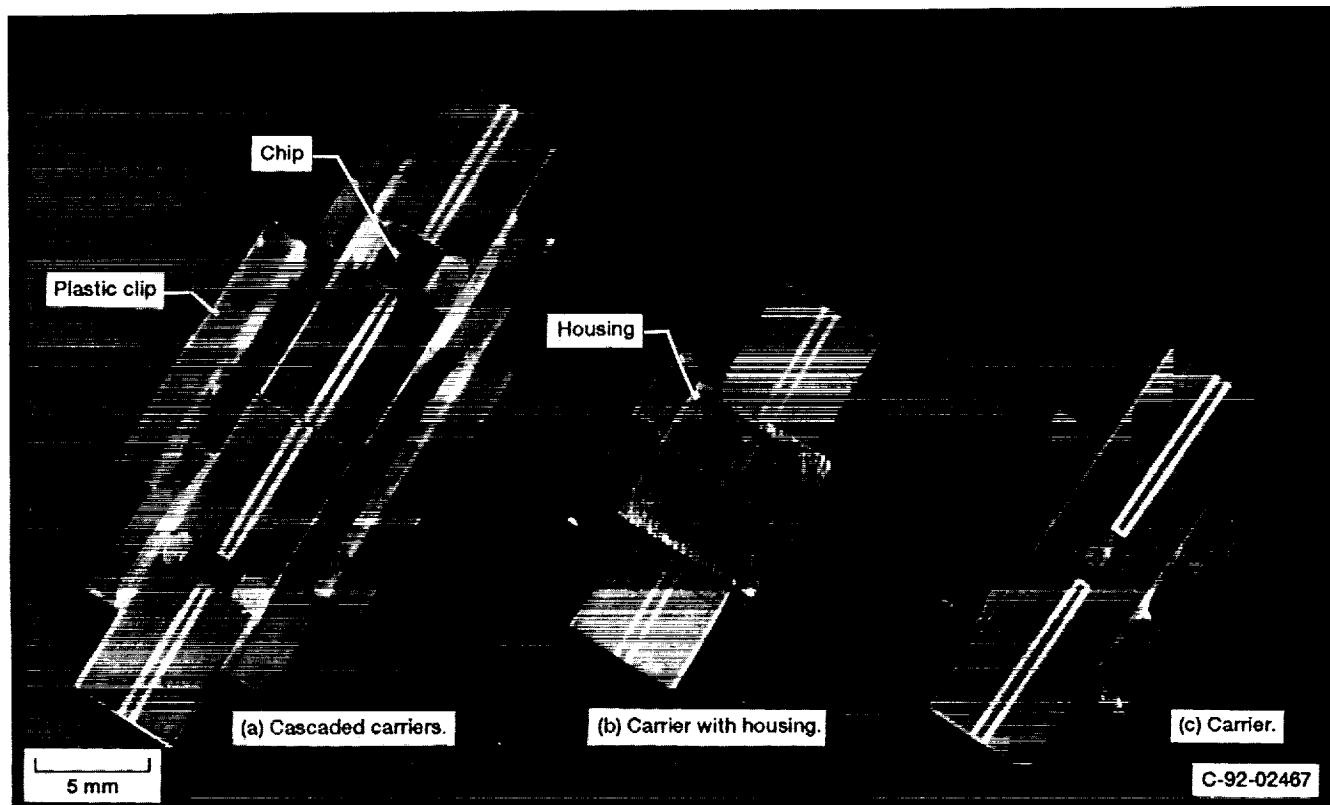


Figure 6.—CPW carriers.

**A 1 W, 30-GHZ, CPW AMPLIFIER FOR ACTS SMALL TERMINAL UPLINK**

Susan R. Taub  
National Aeronautics and Space Administration  
Lewis Research Center  
Cleveland, Ohio 44135

and

Rainee N. Simons  
Sverdrup Technology, Inc.  
Lewis Research Center Group  
Brook Park, Ohio 44135

**Abstract**

This paper describes the progress to date of the development of a 1-W, 30-GHz, coplanar waveguide (CPW) amplifier for the Advanced Communication Technology Satellite (ACTS) Small Terminal Uplink. The amplifier is based on Texas Instruments' monolithic microwave integrated circuit (MMIC) amplifiers; a three-stage, low-power amplifier and a single-stage, high-power amplifier. The amplifiers have a power output of 190 mW and 0.710 W, gain of 23 and 4.2 dB, and efficiencies of 30.2 and 24 percent for the three-stage and one-stage amplifiers, respectively. The chips are to be combined via a CPW power divider/combiner circuit to yield the desired 1 W of output power.

**Introduction**

MMIC amplifiers find extensive applications in satellite communications due to their small size and efficiency. In this paper we describe the design and development of an MMIC amplifier for the ACTS Small Terminal Uplink. The amplifier is based on Texas Instruments' monolithic microwave integrated circuit (MMIC) amplifier chips; a three-stage, low-power amplifier chip and a single-stage, high-power amplifier chip. The chips are to be combined via a CPW power divider/combiner circuit to yield the required 1 W of output power. Table 1 shows the amplifier requirements. Henceforth in this paper the term "MMIC chips" will refer to the Texas Instruments amplifier chips and the term "amplifier" will refer to the entire amplifier assembly.

**Amplifier Design and Performance**

A configuration drawing of the amplifier is shown in figure 1. The signal is brought into the amplifier via a coaxial input line and a coaxial-to-CPW transition. The power is divided three ways by a CPW power divider. The output of the power divider is coupled to the cascaded MMIC chips. The MMIC chips are mounted on the amplifier using a novel carrier. The output of the MMIC chips are combined in a three-way CPW power combiner. The power divider and combiner are on two separate substrates, connected back-to-back using a novel post coupler. The output of the combiner is fed into a coax to waveguide transition which forms the input to the antenna. An alternate amplifier configuration is shown in figure 2. This is a nonplanar design that eliminates the need for the post coupler. The output of the power divider and combiner connects directly to each of the TI MMIC chips.

**Power Divider/Combiner**

A coax-to-CPW in-phase three-way radial, nonplanar power divider/combiner is formed by the intersection of three CPW lines. Power is coupled to this junction from a coaxial cable, the outer conductor of coaxial cable is slotted lengthwise to prevent shorting of the CPW lines. The center pin of the coaxial line meets the intersecting CPW center conductors and the three outer conductors meet the ground plane. This arrangement has the advantage of holding the ground planes at the same potential and exciting the three CPW lines in equal amplitude and phase without the use of bond wires.

### Post Coupler

A CPW-to-CPW post coupler is shown in figure 3. The CPW's share a common ground plane that has an aperture. The coupler is formed by a metal post which passes through the aperture and contacts the strip conductors of the CPW. A pair of wire located to the sides of the post, tie the CPW ground planes to a common potential. The S-parameters for the coupler are shown in figure 4. The coupler works only marginally at 30 GHz, but shows excellent characteristics at 7 GHz. Work is being done, including computer simulations to better understand the behavior of this coupler.

### MMIC Chips

Two MMIC chips were used, a three-stage and a single-stage amplifier chip. The gain compression of the three-stage chip is shown in figure 5. A typical chip has a power output of 190 mW, gain of 23 dB, and efficiency of 30.2 percent. Typical characteristics for the single-stage chip are: power output of 710 mW, gain of 4.2 dB, and efficiency of 24 percent. In order to achieve the required 1 W of output power, the MMIC chips were cascaded. The cascading configuration is shown in figure 6.

### MMIC Carrier

A novel package, which consist of a carrier and housing, was developed to mount the MMIC chips in the amplifier. The carrier with housing is shown in figure 7. The carrier has CPW interconnects and provides heat-sinking, tuning, and cascading capabilities. The housing provides electrical isolation, mechanical protection, and a feed-through for biasing. Figure 8 shows the measured insertion and return loss of the carrier with a 50- $\Omega$  microstrip line in place of the MMIC. After subtracting the losses due to the test fixture, the insertion loss of the carrier is about 1.0 dB and the return loss is better than 15 dB.

### Conclusions

The paper presents two schemes for the assembly of a 1-W, 30-GHz MMIC amplifier for the ACTS small terminal. The characteristics of TI MMIC chips, the post coupler, and the carrier have been presented. Future work includes: characterizing the power divider/combiner, tuning the MMIC chips, and assembling the amplifier.

## References

1. Saunier, P.; and Tserng, H.O.: AlGaAs/InGaAs Heterostructures with Doped Channels for Discrete Devices and Monolithic Amplifiers. IEEE Trans. Electron Devices, vol. 36, Oct. 1989, pp. 2231-2235.

2. Simons, R.N.; and Taub, S.R.: A Flexible CPW Package for a 30-GHz MMIC Amplifier. Presented at the IEEE Topical Meeting on Electrical Performance of Electronic Packaging, Apr. 22-24, 1992, Tuscon, AZ. NASA TM-105630, 1992.

|                  |              |
|------------------|--------------|
| Power input      | -25 dBm      |
| Power output     | 1 W          |
| Center frequency | 29.634 GHz   |
| Bandwidth        | 29.1-30 GHz  |
| Input connector  | 2.4 mm OS-50 |
| Output waveguide | WR 28        |

Table 1: Amplifier requirements.

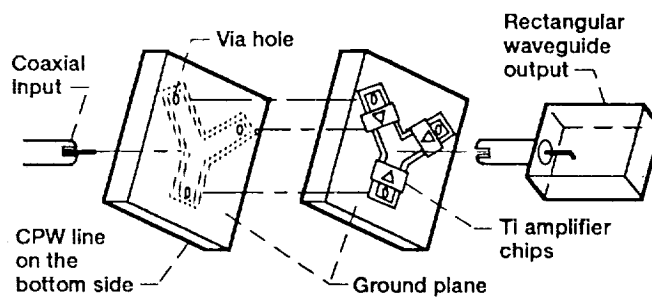
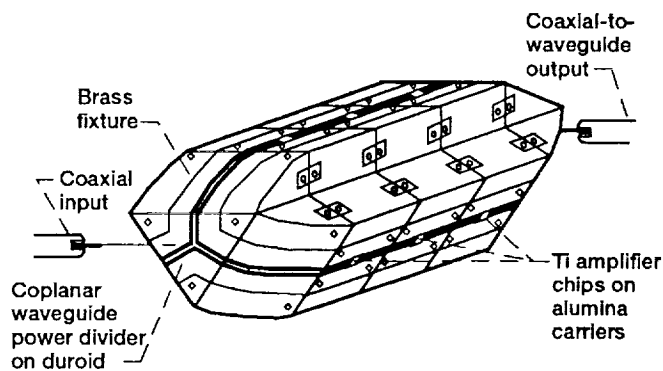


Figure 1.—Amplifier configuration.



(a) Alternate amplifier configuration.

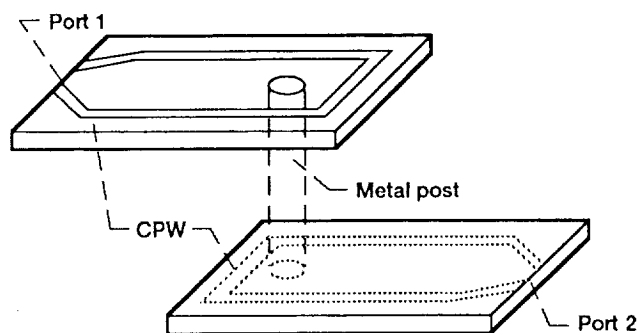
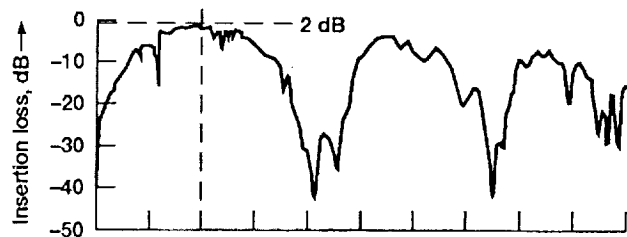


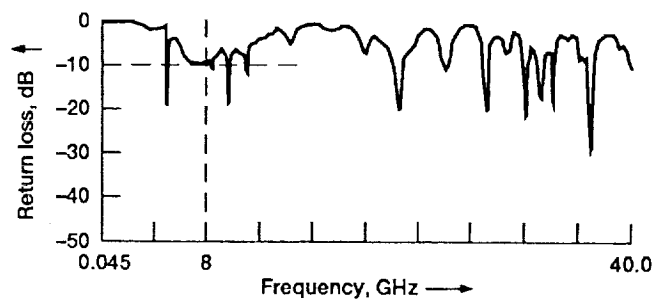
Figure 3.—CPW-to-CPW post coupler.



(b) Coax-to-CPW in-phase three-way radial nonplanar power divider/combiner.



(a)



(b)

Figure 4.—Post coupler S-parameters.

Figure 2.

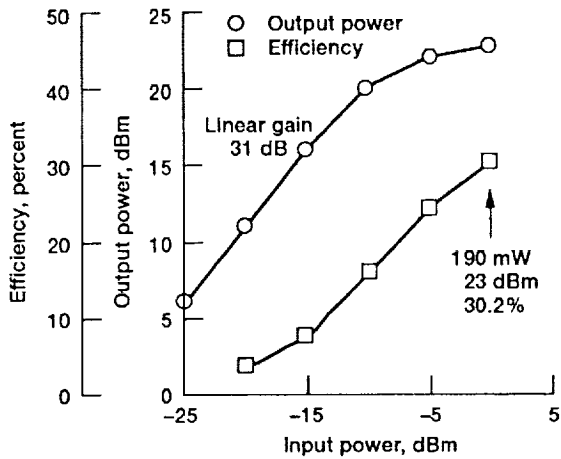


Figure 5.—Gain compression diagram of three-stage amplifier.

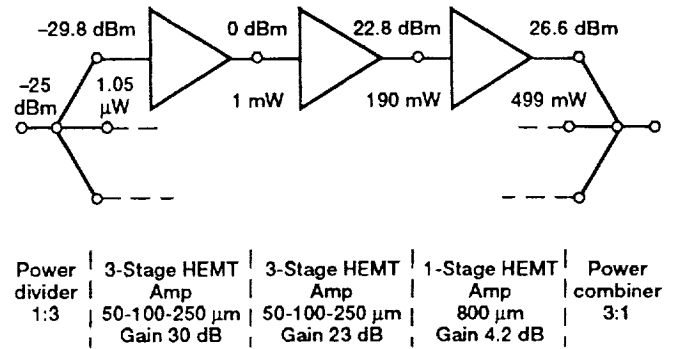


Figure 6.—MMIC combination scheme.

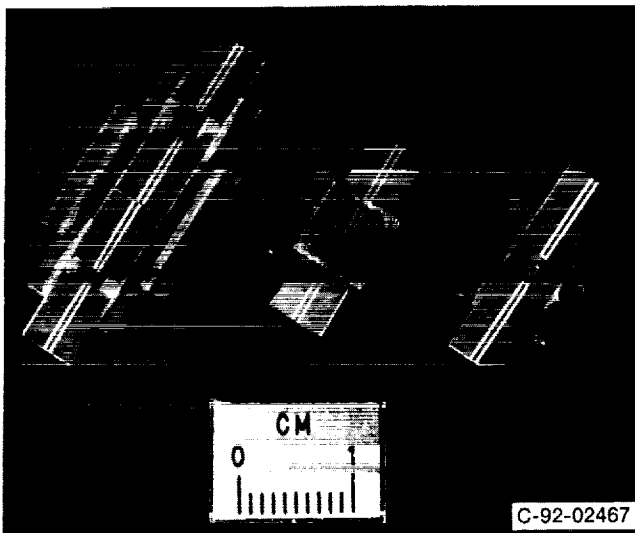


Figure 7.—Carrier with housing.

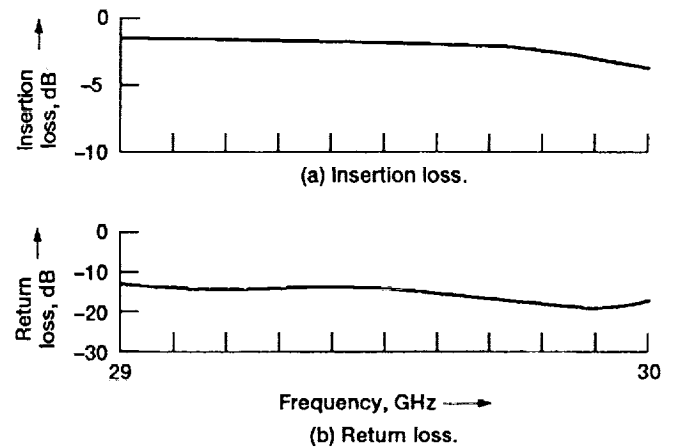


Figure 8.—Measured Insertion loss and return loss of the carrier.

ORIGINAL PAGE  
BLACK AND WHITE PHOTOGRAPH

# Comparative Evaluation of Optical Waveguides as Alternative Interconnections for High Performance Packaging

S. E. Schacham, Henri Merkelo, L.-T. Hwang, *Member, IEEE*, Bradley D. McCredie, Mark S. Veatch, and I. Turlik, *Senior Member, IEEE*

Permission to copy without fee all or part of this material is granted provided that the copies are not made or distributed for direct commercial advantage. Copying is by permission of the Institute of Electrical and Electronics Engineers. To copy otherwise, or to republish, requires a fee and specific permission.

## I. INTRODUCTION

As both silicon and GaAs based technologies drive device speeds into the multigigabit per second ranges, and rise times down to small fractions of a nanosecond, the quality of all circuit components including interconnections assumes ever increasing importance. Digital systems supported by these technologies are designed to operate in the multigigabit per second data regime, where synchronous clock and data distribution are extremely difficult to maintain. This means that for many geometries the interconnection lines have to be treated as broad-band transmission systems. Skin effect, dielectric properties and imperfections, and electromagnetic discontinuities can cause severe signal distortion in addition to randomizing propagation delays. Thin-film multichip package technology offers high density interconnection capability and design trade-off flexibility. However, conductor resistivity, cross section, length, choice of dielectrics, and driver/receiver characteristics must be all compatibly incorporated into each design in order for the system to function properly. The increased density of components within integrated circuits requires hundreds of electrical interconnections for each chip, and thousands of I/O ports for the entire package. Optical interconnections offer a potential solution to these increased requirements. The advantages of optical links are receiving wide acceptance, with the most relevant ones being: low attenuation in good structures, noise immunity, low cross talk, extremely high carrier frequencies (multiplexing capability), propagation delays being independent of fan out, and, in some cases, isolation of various parts of a circuit (e.g., the driver electronics from the receiver electronics). Optoelectronics offer an important supplement to the electrical signal transmission but poses its own set of technological challenges.

In the following sections, a comparative analysis of conventional conductors versus optical interconnections is presented. The discussion is focused on limitations of electrical transmission lines and the applicability of short range optical links in packages of high performance digital systems intended to operate at multigigabit rates. An effort is presented to define the conditions for which the optical alternative benefits system performance. Finally, the implementation of optical waveguides with polyimides, as part of the MCNC high performance package, is described.

*Abstract*— The well-known advantages of optical interconnections include high carrier frequency, low attenuation, high noise immunity, and, in ideal guides, low cross talk. In this paper, a detailed comparison between optical and electrical interconnections is presented, with the emphasis on advantages and drawbacks of optical link utilization. The impact of attenuation, dispersive degradation, and fan out on signal integrity is discussed. Reflections from discontinuities are taken into account in the section on fan out, but the issue of reflection is omitted in the remainder of the paper, not because it is unimportant, but because these reflections do not give either system an advantage. If anything, reflections are more troublesome in optical waveguide circuits than in electrical circuits. Bends in optical waveguides cannot exceed the limitations imposed by the index difference which precludes the existence of abrupt bends that mimic corners or vias in electrical interconnections. According to our results, there is no obvious advantage of using optical interconnections for the distribution of digital signals containing significant frequency components in excess of 10 GHz, unless substantial distances are involved, for which low dispersion optical waveguides could provide a solution. The actual electronic digital signal speeds for which suitable interconnections can be provided still depend as much on the skill of the designer as on the availability of materials or processes. Therefore, in high-speed digital systems, a detailed study has to be performed on the entire system before a decision is made as to which interconnection scheme is superior for a given application. Moreover, the reduction of the number of lines and ports by multiplexing and demultiplexing is limited by the electronics, for both electrical and optical approaches. Retention of waveform amplitude and integrity and tolerance of cross talk eventually become the key parameters that force the transition to the optical channel at ultra-high digital speeds. Approaching tens of picosecond rise time, dispersion and attenuation of electrical signals is detrimental, while optical waveforms are basically unaffected in low dispersion waveguides, making the transition to optical interconnections essential. The implementation of a polyimide optical waveguide in the MCNC package is discussed.

Manuscript received April 25, 1990; revised May 14, 1991.

S. E. Schacham was with the MCNC Center for Microelectronics Research Triangle Park, NC. He is now with the Department of Electrical Engineering, Technion-Israel Institute of Technology, Haifa 32000 Israel.

H. Merkelo and M. S. Veatch are with the Department of Electrical and Computer Engineering, University of Illinois, Urbana, IL 61801-2991.

L.-T. Hwang and I. Turlik are with the MCNC Center for Microelectronics, Research Triangle Park, NC 27709.

B. D. McCredie was with the Department of Electrical and Computer Engineering, University of Illinois, Urbana, IL. He is now with IBM, East Fishkill, NY.

IEEE Log Number 9104827.

## II. ATTENUATION

Optical techniques promise interconnections that overcome important limitations of conventional electrical interconnections [1]–[4], such as attenuation, dispersion, and cross talk (coupling noise). Computations of the attenuation as a function of frequency for transmission lines of arbitrary cross sections are relatively involved [5]–[7], and require a substantial amount of numerical computation. Generally, the line attenuation per unit length is

$$\alpha = \frac{R(\omega)}{2 \cdot \text{Re}\{Z_0\}} \quad (1)$$

where  $\text{Re}\{Z_0\}$  is the real part of the characteristic impedance. Since  $R$  is a function of frequency, this attenuation incorporates the conductor series resistance loss factor including the skin effect. Dielectric loss is neglected here. Then, for those geometries for which the internal and external inductances can be separated, the characteristic impedance of a transmission line is given by

$$Z_0 = \sqrt{\frac{R + jX + j\omega L_{\text{ext}}}{j\omega C_{\text{ext}}}} \quad (2)$$

where  $R$  and  $X = \omega L_{\text{int}}$  are the real and imaginary parts of the internal impedance of the line,  $L_{\text{int}}$  is the internal inductance of the line, and  $L_{\text{ext}}$  and  $C_{\text{ext}}$  are the external inductance and capacitance of the line. It should be noted that  $R$ ,  $L_{\text{int}}$ ,  $L_{\text{ext}}$ , and  $C_{\text{ext}}$  can be all implicitly frequency dependent. At high frequencies,  $Z_0$  approaches  $R_0 = \sqrt{L_{\text{ext}}/C_{\text{ext}}}$  which does not change with frequency in homogeneous dielectrics such as clad microstrip lines. For conventional, unclad microstrips, even this  $R_0$  term continues to change with frequency [7], [8], asymptotically approaching the value of the characteristic impedance of a parallel plate waveguide. All these differences directly affect high-speed electrical signal propagation. For example, the attenuation is calculated for a polyimide supported microstrip, homogeneously capped by the same material. The trace of the microstrip is made of copper  $8 \mu\text{m}$  wide and  $4 \mu\text{m}$  thick such that nominal  $R_0 \approx 58 \Omega$ . The frequency dependence of  $R = R(\omega)$  is totally determined by the current distribution in the metal which is shown in Fig. 1 for the  $8 \mu\text{m}$  by  $4 \mu\text{m}$  lead of the strip. Fig. 1(a) corresponds to the distribution of the 200-MHz frequency component of the current, and is contrasted with the 10-GHz component shown in Fig. 1(b). The attenuation  $\alpha(\omega)$  clearly rises with frequency as a result of the current crowding at the corners and at the bottom of the strip. The bottom of the strip is at  $y = 0$  in Fig. 1(a) and (b). Moreover, for frequencies up to approximately 0.2 GHz, the attenuation increases, as shown in Fig. 2, due to decreasing characteristic impedance caused by an increasing capacitive reactance. With a further increase in frequency, the capacitive reactance is compensated by the inductive reactance, and the signal attenuation is determined by the line resistance which includes the skin effect at high frequencies. Above 1 GHz, there is a substantial increase in attenuation due to current crowding as shown in Fig. 1, which increases resistance and decreases internal inductance.

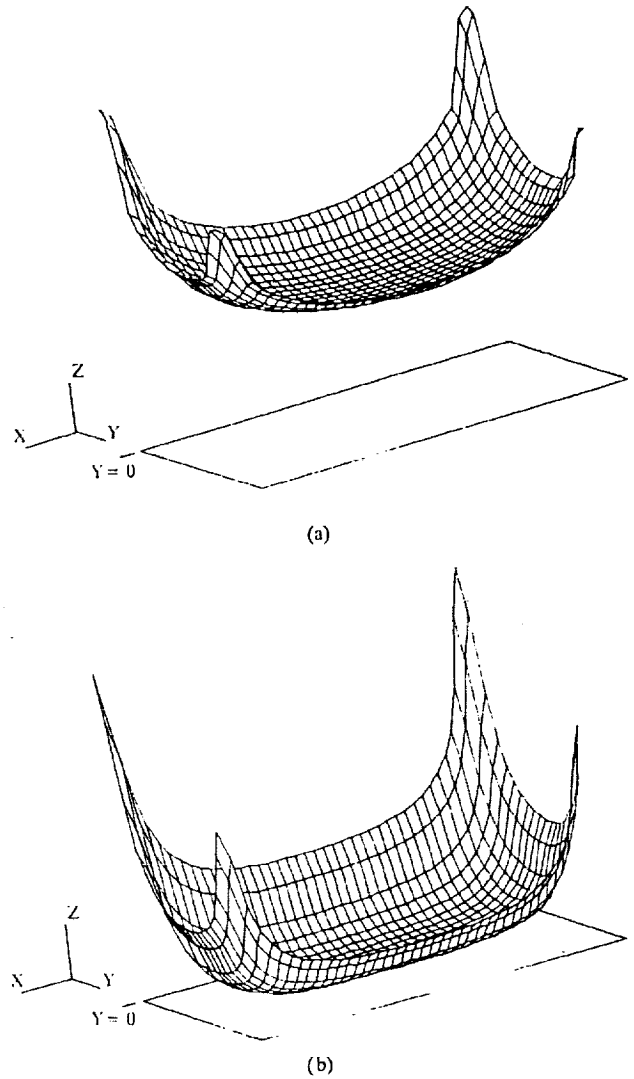


Fig. 1. Magnitude of current distribution within a  $8 \mu\text{m}$  by  $4 \mu\text{m}$  copper strip of a microstrip geometry of height  $H = 8 \mu\text{m}$ , width  $W = 8 \mu\text{m}$ , and thickness  $T = 4 \mu\text{m}$ , entirely embedded in a dielectric of  $\epsilon_r = 3.5$ . (a) At 200 MHz. (b) At 10 GHz.

Comparing this result to the optical alternative, it is obvious that the attenuation of communication quality optical fibers is lower by many orders of magnitude. However, the use of such fibers in a high performance package is highly impractical. The density and complexity of thin film multichip packages rule out the insertion and coupling of optical fibers, but allow the fabrication of optical waveguides directly in the package. The lowest losses for these waveguides are about 0.01 dB/cm, and are obtained with laser annealed polycrystalline ZnO. However, typical losses are in the range of 0.1–5.0 dB/cm [9]. Recently, transparent polyimides have been introduced for waveguide applications with attenuations in the range of 0.3–4.0 dB/cm [10]–[11]. In addition to the attenuation, optical interconnections suffer from various coupling losses (i.e., coupling of light source to the waveguide and the waveguide to the detector, or coupling/splitting between waveguides). It is important to point out that the losses of optical links are

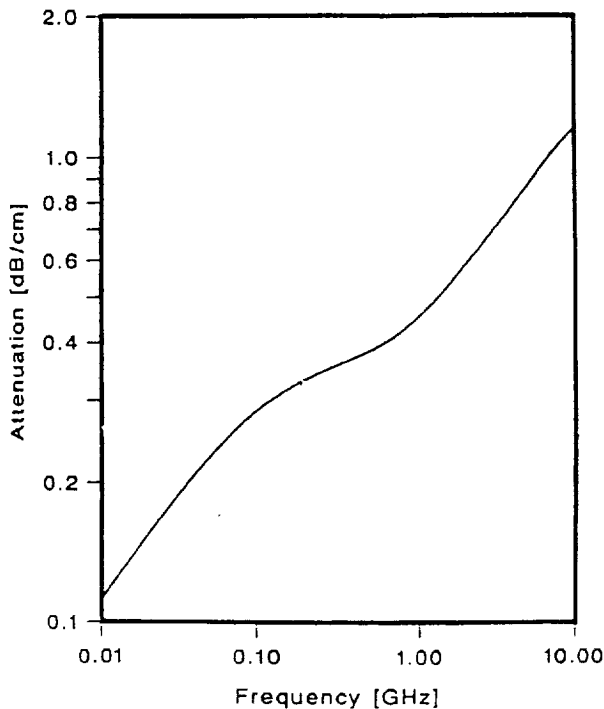


Fig. 2. Functional dependence of electrical attenuation for the microstrip specified in Fig. 1:  $H = W = 8 \mu\text{m}$ ,  $T = 4 \mu\text{m}$  (strip thickness),  $\epsilon_r = 3.5$ , and  $R_0 \approx 58 \Omega$ .

not dependent on digital rates and, therefore, not frequency dependent throughout the whole signal spectrum, but, as shown, the attenuation of electrical interconnections increases with frequency and eventually becomes larger than its optical counterpart.

### III. EFFECT OF FAN OUT ON OPTICAL SENSITIVITY

The derivation of the effect of optical fan out on the maximum operating rate of an optical interconnection is based on the reduction of the output power which, under ideal conditions, is equally split among  $N$  loads. In practice, however, more than half of the total power is lost in the fan out process. Since the noise increases with bandwidth, maintaining a specified bit error rate (BER) at a reduced output power implies a reduction in data rate. Assuming a Gaussian distribution, the BER is given by [12]

$$P(E) = \frac{1}{\sqrt{2\pi}} \int_Q^{\infty} e^{-x^2/2} dx \quad (3)$$

where

$$Q = \frac{|D - i|}{\langle i_n^2 \rangle^{0.5}} \quad (4)$$

with  $D$  defined as the decision level (current level above which the state is "1" and below which it is "0"),  $i$  is the expected signal current, and  $\langle i_n^2 \rangle^{0.5}$  is the rms noise.

Several sources contribute to the noise involved in the detection of optical signals, some of them are dependent on the

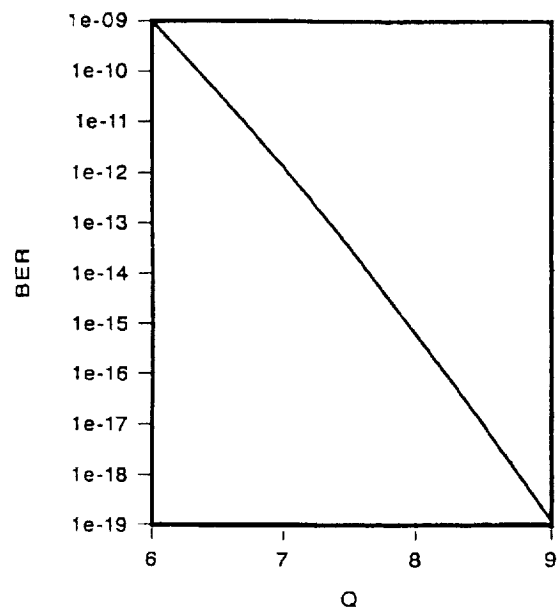


Fig. 3. BER versus  $Q$ .

photonic signal. The major sources are due to the photocurrent of the detector, the thermal noise generated by the biasing circuitry, and the noise due to the preamplifier. In digital receivers, the noise is dominated by circuit noise,  $\langle i^2 \rangle_c$ , while noise due to the detected signal is negligible [12]–[16]. For a quantum detector such as a p-n or a p-i-n photodiode, the optical power  $\eta\bar{P}$  required to achieve a desired error rate (i.e., receiver sensitivity) is determined by  $Q$ . If the decision level  $D$  is the half way between the "0" and "1" states, and if the "0" level is close to zero, then

$$\eta\bar{P} = \left(\frac{h\nu}{q}\right) Q \langle i^2 \rangle_c^{0.5} \quad (5)$$

where  $h\nu$  is the photon energy. For long distance communications, a BER of  $10^{-9}$  is usually assumed for a rate of 1 Gb/s. When manipulating words rather than single bits, a much lower BER must be imposed, typically  $10^{-17}$  at 1 Gb/s [2]. Fig. 3 shows the BER as a function of  $Q$  for the  $10^{-9}$  to  $10^{-19}$  range. Note that due to the exponential nature of (3), this tenth order of magnitude change in the BER is obtained by an increase in  $Q$  of only 50%. For a BER of  $10^{-17}$ ,  $Q = 8.5$ . Thus at a wavelength of 800 nm,  $\eta\bar{P} = 13.15 \langle i^2 \rangle_c^{0.5}$ , while for the 1300–1550 nm range,  $\eta\bar{P} = 8.1 \sim 6.8 \langle i^2 \rangle_c^{0.5}$ . The additional power required for achieving an improvement of eight orders of magnitude in the BER is less than 3 dB. This is, of course, a minimum value since degradation factors such as power rail noise and clock feedthrough require an increased optical signal to maintain the same BER.

The circuit noise of the receiver depends on the semiconductor technology and circuit design employed. The conventional approach to obtain a wide-band low noise front-end is by a transimpedance amplifier with a large feedback resistor. Even though the bandwidth is increased by a factor of  $A + 1$ , where  $A$  is the open loop gain, the use of such a design is limited due to the phase shift generated by the amplifier [13]. For

very high frequencies, a high impedance front-end such as a field effect transistor (FET) is utilized. The large  $RC$  time constant is corrected by a proper equalizer [13]. Indeed, a combination of a InGaAs avalanche photodiode and a GaAs FET in a high impedance configuration was employed to measure data at a rate of 8 Gb/s [17]. The receiver sensitivity was  $-25.8$  dBm for a BER of  $10^{-9}$ . The same data rate was detected with the same detector FET combination, but using a low input impedance configuration, required a minimum power of  $-15.5$  dBm for an equal BER [18].

The circuit noise current for a FET receiver is given by [12]–[15]

$$\langle i^2 \rangle_c = \frac{4kT}{R_L} I_2 B + 2qI_{\text{gate}} I_2 B + \frac{4kT\Gamma}{g_m} (2\pi C_T)^2 f_c I_f B^2 + \frac{4kT\Gamma}{g_m} (2\pi C_T)^2 I_3 B^3. \quad (6)$$

Here  $B$  is the bit rate,  $R_L$  is the load resistance,  $I_{\text{gate}}$  is the FET leakage current,  $g_m$  is its transconductance, and  $f_c$  is the  $1/f$  noise corner frequency. The total capacitance  $C_T$  is the sum of the FET gate capacitance, the detector capacitance  $C_d$ , and the stray capacitance  $C_s$ . The numerical factor  $\Gamma$  is a noise factor associated with channel thermal noise and gate induced noise of the FET. It is about 0.7 for Si and 1.1 for GaAs FET's. The definite integrals  $I_2$ ,  $I_3$ , and  $I_f$  depend only on the output pulse shape. For a rectangular pulse,  $I_2$  can be taken as 0.4,  $I_3$  as 0.03, and  $I_f$  as 0.1.

Originally derived for intermediate frequencies in the range of few hundred megabits per second [12], these formulas can also be adapted to very high frequencies. Thus since at these high data rates the drain load resistor  $R_D$  must be decreased in order to reduce the  $RC$  time constant,  $R_D$  may become a source for significant noise. This noise is taken into account by defining an equivalent  $\Gamma$  given by  $\Gamma_{\text{eq}} = \Gamma + 1/g_m R_D$  [16], [19]. This noise and the channel noise (the fourth term in (6)) can be minimized by optimizing the gate width upon which both  $g_m$  and  $C_T$  depend. For a well-designed FET preamplifier with a small leakage current, the circuit noise is dominated by Johnson noise due to the channel. To reach this limit,  $R_L$  should be made as large as possible to reduce the thermal noise (the first term in (6)). There is a trade-off between bandwidth and sensitivity, however, since this thermal noise is proportional to the first power of  $B$ , while Johnson noise is proportional to the third power. At a bit rate of 20 Gb/s with a  $g_m$  of 50 mmho and  $C_T = 1.5$  pF, Johnson noise is larger if  $R_L$  is more than 10  $\Omega$  (!). Indeed, these equations were utilized to analyze the noise of the amplifier for bit rates up to 20 Gb/s [16]. A detailed consideration of the various aspects of very high bit rates is given in [19].

The calculated sensitivity of p-i-n receivers as a function of data bit rate, up to 50 Gb/s, is shown in Fig. 4. As can be derived from (5) and (6), the minimal optical power required at the detector is proportional to  $B^{1.5}$ . In addition, the BER is rate dependent. Assuming a constant number of errors per unit time, the BER is linearly proportional to the inverse of the bandwidth. Since the change in  $Q$  is minimal, this effect is secondary. The parameters used in (6) for deriving the

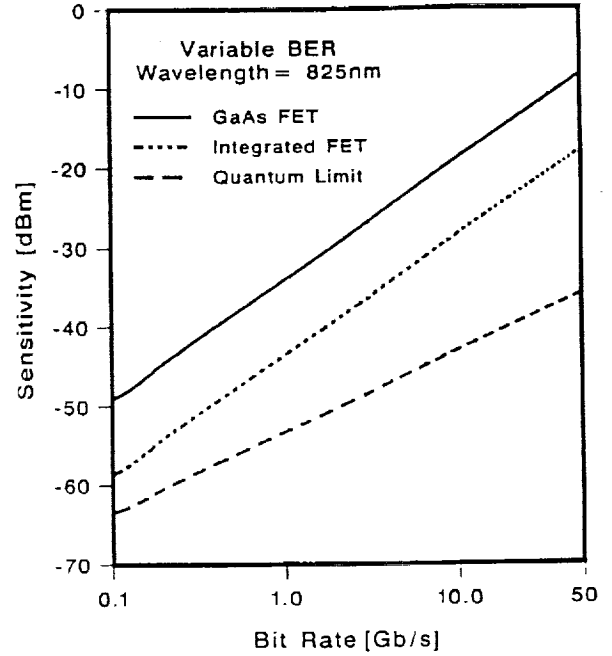


Fig. 4. Receiver sensitivity versus data rate at wavelength of 825 nm. BER ( $10^{-17}$  at 1 Gb/s) varies with the rate.  $C_T = 1.5$  pF for GaAs FET and  $C_T = 0.5$  pF for integrated FET.

noise generated by the FET were based on data of state-of-the-art GaAs transistors, capable of operating at these high frequencies. These were  $g_m = 50$  mmho and  $C_T = 1.5$  pF. Then, for a wavelength of 825 nm, at room temperature:

$$\eta\bar{P} = 4.68 \times 10^{-8} \cdot QB^{1.5} \quad (7)$$

when  $B$  is expressed in gigabits per second. The quantum limit curve reflects the minimum average number of photons per pulse required to assure that the probability of zero photoelectrons generated is below the dictated BER (e.g., 39 for BER =  $10^{-17}$  as compared to 21 for  $10^{-9}$ ). In addition, a third curve is added to represent the improved sensitivity attainable with integration of the detector and the FET on a single chip, thereby reducing the total capacitance to 0.5 pF.

When a bipolar transistor is used in the common emitter configuration as the front end, the circuit noise current is generated by the base current  $I_b$ , the collector current  $I_c$ , and the base spread resistance  $r_{b'b}$ . This current is given by [12]–[14], [16]:

$$\langle i^2 \rangle_c = \frac{4kT}{R_L} I_2 B + 2qI_b I_2 B + \frac{2qI_c}{g_m^2} (2\pi C_T)^2 I_3 B^3 + 4kTr_{b'b} [2\pi(C_d + C_s)]^2 I_3 B^3. \quad (8)$$

Here  $C_T$  includes the base-emitter capacitance  $C_{b'e}$  and the base-collector capacitance  $C_{b'c}$ . The third term is inversely proportional to the collector current since the transconductance  $g_m = qI_c/kT$ . In addition, the diffusion part of the capacitance  $C_{b'e}$  depends linearly on  $I_c$ , so an optimum collector current can be derived. At low frequencies, the optimum  $I_c$  is linearly

proportional to the bit rate, so both the shot noise generated by the base and by the collector render (equal) terms proportional to  $B^2$  [12]. Neglecting the contribution of the shot noise generated by the base current and assuming a large enough load resistor, one obtains for the low frequency range [12], [16]

$$\langle i^2 \rangle_c = 8\pi kTC_T \left( \frac{I_2 I_3}{\beta} \right)^{0.5} B^2 + 4kTr_{b'b} [2\pi(C_d + C_s)]^2 I_3 B^3. \quad (9)$$

Here  $\beta$  is the common emitter current gain. At very high bit rates, the optimum collector current is independent of  $B$ , that is,  $I_c = 2\pi kTC_o f_T / q$ , where  $C_o$  is the total low frequency capacitance and  $f_T$  is the current gain-bandwidth product. Under these conditions,  $C_T = 2C_o$  and the noise current is given by [13], [14], [16]

$$\langle i^2 \rangle_c = \frac{4kT}{R_L} I_2 B + \frac{16\pi kTC_o}{f_T} I_3 B^3 + 4kTr_{b'b} [2\pi(C_d + C_s)]^2 I_3 B^3. \quad (10)$$

The cross-over point between the low and the high bit rate regimes is at  $B = f_T(I_2/\beta I_3)^{0.5}$ . The last term in (10) is dominant at high frequencies provided that  $f_T$  and the load resistor are large enough. For typical values of  $r_{b'b} = 100 \Omega$  and  $C_d + C_s = 1$  pF, the receiver sensitivity at 825 nm is given by

$$\eta \bar{P} = 6.62 \times 10^{-8} \cdot QB^{1.5} \quad (11)$$

for  $B$  in gigabits per second. Comparing to the expression presented in (7) for an FET front-end, the bipolar circuitry does not seem to have any advantage over the FET. Even if the stray capacitance  $C_s$  is substantially reduced by integration, the effect on the sensitivity is not dominant. Only with an improvement in technology resulting in a significant reduction in the base resistance  $r_{b'b}$ , can the bipolar transistors become more competitive. Fig. 5 shows the receiver sensitivity for GaAs FET and bipolar front-ends for the parameters specified in Fig. 4 except that the wavelength is 1550 nm.

The mathematical process of evaluating the effect of fan out on the maximum bit rate is quite intricate since the relationships between the detected power,  $Q$ , and the BER are not explicit. The computation is based on the assumption that the system is operating at its maximum data rate for a one to one link ( $N = 1$ ). The optical power is now split between  $N (>1)$  receivers equally. Knowing the reduced power, the data bit rate is derived. Starting with maximum bit rates of 0.1, 1, and 10 Gb/s for  $N = 1$ , Fig. 6 illustrates the effect of fan out on the maximum bit rate. No excess losses, in either the waveguide or the coupling and splitting, are taken into account in these plots. With 10 Gb/s for  $N = 1$ , a similar analysis is shown in Fig. 7, for which four different levels of total losses are assumed. The effect of these losses is quite devastating. When the excess losses (including coupling, splitting, and total attenuation) are 4 dB per link, the maximum operating data rate is reduced more than 3 orders of magnitude for a fan out of 10.

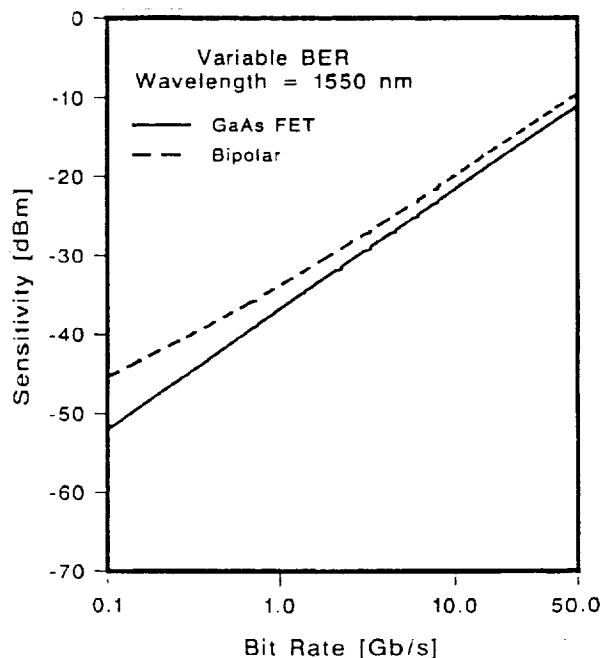


Fig. 5. Receiver sensitivity versus data rate at wavelength of 1550 nm for GaAs FET and bipolar.

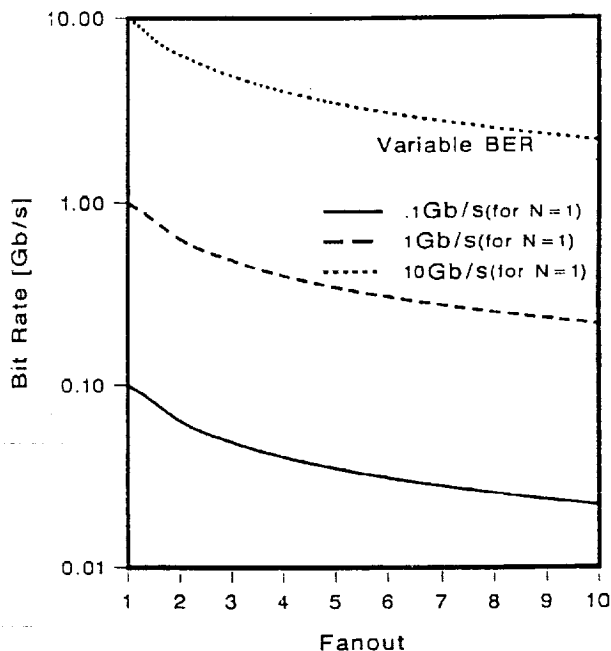


Fig. 6. Maximum bit rate as a function of fan out for various bit rates of lossless links.

#### IV. FAN OUT IN ELECTRICAL NETWORKS

Turning the attention to fan out in electrical circuits, it should be noted that there is a tradition of thinking about fan out in electrical circuits as being distinct from that of fan out in optical channels by the fact that line charging takes place in one and not the other. This difference is indeed real but only in the sense that it is much easier to accumulate electrons than it

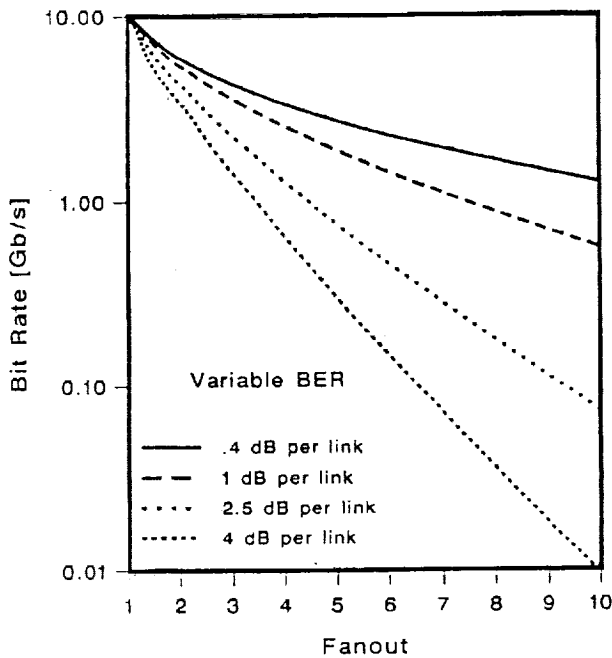


Fig. 7. Maximum bit rate as a function of fan out for various levels of overall losses at 10 Gb/s,  $N = 1$ .

is to accumulate photons. This distinction vanishes when first-incidence logic is considered for both optical and electrical systems, which is the only logic that can be considered for optical networks, unless optical resonators are built into the channels. For charge-accumulation logic to take place, the propagation time through the interconnections must be shorter than or comparable to the significant waveform features, particularly fall and rise times. Because of the advantages and the feasibility of fully charging short electrical lines, such accumulation logic is frequently assumed for electrical networks (e.g., interconnections in VLSI chips) which, of course, is not without penalties. Thus when assuming accumulation logic for electrically interconnected networks, some of the effects of fan out on electrical interconnections are presented by Haugen *et al.* [1]. For this mode of operation, an increased fan out results in a lower effective characteristic impedance, e.g., a 50- $\Omega$  line impedance is effectively reduced to a lower value depending on the dielectric constant, the relative lengths of lines, and the degree of fan out. For example, for a polyimide stripline structure (with capacitance 1.25 pF/cm), the loading density is limited to approximately 3 pF every 2 cm to ensure that the reflection coefficient  $\rho$  is less than 0.2. Again for charge accumulation logic, a larger fan out requires a larger driving power and it results in slower signal response.

In contrast, when first incidence logic is assumed, many of the considerations for electrical systems are similar to optical networks, with square law detection for photonics being the principal distinction. Assuming first incidence logic, a load on a terminated electrical line (i.e., fan out  $N > 1$ ) may limit the maximum bit transmission rate, depending on load and line length. Two fan-out schemes are discussed here: one with loads at the end of the line (Fig. 8(a)), and the other with loads at

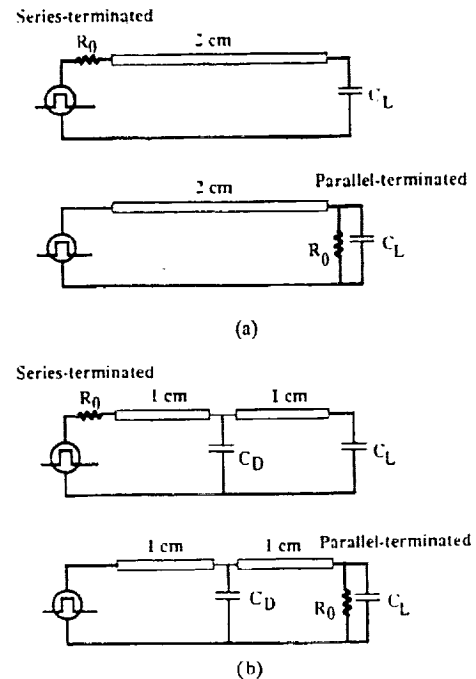


Fig. 8. Circuit diagrams for two different fan out schemes with both series and parallel terminations, (a) Loads at the end of the line. (b) Loads at the end and the middle of the line.

the middle of the line (Fig. 8(b)). In each fan-out scheme, both termination methods (i.e., series termination and parallel termination) are considered. The termination resistor,  $R_0$ , is the high frequency limit characteristic impedance (i.e.,

$$R_0 = \lim_{\omega \rightarrow \infty} Z_0$$

where  $Z_0$  is defined in (2)). Since the wire segment connecting the transmission line and the receiving pad is only 0.5 mm, it was considered as a lumped circuit. A total capacitance of 0.1 pF is assumed for each electrical fan out, which consists of contributions from the wire segment, the receiving pad, and the receiver gate. Fig. 9 shows the output signal waveforms derived for a 2-cm copper line of the cross section given earlier (8  $\mu$ m by 4  $\mu$ m) with a fan out of 1 ( $N = 1$ ), while Fig. 10(a) and (b) shows the same for a fan out of 3 ( $N = 3$ ); all waveforms are calculated by assuming a trapezoidal input shown in the same figures. Output waveforms in Fig. 9 ( $N = 1$ ) can be obtained either by using Fig. 8(a) with  $c_L = 0.1$  pF or using Fig. 8(b) with  $c_L = 0.1$  pF and  $c_D = 0$  pF. Output waveforms in Fig. 10(a) were obtained using Fig. 8(a) with  $c_L = 0.3$  pF, while those in Fig. 10(b) were obtained using Fig. 8(b) with  $c_L = 0.1$  pF and  $c_D = 0.2$  pF. For  $N = 1$ , the peak of the output waveforms is greater than 50% of the input, and the amplitude of the reflections is small, the output waveforms are considered as adequate for switching the receiving devices. For  $N \geq 3$ , the peak of the output waveforms is reduced, and the amplitude of the reflections is increased. The transient output waveforms are seriously degraded. The noise margin is greatly reduced, and the waveforms might fail to switch the receiving gates. It is

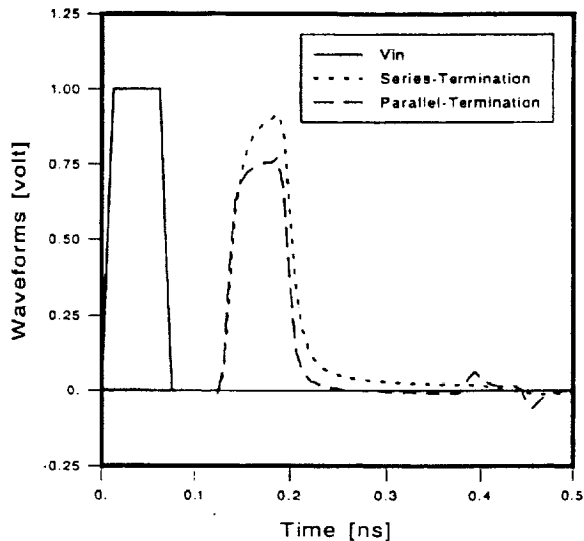


Fig. 9. Output waveforms of a 2-cm long microstrip described in Fig. 1 for both series and parallel terminations, at 8 Gb/s, fan out  $N = 1$  (i.e.,  $c_L = 0.1$  pF in Fig. 8(a)).

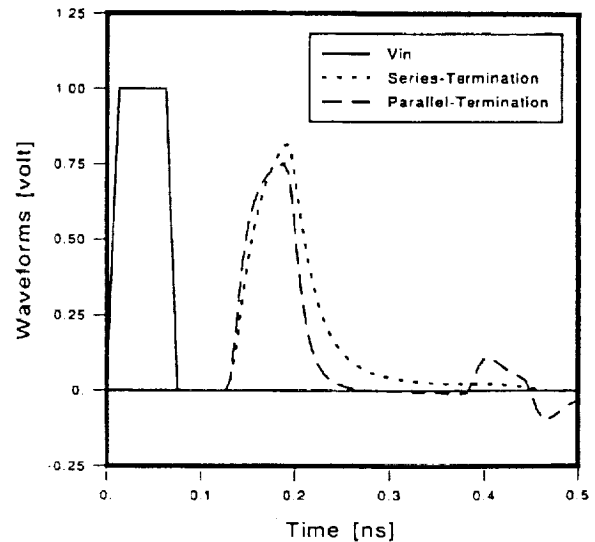
also observed that the attenuation of a 10-cm long line is such that even for a single load (i.e.,  $N = 1$ ) the output signal at 8 Gb/s is below 50% for both terminations.

Because modeling and simulation of the propagation of digital electrical signals has achieved a high degree of precision, even in networks of high complexity [20], [21], actual examples of signal damping and dispersion are shown in the next section for first incidence logic design considerations.

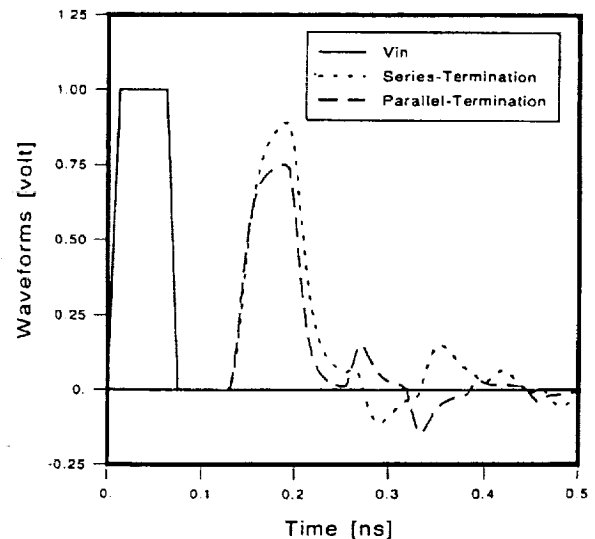
#### V. EFFECT OF DAMPING AND DISPERSION ON MAXIMUM BIT RATE

As discussed in the previous section, the limitation on the maximum operating data bit rate of an optical interconnection is the power reaching the receiver of a compatible bandwidth. Improving coupling efficiency, reducing waveguide attenuation, and developing more powerful sources can all contribute to higher operating speeds. Avalanche photodiodes provide better signal-to-noise ratio [12]–[16], however, higher voltages (tens of volts) are required for their biasing, which may be not acceptable within a package. Monolithic integration on III-IV semiconductors or flip-chip interconnection for the optoelectronics [22] should help reduce the noise at extremely high frequencies. Moreover, single mode optical waveguides are assumed throughout, which is not always achievable in practice. Also, of course, it is well known that modal dispersion can very quickly dominate all other effects [21].

The considerations for electrical transmission lines as discussed above range from charge accumulation logic to first incidence logic. For a better comparison to the optical alternative, first incidence logic, which does not suffer from the  $RC$  type of pulsewidth broadening described previously, is under the influence of several propagation induced high frequency effects which are principally dispersive damping and dispersive phase distribution. These dispersive effects,



(a)



(b)

Fig. 10. Waveform distortion due to fan out for microstrips described in Fig. 1 for both series and parallel terminations, at 8 Gb/s, fan out  $N = 3$ . (a) Using Fig. 8(a) with  $c_L = 0.3$  pF. (b) Using Fig. 8(b) with  $c_L = 0.1$  pF and  $c_D = 0.2$  pF.

which also manifest themselves in the design of multiple transmission line matching and termination matching, cause the most deleterious high-speed network phenomena. The positive aspect of electrical network technologies is that fabrication and processing are at a very high level of development. What's more, methods and tools for designing and analyzing ultra-high-speed networks with high precision are also developing rapidly [22]. Therefore, very exacting rules of electromagnetic propagation can be applied to the engineering of ultra-high-speed digital electronic networks of high complexity.

Several specific examples of high-speed digital pulse propagation are shown for illustrating the damaging effects of damping and dispersion but also for demonstrating the relative tolerance of high-speed signals to these effects in the context

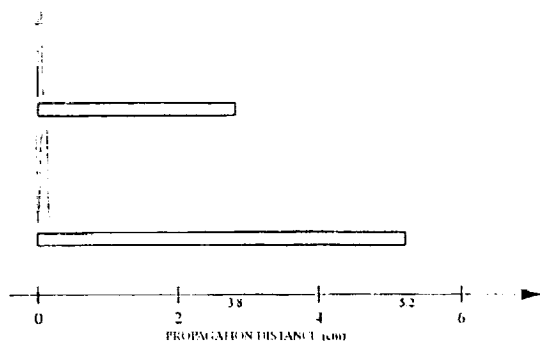


Fig. 11. Illustration of the propagation of high-speed digital signals on the microstrip described in Fig. 1. The effects of metal conductivity  $\sigma = 5.8 \times 10^7$  mho/m on both damping and dispersion are included without approximations. Rounded corner trapezoidal signals of full-width at half maximum (FWHM) of 5 ps (top) and 10 ps (bottom) are propagated to distance at which 50% of amplitude is lost.

of electronic interconnections. Rounded trapezoids are chosen to approximate practical waveforms. Rise time and pulse spacings are such that the signals correspond to ultra-high digital rates; namely, 67 and 133 Gb/s. The individual signals in these waveforms are 5 and 10 ps full width at half-maximum (FWHM) with 7.5- and 15-ps spacing, respectively. Fig. 11 shows the propagation of these digital waveforms on a 8- $\mu\text{m}$  by 4- $\mu\text{m}$  copper strip placed on a polyimide dielectric in a microstrip configuration for which Figs. 1 and 2 were prepared. The propagation in this geometry is nearly totally dominated by loss with a mild phase dispersion caused by the resistance of the strip, regardless whether the strip is clad or unclad. The criteria for maximum distance propagation are that either one of the signals diminished to 50% of its launched magnitude or that the peaks separated in time such that the amplitude is effectively 50% of the initial amplitude. For the purpose of discussion, signal levels above 50% are considered "1" and signals below 50% are considered "0." By these criteria, digital signals of 5-ps FWHM propagate 3.8 cm and signals of 10-ps FWHM propagate 5.2 cm. These are not long distances but, of course, these are ultra-high-speed digital signals.

Figs. 12 and 13 illustrate the propagation of the same signals on much wider microstrips ( $W = 100 \mu\text{m}$ ) fabricated on the same dielectric,  $\epsilon_r = 3.5$ . Fig. 12 shows the effect of dispersion in an unclad microstrip when loss is neglected. Nearly an order of magnitude greater distance is traversed by 10-ps signals than by 5-ps signals. This advantage is reduced to a factor of two when dispersive attenuation is taken into account as shown in Fig. 13.

Clearly, even though these limiting examples show severely damaging effects of ordinary conductors, it is evident that ample range exists between the rates of systems operating to date and the rates at which systems can be designed in the future.

## VI. POLYIMIDE WAVEGUIDES

The implementation of optical interconnections into a high performance multichip module was studied. Since polyimide materials are used as the dielectrics for the thin-film inter-

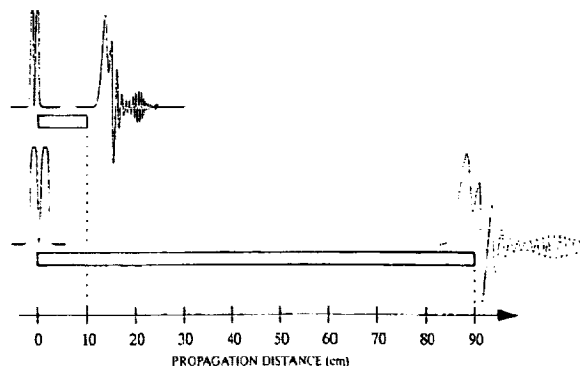


Fig. 12. Illustration of the propagation of high-speed digital signals on a lossless, unclad microstrip of  $W = 100 \mu\text{m}$ ,  $H = 44 \mu\text{m}$ ,  $T = 1 \mu\text{m}$ ,  $\epsilon_r = 3.5$  (i.e., nominal  $R_0 \approx 50 \Omega$ ) showing dispersion dominated signal degradation for 5-ps FWHM (top) and 10-ps FWHM (bottom) waveforms. Here, because of destructive interference, 50% of magnitude at the location of the second digit is reached before the entire magnitude of the second digit has lost 50% of its value.

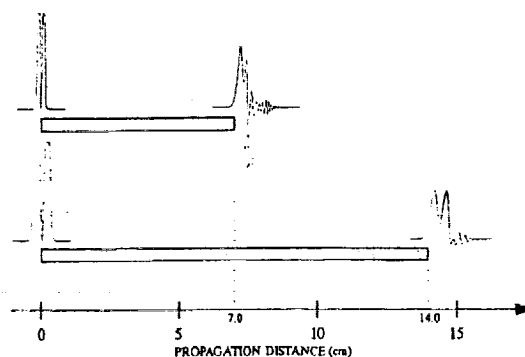


Fig. 13. Same illustration as Fig. 12 with conductor losses ( $\sigma = 5.8 \times 10^7$  mho/m) taken fully into account.

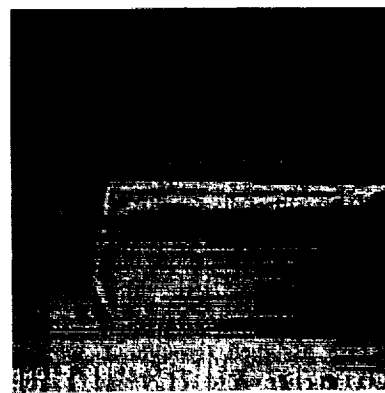


Fig. 14. Cross section of a polyimide waveguide. Core material: DuPont PI2525; cladding material: PI2566. Core dimensions are  $20 \mu\text{m} \times 10 \mu\text{m}$ .

connections, various combinations of polyimides are being explored to establish their suitability as optical links. Fig. 14 shows the cross section of one such waveguide. The core material is a DuPont PI2525, with refractive index  $n = 1.70$ . The cladding material is either  $\text{SiO}_2$  or DuPont PI2566 with refractive indexes of  $n = 1.48$  and  $n = 1.58$ . These materials and the related processing schemes are compatible with

processes involved in the manufacturing of the MCNC high performance multichip package. Various cross-sectional dimensions are characterized, ranging from  $5 \times 10 \mu\text{m}^2$  and up to  $100 \times 20 \mu\text{m}^2$ . Typical losses measured for these waveguides are on the order of 3 dB/cm. Obviously, since multimoding has not been taken into account, the size of the waveguides have to be moderated, especially when the normalized waveguide cladding index differences can be as high as 0.15. Fluorinated polyimides, known to have lower attenuation [10], are currently under investigation as core material for these waveguides.

## VII. CONCLUSIONS

The comparison between optical and electrical interconnections for high performance applications involves a large number of parameters. With the exception of reflections from discontinuities, the key issues are discussed in this paper. It is shown that the attenuation of a transmission line increases with frequency due to the skin effect, and approaches 1 dB/cm at 10 GHz for particularly miniaturized structures. The attenuation of an optical link also depends on the material used for implementing the waveguide; however, it is independent of modulation frequency. However, unless single mode optical waveguides are assumed, modal dispersion can very quickly dominate all other considerations when the dimensions of the guide and the index difference are large. If pulse spreading in a step-index waveguide of length  $L$  is written as

$$\delta = Ln_1 \frac{\Delta}{c} \frac{1}{2\sqrt{3}} \quad (12)$$

where  $\Delta = (n_1 - n_0)/n_0$  is the normalized index difference [23],  $c$  is the speed of light, then  $\delta$  can range from 12.5 to 25 ps for a 10-cm length when the range of  $n_0$  is between 1.48 and 1.58, as for the cited materials.

Fan out reduces the maximum bit rate throughout the spectrum for optical interconnections, while its effect is noticeable only in the gigabits per second regime for a terminated electrical line when charge accumulation principles are valid. When first incidence logic considerations apply, an electrically interconnected system is analyzed in the same manner as an optically interconnected system without the optical square law provision. Then, even higher digital rates can be achieved. Other parameters, such as power consumption, depend on the specific technology and devices employed [1], [3], [4].

The reduction of the number of I/O ports by multiplexing the signal over a single link seems to be a very attractive approach. Still, the technology is limited and the fastest multiplexers commercially available are in the few gigabits per second range and could be used in electric connections as well. The realization of optical sources and detectors along with the waveguides for optical interconnections, including all the supporting electronics, is complex and is not likely to be widely implemented presently. In spite of that, as frequency content increases, optical interconnections can become advantageous. At ultra-high data rates, the retention of pulse shape over significant distances becomes the key parameter that forces the transition from electrical interconnections to the optical

channel. The electro-optical components must be integrated in order to minimize the required area and to assure performance enhancement. At such high digital rates, additional electronics is required to generate and detect optical signals, maintaining an extremely high signal-to-noise ratio. At that point, the entire package configuration is driven by the trade-off between core components and supporting electronics. In the meantime, dielectric materials with low relative permittivity must be employed for electrical signal distribution, not only because of the shorter propagation delays but also because of the dispersive effects that are illustrated.

## ACKNOWLEDGMENT

The authors would like to thank Theodore (Ted) G. Tessier for his help in fabricating the polyimide waveguides, and Glenn A. Rinne for proofreading the manuscript.

## REFERENCES

- [1] P. H. Haugen, S. Rychnovsky, A. Husain, and L. D. Hutcheson, "Optical interconnects for high speed computing," *Opt. Eng.*, vol. 25, no. 10, pp. 1076-1085, 1986.
- [2] D. H. Hartman, "Digital high speed interconnects: a study of the optical alternative," *Opt. Eng.*, vol. 25, no. 10, pp. 1086-1102, 1986.
- [3] R. K. Kostuk, J. W. Goodman, and L. Hesselink, "Optical imaging applied to microelectronic chip-to-chip interconnections," *Appl. Opt.*, vol. 24, pp. 2851-2858, 1985.
- [4] M. R. Feldman, S. C. Esner, C. C. Guest, and S. H. Lee, "A comparison between optical and electrical interconnections based on power and speed considerations," *Appl. Opt.*, vol. 27, pp. 1742-1751, 1988.
- [5] W. T. Weeks, L. L. Wu, M. F. McAllister, and A. Singh, "Resistive and inductive skin effect in rectangular conductors," *IBM J. Res. Develop.*, vol. 23, pp. 652-660, 1979.
- [6] C. S. Yen, Z. Fazarinc, and R. L. Wheeler, "Time-domain skin-effect model for transient analysis of lossy transmission lines," *Proc. IEEE*, vol. 70, pp. 750-757, July 1982.
- [7] B. D. McCredie, M. S. Veatch, and H. Merkelo, "Issues and results in modeling dielectrically inhomogeneous propagation channels for high speed digital applications," in *Proc. Int. Electronics Packaging Society*, Marlborough, MA, Sept. 10-12, 1990, pp. 719-755.
- [8] M. S. Veatch, B. D. McCredie, and H. Merkelo, "Ultra-high speed, ultra-broadband characteristics of microstrips," in *Proc. Int. Electronics Packaging Society*, Marlborough, MA, Sept. 10-12, 1990, pp. 699-718.
- [9] F. S. Hickernell, "Optical waveguides on silicon," *Solid State Technol.*, vol. 31, pp. 83-88, Nov. 1988.
- [10] R. Reuter, H. Franke, and C. Feger, "Evaluating polyimides as lightguide materials," *Appl. Opt.*, vol. 27, no. 21, pp. 4565-4571, Nov. 1988.
- [11] R. Selvaraj, H. T. Lin, and J. F. McDonald, "Integrated optical waveguides in polyimide for wafer scale integration," *J. Lightwave Technol.*, vol. 6, pp. 1034-1044, June 1988.
- [12] R. G. Smith and S. D. Personick, "Receiver design for optical fiber communication systems," in *Semiconductor Devices for Optical Communications*. New York: Springer-Verlag, 1980, ch. 4, pp. 89-160.
- [13] B. L. Kasper, "Receiver design," in *Optical Fiber Telecommunications II*, S. E. Miller and I. P. Kaminow, eds. San Diego, CA: Academic, 1988, ch. 18.
- [14] T. V. Muoi, "Receiver design for high-speed optical-fiber systems," *J. Lightwave Technol.*, vol. LT-2, pp. 243-267, 1984.
- [15] S. R. Forrest, "Optical detectors for lightwave communication," in *Optical Fiber Telecommunications II*, S. E. Miller and I. P. Kaminow, eds. San Diego, CA: Academic, 1988, ch. 14.
- [16] B. L. Kasper and J. C. Campbell, "Multigigabit-per-second avalanche photodiode lightwave receivers," *J. Lightwave Technol.*, vol. LT-5, pp. 1351-1364, 1987.
- [17] B. L. Kasper, J. C. Campbell, J. R. Talman, A. H. Gnauck, J. E. Bowers, and W. S. Holden, "An APD/FET optical receiver operating at 8 Gbit/s," *J. Lightwave Technol.*, vol. LT-5, pp. 344-347, 1987.
- [18] A. H. Gnauck, J. E. Bowers, and J. C. Campbell, "8 Gbit/s transmission over 30 km of optical fiber," *Electron Lett.*, vol. 22, pp. 600-602, 1986.
- [19] M. Brain and T. P. Lee, "Optical receivers for lightwave communications systems," *J. Lightwave Technol.*, vol. LT-3, pp. 1281-1300, 1985.

- [20] H. Merkelo, IEEE Computer Packaging Workshop, Brussels, Belgium, Sep. 20–23, 1987.
- [21] H. Merkelo, B. D. McCredie, M. S. Veatch, D. L. Quinn, M. C. Dorneich, and Y. Doi, "Methods for comparative analysis of waveform degradation in electrical and optical high performance interconnections," in *Proc. 1990 IEEE/SPIE Symp. on Advances in Interconnects and Packaging*, Boston, MA, Nov. 5–9, 1990, pp. 91–163.
- [22] K. Katsura, T. Hayashi, F. Ohira, S. Hata, and K. Katashita, "A novel flip-chip interconnection technique using solder bumps for high-speed photoreceivers," *J. Lightwave Technol.*, vol 8, pp. 1323–1327, 1990.
- [23] J. E. Midwinter, *Optical Fibers for Transmission*. New York: Wiley, 1979.

***SECTION  
TWO***

***DEVELOPMENT OF  
HETEROJUNCTION  
MATERIALS AND DEVICES***



## NEW MATERIALS AND TECHNIQUES FOR IMPROVED mm WAVE DEVICES

Samuel A. Alterovitz  
Space Electronics Division  
NASA Lewis Research Center, Cleveland, Ohio 44135

### Abstract

This paper summarizes the work performed at or for the Lewis Research Center with the goal of improved microwave and mm wave three terminal semiconductor devices. In particular, we will dwell on the work devoted to the development of the pseudomorphic InGaAs modulation doped field effect transistor (MODFET) made on the commercial semi-insulating substrates GaAs and InP. The work includes the conceptual development, the molecular beam epitaxy (MBE) growth of the material, the first operating device on GaAs substrate and its subsequent optimization. Results greatly superior to the AlGaAs/GaAs MODFET were obtained. Our efforts in technology transfer of this device, which continue to date using a non-MBE growth method, resulted in a widely accepted device in the industrial microwave community. Our present work in the application of high indium concentration MODFET grown on InP in the temperature range of 120-150K (or lower) will also be described.

### Introduction

The main goal of the technology base research on new electronic materials and devices at the Solid State Technology Branch of the NASA Lewis Research Center is the improved performance of active and passive devices for space communications. A secondary but very important goal is technology transfer. In this paper we will describe both the performance results actually obtained and the way technology transfer has been successfully achieved in this project in the area of an advanced three terminal device, namely the pseudomorphic InGaAs MODFET (modulation doped field effect transistor).

The progress in the new electronic materials' development in the last decade was driven by the epitaxial growth of III-V semiconductors using either molecular beam epitaxy (MBE)

or metal organic chemical vapor epitaxy (MOCVD). As these two methods require a large commitment of funds and manpower, the budget constraints forced us to choose awarding and monitoring grants and contracts done outside Lewis Research Center to achieve our goals in materials development, with the in house lab work devoted to material characterization and some device testing. This fact has helped markedly in the technology transfer goal.

A MODFET device includes a low bandgap undoped material, InGaAs in this case, grown adjacent to a higher bandgap doped semiconductor, AlGaAs, GaAs, or InAlAs in the present case. This combination creates a quantum well in the InGaAs, where quantum confined electrons will accumulate. It turns out that MODFET devices have superior performance vs. single material field effect transistors (FET) due to a combination of factors, mostly due to the quantum well structure and to the properties of the material of the well.

The paper is divided in two main parts: program description and technological results. In each part, the effort done by the three material growth groups that worked with our support and collaboration, namely University of Illinois, University of Michigan and Spire Corp., will be described.

### Program Description

The work started in 1984, when several grant proposals were received and evaluated at Lewis Research Center. The funding source for this new subject was the "Fund for Independent Research" (F.I.R.), which is a center wide fund. High risk, high reward grant proposals are summarized and highlighted by NASA scientists for their merits, both for NASA and for general applications. This new shorter version of the grant proposals compete for a limited number of grants under the F.I.R.

sponsorship. The highest risk-reward proposal in the electronic materials subject was received from Prof. H. Morkoc from the University of Illinois. The group at Illinois had developed successfully the first generation GaAs/AlGaAs MODFET and was looking to a new concept: strain lattice MBE epitaxial growth. Their proposal called for epitaxial growth of InGaAs on GaAs. The problem here was the fact that  $\text{In}_x\text{Ga}_{1-x}\text{As}$  even for low  $x$  values is not lattice matched to GaAs, while the materials used previously (AlGaAs and GaAs) are almost perfectly lattice matched. The electronic properties<sup>(1,2)</sup> of  $\text{In}_{0.53}\text{Ga}_{0.47}\text{As}$  are much better than GaAs. By interpolation, any  $\text{In}_x\text{Ga}_{1-x}\text{As}$  material with  $x > 0$  is better than GaAs. Using this fact and the reduced device channel thickness (to reduce strain) I was able to make a case in the F.I.R. competition that this proposal was (marginally) feasible and F.I.R. funding was approved. It turned out that two other groups were working at the same time on an InGaAs strained layer single quantum well MODFET, namely Sandia National Labs<sup>(3)</sup> and IBM<sup>(4)</sup>. All three groups published their results in a two month period. However, the University of Illinois device itself and the concept behind it<sup>(5)</sup> turned up superior to the others. The most important point of the University of Illinois device was the use of the combination AlGaAs/InGaAs/GaAs vs. GaAs/InGaAs/GaAs,<sup>(3,4)</sup> a fact that allowed a larger bandgap discontinuity in the device, with accompanying better confinement and better current carrying capability. The MODFET material growth was optimized by the Univ. of Illinois,<sup>(6-8)</sup> but they were limited by their lithography. Some material characterization, using the complex technique of Shubnikov de Haas<sup>(9)</sup> was done at Lewis Research Center. In 1986, a 0.25 micron gate MODFET was fabricated using the Illinois grown material by G.E. Syracuse Electronics Laboratory<sup>(10)</sup> and the results were absolutely spectacular. As the InGaAs based MODFET could easily be made with the hardware available in the industry for GaAs/AlGaAs MODFET and using commercial GaAs substrates, most microwave industries moved to the new device, and it became the

device of choice. A recent paper<sup>(11)</sup> describes the wide applicability of this device for monolithic microwave integrated circuits (MMIC). Our own group at Lewis Research Center went one step further in the application of InGaAs on GaAs MODFET by releasing an RFP (request for proposal) for a MMIC transmitter technology in the 30-70 GHz range in May 1987. The contract was subsequently awarded to Hughes Aircraft and included the new devices. This way both space communications applications and complete technology transfer were achieved for this new material and device.

The next step was again driven by the general considerations given in references 1 and 2, namely the higher the indium concentration in  $\text{In}_x\text{Ga}_{1-x}\text{As}$ , the better will the device perform. The easiest material to grow is a lattice-matched epitaxial film. Thus  $\text{In}_{0.53}\text{Ga}_{0.47}\text{As}$  material, grown on InP, looked very promising. High quality microwave performance devices were made at University of Illinois under our grant<sup>(12)</sup> using InP substrates and  $\text{In}_{0.52}\text{Al}_{0.48}\text{As}$  as the high bandgap material. However, room for improvement was possible by going to even higher indium concentrations and again using strain layer epitaxy. Pioneering work in this area was published<sup>(13)</sup> in 1986 and the University of Illinois extended the idea by growing  $\text{In}_x\text{Ga}_{1-x}\text{As}$  material on InP with indium concentration up to  $x=0.70$  and using a graded interface.<sup>(14)</sup> Similar work and device fabrication has been done at the University of Michigan<sup>(15)</sup> and other places. These devices will be brought into larger scale application when InP substrate material of 3" or more with proven reliability is available. At this stage, we decided to leapfrog the regular progress by adding another parameter to improve performance, i.e. cooling. In 1989 a grant was awarded to Prof. P.K. Bhattacharya at the University of Michigan to develop cryogenic MODFET's. Most of the work used high indium concentration MODFET devices made on InP. All high frequency cryogenic tests down to 40K were done at Lewis Research Center, using wire bonded devices.<sup>(16,17)</sup> A new cryostat, using probes, is now being fabricated at Lewis Research Center to

facilitate the calibration and measurement procedures. The cryogenic results obtained for pseudomorphic MODFET on InP substrates, which are the first ever measured anywhere, point to a marked improvement in the properties of the device. A complete device modelling was also performed, showing a good agreement with the experiments.<sup>(17)</sup>

In parallel, a Lewis Research Center in house program was conducted to study the optical properties<sup>(18)</sup> of InGaAs and to apply the results to characterize the material grown for the MODFET devices using ellipsometry. In this technique, a non-destructive simultaneous estimate of the various layers' thicknesses and ternary material composition is possible.<sup>(19,20)</sup> The application of ellipsometry to semiconductor multilayer characterization, including ternary material composition, was pioneered by a collaboration of University of Nebraska and Lewis Research Center.<sup>(21)</sup> A large variety of applications to III-V semiconductors was found.<sup>(22)</sup> Recently, a spin-off company from University of Nebraska (J.A. Woollam Co.) began to manufacture research spectroscopic ellipsometers and work toward application of this technique to in-situ semiconductor growth using MBE and MOCVD. This is another example of technology transfer under our program.

We are also pursuing another approach, offered to us by the SBIR (Small Business Innovative Research) program. Improved surface morphology and increased material production in III-V epitaxial semiconductors are achieved using MOCVD rather than the conventional MBE technique. An SBIR contract, which is now in phase II, has been awarded to Spire Corporation for the growth of  $\text{In}_x\text{Ga}_{1-x}\text{As}$  on GaAs. The contract calls for indium concentrations up to  $x=0.30$  and for device fabrication and testing. All process steps will be optimized and the device results will be correlated with material parameters. The phase II contract was awarded in April 91.

#### Technical Results

Device performance can be measured by several parameters. In the case of

III-V semiconductors some of the important characteristics are power and current gain cutoff frequencies ( $f_{\text{max}}$  and  $f_t$  respectively), gain, power and power added efficiency, noise figure and its associated gain, third order intermodulation and others. Most of these figures are limited by the material properties, although lithography and processing (e.g., making a reduced resistance "mushroom" type gate) are also very important. In the case of III-V semiconductors, the critical material parameters are saturated velocity, mobility, bandgap, carrier concentration, carrier confinement and the  $\Gamma$ -L intervalley gap. In an early paper<sup>(1)</sup>, a complete FET Monte Carlo simulation shows the importance of a large intervalley gap for improved device performance. This gap increases by over 50% between GaAs (0.36eV) and  $\text{In}_{0.53}\text{Ga}_{0.47}\text{As}$ <sup>(23)</sup> (0.55eV). In addition, the larger mobility and saturated velocity in  $\text{In}_{0.53}\text{Ga}_{0.47}\text{As}$  vs. GaAs<sup>(1,14)</sup> are important benefits. These parameters improve even more as the indium concentration in  $\text{In}_x\text{Ga}_{1-x}\text{As}$  increases toward  $x=1$ . However, the bandgap of InAs is so low (0.35eV) that room temperature application is not possible. That of  $\text{In}_{0.53}\text{Ga}_{0.47}\text{As}$  however, is 0.75eV and is still acceptable. In general, the higher the indium concentration  $x$  in  $\text{In}_x\text{Ga}_{1-x}\text{As}$ , the better are the electronic properties, except for the low bandgap for  $x$  near 1. The most important consideration for the material grower is the lattice mismatch of  $\text{In}_x\text{Ga}_{1-x}\text{As}$  to the substrate. The InGaAs will not have excess dislocations and will give pseudomorphic growth if the strained layer thickness is below the critical thickness<sup>(24)</sup>  $t_c$ . For  $\text{In}_x\text{Ga}_{1-x}\text{As}$  on GaAs,  $t_c$  is just below 100Å at  $x=0.30$  and grows with decreasing  $x$ . As the device channel thickness should be able to carry current, the value of  $x$  is limited to  $x \leq 0.30$  for GaAs substrates. Increasing carrier concentration and carrier confinement is achieved by using  $\text{Al}_y\text{Ga}_{1-y}\text{As}$  and not GaAs as the MODFET donor layer. The value of  $y$  is limited, usually to  $y \leq 0.20$ , to keep the AlGaAs DX trap centers to a minimum.

We will now show several actual results obtained in this program.

(All graphs in this paper that were previously published are reprinted here with permission). Fig. 1 (reprinted from reference 6) shows the actual MODFET structure used at the University of Illinois. As InGaAs has a smaller bandgap than either AlGaAs or GaAs, an almost square quantum well is achieved. Results showing the short-circuit current gain and the maximum available gain (MAG) vs. frequency for 1 micron gate length devices are given in Fig. 2, which is reprinted from reference 6. Both  $f_1$  and  $f_{max}$  show a large improvement of over 50% and 30% respectively vs. a AlGaAs/GaAs MODFET. The same devices show a reduction<sup>(7)</sup> of a factor of 10 (or more) in the gate noise spectrum

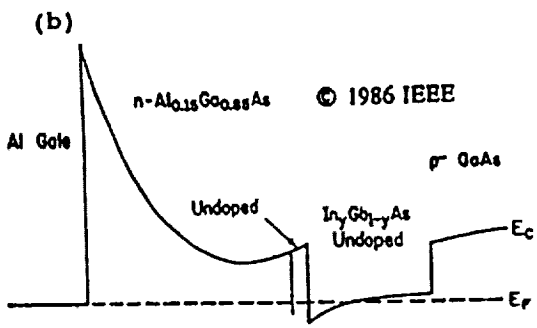
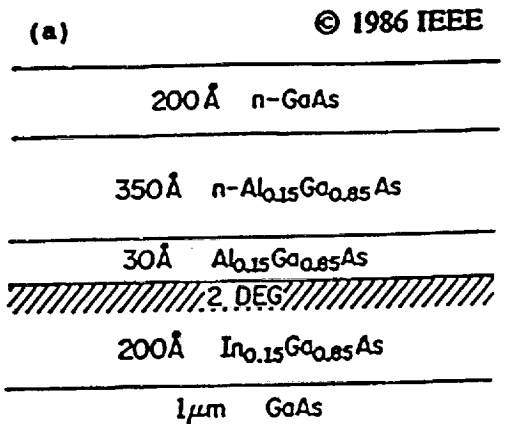


Fig. 1. (a) Typical structure for MBE-grown InGaAs/AlGaAs pseudomorphic MODFET and (b) the associated conduction band diagram. The conducting channel forms a two dimensional electron gas in the strained-layer InGaAs quantum well. (Reprinted from reference 6, with permission).

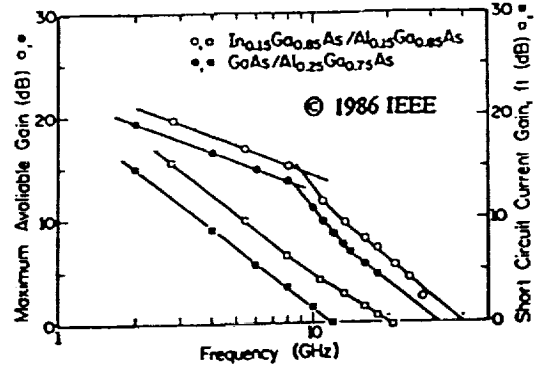


Fig. 2. Maximum available gain and short circuit current gain of In<sub>0.15</sub>Ga<sub>0.85</sub>As/Al<sub>0.15</sub>Ga<sub>0.85</sub>As and GaAs/Al<sub>0.25</sub>Ga<sub>0.75</sub>As. (Reprinted from reference 6, with permission).

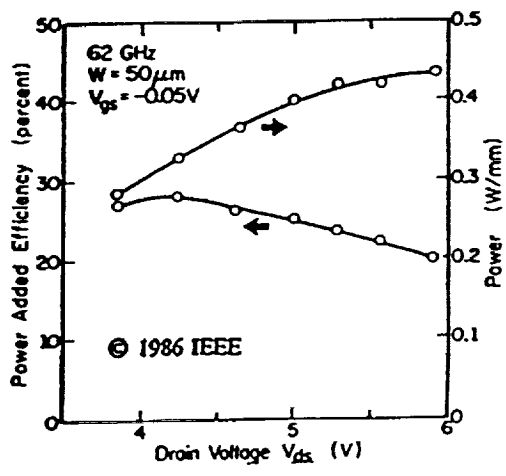


Fig. 3. Output power and power-added efficiency as a function of drain voltage for a 0.25 x 50-μm<sup>2</sup> pseudomorphic MODFET. The device is tuned for maximum output power with 3-dB gain. (Reprinted from reference 10, with permission).

vs. the AlGaAs/GaAs device, mainly due to the reduction of the DX trap centers in the AlGaAs layer. A structure similar to Fig. 1, but with 400 Å of cap GaAs layer, made at the University of Illinois was used by the G.E. Electronics Laboratory to make a quarter micron device. A representative result is shown in Fig. 3 (reprinted from reference 10). This device, with a transconductance of 495 mS/mm, had the following performance<sup>(10)</sup> around 60 GHz: MAG of 11.7 dB, noise figure of 2.4 dB and associated gain of 4.4 dB, 28% power

added efficiency and 0.43 W/mm power output level. The estimated  $f_{\max}$  was over 200 GHz. This result was such a large improvement over the best existing three terminal mm wave device (the AlGaAs/GaAs MODFET) that it became instantly the device of choice for these high frequencies.

The work on MOCVD growth of pseudomorphic MODFET material on GaAs substrates at Spire Corporation is in the early stages. The first results show that a 1 micron undoped GaAs buffer gives leaky devices and the solution is a 1000Å undoped  $\text{Al}_{0.20}\text{Ga}_{0.80}\text{As}$  and a 9000Å undoped GaAs. A schematic of the MODFET structure used is given in Fig. 4. The work is concentrated on  $x=0.30$  and uses channel thicknesses of 50Å and 100Å. Transmission electron microscopy shows defect free 100Å thick channels, but device results point to better performance for the 50Å thick channel. The material is not yet optimized, and the best device gave a transconductance of 300 mS/mm.

A spectroscopic ellipsometry characterization<sup>(16,20)</sup> was performed on several MOCVD grown samples assuming that the optical properties of the  $\text{In}_{0.3}\text{Ga}_{0.7}\text{As}$  layer in the MODFET structure are equal to that in an unstrained, thick layer of equal composition. However, strain effects in the MODFET structure are changing the properties of the InGaAs layer. Work done on strained InGaAs layers<sup>(20)</sup> with  $x=0.65$  and  $0.70$  show that the strained  $\text{In}_x\text{Ga}_{1-x}\text{As}$  layer has optical properties similar to an unstrained  $\text{In}_y\text{Ga}_{1-y}\text{As}$  layer with  $y$  lower than  $x$ . Here,  $y$  is only an apparent indium concentration. We will now present the newest ellipsometric results on the MOCVD grown material from Spire Corp. As ellipsometry cannot distinguish doped and undoped material, we have shown the nominal ellipsometric thicknesses of this structure in the right hand side of Fig. 4. Results of the different layer thicknesses  $t_i$  ( $i=1$  to 4) for one sample, assuming different values of the indium concentration  $x$ , are given in Table I. The quality of the least square fit is given by the column "Trig. MSE" (i.e., trigonometric mean square error). This quality parameter shows that the actual result is obtained at an

apparent indium concentration of  $y=0.24$ . The thicknesses of all layers are in good agreement with the nominal values, but the ellipsometrically evaluated aluminum concentration in the AlGaAs layer is low compared to the nominal value. The low aluminum concentration was

MOCVD MODFET STRUCTURE

| Actual Structure                               |         | Nominal Structure For Ellipsometry             |      |
|--|---------|--|------|
| $n^+$ GaAs                                     | 100Å    | $t_1$ GaAs Oxide                               | 20Å  |
| $n^+$ Al <sub>0.20</sub> Ga <sub>0.80</sub> As | 400Å    | $t_2$ GaAs                                     | 100Å |
| $i$ Al <sub>0.20</sub> Ga <sub>0.80</sub> As   | 50Å     | $t_3$ Al <sub>0.20</sub> Ga <sub>0.80</sub> As | 450Å |
| $i$ In <sub>0.30</sub> Ga <sub>0.70</sub> As   | 100Å    | $t_4$ In <sub>0.30</sub> Ga <sub>0.70</sub> As | 100Å |
| Buffer   | 10,000Å | GaAs Substrate                                 |      |
| SI GaAs Substrate                              |         |  |      |

Fig. 4. Actual and nominal structure used in the ellipsometric analysis for a MOCVD grown MODFET structure.

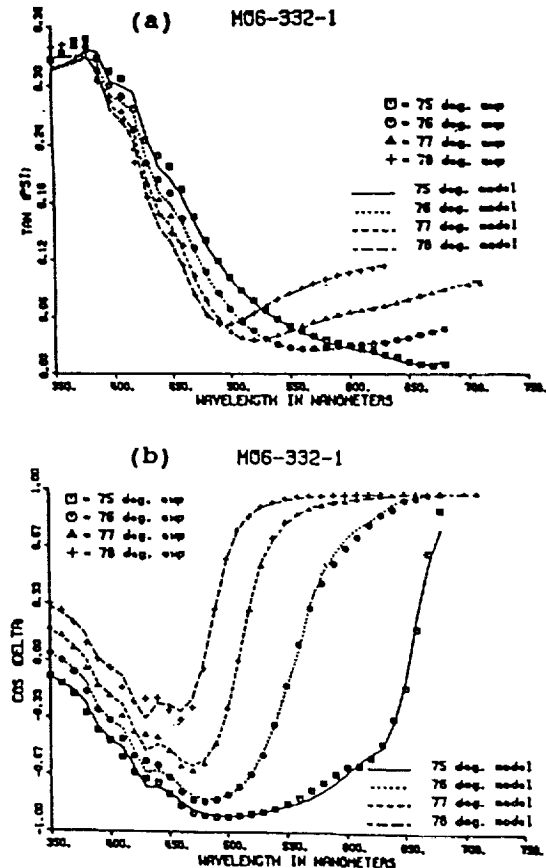


Fig. 5. Experimental and model simulation for (a)  $\tan(\Psi)$  and (b)  $\cos(\Delta)$  vs. wavelength for the MOCVD grown MODFET structure of Fig. 4.

also found in another sample and it seems to be real. A comparison of the experimental results (called  $\cos(\Delta)$  and  $\tan(\Psi)$ ) and a model calculating the expected  $\cos(\Delta)$  and  $\tan(\Psi)$  values using the structure given in Table I for  $x=0.24$  is shown in Figs. 5(a) and 5(b). The good agreement between the experimental and the calculated results is evident.

The low temperature device work was motivated by several considerations. First, we expect improved circuit performance as decreased temperature will give increased device speed due to higher drift velocity<sup>(25)</sup> and mobility, lower device noise, lower metal interconnect resistivity that gives faster and lower loss circuits, better reliability due to reduction of diffusion driven processes, and possible integration with superconducting elements. Second, no new technology has to be developed, and thus the applications are immediate. This second point is especially important in space<sup>(26)</sup> as passive cooling is projected to achieve the 120K-150K range for front end electronics.

© 1990 IEEE

|           |  |  |
|-----------|--|--|
| 100 Å     | $\text{In}_{0.53}\text{Ga}_{0.47}\text{As}$  | $n^+ 5 \times 10^{18} \text{ cm}^{-3}$ |
| 200 Å     | $\text{In}_{0.52}\text{Al}_{0.48}\text{As}$  |  |
| 150 Å     | $\text{In}_{0.53}\text{Al}_{0.47}\text{As}$  | $n^+ 5 \times 10^{18} \text{ cm}^{-3}$ |
| 50 Å      | $\text{In}_{0.52}\text{Al}_{0.48}\text{As}$  |  |
| 100-150 Å | $\text{In}_x\text{Ga}_{1-x}\text{As}$  |  |
|           | $0.53 \leq x \leq 0.70$  |  |
| 400 Å     | $\text{In}_{0.53}\text{Ga}_{0.47}\text{As}$  |  |
| 3000 Å    | $\text{In}_{0.52}\text{Al}_{0.48}\text{As}$  |  |
| 1800 Å    | 30 Å $\text{In}_{0.53}\text{Ga}_{0.47}\text{As}/$<br>30 Å $\text{In}_{0.52}\text{Al}_{0.48}\text{As}$ SL |  |
|           | SI InP Substrate   |  |

Fig. 6. Layer schematic of pseudomorphic  $\text{In}_x\text{Ga}_{1-x}\text{As}/\text{In}_{0.52}\text{Al}_{0.48}\text{As}$  ( $x=0.53, 0.60, \text{ and } 0.70$ ) channel MODFET's on InP substrates. (Reprinted from reference 16, with permission).

Although significant progress was achieved in Sb based devices under our grant to the University of Michigan,<sup>(27,28)</sup> we will limit ourselves in this paper only to results obtained in the strained layer  $\text{In}_x\text{Ga}_{1-x}\text{As}$  MODFET devices grown on InP. Ellipsometry work on these

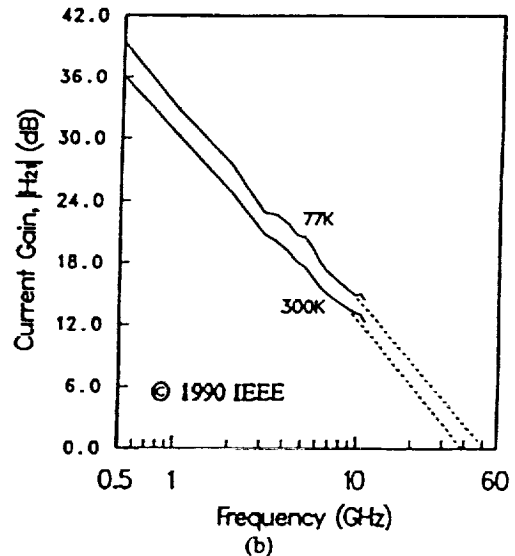
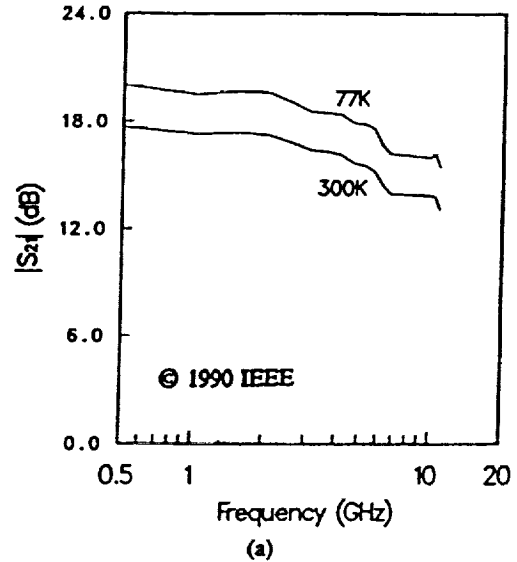


Fig. 7. Magnitude of  $S_{21}$  (a) and current gain  $h_{21}$  (b) vs. frequency for a pseudomorphic  $\text{In}_{0.70}\text{Ga}_{0.30}\text{As}/\text{In}_{0.52}\text{Al}_{0.48}\text{As}$  channel MODFET at 77K and 300K with  $V_{ds}=1.5$  volts and  $V_{gs}=0$  volts. (Reprinted from reference 16, with permission).

structures<sup>(19,20)</sup> will also not be given here. In this project, devices with gate lengths down to 0.1 micron and  $x$  up to 0.70 were made. The structures used are shown in Fig. 6, reprinted from reference 16. The channel thickness is 100Å for the  $x=0.70$  channel, and 150Å for the other indium concentrations.

The best device had an extrapolated  $f_t$  of 210 GHz, at 0.1 micron gate and  $x=0.70$ . 0.2 and 0.8 micron devices with  $x=0.53$ , 0.60, and 0.70 were DC and RF characterized in the temperature range 40K-300K. Results for the  $S_{21}$  parameter and the current gain of the 0.8 micron gate are shown in Fig. 7, reprinted from reference 16. An increase of approximately 35% in  $f_t$  or 3 dB in gain can be deduced from this figure for the 300K to 77K cooling. Other results for the same device were a 30% increase in transconductance, over an order of magnitude reduction in gate leakage and a 20% decrease in output conductance. Most of the improvement was achieved with cooling to the 120K range, a very important point for potential space applications. The results for the 0.2 micron devices show less improvement with decreasing temperature, with  $f_t$  increase of only 25%. A detailed device modelling,<sup>(17)</sup> including Monte Carlo calculation of the carrier transit times, also shows a smaller improvement of the 0.2 micron device vs. the 0.8 micron one. This result is explained by a much larger contribution of ballistic electron transport to the total electrical transport in the smaller gate length device vs. the longer gate device. This contribution is not affected by the temperature, as no scattering is involved.

#### Conclusions

Three terminal devices for microwave and mm-wave frequencies are now the backbone for the large majority of solid state circuit applications. In this paper we have shown the contribution of Lewis Research Center in the research and development of pseudomorphic InGaAs MODFET devices. This contribution included the early development of the device on GaAs substrates using MBE and the subsequent technology transfer, the work presently done to develop a

viable device on GaAs substrate using MOCVD and the pioneering work done on low temperature (of the order 120K-150K) applications of pseudomorphic InGaAs MODFET on InP substrates.

#### Acknowledgement

I would like to thank Prof. H. Morkoc, Prof. P.K. Bhattacharya and P.A. Sekula-Moise for the excellent work performed under their grants and contract respectively, and for their close collaboration with me in every aspect. I would also like to thank R.M. Sieg for the ellipsometric analysis of the MOCVD grown samples.

#### References

- (1) A. Cappy, B. Carnez, R. Fanguembergues, G. Salmer and E. Constant, "Comparative Potential Performance of Si, GaAs, GaInAs, InP Submicrometer-Gate FET's," IEEE Trans. Electron Dev. ED-27, 2158-2160 (1980).
- (2) J. M. Golio and R. J. Trew, "Optimum Semiconductors for High-Frequency and Low-Noise MESFET Applications," IEEE Trans. Electron. Dev. ED-30, 1411-1413 (1983).
- (3) T. E. Zipperian and T. J. Drummond, "Strained Quantum Well, Modulation Doped, Field Effect Transistor," Electron. Lett. 21, 823-824 (1985).
- (4) J. J. Rosenberg, M. Benlamri, P. D. K. Kircher, J. M. Woodall and G. D. Pettit, "An  $In_{0.15}Ga_{0.85}As/GaAs$  Pseudomorphic Single Quantum Well HEMT," IEEE Electron. Dev. Lett. EDL-6, 491-493 (1985).
- (5) W. T. Masselink, A. Ketterson, J. Klem, W. Kopp and H. Morkoc, "Cryogenic Operation of Pseudomorphic AlGaAs/InGaAs Single Quantum-Well MODFET's," Electron. Lett. 21, 937-939 (1985).
- (6) A. A. Ketterson, W.T. Masselink, J. S. Gedymin, J. Klem, C. K. Peng, W. F. Kopp, H. Morkoc and K. R. Gleason, "Characterization of InGaAs/AlGaAs Pseudomorphic Modulation-Doped Field-Effect Transistors," IEEE Trans. Electron. Dev. ED-33, 564-571 (1986).
- (7) S. M. Liu, M. B. Das, C. K.

Peng, J. Klem, T. S. Henderson, W. F. Kopp and H. Morkoc, "Low-Noise Behavior of InGaAs Quantum-Well-Structured Modulation-Doped FET's from  $10^2$  to  $10^8$  Hz," IEEE Trans. Electron. Dev. ED-33, 576-582 (1986).

(8) H. Morkoc, T. Henderson, W. Kopp and C.K. Peng, "High Frequency Noise of  $\text{In}_x\text{Ga}_{1-x}\text{As}/\text{Al}_x\text{Ga}_{1-x}\text{As}$  MODFET's and Comparison to  $\text{GaAs}/\text{Al}_x\text{Ga}_{1-x}\text{As}$  MODFET's," Electron. Lett. 22, 578-580 (1986).

(9) S. A. Alterovitz, E.J. Haugland, C. Soehn, J. J. Klem and H. Morkoc, "Shubnikov de Haas Measurements of 2D Electron Gas in Thin Layers of  $\text{In}_x\text{Ga}_{1-x}\text{As}$  ( $x \leq 0.15$ )," Bull. Am. Phys. Soc. 31, 1077 (1986), and P.P. Szydlik, S.A. Alterovitz, E.J. Haugland, B. Segall, T. Henderson, J. Klem and H. Morkoc, "Shubnikov de Haas Measurements of the 2D Electron Gas in Pseudomorphic InGaAs Grown on GaAs," Superlattices and Microstructures 4, 619-629 (1988).

(10) T. Henderson, M.I. Aksun, C.K. Peng, H. Morkoc, P.C. Chao, P.M. Smith, K.H.G. Duh and L.F. Lester, "Microwave Performance of a Quarter-Micrometer Gate Low-Noise Pseudomorphic InGaAs/AlGaAs Modulation-Doped Field Effect Transistor," IEEE Electron. Dev. Lett. EDL-7, 649-651 (1986).

(11) R. Ramachandran and G. Metze, "Design and Processing Considerations for mm-Wave Multifunction MMIC's," Microwave Jour. 34, 113-122 (1991).

(12) C. K. Peng, M. I. Aksun, A. A. Ketterson, H. Morkoc and K. R. Gleason, "Microwave Performance of InAlAs/InGaAs/InP MODFET's," IEEE Electron Dev. Lett. EDL-8, 24-26 (1987).

(13) J. M. Kuo, B. Lalevic and T.Y. Chang, "New Pseudomorphic MODFET's Utilizing  $\text{Ga}_{0.47-x}\text{In}_{0.53+x}\text{As}/\text{Al}_{0.48-x}\text{In}_{0.52-x}\text{As}$  Heterostructures," IEEE IEDM Tech. Dig. 460-463 (1986).

(14) C. K. Peng, S. Sinha and H. Morkoc, "Characterization of Graded Interface  $\text{In}_x\text{Ga}_{1-x}\text{As}/\text{In}_{0.52}\text{Ga}_{0.48}\text{As}$  ( $0.53 \leq x \leq 0.70$ ) Structures Grown by Molecular-Beam-Epitaxy," J. Appl. Phys. 62, 2880-2884 (1987).

(15) G.I. Ng, W.P. Hong, D. Pavlidis, M. Tutt and P.K. Bhattacharya, "Characteristics of Strained  $\text{In}_{0.65}\text{Ga}_{0.35}\text{As}/\text{In}_{0.52}\text{Al}_{0.48}\text{As}$  HEMT with Optimized Transport Parameters," IEEE Electron. Dev. Lett. EDL-9, 439-441 (1988).

(16) R. Lai, P.K. Bhattacharya, S.A. Alterovitz, A.N. Downey and C. Chorey, "Low Temperature Microwave Characteristics of Pseudomorphic  $\text{In}_x\text{Ga}_{1-x}\text{As}/\text{In}_{0.52}\text{Al}_{0.48}\text{As}$  Modulation Doped Field-Effect Transistors," IEEE Electron. Dev. Lett. EDL-11, 564-566 (1990).

(17) R. Lai, P.K. Bhattacharya, D. Yang, T. Brock, S.A. Alterovitz and A.N. Downey, "Characteristics of 0.8  $\mu\text{m}$  and 0.2  $\mu\text{m}$  Gate Length  $\text{In}_x\text{Ga}_{1-x}\text{As}/\text{In}_{0.52}\text{Al}_{0.48}\text{As}$  ( $0.53 \leq x \leq 0.70$ ) Modulation-Doped Field Effect Transistors at Cryogenic Temperatures," submitted for publication.

(18) S.A. Alterovitz, R.M. Sieg, H.D. Yao, P.G. Snyder, J.A. Woollam, J. Pamulapati, P.K. Bhattacharya and P.A. Sekula-Moise, "Dielectric Function of InGaAs in the Visible," Proc. 2nd Int'l. Conf. on Electron. Mat., T. Sugano, R.P.H. Chang, H. Kamimura, I. Hayashi and T. Kamiya eds., 187-192 (MRS Int'l. Proc. 1990).

(19) S.A. Alterovitz, R.M. Sieg, H.D. Yao, P.G. Snyder, J.A. Woollam, J. Pamulapati and P.K. Bhattacharya, "Ellipsometric Study of InGaAs MODFET Material," Mat. Res. Soc. EA-21, 299-302 (1990).

(20) S. A. Alterovitz, R.M. Sieg, H.D. Yao, P.G. Snyder, J.A. Woollam, J. Pamulapati, P.K. Bhattacharya and P.A. Sekula-Moise, "Study of InGaAs-Based MODFET Structures using Variable Angle Spectroscopic Ellipsometry," Thin Solid Films - accepted for publication.

(21) P.G. Snyder, M.C. Rost, G.H. Bu Abbud, J.A. Woollam and S.A. Alterovitz, "Variable Angle of Incidence Spectroscopic Ellipsometry: Application to  $\text{GaAs}-\text{Al}_x\text{Ga}_{1-x}\text{As}$  Multiple Heterostructures," J. Appl. Phys. 60, 3293-3302 (1986).

(22) S.A. Alterovitz, J.A. Woollam

and P.G. Snyder, "Variable Angle Spectroscopic Ellipsometry," Solid State Technology 31, 99-102 (1988).

(23) K.Y. Cheng, A.Y. Cho, S.B. Christman, T.P. Pearsall and J.E. Rowe, "Measurement of the  $\Gamma$ -L Separation in  $\text{Ga}_{0.47}\text{In}_{0.53}\text{As}$  by Ultraviolet Photoemission," Appl. Phys. Lett. 40, 473-475 (1982).

(24) J.W. Matthews and A.E. Blakeslee, "Defects in Epitaxial Multilayers," J. Cryst. Growth 27, 118-125 (1974).

(25) A. Bhattacharya, A. Ghosal and D. Chattopadhyay, "Temperature Dependence of Peak Drift Velocity and Threshold Field in n- $\text{In}_{0.53}\text{Ga}_{0.47}\text{As}$ ," IEEE Trans. Electron. Dev. ED-31, 1918-1919 (1984).

(26) P.F. Goldsmith et.al., "The Submillimeter Wave Astronomy Satellite," IEEE MTT-S Digest, 395-398 (1991).

(27) S. Tsukamoto, P.K. Bhattacharya, Y.C. Chen and J.H. Kim, "Transport Properties of  $\text{InAs}_x\text{Sb}_{1-x}$  ( $0 \leq x \leq 0.55$ ) on InP Grown by Molecular Beam Epitaxy," J. Appl. Phys. 67, 6819-6822 (1990).

(28) J.H. Kim, D. Yang, Y.C. Chen and P.K. Bhattacharya, "Growth and Properties of  $\text{InAs}_x\text{Sb}_{1-x}$ ,  $\text{Al}_y\text{Ga}_{1-y}\text{Sb}$  and  $\text{InAs}_x\text{Sb}_{1-x}/\text{Al}_y\text{Ga}_{1-y}\text{Sb}$  Heterostructures," J. Crystal Growth, to be published.

Table I

Best Fits for MOCVD-grown InGaAs/AlGaAs MODFET structure using the unstrained InGaAs calibration functions, with In concentration as a parameter.

| Trig MSE | In Conc. | InGaAs Thick. | AlGaAs Thick. | Al Conc.  | GaAs Thick. | GaAs Ox. Thick. |
|----------|----------|---------------|---------------|-----------|-------------|-----------------|
| 5.71E-4  | 20%      | 111±7         | 436±5         | .143±.004 | 94.3±3      | 16.0±0.6        |
| 5.40E-4  | 22%      | 105±6         | 437±4         | .144±.004 | 93.8±3      | 16.2±0.5        |
| 5.33E-4  | 23%      | 101±6         | 437±4         | .145±.004 | 93.9±3      | 16.3±0.5        |
| 5.30E-4  | 24%      | 97.9±5        | 438±4         | .145±.004 | 93.5±3      | 16.3±0.5        |
| 5.36E-4  | 25%      | 94.0±5        | 438±4         | .146±.004 | 93.6±3      | 16.4±0.5        |
| 5.47E-4  | 26%      | 92.2±5        | 438±4         | .147±.004 | 93.3±3      | 16.5±0.5        |
| 5.59E-4  | 28%      | 87.8±5        | 439±4         | .147±.004 | 92.9±3      | 16.6±0.5        |
| 5.64E-4  | 30%      | 84.7±5        | 438±4         | .148±.004 | 93.1±3      | 16.7±0.5        |
| Nominal  | 30%      | 100           | 450           | 0.20      | 100         | 20              |

All thicknesses are in Angstroms.



## Intermodulation in the oscillatory magnetoresistance of a two-dimensional electron gas

S. E. Schacham,\* E. J. Haugland, and S. A. Alterovitz  
 NASA Lewis Research Center, M/S 54-5, Cleveland, Ohio 44135  
 (Received 23 December 1991)

The oscillatory magnetoresistance wave form of a two-dimensional electron gas shows multiple structures when two subbands are populated. In addition to high-field oscillations at a frequency equal to the sum of the two frequencies corresponding to the concentrations of the subbands, and to a superposition at intermediate fields, we observed oscillations at the difference frequency at low fields and higher temperatures. The field range at which the frequency difference is observed increases with increasing temperature. The crossover from superposition to frequency difference is accompanied by a beat. Similar beats, whose field location shows identical temperature dependence, can be observed in data obtained by other groups on different structures. The various components of the wave form can be attributed to different phase relations between the diagonal and off-diagonal elements of the conductivity tensor. It is shown how the intermodulation term, when inserted into the extended oscillatory equation, can give rise to all three structures.

## INTRODUCTION

The oscillatory pattern of magnetoresistance, the Shubnikov-de Haas (SdH) effect, is extremely useful in the characterization of a two-dimensional electron gas (2DEG). As a function of the inverse magnetic field, the frequency of oscillation is linearly proportional to the concentration of the carriers generating the given oscillations. In addition, the decay of the oscillation amplitude with increasing temperature at a given magnetic field or with decreasing field at a given temperature allows for the determination of the effective mass or the quantum relaxation time within the subband. The wave form becomes complex when either more than one subband is populated, or more than one carrier type takes part in the conduction process. This complex SdH pattern is generated by the presence of two Landau-level ladders, one for each carrier type or subband. At large enough magnetic fields, when all the levels are sharp, a single oscillatory wave form is obtained, the frequency of which corresponds to the sum of the concentrations of the various carriers.<sup>1</sup> At lower fields, a superposition of the two frequencies is usually observed, whereby the oscillations at the higher frequency, corresponding to the ground subband concentration,  $f_1$ , are modulated by the lower oscillation frequency associated with the excited subband  $f_2$ .<sup>2,3</sup>

An abrupt change in the frequency of magnetoresistance oscillations as a function of the inverse magnetic field is encountered under various conditions. Most common is a doubling of the frequency when the spin degeneracy is removed, usually at fields of several teslas.<sup>4,5</sup> For some particular structures, a frequency shift was observed due to the different types of carriers present in the 2D gas. When an asymmetric quantum-well structure was investigated in  $\text{Ga}_{1-x}\text{Al}_x\text{As}/\text{GaAs}$  heterojunction,<sup>4</sup> the frequency of oscillation increased by a factor of 3.4 from low to high fields. The oscillations at low fields were attributed to the light holes only, for which the

lower effective mass  $m^*$  results in a larger cyclotron-resonance frequency  $\omega_c = qB/m^*$ , where  $B$  is the magnetic field. Since the separation between the Landau levels is  $\hbar\omega_c$ , only the ladder produced by the light holes generates oscillations detectable at low fields. In a second paper,<sup>5</sup> a similar asymmetric well was investigated in a GaSb/AlSb system. Here, too, the oscillation frequency of the SdH pattern recorded for this structure increases rather abruptly. However, the change in frequency is much smaller than in the previous sample, only a factor of 1.27. The authors attributed the low-field oscillations to the heavy holes.

In this paper, we report the observation of a third SdH frequency recorded on a modulation-doped field-effect transistor (MODFET) structure when two subbands are populated. At lower fields, a single intermediate frequency  $f_I$  is present, while at higher fields a higher frequency  $f_H$  prevails, modulated by a third, much lower frequency,  $f_L$ . This feature is temperature dependent, i.e., the crossover magnetic field between  $f_I$  and  $f_H$  decreases with decreasing temperature such that at very low temperatures the intermediate frequency is absent. The theory behind these phenomena is discussed. Various possible mechanisms are investigated, and it is shown that the presence of three frequencies and their temperature dependence is closely related to the intermodulation between the subbands, recently introduced by Coleridge.<sup>3</sup>

## Experimental Results

The sample measured in this paper is a MODFET structure composed of an  $\text{Al}_x\text{Ga}_{1-x}\text{As}/\text{GaAs}$  heterojunction with  $x=0.3$ . The  $\text{Al}_x\text{Ga}_{1-x}\text{As}$  barrier is 500-Å layer doped with Si ( $3 \times 10^{18} \text{ cm}^{-3}$ ) and a 60-Å undoped spacer. The 2DEG concentration of the sample at dark was measured by both Hall and SdH techniques, and was found to be  $6.10 \times 10^{11} \text{ cm}^{-2}$  with a Hall mobility  $\mu_H = 295\,000 \text{ cm}^2/\text{Vs}$  at 4.2 K. After exposing the sample to light, the Hall concentration increased to

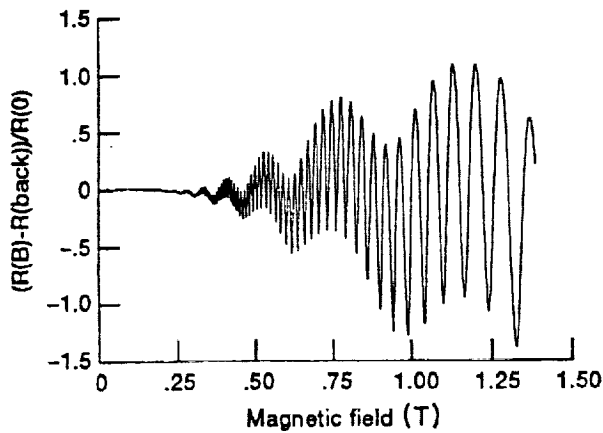


FIG. 1. SdH wave form taken at 1.45 K, showing the superposition of the two frequencies corresponding to two populated subbands.

$1.066 \times 10^{12} \text{ cm}^{-2}$ , due to persistent photoconductivity, with a mobility of  $\mu_H = 415\,000 \text{ cm}^2/\text{V s}$ . The SdH wave form measured on the exposed sample at 1.45 K is presented in Fig. 1. A superposition of two frequencies can be clearly observed. The high frequency,  $f_H = 19.9 \text{ T}$ , corresponds to a 2DEG concentration of  $9.65 \times 10^{11} \text{ cm}^{-2}$ , while the low frequency,  $f_L = 1.83 \text{ T}$ , renders a concentration of  $8.9 \times 10^{10} \text{ cm}^{-2}$ . The sum of these two concentrations equals the result obtained from the Hall experiment. At this temperature, these two frequencies prevail throughout the experimentally available magnetic field, i.e., 1.4 T.

As the temperature is increased, a third frequency of 18.1 T is observed at the lower magnetic fields. This intermediate frequency  $f_I$  is equal to the difference between the two previous frequencies, i.e.,  $f_I = f_H - f_L$ . The three frequencies  $f_L$ ,  $f_I$ , and  $f_H$  are observed as three peaks in the fast Fourier transform (FFT) of Fig. 2. The presence of a difference frequency was recently reported by Coleridge.<sup>3</sup>

Figure 3 shows an expanded view of the SdH pattern as a function of the inverse magnetic field. The oscilla-

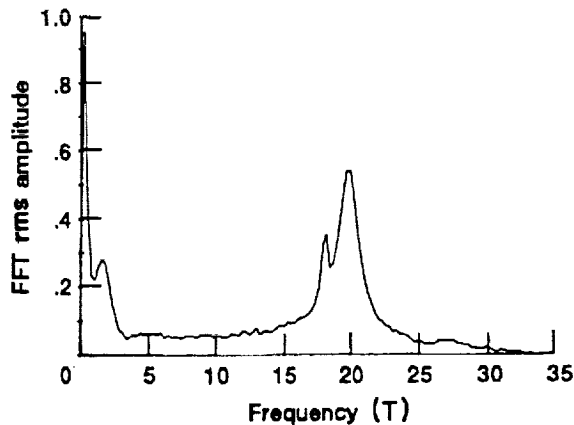


FIG. 2. FFT of the SdH pattern measured at 3.9 K, showing the peaks at  $f_H$  (19.9 T),  $f_L$  (1.8 T), and  $f_I$  (18.1 T).

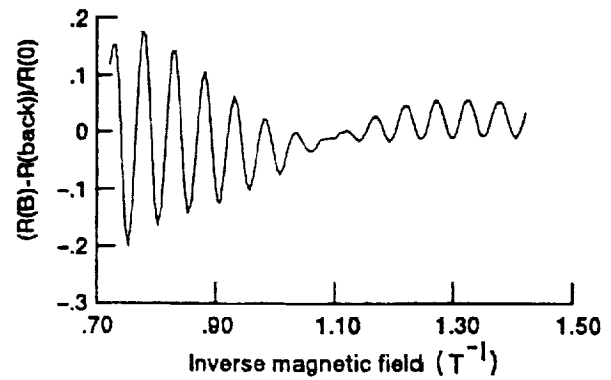


FIG. 3. SdH pattern vs the inverse magnetic field measured at 5.28 K. Two frequencies ( $f_H$  and  $f_I$ ) are observed. A beat is clearly seen at the crossover point.

tions at  $f_H$  are observed at the left part of the wave form (low  $1/B$ ), while  $f_I$  is at the right side. A beat appears at the crossover field. The indexed extrema are present in Fig. 4. Although the slopes are very close to one another, they are clearly distinct, and the two frequencies are properly resolved by the computer to render the above concentrations. Such intersects were employed in order to determine the crossover field at the various temperatures of measurement.

The increase in the crossover field with increasing temperature is shown in Fig. 5. The SdH spectrum measured at 1.6 K shows only one high frequency, namely  $f_H$ . (There is also a FFT peak at  $f_L$ , but this frequency is not relevant to the crossover estimate.) The reason is that the crossover field at this temperature should be about 0.3 T,

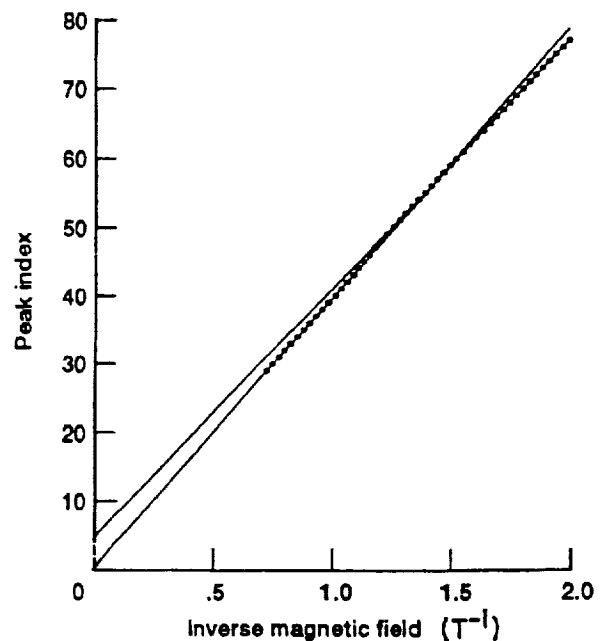


FIG. 4. Indices of extrema points in the experimental SdH pattern vs the inverse magnetic field at 4.6 K. Two slopes and a crossover are clearly observed.

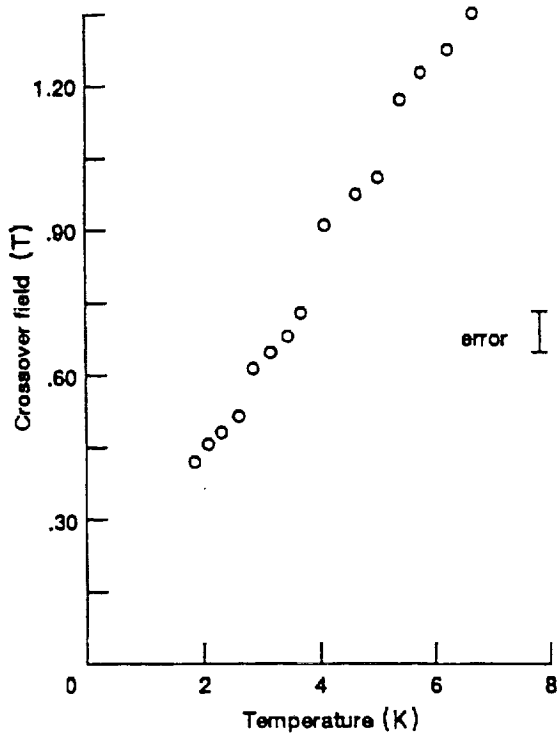


FIG. 5. Magnetic field at which a transition between  $f_H$  and  $f_I$  takes place vs temperature.

and at these low-field values the oscillatory magnetoresistance was not detectable. At the other extreme, the SdH spectrum measured at 9 K also shows only one high frequency; this time it is  $f_I$ . The reason this time is the crossover field is above 1.4 T, which is the maximum value attainable in our experimental setup. In between these temperatures, the amplitude of the FFT peak corresponding to  $f_H$  diminishes, while that due to  $f_I$  increases with temperature. It is possible to isolate  $f_H$  and  $f_I$  frequencies completely by obtaining the transforms of the lower fields and higher fields separately. The analysis of the SdH pattern was extended to temperatures as high as

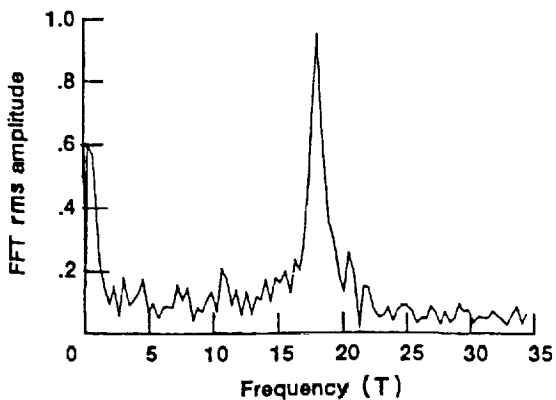


FIG. 6. FFT of the SdH wave form measured at 13 K, showing a single peak at 18.1 T.

15 K. A FFT of a wave form recorded at 13 K is shown in Fig. 6. The only peak observed is, as expected, at the intermediate frequency  $f_I$ .

Even though the temperature dependence of this effect has not been reported previously, a close examination of two recent publications which present SdH patterns recorded at various temperatures<sup>2,3</sup> shows beats at magnetic fields which are very close to the crossover fields shown in Fig. 5. Thus, it seems that the presence of an intermediate frequency and its temperature dependence are general phenomena, appearing in samples of different structures and composition.

## DISCUSSION

The presence of oscillations at difference frequencies is not apparent from previous analyses. The fact that the two peaks of the FFT corresponding to  $f_H$  and  $f_I$  can be isolated by choosing appropriate field regions indicates that we are not dealing with a "conventional" wave form in which a superposition of two frequencies is observed.<sup>6</sup>

The interpretation of the data depends first and foremost on the way the three frequencies are associated with the carriers in the various subbands. While  $f_L$  definitely corresponds to the concentration of carriers in the excited subband  $f_2$ , there are two possible approaches to associate the two high frequencies with  $f_1$ . For the sake of the clarity we will call these interpretations model 1 and model 2. In model 1,  $f_H$  is associated with the 2DEG in the ground subband, i.e.,  $f_H = f_1$ . Hence, for this model,  $f_I$  corresponds to the difference between the two concentrations, i.e.,  $f_I = f_1 - f_2$ . Alternatively, in model 2,  $f_I$  is assumed to be generated only by the ground subband carriers,  $f_I = f_1$ , so that  $f_H$  corresponds to the sum of the concentrations  $f_H = f_1 + f_2$ . While for model 1 the sum of the concentrations derived from  $f_H$  and  $f_L$  agrees perfectly with the Hall data, it necessitates the introduction of a difference frequency into the system. The only previous report of such a frequency is that of Coleridge,<sup>3</sup> who attributes this frequency to a result of the intermodulation between the two subbands generating frequency modulation (FM). FM produces two side frequencies of equal amplitudes, one at the difference and the other at the sum frequency. However, no sum and difference frequencies are observed simultaneously at the same magnetic-field range.

According to model 2,  $f_H$  is due to the sum of the subband concentrations. The presence of oscillations at the sum frequency is documented and the theory is established.<sup>1</sup> However, the sum frequency usually appears as a single frequency at fields of several teslas, following a region of superposition of the two constituent frequencies. On our data,  $f_H$  is a part of a superposition wave form. More important, since this model assumes that  $f_H = f_1 + f_2$ , one concludes that at fields below the crossover point the oscillations are generated by the ground subband only, i.e.,  $f_I = f_1$ . Thus, for model 2 to be valid it is essential to find the physical justification for the absence of oscillations due to the excited subband at these fields. This can be the case only if the Landau ladder

produced by the excited subband is not sharp enough. One condition for clearly resolved SdH oscillations is that the separation between these levels,  $\hbar\omega_c$ , will be larger than the scattering-induced energy broadening of a single level. The width of each level,  $\Gamma$ , is related to the quantum scattering time  $\tau_q$  by  $\Gamma = \hbar/2\tau_q$ . A second condition is that  $\hbar\omega_c$  should be larger than the thermal energy broadening  $kT$ . Translated to magnetic fields, these conditions can be expressed as

$$\begin{aligned} B &> 8.64 \times 10^3 (m^*/m_0) \Gamma, \\ B &> 0.744 (m^*/m_0) T, \end{aligned} \quad (1)$$

where  $B$  is in teslas,  $\Gamma$  in eV, and  $T$  in kelvin. For GaAs, with  $m^*/m_0 = 0.068$  one obtains

$$\begin{aligned} B &> 587 \Gamma = 1.93 \times 10^{-13} / \tau_q, \\ B &> 5.06 \times 10^{-3} T. \end{aligned} \quad (2)$$

If both broadening mechanisms are significant and if they are not correlated, they can be combined to give the condition  $\hbar\omega_c > [(kT)^2 + \Gamma^2]^{1/2}$ . The value of  $\tau_q$  is derived from the decay of the SdH amplitude with decreasing magnetic field. Unfortunately, the calculated value of  $\tau_q$  depends on the mathematical formalism assumed.<sup>6,7</sup> Typically  $\tau_q$  is about  $10^{-12}$  s for both the first and the excited subbands. Thus, the threshold of resolution is within the range of fields discussed in this work and it increases with temperature.

According to Eq. (1), it is possible that at lower magnetic fields the magnetoresistance oscillations due to the excited subband are not observed, if either the effective mass of electrons in the excited subband is substantially larger than that in the ground level, or the relaxation time  $\tau_q$  is significantly shorter in the former, or both. Practically neither of these statements seems correct. All reported data indicate that the quantum relaxation time of electrons in the excited subband is three to five times larger than that in the ground level.<sup>3,8</sup> The difference between the effective masses of carriers in the two subbands is minimal and again seems to be in the opposite direction, i.e., it is larger for the ground level.<sup>9</sup> Moreover, even though Eq. (1) in the combined form  $\hbar\omega_c > [(kT)^2 + \Gamma^2]^{1/2}$  indicates that the crossover field should increase with temperature, the predicted increase is much less steep than that measured, as shown in Fig. 5. In addition, according to the present model, there is a discrepancy (of about 10%) between the SdH and the Hall data. Thus we rule out model 2, associating  $f_H$  with the sum of the concentrations.

Let us return to model 1, in which  $f_H$  corresponds to

$$\begin{aligned} \frac{\partial^2 \rho_{xx}}{\partial x_1 \partial x_2} = \frac{1}{D^2} & \left[ -6(\sigma_{xx_1} + \sigma_{xx_2})(\sigma_{x_1} \sigma_{x_2} \alpha_1 \alpha_2 + \sigma_{y_1} \sigma_{y_2} \beta_1 \beta_2) - 2(\sigma_{xy_1} + \sigma_{xy_2})(\sigma_{x_1} \sigma_{y_2} \alpha_1 \beta_2 + \sigma_{x_2} \sigma_{y_1} \alpha_2 \beta_1) \right. \\ & + \frac{8(\sigma_{xx_1} + \sigma_{xx_2})}{D} [(\sigma_{xx_1} + \sigma_{xx_2})^2 \sigma_{x_1} \sigma_{x_2} \alpha_1 \alpha_2 + (\sigma_{xy_1} + \sigma_{xy_2})^2 \sigma_{y_1} \sigma_{y_2} \beta_1 \beta_2 \\ & \left. + (\sigma_{xx_1} + \sigma_{xx_2})(\sigma_{xy_1} + \sigma_{xy_2})(\sigma_{x_1} \sigma_{y_2} \alpha_1 \beta_2 + \sigma_{x_2} \sigma_{y_1} \alpha_2 \beta_1) \right], \end{aligned} \quad (6)$$

the concentration of the ground subband. To validate this model, it is essential to provide for a mechanism through which oscillations at the difference frequency  $f_i = f_1 - f_2$  can be generated. We intend to show that this is the result of the intermodulation which prevails when more than one subband is occupied.

The theory of Isihira and Smrcka<sup>10</sup> for the oscillatory behavior of conductivity under magnetic fields was extended by Coleridge to the case of two subbands.<sup>3</sup> Based on the introduction of intrasubband and intersubband scattering in the presence of carriers in two subbands, the oscillatory part  $\Delta R_{xx}$  of the resistance  $R_{xx}$  (with a zero-field value of  $R_0$ ) was expressed by<sup>3</sup>

$$\frac{\Delta R_{xx}}{R_0} = A_1 \frac{\Delta g_1}{g_0} + A_2 \frac{\Delta g_2}{g_0} + B_{12} \frac{\Delta g_1 \Delta g_2}{g_0^2}. \quad (3)$$

Here  $g_0$  is the zero-field density of states and  $\Delta g$  is its oscillatory part.  $A_1$  and  $A_2$  are the amplitudes of single-subband oscillations.

The intermodulation, which prevails when two subbands are occupied, is represented by the  $B_{12}$  term. We intend to show that this component incorporates several mixed conductivity terms leading to various oscillatory wave patterns. We start from the equations describing a material with a single carrier type. The conductivity tensor elements as obtained in Ref. 10 for this structure are

$$\begin{aligned} \sigma_{xx} &= \frac{\sigma_0}{1 + \omega_c^2 \tau_0^2} \left[ 1 + \frac{2\omega_c^2 \tau_0^2}{1 + \omega_c^2 \tau_0^2} \frac{\Delta g}{g_0} \right], \\ \sigma_{xy} &= -\frac{\sigma_0 \omega_c \tau_0}{1 + \omega_c^2 \tau_0^2} \left[ 1 - \frac{3\omega_c^2 \tau_0^2 + 1}{\omega_c^2 \tau_0^2 (1 + \omega_c^2 \tau_0^2)} \frac{\Delta g}{g_0} \right], \end{aligned} \quad (4)$$

where  $\sigma_0$  is the zero-field longitudinal conductivity and  $\tau_0$  is the mobility scattering time.<sup>11</sup> When the magnetoresistance in a sample with two subbands is analyzed, the two components of the conductivity tensor must be combined and the matrix inverted. This results in

$$\rho_{xx} = \frac{\sigma_{xx_1} + \sigma_{xx_2}}{(\sigma_{xx_1} + \sigma_{xx_2})^2 + (\sigma_{xy_1} + \sigma_{xy_2})^2}. \quad (5)$$

The intermodulation component is obtained from the second derivative term in the expansion of the resistivity as series in  $\Delta g/g_0$ . To reduce the complexity of the following expressions, we will denote the nonoscillatory part of  $\sigma_{xx}$  as  $\sigma_x$ , that of  $\sigma_{xy}$  as  $\sigma_y$  [ $\sigma_y = -\sigma_0 \omega_c \tau_0 / (1 + \omega_c^2 \tau_0^2)$ ], and the denominator of Eq. (5) by  $D$ .

The mixed derivative provides the following term:

where  $i$  represents the subband ( $i=1,2$ ) and  $\sigma_{xx_i} = \sigma_{x_i}(1 + \alpha_i x_i)$ ;  $\sigma_{xy_i} = \sigma_{y_i}(1 + \beta_i x_i)$  with  $x_i = |\Delta g_i / g_0|$ ;  $\alpha_i = \alpha_0 \cos(2\pi f_i / B + \phi_i)$ ;  $\beta_i = \beta_0 \cos(2\pi f_i / B + \theta_i)$ . The temperature reduction factor and the exponential decay due to the quantum relaxation time  $\tau_q$  are included in the oscillatory part of the density of states  $\Delta g_i$ , i.e., in  $x_i$ . One should note that both  $\omega_c$  and  $\tau_0$  depend on the carrier type and therefore are different for the two subbands. In our case this prevents the very simple representation that was shown in the single-subband case.<sup>10</sup> No *a priori* assumption is made regarding the relative phase between the two oscillation phases  $\phi_i$  and  $\theta_i$ .

Equation (6) can be simplified assuming that  $\omega_c \tau_0 \gg 1$  since  $\tau_0$  is the mobility scattering time not the quantum relaxation time<sup>11</sup> and is related to the electron mobility  $\mu_e$  through  $\omega_c \tau_0 = \mu_e B$ . In all high-mobility structures this condition is fulfilled at fields as low as a few tenths of a tesla. The relative magnitude of the various conductivity components should be examined. The ratio between the longitudinal and transverse nonoscillatory conductivities is well known,  $\sigma_{y_i} = -\omega_c \tau_0 \sigma_{x_i}$ . It is important to notice that this is not the case for the oscillatory part of  $\sigma_{xx}$ ,  $\Delta \sigma_{xx_i} = \sigma_{xx_i} - \sigma_{xx_i}(\Delta g_i = 0)$ , according to the

derivation of Ishihara and Smrcka.<sup>10</sup> Rather, from Eq. (4) one obtains the inverse relationship, i.e.,  $\Delta \sigma_{xx_i} \approx \frac{2}{3} \omega_c \tau_0 \Delta \sigma_{xy_i}$  for  $\omega_c \tau_0 \gg 1$ . Thus, for this approximation  $\alpha \approx \frac{2}{3} \omega_c^2 \tau_0^2 \beta$ . Hence,  $\sigma_{x_i}^2 \sigma_{x_j} \alpha_i \alpha_j$  is of the same order of magnitude as  $\sigma_{x_i} \sigma_{y_1} \sigma_{y_2} \alpha_i \beta_j$ , while  $\sigma_{x_i} \sigma_{y_1} \sigma_{y_2} \beta_1 \beta_2$  and  $\sigma_{x_i}^4 \sigma_{x_j} \alpha_i \alpha_j / D$  are smaller by a factor of  $\omega_c^{-2} \tau_0^{-2}$  ( $j$  equals either 1 or 2 but is different from  $i$ ). Since all the terms multiplied by  $8(\sigma_{x_1} + \sigma_{x_2}) / D$  are of the same order of magnitude, this component is negligible as well as the second term in the first set of parentheses. Therefore, Eq. (6) can be reduced to

$$\frac{\partial^2 \rho_{xx}}{\partial x_1 \partial x_2} \approx \frac{1}{(\sigma_{xy_1} + \sigma_{xy_2})^4} \times [-6(\sigma_{xx_1} + \sigma_{xx_2}) \sigma_{x_1} \sigma_{x_2} \alpha_1 \alpha_2 - 2(\sigma_{xy_1} + \sigma_{xy_2})(\sigma_{x_1} \sigma_{y_2} \alpha_1 \beta_2 + \sigma_{x_2} \sigma_{y_1} \alpha_2 \beta_1)]. \quad (7)$$

Thus, the mixed term in the expansion of the resistivity can be written as

$$\frac{\partial^2 \rho_{xx}}{\partial x_1 \partial x_2} \Big|_0 x_1 x_2 \approx \frac{1}{(\sigma_{y_1} + \sigma_{y_2})^4} [-6(\sigma_{x_1} + \sigma_{x_2}) \Delta \sigma_{xx_1} \Delta \sigma_{xx_2} - 2(\sigma_{y_1} + \sigma_{y_2})(\Delta \sigma_{xx_1} \Delta \sigma_{xy_2} + \Delta \sigma_{xx_2} \Delta \sigma_{xy_1})]. \quad (8)$$

The first term represents a product of cosines at the two frequencies which is an amplitude modulation. This result is a superposition as described by Leadley *et al.*<sup>2</sup> and Coleridge.<sup>3</sup> The last two terms of Eq. (8) include the mixed oscillations due to the longitudinal conductivity of one subband, and the transverse conductivity of the other, and therefore are of equal amplitudes, independent of the model assumed, since the ratios between the  $xx$  and  $xy$  components are crossed. The wave form generated by these terms depends on the relative phase between the longitudinal and transverse oscillatory conductivities, and between the oscillations in the first and the second subbands. The issue of the phases in a single-carrier-type system was addressed by Coleridge, Stoner, and Fletcher,<sup>11</sup> who have measured the phase difference between  $\sigma_{xx}$  and  $\sigma_{xy}$ . According to their findings,  $\phi$  is equal to  $\pi$ , while  $\theta$  increases from  $3\pi/2$  to  $2\pi$  with decreasing field. Thus, the phase difference increases from  $\pi/2$  to  $\pi$ . The presence of the difference frequency at high temperatures and low magnetic fields, as verified experimentally, implies that at the lowest fields there is another change in the relative phases of the four components of conductivity; this time they will be in antiphase to the high-field configuration. Indeed, one can observe in Fig. 3 that the beat is accompanied by a change of phase of  $\pi$  in the wave form. If these terms are dominant, as discussed below, then, taking  $\phi_1 = \phi_2 = \pi$ , while  $\theta_1 = \frac{1}{2}\pi$  and  $\theta_2 = \frac{3}{2}\pi$ , one obtains

$$\frac{\partial^2 \rho_{xx}}{\partial x_1 \partial x_2} \Big|_0 x_1 x_2 \approx \frac{2\Delta \sigma_{xx_1} \Delta \sigma_{xy_2}}{(\sigma_{y_1} + \sigma_{y_2})^3} \sin \left[ \frac{2\pi f_1}{B} - \frac{2\pi f_2}{B} \right]. \quad (9)$$

Thus, the difference frequency can be derived from the intermodulation term with the appropriate choice of phases. At higher fields, assuming the phases reported in Ref. 11,  $\phi_1 = \phi_2 = \pi$  and  $\theta_1 = \theta_2 = 2\pi$ , one gets

$$\frac{\partial^2 \rho_{xx}}{\partial x_1 \partial x_2} \Big|_0 x_1 x_2 \approx \frac{2\Delta \sigma_{xx_1} \Delta \sigma_{xy_2}}{(\sigma_{y_1} + \sigma_{y_2})^3} \cos \left[ \frac{2\pi f_1}{B} \right] \times \cos \left[ \frac{2\pi f_2}{B} \right], \quad (10)$$

which is an amplitude modulation as discussed before. Finally, at the highest fields, where  $\phi_1 = \phi_2 = \pi$ , while  $\theta_1 = \theta_2 = \frac{1}{2}\pi$ , one obtains

$$\frac{\partial^2 \rho_{xx}}{\partial x_1 \partial x_2} \Big|_0 x_1 x_2 \approx \frac{2\Delta \sigma_{xx_1} \Delta \sigma_{xy_2}}{(\sigma_{y_1} + \sigma_{y_2})^3} \sin \left[ \frac{2\pi f_1}{B} + \frac{2\pi f_2}{B} \right]. \quad (11)$$

This is the sum of the frequencies observed at large fields (of several teslas, beyond our range), as observed experimentally.

The intermodulation can generate several wave patterns, the relative amplitude of which depends on the effect of the various scattering mechanisms on the relaxation time, as outlined by Coleridge.<sup>3</sup> On the other hand, the intermodulation is one of three components contributing to the oscillatory wave form of a system with two occupied subbands, as presented in Eq. (3). If all three

terms were significant, the measured line shape would not manifest a pure oscillation at the difference frequency, as we have recorded. However, the amplitude of oscillation due to the separate subbands decays exponentially with increasing temperature. On the other hand, the intermodulation increases markedly as the temperature is raised.<sup>3</sup> Thus, at higher temperatures, this term becomes more dominant, and oscillations at the difference frequency are observed throughout larger magnetic-field ranges.

### CONCLUSIONS

The presence of a third frequency in the SdH wave form was experimentally verified. The analysis shows that this frequency corresponds to the difference between

the concentration of the ground and the excited subband. It seems that this feature is present in other structures as well. All three frequencies of the wave form, starting from the sum frequency at high fields, through the superposition at intermediate fields, and down to the difference frequency at the lowest fields, can be attributed to the various relative phases between the longitudinal and transverse conductivities in the intermodulation.

### ACKNOWLEDGMENT

This work was done while one of us (S.E.S.) was at NASA Lewis Research Center with financial support from the National Research Council.

---

\*On leave from the Department of Electrical Engineering and Solid State Institute, Technion, Haifa 32000, Israel.

<sup>1</sup>B. Vinter and A. W. Overhauser, *Phys. Rev. Lett.* **44**, 47 (1980).

<sup>2</sup>D. R. Leadley, R. J. Nicholas, J. J. Harris, and C. T. Foxon, *Semicond. Sci. Technol.* **4**, 885 (1989).

<sup>3</sup>P. T. Coleridge, *Semicond. Sci. Technol.* **5**, 961 (1990).

<sup>4</sup>J. P. Eisenstein, H. L. Störmer, V. Narayanamurti, A. C. Gosard, and W. Wiegmann, *Phys. Rev. Lett.* **53**, 2579 (1984).

<sup>5</sup>W. Hansen, T. P. Smith III, J. Piao, R. Beresford, and W. I. Wang, *Appl. Phys. Lett.* **56**, 81 (1990).

<sup>6</sup>J. J. Harris, J. M. Lagemaat, S. J. Battersby, C. M. Hellon, C.

T. Foxon, and D. E. Lacklison, *Semicond. Sci. Technol.* **3**, 773 (1988).

<sup>7</sup>S. E. Schacham, E. J. Haugland, and S. A. Alterovitz (unpublished).

<sup>8</sup>T. P. Smith III, E. F. Fang, U. Meirav, and M. Heiblum, *Phys. Rev. B* **38**, 12 744 (1988).

<sup>9</sup>V. Altschul, A. Fraenkel, and E. Finkman, *J. Appl. Phys.* (to be published).

<sup>10</sup>A. Isihara and L. Smrcka, *J. Phys. C* **19**, 6777 (1986).

<sup>11</sup>P. T. Coleridge, R. Stoner, and R. Fletcher, *Phys. Rev. B* **39**, 1120 (1989).

REDUCED MOBILITY AND PPC IN  $\text{In}_{.20}\text{Ga}_{.80}\text{As}/\text{Al}_{.23}\text{Ga}_{.77}\text{As}$  HEMT STRUCTURE

S. E. Schacham\*, R. A. Mena, E. J. Haugland and S. A. Alterovitz  
 NASA Lewis Research Center

## ABSTRACT

Transport properties of a pseudomorphic  $\text{In}_{.20}\text{Ga}_{.80}\text{As}/\text{Al}_{.23}\text{Ga}_{.77}\text{As}$  HEMT structure have been measured by Hall and SdH techniques. Two samples of identical structures but different doping levels were compared. Low temperature mobility measurements as a function of concentration shows a sharp peak at a Hall concentration of  $1.9 \cdot 10^{18}/\text{cm}^2$ . This concentration coincides with the onset of second subband occupancy, indicating that the decrease in mobility is due to intersubband scattering. In spite of the low Al content (23%) large PPC was observed in the highly doped sample only, showing a direct correlation between the PPC and doping concentration of the barrier layer.

## I. INTRODUCTION

An important aspect of 2DEG transport is the effect of the second subband occupancy on carrier mobilities in HEMT structures. Several studies have been carried out on GaAs/AlGaAs structures and have shown that carrier mobilities decrease as a result of the larger inter-subband scattering effects that come about from second subband occupancy [1,2]. Here we report on an  $\text{In}_{.20}\text{Ga}_{.80}\text{As}/\text{Al}_{.23}\text{Ga}_{.77}\text{As}$  structure where the energy band separation between the subbands in the quantum well is larger due to a larger energy band discontinuity at the heterojunction [3]. Therefore larger carrier concentrations are required before population of the second subband can occur [4,5]. The large energy band discontinuity at the interface leads to better quantum confinement of the carriers and very high electron sheet carrier densities are possible. The larger doping concentrations however, bring up the interesting question as to how this affects the generation of DX centers in the AlGaAs layer leading to a persistent photoconductivity (PPC) effect [6].

It is generally believed that PPC decreases rapidly as the Al content fall below 30%, becoming negligibly small at 23% [7]. In this study, a comparison is made between two identical samples with a 23% Al concentration, with a single difference in the doping concentrations. Excess carriers were generated by illumination of the samples and measured by the Shubnikov-de Haas (SdH) oscillations, the Hall effect and magneto-resistance measurements. While the total carrier concentration,  $n_t$ , is obtained from the Hall voltage, the frequency (in  $1/B$ , where B is the magnetic field) of the SdH oscillation renders the electron concentration in the subbands of the 2DEG. When a parallel conducting path is present in the AlGaAs layer, the Hall concentration will be different from of the SdH value. Magneto-resistance measurements are used to confirm that the difference is due to a parallel conducting path and not as a result of second subband occupancy at the lower carrier concentrations.

\*Permanent Address: Dept. Elect. Engr., Technion, Haifa, Israel

Published in the Proceedings of the Fall 1991 Meeting of the MRS.



Persistent photoconductivity generated by the AlGaAs layer is known to decrease very rapidly as the aluminum content falls below 30% [7]. At a concentration of 23% one would expect hardly any PPC. Thus the pronounced increase in the concentration observed after illumination sequence that persists to 150K is quite surprising. On the other hand, for the lower doped sample #2 very little PPC was observed, as one would expect from this low Al ratio. Following the same illumination procedure as for sample #1, the concentration of the 2DEG for sample #2 hardly changed. It is apparent that the PPC effect is not only a function of the aluminum content but is also directly dependent on the doping concentration of the AlGaAs layer.

This is further illustrated by magneto-resistance measurements performed on both samples. Sample #1 showed a considerable amount of magneto-resistance indicating the existence of a parallel conducting path through the AlGaAs layer. On the other hand, sample #2 hardly had any magneto-resistance associated with it. In order to determine that the observed magneto-resistance was due to a parallel conducting path, a fit of the magneto-resistance was done using a two band model [8,9]. It is assumed that concentrations obtained from oscillatory magneto-resistance measurements, i.e. the Shubnikov-de Haas (SdH) technique, represent the accurate 2DEG concentration. The mobilities obtained from the fit consist of a high mobility carrier,  $u_h$ , which would correspond to the 2DEG and a low mobility carrier,  $u_l$ , corresponding to a carrier in the AlGaAs layer. Typical mobilities obtained from the fit are  $u_h=3.8 \cdot 10^4 \text{ cm}^2/\text{V.s}$  and  $u_l=.1 \cdot 10^4 \text{ cm}^2/\text{V.s}$ . As a result of the parallel conducting path in sample #1, carrier concentrations obtained by Hall measurements will be larger than the actual 2D concentration in the quantum well. For example, under dark conditions, a Hall carrier concentration of  $1.78 \cdot 10^{12}/\text{cm}^2$  was obtained compared to a SdH value of  $1.5 \cdot 10^{12}/\text{cm}^2$ . The fit was verified by comparing the Hall coefficient calculated based on mobilities and concentrations derived from the procedure with that obtained from the measured Hall voltage. The agreement between the two results was excellent. For sample #2, Hall and SdH values are almost identical which is again a prove of the absence of parallel conduction in this sample.

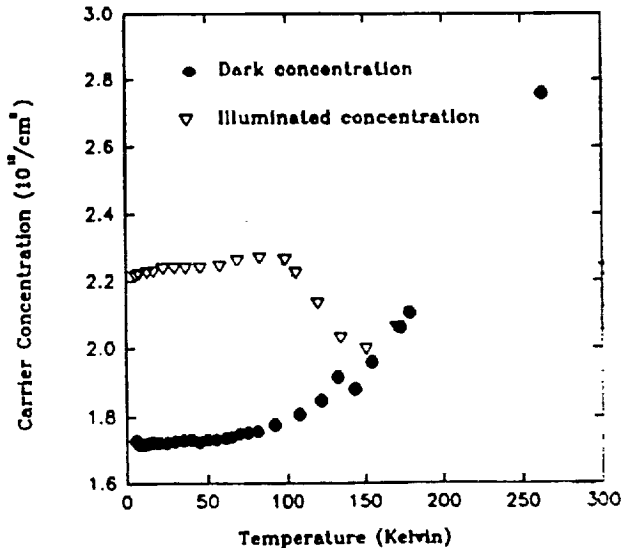


Fig.2 Temp. dependence of the carrier concentration for sample#1; before and after illumination.

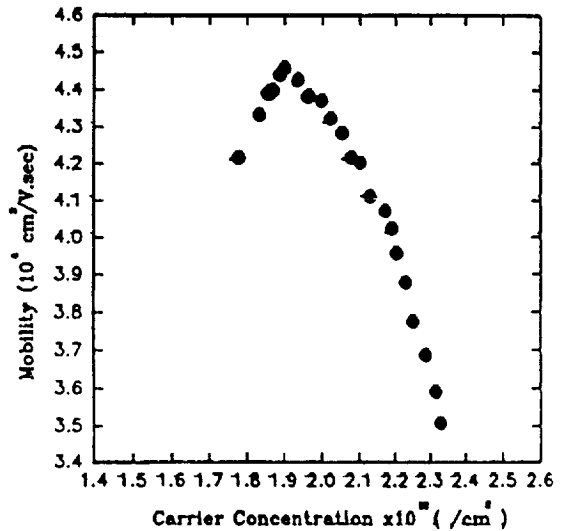


Fig.3 Measured Hall mobility for sample#1 as a function of carrier concentration.

Plotted in Fig. 3 are the carrier mobilities as a function of concentration as determined by Hall measurements. The measurements were carried out at 4.2K where phonon interactions are very small. The carrier mobility of the sample increases initially from a dark current mobility of  $4.2 \cdot 10^4 \text{ cm}^2/\text{V.s}$  to a maximum of  $4.45 \cdot 10^4 \text{ cm}^2/\text{V.s}$  as the concentration is increased. For this highly doped sample, a rather abrupt peak in the mobility occurred at a 2D concentration of  $1.9 \cdot 10^{12}/\text{cm}^2$ . At this point in the concentration, the mobility begins to drop as the concentration was increased further. The drop in mobility has two well defined linear slopes as a function of concentration. The change in slopes occurs at a concentration of about  $2.2 \cdot 10^{12}/\text{cm}^2$ . This corresponds to the point in the illumination where the neutral density filter was removed.

#### IV. DISCUSSION

An important finding of this work is the dependence of the 2DEG mobility on carrier concentration as presented in Fig. 3. Initially, as the concentration increased in sample #1 so did the mobility. This occurs as a result of the increased screening of scattering impurities by the generated excess electrons [10]. As the concentration went beyond a certain threshold however, a sharp peak is experienced and the mobility begins to drop in a linear fashion. This behavior in the mobility can be explained by the onset of the population of a second subband in the quantum well. At the onset of population, inter-subband scattering becomes more prominent and has an adverse effect on the mobility. This drop in mobility will continue until there are sufficient carriers to once again screen the impurity potential. Similar drops in mobilities were recorded in GaAs/AlGaAs structures by several groups and were attributed to the onset of the population of a second subband which occurs at concentrations between  $5 \cdot 10^{11}/\text{cm}^2$  to  $8 \cdot 10^{11}/\text{cm}^2$  [1,2]. The measured data showed decrease which were usually much less abrupt than predicted by theory [11].

For the  $\text{In}_{.20}\text{Ga}_{.80}\text{As}/\text{Al}_{.23}\text{Ga}_{.77}\text{As}$  structure the subband separation is greater due to a larger energy band discontinuity at the semiconductor interface. Thus larger 2D concentrations are required before a second subband population can occur. From the theoretical calculations by G. Ji et al. [4] on an  $\text{In}_{.16}\text{Ga}_{.86}\text{As}/\text{Al}_{.16}\text{Ga}_{.86}\text{As}$  HEMT structure, one can estimate that the second subband starts to be populated when the total concentration is approximately  $1.7 \cdot 10^{12}/\text{cm}^2$ . For the structure used in this study one would expect a larger separation of the energy bands due to a larger conduction band discontinuity. From Fig. 3 we see that the peak in the mobility occurs at a Hall concentration of  $1.9 \cdot 10^{12}/\text{cm}^2$ . As mentioned earlier, Hall concentrations are higher than the actual 2D concentration due to the parallel conducting path through the AlGaAs layer. SdH analysis at this point in the illumination gives a value of  $1.7 \cdot 10^{12}/\text{cm}^2$ . This value would correspond to a concentration below that of second subband population and is consistent with the comparison with G. Ji et al. calculations. At the final saturated Hall concentration of  $2.32 \cdot 10^{12}/\text{cm}^2$ , SdH analysis showed that the second subband was beginning to be populated. This is evident by the slight amplitude modulation of the SdH waveform shown in Fig. 4. It should be pointed out that we were not able to increase the population enough to reach a point where we would expect the decline to end and the rise to resume.

One of the most important aspects of this PPC study was the comparison of sample #1 with sample #2. This study shows that even when a low Al fraction is present, namely 23%, a large amount of PPC was observed for the higher doped sample, while for the lower doped sample, the PPC was completely negligible. Thus it is obvious that there is a direct correlation of the PPC effect with the doping concentration of the structure.

Finally from Fig. 1 we see that the concentration increased very rapidly after only a few seconds of illumination. This abrupt increase in concentration could possibly be due to the generation of electron-hole pairs in the channel region [1]. Following this abrupt increase, the carrier density as a function of illumination, took on an exponential behavior which is consistent with the excitation of DX centers in the AlGaAs region [12].

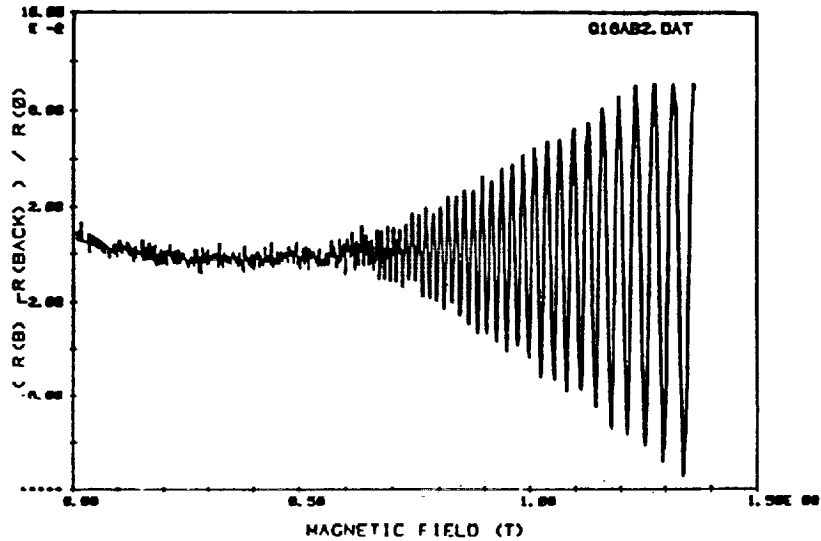


Fig.4 SdH oscillations with least-squares background subtraction.

## V. CONCLUSION

The transport properties of a pseudomorphic  $\text{In}_{0.20}\text{Ga}_{0.80}\text{As}/\text{Al}_{0.23}\text{Ga}_{0.77}\text{As}$  HEMT structure have been measured by Hall and SdH techniques. It was observed that as the second subband became occupied by excess carriers generated through illumination, carrier mobilities were lower than their dark current values. This result can be explained as a result of a more pronounced inter-subband scattering effect at the onset of second subband population. The difference in the observed PPC for two samples doped at different concentrations in the AlGaAs layer also leads to a direct correlation of the PPC effect and doping concentrations. It was seen that the higher doping concentrations result in a more pronounced PPC effect regardless of the Al content in the AlGaAs layer. There are several interesting points that are still unresolved. For example, at what point in the carrier concentration does the screening mechanism resume and carrier mobilities once again begin to increase. Also, what is the effect of different illumination wavelength on the drop in mobility due to second subband occupancy.

## ACKNOWLEDGMENT

The authors wish to thank Paul Young for the many useful discussions and Quantum Epitaxial Designs Inc. for the growth of the material structures.

## REFERENCES

1. R. Fletcher and E.Zaremba, Phys. Rev.B, 38(11), 7866(1988).
2. J.J.Harris, D.E.Lacklison, C.T.Foxon, F.M.Selten, A.M.Suckling, R.J.Nicholas and K.W.J.Barnham, Semicond. Sci. Technol. 2, 783, (1987).
3. M.Jaffe, Y.Sekiguchi, J.East and J.Singh, Superlattices and Microstructures, 4(4/5), 395, (1988).
4. G.Ji, T.Henderson, C.K.Peng, D.Huang and H.Morkoc, Solid-State Electronics, 33(2), 247, (1990).
5. F.Schubert and K.Ploog, IEEE Transactions on Electron Devices, 32(9), 1868, (1985).
6. P.M.Mooney, J. Appl. Phys., 67(3), R1, (1990)
7. T.N.Theis and S.L.Wright, Appl. Phys. Lett., 48, 1374, (1986).
8. S.T. Battersby, F.M. Selten, J.J. Harris and C.T.Foxon, Solid State Electronics, 31, 1083, (1988).
9. M.J. Kane, N.Aspley, D.A.Anderson, L.L.Taylor and T.Kerr, J. Phys. C, 18, 5629, (1985).
10. P.J.Price, J. Vac. Sci. Technol., 19(3), 599, (1981).
11. T.Ando, J. Phys. Soc. Jpn., 37, 1233, (1974).
12. D.E.Lacklison, J.J.Harris, C.T.Foxon, J.Hewett, D.Hilton and C.Roberts, Semicond. Sci. Technol., 3, 633, (1988).

# Study of InGaAs-based modulation doped field effect transistor structures using variable-angle spectroscopic ellipsometry

S. A. Alterovitz

*National Aeronautics and Space Administration, Lewis Research Center, Cleveland, Ohio 44135 (U.S.A.)*

R. M. Sieg\*

*Cleveland State University, Department of Electrical Engineering, Cleveland, Ohio 44115 (U.S.A.)*

H. D. Yao, P. G. Snyder and J. A. Woollam

*University of Nebraska, Department of Electrical Engineering, Lincoln, NE 68588 (U.S.A.)*

J. Pamulapati and P. K. Bhattacharya

*University of Michigan, Department of Electrical Engineering and Computer Science, Ann Arbor, MI 48109 (U.S.A.)*

P. A. Sekula-Moise

*Spire Corporation, Bedford, MA 01730 (U.S.A.)*

## Abstract

Variable-angle spectroscopic ellipsometry was used to estimate the thicknesses of all layers within the optical penetration depth of InGaAs-based modulation doped field effect transistor structures. Strained and unstrained InGaAs channels were made by molecular beam epitaxy (MBE) on InP substrates and by metal-organic chemical vapor deposition on GaAs substrates. In most cases, ellipsometrically determined thicknesses were within 10% of the growth-calibration results. The MBE-made InGaAs strained layers showed large strain effects, indicating a probable shift in the critical points of their dielectric function toward the InP lattice-matched concentration.

## 1. Introduction

$\text{In}_x\text{Ga}_{1-x}\text{As}$  can be grown epitaxially on InP or GaAs substrates, mostly as a strained layer. At a concentration of  $x = 0.53$ , it is lattice matched to InP. Although many applications in electronics and optoelectronics have been demonstrated using the lattice-matched concentration, superior properties of the strained-layer material have shifted the direction of applied research to  $x \neq 0.53$ . Modulation doped field effect transistors (MODFETs) with a strained-layer InGaAs channel have been demonstrated on InP [1] and on GaAs [2] substrates. Strain effects also play an important role in optoelectronic applications [3], especially near the band edge. Important parameters for any applications are the thicknesses of the layers, composition, interface quality and overlayer contamination or oxidation.

Ellipsometry, particularly variable-angle spectroscopic ellipsometry (VASE) in the visible, has been shown to characterize MODFETs [4] and optoelec-

tronic structures [5] in the GaAs/AlGaAs family. This non-destructive optical technique can be used to perform a detailed analysis of all layers within the optical penetration depth. For InGaAs, this depth is of the order of 1000 Å, *i.e.* it covers all interesting layers in a MODFET structure. Ellipsometry has only been used twice in the past for InGaAs-based MODFETs [6, 7]. The  $\text{In}_x\text{Ga}_{1-x}\text{As}/\text{InP}$  MODFET with  $x = 0.53$  made by metal-organic chemical vapor deposition (MOCVD) was analyzed in detail, including interface quality, by Erman *et al.* [6]. However, the more common MODFET growth technique is molecular beam epitaxy (MBE) rather than MOCVD. In this technique, InP cannot be grown and is replaced by  $\text{In}_{0.52}\text{Al}_{0.48}\text{As}$ , which is lattice matched to the InP substrate and provides the high band gap layer needed for the MODFET. Preliminary results on lattice-matched  $\text{In}_x\text{Ga}_{1-x}\text{As}/\text{InAlAs}/\text{InP}$  MODFETs were published by Alterovitz *et al.* [7]. However, no strain effects were reported in ref. 7. In this paper, we report on an ellipsometric study showing strain effects for the first time. The work included strained and lattice-matched InGaAs MODFETs made by MBE, as well as strained InGaAs MODFETs made by MOCVD on GaAs and

\*Undergraduate Student Intern at NASA Lewis Research Center.

| MBE MODFET Structure                |  |                               |   |
|-------------------------------------|--|-------------------------------|---|
| Actual MBE Grown Structure          |  | Nominal Structure for Ellips. |   |
|                                     |  | $t_1$                         | GaAs oxide 0 Å                                    |
| $n^+$                               | $\text{In}_{x,y}\text{Ga}_{1-x,y}\text{As}$ 100 Å  | $t_2$                         | $\text{In}_{x,y}\text{Ga}_{1-x,y}\text{As}$ 100 Å |
| $i$                                 | $\text{In}_{x,y}\text{Al}_{1-x,y}\text{As}$ 200 Å  |                               |   |
| $n^+$                               | $\text{In}_{x,y}\text{Al}_{1-x,y}\text{As}$ 150 Å  | $t_3$                         | $\text{In}_{x,y}\text{Al}_{1-x,y}\text{As}$ 400 Å |
| $i$                                 | $\text{In}_{x,y}\text{Al}_{1-x,y}\text{As}$ 50 Å   |                               |   |
| $i$                                 | $\text{In}_x\text{Ga}_{1-x}\text{As}$ $d$          | $t_4$                         | $\text{In}_x\text{Ga}_{1-x}\text{As}$ $d$         |
| $i$                                 | $\text{In}_{x,y}\text{Ga}_{1-x,y}\text{As}$ 400 Å  | $t_5$                         | $\text{In}_{x,y}\text{Ga}_{1-x,y}\text{As}$ 400 Å |
| $i$                                 | $\text{In}_{x,y}\text{Al}_{1-x,y}\text{As}$ 4000 Å |                               | $\text{In}_{x,y}\text{Al}_{1-x,y}\text{As}$ -     |
| 30 prd 30 Å/30 Å S.L. InGaAs/InAlAs |  |                               |   |
| Si InP Substrate                    |  |                               |   |

Fig. 1. Actual and nominal structures used in ellipsometry for the MBE-grown MODFET structures:  $d = 150 \text{ \AA}$  for  $x = 0.53$  and  $0.65$ ;  $d = 100 \text{ \AA}$  for  $x = 0.70$ .

using AlGaAs as the donor layer. Results will be compared with growth-calibration data obtained during the crystal growth.

## 2. Experimental details

The structures grown on semi-insulating InP substrates were prepared by MBE at the University of Michigan. The structures are shown in Fig. 1. The 30-period  $30 \text{ \AA}/30 \text{ \AA}$  superlattice buffer made of InGaAs/InAlAs acts as a dislocation filter. The role of all the other layers is explained in ref. 7. Growth conditions are given in ref. 8. For ellipsometry purposes, the  $4000 \text{ \AA}$  thick InAlAs serves as the substrate, as the optical penetration depth in most of the experimental range is smaller than the thickness of all layers above the superlattice. Three indium concentrations  $x$  were tested:  $0.53$ ,  $0.65$ , and  $0.70$ . Nominal channel thicknesses derived from growth-calibration data are shown in Fig. 1.

Three samples grown by MOCVD at Spire Corporation on semi-insulating GaAs were also tested. The structures are shown in Fig. 2. The  $1 \mu\text{m}$  buffer is made mainly of iGaAs and is regarded as the substrate for ellipsometry purposes. Growth parameters are given in ref. 8.

The ellipsometric technique used was similar to that described previously [9]. In this work, we minimized the mean square error  $\sigma$  as defined in eqn. (1)

$$\sigma \equiv (N^{-1}) \sum_i [(\tan \psi_{e,i} - \tan \psi_{c,i})^2 + (\cos \Delta_{e,i} - \cos \Delta_{c,i})^2] \quad (1)$$

Here  $\tan \psi_{e,i}$ ,  $\cos \Delta_{e,i}$  are the experimental results and  $\tan \psi_{c,i}$ ,  $\cos \Delta_{c,i}$  are the model calculations. The summation is over all  $N$  experimental points, *i.e.* all wavelengths and angles of incidence. Ellipsometric dielectric

## MOCVD MODFET STRUCTURE

| Actual Structure  |  | Nominal Structure For Ellipsometry |  |
|-------------------|--|------------------------------------|--|
|                   |  | $t_1$                              | GaAs Oxide 20 Å  |
| $n^+$             | GaAs 100 Å   | $t_2$                              | GaAs 100 Å   |
| $n^+$             | $\text{Al}_x\text{Ga}_{1-x}\text{As}$ 400 Å              |                                    |  |
| $i$               | $\text{Al}_x\text{Ga}_{1-x}\text{As}$ 50 Å               | $t_3$                              | $\text{Al}_x\text{Ga}_{1-x}\text{As}$ 450 Å              |
| $i$               | $\text{In}_{x,y}\text{Ga}_{1-x,y}\text{As}$ 50 Å (100 Å) | $t_4$                              | $\text{In}_{x,y}\text{Ga}_{1-x,y}\text{As}$ 50 Å (100 Å) |
|                   |  | GaAs Substrate                     |  |
| Buffer            | 10,000 Å   |                                    |  |
| Si GaAs Substrate |  |                                    |  |

Fig. 2. Actual and nominal structures used in ellipsometry for the MOCVD-grown MODFET structures. The aluminum concentration in  $\text{Al}_x\text{Ga}_{1-x}\text{As}$  is a variable. Some samples have a  $50 \text{ \AA}$   $\text{In}_{0.3}\text{Ga}_{0.7}\text{As}$  layer and others have a  $100 \text{ \AA}$  layer.

calibration functions were taken from the following:  $\text{In}_x\text{Ga}_{1-x}\text{As}$  from the algorithm developed in ref. [8], AlGaAs from the algorithm given in ref. 10, GaAs from ref. 11,  $\text{In}_{0.52}\text{Al}_{0.48}\text{As}$  from previous measurements at NASA Lewis Research Center and the oxide from ref. 12. The dielectric function for the oxide was measured on GaAs oxides, but it gives a good description of the oxide on  $\text{In}_{0.53}\text{Ga}_{0.47}\text{As}$  [13].

## 3. Results and discussion

Results for three indium compositions grown by MBE are given in Table 1. The thicknesses  $t_i$  correspond to Fig. 1. The quality of the fits, as measured by the value of the mean square error, is good. However, two features of these results were unexpected: the very low values of the cap InGaAs layer thicknesses and the negative values for the strained layer thicknesses. The low values obtained for the cap layers can be explained by the very short growth time of these layers and the accompanying experimental errors, and by possible loss of material due to oxidation. We found this result for the InGaAs cap layer in all our MBE samples. Another explanation might involve an interface layer between the InAlAs and the cap layer. However, for our structures it is almost impossible to study this interface by ellipsometry. We already have 4–5 parameters and an interface layer would introduce another parameter. In addition, we already have a high correlation parameter ( $0.9$  or higher) between  $t_2$  and  $t_3$ , the cap layer and the InAlAs layer thicknesses respectively. The correlation problem was discussed in refs. 14 and 15. The high correlation between  $t_2$  and  $t_3$  means that ellipsometry has difficulty in estimating accurately the value of each one of these two parameters, but the sum  $t_2 + t_3$  is not affected by the correlation. Results given in Table 1 support this conclusion, with experimental  $t_2 + t_3$  values

TABLE 1. Best fits for MBE-grown InGaAs/InAlAs MODFET structures using the strain-free calibration functions (wavelength range 3300–7500 Å)

|          | $x = 0.53$ |                      | $x = 0.65$ |                      | $x = 0.70$ |                      |
|----------|------------|----------------------|------------|----------------------|------------|----------------------|
|          | Nominal    | Ellipsometry         | Nominal    | Ellipsometry         | Nominal    | Ellipsometry         |
| $t_1$    | 0          | 20.8                 | 0          | 27.6                 | 0          | 25.8                 |
| $t_2$    | 100        | 45.7                 | 100        | 41.4                 | 100        | 50.3                 |
| $t_3$    | 400        | 443                  | 400        | 452                  | 400        | 424                  |
| $t_4$    | 150        | 553                  | 150        | -0.5                 | 100        | -28.8                |
| $t_5$    | 400        |                      | 400        | 566                  | 400        | 559                  |
| $\sigma$ | —          | $3.2 \times 10^{-3}$ | —          | $2.7 \times 10^{-3}$ | —          | $1.8 \times 10^{-3}$ |

InGaAs or InP in the visible. However, we expect the critical points and, accordingly, the dielectric function [10] to change continuously as a function of composition. In the case of pseudomorphic InGaAs, we find a split of the valence band [16] and the resulting band structure with the associated critical points is expected to be more complex than the case for AlGaAs. However, in a very rough approximation and extension of the result in ref. 16, the band gap of strained-layer  $\text{In}_x\text{Ga}_{1-x}\text{As}$  is similar to unstrained  $\text{In}_y\text{Ga}_{1-y}\text{As}$ , where  $x > y$  for  $y > 0.53$ , *i.e.* for compressive strain. Assuming that all critical points move in the same direction we have to use as a calibration dielectric function for our strained  $\text{In}_x\text{Ga}_{1-x}\text{As}$  the dielectric function obtained for unstrained  $\text{In}_y\text{Ga}_{1-y}\text{As}$  from ref. 8 with  $x > y$ . We used the dielectric function of the unstrained  $\text{In}_{0.53}\text{Ga}_{0.47}\text{As}$  to fit the  $\text{In}_x\text{Ga}_{1-x}\text{As}$  strained-lattice layers for both  $x = 0.65$  and 0.70. The results are given in Table 2. The quality of the fits is good, and there are no unphysical results for layer thicknesses. Results are also shown in Fig. 3(a) and (b) for the fit given in Table 2 for the  $x = 0.70$  sample. There is a remarkably good fit of the experimental and the modeled data, including the sharp jumps in the values of  $\cos \Delta$ .

Two comments on the results given in Table 2 will now be discussed. First comment is with regard to

TABLE 2. Best fits for MBE-grown strained-layer channel samples, assuming all InGaAs layers are lattice matched to InP, *i.e.*  $x = 0.53$  (wavelength range 3300–7500 Å)

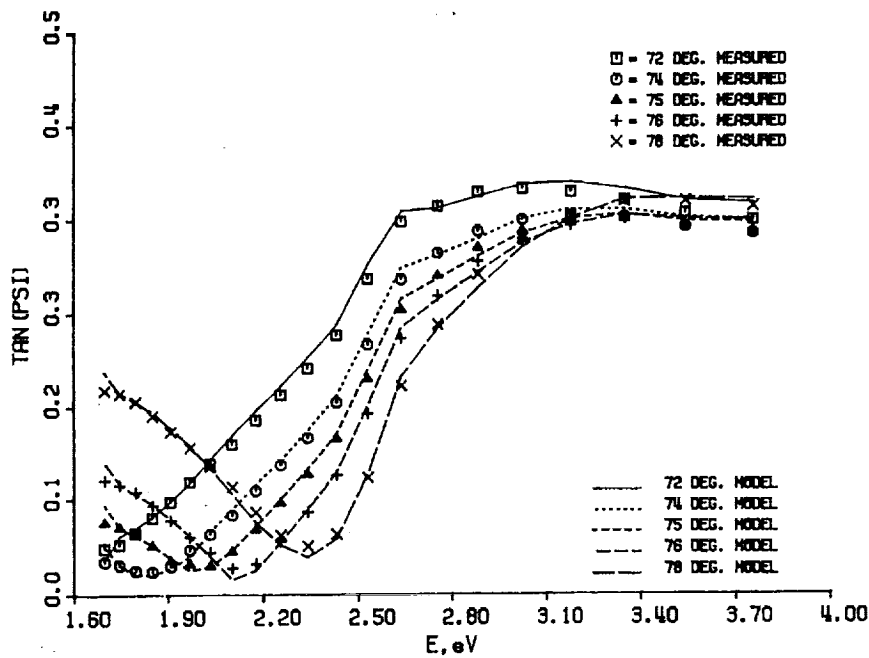
|          | $x = 0.65$ |                      | $x = 0.70$ |                      |
|----------|------------|----------------------|------------|----------------------|
|          | Nominal    | Ellipsometry         | Nominal    | Ellipsometry         |
| $t_1$    | 0          | 27.5                 | 0          | 26.7                 |
| $t_2$    | 100        | 41.5                 | 100        | 48.9                 |
| $t_3$    | 400        | 452                  | 400        | 433                  |
| $t_4$    | 150        | 564                  | 100        | 530                  |
| $t_5$    | 400        |                      | 400        |                      |
| $x$      | 0.65       | 0.53                 | 0.70       | 0.53                 |
| $\sigma$ | —          | $2.6 \times 10^{-3}$ | —          | $1.8 \times 10^{-3}$ |

in the range 474–493 Å, while the nominal value is 500 Å.

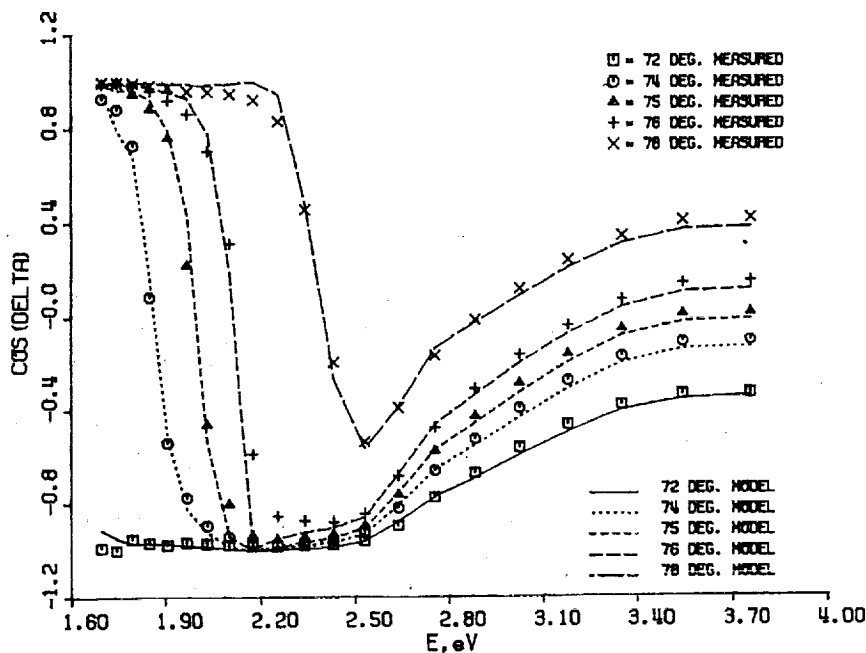
The other unexpected result, the negative values for  $t_4$ , is definitely related to the special property of this layer, namely that it is a pseudomorphic strained layer. The ellipsometric dielectric calibration functions that were used for the calculations were taken from ref. 8, where a study of strain-free  $\text{In}_x\text{Ga}_{1-x}\text{As}$  material was done. It is known that the band gap of pseudomorphic InGaAs grown on InP is different from that of unstrained bulk InGaAs [16]. There are no theoretical calculations of the dielectric function of pseudomorphic

TABLE 3. Best fits for MOCVD-grown InGaAs/AlGaAs MODFET structures using the strain-free calibration functions (wavelength range 3500–6800 Å)

|          | MO6-316-3 |                      | MO6-332-1 |                      | MO6-334-1 |                      |
|----------|-----------|----------------------|-----------|----------------------|-----------|----------------------|
|          | Nominal   | Best fit             | Nominal   | Best fit             | Nominal   | Best fit             |
| $t_1$    | 20        | 20.6                 | 20        | 17.7                 | 20        | 18.3                 |
| $t_2$    | 300       | 341                  | 100       | 101                  | 100       | 103                  |
| $x$      | 0.2       | 0.223                | 0.2       | 0.166                | 0.2       | 0.155                |
| $t_3$    | 450       | 374                  | 450       | 443                  | 450       | 491                  |
| $t_4$    | 100       | 86.0                 | 100       | 94.5                 | 50        | 52.8                 |
| $\sigma$ | —         | $3.3 \times 10^{-4}$ | —         | $5.7 \times 10^{-4}$ | —         | $5.0 \times 10^{-4}$ |



(a)

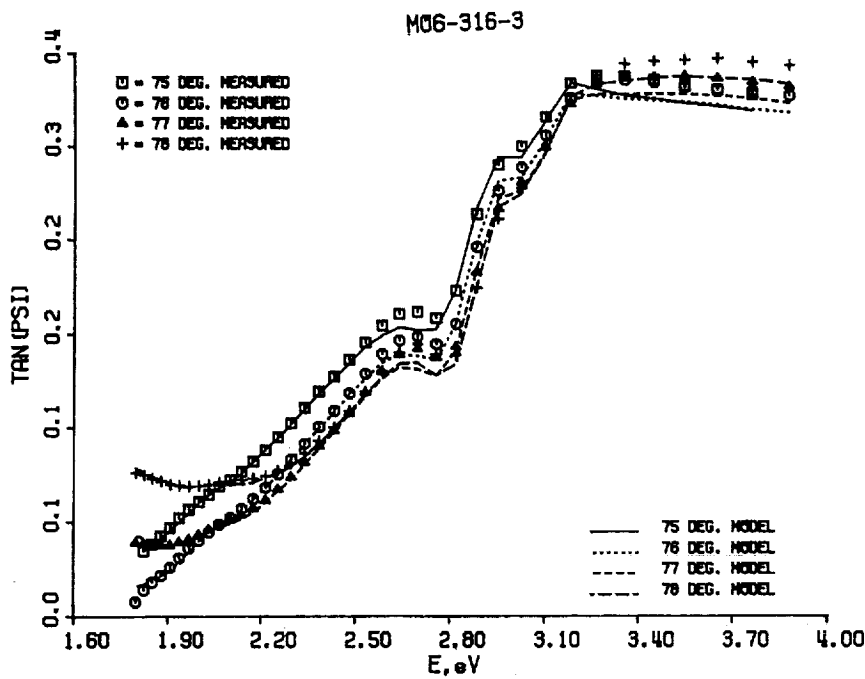


(b)

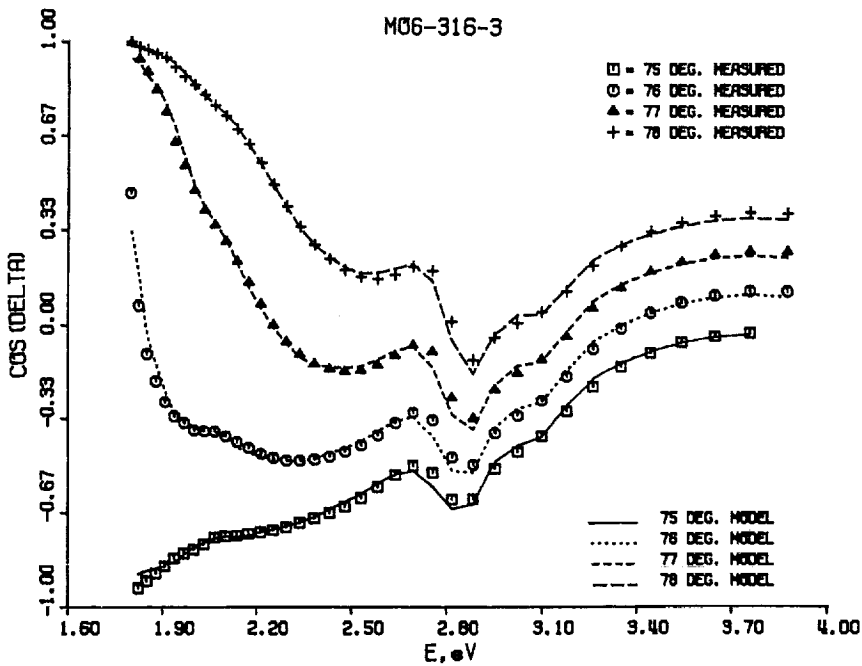
Fig. 3. Experimental and model simulation for (a)  $\tan \psi$  and (b)  $\cos \Delta$  vs. energy for five angles of incidence for the MBE-grown  $v = 0.70$  sample. All of the InGaAs material is assumed to be lattice matched to InP.

correlations. The same correlation problem between  $t_2$  and  $t_3$  mentioned previously was also observed for the results given in Table 2. We will now combine the results of Table 1 (for the lattice-matched sample) and Table 2 (for the strained-lattice sample) for the parameter  $t_2 + t_3$ : while the nominal value is 500 Å for all

samples, the range of experimental results is 482–493 Å, even smaller than the range mentioned above. The second comment is with regard to the concentration parameter  $x$ , especially for the strained-lattice samples. This parameter was obtained from growth-calibration data, which were cross checked by X-rays



(a)



(b)

Fig. 4. Experimental and model simulation for (a)  $\tan \psi$  and (b)  $\cos \Delta$  vs. energy for four angles of incidence for an MOCVD-grown  $x = 0.30$  sample.

for strain-free material. A positive confirmation that  $x$  for the strained-lattice samples is not 53% was obtained from electrical measurements of devices made from the same wafers or similarly prepared wafers [17, 18]. The measured device parameters show a clear dependence on the nominal value of  $x$ .

Three MOCVD-grown MODFET structures of pseudomorphic  $\text{In}_{0.3}\text{Ga}_{0.7}\text{As}$  on GaAs were measured. The results are shown in Table 3. For one of the samples, we also show a complete comparison of experiment and model in Fig. 4. The mean square errors  $\sigma$  are much smaller than those for the  $\text{InGaAs/InAlAs/InP}$

samples. In addition, all results pertaining to the InGaAs and the GaAs layer thicknesses are in good agreement with the nominal values. There are some discrepancies between the ellipsometric estimates and the AlGaAs nominal concentrations or thicknesses. At the present time, we believe that the ellipsometric result may be a more accurate description of the sample. The low values for  $\sigma$  are probably due to better calibration spectra for the constituents and the fact that the aluminum concentration in AlGaAs is a free parameter, while the composition in  $\text{In}_{0.52}\text{Al}_{0.48}\text{As}$  is held constant.

#### 4. Conclusions

A variety of InGaAs MODFET structures, made by both MBE and MOCVD were studied by variable-angle spectroscopic ellipsometry. The thicknesses of all layers involved in the electric conduction were estimated and reasonably good fits to the nominal values were obtained. We have clearly seen, for the first time, strain effects in pseudomorphic InGaAs. These effects were explained qualitatively as a shift of the critical points in the strained *vs.* the unstrained InGaAs material. In addition, in the case of MOCVD, we have seen possible problems in an AlGaAs layer, showing that ellipsometry can be used as a quality control tool for a complex material.

#### Acknowledgment

We would like to thank Mark Drotos for technical help in the ellipsometric analysis.

#### References

- 1 G. I. Ng, W. P. Hong, D. Pavlidis, M. Tutt and P. K. Bhattacharya, *IEEE Electron Devices Lett.*, **9** (1988) 439.
- 2 W. T. Masselnik, J. Klem, T. Henderson, A. Ketterson, J. S. Gedjmin, H. Morkoc and K. R. Gleason, *Proc. Int. Electron Devices Meet. (IEDM) 1985*, p. 755.
- 3 S. C. Hong, G. P. Kothigal, N. Debbbar, P. K. Bhattacharya and J. Singh, *Phys. Rev. B*, **37** (1988) 878.
- 4 P. G. Snyder, M. C. Rost, G. H. Bu-Abbud, J. A. Woollam and S. A. Alterovitz, *J. Appl. Phys.*, **60** (1986) 3293.
- 5 S. A. Alterovitz, J. A. Woollam and P. G. Snyder, *Solid State Technol.*, **31** (1988) 99.
- 6 M. Erman, J. P. Andre and J. LeBris, *J. Appl. Phys.*, **59** (1986) 2019.
- 7 S. A. Alterovitz, R. M. Sieg, H. D. Yao, P. G. Snyder, J. A. Woollam, J. Pamulapati and P. K. Bhattacharya, *Mater. Res. Soc., EA-21* (1990) 299.
- 8 S. A. Alterovitz, R. M. Sieg, H. D. Yao, P. G. Snyder, J. A. Woollam, J. Pamulapati, P. K. Bhattacharya and P. A. Sekula-Moise, *Proc. ICEM-90*, in the press.
- 9 S. A. Alterovitz, R. M. Sieg, N. S. Shoemaker and J. J. Pouch, *Mater. Res. Soc. Symp. Proc.*, **152** (1989) 21.
- 10 P. G. Snyder, J. A. Woollam, S. A. Alterovitz and B. Johs, *J. Appl. Phys.*, **68** (1990) 5925.
- 11 D. E. Aspnes and A. A. Studna, *Phys. Rev. B*, **27** (1983) 985.
- 12 D. E. Aspnes, G. P. Schwartz, G. J. Gualtieri, A. A. Studna and B. Schwartz, *J. Electrochem. Soc.*, **128** (1981) 590.
- 13 D. E. Aspnes and H. J. Stocker, *J. Vac. Sci. Technol.*, **21** (1982) 413.
- 14 S. A. Alterovitz, G. H. Bu-Abbud, J. A. Woollam and D. C. Liu, *J. Appl. Phys.*, **54** (1983) 1559.
- 15 G. H. Bu-Abbud, N. M. Bashara and J. A. Woollam, *Thin Solid Films*, **138** (1986) 27.
- 16 R. People, *Appl. Phys. Lett.*, **50** (1987) 1604.
- 17 R. Lai, P. K. Bhattacharya, S. A. Alterovitz, A. N. Downey and C. Chorey, *Electron Devices Lett.*, **11** (1990) 564.
- 18 J. Pamulapati, R. Lai, G. I. Ng, Y. C. Chen, P. R. Berger, P. K. Bhattacharya, J. Singh and D. Pavlidis, *J. Appl. Phys.*, **68** (1990) 347.

MICROWAVE PROPERTIES OF "PEELED" HEMT DEVICES  
SAPPHIRE SUBSTRATES

Paul G. Young\*, Samuel A. Alterovitz\*\*, Rafael A. Mena\*\* and Edwyn D. Smith\*

\*University of Toledo  
Electrical Engineering Department  
Toledo, Ohio 43606

\*\*NASA Lewis Research Center  
Cleveland, Ohio 44135

The use of an AlAs layer buried between the GaAs substrate and the active device layer of high electron mobility transistor (HEMT) material has allowed the development of "peeled" devices. Work by Konagai<sup>1</sup> and Yablonovitch<sup>2</sup> in the area of "peeled" layers using selective etching has opened a new technology in transferable devices and circuits. MESFET rf operation<sup>3</sup> and some work in the area of DC HEMT performance<sup>4</sup> of "peeled" devices has been demonstrated.

Interest in peeled technology has arisen because the 1 to 2 um active layer of a microwave device can be "peeled" from the GaAs and attached to a suitable host with the desired permittivity and thermal properties. The small thickness of the active layer permits interconnections between devices and transmission lines to be made using standard photolithographically produced metal lines eliminating the need for bond wires resulting in improved rf performance. The focus of this research will be to demonstrate the first full rf characterization of HEMT device parameters. The results of this research will be used in the design of circuits with peeled HEMT devices, e.g. 10GHz amplifier<sup>5</sup>.

Devices were fabricated using two HEMT structures grown by MBE methods. A 500Å AlAs release layer for "peel off" was included under the active layers of the structure. The structures are a homogeneously doped Al<sub>0.3</sub>Ga<sub>0.7</sub>As/GaAs and a delta doped square well Al<sub>0.23</sub>Ga<sub>0.77</sub>As/GaAs HEMT structure as shown in figure 1. Devices were fabricated using a mesa isolation process. Contacts were done by sequentially evaporating Au/Ge/Au/Ni/Au followed by rapid thermal anneal at 400C for 15 seconds. Gates were wet etch recessed and 1um to 1.4um Ti/Au gate metal was deposited. Devices were peeled off the GaAs substrate using Apiezon wax to support the active layer and a HF:DI (1:10) solution to remove the AlAs separation layer. Devices were then attached to sapphire substrates using van der Waals bonding.

DC testing of the devices was conducted to determine contact resistivity, channel resistivity, extrinsic transconductance and Hall mobility. Transmission lines were used to determine contact resistivity and channel resistivity. Results of these tests showed a contact resistivity of  $7 \cdot 10^{-7}$  ohm-cm<sup>2</sup> before and after peel off with no degradation in the measured channel resistivity. This indicates that parameters associated with the source drain series resistance of a transistor are unaffected by "peel-off" process.

The extrinsic transconductance for a square well delta doped structure is shown in figure 2 illustrating that no device degradation was experienced when peeling off the devices. Similar results were obtained for the homogeneously doped structure with a peak extrinsic transconductance of 120 mS/mm for a 1.4um device. It appears that the parameters associated with the DC operation of the devices are unaffected by the peel off process. Further proof of this is seen in the Hall mobility results as shown in figure 3. The Hall mobility for a non-peeled and peeled homogeneously doped HEMT structure is plotted as a function of temperature showing no apparent degradation in the mobility over the temperature range. Peak electron concentrations for both the peeled and non-peeled structures are of the order of  $3 \cdot 10^{12}$ /cm<sup>2</sup> as measured by Hall techniques.

Rf testing of devices were also conducted using a Cascade probe station and the HP8510A automatic network analyzer. The S parameters verses frequency were measured and the rf results are plotted in figure 4 for a square well, delta doped device before and after peel off. As can be seen, the device exhibits no change in  $F_{max}$  but there appears to be an improvement in the maximum available gain ( $G_{max}$ ) and the S parameter response at lower frequencies.  $G_{max}$  has increased by 2 dB for the peeled versus the unpeeled device. Similar results were achieved for the homogeneously doped structure. The S parameters show an improvement in the forward ( $S_{21}$ ) and reverse transmission ( $S_{12}$ ) parameters resulting in the improved gain response.

The parameters indicated that while DC parameters are unaffected by peel off while the rf performance is slightly improved. It can be assumed that the sapphire substrate does affect the frequency response of the device resulting in the improvements of  $G_{max}$ .

1. M. Konagai, M. Sugimoto and K. Takahshi, J. of Crystal Growth 45, 277 (1978).
2. E. Yablonovitch, D. Hwang, T. Gmitter, J. Harbison and R. Bhat, Appl. Phys. Lett. 51(26), 28 Dec. 1987.

3. D. Shah, W. Chan, T. Gmitter, L. Florez, H. Shumacher, B. Van Der Gaag, Electronics Lett., Vol. 26, No. 22, 25 Oct. 1990.

4. D. Myers, J. Klem, and J. Lott, 1988 IEDM Conference Proceedings, pg. 704

5. P. G. Young, R. R. Romanofsky, S. A. Alterovitz and E. D. Smith, to be published.

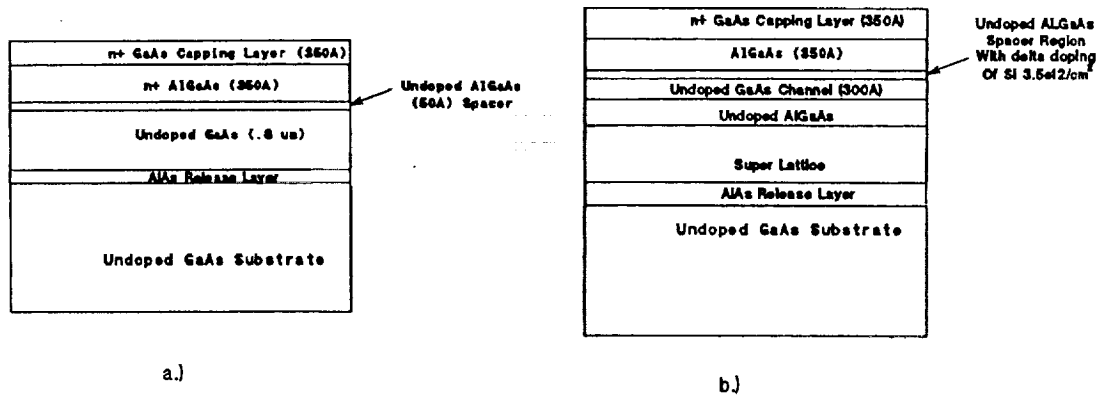


Figure 1. a.) Homogeneously doped and b.) delta doped HEMT structures with the ALAs release layer.

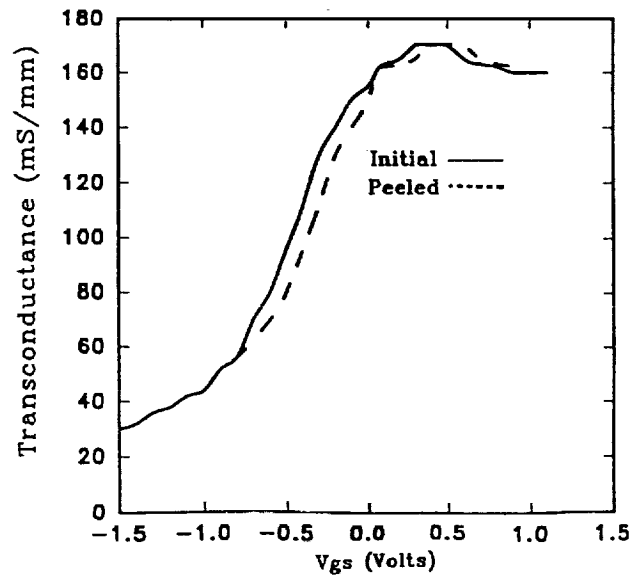


Figure 2. Extrinsic transconductance for a 1 μm gate delta doped structure.

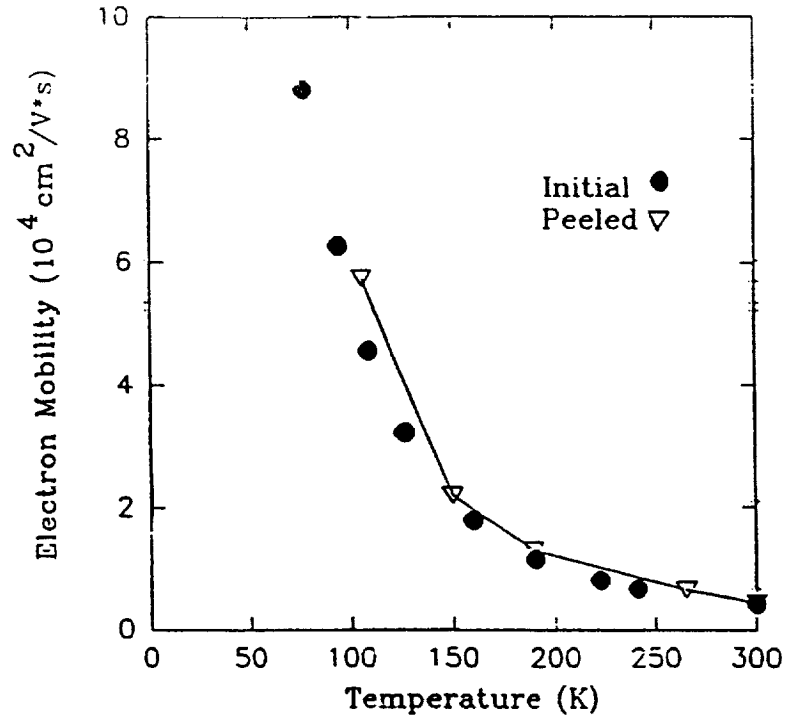


Figure 3. Hall mobility for a homogeneously doped HEMT structure.

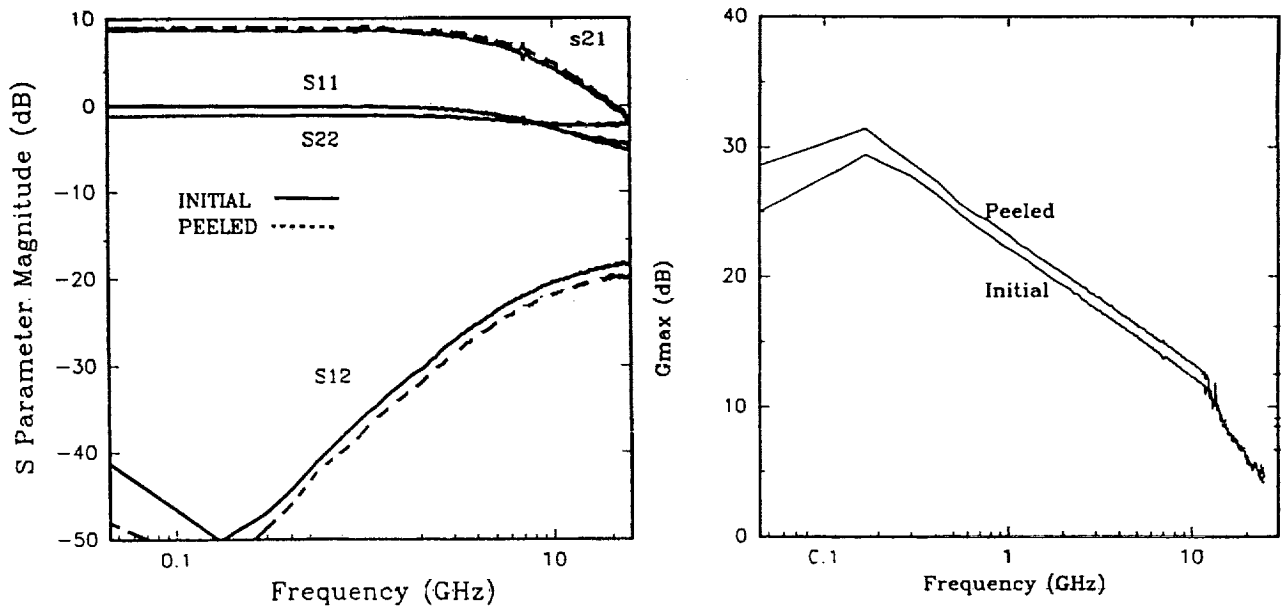


Figure 4. Rf response for a delta doped HEMT structure with a 1 um gate.

# A Model for the Trap-Assisted Tunneling Mechanism in Diffused n-p and Implanted n<sup>+</sup>-p HgCdTe Photodiodes

David Rosenfeld and Gad Bahir

Permission to copy without fee all or part of this material is granted provided that the copies are not made or distributed for direct commercial advantage. Copying is by permission of the Institute of Electrical and Electronics Engineers. To copy otherwise, or to republish, requires a fee and specific permission.

**Abstract**—In this paper we present a theoretical model for the trap-assisted tunneling process in diffused n-on-p and implanted n<sup>+</sup>-on-p HgCdTe photodiodes. The model describes the connection between the leakage current associated with the traps and the trap characteristics: concentration, energy level, and capture cross sections. We have observed that the above two types of diodes differ in the voltage dependence of the trap-assisted tunneling current and dynamic resistance. Our model takes this difference into account and offers an explanation of the phenomenon. The good fit between measured and calculated dc characteristics of the photodiodes (for medium and high reverse bias and for temperatures from 65 to 140 K) supports the validity of the model.

## I. INTRODUCTION

THE MAIN interest in ternary alloys HgCdTe stems from their potential use in infrared detectors. One of the parameters affecting the performance of such devices is the trap concentration in the neutral as well as the depletion regions. Traps in the neutral region serve as Shockley-Read-Hall centers and bring about two short thermal transitions instead of one longer transition. They may cause a dramatic decrease in the minority-carrier lifetime in these regions [1]. The reduction of lifetime at a distance smaller than a diffusion length from the edge of the depletion region is of great importance, since it increases the diffusion leakage current and decreases the quantum efficiency as well as the photodiodes cutoff wavelength [2].

The role played by traps in the depletion region is more complicated. The existence of an electric field in the depletion region gives rise to two additional nonthermal transitions: a) tunneling of electrons from the valence band to the traps and b) tunneling from the traps to the conduction band. In addition to the thermal-thermal path that takes place in centers located in the neutral region, three

more paths are possible in centers located within the depletion region: thermal-tunnel, tunnel-thermal, and tunnel-tunnel paths. The Shockley-Read-Hall mechanism is therefore replaced by a more complex mechanism, often called trap-assisted tunneling. The three additional paths add significant leakage current and therefore degrade the performance of photodiodes operated at low temperatures and reverse biases higher than 50 mV.

The negative effect of traps on the performance of HgCdTe diodes is not limited to the low-temperature high-bias region. In previously published works [3], [4] we demonstrated the correlation between tunneling currents and  $1/f$  noise measured on HgCdTe diodes. It was shown that the low-frequency noise associated with tunneling mechanisms is much higher than that associated with diffusion and generation-recombination mechanisms. It was also found that the dark current of photodiodes, operated at the usual working conditions, is dominated by the diffusion mechanism, while the low-frequency noise is often dominated by tunneling mechanisms. The concentration and nature of the traps within the depletion region are therefore important parameters, which determine the low-frequency noise and may degrade the detector's signal-to-noise ratio, even when trap-assisted tunneling current is negligible.

Since each of the four paths involved in the trap-assisted tunneling process has different temperature and voltage dependencies, the overall temperature and voltage dependencies of the trap-assisted tunneling current is very complicated. Several published papers deal with the phenomena of trap-assisted tunneling in HgCdTe diodes [5]–[8] and capacitors [9]–[11], and present comparisons between theory and measured data. Most of these models seem to fit certain observed behavior within a limited range of operating conditions; namely, temperature and bias; but none in a wide range of these parameters. In this paper we model the trap-assisted tunneling current of front-illuminated diffused n-p and implanted n<sup>+</sup>-p Hg<sub>1-x</sub>Cd<sub>x</sub>Te photodiodes with  $x \approx 0.22$ . We compare measured and calculated characteristics in a wide range of temperatures (65–140 K) and biases (0.3–0.8 V). We also demonstrated the different voltage dependence of the trap-assisted tunneling mechanism in the high-temperature region and suggest an explanation for this difference.

Manuscript received February 18, 1991; revised December 20, 1991. The review of this paper was arranged by Associate Editor N. Moll.

D. Rosenfeld was with the Kidron Microelectronics Research Center, Department of Electrical Engineering, Technion—Israel Institute of Technology, Haifa 32000, Israel. He is now with NASA Lewis Research Center, Cleveland, OH 44135.

G. Bahir is with the Kidron Microelectronics Research Center, Department of Electrical Engineering, Technion—Israel Institute of Technology, Haifa 32000, Israel.

IEEE Log Number 9200386.

## II. DEVICE PROCESSING AND SURFACE POTENTIAL

The model and the measured data presented in the following sections characterize front-illuminated bulk HgCdTe photodiodes with  $x \approx 0.22$ . The starting material is undoped p-type bulk material grown by the traveling heater method (THM), either a) with  $|N_A - N_D| \approx 10^{16} \text{ cm}^{-3}$  at 77 K, or b) with  $|N_A - N_D| \approx 3 \times 10^{17} \text{ cm}^{-3}$  at 77 K.

In the case of the material with  $N_A \approx 10^{16} \text{ cm}^{-3}$ ,  $n^+$ -p junctions were formed by implanting boron with a relatively low dose and low energy. The photodiodes were passivated with a thin film of native sulfides and covered with a 1- $\mu\text{m}$  evaporated ZnS layer, which serves as an AR coating. After passivation the devices were exposed to a low-temperature post-implantation anneal (80°C). In the case of the heavily doped material ( $N_A \approx 3 \times 10^{17} \text{ cm}^{-3}$ ), n-p diodes were fabricated by diffusing Hg into the bulk p. The n-p diodes were passivated with evaporated ZnS.

A small number of gate-controlled diodes and capacitors were fabricated near the  $n^+$ -p and n-p diodes. The gate-controlled diodes dc characteristics, as well as the capacitors  $C$ - $V$  characteristics, were used to study the role played by the surface potential and to determine the relative contribution of surface-induced leakage currents. Using capacitors and gate-controlled diodes it has been shown that in properly processed passivated  $n^+$ -p [4], [12] and n-p [13] diodes, surface effects do not contribute significant dark current even at reverse biases as high as 1 V and temperature below 65 K. Hence, the model presented in the following section rightly ignores the negligible amount of surface-induced currents and concentrates on various leakage processes that take place in the bulk.

## III. MODELING OF THE TRAP-ASSISTED TUNNELING MECHANISM

In general, three distinct mechanisms dominate the leakage current and the dynamic resistance in HgCdTe diodes with  $x \approx 0.22$ : diffusion, band-to-band (direct) tunneling, and trap-assisted tunneling [4]. The diffusion mechanism dominates the leakage current and dynamic resistance in zero bias and low bias and in high temperatures. Band-to-band tunneling is the dominant leakage mechanism in high reverse biases and low temperatures, in diodes fabricated on doped material. Trap-assisted tunneling is the dominant mechanism in medium biases and medium temperature regions in diodes fabricated on doped material, and in wider regions in diodes realized on undoped material. It has been lately shown by Nemirovsky *et al.* [4], [12] that the trap-assisted tunneling dominates the current and dynamic resistance in HgCdTe diodes fabricated on undoped material even in temperatures down to 65 K and reverse biases up to 1 V.

Modeling of the trap-assisted tunneling mechanism is rather complicated since the dc characteristics are mostly defined by the nature of the depletion region. The current and dynamic resistance are determined by the concentration of traps in the depletion region, by their distance from

the edges of the bands, by their capture cross section, and by the depletion-region doping level. Since in both ion-implanted and diffused HgCdTe diodes the doping level and the trap concentration may depend on the distance from the junction—a simple model describing the voltage dependence of that mechanism will not be accurate. Modeling of the temperature dependence is even more complicated since the temperature behavior of the capture cross section depends on the origin of the material and on the type of trap and therefore may vary with each sample.

Fig. 1 shows the energy bands of a diode with a mid-gap level in high (Fig. 1(a)) and low (Fig. 1(b)) reverse biases. It is clearly seen that thermal transitions are always possible for all traps while tunnel transitions are not. An essential condition for the electron tunneling process is a trap energy "higher" than the bottom of the conduction band. Similarly, holes can tunnel from a trap to the valence band only if the trap energy is "lower" than the top of the valence band. Fig. 1 shows that traps can be divided into four major groups according to the following allowed carrier transitions:

- a) Traps that can exchange carriers with the valence band by thermal transition only, and with the conduction band using both thermal and tunnel transitions.
- b) Traps that can exchange carriers with both bands using thermal transitions only (Shockley-Read-Hall centers).
- c) Traps that can exchange carriers with the valence band by thermal and tunnel transitions, and with the conduction band by thermal transition only.
- d) Traps that can exchange carriers with both bands by thermal and tunnel transitions.

In the case of degenerate  $n^+$ -p diodes, two additional groups of traps are added (see Fig. 2):

- e) Traps with thermal and tunnel transitions such as (c), but with a higher thermal barrier due to the Burstein-Moss shift.
- f) Traps with only thermal transitions such as (b), but with a higher thermal barrier due to the Burstein-Moss shift.

Since each group has its characteristic carrier transition paths, each is associated with different occupation probability as well as with different probabilities for tunnel and thermal transitions, and hence different contributions to the overall current. In addition, the relative number of traps associated with each group depends strongly on temperature and bias. For example: the trap-assisted tunneling current in a diode with mid-gap traps operated at high reverse bias is dominated by the contribution of group (d), while in the case of low reverse bias the contribution of that group is negligible (see Fig. 1). Hence, modeling of the trap-assisted tunneling current should include detailed calculations of the relative concentration of traps in each group as well as their special characteristics.

The different role played by the two types of holes should be noted. Since the tunneling rate of carriers is inversely proportional to the exponent of their mass, the tunneling probability of heavy holes is much smaller than

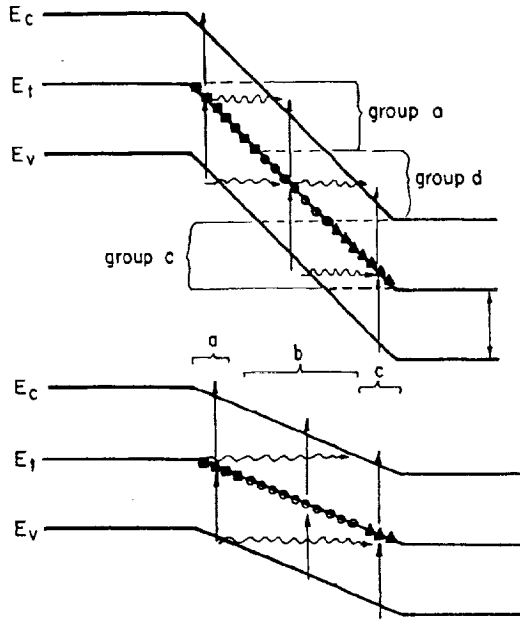


Fig. 1. The energy bands of an n-p diode with a mid-gap trap level in high (upper) and low (lower) reverse biases. The traps are divided into four major groups according to the allowed carrier transitions.

that of light ones and therefore can be ignored. On the other hand, due to the higher density of states in the heavy-hole band, the thermal transition of heavy holes is much higher than that of light ones. As a result, the hole thermal transition is dominated by heavy holes while the hole tunnel transition is dominated by light ones.

Let us consider the generation-recombination transition path of group (d) in which all tunnel and thermal transitions are allowed. The net capture rate of electrons into centers located at a distance  $x$  from the junction and with energy  $E_T$  and concentration  $N_{Td}$  is

$$U_{nd} = \gamma_n n(x) N_{Td} (1 - f) - \gamma_n n_1 N_{Td} f + \omega_c n(x + x_{ic}) N_{Td} (1 - f) - N_C \omega_c N_{Td} f \quad (1)$$

and the net capture rate of holes into the same traps is

$$U_{pd} = \gamma_p p_h(x) N_{Td} f - \gamma_p p_l N_{Td} (1 - f) + \omega_v p_L(x - x_{iv}) N_{Td} f - \omega_v N_c N_{Td} (1 - f) \quad (2)$$

where  $x_{iv}$  and  $x_{ic}$  are the tunneling distances for electrons and holes (see Fig. 3)), and  $f = f(x)$  is the trap occupation probability.  $\gamma_p$  and  $\gamma_n$  are the electron and holes capture coefficients,  $p_h$ ,  $p_l$ , and  $n$  are the concentration of heavy holes, light holes, and electrons, and  $N_v$  and  $N_c$  are the light holes and the electron effective densities of states.  $\omega_v$  and  $\omega_c$  represent the carriers tunneling probabilities be-

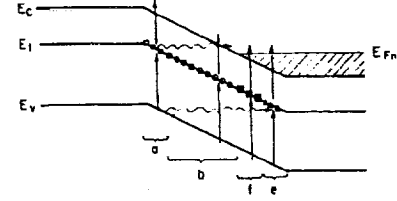


Fig. 2. The energy bands of an  $n^+$ -p diode. Two additional groups of traps, (e) and (f), are added due to the Burstein-Moss shift.

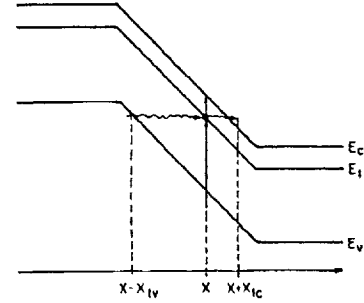


Fig. 3. The four transitions of group (d) and the tunneling distances.

tween the center and the bands. The temperature dependence of the thermal emission rates is given by  $n_1 = N_C \cdot \exp(-(E_g - E_T)/kT)$  for electrons and by  $p_1 = N_{vh} \cdot \exp(-E_T/kT)$  for heavy holes (where  $N_{vh}$  is their effective density of states).

Assuming quasi-equilibrium situation,  $U_{nd} = U_{pd}$ ,  $n \cdot p_h = n_l^2 \cdot \exp(qV/kT)$ , and  $n$ ,  $p_l$ ,  $p_h \rightarrow 0$  in the depletion region, the net generation rate of group (d)  $U_d$  is given by

$$U_d = N_{Td} \left[ \frac{-\gamma_n \gamma_p n_l^2 (e^{(qV/kT)} - 1) + \omega_c N_C \omega_v N_v + \gamma_n n_1 \omega_v N_v + \gamma_p p_1 \omega_c N_C}{\gamma_n n_1 + \gamma_p p_1 + \omega_c N_C + \omega_v N_v} \right] \quad (3)$$

The net generation rates of groups (a), (b), and (c) can be easily obtained using (3). Assuming  $\omega_v N_v \rightarrow 0$  for group (a),  $\omega_v N_v \rightarrow 0$ ,  $\omega_c N_C \rightarrow 0$  for group (b), and  $\omega_c N_C \rightarrow 0$  for group (c) one obtains

$$U_a = N_{Ta} \left[ \frac{-\gamma_n \gamma_p n_l^2 (e^{(qV/kT)} - 1) + \gamma_p p_1 \omega_c N_C}{\gamma_n n_1 + \gamma_p p_1 + \omega_c N_C} \right] \quad (4)$$

$$U_b = N_{Tb} \left[ \frac{-\gamma_n \gamma_p n_l^2 (e^{(qV/kT)} - 1)}{\gamma_n n_1 + \gamma_p p_1} \right] \quad (5)$$

$$U_c = N_{Tc} \left[ \frac{-\gamma_n \gamma_p n_l^2 (e^{(qV/kT)} - 1) + \gamma_n n_1 \omega_v N_v}{\gamma_n n_1 + \gamma_p p_1 + \omega_v N_v} \right] \quad (6)$$

where  $N_{Ta}$ ,  $N_{Tb}$ , and  $N_{Tc}$  represent the concentration of traps in groups (a), (b), and (c), respectively.

The net generation rates of group (e) and (f) (shown in Fig. 2), can also be obtained by replacing the electron thermal barrier  $(E_g - E_T)$  with  $(E_g - E_T + BS)$ , where  $BS$  is the average additional barrier caused by the Burstein-Moss effect. The temperature dependence of the

thermal emission rate is given now by

$$n_2 = N_C \exp \left[ \frac{-(E_g - E_T + BS)}{kT} \right] = n_1 e^{(-BS/kT)} \quad (7)$$

and the generation rates (of  $N_{Te}$  traps in group (e) and  $N_{Tf}$  traps in group (f)) by

$$U_e = N_{Te} \left[ \frac{-\gamma_n \gamma_p n_i^2 (e^{(qV/kT)} - 1) + \gamma_n n_i \omega_v N_V}{\gamma_n n_i e^{(BS/kT)} + \gamma_p p_1 + \omega_r N_V} \right] \cdot e^{(BS/kT)} \quad (8)$$

$$U_f = N_{Tf} \left[ \frac{-\gamma_n \gamma_p n_i^2 (e^{(qV/kT)} - 1)}{\gamma_n n_i + \gamma_p p_1 e^{(-BS/kT)}} \right] \quad (9)$$

The magnitude of the tunneling rates  $\omega_c N_C$  and  $\omega_v N_V$  are obviously important in determining the trap-assisted tunneling current. The tunnel diode theory of Sah [14] indicates that the tunneling rates out of a group of traps located at a distance  $E_T$  from the valence band are given by

$$\omega_c N_C = \frac{\pi^2 q m_c^* E M^2}{h^3 (E_g - E_T)} \cdot \exp \left[ \frac{-8\pi (2m_c^*)^{1/2} (E_g - E_T)^{3/2}}{3hqE} \right] \quad (10)$$

$$\omega_v N_V = \frac{\pi^2 q m_v^* E M^2}{h^3 E_T} \cdot \exp \left[ \frac{-8\pi (2m_v^*)^{1/2} E_T^{3/2}}{3hqE} \right] \quad (11)$$

where  $E$  is the maximum electric field in the depletion region,  $M$  is the matrix element of the trap potential energy, and  $m_v^*$  and  $m_c^*$  are the effective masses of carriers in the valence and conduction bands. The tunneling probability of light holes is much greater than that of heavy holes and therefore is the only probability to be considered. Following Kinch [9], we assume that the effective masses of light holes and electrons are given by  $m_v^* = m_c^* = 0.07 m_0 E_g$ , where  $m_0$  is the electron rest mass and  $E_g$  is the bandgap in electron-volts. We use the experimentally determined value [9] for  $m_v^* M^2 = m_c^* M^2 = 10^{-23} \text{ V} \cdot \text{cm}^3$  and finally obtain

$$\omega_c N_C = \frac{6 \times 10^5 E}{E_g - E_T} \cdot \exp \left[ \frac{-1.7 \times 10^7 E_g^{1/2} (E_g - E_T)^{3/2}}{E} \right] \quad (12)$$

$$\omega_v N_V = \frac{6 \times 10^5 E}{E_T} \cdot \exp \left[ \frac{-1.7 \times 10^7 E_g^{1/2} E_T^{3/2}}{E} \right] \quad (13)$$

The magnitude and temperature dependence of the capture coefficients are also important in determining the trap-assisted tunneling current. In general, the capture coeffi-

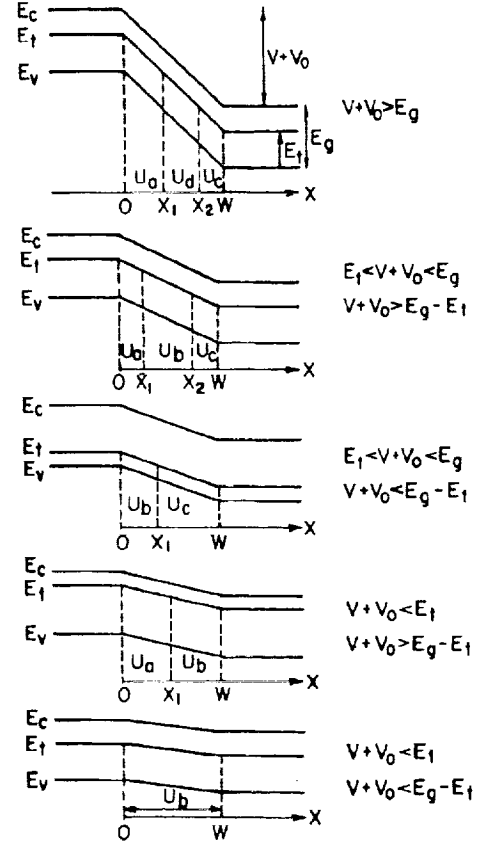


Fig. 4. The energy bands of an n-p diode and the five possible relations (between  $V$ ,  $V_0$ ,  $E_g$ , and  $E_T$ ), as well as the various groups of traps and their position within the depletion region.

icients  $\gamma_p$  and  $\gamma_n$  are given by

$$\gamma_p = \sigma_p V_{ip} \quad \gamma_n = \sigma_n V_{in} \quad (14)$$

$$V_{ip} = \left[ \frac{kT}{3m_{ih}^*} \right]^{1/2} \quad v_{in} = \left[ \frac{kT}{3m_c^*} \right]^{1/2} \quad (15)$$

$$m_{ih}^* = 0.55 \cdot m_0 \quad m_c^* = 0.07 \cdot m_0 \cdot E_g$$

where  $\sigma_p$ ,  $\sigma_n$ ,  $V_{ip}$ ,  $V_{in}$ ,  $m_{ih}^*$ , and  $m_c^*$  are capture cross sections, thermal velocities, and effective masses of heavy holes and electrons, respectively. Since the two effective masses are linear functions of the temperature we can use Lax estimation [15] for the temperature dependence of electron and hole capture cross sections  $\sigma_n \propto T^{-\beta_n}$  and  $\sigma_p \propto T^{-\beta_p}$ , and estimate the temperature dependence of electron and hole capture coefficients to be

$$\gamma_p(T) = \gamma_{p0} \left[ \frac{T}{77} \right]^{-\beta_p} \quad (17a)$$

$$\gamma_n(T) = \gamma_{n0} \left[ \frac{T}{77} \right]^{-\beta_n} \quad (17b)$$

where  $\gamma_{p0}$  and  $\gamma_{n0}$  are the capture coefficients at 77 K and  $\beta_p$  and  $\beta_n$  are fitting parameters.

The overall trap-assisted tunneling current can now be obtained by integrating the net generation rate across the depletion region. To do so one should take into account the generation rate and the number of traps associated with each group.

Detailed calculations of energy bands in p-type HgCdTe which take into account the high density of states in the valence band show that for  $60 \text{ K} < T < 150 \text{ K}$  the material does not become degenerate even with doping levels higher than  $10^{18} \text{ cm}^{-3}$ . Therefore, in the case of n-p diodes the traps can be divided into four groups. The relative number of traps in each group is determined by the relations between the built-in voltage, the applied voltage, the bandgap, and the energy level of the traps.

Fig. 4 shows the five significant relations possible in n-p diodes as well as the various groups of traps and their position within the depletion region. By integrating the net generation rate across the depletion region we obtain the total generation rate in each one of the five cases

where  $J_{\text{TAT}}$  is the trap-assisted tunneling current and  $E_g$ ,  $E_T$ ,  $V_0$ ,  $V$ , and  $W$  represent the bandgap, the trap energy, the built-in voltage, the applied voltage, and the depletion region width, respectively.

In the case of degenerate n<sup>+</sup>-p diodes the additional thermal barrier caused by the Burstein-Moss effect considerably increases the number of groups and the number of relations between  $E_g$ ,  $E_T$ ,  $V_0$ ,  $V$ , and  $BS$ . The result is more than 15 significant relations which involve six different groups of traps. However, in reverse bias above 50 mV only two significant cases are possible:  $E_g + BS < V_0 + V$  and  $E_g < V_0 + V < E_g + BS$ . Fig. 5 shows the energy bands associated with the two cases as well as the five groups involved and their position within the de-

$$U = \begin{cases} \int_0^{W(E_T/(V+V_0))} U_a dx + \int_{W(E_T/(V+V_0))}^{W(1-(E_g-E_T)/(V+V_0))} U_d dx + \int_{W(1-(E_g-E_T)/(V+V_0))}^W U_c dx, & V + V_0 > E_g \\ \int_0^{W(1-(E_g-E_T)/(V+V_0))} U_a dx + \int_{W(1-(E_g-E_T)/(V+V_0))}^{W(E_T/(V+V_0))} U_d dx + \int_{W(E_T/(V+V_0))}^W U_c dx, & E_T < V + V_0 < E_g, V + V_0 > E_g - E_T \\ \int_0^{W(E_T/(V+V_0))} U_b dx + \int_{W(E_T/(V+V_0))}^W U_c dx, & E_T < V + V_0 < E_g, V + V_0 < E_g - E_T \\ \int_0^{W(1-(E_g-E_T)/(V+V_0))} U_a dx + \int_{W(1-(E_g-E_T)/(V+V_0))}^W U_b dx, & V + V_0 < E_T, V + V_0 > E_g - E_T \\ \int_0^W U_b dx, & V + V_0 < E_T, V + V_0 < E_g - E_T \end{cases} \quad (18)$$

Since  $U_a$ ,  $U_b$ ,  $U_c$ , and  $U_d$  are constant, the integration yields

$$J_{\text{TAT}} = \begin{cases} qW \cdot N_T \cdot \left( U_a \left( \frac{E_T}{V+V_0} \right) + U_d \left( 1 - \frac{E_g}{V+V_0} \right) + U_c \left( \frac{E_g - E_T}{V+V_0} \right) \right), & V + V_0 > E_g \\ qW \cdot N_T \cdot \left( U_a \left( 1 - \frac{E_g - E_T}{V+V_0} \right) + U_b \left( \frac{E_g}{V+V_0} - 1 \right) + U_c \left( 1 - \frac{E_T}{V+V_0} \right) \right), & E_T < V + V_0 < E_g, V + V_0 > E_g - E_T \\ qW \cdot N_T \cdot \left( U_b \left( \frac{E_T}{V+V_0} \right) + U_c \left( 1 - \frac{E_T}{V+V_0} \right) \right), & E_T < V + V_0 < E_g, V + V_0 < E_g - E_T \\ qW \cdot N_T \cdot \left( U_a \left( 1 - \frac{E_g - E_T}{V+V_0} \right) + U_b \left( \frac{E_g - E_T}{V+V_0} \right) \right), & V + V_0 < E_T, V + V_0 > E_g - E_T \\ qW \cdot N_T \cdot U_b, & V + V_0 < E_T, V + V_0 < E_g - E_T \end{cases} \quad (19)$$

pletion region. The total generation rate for  $V_0 + V > E_g + BS$  is given now by

$$U = \int_0^{W(E_T/(V+V_0))} U_a dx + \int_{W(E_T/(V+V_0))}^{W(1-(E_g-E_T+BS)/(V+V_0))} U_d dx + \int_{W(1-(E_g-E_T+BS)/(V+V_0))}^{W(1-BS/(V+V_0))} U_c dx + \int_{W(1-BS/(V+V_0))}^W U_c dx. \quad (20a)$$

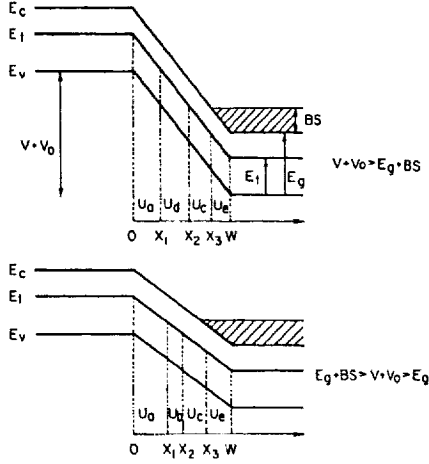


Fig. 5. The energy bands of an  $n^+$ -p diode and the two relations between  $V$ ,  $V_0$ ,  $E_g$ ,  $E_T$ , and  $BS$ , possible for reverse bias above 50 mV. The various groups of traps and their position within the depletion region are also plotted.

Similarly, for  $E_g < V_0 + V < E_g + BS$  the net generation rate is given by

$$\begin{aligned}
 U = & \int_0^W \frac{1 - (E_g - E_T - BS)/(V + V_0)}{W} U_a dx \\
 & + \int_0^W \frac{E_T/(V + V_0)}{W(1 - (E_g - E_T - BS)/(V + V_0))} U_d dx \\
 & + \int_0^W \frac{1 - BS/(V + V_0)}{W(E_T/(V + V_0))} U_c dx + \int_0^W \frac{1 - BS/(V + V_0)}{W} U_e dx.
 \end{aligned} \quad (20b)$$

The associated trap-assisted tunneling current  $J_{TAT}$  is now given by

$$\begin{aligned}
 J_{TAT} = & qWN_T \left[ U_a \left( \frac{E_T}{V + V_0} \right) + U_d \left( 1 - \frac{E_g + BS}{V + V_0} \right) \right. \\
 & \left. + U_c \left( \frac{E_g - E_T}{V + V_0} \right) + U_e \left( \frac{BS}{V + V_0} \right) \right] \quad (21a)
 \end{aligned}$$

for  $V_0 + V > E_g + BS$ , and for  $E_g < V_0 + V < E_g + BS$  by

$$\begin{aligned}
 J_{TAT} = & qWN_T \left[ U_a \left( 1 - \frac{E_g + BS - E_T}{V + V_0} \right) + U_b \right. \\
 & \cdot \left( \frac{E_g + BS}{V + V_0} - 1 \right) + U_c \left( 1 - \frac{E_T + BS}{V + V_0} \right) \\
 & \left. + U_e \left( \frac{BS}{V + V_0} \right) \right]. \quad (21b)
 \end{aligned}$$

#### IV. RESULTS AND DISCUSSION

Figs. 6 and 7 represent typical resistance-temperature characteristics ( $R$ - $T$ ) of two one-sided HgCdTe photo-diodes fabricated on undoped THM material. We chose

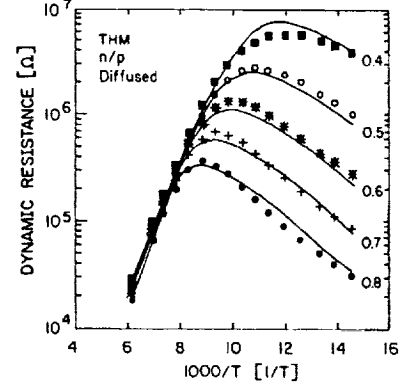


Fig. 6. Measured and calculated characteristics of a diffused n-p diode with  $x = 0.219$ ,  $N_D = 2 \times 10^{15} \text{ cm}^{-3}$ , and junction area of  $A_j = 2 \times 10^{-5} \text{ cm}^2$ . The dynamic resistance associated with the trap-assisted tunneling mechanism versus reciprocal temperature is plotted, with the diode reverse bias as a parameter. The symbols represent measured data while the solid curves represent theory. The fit was obtained for  $N_T = 4.3 \times 10^{16} \text{ cm}^{-3}$ ,  $E_T = 0.6E_g$ ,  $\gamma_{n0} = 3.2 \times 10^{-7} \text{ [cm}^3/\text{S]}$ ,  $\beta_n = 1$ ,  $\gamma_{p0} = 9.8 \times 10^{-7} \text{ [cm}^3/\text{S]}$ , and  $\beta_p = 0.3$ .

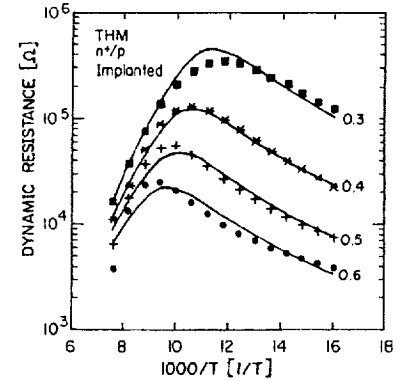


Fig. 7. Measured and calculated characteristics of an ion-implanted  $n^+$ -p diode with  $x = 0.225$ ,  $N_A = 10^{16} \text{ cm}^{-3}$ , and junction area of  $A_j = 2 \times 10^{-5} \text{ cm}^2$ . The dynamic resistance associated with the trap-assisted tunneling mechanism versus reciprocal temperature is plotted, with the diode reverse bias as a parameter. The symbols represent measured data while the solid curves represent theory. The fit was obtained for  $E_T = 0.6E_g$ ,  $\gamma_{n0} = 2.1 \times 10^{-6} \text{ [cm}^3/\text{S]}$ ,  $\beta_n = 1.3$ ,  $\gamma_{p0} = 6.6 \times 10^{-5} \text{ [cm}^3/\text{S]}$ , and  $\beta_p = 0.3$ . The effective trap concentration for  $V = 0.6 \text{ V}$  is  $N_T = 1.8 \times 10^{16} \text{ cm}^{-3}$ . For smaller bias we multiply both the carrier concentration and the traps concentration by a factor  $\eta < 1$ , maintaining the same ratio between the trap and acceptor concentrations. The obtained values for  $\eta$  were 0.93, 0.86, and 0.78 for reverse biases of  $V = 0.5, 0.4$ , and  $0.3 \text{ V}$ , respectively.

to compare measured and calculated resistance instead of currents because small changes in the characteristics become evident. Being the derivative of the current, the dynamic resistance reveals small changes that are masked in the current characteristics.

Fig. 6 shows the characteristics of a representative diffused n-p diode with  $x = 0.219$  and  $n = 2 \times 10^{15} \text{ cm}^{-3}$  (at 77 K). Fig. 7 shows the characteristics of an implanted  $n^+$ -p diode with  $x = 0.225$  and  $p = 10^{16} \text{ cm}^{-3}$  (at 77 K). The two figures show dynamic resistance versus reciprocal temperature, with the diode's reverse bias as a parameter. The symbols represent measured data while the solid curves represent the theoretical model presented in (3)-(21); namely, the numerical derivatives of (19) and

(21). As indicated by Nemirovsky *et al.* [4], in the entire temperature and bias regions of Figs. 6 and 7, the leakage current and dynamic resistance of undoped diodes are dominated by the trap-assisted tunneling mechanism. Therefore, our calculations of leakage current disregard the contribution of other leakage mechanisms such as diffusion and band-to-band tunneling.

The complex temperature dependence of the trap-assisted tunneling process is seen clearly in both figures. The high-temperature regions are dominated by Shockley-Read-Hall thermal-thermal transitions as indicated by straight lines on a semilog scale. The low-temperature regions, on the other hand, are dominated by the tunnel-tunnel transitions as indicated by the decrease in the dynamic resistance with decreasing temperature.

In addition to the difference in the average resistances, caused mainly by the different compositions, the two diodes differ in their voltage dependence in the high-temperature region. The diffused n-p diode represented in Fig. 6 exhibits almost no voltage dependence in the region dominated by thermal-thermal transitions. Fig. 7, on the other hand, demonstrates the strong voltage dependence of the dynamic resistance of the n<sup>+</sup>-p implanted photodiode in the same temperature region. This last figure shows that the dynamic resistance is degraded by a factor of 5, as the reverse bias is increased from 300 to 600 mV. This is unexpected behavior since both current and dynamic resistance in this temperature region are dominated by thermal-thermal transitions and therefore should exhibit negligible field dependence. The suggested explanation for this behavior is related to the profile of vacancies close to the junction, and will be discussed in the next paragraph.

Tobin [16] and Riley [17] have both observed a linear relationship between the shallow acceptor concentration due to Hg vacancy and the deep trap concentration. They have suggested that the traps are either a different (and additional) state of the Hg vacancy or a complex involving the Hg vacancy. Both Tobin and Riley did not rule out either the additional vacancy-state model or the vacancy-complex model. However, the correlation between trap and vacancy concentrations they observed is of great importance, since it indicates that the vacancies produce both the shallow level (responsible for p-type conductivity) and the deep level (traps). Also, it has been found and demonstrated by Bubulac *et al.* [18], that in undoped material, Hg freed by the implant annihilates vacancies and decreases the doping level in the region adjacent to the n<sup>+</sup> region. Fraenkel *et al.* [19], and more recently Nemirovsky *et al.* [4], used *C-V* profiling techniques to characterize the carrier profile of HgCdTe photodiodes realized by implanting boron into undoped material. They have found that n<sup>+</sup>-p<sup>-</sup> junctions are formed with very low p doping near the junction, and that the doping increases gradually until it reaches the bulk doping level. In order to explain the thermal-thermal transitions voltage dependence in implanted diodes we rely on these two phe-

nomena. By considering the gradual profile of the Hg vacancy and the correlation between vacancy and trap concentrations, we suggest that the trap concentration is gradual as well. Therefore, as the reverse bias increases and the depletion region expands, regions with higher trap concentration are introduced and the average number of traps increases. As a result, even in temperature regions dominated by thermal-thermal transitions, the trap-assisted tunneling current and dynamic resistance depend strongly on bias.

The good fit between measured and calculated dynamic resistance of the two diodes supports the validity of the model as demonstrated in Figs. 6 and 7. In the case of a diffused n-p photodiode, the fit was obtained for trap energy of  $E_T = 0.6E_g$  and trap concentration of  $N_T = 4.3 \times 10^{16} \text{ cm}^{-3}$ . The obtained values of the electron capture coefficients were  $\gamma_{n0} = 3.2 \times 10^{-7} \text{ [cm}^3/\text{S]}$  and  $\beta_n = 1$  and the hole capture coefficients were  $\gamma_{p0} = 9.8 \times 10^{-7} \text{ [cm}^3/\text{S]}$  and  $\beta_p = 0.3$ . Using (14)-(16) the capture cross sections at 77 K were calculated to be  $\sigma_n = 4.7 \times 10^{-15} \text{ cm}^2$  and  $\sigma_p = 1.2 \times 10^{-13} \text{ cm}^2$ .

In the case of implanted n<sup>+</sup>-p photodiodes, a good fit was obtained for trap energy of  $E_T = 0.75E_g$ . Since the vacancy concentration (and therefore the carrier concentration as well) was assumed to depend on the distance from the junction in these diodes, different effective carrier and trap concentrations for each bias were used. The values derived from the fitting process for  $V = 0.6 \text{ V}$  were  $N_T = 1.8 \times 10^{16} \text{ cm}^{-3}$  and  $N_A = 10^{16} \text{ cm}^{-3}$ . For smaller bias values we multiply both the acceptor concentration and the trap concentration by a factor  $\eta < 1$ , maintaining the same ratio between trap and acceptor concentrations. The obtained values for  $\eta$  were 0.93, 0.86, and 0.78 for reverse biases of  $V = 0.5, 0.4, \text{ and } 0.3 \text{ V}$ , respectively. The attained values of the electron capture coefficients were  $\gamma_{n0} = 2.1 \times 10^{-6} \text{ [cm}^3/\text{S]}$  and  $\beta_n = 1.3$  and that of holes were  $\gamma_{p0} = 6.6 \times 10^{-5} \text{ [cm}^3/\text{S]}$  and  $\beta_p = 0.3$ . The capture cross sections calculated using (14)-(16), were  $\sigma_n = 3.3 \times 10^{-14} \text{ cm}^2$  and  $\sigma_p = 8.2 \times 10^{-12} \text{ cm}^2$  at 77 K, for the electrons and the holes, respectively.

The values for trap energy levels, concentrations, and capture cross sections, obtained from the fit between measured and calculated characteristics, are in agreement with those published in the literature, mostly by Polla, Jones and co-authors [20]-[22]. In this work data on traps in undoped HgCdTe based on DLTS measurements were provided. Although they have reported the existence of two energy levels associated with the deep traps  $0.4E_g$  and  $0.75E_g$ , they have found that only the  $0.75E_g$  level determines the *R-T* characteristics [22]. The trap concentrations reported by them ranged from approximately  $0.1N_A$  to  $10N_A$  (where  $N_A$  is the shallow acceptor concentration), and therefore are also in agreement with our values. However, our results differ from previously published values since we obtained acceptor-like centers with  $\sigma_p > \sigma_n$ . Such centers with  $\sigma_p > \sigma_n$  were found only in As doped material [23].

## V. SUMMARY

In this paper we modeled the trap-assisted tunneling mechanism of n-p and n<sup>+</sup>-p Hg<sub>1-x</sub>Cd<sub>x</sub>Te photodiodes. The model describes the connection between the leakage current and dynamic resistance associated with the traps, the trap characteristics (energy level, concentration, and capture cross sections), and the bulk properties (dopant concentration and composition). We demonstrated the difference between these two types of photodiodes in the voltage dependence of the trap-assisted tunneling current and resistance, and suggested an explanation for this difference. Finally, we supported the validity of the model by comparing measured and calculated characteristics in a wide range of temperatures (65–140 K) and biases (0.3–0.8 V). Good fits between measured and calculated characteristics were obtained for trap concentrations, energy levels, and capture cross sections, close to those presented in the literature. Unfortunately, only a handful of published works [20]–[23] deal with the nature of traps in undoped HgCdTe. Therefore, the validity of our model should be farther confirmed, by replacing the published characteristics of the traps with DLTS data measured on our samples [24]. In addition, more detailed studies of the trap profile and their connection with the shallow acceptor level are needed.

## ACKNOWLEDGMENT

The authors wish to thank the scientific team at Semiconductor Devices, Jerusalem, Israel, for the fabrication of the diodes of Fig. 7. The authors are grateful to E. Haugland from NASA Lewis Research Center, and to S. E. Schacham from the Department of Electrical Engineering at Technion for their useful remarks. The technical assistance of D. Schoenmann, A. Zohar, N. Steinbrecher, S. Dolev, P. Elyau, and Y. Betser from the Kidron Microelectronics Research Center are also acknowledged with thanks. Special thanks are given to I. Rosenfeld and R. Rosenfeld for their editorial assistance.

## REFERENCES

- [1] M. B. Reine, A. K. Sood, and T. J. Tredwell, "Photovoltaic detectors," in *Semiconductors and Semimetals*, vol. 18, R. K. Willarson and A. C. Beer, Eds. New York: Academic Press, 1981, ch. 6.
- [2] Y. Nemirovsky and D. Rosenfeld, "The cut-off wavelength and minority carrier lifetime in implanted n<sup>+</sup> on bulk p HgCdTe photodiodes," *J. Appl. Phys.*, vol. 83, no. 7, no. 1, p. 2435, 1988.
- [3] D. Rosenfeld and Y. Nemirovsky, "Tunneling induced 1/f noise in HgCdTe photodiodes," presented at The 16th Conf. of Electrical and Electronics Engineering in Israel, Convention Center, Tel-Aviv Grounds, Israel, Mar. 7–9, 1989.
- [4] Y. Nemirovsky, D. Rosenfeld, R. Adar, and A. Kornfeld, "Tunneling and dark currents in HgCdTe photodiodes," *J. Vac. Sci. Technol. A*, vol. 7, p. 529, 1989.
- [5] R. E. Dewames, J. G. Pasko, E. S. Yao, A. H. B. Vanderwyck, and G. M. Williams, "Dark current generation mechanisms and spectral noise current in long-wavelength infrared photodiodes," *J. Vac. Sci. Technol. A*, vol. 6, p. 2655, 1988.
- [6] R. E. Dewames, G. M. Williams, J. G. Pasko, and A. H. B. Vanderwyck, "Current generation mechanisms in small band gap HgCdTe pn fabricated by ion implantation," *J. Crystal Growth*, vol. 86, p. 948, 1988.

- [7] Y. Nemirovsky, R. Fastow, M. Meyassed, and A. Unikovsky, accepted for publication in *J. Vac. Sci. Technol.*, Apr. 1991.
- [8] W. W. Anderson and J. Hoffman, "Field ionization of deep levels in semiconductors with applications to HgCdTe pn junctions," *J. Appl. Phys.*, vol. 53, p. 9130, 1982.
- [9] M. A. Kinch, "Metal insulator semiconductor infrared detectors," in *Semiconductors and Semimetals*, vol. 18, R. K. Willarson and A. C. Beer, Eds. New York: Academic Press, 1981, ch. 7.
- [10] D. K. Blanks, J. D. Beck, M. A. Kinch, and L. Colombo, "Band-to-band processes in HgCdTe: Comparison of experimental and theoretical studies," *J. Vac. Sci. Technol. A*, vol. 6, p. 2790, 1988.
- [11] P. Omaggio, "Analysis of dark current in IR detectors on thinned p-typed HgCdTe," *IEEE Trans. Electron Devices*, vol. 37, no. 1, pp. 141–152, 1990.
- [12] Y. Nemirovsky and D. Rosenfeld, "Surface passivation and 1/f noise phenomena in HgCdTe photodiodes," *J. Vac. Sci. Technol. A*, vol. 8, p. 1159, 1990.
- [13] D. Rosenfeld and G. Bahir, to be published.
- [14] C. T. Sah, "Electronic processes and excess currents in gold-doped narrow junctions," *Phys. Rev.*, vol. 109, p. 1594, 1958.
- [15] M. Lax, "Cascade capture of electrons in solids," *Phys. Rev.*, vol. 119, p. 1502, 1960.
- [16] S. P. Tobin, M.S. thesis, MIT, 1979.
- [17] K. J. Reily, P. R. Pratt, and A. H. Lockwood, in *IRIS Meet. of the Specialty Groups on Infrared Detectors and Imaging*, vol. 1, p. 333, 1978.
- [18] L. O. Bubulac and W. E. Tennant, "Role of Hg in junction formation in ion-implanted HgCdTe," *Appl. Phys. Lett.*, vol. 51, p. 355, 1987.
- [19] A. Fraenkel, S. E. Schacham, G. Bahir, and E. Finkman, "Lifetime and carrier concentration profiles of B implanted p-type HgCdTe," *J. Appl. Phys.*, vol. 60, p. 3916, 1986.
- [20] D. L. Polla and C. E. Jones, "Deep level studies of HgCdTe. I: Narrow bandgap space charge spectroscopy," *J. Appl. Phys.*, vol. 52, no. 8, p. 5118, 1981.
- [21] D. L. Polla, M. B. Reine, and C. E. Jones, "Deep level studies of HgCdTe. II: Correlation with photodiode performance," *J. Appl. Phys.*, vol. 52, no. 8, p. 5132, 1981.
- [22] C. E. Jones, V. Nair, and D. L. Polla, "Generation-recombination centers in p-type HgCdTe," *Appl. Phys. Lett.*, vol. 39, no. 3, p. 248, 1981.
- [23] C. E. Jones, *et al.*, "Status of point defects in HgCdTe," *J. Vac. Sci. Technol.*, vol. A3, no. 1, p. 131, 1985.
- [24] S. J. Zackman, M.Sc. thesis, Technion, Haifa, Israel, to be published.

***SECTION  
THREE***

***HIGH TEMPERATURE  
SUPERCONDUCTIVITY***



**HIGH TEMPERATURE SUPERCONDUCTOR ANALOG ELECTRONICS  
FOR MILLIMETER-WAVELENGTH COMMUNICATIONS**

R. R. Romanofsky and K. B. Bhasin

NASA Lewis Research Center  
21000 Brookpark Road  
Cleveland, Ohio 44135

**ABSTRACT**

The performance of high-temperature superconductor (HTS) passive microwave circuits up to X-band has been encouraging when compared to their metallic counterparts. The extremely low surface resistance of HTS films up to about 10 GHz enables a reduction in loss by as much as 100 times compared to copper when both materials are kept at about 77K. However, a superconductor's surface resistance varies in proportion to the frequency squared. Consequently, the potential benefit of HTS materials to millimeter-wave communications requires careful analysis. A simple ring resonator has been used to evaluate microstrip losses at Ka-band. We have also investigated additional promising components such as antennas and phase shifters. Prospects for HTS to favorably impact millimeter-wave communications systems are discussed.

**INTRODUCTION**

Thin film analog signal processing electronics was envisioned as the first practical application for high temperature superconductors. The major prerequisite for microwave circuits was comparatively low surface resistance as opposed to high current density or high critical magnetic field performance, although the parameters are correlated. The surface resistance ( $R_s$ ) of normal conductors varies in proportion to the square root of frequency due to the skin effect, whereas for a superconductor the surface resistance is proportional to the frequency squared. The strong dependence of  $R_s$  on frequency for superconductors is a consequence of the reactive voltage associated with the oscillating supercurrent interacting with unpaired (normal) electrons to induce loss. The proportion of normal electrons varies from 0 at  $T=0$  to 1 at  $T=T_c$ .

This property can be exploited to enhance passive microstrip circuitry, such as filters and phased array beam forming networks (BFNs). HTS microstrip enables tremendous miniaturization of filters without any concomitant degradation in performance compared to a waveguide implementation. HTS microstrip may also enable high directivity arrays because of

the greatly reduced gain degradation in BFNs. Antennas, phase shifters, hybrid superconductor/semiconductor circuits and other components are likely to profit from this property as well. This paper will examine the potential of passive HTS circuitry to favorably impact millimeter-wave communications.

The greatest contribution to millimeter-wave communications may ultimately result from active low- or high- $T_c$  superconducting electronics. Digital signal processors utilizing Josephson junction (JJ) technology will almost surely evolve because of the three-to-four orders of magnitude improvement in the delay-power product. Low- $T_c$  JJs operate ten times faster than any high density semiconductor device and consume 1000 times less power. The eventual possibility of high- $T_c$  JJ chips has been suggested as researchers learn to intentionally manufacture arrays of large angle grain boundary junctions. It has been established for conventional superconductors that energy gap is approximately  $3.5 kT_c$  at zero temperature where  $k$  is Boltzmann's constant. This gap varies slowly with temperature up to about  $1/2 T_c$ . Beyond about  $2/3 T_c$ , the gap diminishes precipitously, becoming zero at  $T=T_c$ . Consequently, in practice, device operation may be restricted to temperatures below  $0.67 T_c$ . It cannot be stated with certainty that this same phenomenon will govern high- $T_c$  electronics. A novel active high- $T_c$  device termed the superconducting flux flow transistor (SFFT), may lead to a new class of microwave electronics. The SFFT uses a current control line to create a magnetic field and induce flux motion which changes the terminal voltage. Hence, the SFFT is the electrical dual of the FET. The SFFT can produce a net gain and has been demonstrated in basic microwave devices. Although this paper will not focus on active high- $T_c$  electronics, revolutionary advances in communications and high speed data processing will likely be derived from this facet of the technology.

**Microstrip Ring Resonator**

Microstrip ring resonators with a design center frequency of 35 GHz were fabricated from laser ablated YBaCuO thin films

deposited on lanthanum aluminate substrates<sup>2</sup>. The ring resonator technique provides a useful method for evaluating patterned film characteristics and includes film-substrate interface effects. Reflection coefficients were measured over a wide temperature range and performance was compared to identical resonators made of evaporated gold. The performance crossover, in terms of resonator "Q" which is inversely proportional to loss, occurred at about 80 K. The unloaded Q of the superconducting resonator was about 4 times better than gold at 20 K. Unloaded Q data as a function of temperature is shown in figure 1. As expected because of the dependence of internal inductance of the strip on the changing normal/superconducting electron densities, the resonant frequency was observed to have a negative temperature coefficient. This prototype device indicated the potential for HTS to enhance millimeter-wave microstrip circuitry.

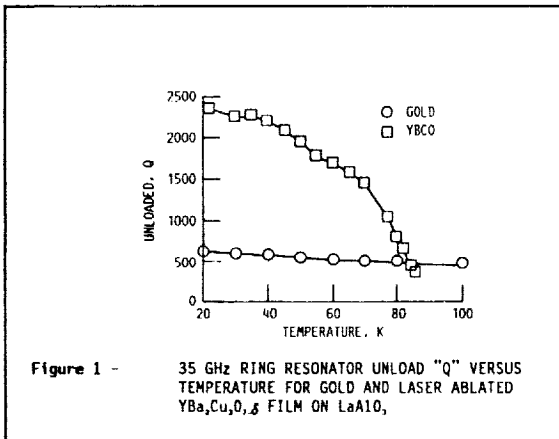


Figure 1 - 35 GHz RING RESONATOR UNLOAD "Q" VERSUS TEMPERATURE FOR GOLD AND LASER ABLATED  $YBa_2Cu_3O_{7.8}$  FILM ON  $LaAlO_3$ .

### Low Noise Receivers

Because of the extraordinary distances involved and scarce transmitter power, receivers for deep-space links have extremely demanding sensitivity requirements. At the present time, maser amplifiers provide the only practical technology for interplanetary communications. The drawback to these systems is cost and the complexity of the necessary 4.5 K refrigeration. A promising alternative to maser technology is cryogenically cooled high electron mobility transistor (HEMT) low noise amplifiers (LNAs). Noise figures of HEMTs cooled below liquid nitrogen temperatures are approaching the performance of maser amplifiers. The minimum noise figure of a metal semiconductor field effect transistor (MESFET) scales as the reciprocal of the cutoff frequency (or transconductance). The high carrier mobility of a HEMT results in a much larger transconductance when compared to a conventional MESFET. Furthermore, the noise conductance is inversely proportional to the square of the

cutoff frequency. This reduces the HEMT's susceptibility to impedance variations and enables high performance over a wide bandwidth. The HEMT's performance also improves much more rapidly upon cooling than a conventional MESFET.

A possible Mars-Earth communications scenario calls for relay satellites in orbit about each planet. Because of the increased operating temperature, reduced cost, and improved reliability, HEMT LNA receivers may prove enabling. In order to assess the performance enhancement that HTS could provide to such a system, mock hypothetical receivers were designed at 10, 32, 60, and 94 GHz. Each simplified receiver consisted of an ideal antenna, 1.5 wavelengths of feed loss, a five-pole band-pass filter, three (10 and 32 GHz), four (60 GHz), or five (90 GHz) gain stages, and a mixer. Scattering and noise parameters of the hypothetical HEMTs were consistent with state-of-the-art performance<sup>3,4</sup>. Since the LNA gain was nearly 40 dB in each case, any marginal improvement in HEMT gain upon cooling was neglected since it would not impact system sensitivity. A surface resistance of 5 milliohms at 30 GHz with a frequency squared dependence was assumed for the HTS. Figure 2 shows the modeled receiver noise figure as a function of frequency for gold microstrip at 300K and 77K and for HTS at about 77K. The shapes of the curves are largely an artifact of the chosen device parameters and the curve fitting algorithm. Obvious advantages of HTS over gold are indicated at lower microwave frequencies. An improvement in sensitivity of about 0.1 dB exists at 60 GHz. The enhancement diminishes to zero at 80-90 GHz.

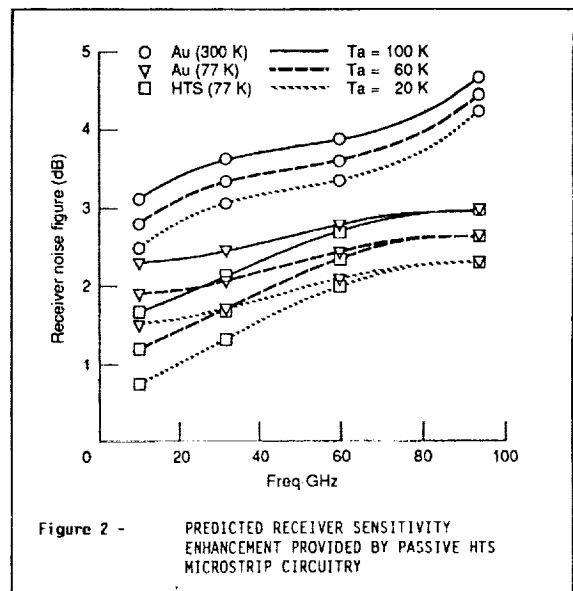
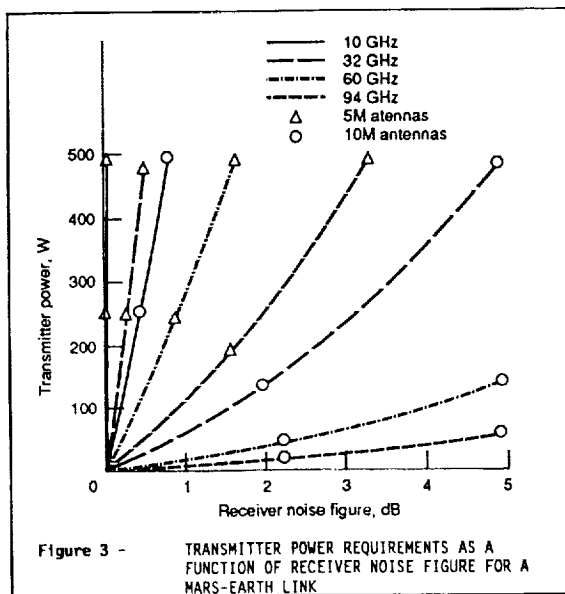


Figure 2 - PREDICTED RECEIVER SENSITIVITY ENHANCEMENT PROVIDED BY PASSIVE HTS MICROSTRIP CIRCUITRY

The salient issue is the significance of the marginal improvements even at

millimeter wavelengths. Figure 3 demonstrates the merit of even minor sensitivity improvements for a Mars-Earth link. Channel assumptions were based primarily on an earlier study<sup>6</sup>. For example, power efficient modulation permitting a receiver (energy per bit)/(noise power) ratio of 1.5 dB was assumed. A different range of  $2.7 \times 10^7$  km, which would place the planets roughly at quadrature, was assumed. Data is plotted for both five and ten meter transmit and receive antennas. A reduction in receiver noise figure by several tenths of a dB corresponds to a transmitter power reduction of tens to perhaps hundreds of watts, or alternatively to a reduction in antenna size. The development of large deployable antennas represents a significant technical challenge. Voyager, for example, utilized a 3.7 meter X-band antenna. The NASA Advanced Communication Technology Satellite's 3.2 meter dish is the largest Ka-band antenna developed to date.

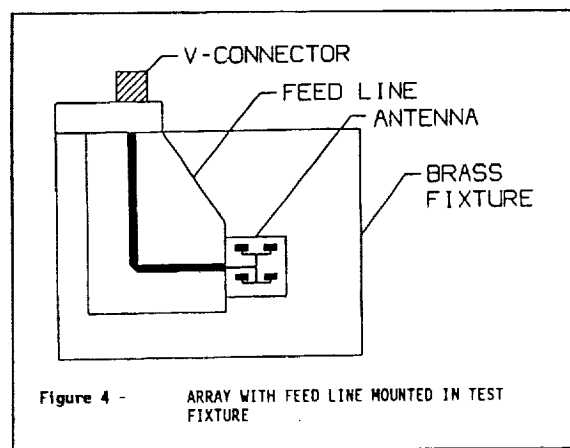


### Superconducting Microstrip Antennas

Application of high  $T_c$  superconductivity to electrically short antennas, superdirective antenna arrays and millimeter wave array feed networks has been analyzed by several researchers recently<sup>6,7</sup>. Their work has shown HTS may be most beneficial when used in the feed and matching networks for microwave and millimeter wave microstrip arrays. This is due to the fact that the maximum obtainable gain from an antenna array is limited by the ohmic losses in the metal microstrip transmission lines which form the feed network. Thus, even though the antenna directivity increases with an increasing number of elements, the gain is limited by the feed network losses. At millimeter waves the problem becomes even

more serious. However, recently Hansen<sup>7</sup> showed an HTS 100 element linear array at 35 GHz could experience a gain increase of 8 to 10 dB over an identical copper array.

NASA Lewis Research Center and Ball Aerospace have designed, fabricated and tested 30 GHz four element superconducting microstrip arrays on various substrates. The antennas were assembled into a brass test fixture with a 50  $\Omega$  gold microstrip feed line patterned on an alumina substrate separating the coax-to-microstrip transition (Wiltron V-connector) from the antenna (Fig. 4). Wire bonds connect the feed line to the antenna. Wire bonds were made directly to the YBCO. To test the devices, each test fixture was in turn mounted at the second stage of a 2-stage closed-cycle helium refrigerator. A hermetically sealed coaxial feedthrough passes the RF into the vacuum chamber. A high-density polyethylene (HDPE) cap serves as both a vacuum jacket and a radome. The entire cryostat was mounted on the rotating pedestal of a far-field antenna range for pattern measurements in the receive mode.



The measured H-plane patterns are shown in Fig. 5 normalized to the highest received power for a magnesium oxide substrate. The antenna demonstrated a received power maxima at approximately 30.3 GHz and 31.7 GHz. H-plane co- and cross-polarization measurements suggest that the lower frequency resonance is primarily due to feedline radiation. The amplitudes of the received antenna patterns at 70K are comparable to gold levels. These results were anticipated for a first experiment because the HTS arrays are not yet fully optimized and the films used had a relatively low (below 85K) critical temperature  $T_c$ . Higher quality films and the use of ohmic contacts are expected to yield greater received powers for the HTS antennas relative to the gold circuits. It should be noted, though, that only 1 dB of improvement over the gold circuits can be expected for such a small number of

elements.

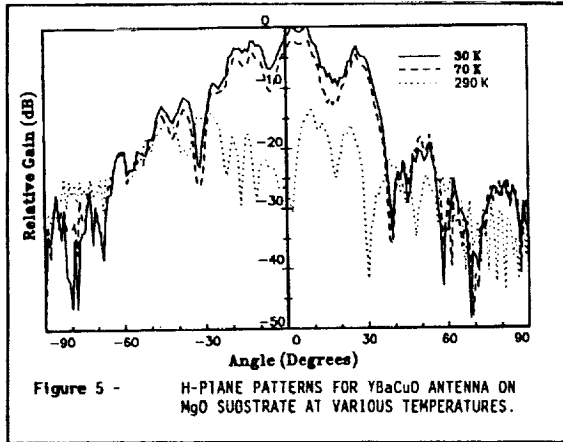


Figure 5 - H-PLANE PATTERNS FOR YBaCuO ANTENNA ON MgO SUBSTRATE AT VARIOUS TEMPERATURES.

The analytical and preliminary experimental work have shown that superconducting microstrip antennas have advantages over conventional antennas. It is also clear that the range of applications of superconducting antennas will be limited due to cryogenic requirements and the performance of superconducting films at frequencies above 50 GHz. However, in applications where high gain from the antenna is desired regardless of other considerations, high performance superconducting antennas will be likely candidates.

#### Microwave Superconductor Switches

The proposed superconductor switch consists of a rectangular patch of HTS material terminated by a quarter-wave radial stub, positioned one quarter wavelength away from a microstrip tee junction. If the switch is superconducting, its path appears as an ideal open circuit at the center frequency. It was determined that a 0.005 inch long, 25:1 aspect ratio HTS patch was nearly optimum for the design of a 32 GHz switched line phase shifter which will be described later.

Two possible modes of operation exist for a superconductor switch. The simplest is the bolometric mode, for which the film is held near its transition temperature. Normally, this technique exploits the fact that in this region, the temperature derivative of resistance is maximum. Incident radiation from an infrared light emitting diode or a laser raises the temperature and consequently causes the film to become resistive. This technique, although seemingly straightforward, has inherent speed limitations due to the high thermal conductivity of HTS compatible substrates. The problem for RF switching is compounded by the highly inductive component of the HTS near  $T_c$ . It is apparent from the observation of HTS resonator Q data that an acceptable reduction in loss

for switching purposes doesn't occur until the temperature falls to about 75% of  $T_c$ . Consequently, it is unlikely that a bolometric switch would be practical except under the most forgiving circumstances. To date, the fastest operation we achieved has been on the order of several seconds. Alternatively, magnetic field induced switching may provide a viable solution. The second operational mode is quantum mechanical. Incident photons with energy exceeding the bandgap break up the Cooper pairs and generate a population of quasiparticles. This effect destroys the superconductivity, resulting in a resistive film. Speed is limited only by carrier recombination time. Implementation of this type of switch is hindered by the need to precisely control film stoichiometry, surface quality, and film thickness. Furthermore, although this effect has been well documented for low- $T_c$  materials, there is still much controversy regarding an analogous response in high- $T_c$  films.

In a typical millimeter-wave device requiring RF switching, such as a phase shifter, the majority of insertion loss can be attributed to the parasitics associated with the switches. For example, metal line loss near 30 GHz on 0.020 inch  $LaAlO_3$  is about 0.14 dB per wavelength. The parasitics of a typical MESFET switch could contribute as much as 0.5 dB to the total insertion loss. An "off" FET can be modeled as an RLC tank circuit. The inductor, L, is external to the FET and is included to resonate the circuit and improve the off-state impedance. The capacitor, C, is the total pinch-off capacitance between the source and drain, and the resistor, R, is the channel and contact resistance. An "off" HTS switch can be modeled by an inductor and resistor. The inductor associated with the HTS switch represents the large kinetic inductance term of the superconductor near  $T_c$ . It is this reactive term which necessitates operating the HTS switch farther below the transition temperature than normal for a "bolometric" type of device. Both switches can be accurately modeled by a single resistor,  $R_{on}$ , in the high conductivity state. Sokolov defined a suitable figure of merit for FET switching devices as:

$$Q^2 = (R_{on}R)^{-1} (\omega C)^{-2} = R_{off}/R_{on}$$

where  $\omega$  is the radian frequency. For a typical switching FET, taking  $R_{on}=10$  ohms,  $C=0.07$  pf, and  $R=5$  ohms,  $R_{off}$  is 1149 ohms at 30 GHz. This yields a figure of merit ( $Q^2$ ) of about 110. If we consider an HTS switch, using a surface resistance of 0.010 ohms in the superconducting state, the equivalent resistivity at 30 GHz is  $8.4e-8$  ohm-cm. Assuming a normal state resistivity of  $1e-3$  ohm-cm, by toggling between the two states, the theoretical figure of merit is about 12,000. It is interesting to note that the semiconductor switching Q will degrade as the frequency

squared; hence, it can be expected that an HTS switch will outperform a MESFET switch throughout the millimeter wavelength portion of the spectrum.

### An HTS Switched Line Phase Shifter

Phased array antennas require variable phase shift components for each radiating element to achieve spatial scanning. A true time delay phase shifter can theoretically provide frequency independent beam steering for large arrays. A popular method for implementing this concept is referred to as the switched line technique. This method achieves true time delay by switching the signal between two alternate routes; either the reference (zero phase shift) path or the delay path. The phase shift is proportional to the path length difference ( $\Delta l$ ) and frequency. Hence the time delay, which is equal to the derivative of phase with respect to radian frequency, will be  $\Delta l/c$ . The array scan angle will be frequency independent since the radiating element spacing and the delay have the same dependence on wavelength. A minimum of three active devices configured as two single-pole double-through switches are required per bit.

Several disadvantages are inherent to this method of implementation: asymmetric insertion loss between the delay and reference paths, high insertion loss overall, and poor isolation between the radio frequency (RF) and bias signals. The effect of switching Q on insertion loss was discussed earlier. An equally vexing problem results from the interaction of the biasing network required to control the switches and the RF signal. Standing wave patterns are set up on the bias lines causing unpredictable performance and sensitivity to bondwire lengths. The proposed phase shifter is shown in figure 6.

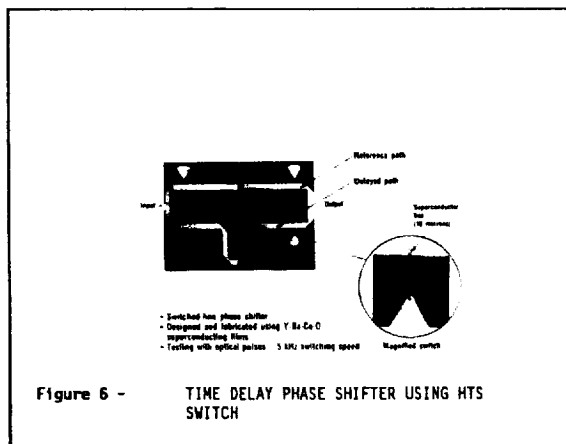


Figure 6 - TIME DELAY PHASE SHIFTER USING HTS SWITCH

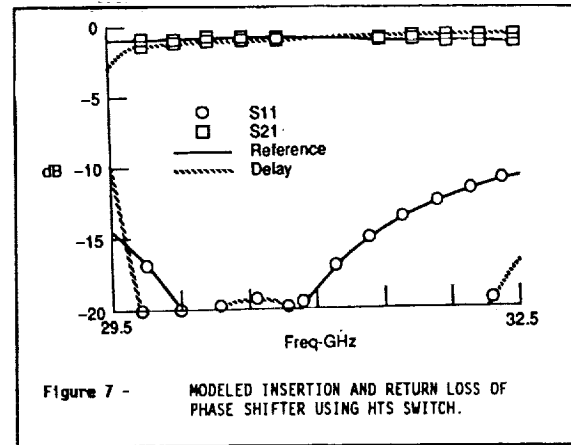


Figure 7 - MODELED INSERTION AND RETURN LOSS OF PHASE SHIFTER USING HTS SWITCH.

If the switches in the reference line, for example, are superconducting they represent a high impedance path from the junction. Concomitantly, the shunt switches in the delay path are caused to become normal (resistive) via optical illumination or magnetic quenching, passing the RF signal. The switches were modeled as thin film resistors of variable sheet resistance in the design, and the influence of the switch reactance was incorporated as part of the radial stub. Figure 7 illustrates the predicted performance and reveals the exceptionally narrow insertion loss envelope and low total insertion loss.

### Conclusions

The potential for HTS devices and circuits to contribute significant performance enhancements to millimeter-wave communications subsystems has been demonstrated. Reproducible, large area films on attractive substrates will be enabling for practical applications, as will economical, compact, and reliable cryogenic cooling systems. It is expected that the combination of superconducting antennas, feed networks, filters, hybrid LNAs, and phase shifters would enormously enhance system performance in terms of the gain/temperature ratio.

### REFERENCES

1. Martens, J. S., Ginley, D. S., Hietala, V. M., and Tigges, C. P., "Novel Applications of Tl-Ca-Ba-Cu-O Thin Films to Active and Passive High Frequency Devices," Third International Symposium on superconductivity, Sendai, Japan, Nov. 6-9, 1990.
2. Bhasin, K. B. et al, "Performance and Modeling of Superconducting Ring Resonators at Millimeter-Wave Frequencies," IEEE MTT-S International Microwave Symposium, Dallas, Tx., May 8-10, 1990, pp. 269-272 (NASA TM-102526).

3. Swanson, A.W., "The Pseudomorphic HEMT," *Microwaves and RF*, March, 1987, pp. 139-150.
4. Duh, K.H.G. et al, "32-GHz Cryogenically Cooled HEMT Low-Noise Amplifiers," *IEEE Trans. Electron Devices*, Vol. 36, No. 8, 1989, pp. 1528-1535.
5. Ponchak, D.S. et al. "A Technology Assessment of Alternative Communications Systems for the Space Exploration Initiative," *AIAA Space Programs and Technology Conference*, Huntsville, Al., Sept. 25-27, 1990 (NASA TM-103243).
6. Dinger, R.J., "Some Potential Antenna Applications of High Temperature Superconductors," *Journal of Superconductivity*, vol. 3, No. 3, pp. 287-296, 1990.
7. Hansen, R.C., "Superconducting Antennas," *IEEE Trans: on Aerospace and Electronic Systems*, vol. 26, No.2, pp. 345-354, March 1990.
8. Richard, M.A. et al, "Performance of a 4-Element K-Band Thin Film Superconducting Microstrip Antenna," submitted to *IEEE Microwave and Guided Wave Letters*.
9. Sokolov, V. et al., "A Ka-Band GaAs Monolithic Phase Shifter," *IEEE. Trans. Microwave Theory and Tech.*, MTT-31, No. 12, 1983, pp. 1077-1082.

## NASA SPACE APPLICATIONS OF HIGH-TEMPERATURE SUPERCONDUCTORS

Vernon O. Heinen  
National Aeronautics and Space Administration  
Lewis Research Center  
Cleveland, Ohio 44135

Martin M. Sokoloski  
National Aeronautics and Space Administration  
Headquarters  
Washington, DC 20546

Paul R. Aron, Kul B. Bhasin,  
Edwin G. Wintucky and Denis J. Connolly  
National Aeronautics and Space Administration  
Lewis Research Center  
Cleveland, Ohio 44135

## SUMMARY

The application of superconducting technology in space has been limited by the requirement of cooling to near liquid helium temperatures. The only means of attaining these temperatures has been with cryogenic fluids which severely limits mission lifetime. The development of materials with superconducting transition temperatures ( $T_c$ ) above 77 K has made superconducting technology more attractive and feasible for employment in aerospace systems. In this paper, potential applications of high-temperature superconducting technology in cryocoolers and remote sensing, communications and power systems will be discussed.

## INTRODUCTION

There has been a great deal of interest in low temperature technology for space applications from the beginning of the space age. The initial interest was chiefly in using cryogenes for rocket fuel and life support systems. The interest shifted later to scientific instruments. An example of such an application is Gravity Probe B (GPB) which is being developed to test certain tenets of Einstein's general theory of relativity. The experiment is designed to measure the gyroscopic precession which should result from the influence of the mass of the Earth on space-time. GPB makes extensive use of superconducting technology. It will have superconducting lead sleeves to attenuate the Earth's magnetic field. Rotating superconducting niobium-coated quartz spheres will act as gyroscopes, and SQUID magnetometers will measure their magnetic moments. There are many other examples of past and planned space missions which require low temperatures. One of the common elements of these missions is the use of liquid helium (up to 4000 L) to reach the low temperatures. Use of helium limits the lifetimes of the missions to less than 5 years.

This limited mission lifetime has been one of the key factors which has limited the applications of superconducting technology. Until the discovery of high temperature superconducting (HTS) materials, liquid helium was necessary to reach the temperatures at which materials were in their superconducting states. HTS materials with transition temperatures above liquid nitrogen temperature significantly reduce the cooling required to use these materials in space. A satellite using liquid nitrogen or hydrogen as a cryogen would have a much longer lifetime than a

satellite which had the same volume of liquid helium. Mechanical coolers capable of cooling to 80 K are much further along in development than coolers capable of cooling to <10 K. Passive cooling can also be used to reach the 70 to 80 K range for very low heat loads. Because of the dramatic increase in transition temperature, superconducting technology may now be feasible for use in space for communication, power, and propulsion systems. Before HTS materials will be used in space, their long term stability must be demonstrated, especially in the space environment. Also, the added weight, power requirements and complexity of the necessary cooling must be included when estimating the benefits of using superconducting technology. Many applications have been suggested and investigated to determine the benefits of incorporating superconducting technology in space systems and are described below.

## APPLICATIONS OF HTS MATERIALS

### Cryocoolers

Space cryocoolers typically operate at or below 77 K and provide a natural cryogenic environment for HTS applications, with no additional weight/energy penalty to refrigerate the HTS component. Applications are being developed that potentially can significantly enhance cryocooler performance, efficiency, reliability and lifetime, such as HTS electrical leads for thermal isolation in space borne liquid helium dewars, damping of vibrations induced in the focal plane by Stirling cycle mechanical cryocoolers and passive magnetic bearings for turboexpander-type cryocoolers.

Some of the future NASA mission such as the Earth Observing System (EOS) will employ cooling of infrared and other types of sensors in order to obtain the required sensitivity and energy resolution. A large number of electrical leads, typically manganin wire, are needed to connect the sensors situated on the cooled focal plane at <10 K to instrumentation at a much higher temperature located outside the dewar. Another mission, the Advanced X-ray Astrophysics Facility (AXAF) will have immersed in liquid helium an adiabatic demagnetization refrigerator requiring nearly 3 A of current for operation. Although the sensor leads usually carry only microamps or less of current, they nevertheless comprise a significant parasitic heat load. For example, in the case of the Spectroscopy of the Atmosphere by Far Infrared Emission (SAFIRE) mission, the sensor leads constitute 33 percent of the instrument and 17 percent of the total heat load.

A high degree of thermal isolation can be achieved if the sensor leads are replaced by HTS copper oxide ceramics, which have thermal conductivities of less than one-fourth that of manganin. Using  $\text{YBa}_2\text{Cu}_3\text{O}_{7-\delta}$  for just the 158 sensor leads in the SAFIRE dewar would reduce the total heat load by at least 8 percent and extend the mission life by more than 5 percent. Much larger extensions of lifetime have been estimated for other missions. Another important benefit of using HTS electrical leads, in addition to thermal isolation, is an estimated 10 to 100 times improvement in signal-to-noise ratio.

Stirling cycle mechanical cryocoolers are a leading candidate to provide the detector cooling required for the many far-infrared ( $>10 \mu\text{m}$ ) experiments planned for the EOS missions of the late 1990's and early 21st century. In order to achieve precision imaging and high optical resolution, vibrations of the detectors induced by the cryocooler operation, as well as spacecraft induced resonances, must be damped. The generally accepted goal is 0.01 to 0.02 lb of force at the focal plane. One approach that is showing some success is back-to-back cooler operation

supplemented by active electronic suppression of the fundamental cryocooler frequency ( $\sim 40$  Hz) and higher harmonics (ref. 1).

This approach, however, is unlikely to satisfy all the vibration damping requirements and it may be that an additional, and preferably passive, damping mechanism will still be required.  $\text{YBa}_2\text{Cu}_3\text{O}_{7-\delta}$  materials, which have an inherent magnetic damping capability due to dissipation of energy by flux motion (ref. 2), could potentially provide this mechanism. Magnetic Technologies, Inc. laboratory experiments using nonoptimum materials and magnetic field geometry have demonstrated that presently available  $\text{YBa}_2\text{Cu}_3\text{O}_{7-\delta}$  materials can provide at least an order of magnitude greater damping at 77 K than with no superconducting material.

Advanced turboexpander-type cryocoolers based on the Brayton thermodynamic cycle are being developed by NASA for future long duration missions. Important advantages offered by the turboexpander type, which use noncontact gas bearings, over the Stirling cycle mechanical cryocooler are potentially vibration free performance and greater reliability and lifetime. A disadvantage of the gas bearings is the need to run warm, which causes a large heat leak between the warm bearing zone and the cold expansion turbine, resulting in inefficient operation at low temperatures. Therefore, the need exists to improve the efficiency. A promising approach to eliminating the heat leak is to replace the rotary gas bearings with HTS passive magnetic (Meissner) bearings. A study by Creare, Inc. of a 1 W, 10 K cryocooler, where the gas bearings for the coldest turboexpander were replaced by Meissner bearings fabricated from currently available HTS materials, showed that a 40 percent decrease in input power was possible.

With  $\text{YBa}_2\text{Cu}_3\text{O}_{7-\delta}$  materials prepared by the melt quench process, levitation forces are now adequate for cryocooler applications although some improvements in stiffness may be required (ref. 3). A rotational speed of 450 000 rpm (surface speed of 150 m/s) has been demonstrated by Creare, Inc. which is more than adequate for cryocooler applications (90 m/s).

### Remote Sensing Applications

Many space-based sensing systems are cooled for improved sensitivity and decreased noise. This is another area of application where including HTS materials would have no cooling penalty when compared against nonsuperconducting systems. Three devices which would provide great benefit to near Earth and deep space missions are bolometers, mixers and signal processors.

In missions to the outer planets lasting ten years or longer, passive radiative cooling is presently the only satisfactory option for cooling the focal plane. This means the detector temperature is 70 K or higher. Studies of planetary atmospheres at wavelengths greater than  $20 \mu\text{m}$  will require the use of thermal detectors (ref. 4). A promising candidate for this application is a transition-edge bolometer that uses the resistive transition of a HTS element as the temperature sensing element. Such bolometers have been demonstrated to be superior to pyroelectric detectors. Another type of bolometer is the kinetic inductance bolometer which potentially has much lower noise and higher sensitivity. The operation of this bolometer depends on the temperature dependence of the magnetic penetration depth just below  $T_c$ .

Submillimeter spectroscopy is an important objective of future missions for astrophysics and Earth atmospheric studies. Principle components for these studies are mixers. Thus far the most sensitive mixers in the millimeter to near submillimeter range have been Nb based superconductor-insulator-superconductor (SIS) tunnel junctions. HTS tunnel junctions could

possible extend this frequency range well into the THz range. However, SIS tunnel junctions fabricated from HTS materials have not yet been demonstrated. An alternative approach is the superconductor-normal-superconductor (SNS) microbridge. Progress in HTS SNS is proceeding rapidly.

Locating a superconducting signal processor on a focal plane has many advantages over a semiconducting processor in terms of speed, power consumption and thermal loading. The higher speed would allow fewer data lines to the focal plane which means lower thermal loading. The development of such a processor is further in the future than development of HTS bolometers or mixers.

### Space Communications Applications

In the past, the need for heavy, short life and complicated cryogenic systems near 20 K prohibited the use of superconducting electronics circuits in space communications systems in spite of their outstanding advantages when compared to room temperature semiconductor electronics circuits. Since this discovery, NASA has been very active in identifying the applications of HTS materials in space communications systems. The approach has been twofold: first to identify subsystems and communications scenarios where superconducting devices and circuits will have the largest impact and second to design, fabricate and characterize generic superconducting devices and components and compare their performance with conventional circuits to quantitatively determine their advantages.

Under the first approach, in-house application analysis (ref. 5) and studies conducted by TRW, Ball Aerospace and Varian were used to identify key applications and are listed below.

1. Ultra Low Noise Hybrid Superconductor/Semiconductor Receivers
2. Phased Array Antennas from 1 to 50 GHz
3. Digital Signal Processors
4. Traveling Wave Tube Amplifiers

These studies included the impact of cryocoolers in their comparison which has often been ignored. One of the key findings is that superconducting circuits can offer outstanding advantages in reducing a spacecraft's power, size and weight in high performance space communications systems. They can also provide low loss, low noise, high data rate subsystems. However, only in a communication scenario where such high performance is required, can one justify the use of cryocoolers.

Under the second approach, NASA has designed, fabricated and characterized microstrip and coplanar resonator circuits from X-band to Ka band frequencies (refs. 6 and 7), X-band filters, phase shifter switches (ref. 8), X-band superconducting resonator stabilized oscillators, Ka-band passive microstrip antenna (ref. 6) and hybrid superconductor/semiconductor low noise amplifiers using  $\text{YBa}_2\text{Cu}_3\text{O}_{7-\delta}$  and thallium thin films on lanthanum aluminate substrates. Superconducting resonator circuits have shown higher "Q" values than gold circuits which translates into low loss passive microwave circuits (ref. 9). Superconducting filters have shown low insertion loss and higher "Q"s (ref. 7). Early evidence of superior performance of high  $T_c$  superconducting passive microwave components at liquid nitrogen temperatures has led Naval Research Laboratories (NRL) to evaluate their performance in several space experiments and expedite technology development (ref. 10). NASA has participated in NRL's High  $T_c$  Super-

conducting Space Experiment (HTSSE) I. NASA is also planning to participate in HTSSE II expected to be launched in 1996. For this experiment NASA Lewis Research Center and the Jet Propulsion Laboratory will be jointly developing an X-band hybrid HTS/semiconductor receiver. Also under planning is a Ka-band superconducting receiver antenna experiment as a part of a link between shuttle and Advanced Communications Technology Satellite.

For space communication applications, the discovery of high  $T_c$  superconductors has led to the development of high performance microwave components operating at 77 K. It is possible that these components may find use in real space communication systems demanding extraordinary performance. However, only the discovery of superconductors operating at 150 K can make their use practical in most of the space communications systems.

### Space Power Applications

When high current density superconductors appeared in the early 1960's their potential for application to space power technologies was carefully explored since it seemed certain that a zero resistance conductor could lower the launch weight by reducing the masses of both the conductors and the power system. Further, it could allow the wide use of magnets which would no longer need large and heavy power supplies and/or massive amounts of iron. The price to be paid however was the need to maintain the conductor below its transition temperature. For the conductors then available this meant refrigeration to well below 20 K (typically 4.2 K). This constraint introduced weight, complexity and reliability issues that effectively foreclosed the use of superconducting technology in space power systems. As was found with terrestrial power applications, the use of superconductors offers an attractive payoff only for the very largest systems.

Now, in the 1990's, this issue is being reexamined as the result of two developments. First, we are seriously considering space missions, such as Moon colonization and Mars exploration, that will require large capacity ( $>100$  kW) electric power systems and second, the discovery of HTS materials.

The most straight forward application of SC is direct power transmission. In this case we look at the wiring harness which carries power and control signals within the power management circuitry and between it and its electrical sources and loads. In reference 11 it was shown that, at a current density of  $2 \times 10^4$  A/cm<sup>2</sup> a superconducting wire can reduce the launch weight dramatically. Since large space systems will require many kilometers of wire carrying many kilowatts, substantial savings are possible if it all could be operated below the SC transition temperature. In general, this is not possible, but it might be practical if the power source must be located a long distance from its load. Not only would a minimum weight penalty be incurred, but the system designer would have additional flexibility in choosing the system operating voltage. A recent design study (ref. 12) has shown that it is possible to use directional radiators to cool such a line to less than 77 K in orbits as close as 1000 km from the Earth and to even lower temperatures in deep space. The mass of such a system, which uses radiation shields and commercially available HTS materials is still substantially less than a comparable system with copper transmission lines and it requires no active cooling system.

About 30 percent of a transformer's weight is conductor, therefore it is another element of a power distribution system where superconductors might be usefully employed. Because the useful current density in superconducting materials is at least 100X greater than that of copper,

the use of superconductors could eliminate more than 99 percent of this mass. In the case of capacitors only a small fraction of a capacitor's mass is conductor and therefore little is to be gained by the direct substitution of superconducting material. Of course, transformers and capacitors are elements of ac systems and the largest impact of superconducting technology on power systems might come from their elimination as the use of superconductivity could make dc systems more interesting (ref. 11).

This long term storage of electrical energy as a magnetic field is only feasible if superconducting inductors are used since the  $I^2R$  losses of normal conductors would quickly dissipate the energy. Early examination (ref. 13) of its potential for use as a space "battery" showed that it has some important advantages. Such a storage system has virtually no losses, allowing the recovery of 95 percent of the input, and would tolerate a wide range of charge/discharge rates. Further, it would have an unlimited cycle life. The specific energy, which is limited by the forces that the field exerts on the conductor, has been estimated at near 50 W-hrs/kg, which is competitive with  $NiH_2$  batteries.

Presently most space systems depend on photovoltaic arrays for primary electrical power and with increased power demands the arrays can reach large sizes. Also, in many orbits there is sufficient plasma density such that arcing can be a problem at  $>150$  V. Therefore power from these large arrays may have to be carried to their loads at high currents. The weights of these conductors, presently 3 to 5 percent (ref. 14) of the array mass and the 1 to 2 percent of the array lost to  $I^2R$  can be substantially reduced by the use of superconductors. Although the percentages are small, in large or multiple systems the absolute weight and money savings can be nontrivial. It remains to be seen if the system complexity introduced by the need to thermally shield the superconducting components will discourage its use in this application.

Many other space applications of superconducting technology in addition to the ones discussed above have also been identified. These include active bearings for rocket engines and magnets for magnetoplasmadynamic thrusters.

## CONCLUSIONS

The discovery of materials which are superconducting above liquid nitrogen temperature has made superconducting technology more attractive and feasible for use in aerospace systems. For some future missions where cooling is necessary to fulfill the mission objectives, the HTS materials meet all the technical requirements and are likely to be used after the material stability issues have been settled. For other missions, the added complexity of cooling must be justified by the improved performance offered by superconducting technology. If materials are developed with higher transition temperatures, cooling will be much less of an issue, and the use of superconducting technology should become much more widespread in space-based systems.

## REFERENCES

1. Ross, R.G.; Johnson, D.L.; and Sugimura, R.S.: Paper presented at the Sixth International Cryocooler Conference, 1991.
2. Moon, F.C.; Weng, K.C.; and Chang, P.Z.: Dynamic Magnetic Forces in Superconducting Ceramics. *J. Appl. Phys.*, vol. 66, no. 11, 1989, pp. 5643-5645.

3. Carlson, L.: Bullish on Bearings. *Supercond. Ind.*, vol. 4, Summer 1991, pp. 22-28.
4. Castles, S., et al.: Research on High Temperature Superconductor Applications at the Goddard Space Flight Center. *World Congress on Superconductivity*, C.G. Burnham and R.D. Kane, eds., World Scientific, 1988, pp. 155-167.
5. Heinen, V.O.; Bhasin, K.B.; and Long, K.J.: Emerging Applications of High Temperature Superconductors for Space Communications. NASA TM-103629, 1991.
6. Richard, M.A., et al.: Measurement Techniques for Cryogenic Ka-Band Microstrip Antennas. NASA TM-105183, 1991.
7. Chew, W., et al.: Design and Performance of a High-Tc Superconductor Coplanar Waveguide Filter. *IEEE Trans. Microwave Theory Tech.*, vol. 39, Sept. 1991, pp. 1455-1461.
8. Bhasin, K.B., et al.: High Temperature Superconducting Thin Film Microwave Circuits: Fabrication, Characterization, and Applications. *Superconductivity Applications for Infrared and Microwave Devices; Proceedings of SPIE*, vol. 1292, SPIE, 1990, pp. 71-82.
9. Chorey, C.M., et al.: YBCO Superconducting Ring Resonators at Millimeter-Wave Frequencies. *IEEE Trans. Microwave Theory Tech.*, vol. 39, Sept. 1991, pp. 1480-1487.
10. Webb, D.C.; and Nisenoff, M.: The High Temperature Superconductivity Space Experiment. *Microwave J.*, vol. 34, Sept. 1991, pp. 85-91.
11. Aron, P.R.; and Myers, I.T.: The Application of High Temperature Superconductors to Space Electrical Power Distribution Components. 1988 IECEC; *Proceedings of the Twenty-Third Intersociety Energy Conversion Engineering Conference*, D.Y. Goswami, ed., ASME, 1988, vol. 2, pp. 501-503. (Also, NASA TM-100901.)
12. Shimko, M.A.; Crowley, C.J.; and Wallis, P.N.: Novel Concept for a Space Power Distribution Busbar Using HTS Materials and Passive Cooling. Presented at the Fifth Conference on Superconductivity and Applications, Buffalo, New York, Sept., 1991.
13. Fickett, F.R.: Space Applications of Superconductivity: High-Field Magnets. *Cryogenics*, vol. 19, no. 12, 1979, pp. 691-701.
14. Meulenberg, A. Jr.: Private communication.



## MEASUREMENT TECHNIQUES FOR CRYOGENIC KA-BAND MICROSTRIP ANTENNAS

M.A. Richard  
Case Western Reserve University  
Department of Electrical Engineering  
Cleveland, Ohio 44106

K.B. Bhasin  
National Aeronautics and Space Administration  
Lewis Research Center  
Cleveland, Ohio 44135

C. Gilbert and S. Metzler  
Ball Communications Systems Division  
Broomfield, Colorado 80020

P.C. Claspy  
Case Western Reserve University  
Department of Electrical Engineering  
Cleveland, Ohio 44106

## ABSTRACT

The measurement of cryogenic antennas poses unique logistical problems since the antenna under test must be embedding in the cooling chamber. In this paper, a method of measuring the performance of cryogenic microstrip antennas using a closed cycle gas-cooled refrigerator in a far field range is described. Antenna patterns showing the performance of gold and superconducting Ka-band microstrip antennas at various temperatures are presented.

## 1. INTRODUCTION

Printed circuit antennas have been the focus of much research in recent years as candidates for applications such as satellites where weight and volume are a premium [1]. In theory, many-element microstrip arrays could rival the gain of traditional parabolic dishes. However, microstrip antennas have high ohmic losses which act to limit the maximum obtainable gain. This problem is compounded at millimeter wave frequencies since the surface resistance of metals increases with  $f^{1/2}$ , causing microstrip transmission lines to be much more lossy.

It is well known that ohmic losses may be reduced significantly by cooling the circuit to cryogenic temperatures. Gold has a resistance temperature coefficient of approximately  $10 \text{ n}\Omega \text{ cm/K}$ . Computer simulations show that a reduction in temperature from 300 K to 77 K translates to 10 dB/m less loss at 30 GHz for a microstrip line on 0.25 mm alumina. The use of cryogenics has the additional benefit of reducing the noise figure of the system, which is critical for radiometric antennas. Recently, much attention has been given to the use of high temperature superconductors (HTS) as a solution to the problem of gain limitation in many-element microstrip array antennas [2,3]. According to [3], an HTS 100 element linear array at 35 GHz could experience a gain increase of 8 to 10 dB over an identical copper array. Measurements of 35 GHz HTS ring resonators have shown an improvement in microstrip line attenuation of 10 dB over identical gold circuits when both are at 77 K. [4]

In a practical sense, measuring the performance of antennas at cryogenic temperatures is quite difficult. If the antenna is to be cooled in a cryogen such as liquid nitrogen or liquid helium, a radio-transparent dewar must be used. In general such an arrangement allows performance measurements only at two temperatures: room temperature and the boiling point of the cryogen. This type of cryostat has been used by [5] to measure electrically small superconducting arrays at 650 MHz and by [6] to measure a 500 MHz HTS dipole. A gas refrigerator, on the other hand, has the advantage that the temperature can be set to any value within its range. However, a vacuum must be maintained, which necessitates the use of some type of radio-transparent vacuum jacket.

In this paper, we discuss the design of a temperature-controlled cryostat which has been used to successfully test planar superconducting microstrip arrays at 30 GHz. To our knowledge this is the first reported use of a gas refrigerator for cryogenic antenna measurements.

## 2. DESIGN

The cryostat used is based upon a CTI-Cryogenics compressor and cold head. The unit is a closed-cycle helium refrigerator. A Lakeshore Cryogenics temperature controller controls the current through a heater element to provide temperature control over the system. The two-stage cold finger is enclosed by a stainless steel tube, capped with a lid machined from high-density polyethylene (HDPE) as shown in Fig. 1. HDPE was chosen because of its low relative permittivity (2.34) [7] and loss tangent and because it is inexpensive in comparison to other polymers such as teflon. The lid is spherical with an inner radius of 12.7 cm and thickness of .508 cm. A hermetically sealed coaxial feedthru (two back-to-back "K" sparkplug launchers) passes the RF into the vacuum chamber. Semirigid coaxial cable connects the feedthru to the antenna test fixture.

The antennas used are 4 element microstrip arrays with a resonance at 31.7 GHz. The antennas were patterned onto their respective substrates, magnesium oxide (MgO) and lanthanum aluminate ( $\text{LaAl}_2\text{O}_3$ ), and assembled into a brass test fixture (Fig. 2). A  $50 \Omega$  gold microstrip feed line patterned on an alumina substrate separates the coax-to-microstrip transition (Wiltron V-connector) from the antenna. The test fixture was made as thin as practically possible to reduce the thermal loading of the cryostat, thereby hastening the cool-down and warmup times involved. Wire bonds connect the feed line to the antenna. To test the antennas, each test fixture was in turn mounted at the second stage of a 2-stage closed-cycle helium refrigerator. A high-density polyethylene (HDPE) cap serves as both a vacuum jacket and a radome. S-parameter ( $S_{11}$ ) measurements using an HP 8510B were done by calibrating to the coaxial connector inside the cryostat while at room temperature. The entire cryostat was mounted on a plexiglass stand, which in turn was fastened to the rotating pedestal of a far-field antenna range for pattern measurements in the receive mode (Fig. 3).

### 3. ANTENNA MEASUREMENTS

This setup was used to measure H-plane patterns of the aforementioned Ka-band microstrip arrays. The arrays were fabricated with high-temperature superconductors (HTS) and, for comparison purposes, with evaporated gold. The antennas were measured at 30 K, 70 K and room temperature (295 K). In addition, the array patterns of the gold antennas were measured with and without the HDPE lid to judge the effect of the radome. The measured patterns are shown in Fig. 2. Comparison of the patterns with and without the lid show the H-plane patterns to be essentially unchanged, except for a 3-dB amplitude decrease when the lid is removed. This is most likely a result of the lid acting as a dielectric lens, thereby weakly focusing the radiation. The thickness of the HDPE lid was chosen arbitrarily, and at the resonant frequency of the antennas is 1.22 dielectric wavelengths. The gold antenna patterns show a 3 dB increase in received power as the temperature is lowered from 295 K to 30 K. The HTS arrays show a distinct difference in pattern below and above the critical temperature ( $T_c$ ), with the received power increasing by more than 10 dB below  $T_c$ .

### 4. CONCLUSIONS

A specially designed cryogenic unit has been developed for the measurement of microstrip antennas at temperature down to 25 K. The use of the unit was demonstrated by measuring far-field patterns and the reflection coefficients of superconducting and gold Ka-band microstrip arrays. H-plane measurements show no substantial effects resulting from the presence of the HDPE radome.

### ACKNOWLEDGMENT

The authors would like to thank Mr. Ed Smith for his help in the measurement of these antennas, and Dr. R.Q. Lee for his constructive suggestions. One of the authors (M.A. Richard)

acknowledges support through a NASA Space Grant / Ohio Aerospace Institute Doctoral Fellowship.

## 5. REFERENCES

1. Ely Levine, Gabi Malamud, Shmuel Shtrikman, and David Treves, "A Study of Microstrip Array Antennas with the Feed Network," *IEEE Trans. Antennas and Propagat.*, vol. AP-37, no. 4, pp. 426-434, Apr. 1989.
2. R.C. Hansen, "Superconducting Antennas," *IEEE Trans. on Aerospace and Electronic Systems*, vol. 26, no. 2, pp. 345-354, March 1990.
3. Robert J. Dinger, "Some Potential Antenna Applications of High Temperature Superconductors," *Journal of Superconductivity*, vol. 3, no. 3, pp. 287-296, 1990.
4. C.M. Chorey, K.B. Bhasin, J.D. Warner, J.Y. Joesfowicz, D.B. Rensch, and C.W. Nieh, "An Experimental Study of High Tc Superconducting Microstrip Transmission Lines at 35 GHz and the Effect of Film Morphology," *IEEE Trans. on Magnetics*, pp. March 1991.
5. G.B. Walker, Clovis R. Haden, and O.G. Ramer, " *IEEE Trans. Antennas and Propagat.*, vol. AP-25, no. 6, pp. 885-887, Nov. 1977.
6. S.K. Khamas, M.J. Mehler, T.S. Maclean, C.E. Gough, "High Tc Superconducting Short Dipole Antenna," *Electronics Letters*, vol.24, no. 8, pp. 460-461, April 1988.
7. Karlheinz Seeger, "Microwave Measurement of the Dielectric Constant of High-Density Polyethylene," *IEEE Trans. Microwave Theory and Tech.*, vol. 39, no. 2, pp. 352-354, Feb. 1991.

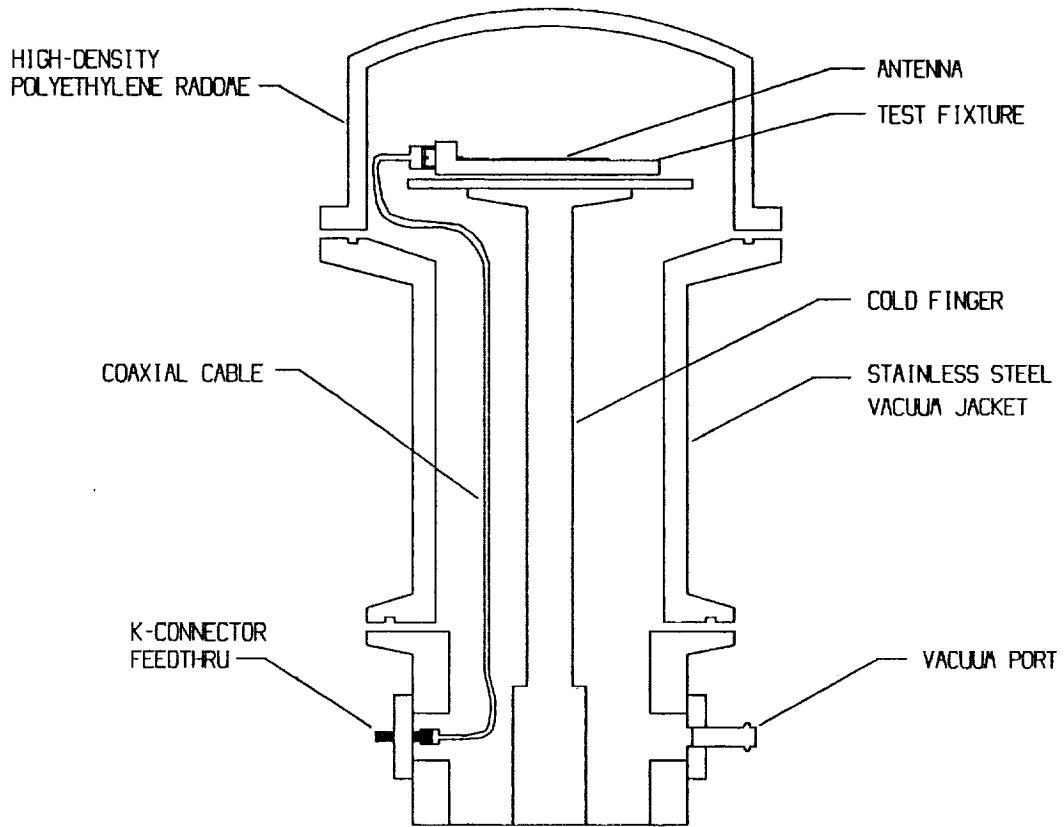


Fig. 1. Cryogenic antenna test unit.

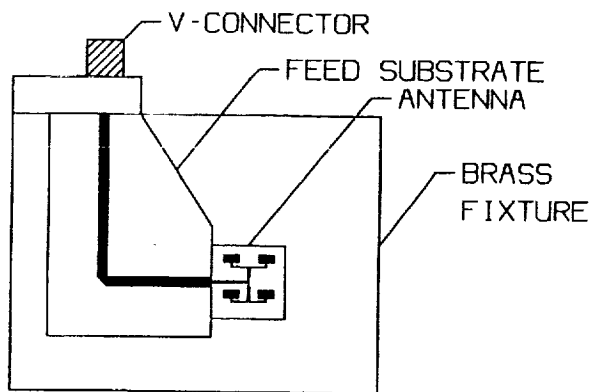


Fig. 2. Four element microstrip antenna in brass test fixture.

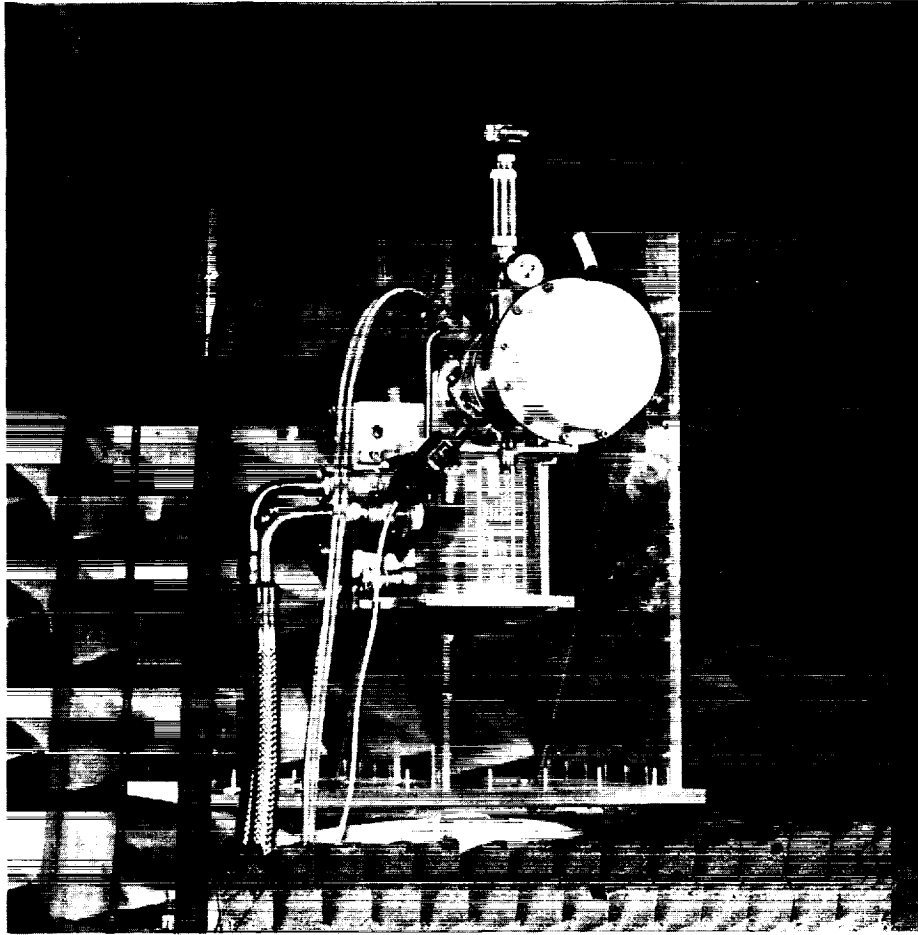


Fig. 3. Cryogenic unit mounted on rotating pedestal of the far field antenna range.

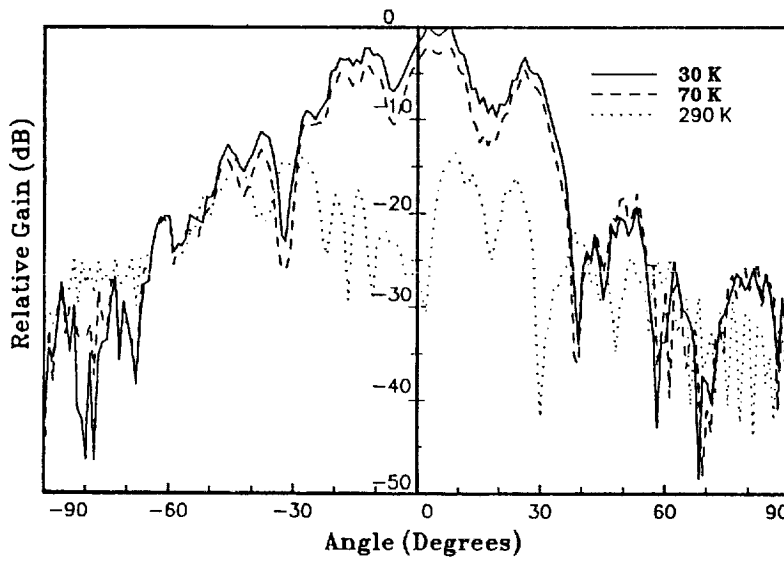


Fig. 4. H-plane patterns of 4-element HTS array on MgO substrate taken at 290, 70, and 30 Kelvin.



# Performance of a Four-Element Ka-Band High-Temperature Superconducting Microstrip Antenna

M. A. Richard, *Student Member, IEEE*, K. B. Bhasin, *Senior Member, IEEE*, C. Gilbert, S. Metzler, G. Koepf, *Member, IEEE*, and P. C. Claspy, *Senior Member, IEEE*

Permission to copy without fee all or part of this material is granted provided that the copies are not made or distributed for direct commercial advantage. Copying is by permission of the Institute of Electrical and Electronics Engineers. To copy otherwise, or to republish, requires a fee and specific permission.

**Abstract**—Superconducting four-element microstrip array antennas operating at 30 GHz have been designed and fabricated on a lanthanum aluminate ( $\text{LaAlO}_3$ ) substrates. The experimental performance of these thin film Y-Ba-Cu-O superconducting antennas is compared with that of identical antenna patterned with evaporated gold. Efficiency measurements of these antennas show an improvement of 2 dB at 70 K and as much as 3.5 dB at 40 K in the superconducting antenna over the gold antenna.

## I. INTRODUCTION

SINCE the advent of high-temperature superconductors (HTS), many superconducting electronics applications have been projected at liquid nitrogen temperatures [1]. More recently, HTS devices such as resonators, delay lines, filters, and phase shifters have been fabricated and tested at X-band frequencies and below [2]. Experimental results have shown that HTS devices typically exhibit significantly better performance than that of identical metallic circuits. Experimental work with Ka-band superconducting ring resonators [3] has shown a factor of 3 improvement in circuit "Q" at 35 GHz over an identical circuit fabricated with evaporated gold. Such results have encouraged the investigation of potential HTS applications in microstrip antenna systems.

To date, experimental investigation of HTS antennas has been very limited in scope, consisting mainly of work done on electrically small antennas at frequencies less than 1 GHz [4]. Analytical work by Dinger [5] has shown that HTS may be most beneficial when used in the feed and matching networks for microwave and millimeter-wave microstrip arrays. This is due to the fact that metal microstrip transmission lines have high ohmic losses which, in the feed network of an antenna array, act to limit the maximum obtainable gain. This problem is especially profound at Ka-band and higher frequencies. With the use of HTS, however, the conductor losses in the feed network are reduced dramatically. According to Dinger [5],

Manuscript received December 4, 1991. M.A. Richard is supported by a NASA Space Grant/Ohio Aerospace Institute Doctoral Fellowship.

M. A. Richard and P. C. Claspy are with the Department of Electrical Engineering, Case Western Reserve University, Cleveland, OH 44106.

K. B. Bhasin is with the National Aeronautics and Space Administration, Lewis Research Center, Cleveland, OH 44135.

C. Gilbert, S. Metzler, and G. Koepf are with the Ball Communication Systems Division, Broomfield, CO 80020.

IEEE Log Number 9107676.

## II. THE ANTENNAS

an HTS 100 element linear array at 35 GHz could experience a gain increase of 8 to 10 dB over an identical copper array.

To experimentally investigate the advantages of HTS in such array antennas we have designed and fabricated a 30 GHz four-element superconducting microstrip array on a lanthanum aluminate ( $\text{LaAlO}_3$ ) substrate. Efficiency measurements are presented and compared with identical gold antennas.

The four-element antenna arrays were designed for a lanthanum aluminate substrate. This material was chosen in spite of its high relative permittivity ( $\epsilon_r$ ) because it allows the growth of high quality YBCO thin films. The design for the antenna consists of four microstrip patches spaced  $\lambda_0/2$  apart in both directions and fed in-phase by a microstrip corporate feed network. The patch feedpoints are inset by approximately 28% and fed via 100- $\Omega$  quarter-wave transformers to match the high-patch input impedance. A substrate thickness of 0.25 mm is used to minimize substrate modes and radiation. The YBCO thin film was deposited by a laser ablation process and had a relatively low critical temperature ( $T_c$ ) of 84 K. The patterning of the circuit was done by standard photolithography using a wet chemical etchant. An evaporated gold ground plane of 100- $\text{\AA}$  titanium followed by 1  $\mu\text{m}$  of gold was used. An identical circuit was made using 1  $\mu\text{m}$  of evaporated gold as metallization for comparison purposes.

The antennas are assembled into a brass test fixture with a 50- $\Omega$  gold microstrip feed line patterned on an alumina substrate separating the coax-to-microstrip transition from the antenna (Fig. 1). Wire bonds connect the feed line on the alumina substrate to the antenna. To test the devices, each test fixture was in turn mounted at the second stage of a two-stage closed-cycle helium refrigerator that has a high-density polyethylene (HDPE) cap serving as both a vacuum jacket and a radome [6].

The efficiency of the HTS antenna relative to the gold antenna was found measuring the power received by the antenna under test at boresight and applying the Friis transmission formula. The antenna under test is used in the receive mode in the presence of a transmitting horn, while  $S_{21}$  and the reflection coefficient ( $S_{11}$ ) of each antenna under test are in turn measured (Fig. 2). With all other factors being equal for the two antennas under test, the efficiency of the HTS antenna

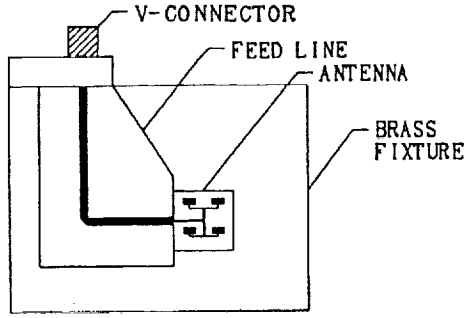


Fig. 1. Four-element array with feedline mounted in test fixture.

relative to the gold may be found as

$$\frac{\eta_{HTS}}{\eta_{Au}} = \frac{|S_{21}|_{HTS}^2}{1 - |S_{11}|_{HTS}^2} \cdot \frac{|S_{21}|_{Au}^2}{1 - |S_{11}|_{Au}^2} \quad (1)$$

### III. RESULTS AND DISCUSSION

The measured E- and H-plane patterns of the gold array at 31 GHz are shown in Fig. 3. The perturbations in the patterns are due to effects such as feed radiation, surface waves, and scattering from the test fixture. As can be seen in Fig. 4, the efficiency of the HTS antenna increases dramatically at the onset temperature but tends to level off at lower temperatures. The efficiency of the four-element arrays can be approximated as

$$\eta_{(dB)} = \alpha_c L - \alpha_o L + \eta_{(dB),misc} \quad (2)$$

Here,  $\alpha_c$  is the conductor attenuation constant (dB/unit length),  $\alpha_o$  is the attenuation constant due to other effects such as substrate losses and feedline radiation losses,  $L$  is the total feedline length, and  $\eta_{misc}$  is any remaining efficiency term including such effects as aperture and surface wave efficiencies. Of the terms involved in (2), to a very good approximation only  $\alpha_c$  is affected by a change in either conductor metallization or ambient temperature. Thus, the relative efficiency as given in (1) is a measure of the difference in metal losses found in the feed network and patches of the two antennas. Loss calculations predict the HTS antenna to have approximately 1.3 dB of increase in gain over the gold antenna at 77 K. Measured relative efficiency data shows 2 dB increase at 70 K and as much as 3.5 dB improvement at 40 K. The better than expected performance at the lower temperatures may be attributed to higher than expected losses in the very narrow (2.8- $\mu$ m width) 100- $\Omega$  gold lines.

To verify the shape of the efficiency curve found in this work, data from measured microstrip ring resonators patterned on identical YBCO thin films [3] was used to find the attenuation constant,  $\alpha$ , as a function of temperature. By assuming this loss to be the only loss in the array, the shape of the gain-versus-temperature curve may be found as

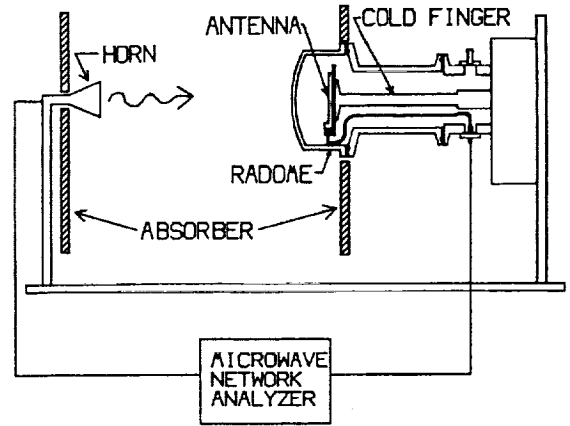


Fig. 2. Antenna efficiency measurement setup.

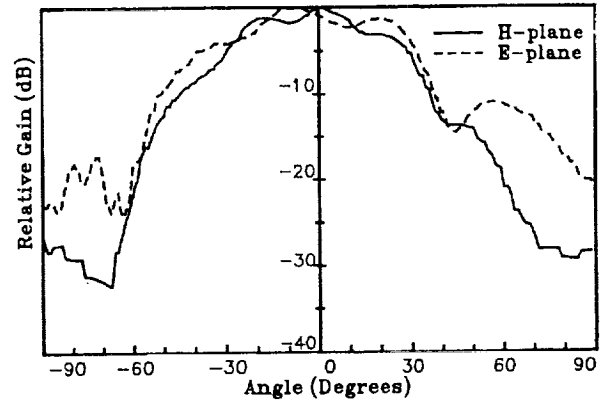


Fig. 3. E- and H-plane patterns of the gold array.

$$G = 10 \log_{10} \frac{(4\pi A)}{\lambda_0} - \alpha L, \quad (3)$$

where  $L$  is the total feed line length (1.5 cm). These values are plotted in Fig. 5 along with the experimental antenna received power quantity

$$\frac{|S_{21}|^2}{1 - |S_{11}|^2} \quad (4)$$

and show the same behavior as measured in the array. Similarity of these curves confirms the shape of the experimentally-found efficiency curve and validates the assumption that conductor loss is the only parameter of the antenna efficiency which changes significantly with temperature.

### IV. CONCLUSION

A superconducting Ka-band microstrip array on lanthanum aluminate has been demonstrated. Efficiency measurements show a distinct improvement in performance over an identical gold circuit at temperatures below 75 K. Comparison with measured data from ring resonators confirm the general shape of the measured efficiency curve.

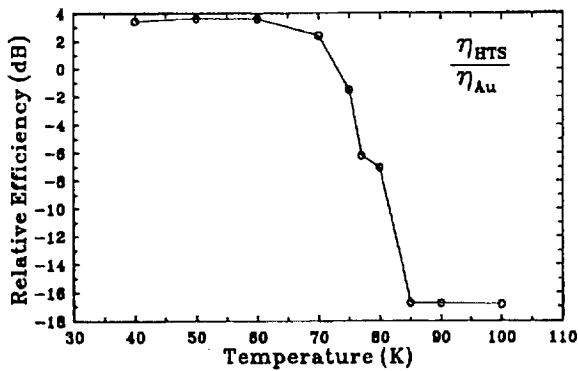


Fig. 4. Relative efficiency of HTS antenna with respect to gold antenna versus temperature.

ACKNOWLEDGMENT

The authors would like to thank Mr. N. Roeher for fabricating the HTS thin films used in this work.

REFERENCES

[1] M. Nisenoff, "Superconducting electronics: current status and future prospects," *Cryogenics*, vol. 28, pp. 47-56, Jan. 1988.  
 [2] *IEEE Trans. Microwave Theory Tech.*, Special Issue, vol. 39, no. 9, Sept. 1991.

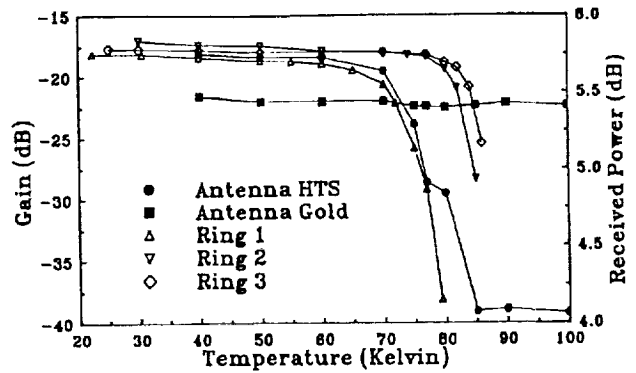


Fig. 5. Gain curves using data from HTS ring resonators compared to received power data.

[3] C. M. Chorey, Keon-Shik Kong, Kul B. Bhasin, J. D. Warner, and Tatsuo Itoh, "YBCO superconducting ring resonators at millimeter-wave frequencies," *IEEE Trans. Microwave Theory Tech.*, vol. 39, pp. 1480-1487, Sept. 1991.  
 [4] C. E. Gough, S. K. Khamas, T. S. Maclean, M. J. Mehler, N. Alfor, and N. M. Harmer, "Critical currents in a high-Tc superconducting short dipole antenna," *IEEE Trans. Magn.*, vol. 25, pp. 1313-1314, Mar. 1989.  
 [5] R. J. Dinger, "Some potential antenna applications of high temperature superconductors," *J. Superconduct.*, vol. 3, no. 3, pp. 287-296, 1990.  
 [6] M. A. Richard, K. B. Bhasin, C. Gilbert, S. Metzler, and P. C. Claspay, "Measurement techniques for cryogenic Ka-band microstrip antennas," *Antenna Measurement Tech. Assoc. Proc.*, 1991, pp. 1.13-1.17.



## PERFORMANCE OF A Y-Ba-Cu-O SUPERCONDUCTING FILTER/GaAs

## LOW NOISE AMPLIFIER HYBRID CIRCUIT

K.B. Bhasin and S.S. Toncich  
National Aeronautics and Space Administration  
Lewis Research Center  
Cleveland, Ohio 44135

C.M. Chorey  
Sverdrup Technology, Inc.  
Lewis Research Center Group  
Brook Park, Ohio 44142

R.R. Bonetti and A.E. Williams  
COMSAT Laboratories  
Clarksburg, Maryland 20871

Abstract

A superconducting 7.3 GHz two-pole microstrip bandpass filter and a GaAs low noise amplifier (LNA) were combined into a hybrid circuit and characterized at liquid nitrogen temperatures. This superconducting/semiconducting circuit's performance was compared to a gold filter/GaAs LNA hybrid circuit. The superconducting filter/GaAs LNA hybrid circuit showed higher gain and lower noise figure than its gold counterpart.

Introduction

Before the discovery of high-Tc superconductivity, the integration of low-Tc superconductors with semiconducting devices was not feasible since many semiconducting devices freeze-out below 10 K. The recent demonstration of high-Tc superconducting passive microwave components operating at liquid nitrogen temperatures<sup>1,2</sup> has enhanced the feasibility of integrating these superconducting components with semiconducting devices to achieve high performance microwave systems. GaAs and heterostructure microwave semiconducting devices make strong candidates for integration since they have shown significantly lower noise figures at liquid nitrogen temperatures.<sup>3,4</sup>

In deep space communications, radio astronomy and radiometer applications, low noise and low loss requirements are frequently met by cooling the microwave components. For the first time we have combined in a hybrid circuit a superconducting microstrip bandpass filter and a GaAs low noise amplifier (LNA), which is a basic building block in these applications. We compared its performance to a hybrid gold filter/LNA circuit operating at the same temperature. The circuit design, fabrication, and experimental results are presented below.

Circuit Design and Fabrication

A two-pole microstrip bandpass filter was designed with a 2.5 percent bandwidth, 0.5 dB passband ripple, and 7.5 GHz center frequency on lanthanum aluminate substrate. The layout of the two-pole filter is shown in Fig. 1. The filter was fabricated using laser ablated YBCO superconducting films (~5000 Å) on a 10 mil lanthanum aluminate substrate. A gold film deposited by E-beam evaporation on the opposite side of lanthanum aluminate substrate

was used as a ground plane. An identical filter using gold film for the microstrip and the ground was also fabricated.

The LNA selected was an Avantek Inc. PGM 11421 with a specified frequency response from 4 to 11 GHz, a minimum gain of 8.0 dB, and a typical noise figure of 2.5 dB. The bandpass filter/GaAs LNA hybrid was mounted in a brass test fixture as shown in Fig. 2. The devices were connected by 10 mil gold bond wires to 50 Ω input/output microstrip lines that were fabricated on 10 mil thick Duroid ( $\epsilon_r = 2.3$ ) substrate. The length of the microstrip lines were chosen so as to minimize the interaction between the launcher pins and the devices.

The coax to microstrip transition was implemented using SMA female flange connectors. Silver paint was used to improve the contact between the center conductor of the launcher and the microstrip line.

Cryogenic Measurements and Results

The LNA and bandpass filters were tested individually to verify their performance at  $T = 300$  and 77 K. An HP 8510B automatic network analyzer (ANA) was used to measure insertion gain or loss, and a HP 8970A noise figure meter was used to determine the noise figure of the LNA. Table 1 presents a summary of the pertinent results that apply for this work. The data for the gold filter shows a reduction in the insertion loss of 1.4 dB between  $T = 300$  and 77 K. This is due to lower ohmic loss in the gold conductor and to a reduction of loss in the dielectric substrate at  $T = 77$  versus 300 K. The HTS filter shows a significantly smaller insertion loss than the gold filter at 77 K. This is due to the near elimination of conductor loss in the YBCO film compared to the loss in the gold conductor. Most of the loss present of the HTS filter is due to the use of a gold ground plane.

The primary advantage in using an HTS filter over a gold filter is that the HTS filter offers a much smaller insertion loss. If the HTS filter's gold ground plane were replaced with HTS material, a further reduction in insertion loss could be achieved.

For the LNA/bandpass filter hybrid measurements, a full two port calibration was performed inside the cryostat so as to move the ANA reference planes to the ends of the semi-rigid cables

inside the cryostat. Since this experiment is concerned only with the relative difference in gain of the hybrid circuit and not with the absolute gain, a two port calibration was selected over a TRL or LRL calibration, which could move the reference planes of the ANA onto the test fixture, thereby removing its effect as well. In all measurements performed, only the filters were changed in the test fixture.

To calibrate the noise figure meter, the LNA/bandpass filter was replaced in the test fixture by a 50  $\Omega$  thru line supplied by Avantek Inc. An ANA measurement was made to determine the total insertion loss of the test fixture and semi-rigid cables over the frequency range of 7.0 to 8.0 GHz. This loss was found to be 2.6 dB in this frequency range. One half of this loss (1.3 dB), representing the loss of that portion of the test fixture that appears at the input of the hybrid, was subtracted away from the noise figure measurements that were made on the hybrid at the appropriate frequency points, leaving only the actual noise figure of the hybrid.

Figure 3 shows the difference in the hybrid's gain when gold and HTS filters, respectively, are used, while Fig. 4 shows the difference in the noise figures. Since the HTS filter becomes functional only after the system reaches cryogenic temperatures, there is no room temperature data provided for it. This particular filter was fabricated on a high quality substrate, it began to conduct at T = 89 K, and reached its minimum insertion loss at T = 85 K.

At 77 K the gold filter/LNA hybrid shows a noise figure improvement of nearly 3.5 dB as compared to 300 K, while the HTS filter/LNA hybrid shows a 5.5 dB improvement in noise figure compared to gold at 300 K. As expected, the overall gain of the HTS filter/LNA hybrid is greater than that of the gold hybrid due to a lower insertion loss of the HTS filter.

As a check on the accuracy of these results, the data obtained for the LNA and filters individually is inserted in the expression for the noise figure of a cascade,  $F_t = F_1 + (F_2 - 1)/G_1$ . Here,  $F_1$  and  $F_2$  are the noise figures of the filter and LNA respectively, and  $G_1$  is the loss of the filter. Table 2 shows the results for the minimum noise figure of the hybrid. There is good agreement between the calculated and measured noise figures for the hybrid.

TABLE 1.—DATA ON THE LNA AND BANDPASS FILTERS  
USED IN THIS EXPERIMENT

[The frequency range is 7.0 to 8.0 GHz. The gain/loss values shown are average values over this frequency band. For the filters, noise figure values were taken to be the magnitude of the respective insertion loss.]

|                 |           | Gain/loss,<br>dB | Noise figure,<br>dB |
|-----------------|-----------|------------------|---------------------|
| LNA (PGM 11421) | T = 300 K | 8.9              | 2.5                 |
|                 | T = 77 K  | 9.5              | 0.9                 |
| Gold filter     | T = 300 K | -4.2             | 4.2                 |
|                 | T = 77 K  | -2.8             | 2.8                 |
| HTS filter      | T = 77 K  | -0.5             | 0.5                 |

## Conclusions

A low loss two-pole Y-Ba-Cu-O superconducting bandpass filter on lanthanum aluminate substrate was connected in series with a packaged GaAs low noise amplifier and fully characterized at 77 K. The noise figure characteristics of the superconducting filter/LNA hybrid circuit when compared to the gold filter/LNA hybrid circuit showed an improvement of 2.1 dB at 77 K. The gain characteristics showed an improvement of 0.5 dB for the HTS filter hybrid over the gold hybrid at 77 K.

This first demonstration of superconducting filter/GaAs LNA hybrid circuit shows potential for applications in radio astronomy, radiometers and deep space communications systems where high performance is desired in spite of the cooling requirements.

## Acknowledgment

The authors wish to acknowledge the assistance of Mr. Ed Rylander, Sr. Test Engineer at Avantek Inc., Folsom, CA for his useful discussions on noise figure measurement and for supplying us with Avantek thru lines for calibration purposes.

## References

1. *IEEE Trans. Microwave Theory Tech.*, vol. 39, no. 9, 1991 (entire issue).
2. D.C. Webb and M. Nisenoff, "The high temperature superconductivity space experiment," *Microwave J.*, vol. 34, pp. 85-91, 1991.
3. M.W. Pospieszalski, S. Weinreb, R.D. Norrod, and R. Harris, "FET's and HEMT's at cryogenic temperatures—their properties and use in low-noise amplifiers," *IEEE Trans. Microwave Theory Tech.*, vol. 36, pp. 552-560, 1988.
4. S. Weinreb, "Low-noise, cooled GASFET amplifiers," *IEEE Trans. Microwave Theory Tech.*, vol. 28, pp. 1041-1054, 1980.

TABLE 2.—CALCULATED AND MEASURED VALUES FOR THE NOISE FIGURE OF THE HYBRID CIRCUIT

|                            | Calculated noise figure, dB | Measured noise figure, dB |
|----------------------------|-----------------------------|---------------------------|
| Gold filter/LNA, T = 300 K | 6.7                         | 7.0                       |
| Gold filter/LNA, T = 77 K  | 3.7                         | 3.6                       |
| HTS filter/LNA, T = 77 K   | 1.4                         | 1.5                       |

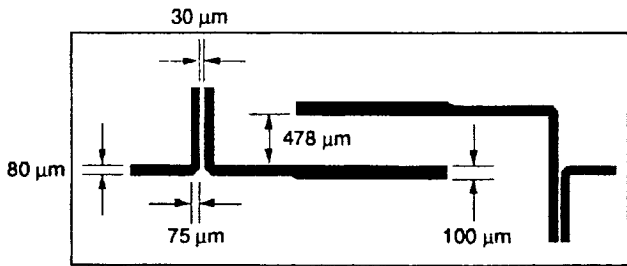


Figure 1.—Layout of the C-band, two pole bandpass filter.

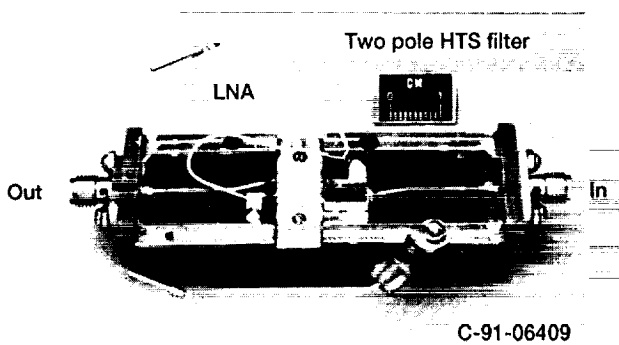


Figure 2.—Test fixture used for measurements on bandpass filter/LNA hybrid.

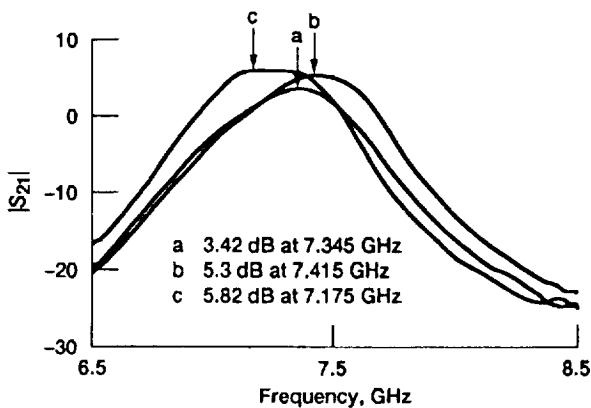
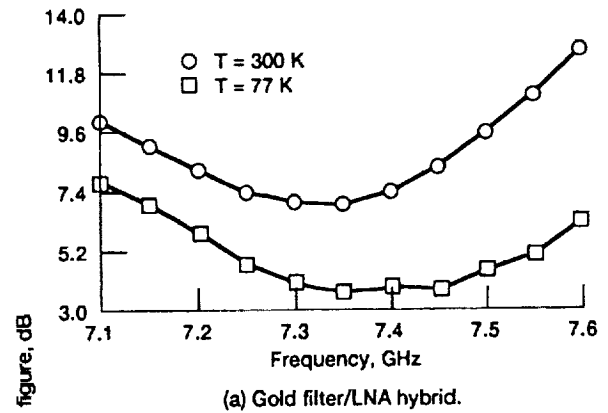
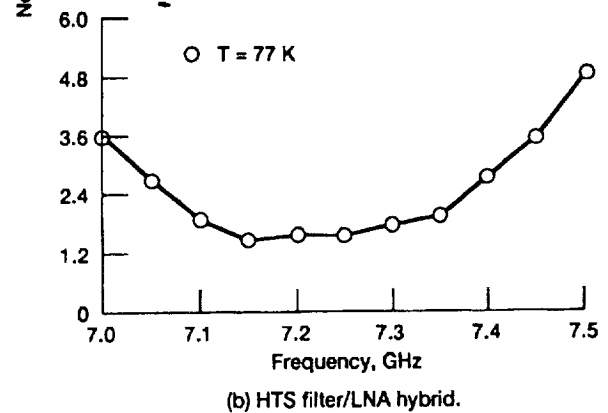


Figure 3.—Forward transmission (gain) of the gold filter/LNA hybrid (a) at T = 300 K, (b) at T = 77 K, and (c) the HTS filter/LNA hybrid at T = 77 K.



(a) Gold filter/LNA hybrid.



(b) HTS filter/LNA hybrid.

Figure 4.—Noise figure measurement as a function of temperature.



# YBCO Superconducting Ring Resonators at Millimeter-Wave Frequencies

Christopher M. Chorey, *Member, IEEE*, Keon-Shik Kong, *Student Member, IEEE*, Kul B. Bhasin, *Senior Member, IEEE*, J. D. Warner, and Tatsuo Itoh, *Fellow, IEEE*

Permission to copy without fee all or part of this material is granted provided that the copies are not made or distributed for direct commercial advantage. Copying is by permission of the Institute of Electrical and Electronics Engineers. To copy otherwise, or to republish, requires a fee and specific permission.

**Abstract**—Superconducting microstrip ring resonators operating at 35 GHz have been fabricated from laser ablated  $\text{YBa}_2\text{Cu}_3\text{O}_{7-x}$  (YBCO) films on lanthanum aluminate substrates. The circuits consist of superconducting strips over normal metal ground planes. The circuits are measured from 20 K to 90 K and with microwave input powers ranging from 0.25 mW to 10 mW. The superconducting resonators show significant improvement in  $Q$  (six to seven times higher) over identical gold resonators at 20 K, but only marginal improvement at 77 K. No variation in the superconductor performance is observed with varying input power. Using a microstrip loss model, the microwave surface resistance of the superconductors is extracted; the lowest value obtained at 77 K is 9 m $\Omega$ . The change in the resonant frequency with temperature is analyzed and a value for the penetration depth computed. “Double resonances” observed in some superconducting ring resonators are described and an explanation for their presence advanced. Factors limiting millimeter-wave high-temperature superconductor circuits are explored and potential performance levels calculated based on current reported values for high-temperature superconductor surface resistances.

## I. INTRODUCTION

CONTINUED refinement in the growth of thin high-temperature superconducting (HTS)  $\text{YBa}_2\text{Cu}_3\text{O}_{7-x}$  (YBCO) films on microwave-suitable substrates has resulted in materials with very low microwave losses. Currently, the best reported films have surface resistivities in the range of 0.1 m $\Omega$  at 77 K and 10 GHz [1]. When extrapolated assuming an  $f^2$  dependence, surface resistivities lower than that of copper are seen to be possible to beyond 100 GHz. The availability of such low-loss films has spurred interest in microwave applications for these films. Frequently mentioned examples of where high-temperature superconductors could have an impact are microstrip filters [2], delay lines, and feed networks for monolithic antenna arrays [3] where overall circuit and system performance may be improved by the low-loss superconducting lines.

The microwave loss of the superconducting films is generally measured by one of several techniques, which

may be grouped into two categories: 1) those that do not require patterning of the film, such as cavity techniques [4] or microwave transmission studies [5], and 2) those that pattern the film into some form of planar transmission line resonator [6]. Measurements on the patterned films are believed to give a more complete assessment of the superconductor performance in planar microwave circuits since factors such as dielectric loss, substrate/film interface imperfections, and edge damage caused by patterning are included in the response of the circuit. Such patterned film techniques have a drawback, however, in that values of the surface resistance ( $R_s$ ) are difficult to extract, and the circuit  $Q$  values have little importance in comparisons between different test circuits. Nevertheless, these techniques, when coupled with reasonable attempts at modeling, can provide valuable insight into HTS microwave circuit performance.

A number of HTS surface resistance measurements exist ranging from 1 to 100 GHz [1]; these represent both cavity-type and patterned resonator measurements, although patterned resonator measurements are generally restricted to below 15 GHz. Because the superconductor's surface resistance increases as the frequency squared, smaller relative improvements over normal metals are expected as the frequency increases. Measurements on patterned resonators at millimeter-wave frequencies are therefore of interest in assessing the performance level possible when high-temperature superconductors are used at these frequencies and in determining the factors that limit such circuits' performance.

In this paper, we present results from the study of microstrip ring resonators at 35 GHz. These resonators were fabricated from single-sided YBCO films deposited by laser ablation on lanthanum aluminate ( $\text{LaAlO}_3$ ). The response of the resonator was observed as a function of temperature, noting the resonator  $Q$  and the resonant frequency as well as the effect of the microwave drive power on the circuit performance. The results were compared with a gold implementation of the circuit. In addition to the comparison with the gold circuit, a microstrip loss model, the phenomenological loss equivalence method (PEM) was used to calculate surface resistances for the HTS films and an effective superconducting penetration depth was calculated. The factors limiting the circuit performance are discussed, and with the aid of the best published values for the superconducting surface resistance, potential circuit performance levels are calculated.

Manuscript received November 19, 1990; revised April 25, 1991.

C. M. Chorey is with the LeRC Group, Sverdrup Technology, 2001 Aerospace Parkway, Brook Park, OH 44142.

K. S. Kong is with the Electrical and Computer Engineering Department, University of Texas at Austin, Austin, TX 78712.

K. B. Bhasin and J. D. Warner are with the NASA Lewis Research Center, 21000 Brookpark Rd., Cleveland, OH 44135.

T. Itoh was with the Electrical and Computer Engineering Department, University of Texas at Austin. He is now with the Department of Electrical Engineering, UCLA, Los Angeles, CA 90024.

IEEE Log Number 9101199.

## II. CIRCUIT FABRICATION AND TESTING

### A. Film Growth and Patterning

The superconducting YBCO films used in this study were produced by laser ablation of a  $\text{YBa}_2\text{Cu}_3\text{O}_{7-x}$  (YBCO) target onto one side of a heated lanthanum aluminate substrate. A 248 nm pulsed excimer laser with a pulse rate of 2 pps and a laser fluence of  $2 \text{ J/cm}^2$  was used to ablate a  $\text{YBa}_2\text{Cu}_3\text{O}_{7-x}$  stoichiometric pellet with a density of 95% of theoretical. The laser was rastered over the target by means of an external lens, and the deposition rate was approximately  $100 \text{ \AA}$  per minute. The substrates were mounted on a heated ( $\sim 755^\circ \text{C}$ ) stainless steel block 7.5 cm from the target and exposed to an ambient oxygen atmosphere of 170 mtorr during deposition. Following deposition, the oxygen pressure was raised to 1 atm, the block temperature lowered to  $450^\circ \text{C}$ , and the sample allowed to anneal at that temperature for two hours. Then the block was slowly cooled in oxygen to room temperature before removing the sample from the growth chamber. Film thicknesses were typically in the range of  $3000 \text{ \AA}$  to  $6000 \text{ \AA}$  and substrates slightly in excess of  $1 \text{ cm}^2$  could be covered.

When observed in an optical or scanning electron microscope, the samples were generally found to be smooth and featureless but occasional surface roughness or particulates from the ablation process could be found. No misaligned platelets or indications of second phases were found in these examinations. X-ray diffraction analysis of the samples confirmed that to within the test resolution, the material was *c*-axis aligned and free of secondary phases. Transition temperatures ( $T_c$ ) of up to 90 K were achieved.

The superconducting films were patterned into resonators by wet etching and standard photolithography. A positive photoresist was spun on, exposed, and developed in normal processing fashion. The films were then etched in a dilute solution of phosphoric acid in water (1:100: $\text{H}_2\text{O}$ : $\text{H}_3\text{PO}_4$ ). The etch was quick, but undercutting was found to be minimized by the use of the very dilute solutions. Following etching, the photoresist was stripped in acetone. Since the samples had superconducting films on only one side of the substrate, a normal metal ground plane was evaporated to complete the circuit. First,  $100 \text{ \AA}$  of titanium was deposited to promote adhesion of the gold layer, which was then evaporated. The ground plane thickness was slightly in excess of  $1 \text{ \mu m}$ .

### B. Circuit Testing

The resonant circuit consisted of a microstrip ring with a  $3\lambda$  resonance near 35 GHz; it is shown schematically in Fig. 1. The strip width was  $143 \text{ \mu m}$  and the mean diameter of the ring was  $1980 \text{ \mu m}$ . The ring was coupled to a single microstrip feed line via a capacitive gap  $47 \text{ \mu m}$  across. The substrate thickness was  $254 \text{ \mu m}$  (10 mils) to avoid substrate modes at 35 GHz. A normal metal ground plane was used and its thickness was  $1 \text{ \mu m}$ . Calculations

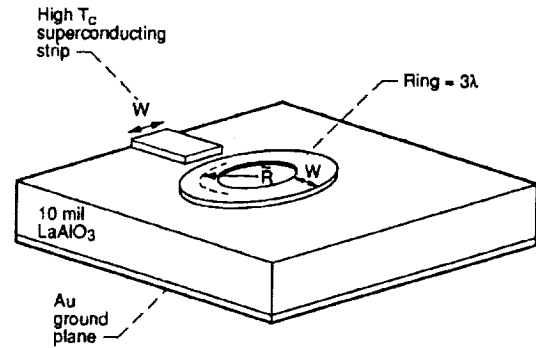


Fig. 1. A schematic drawing of the circuit used in this study. The microstrip ring was three wavelengths in circumference at 35 GHz. The line width was  $143 \text{ \mu m}$  and the substrate thickness  $254 \text{ \mu m}$ . The calculated line impedance was  $38 \text{ \Omega}$ .

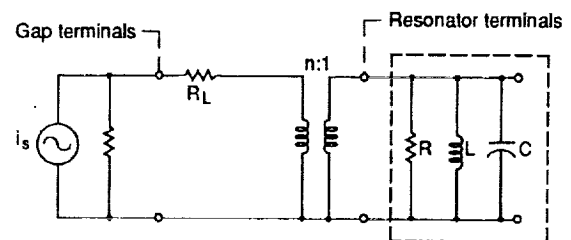


Fig. 2. The circuit model used to extract the unloaded  $Q$ . The coupling gap between the ring and feedline is modeled as an ideal transformer plus a series loss.

of the line impedance by the method of Wheeler [7] and using the observed effective dielectric constant gave values of  $\sim 38 \text{ \Omega}$ .

Since the ring had only one port, the resonance was measured via the reflected power. The circuits were measured using a Hewlett Packard 8510 network analyzer with a WR-28, Ka-band waveguide option. Transition from the waveguide mode to the microstrip was accomplished by a cosine tapered *E*-plane ridge in a section of WR-28 waveguide [8]. The ridge contacted the end of the microstrip feedline at the edge of the substrate and launched the quasi-TEM microstrip mode. A standard waveguide calibration was performed at the plane where the tapered ridge fixture was connected. This calibration was performed at room temperature only and was assumed to be valid over the entire temperature range. Measurements were made using a closed-cycle helium refrigerator with a vacuum enclosure around the cold finger. Sample temperatures could be controlled from room temperature to between 10 K and 20 K. Normal signal levels at the calibration plane were  $0.45 \text{ mW}$ ; however the level could be varied from  $0.10$  to  $10 \text{ mW}$  for study of the power dependence of the HTS film properties.

The reflection data from the resonators provided a measure of the loaded  $Q$ ; the unloaded  $Q$ 's were calculated from these data using the model shown in Fig. 2 [9], where the ring resonance is modeled as a simple *RLC*

circuit and the coupling gap as an ideal transformer with series loss. By circuit analysis of the model, the impedance of the isolated ring, and its  $Q$  (the unloaded  $Q$  or  $Q_0$ ) is found to be

$$Z_{res} = \left[ \frac{1}{R} + j \left( \omega C - \frac{1}{\omega L} \right) \right]^{-1} \quad (1)$$

$$Q_0 = \omega_0 CR \quad (2)$$

where  $\omega$  is the angular frequency,  $\omega_0$  the resonant frequency, and  $R$ ,  $C$ , and  $L$  the distributed resistance, capacitance, and inductance of the line. This represents the impedance and  $Q$  of the ring only, unperturbed by the input line. The loaded  $Q$ , the quantity actually measured, is the response of the ring loaded by the line impedance and coupling loss as transformed by the coupling gap. The impedance of this equivalent circuit and its  $Q_L$  (the loaded  $Q$ ) is

$$Z_{loaded} = \left[ \frac{n^2}{(Z_0 + R_L)} + \frac{1}{R} + j \left( \omega C - \frac{1}{\omega L} \right) \right]^{-1} \quad (3)$$

$$Q_L = \frac{\omega_0 CR(1 + \sigma)}{(1 + \sigma + \kappa)} = \frac{Q_0(1 + \sigma)}{(1 + \sigma + \kappa)} \quad (4)$$

where  $\sigma = R_L/Z_0$  and  $\kappa = Rn^2/Z_0$ . The values of  $\sigma$  and  $\kappa$  relating the loaded and unloaded  $Q$ 's can be determined from the reflection coefficient of the resonator. Far from the resonance, the reflection coefficient is given by

$$\Gamma = \frac{(\sigma - 1)}{(\sigma + 1)} \quad (5)$$

while at resonance

$$\Gamma = \frac{(\sigma + \kappa - 1)}{(\sigma + \kappa + 1)}. \quad (6)$$

Using the values of  $\sigma$  and  $\kappa$  obtained through  $\Gamma$  at these points and the measured loaded  $Q$ , the unloaded  $Q$  was determined using (4). The determination of whether the resonator was overcoupled or undercoupled was made from an examination of the Smith chart.

### III. CIRCUIT PERFORMANCE

#### A. Resonator $Q$ and Surface Resistance

Several superconducting resonators were fabricated and tested. In all cases the YBCO resonators showed no resonance above  $T_c$  owing to the high normal state resistivity of the YBCO material. At a point a few degrees below  $T_c$ , low- $Q$  resonances appeared which quickly sharpened and rose above the unloaded  $Q$  values measured for gold resonators at those temperatures. The temperature at which the crossover between the superconducting resonator and the gold resonator occurred was dependent on the quality of the superconducting film, with the film  $T_c$  being a first-order indicator of the quality. Unloaded  $Q$ 's for the superconducting resonators

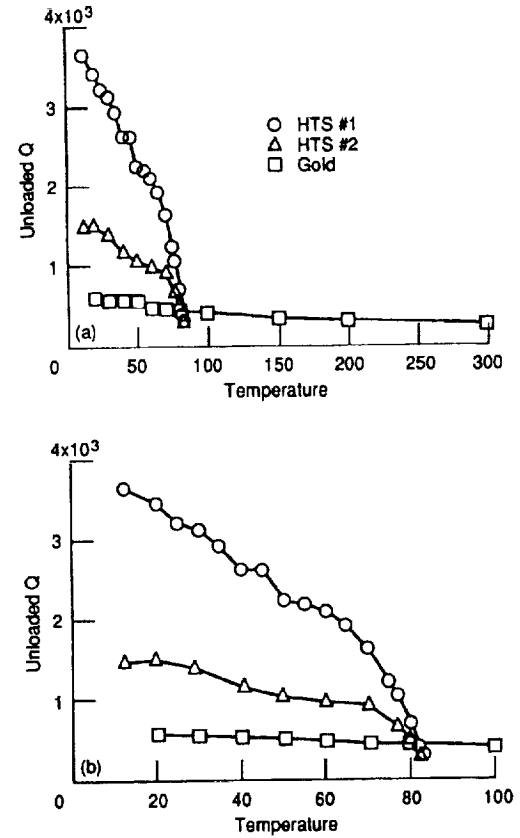


Fig. 3. Measured  $Q$  values for gold and superconducting resonators over the range (a) 0 to 300 K and (b) 0 to 100 K. The  $Q$  of the gold resonator increases by only a factor of 2 in cooling from 300 K to 20 K. The superconducting resonators show only marginal improvement over the gold resonator at 77 K, while operation at lower temperatures provides more substantial improvement.

continued to rise with decreasing temperature, though at a decreasing rate. Fig. 3 shows the unloaded  $Q$  versus temperature between 0 and 300 K (a) and 0 and 100 K (b) for two superconducting resonators and a gold resonator. The difference in the  $Q$  values between samples HTS#1 and HTS#2 is typical of the spread among the many superconducting resonators that were measured. Circuit performance ranged from only slightly better than gold across a wide temperature range to the best results as shown for HTS#1. A strong correlation was observed between the unloaded  $Q$  values and the film  $T_c$  [10]; films with higher  $T_c$ 's generally had higher  $Q$ 's. Film  $T_c$ 's included in this study ranged from  $\sim 84$  to 89 K.

The effect of the microwave drive power on the  $Q$  of superconducting films HTS#1 and HTS#2 is shown in parts (a) and (b) of Fig. 4, respectively, where the  $Q$  is plotted versus the microwave input power at three temperatures. The microwave power, as measured at the calibration plane, was varied from 0.25 mW to 10 mW. It is seen that there is no degradation in the performance for either film for this range of powers. In general, the laser-ablated films tended to show no power dependence up to at least 10 mW unless the film was of particularly

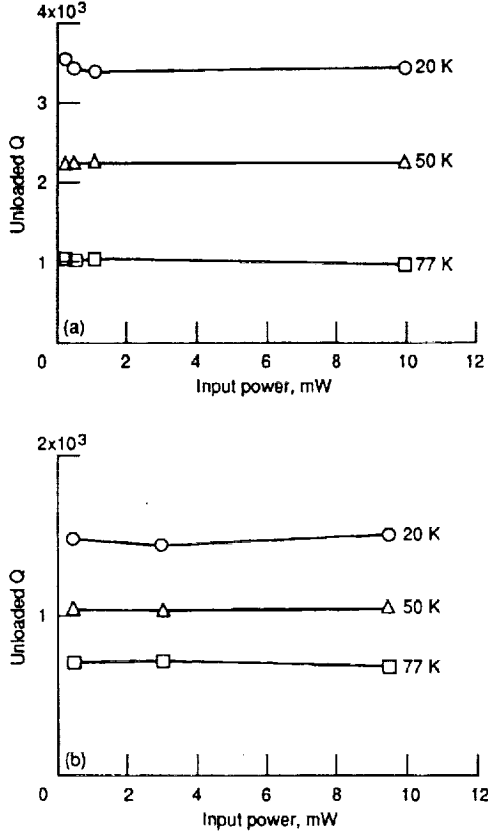


Fig. 4. Dependence of the superconducting resonator  $Q$  on the microwave input power for (a) HTS#1 and (b) HTS#2. The laser-ablated films did not show any power dependence.

low quality (i.e.,  $T_c < 80$  K and/or poor morphology).

The performance of the superconducting resonators, as shown in Fig. 3, provides some improvement over the gold circuit, with a factor of 2 increase in the unloaded  $Q$  at 77 K which grows to a factor of 7 at 20 K. This level of improvement is below the levels reported for X-band resonators, where order of magnitude improvements at 77 K are reported [11]. However, when the  $f^2$  dependence of the superconducting surface resistance is considered, it is seen that smaller improvements over normal metal circuits are expected at higher frequencies. To assess the magnitude of the observed improvements and to determine whether better performance may be expected, modeling of the microstrip is necessary to account for the superconductor surface resistance. Such a model will not only allow prediction of circuit performance given the surface resistance; it will also allow the surface resistance to be inferred from measured  $Q$  data. The development of accurate equations for the superconducting microstrips is limited by the lack of precise values for the dielectric constant and loss tangent of the  $\text{LaAlO}_3$  substrates and because the accuracy of existing closed-form expressions for microstrip structures is unknown when applied to high-dielectric-constant substrates such as  $\text{LaAlO}_3$ . Nevertheless, by matching experimental results from thin gold

circuits where the surface resistance is reasonably known, sufficiently accurate expressions may be found to model the superconducting strips. For this work we have used the PEM [12].

The basis of the PEM method is that the internal impedance of the conductors (meaning the resistance and reactance arising from the field penetration into the strip and ground plane) can be calculated as the product of the surface impedance of the material, a geometric factor ( $G$ ) determined by the line geometry, and a corrective term for the conductor thickness:

$$Z_{\text{internal}} = Z_{\text{surface}} \cdot G \cdot \coth[\tau t_c]. \quad (7)$$

Separate  $G$  factors are calculated for the strip and ground plane. The thickness correction for the strip is calculated from an effective thickness for the conductor,  $t_e$ , and a complex decay constant,  $\tau$ , which accounts for the field decay into the conductor. These are calculated as

$$t_e = G \times (\text{cross-sectional area of strip})$$

$$\tau = (j\omega\mu\sigma)^{1/2}$$

where  $\mu$  is the permeability of vacuum and  $\sigma$  the complex conductivity. The thickness correction for the ground plane is determined from the actual conductor thickness and the decay constant,  $\tau$ . The geometric factors for the strip and ground plane are calculated by the incremental inductance rule [13]:

$$G = \frac{1}{\mu} \sum_i \frac{\partial L}{\partial n_i} \quad (8)$$

where  $\partial L / \partial n_i$  is the derivative of the external inductance with respect to an incremental recession of the wall  $i$ .

We have used the equations of [11] to calculate the  $G$  factors for the strip and ground plane:

$$G_{\text{strip}} = \frac{2}{2\pi d} \cdot \left[ 1 - \left[ \frac{w}{4d} \right]^2 \right] \cdot \left[ \frac{1}{2} + \frac{d}{w} + \frac{d}{\pi w} \ln(2d/t) \right] \quad (9)$$

$$G_{\text{ground}} = \frac{1}{2\pi d} \cdot \left[ 1 - \left[ \frac{w}{4d} \right]^2 \right] \quad (10)$$

where  $d$  is the substrate thickness,  $w$  is the strip width, and  $t$  is the conductor thickness.  $Q$ 's were calculated by the standard formula:

$$Q = \frac{\beta}{2\alpha} = \frac{\beta}{2(\alpha_{\text{conductor}} + \alpha_{\text{dielectric}} + \alpha_{\text{radiation}})}. \quad (11)$$

The  $\alpha_{\text{conductor}}$  is computed from the real part of the internal impedance as calculated from the PEM. The  $\alpha_{\text{dielectric}}$  is computed from the expression [11]

$$\alpha_{\text{dielectric}} = \frac{27.3}{8.68} \cdot \left[ \frac{qk}{k_{\text{eff}}} \right] \cdot \frac{\tan \delta}{\lambda_g} \quad \left[ \frac{\text{nepers}}{\text{meters}} \right]$$

$$q = \left[ \frac{k_{\text{eff}} - 1}{k - 1} \right] \quad (12)$$

where  $k$  is the dielectric constant of the substrate and  $k_{\text{eff}}$

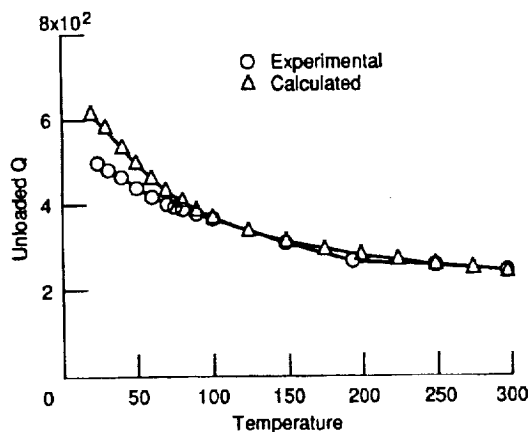


Fig. 5. Measured  $Q$  values for a thin gold resonator and values calculated using PEM. The agreement is within 10% to about 100 K. Increasing deviation below 100 K is due to errors in the calculated  $R_s$  value for gold at those temperatures.

is the effective dielectric constant experienced by the propagating wave. The radiation loss is assumed to be negligible owing to shielding of the circuit. Values for  $\beta$  were determined experimentally from the resonant frequency of the ring and the known circumference.

As a test of the PEM method, the  $Q$  values were calculated for a thin gold resonator (1  $\mu\text{m}$  thick gold) and compared with the experimentally determined values. The dc resistivity of the gold in the ring was measured across the temperature range using a four point probe technique. The values of the resistivity were then used to calculate the microwave surface resistance ( $R_s$ ) and penetration depth ( $\delta_s$ ) at the different temperatures using  $R_s = (\omega\mu/2\sigma)^{1/2}$  and  $\delta_s = (2/\omega\mu\sigma)^{1/2}$ . A value of  $8.3\text{E-}5$  was used for the dielectric loss tangent. The results of the calculation are shown in Fig. 5. The match is within 10% across most of the temperature range, with increasing deviation below 100 K. Comparisons between experimental and computed values for 0.45 and 1.5  $\mu\text{m}$  thick gold resonators also showed agreement within 10% above 100 K with increasing deviation below. The larger deviations at low temperatures do not appear to be a defect of the model, but rather appear to derive from incorrect values for the surface resistance of the gold. Nonidealities such as surface scattering are not accounted for by the simple surface resistance equation used, and probably result in an underestimation of the actual surface resistance. Thus the PEM equations adequately model the losses for the microstrip structure.

The PEM method was next applied to the superconducting resonator results using  $R_s$  values for the gold ground plane that were corrected to match the gold resonator experimental results below 100 K. The same value for  $\tan \delta$  as used in the gold resonator calculations was used here. Calculations were done with three values of the penetration depth, since this parameter is not known with a high degree of certainty. (Calculations in the following section give a value of approximately 3000

TABLE I  
MICROWAVE SURFACE RESISTIVITY COMPUTED  
FROM THE SUPERCONDUCTING RESONATOR  
 $Q$  VALUES USING PEM

| HTS#1: 0° Penetration Depth, $\lambda_0$ |         |        |        |
|--|---------|--------|--------|
|  | 1500 Å  | 3000 Å | 4500 Å |
| 20°                                      | 1 mΩ    | 0.8 mΩ | 0.7 mΩ |
| 50°                                      | 3.4 mΩ  | 2.9 mΩ | 2.5 mΩ |
| 77°                                      | 12 mΩ   | 9 mΩ   | 7 mΩ   |
| HTS#2: 0° Penetration Depth, $\lambda_0$ |         |        |        |
|  | 1500 Å  | 3000 Å | 4500 Å |
| 20°                                      | 7 mΩ    | 5 mΩ   | 3.7 mΩ |
| 50°                                      | 10.4 mΩ | 7.1 mΩ | 5.5 mΩ |
| 77°                                      | 15 mΩ   | 9.1 mΩ | 6.3 mΩ |

Å.) The results are summarized in Table I, where we see that  $R_s$  values computed at 77 K for HTS#1 lie in the range from 12 mΩ to 7 mΩ, and those for HTS#2 from 15 mΩ to 6 mΩ. These computed values of  $R_s$  at 77 K are somewhat higher than those for the best reported films (1–4 mΩ) [1]. If surface resistance values of the order of the best reported can be achieved in patterned strips, then better circuit performance than observed here can be achieved.

To determine the levels of performance possible in this circuit, the PEM can be used to calculate projected  $Q$  values. If a best value of  $R_s = 1$  mΩ at 77 K is assumed and the present gold ground plane retained, a circuit  $Q$  of  $\sim 2500$  is calculated, a factor of 5 higher than that for the all-gold circuit. The gold ground plane, in this case, limits the circuit  $Q$ . To achieve higher circuit  $Q$ 's a superconducting ground plane is needed. If the gold ground is replaced with a 1 mΩ superconductor the  $Q$  rises to  $\sim 5000$ , an order of magnitude higher than for the gold circuit. Thus an order of magnitude improvement is possible at 77 K if surface resistivities of  $\sim 1$  mΩ can be achieved and superconducting strips and ground planes are used. It should be noted, though, that this  $R_s$  value of 1 mΩ at 77 K, 35 GHz represents the lowest reported value for current YBCO material. For superconducting films with surface resistances higher than this, operation at lower temperatures would be necessary to achieve comparable improvements. The effect of the dielectric loss (assuming  $\tan \delta = 8.3\text{E-}5$ ), while not dominant for the above conditions, is comparable in magnitude ( $\alpha_{\text{dielectric}} = 0.12$  nepers/meter) to the conductor losses and contributes to the total  $Q$  by an amount that cannot be neglected. As the conductor losses decrease, because of either improved film quality or lower operating temperature, the dielectric loss becomes dominant and will begin to limit the circuit performance.

### B. Resonant Frequency Shift and Penetration Depth

Fig. 6 shows the resonant frequency as a function of temperature for both a superconducting ring and a gold ring. It is seen that both circuits undergo a shift in the resonant frequency to higher values as the temperature is decreased. The resonant frequencies do not coincide in the common temperature range of the two films owing to

scatter in the substrate thicknesses among samples as well as differences in the line widths (a consequence of minor undercutting during etching). The magnitude of the shift for both the superconducting ring and the gold ring is of the order of 1% for the temperature range over which each circuit is operational. For the superconducting circuit, there is a very rapid change just below  $T_c$  and any practical circuit operating in this region would be susceptible to drift with any thermal fluctuations. Such drift would be most severely felt in narrow-band circuits or applications requiring a high degree of stability. Operation at 77 K is on the edge of this region and may or may not provide adequate stability depending on the requirements of the circuit.

The causes for the resonance shifts are different for the two circuits. The gold circuit has been analyzed with the data available on lanthanum aluminate, and the resonance shift was found to correspond to that which would be expected from the thermal contraction in the substrate. The shift of the superconducting resonator is due mostly to the change in the magnetic penetration depth in the superconducting strip with temperature, although other effects, among them thermal contraction, are embedded in the response also. By analysis of the frequency shift it is possible to extract a value for the penetration depth.

As a first approximation in this analysis, it is assumed that the shift of the superconducting resonator is due entirely to the changing penetration depth. The penetration depth affects the resonant frequency through the distributed inductance of the line. Specifically, the changing field penetration in the conductors results in a change in the internal reactance of the line. The resonant frequency may be related to the inductance through the standard expression for the propagation constant of a transmission line:

$$\beta = \frac{2\pi}{\lambda_g} = 2\pi f(LC)^{1/2}$$

where  $\lambda_g$  is the guide wavelength,  $f$  the frequency, and  $L$  and  $C$  the distributed inductance and capacitance of the line. For the ring resonator at resonance, we know that the circumference ( $D$ ) is equal to an integral number of wavelengths (for this resonator,  $n = 3$ ); thus,

$$\lambda_g = D/3 \quad \text{and} \quad f_0\{T\} = \frac{3}{D\{T\}} \cdot \frac{1}{(L\{T\}C\{T\})^{1/2}} \quad (13)$$

where  $f_0$  is the resonant frequency and the notation " $\{T\}$ " denotes that the terms are functions of temperature. If we call  $f_0\{0\}$  the resonant frequency at 0 K, then

$$\frac{f_0\{T\}}{f_0\{0\}} = \frac{D\{0\}(L\{0\}C\{0\})^{1/2}}{D\{T\}(L\{T\}C\{T\})^{1/2}} \quad (14)$$

As a first-order approximation we assume that  $C\{T\} = C\{0\}$  and  $D\{T\} = D\{0\}$ ; i.e., we ignore any thermal contraction

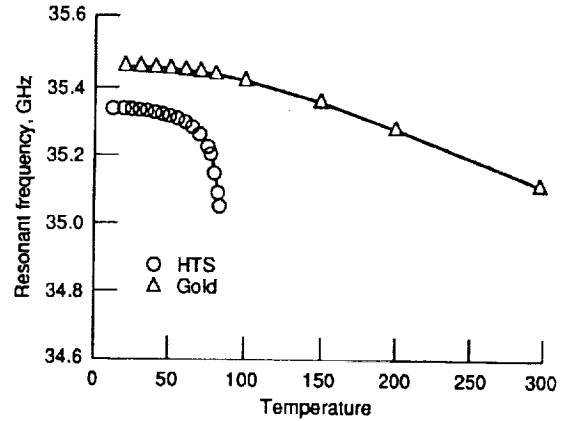


Fig. 6. The resonant frequency as a function of temperature for superconducting and gold resonators. The shift in the gold resonator is due mostly to thermal contraction in the substrate. The shift in the superconducting resonator is primarily due to the changing magnetic penetration depth with temperature.

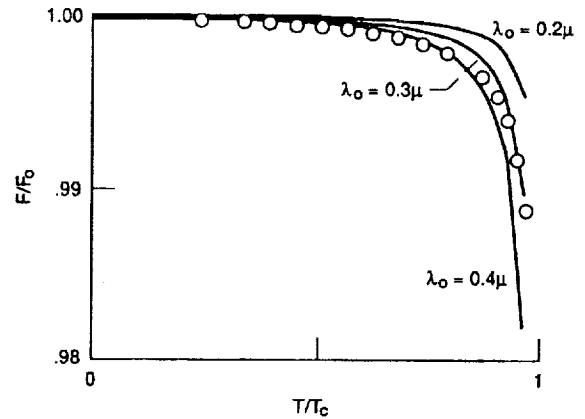


Fig. 7. Analysis to determine the penetration depth. The best fit to the experimental points gives a value of 3000 Å for the penetration depth.

in the substrate. Then

$$\frac{f_0\{T\}}{f_0\{0\}} = \left[ \frac{L\{0\}}{L\{T\}} \right]^{1/2} \quad (15)$$

Now the inductance of the transmission line is composed of three components, from the fields external to the conductors and the fields inside the strip and ground plane. The inductance due to the penetration into the strip and ground is attained from the imaginary part of the internal impedance as calculated from the PEM (preceding section). The expression used for the external inductance is the one that formed the basis for calculating the  $G$  factors in the PEM [13]:

$$L_e = \frac{\mu_0}{2\pi} \left[ \ln(8d/w) + \frac{1}{32} (w/d)^2 \right] \quad (16)$$

An analysis for HTS#1 is shown in Fig. 7. The best fit to the data gives a  $\lambda_0$  value of 3000 Å; similar analysis for HTS#2 also gave a value of  $\sim 3000$  Å.

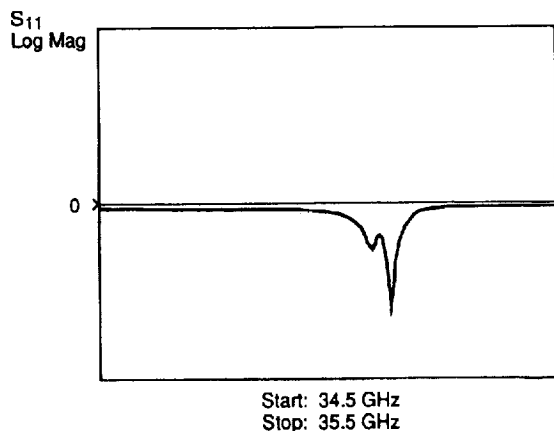


Fig. 8. An example of the double resonance that was seen in several superconducting resonators. The appearance of two peaks can be explained by an discontinuity within the ring. This discontinuity may be due to inhomogeneities in the superconducting film or in the substrate.

### C. Double Resonances in Superconducting Rings

A phenomenon seen in superconducting resonators several times in the course of this study was the splitting of the single resonance peak into two or more overlapping peaks, as illustrated in Fig. 8. Analysis of such resonators was hampered because the overlapping resonances did not allow  $Q$  values to be calculated with a degree of accuracy. The splitting of a ring resonance can be explained by a discontinuity in some region of the ring [14]. This discontinuity can be in either the HTS film or the substrate, but in either case it will set up standing waves which vary slightly in frequency, thus producing two closely spaced resonance peaks. Examination in an optical microscope of the superconducting resonators that showed the splitting did not reveal any obvious defects in the strip. The lanthanum aluminate substrates contain a large number of twins and it is possible that the splitting may be traced to this. At this point, however, no clear determination of the cause can be arrived at. It can only be noted that superconducting films, including films that otherwise appear of high quality, are susceptible to regions of inhomogeneity that can produce such discontinuities. It should be pointed out that similar effects will not be seen in linear resonators since a discontinuity would divide the line into two smaller sections that would show resonances at frequencies above the primary resonance of the line and so be missed.

## IV. CONCLUSIONS

Microstrip ring resonators with YBCO superconducting strips and gold ground planes have been fabricated and tested at 35 GHz. These circuits showed higher unloaded  $Q$ 's than identical resonators with gold strips and ground planes; the best circuit achieved a factor of 2 improvement at 77 K and reached a factor of 7 improvement at 20 K. Because of the  $f^2$  dependence of the superconductor surface resistance, smaller relative improvements over

normal metal circuits are expected at millimeter-wave frequencies. However, modeling using PEM indicated an  $R_s$  value of  $\sim 10$  m $\Omega$  at 77 K, which is higher than the best reported value of 1–4 m $\Omega$  at that frequency and temperature. This indicates that improvements in circuit performance over those observed here are possible if patterned strips exhibiting lower surface resistance can be fabricated. To achieve an order-of-magnitude increase in unloaded  $Q$  at 77 K over the normal metal circuit, calculations suggest that a normal ground plane cannot be used. If both strip and ground were superconducting material with an  $R_s$  of 1 m $\Omega$ , which represents the lowest values reported to date at 35 GHz and 77 K, then an order-of-magnitude improvement at 77 K would be possible.

Observation of the resonant frequency versus temperature of the superconducting resonator showed a shift of approximately 1% from just below  $T_c$  to 20 K. Operation at 77 K places the circuit away from the steepest part of the frequency versus temperature curve, but still on the "knee," indicating possible thermal stability problems for very narrow band circuits operated at that point. An analysis of the frequency shift indicated a value of 3000 Å for the effective penetration depth,  $\lambda_0$ .

Millimeter-wave superconducting circuits were found to severely test the quality of superconducting films. To achieve significant improvements in loss characteristics over normal metal lines at these frequencies, the highest quality films and/or operation below 77 K are required.

## REFERENCES

- [1] H. Piel and G. Muller, "The microwave surface impedance of high- $T_c$  superconductors," *IEEE Trans. Magn.*, vol. 27, pp. 854–862, Mar. 1991.
- [2] D. B. Rensch *et al.*, "Fabrication and characterization of high- $T_c$  superconducting X-band resonators and bandpass filters," *IEEE Trans. Magn.*, vol. 27, pp. 2553–2556, Mar. 1991.
- [3] R. C. Hansen, "Superconducting antennas," *IEEE Trans. Aerosp. Electron. Syst.*, vol. 26, pp. 345–355, Mar. 1990.
- [4] N. Klein *et al.*, "Millimeter wave surface resistance of epitaxially grown  $\text{YBa}_2\text{Cu}_3\text{O}_{7-x}$  thin films," *Appl. Phys. Lett.*, vol. 54, pp. 757–759, Feb. 1989.
- [5] F. A. Miranda, W. L. Gordon, K. B. Bhasin, J. D. Warner, and G. J. Valco, "Millimeter wave transmission studies of  $\text{YBa}_2\text{Cu}_3\text{O}_{7-x}$  thin films in the 26.5 to 40 GHz frequency range," in *Superconductivity and applications*, H. S. Kwok *et al.*, Eds. New York: Plenum Press, 1990, pp. 163–167.
- [6] A. A. Valenzuela and P. Russer, "High  $Q$  coplanar transmission line resonator of  $\text{YBa}_2\text{Cu}_3\text{O}_{7-x}$  on  $\text{MgO}$ ," *Appl. Phys. Lett.*, vol. 55, no. 10, pp. 1029–1031, Sept. 1989.
- [7] K. C. Gupta, R. Garg, and I. J. Bahl, *Microstrip Lines and Slotlines*. Norwood, MA: Artech House, 1979, pp. 7–13.
- [8] R. R. Romanofsky and K. A. Shalkhauser, "Universal test fixture for monolithic mm-wave integrated circuits calibrated with an augmented TRD algorithm," NASA Technical Paper, TP-2875, Mar. 1989.
- [9] E. L. Ginzton, *Microwave Measurements*. New York: McGraw-Hill, 1957, pp. 391–434.
- [10] C. M. Chorney *et al.*, "An experimental study of high  $T_c$  superconducting microstrip transmission lines at 35 GHz and the effect of film morphology," *IEEE Trans. Magn.*, vol. 27, pp. 2940–2943, Mar. 1991.
- [11] P. A. Polakos, C. E. Rice, M. V. Schneider, and R. Trambarulo, "Electrical characteristics of thin-film  $\text{Ba}_2\text{YCu}_3\text{O}_{7-x}$  supercon-

- ducting ring resonators," *IEEE Microwave and Guided Wave Lett.*, vol. 1, pp. 54–56, Mar. 1991.
- [12] H. Y. Lee and T. Itoh, "Phenomenological loss equivalence method for planar quasi-TEM transmission lines with a thin normal conductor or superconductor," *IEEE Trans. Microwave Theory Tech.*, vol. 37, pp. 1904–1909, Dec. 1989.
- [13] R. A. Pucel, D. J. Masse, and C. P. Hartwig, "Losses in microstrip," *IEEE Trans. Microwave Theory Tech.*, vol. MTT-16, pp. 342–350, 1968; correction, vol. MTT-16, p. 1064, 1968.
- [14] N. J. Rohrer *et al.*, "Sequentially evaporated thin film  $\text{YBa}_2\text{Cu}_3\text{O}_{7-x}$  superconducting microwave ring resonator," in *Proc. Conf. Science and Technology of Thin Film Superconductors* (Denver CO), May 1990.

# PERFORMANCE OF A K-BAND SUPERCONDUCTING ANNULAR RING ANTENNA

M. A. Richard

Department of Electrical Engineering and Applied Physics  
Case Western Reserve University  
Cleveland, Ohio 44106

K. B. Bhasin and R. Q. Lee

National Aeronautics and Space Administration  
Lewis Research Center  
Cleveland, Ohio 44135

P. C. Claspy

Department of Electrical Engineering and Applied Physics  
Case Western Reserve University  
Cleveland, Ohio 44106

## KEY TERMS

Annular ring, microstrip antenna, high-temperature superconductors

## ABSTRACT

Superconducting annular ring antennas operating in the  $TM_{12}$  mode at 21 GHz have been designed and fabricated on lanthanum aluminate substrate using a YBCO high-temperature superconducting thin film. The efficiencies and far-field antenna patterns have been measured and are compared with an identical antenna patterned with silver. The resonant frequencies and experimental far-field patterns agree well with published models, and efficiency measurements show a maximum improvement of 6% at 20 K in the efficiency of the HTS antenna when compared to the silver ring at the same temperature.

## INTRODUCTION

The recent discovery of the ceramic high-temperature superconductors (HTS) has generated much speculation into their use in microwave antenna systems. Experimental investigations of passive microwave devices such as delay lines, resonators, and filters at X-band frequencies have shown that HTS provides a substantial loss reduction over identical circuits fabricated with metals (gold, silver, or copper) [1]. However, very little experimental work has been reported in applying HTS to microstrip antennas. In this Letter, we present the first reported experimental performance of a superconducting annular ring microstrip antenna.

## THE ANTENNAS

The geometry of the annular ring microstrip antenna used in this investigation is shown in Figure 1. The antenna substrate is lanthanum aluminate. Although this material is less than ideal for microstrip antennas because of its high permittivity ( $\epsilon_r = 23$ ), it has been used extensively as a substrate for HTS circuits because of its low dielectric loss tangent and its excellent lattice match with YBCO, leading to high-quality (low-loss) films. The inner radius  $a$  is 1.36 mm and the outer radius

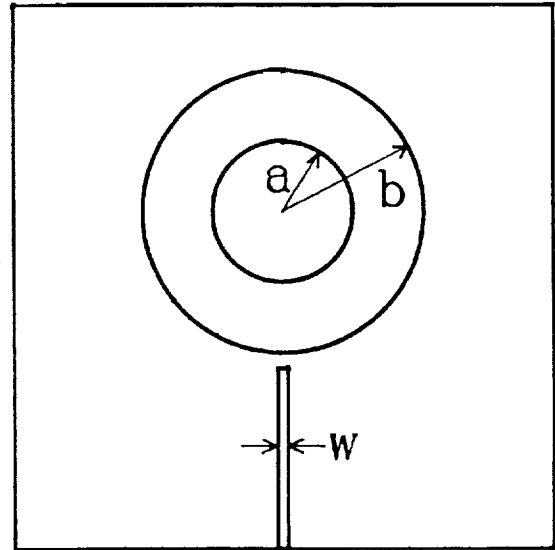


Figure 1 Annular ring antenna. Parameters are  $a = 1.36$  mm,  $b = 2.64$  mm,  $w = 0.1$  mm, and gap size  $g = 0.010$  mm. Dielectric thickness  $d = 0.254$  mm

$b$  is 2.64 mm. These dimensions were chosen for a  $TM_{12}$  mode operation in the K band. The substrate thickness  $d$  was chosen to be the minimum practical thickness of 0.254 mm to reduce surface wave generation. The antenna is capacitively gap-coupled to a 100- $\mu$ m-wide 50- $\Omega$  microstrip line via a 15- $\mu$ m-wide gap. The HTS thin film was deposited by a laser ablation process [2] and had a transition temperature ( $T_c$ ) of 89 K. A standard photolithography and wet etching process were used for fabrication. A silver contact of 2500  $\text{\AA}$  was deposited at the end of the microstrip feedline as a bonding pad. An identical antenna was fabricated with 1.6  $\mu$ m of silver for comparison purposes. Both circuits had 1.6  $\mu$ m of evaporated silver as ground planes.

## EXPERIMENTAL RESULTS

The antennas had a fundamental ( $TM_{11}$  mode) resonance at 5.52 GHz and the higher-order  $TM_{12}$ -mode resonance at 21.65 GHz. The resonant frequencies of annular rings are found by solving [3]

$$J'_n(ka)Y'_n(ka) - J'_n(kb)Y'_n(ka) = 0,$$

where  $k = 2\pi/\lambda$ . It has been shown [4] that good agreement between predicted and experimental values can only be obtained by using an effective dielectric constant  $\epsilon_{eff}$  and modified radii of

$$a_e = a - \frac{3}{4}d,$$

$$b_e = b + \frac{3}{4}d.$$

For this work, a value of 20 for  $\epsilon_{eff}$  gave agreement within 2% for all measured resonances. The computed and measured resonant frequencies of the first few resonances are given in Table 1.

For pattern measurements, the antennas were mounted in a brass test fixture and placed in a closed-cycle helium refrigerator [4]. A 2-cm-long microstrip line on alumina with a K-connector launcher was wire-bonded to the feed line on the annular ring antenna. The E- and H-plane antenna patterns for the  $TM_{12}$  mode were measured and are shown in Figure 2. These patterns compare quite well with the patterns predicted by the cavity model as given by Lee and Dahele [5] (also shown in Figure 2). Deviations of the experimental data from the predicted patterns are due to the finite ground plane, surface waves, and scattering from the test fixture.

The efficiency of these antennas were measured using the Wheeler-cap method [6]. The method consists of measuring

the input resistance at resonance with and without a radiation shield and calculating the efficiency as

$$\eta = \frac{R_{wo} - R_w}{R_{wo}}$$

where  $R_w$  and  $R_{wo}$  are the input resistances with and without the radiation shield, respectively. Newman, Bohley, and Walter [7] and Pozar and Kaufman [8] have shown that the cap size, shape, and conductivity have little effect, while good electrical contact has significant effects on antenna efficiency. For this work an aluminum cap with inner dimensions of 1.25 cm wide and deep by 0.64 cm high was used. Copper tape and silver paint ensured good electrical contact of the cap to the test fixture. The measured efficiencies are shown in Figure 3 as a function of temperature. The HTS antenna is seen to surpass the performance of the metal antenna at temperatures below 80 K, reaching a peak efficiency of 74%. A substantial portion of the lost power is dissipated as surface waves; Pozar [9] showed that about 23% of the power is dissipated as surface waves at 20 GHz due to the high permittivity of the substrate.

TABLE 1 Measured and Calculated Resonances

| Mode      | $F_{meas}$<br>(GHz) | $F_{calc}$<br>(GHz) |
|-----------|---------------------|---------------------|
| $TM_{11}$ | 5.52                | 5.46                |
| $TM_{21}$ | 10.61               | 10.65               |
| $TM_{31}$ | 15.35               | 15.44               |
| $TM_{41}$ | 19.79               | 19.89               |
| $TM_{51}$ | 24.08               | 24.14               |
| $TM_{12}$ | 21.65               | 21.70               |

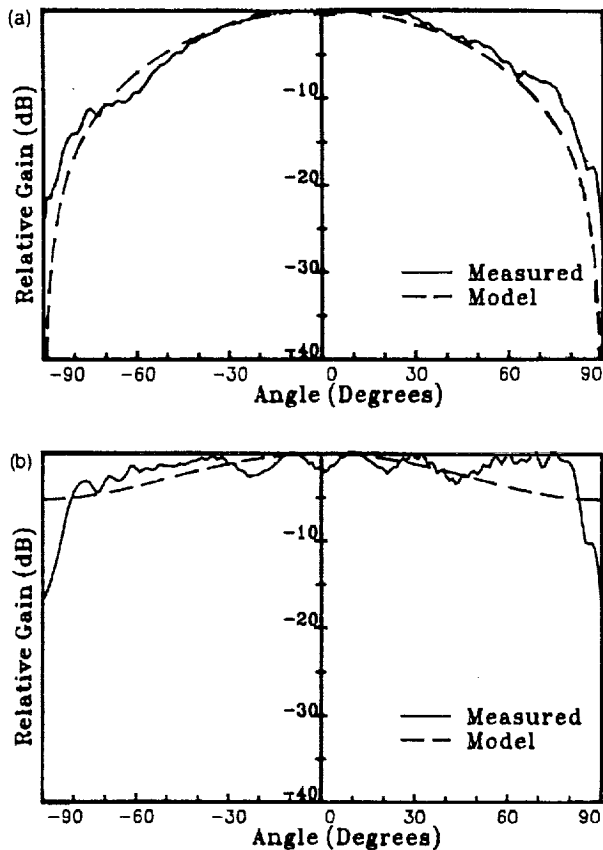


Figure 2 (a) Measured H-plane pattern, (b) measured E-plane pattern

### CONCLUSION

The performance of a superconducting annular ring antenna has been evaluated and compared with that of an identical silver antenna. Efficiency measurements show a 5% increase in performance of the HTS antenna over the silver at 77 K, and 10% at 20 K, due to the lower conductor losses of the

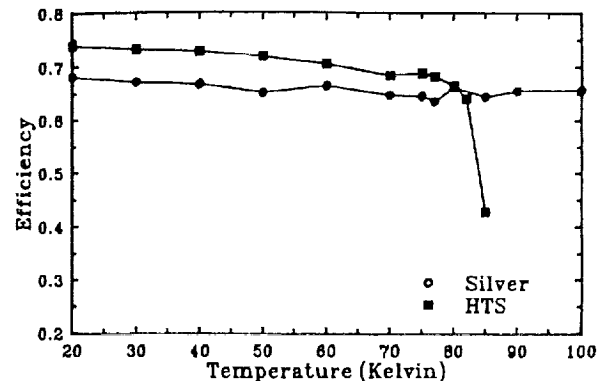


Figure 3 Efficiency of the annular rings measured using the Wheeler-cap method

HTS. Pattern measurements compare favorably with published models. Surface wave efficiency approximations show that the performance of these antennas is limited by surface wave losses.

### ACKNOWLEDGMENTS

The authors wish to acknowledge Mr. Joseph Warner for fabricating the HTS thin films used in this work. One of the authors (M. A. Richard) acknowledges support through the Ohio Aerospace Institute Doctoral Fellowship.

## REFERENCES

1. *IEEE Microwave Theory Tech.*, Special Issue, Vol. 39, No. 9, Sept. 1991.
2. J. D. Warner, K. B. Bhasin, N. J. Varaljay, D. Y. Bohman, and C. M. Chorey, "Growth and Patterning of Laser Ablated Superconducting YBCO Films on LaAlO<sub>3</sub> Substrates," NASA Report No. TM-102336.
3. Y. S. Wu and F. J. Rosenbaum, "Mode Chart for Microstrip Ring Resonators," *IEEE Trans. Microwave Theory Tech.*, Vol. MTT-20, No. 7, July 1972, pp. 487-489.
4. M. A. Richard, K. B. Bhasin, C. Gilbert, S. Metzler, and P. C. Claspy, "Measurement Techniques for Cryogenic Ka-Band Microstrip Antennas." *Antenna Measurement Techniques Association Proceedings*, Oct. 1991, pp. 1.13-1.18.
5. K. F. Lee and J. S. Dahele, "Characteristics of Microstrip Antennas and Some Methods of Improving Frequency Agility and Bandwidth," in J. R. James and P. S. Hall (Eds.), *Handbook of Microstrip Antennas*, Peter Peregrinus, London, 1989.
6. H. A. Wheeler, "The Radiansphere around a Small Antenna." *Proc. IRE*, Vol. 47, Aug. 1959, pp. 1325-1331.
7. Edward H. Newman, Peter Bohley, and C. H. Walter, "Two Methods for the Measurement of Antenna Efficiency." *IEEE Trans. Antennas Propagat.*, Vol. AP-23, No. 4, July 1975, pp. 457-461.
8. David M. Pozar and Barry Kaufman, "Comparison of Three Methods for the Measurement of Printed Antenna Efficiency." *IEEE Trans. Antennas Propagat.*, Vol. 36, No. 1, Jan. 1988, pp. 136-139.
9. D. M. Pozar, "Rigorous Closed-Form Expressions for the Surface Wave Loss of Printed Antennas," *Electron. Lett.*, Vol. 26, No. 13, 1990, pp. 954-956.

Received 1-14-92



# LASER ABLATED $\text{YBa}_2\text{Cu}_3\text{O}_{7-x}$ HIGH TEMPERATURE SUPERCONDUCTOR COPLANAR WAVEGUIDE RESONATOR

G. J. Valco and A. R. Blemker  
Department of Electrical Engineering  
Ohio State University  
Columbus, Ohio 43210

K. B. Bhasin  
National Aeronautics and Space Administration  
Lewis Research Center  
Cleveland, Ohio 44135

## KEY TERMS

High- $T_c$  superconductor, coplanar waveguide, resonator, laser ablated thin film

## ABSTRACT

We have fabricated and tested several 8.8-GHz coplanar waveguide resonators made from laser ablated  $\text{YBa}_2\text{Cu}_3\text{O}_{7-x}$  thin films on  $\text{LaAlO}_3$  substrates. A quality factor of 1250 at 77 K was measured. A correlation between the microwave performance of the resonators and the critical temperature and morphology of the films was observed.

## INTRODUCTION

The development and continuing improvement of thin high-temperature superconducting  $\text{YBa}_2\text{Cu}_3\text{O}_{7-x}$  (YBCO) films has been accompanied by much interest in their application in microwave circuits. Many investigations of the microwave properties of these films have been reported [1]. Many of these investigations have employed microstrip [2, 3] and stripline [4] resonators and filters. A disadvantage of these approaches is that they require films on both sides of the substrate or on several substrates which are assembled into the appropriate structure. The coplanar transmission line geometry eliminates this difficulty. We report here the results of measurements at 8.8 GHz on several coplanar waveguide (CPW) resonators fabricated from YBCO films deposited by laser ablation onto  $\text{LaAlO}_3$  substrates. Unloaded quality factors of 1250 at 77 K and 1700 at 20 K have been observed.

## EXPERIMENTAL PROCEDURES

The YBCO films were deposited onto 0.5-mm-thick, 1 cm  $\times$  1 cm  $\text{LaAlO}_3$  substrates by laser ablation. The substrates were mounted on the surface of a heater whose temperature was measured with an imbedded thermocouple. The depositions were performed in 23-Pa oxygen at temperatures from 765 to 805 °C. A pulsed Kr-F excimer laser beam (248 nm) was scanned in one dimension across a 95% dense YBCO target which was rotating. The pulse rate was two per second and the energy density was 0.8 J/cm<sup>2</sup>. Following deposition, the temperature was ramped down to 450 °C at a rate of 2 °C/min, while the oxygen pressure was increased to 1 atm. The temperature was held there for 2 h and then ramped down to room temperature at 2 °C/min. Optical and scanning electron microscopy were used to observe the morphology of the films.

The films were patterned into CPW resonators by photolithography with Shipley 1400-31 photoresist and 100:1 deionized  $\text{H}_2\text{O}$ :phosphoric acid etchant. A plan drawing of the resonator is shown in Figure 1. The length of the resonator was 4.55 mm, while its width was 0.275 mm. The gap on each

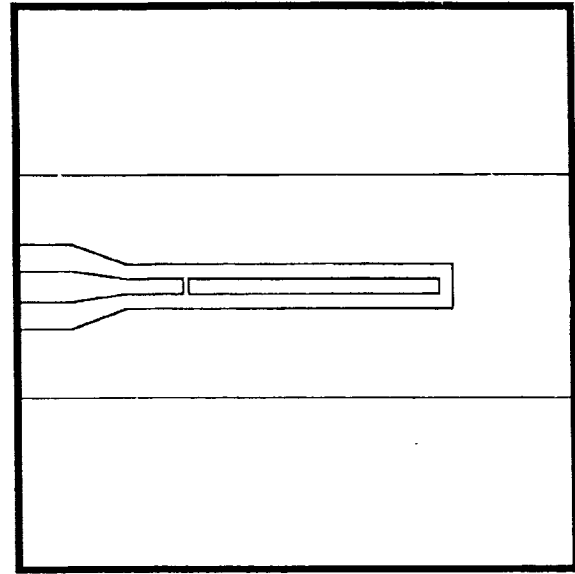


Figure 1 Plan view of a CPW resonator on a 10  $\times$  10  $\times$  0.5 mm<sup>3</sup>  $\text{LaAlO}_3$  substrate. Dimensions are given in the text. The regions outside the ground plane contain additional test structures

side of the resonator was 0.25 mm. The feed line tapered from 0.55 mm to the width of the resonator over a length of 1.0 mm. Capacitive coupling to the resonator was achieved across gaps ranging from 35  $\mu\text{m}$  to 150  $\mu\text{m}$ . A resonator of identical geometry was also fabricated from a 2.4- $\mu\text{m}$ -thick gold film.

The critical temperatures ( $T_c$ ) of the films were measured by a four contact method. Before patterning, contacts were made by wire-bonding directly to the film. After patterning they were made by wire-bonding to silver contacts on several test structures surrounding the resonator. The resonators were mounted in a gold-plated copper measurement jig which was mounted in a closed cycle cryostat. A 5-mm-deep, 6-mm-wide cavity underlaid the CPW transmission line. The reflection coefficients of the resonators were measured with an HP 8510 network analyzer with typical signal levels of 1 mW. The unloaded quality factors were determined following the procedures described in References [2] and [3], taking into account the coupling coefficient and losses.

## RESULTS

The conductor quality factor was determined from the unloaded quality factor using  $\tan \delta$  values for  $\text{LaAlO}_3$  from Reference [5]. The effective surface resistance [4, 6] was extracted from the conductor quality factor [7, 8].

The results of measurements of five superconducting resonators and one gold resonator are summarized in Table 1. The  $T_c$ 's shown were measured after patterning. The unloaded quality factors, effective surface resistances, and resonant frequencies which are listed were measured at 77 K. Sample A had an anomalously low  $T_c$ , a large number of particles on its surface (3 orders of magnitude more than the other samples), and exhibited the poorest microwave performance. Sample E had the best microwave performance. Its unloaded quality factor at 8.8 GHz and 77 K was 1250, which is nearly seven times better than that of the gold resonator. The effective surface resistance of Sample E shows a sharp drop as temperature is decreased below the critical temperature, a plateau and then a slight decrease again at low temperature.

**TABLE 1** Summary of film properties and microwave results. The microwave results are for measurements at 77 K

| Sample | Deposition Temperature (C) | Film Thickness (nm) | Critical Temperature (K) | Unloaded Quality Factor | Effective Surface Resistance (m $\Omega$ ) | Resonant Frequency (GHz) |
|--------|----------------------------|---------------------|--------------------------|-------------------------|--|--------------------------|
| Gold   | —                          | 2400                | —                        | 184                     | 28.5                                       | 8.822                    |
| A      | 805                        | 670                 | 83.7                     | 137                     | 34.1                                       | 8.658                    |
| B      | 765                        | 570                 | 87.6                     | 334                     | 13.6                                       | 8.905                    |
| C      | 765                        | 370                 | 88.2                     | 1070                    | 3.9  | 8.695                    |
| D      | 785                        | 480                 | 88.8                     | 760                     | 5.7  | 8.882                    |
| E      | 805                        | 280                 | 90.4                     | 1250                    | 3.2  | 8.852                    |

The plateau with low-temperature decrease is similar to but not as pronounced as the behavior reported in Reference [4], and was not observed in the other samples.

The unloaded quality factor is plotted as a function of temperature in Figure 2 for the gold resonator and Samples B, C, D, and E. Upon reviewing these curves and the data presented in Table 1, it can be seen that there is a tendency for the unloaded quality factor to increase and the effective surface resistance to decrease as the  $T_c$  of the film increases. Some variation with  $T_c$  is expected, particularly for films with low  $T_c$ , as the reduced temperature  $T/T_c$  for them approaches unity and 77 K would be on or near the steep transition. To study this further, the unloaded quality factors and effective surface resistances at  $T/T_c = 0.85$ , which corresponds to 77 K for Sample E, were extracted from the measurements for each sample. This places the point of comparison on the relatively flat portion of the curve for each sample. A strong variation with  $T_c$  remained, showing that the variation with  $T_c$  was not merely a result of the variation in the difference between the measurement temperature and the critical temperature.

Sample D does not fit this trend perfectly. While its  $T_c$  is better than that of both Samples B and C, its microwave properties are better than those of Sample B but worse than those of Sample C. This may be a result of the morphology of the films. Optical microscopy showed that Samples B and D had defect densities approximately three to four times higher than Sample C. The density on Sample C was such that four defects occurred in the 0.0125-cm<sup>2</sup> area of the re-

sonator. These defects were typically on the order of 5–10  $\mu\text{m}$  in size and were the result of YBCO particles being dislodged from the target during ablation. The resonator of Sample E was free of three particles.

Scanning electron micrographs of the surfaces of the films were obtained to further investigate the morphology. Sample E was observed to be very smooth and continuous. Submicron pits and voids were observed in the surfaces of the other samples. The samples can be ranked according to the density of voids in the order A, B, D, C, E, with A having the largest density of voids and E having none. This correlates exactly with the measured microwave performance.

## CONCLUSIONS

Coplanar waveguide resonators have been patterned from several laser ablated  $\text{YBa}_2\text{Cu}_3\text{O}_{7-x}$  thin films on  $\text{LaAlO}_3$  substrates and have been tested. A quality factor of 1250 at 8.8 GHz and 77 K was measured. This is nearly a factor of 7 better than a gold resonator of like geometry. A correlation between the critical temperature and the quality factor is suggested by our results. A good critical temperature is a necessary but not sufficient indicator of the microwave performance of the films. We have observed that flaws in the morphology such as particles and voids cause films with good critical temperatures to exhibit inferior microwave performance.

## ACKNOWLEDGMENTS

This material is based upon work supported by the National Aeronautics and Space Administration under Award No. NCC-3-197. The authors are grateful to Mr. Chris Chorey for his assistance with the microwave measurements.

## REFERENCES

1. H. Peil and G. Muller, "The Microwave Surface Impedance of High- $T_c$  Superconductors," *IEEE Trans. Magn.*, Vol. MAG-27, March 1991, pp. 854–862.
2. N. J. Rohrer, H. Y. To, G. J. Valco, K. B. Bhasin, C. Chorey, and J. Warner, "Sequentially Evaporated Thin Film  $\text{YBa}_2\text{Cu}_3\text{O}_{7-x}$  Superconducting Microwave Ring Resonator," In R. D. McConnell and R. Noufi (Eds.), *Science and Technology of Thin Film Superconductors 2*, Plenum, New York, 1990, pp. 615–624.
3. C. M. Chorey, K.-S. Kong, K. B. Bhasin, J. D. Warner, and T. Itoh, "YBCO Superconducting Ring Resonators at Millimeter-Wave Frequencies," *IEEE Trans. Microwave Theory Tech.*, Vol. MTT-39, Sept. 1991, pp. 1480–1487.
4. D. E. Oates, A. C. Anderson, D. M. Sheen, and S. M. Ali, "Stripline Resonator Measurements of  $Z_0$  Versus  $H_{c1}$  in  $\text{YBa}_2\text{Cu}_3\text{O}_{7-x}$  Thin Films," *IEEE Trans. Microwave Theory Tech.*, Vol. MTT-39, Sept. 1991, pp. 1522–1529.

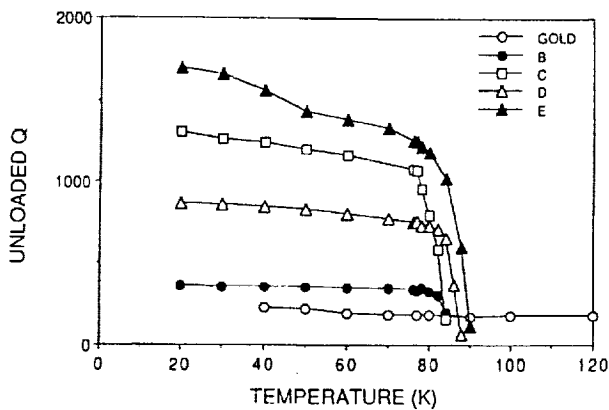


**Figure 2** Unloaded quality factor as a function of temperature for the gold resonator (open circle), Sample B (solid circle), Sample C (open square), Sample D (open triangle), and Sample E (filled triangle)

5. R. W. Simon, C. E. Platt, A. E. Lee, G. S. Lee, K. P. Daly, M. S. Wirc, J. A. Luine, and M. Urbanik, "Low-Loss Substrate for Epitaxial Growth of High-Temperature Superconducting Thin Films," *Appl. Phys. Lett.*, Vol. 53, Dec. 1988, pp. 2677-2679.
6. N. Klein, H. Chaloupka, G. Muller, S. Orbach, H. Piel, B. Roas, L. Schultz, U. Klein, and M. Peiniger, "The Effective Microwave Surface Impedance of High- $T_c$  Thin Films," *J. Appl. Phys.*, Vol. 67, June 1990, pp. 6940-6945.
7. A. A. Valenzuela and P. Russer, "High  $Q$  Coplanar Transmission Line Resonator of  $\text{YBa}_2\text{Cu}_3\text{O}_{7-x}$  on  $\text{MgO}$ ," *Appl. Phys. Lett.*, Vol. 55, Sept. 1989, pp. 1029-1031.
8. G. Ghione, C. Naldi, and Z. Rodolfo, " $Q$ -Factor Evaluation for Coplanar Resonators," *Alta Freq.*, 52, 1983, pp. 191-193

*Received 11-15-91*



# Coaxial Line Configuration for Microwave Power Transmission Study of $\text{YBa}_2\text{Cu}_3\text{O}_{7-\delta}$ Thin Films

C. M. Chorey, F. A. Miranda, and K. B. Bhasin

**Abstract**—Microwave transmission measurements through  $\text{YBa}_2\text{Cu}_3\text{O}_{7-\delta}$  (YBCO) high transition temperature superconducting (HTS) thin films on lanthanum aluminate ( $\text{LaAlO}_3$ ) have been performed in a coaxial line at 10 GHz.  $\text{LaAlO}_3$  substrates were ultrasonically machined into washer shaped discs, polished, and coated with laser ablated YBCO. These samples were mounted in the 50- $\Omega$  coaxial air line to form a short circuit. The power transmitted through the films as a function of temperature was used to calculate the normal state conductivity and the magnetic penetration depth for the films.

## I. INTRODUCTION

Microwave applications of high transition temperature superconductors (HTS's) have generated considerable interest because of the low surface resistance of these superconducting compounds compared to metallic films. Presently, typical microwave HTS circuits take the form of passive planar transmission line structures such as resonators, filters, and delay lines, where the low surface resistance leads to high- $Q$ , low-loss circuits [1], [2]. Passive applications in other than planar transmission line form are generally less common due to the difficulties in forming high quality bulk superconducting parts or in coating complex shapes with a HTS film. In this paper we report on the implementation of a novel coaxial line configuration for the microwave characterization of HTS thin films. This technique was used to determine the conductivity and magnetic penetration depth of  $\text{YBa}_2\text{Cu}_3\text{O}_{7-\delta}$  (YBCO) HTS films at 10 GHz via the transmitted microwave power as a function of temperature.

## II. SAMPLE PREPARATION

The configuration used for this paper consisted of mounting the HTS sample transversely in a coaxial line to form a short circuit. A 50- $\Omega$  air dielectric line, 1.5625 in long with an inner diameter of 0.1378 in and a 0.0580-in diameter center pin was used. The body of the line separated into three pieces: two female APC 3.5 connector sections attached to a 0.75-in center barrel. The center pin also separated into three pieces: two female pin contacts which threaded into the center section of the pin. The center pin was supported in the body of the line by two air articulated rexolite beads which rested in 0.159 diameter recesses in the connector/barrel flanges (Fig. 1(a)). Both the body of the line and the center pin were made of beryllium copper and were gold plated.

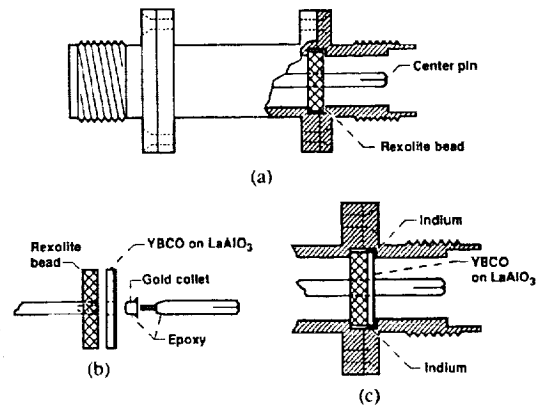


Fig. 1. Schematic drawings of the coaxial line and the mounting of the HTS sample. (a) Schematic of the coaxial line with a cutaway showing the position of the support bead and center pin. (b) Detail of the mounting of the HTS sample to the center pin. (c) Cutaway view showing the HTS sample mounted in the coaxial line and the location of the indium gasket.

To produce the HTS samples, raw cut slices of (001)  $\text{LaAlO}_3$  approximately 30 mils thick were obtained. These were ultrasonically machined into washer shaped discs with an outer diameter of 0.158 in and a center hole of 0.059-in diameter. Glass cover slips were used during the machining to help minimize edge chipping and cracking. The machined pieces were then lapped from one side to a thickness of 20 mils to remove edge and surface damage and then polished to an epitaxial finish. The substrates, when done, had a bright finish but were slightly bowed in the radial direction due to preferential polishing along the outer edge and around the center hole.

The YBCO superconducting films were deposited on the washer-shaped  $\text{LaAlO}_3$  substrates by a pulsed laser ablation technique [3]. The deposition was performed using a 248-nm KrF laser on a stoichiometric target 95% or more of the theoretical density. The substrate temperature was held at 750°C and the ambient oxygen pressure was maintained at 170 mtorr. The resulting films were typically 2500–3000 Å thick, with a transition temperature ( $T_c$ ,  $R = 0$ ) between 85–90K.

The HTS samples were mounted in the coaxial line with the aim of achieving electrical contact between the HTS film and the inner and outer coaxial conductors, and providing good thermal contact between the HTS sample and the body of the line. Electrical contact was required along the entire junction between the HTS sample and the coaxial conductors to prevent leakage coupling of microwave power around the film. Providing mechanical support to the sample was also an important consideration because the  $\text{LaAlO}_3$  substrates were quite fragile. These various needs were found to be best served by machining the existing recess for the rexolite support bead an additional 20 mils in depth and inserting the sample next to the bead. This provided mechanical support as the rexolite bead backed the lanthanum aluminate, and also facilitated electrical contact to the coaxial line because of the overlap of the outer metal tube with the HTS film.

In assembly, the sample was first attached to the center pin. One of the female contact sections of the center pin was unscrewed from the rest of the pin assembly and slightly tapered using emery paper near the connection with the rexolite bead. Because the YBCO film did not extend down into the center hole of the sample, merely sliding the sample onto the tapered pin did not produce adequate electrical contact between the pin and the HTS film. Using solder to

Manuscript received July 8, 1991; revised August 29, 1991.  
C. M. Chorey is with the LeRC Group, Sverdrup Technology, Brook Park, OH 44135.  
F. A. Miranda and K. B. Bhasin are with the NASA Lewis Research Center, Cleveland, OH 44135.  
IEEE Log Number 9103939.

achieve a better connection between the two was not feasible because the heat necessary for soldering degraded the film's superconducting properties and also because the soldering flux attacked the YBCO film. A conductive epoxy was also tried, but when applied to the superconducting film it also caused the film to degrade. The best results were obtained by forming a gold-foil collet which was inserted into the center hole of the sample. Small amounts of conductive epoxy were applied to the inner hole of the sample (away from the HTS film) and to the tapered center pin to fix the collet to the sample and pin. The sample and collet were pressed snugly onto the tapered pin, the pin reassembled and the epoxy allowed to dry (Fig. 1(b)). The press fit between the tapered pin and the gold collet caused the gold to overlap the HTS film, providing contact between the film and the pin.

To achieve electrical and thermal contact to the outer tube, an indium gasket was used. The gasket was loosely inserted into the machined recess in the connector flange. The flange was then pressed over the HTS sample on the center pin which had been reinserted into the rest of the coaxial line. The HTS sample pressed into the soft indium with a "cookie-cutter" effect, forming a complete electrical "seal" around the outer edge of the HTS sample and the coax tube (Fig. 1(c)). Any excess indium was trimmed from between the flanges before they were clamped together. No heat was applied to the indium at any time. This indium "seal" provided good electrical contact and excellent thermal contact for the sample.

### III. MEASUREMENTS AND RESULTS

The coaxial line was tested by mounting the sample at the second stage of a closed-cycle helium gas refrigerator inside a custom made vacuum shroud. While the coaxial configuration is inherently wide band, measurements here were limited to 10 GHz, which corresponds to the center frequency of a narrow test band in the Naval Research Laboratory's High Temperature Superconductivity Space Experiment (HTSSE I) [4]. An HP 8350 sweep oscillator provided the input signal at a power level of 1.0 mW. The input power (via a 10-dB coupler) and the output power were measured with power meters (HP 436A with 8485A sensors), and the system was calibrated by referencing the measurements to the power transmitted through an open air line (i.e., without an HTS sample).

Fig. 2(a) shows the normalized transmitted power ( $P/P_{\max}$ ) versus temperature ( $T$ ) for three HTS samples, where  $P_{\max}$  is the largest measured value for the power transmitted through the sample. In the normal state ( $T > T_c$ , where  $T_c$  is the transition temperature) the YBCO film has a moderately high resistance and lossy transmission occurs through the film and dielectric. The metallic character of the films in the normal state is shown by the positive slope of the transmitted power.

The power transmission signal can be used to determine transport properties at microwave frequencies such as the conductivity ( $\sigma$ ). In the normal state the conductivity ( $\sigma_N$ ) of the film can be expressed conveniently in terms of the power transmission as [5], [6]

$$\sigma_N = \frac{\left\{ -RP_N + \left[ (RP_N)^2 - 4QP_N(SP_N - 8\eta^2) \right]^{1/2} \right\}}{2QP_N dZ_c} \quad (1)$$

where

$$Q = (\eta^2 + 1) + (\eta^2 - 1) \cos(2kt) \quad (2.a)$$

$$R = 2(3\eta^2 + 1) + 2(\eta^2 - 1) \cos(2kt) \quad (2.b)$$

$$S = \eta^4 + 6\eta^2 + 1 - (\eta^2 - 1)^2 \cos(2kt) \quad (2.c)$$

and  $P_N$  is the power transmission coefficient in the normal state,  $d$  is the film thickness,  $Z_c$  is the characteristic impedance of the

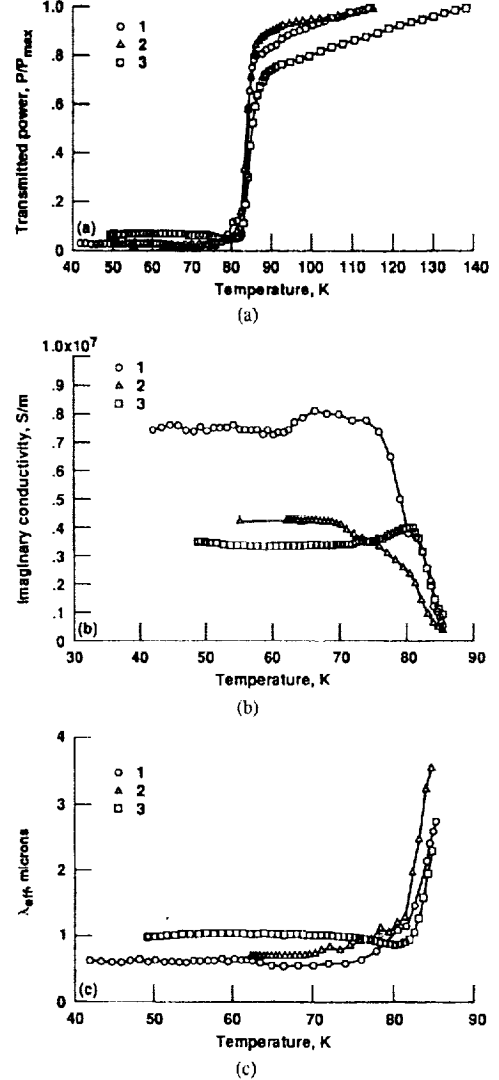


Fig. 2. (a) Normalized transmitted power ( $P/P_{\max}$ ) versus temperature ( $T$ ) at 10 GHz for  $\text{YBa}_2\text{Cu}_3\text{O}_{7-\delta}$  thin films (3000 Å) on  $\text{LaAlO}_3$  (20 mils). (b) Conductivity ( $\sigma_2$ ) versus temperature ( $T$ ) at 10 GHz for  $\text{YBa}_2\text{Cu}_3\text{O}_{7-\delta}$  thin films (3000 Å) on  $\text{LaAlO}_3$  (20 mils). (c) Effective magnetic penetration depth ( $\lambda_{eff}$ ) versus temperature ( $T$ ) at 10 GHz for  $\text{YBa}_2\text{Cu}_3\text{O}_{7-\delta}$  thin films (3000 Å) on  $\text{LaAlO}_3$  (20 mils).

coaxial line,  $t$  is the substrate thickness, and  $k = 2\pi\eta/L$  is the wavenumber with  $\eta$  the refractive index of the substrate and  $L$  the wavelength of the microwave signal. Values of  $\sigma_N$  at 100K for films 1-3 were  $\sim 1.2 \times 10^6$ ,  $3.8 \times 10^5$ , and  $7.6 \times 10^5$  S/m, respectively. Taking the reciprocal of these values we obtained resistivity values for samples 1-3 of  $\sim 83$ , 263, and 132  $\mu\Omega\text{-cm}$ , respectively. These values are consistent with those obtained by others [7] using dc measurements techniques.

In the superconducting state ( $T < T_c$ ) the conductivity can be expressed as ( $\sigma^* = \sigma_1 - j\sigma_2$ ) where  $\sigma_1$  is the part of the conductivity associated with the normal carriers and  $\sigma_2$  is that associated with the superconducting carriers. The power transmission data can be used to determine  $\sigma_2$  through the expression [5], [6]:

$$\sigma_2/\sigma_c = \left\{ -\beta(2\sigma_c dZ_c)^{-1} + \left\{ (\sigma_c dZ_c)^{-2} [(\beta/2)^2 - \gamma] - \alpha\sigma_1(\sigma_c^2 dZ_c)^{-1} - (\sigma_1/\sigma_c)^2 + (P_c/P_s) \cdot [1 + \alpha(\sigma_c dZ_c)^{-1} + \gamma(\sigma_c dZ_c)^{-2}] \right\}^{1/2} \right\} \quad (3)$$

where  $\sigma_c$  and  $P_c$  are the conductivity and the power transmission coefficient, respectively, at  $T = T_c$ ,  $P_s$  is the power transmission coefficient in the superconducting state,  $\alpha = R/Q$ ,  $\gamma = S/Q$ , and  $\beta = [-2\eta(\eta^2 - 1)\sin(2kt)]/Q$ . Note that although  $\sigma_1$  can be determined directly from experimental measurements of the magnitude and phase of the transmitted power [8], we have not determined this parameter directly because the experiment was not configured to measure the phase of the transmitted signal. Therefore, we have used in (3) the temperature dependence of  $\sigma_1$  according to the two-fluid model approximation [5]

$$\sigma_1 = \sigma_c(T/T_c)^4 \quad (4)$$

which has been used in the modeling of HTS microwave circuits. Fig. 2(b) shows a plot of  $\sigma_2$  versus temperature for the samples under discussion. The effects of leakage sources (possibly pin holes or cracks) in film 3, and to some extent in film 1, are evidenced by the decrease of  $\sigma_2$  after reaching a maximum at a temperature not far below  $T_c$ . Values of  $\sigma_2$  at  $\sim 77\text{K}$  for samples 1-3 were  $\sim 6.5 \times 10^6$ ,  $3.2 \times 10^6$ , and  $3.7 \times 10^6$  S/m, respectively.

When the HTS films thickness is of the order of the magnetic penetration depth the surface impedance ( $Z_s = R_s + jX_s$ ) of the films is enhanced and will be influenced by the film thickness as well as by the substrates properties [9]. For thin films the effective surface reactance ( $X_{\text{eff}}$ ) can be defined in terms of the transmitted power and the magnetic penetration depth,  $\lambda$  [10]:

$$X_{\text{eff}} = R_N |P_s/P_c|^{1/2} \cosh(d/\lambda) \quad (5)$$

where  $R_N = (\mu_0 \omega / 2\sigma_c)^{1/2}$  is the surface resistance of the film at  $T_c$ ,  $\mu_0$  is the permeability of free space and  $\omega = 2\pi f$  is the angular frequency. Since in general  $X_{\text{eff}}$  for good superconducting films can be expressed as [9]

$$X_{\text{eff}} = \mu_0 \omega \lambda_{\text{eff}} = \mu_0 \omega \lambda \coth(d/\lambda) \quad (6)$$

then the effective value of the penetration depth can be obtained by solving (5) and (6) simultaneously. The details of this calculation can be found elsewhere [11]. Fig. 2(c) shows a plot of  $\lambda_{\text{eff}}$  versus  $T$  for films 1-3. This corresponds to values of  $\lambda$  at approximately 77K for samples 1-3 of 0.45, 0.50, and 0.50  $\mu\text{m}$ , respectively. At 41K the value of  $\lambda$  for film 1 was  $\sim 0.39 \mu\text{m}$ . The advantage of using (5) and (6) to determine  $\lambda_{\text{eff}}$  is that they are independent of any model of superconductivity in these materials. It is evident that the values for the penetration depth obtained for these films are larger than those previously reported for high quality YBCO thin films and single crystals [7], [11]. This is not unexpected mainly because of the difficulties in film deposition for the film shape needed in this paper. The presence of film inhomogeneities, and the possible film deterioration, especially close to the outer and inner rims of the washer-shaped samples, will certainly increase the magnetic penetration depth.

#### IV. CONCLUSIONS

Microwave power transmission measurements have been made through YBCO thin films on  $\text{LaAlO}_3$  mounted in a coaxial line. Calculations of the conductivity and penetration depth show that the superconducting properties of the films after fabrication and mounting procedures are still suitable for microwave applications. Modifications to this novel mounting scheme, in order to allow the determination of other transport parameters, such as the surface resistance ( $R_s$ ), may lead to microwave applications alternate to traditional microstrip transmission line circuits.

#### ACKNOWLEDGMENT

The authors would like to acknowledge the helpful comments of the reviewers.

#### REFERENCES

- [1] C. M. Chorey, K. B. Bhasin, J. D. Warner, J. Y. Josefowicz, D. B. Rensch, and C. W. Nieh, "An experimental study of high  $T_c$  superconducting microstrip transmission lines at 35 GHz and the effect of film morphology," *IEEE Trans. Magn.*, vol. 27, pp. 2940-2943, Mar. 1991.
- [2] D. Kalokitis, A. Fathy, V. Pendrick, E. Belohoubeck, A. Findikoglu, A. Inam, X. X. Xi, T. Venkatesan, and J. B. Barner, "Performance of a narrow band microwave filter implemented in thin film  $\text{YBa}_2\text{Cu}_3\text{O}_{7-\delta}$  with ohmic contacts," *Appl. Phys. Lett.*, vol. 58, no. 5, pp. 537-539, Feb. 1991.
- [3] J. D. Warner, J. E. Meola, and K. A. Jenkins, "Study of deposition of  $\text{YBa}_2\text{Cu}_3\text{O}_{7-x}$  on cubic zirconia," in *Superconductivity and Applications*, H. S. Kwok, Y. H. Kao, and D. T. Shaw, eds. New York: Plenum, 1990, pp. 163-166.
- [4] J. C. Ritter, M. Nisenoff, G. Price, and S. A. Wolf, "High temperature superconductivity space experiment (HTSSE)," *IEEE Trans. Magn.*, vol. 27, pp. 2533-2536, Mar. 1991.
- [5] R. E. Glover III and M. Tinkham, "Conductivity of superconducting films for photon energies between 0.3 and 40  $k_B T_c$ ," *Phys. Rev.*, vol. 108, no. 2, pp. 243-256, Oct. 1957.
- [6] F. A. Miranda, W. L. Gordon, K. B. Bhasin, V. O. Heinen, J. D. Warner, and G. J. Valco, "Millimeter wave transmission studies of  $\text{YBa}_2\text{Cu}_3\text{O}_{7-\delta}$  thin films in the 26.5 to 40.0 GHz frequency range," in *Superconductivity and Applications*, H. S. Kwok, Y. H. Kao, and D. T. Shaw, eds. New York: Plenum, 1990, pp. 735-748.
- [7] N. Klein, G. Muller, H. Piel, B. Roas, L. Schultz, U. Klein, and M. Peiniger, "Millimeter wave surface resistance of epitaxially grown  $\text{YBa}_2\text{Cu}_3\text{O}_{7-x}$  thin films," *Appl. Phys. Lett.*, vol. 54, no. 8, pp. 757-759, Feb. 1989.
- [8] K. B. Bhasin, J. D. Warner, F. A. Miranda, W. L. Gordon, and H. S. Newman, "Determination of surface resistance and magnetic penetration depth of superconducting  $\text{YBa}_2\text{Cu}_3\text{O}_{7-\delta}$  thin films by microwave power transmission measurements," *IEEE Trans. Magn.*, vol. 27, pp. 1284-1287, Mar. 1991.
- [9] N. Klein, H. Chaloupka, G. Muller, S. Orbach, H. Piel, B. Roas, L. Schultz, U. Klein, and M. Peiniger, "The effective microwave surface impedance of High- $T_c$  thin films," *J. Appl. Phys.*, vol. 67, p. 6940, 1990.
- [10] S. Sridhar, "Microwave response of thin films superconductors," *J. Appl. Phys.*, vol. 63, no. 1, pp. 159-166, Jan. 1988.
- [11] F. A. Miranda, W. L. Gordon, K. B. Bhasin, V. O. Heinen, and J. D. Warner, "Microwave properties of  $\text{YBa}_2\text{Cu}_3\text{O}_{7-\delta}$  high transition temperature superconducting thin films measured by power transmission method," to be published.



# Microwave properties of $\text{YBa}_2\text{Cu}_3\text{O}_{7-\delta}$ high-transition-temperature superconducting thin films measured by the power transmission method

F. A. Miranda<sup>a)</sup> and W. L. Gordon

*Department of Physics, Case Western Reserve University, Cleveland, Ohio 44106*

K. B. Bhasin, V. O. Heinen, and J. D. Warner

*National Aeronautics and Space Administration, Lewis Research Center, Cleveland, Ohio 44135*

(Received 8 May 1991; accepted for publication 26 July 1991)

The microwave response of  $\text{YBa}_2\text{Cu}_3\text{O}_{7-\delta}$  superconducting thin films has been studied by performing power transmission measurements. The measurements were made at frequencies within the 26.5–40.0-GHz frequency range, and at temperatures from 20 to 300 K. The films were deposited on  $\text{LaAlO}_3$ ,  $\text{MgO}$ , yttria-stabilized zirconia, and  $\text{LaGaO}_3$  substrates by laser ablation and dc off-axis magnetron sputtering. From these measurements the complex conductivity  $\sigma^* = \sigma_1 - j\sigma_2$ , the magnetic penetration depth  $\lambda$ , and the surface resistance  $R_s$  of the films have been determined. It was observed that both  $\sigma_1$  and  $\sigma_2$  increased when cooling the films below their transition temperature. This behavior disagreed with that expected from the two-fluid model. In addition, it was observed that the temperature behavior of  $\sigma_1$  deviates from the predictions of the Bardeen–Cooper–Schrieffer theory. Values of  $\lambda$  have been obtained that are in good agreement with the best reported values for high quality *c*-axis-oriented thin films and single crystals ( $\sim 140$  nm). The anisotropy of  $\lambda$  was determined by measuring this parameter in *c*- and *a*-axis-oriented films. An intrinsic penetration depth value ( $\lambda \sim 90 \pm 30$  nm) has been estimated from the film thickness dependence of  $\lambda$ . Values of  $R_s$  for the  $\text{YBa}_2\text{Cu}_3\text{O}_{7-\delta}$  films were calculated and found to be comparable or lower than that of copper at temperatures below 80 K. These  $R_s$  values were consistent with those found on the same films using resonant-cavity techniques.

## I. INTRODUCTION

Since the discovery of the high-transition-temperature superconductors (HTS) by Bednorz and Muller<sup>1</sup> and Wu *et al.*<sup>2</sup> numerous studies have been done to understand the phenomenon of superconductivity in these materials. In particular, considerable attention has been paid to the response of these oxides to electromagnetic radiation because this type of interaction can give information on aspects such as pair coupling mechanisms, density of states, excitations of quasiparticles, gap characteristics, and general material properties.<sup>3</sup> Furthermore, these studies allow the determination of material parameters such as the complex conductivity  $\sigma^* = \sigma_1 - j\sigma_2$ , the magnetic penetration depth  $\lambda$ , and the surface resistance  $R_s$ . These parameters are important for new applications such as superconductor-insulator-superconductor mixers,<sup>4</sup> ring resonators for local oscillator applications,<sup>5</sup> superconductor-based antennas,<sup>6</sup> and high-power microwave switches,<sup>7</sup> among others.

In the past, millimeter and microwave transmission and reflection experiments have been used to study the properties of low-transition-temperature superconducting films. Glover and Tinkham<sup>8</sup> analyzed the microwave properties of Pb and Sn films and obtained the complex conductivity and an effective value for the energy gap of these films from microwave transmission data. Rugheimer, Lehoczký, and Briscoe<sup>9</sup> measured the reflection and transmis-

sion coefficients of thin ( $\sim 50$  Å) films of Sn and In at 1.2-, 0.8-, and 0.4-mm wavelengths and at temperatures below the transition temperature  $T_c$ . They found a good correlation between their experimental results and the transmission and reflection ratios calculated on the basis of the Bardeen–Cooper–Schrieffer (BCS) theory.<sup>10</sup> Subsequent studies by Lehoczký and Briscoe,<sup>11</sup> based on measurements of the microwave transmission and reflection coefficients for thin ( $< 150$  Å) superconducting Pb films, were consistent with the BCS-based Mattis and Bardeen expressions for the conductivity.<sup>12</sup>

The information obtained from these studies provided strong fundamental evidence for the validity of the BCS theory in explaining the microscopic properties of low- $T_c$  superconductors. More recently, Sridhar<sup>13</sup> explored the interaction of microwaves with superconductors by performing extensive measurements of the  $R_s$  and  $X_s$  for superconducting Sn using a right  $\text{TE}_{011}$ -mode cylindrical Pb-plated Cu cavity resonating at 10 GHz. The results obtained by Sridhar for the surface impedance ( $Z_s = R_s - jX_s$ ) were consistent with those predicted by the BCS theory even though  $Z_s$  varied over several orders of magnitude.

A variety of tests has been performed in order to analyze the microwave properties of the new HTS superconducting oxides. However, studies of HTS films by using transmission and reflection coefficient measurements at millimeter and microwave frequencies have not been as abundant as other related tests such as  $R_s$ , critical current density  $j_c$ , and ac magnetic susceptibility  $\chi_s$  measurements.

<sup>a)</sup>Presently with NASA-Lewis Research Center.

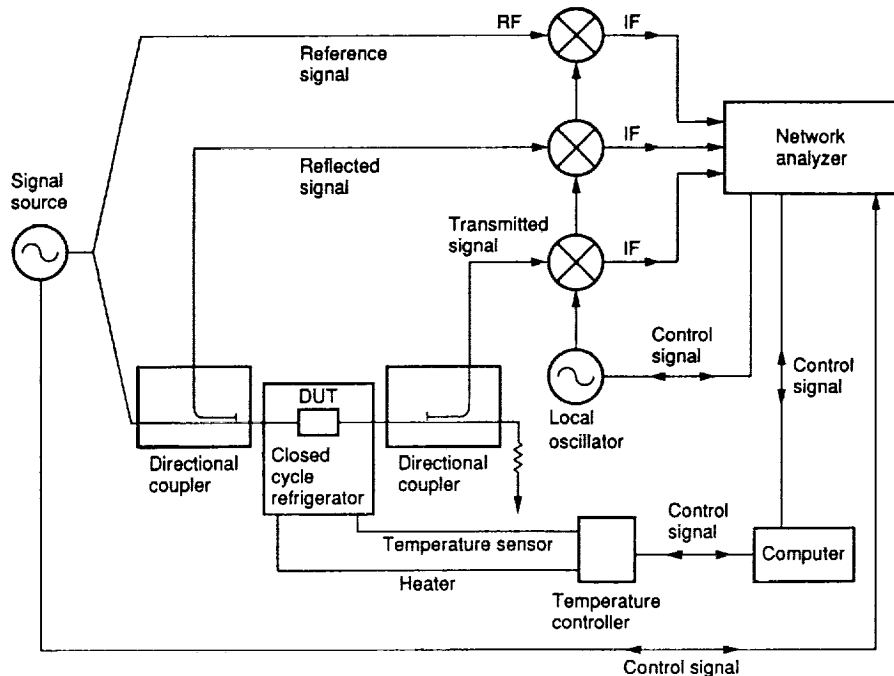


FIG. 1. Apparatus for measuring the microwave-transmitted power.

To our knowledge, the first study of this nature on HTS thin films was done at 60 GHz by Ho *et al.*<sup>14</sup> on Bi-Sr-Ca-Cu-O superconducting thin films (1000–5000 Å) deposited on MgO. Their results suggested that the behavior of the millimeter-wave complex conductivity at temperatures below the beginning of the transition  $T_{\text{onset}}$  could be explained in terms of a model of superconducting grains nucleating in a normal conducting matrix. A similar analysis at 9.0 GHz was done by Nichols *et al.*<sup>15</sup> for  $\text{YBa}_2\text{Cu}_3\text{O}_{7-\delta}$  thin films ( $\sim 1 \mu\text{m}$  thickness,  $T_c \sim 80\text{--}85 \text{ K}$ ) on  $\text{Al}_2\text{O}_3$ , MgO, and yttria-stabilized zirconia (YSZ) substrates. These results indicated that the microwave conductivity behaved qualitatively as expected for a BCS-type superconductor but deviated from the quantitative predictions of this theory, as evidenced by the distribution of gap values obtained ( $2\Delta_0/k_B T_c = 1.3\text{--}6.5$ ). A more recent work by Golosovsky *et al.*<sup>16</sup> reports on the effects of an external magnetic field on the microwave transmission at 9.5 GHz through superconducting films ( $T_c \sim 80\text{--}85 \text{ K}$ ) of  $\text{YBa}_2\text{Cu}_3\text{O}_{7-\delta}$  on MgO substrates. These researchers found that, in the superconducting state,  $\sigma_1$  increases and  $\sigma_2$  decreases when the sample is under the influence of an external magnetic field, and that these changes may be caused by the appearance of vortices in the weak links formed at the grain boundaries.

Valuable information about the properties of thin films of the HTS materials has been provided by the studies mentioned so far. However, since these studies were performed, films of higher quality have been produced due to the improvements of film deposition techniques such as laser ablation and off-axis magnetron sputtering. Furthermore, knowledge of the performance of these films at microwave frequencies well above the x band ( $\sim 8\text{--}12 \text{ GHz}$ ) is becoming more necessary for modeling and development

of new integrated circuits for microwave applications.<sup>5,17</sup>

In this paper we present results of the interaction of microwaves with  $\text{YBa}_2\text{Cu}_3\text{O}_{7-\delta}$  superconducting thin films deposited on  $\text{LaAlO}_3$ , MgO, YSZ, and  $\text{LaGaO}_3$  substrates. Results for  $\sigma^*$ ,  $\lambda$ , and  $R_s$  of the thin films over a wide range of temperatures  $T$  and film thickness  $d$  are discussed.

This paper is organized as follows. A brief review of the experimental configuration for the microwave measurements is presented in Sec. II. Sections III and IV present sample preparation techniques and a brief discussion of the calculation of  $\sigma^*$  from the measured magnitude and phase of the microwave transmitted power. Section V presents a description of and results from the measurements of sample parameters, and Secs. VI and VII briefly discuss the theoretical considerations for the determination of  $X_s$  and  $R_s$ , respectively. Section VIII provides the results obtained in this study and their interpretation. Finally, Sec. IX presents the conclusions drawn from this work and suggestions for future research.

## II. MICROWAVE MEASUREMENTS

A schematic of the configuration used to measure the microwave power transmission is shown in Fig. 1. Note that this experimental configuration also allows the measurement of the power reflected from the sample. However, it was found that for the thickness of films considered in this study ( $\sim 800\text{--}5000 \text{ Å}$ ) and for the maximum power level available ( $\sim 16 \text{ mW}$ ) the reflected power barely changes on the films' transition from the normal to the superconducting state. We did not use the fractional reflection coefficient data for our analysis because it has been shown that it is less sensitive to changes in  $\sigma^*$  than the

transmission coefficient.<sup>11</sup> Furthermore, we found that it was more difficult to account for systematic errors in the reflection data than it was for the transmission data. Similar observations were made earlier by other researchers who measured the transmitted and reflected microwave power of low- $T_c$  superconducting thin films ( $\sim 20$ – $150$  Å).<sup>9,11</sup> These researchers found that the fractional change in the reflected power on cooling a film from the normal to the superconducting state is larger for thinner films than for thicker ones. However, we have not examined thinner films since good HTS films of thickness less than  $500$  Å are difficult to obtain. The deposition factors affecting the quality of very thin HTS films have been discussed by others.<sup>18</sup>

The main components of the experimental apparatus are an HP-8510B network analyzer and a closed-cycle helium gas refrigerator, which are both controlled by an HP 9000-216 computer. The network analyzer is coupled to the refrigerator by  $Ka$  band ( $26.5$ – $40.0$  GHz) rectangular waveguides. The measurement technique compares the reflected and the transmitted signals against the incident microwave signal to determine the reflection and transmission coefficients. The data measured in this way are then stored by the computer for subsequent analysis.

All the measurements were made under vacuum ( $< 10^{-3}$  Torr) in a custom-made aluminum vacuum chamber designed to fit on top of the external shield of the refrigerator and to give access to the waveguides connecting the network analyzer with the refrigerator. Natural mica windows were used as vacuum windows in the waveguide because mica has a low loss and a thermally stable relative dielectric constant; furthermore, it is transparent in the frequency range considered in this study. Inside the vacuum chamber the sample was oriented perpendicular to the microwave source by clamping it between two waveguide flanges thermally connected to the cold head of the refrigerator through a Au-plated Cu plate. The film side of the sample was directed toward the incident microwave signal. The system was calibrated before the beginning of each measurement cycle to account for the impedance of the waveguide network. The noise level for our measurements was determined to be below  $-60$  dB. Background attenuation and phase corrections were made by subtracting the transmitted power as a function of temperature in

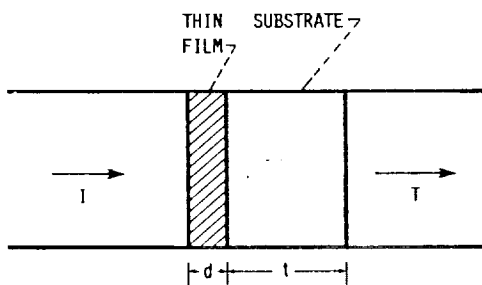


FIG. 2. Side view of a rectangular waveguide propagating the  $TE_{10}$  mode with its entire cross section covered by a high- $T_c$  superconducting thin film of thickness  $d$  deposited on a dielectric substrate of thickness  $t$  and refractive index  $n$ .

the absence of the sample from the data obtained with the sample in place. Measurements of bare substrates were used to determine any temperature dependence of their dielectric constant. These results are reported in Refs. 19 and 20. The temperature of the film was measured with two silicon diodes placed in a  $\frac{1}{8}$ -in.-diam hole on top of each of the sample's supporting flanges. The accuracy of these diodes is  $\pm 1.0$  K from  $1.4$ – $100$  K and  $1\%$  of the temperature in the range from  $100$ – $325$  K. The difference in temperature readings of the two sensors was less than  $0.2$  K over the entire temperature range. An additional sensor was located next to the heater attached to the cold head of the refrigerator and was used to control the temperature of the cold head.

### III. SAMPLE PREPARATION

The  $YBa_2Cu_3O_{7-\delta}$  superconducting thin films considered in this study were deposited either by pulsed laser ablation or by a dc off-axis magnetron sputtering technique with an *in situ* anneal in oxygen. Most of the samples were deposited on  $LaAlO_3$  substrates, but films were also deposited on  $MgO$ ,  $YSZ$ , and  $LaGaO_3$ . All of the substrates were approximately  $1.0$  cm<sup>2</sup>, with thickness of  $10$ – $20$  mils, and had a (100) crystallographic orientation. The thickness of the films ranged from approximately  $800$  to  $5000$  Å, as determined by using a surface profilometer over steps etched at the corner of each film with undiluted phosphoric acid ( $H_3PO_4$ ).

Most of the  $YBa_2Cu_3O_{7-\delta}$  films were deposited by us at NASA-Lewis Research Center using a pulsed laser ablation technique,<sup>21</sup> while the dc off-axis magnetron-sputtered films were deposited at Westinghouse Research Center in Pittsburgh.<sup>22</sup> A brief description of the laser ablation technique used to deposit the films is given below. The deposition was performed with a stoichiometric target of at least  $95\%$  of the theoretical density. The target was polished with  $400$  grit  $Al_2O_3$  sandpaper before each deposition. The deposition process was carried out at a substrate temperature of  $750$  °C and at an ambient  $O_2$  pressure of  $170$  mTorr. The laser wavelength was  $248$  nm, the pulse length was  $20$ – $30$  ns, the pulse rate was  $2$  pulses/s, and the laser fluence on the sample was  $\sim 2.0$  J/cm<sup>2</sup> per pulse. During deposition, the distance between the target and the sample was kept at  $7.5$  cm. Throughout the deposition process the laser beam was rastered  $1$  cm in two orthogonal directions across the target using an external lens on a translator. This gave uniform ablation of the target. At the end of the deposition, the  $O_2$  pressure was increased to  $1$  atm and then the temperature lowered to  $450$  °C at a rate of  $2$  °C/min. The temperature was held at  $450$  °C for  $2$  h, in order to optimize its oxygen content, before it was lowered to  $250$  °C at a rate of  $2$  °C/min. Then the heater power was turned off, and the sample was allowed to cool to  $40$  °C or less before it was removed from the chamber.

#### IV. CALCULATION OF COMPLEX CONDUCTIVITY FROM THE MEASURED MAGNITUDE AND PHASE OF MICROWAVE-TRANSMITTED POWER

By measuring the transmission of a microwave signal through a superconducting thin film we were able to determine the changes in the conductivity of the film as a function of temperature. For a film of thickness  $d$  deposited onto a substrate of thickness  $t$  and refractive index  $n$ , that covers the entire cross section of a rectangular wave-

guide propagating the TE<sub>01</sub> mode (see Fig. 2), the fractional transmitted power coefficient  $T$  and the phase shift  $\phi$  may be written as

$$T = 4n^2 \{ n^2 \cos^2(k_0nt) [(k_0dR)^2 + (2 + k_0dI)^2] + \sin^2(k_0nt) [(k_0dR)^2 + (n^2 + 1 + k_0dI)^2] + (2nk_0dR) \sin(k_0nt) \cos(k_0nt) (n^2 - 1) \}^{-1}, \quad (1)$$

$$\phi = \arctan \{ \cos(k_0t) [(nk_0dR) \cos(k_0nt) + (n^2 + 1 + k_0dI) \sin(k_0nt)] - \sin(k_0t) [n(2 + k_0dI) \cos(k_0nt) - (k_0dR) \sin(k_0nt)] \} / \{ \cos(k_0t) [(-k_0dR) \sin(k_0nt) + n(2 + k_0dI) \cos(k_0nt)] + \sin(k_0t) [(k_0dR) \cos(k_0nt) + (n^2 + 1 + k_0dI) \sin(k_0nt)] \}^{-1}, \quad (2)$$

where  $k_0$  is the magnitude of the propagating wave vector in the rectangular waveguide. The dispersion coefficient ( $R + jI$ ) of the thin film is related to  $\sigma^*$  by  $R = 1 + 4\pi\sigma_2/\omega\epsilon$ , and  $I = 4\pi\sigma_1/\omega\epsilon$ , where  $\omega/2\pi = f$  is the frequency of the wave, and  $\epsilon$  is the relative dielectric constant of the HTS material. Thus,  $\sigma^*$  is given in terms of  $T$  and  $\phi$  by

$$R = \frac{\{(2n/T^{1/2}) [n \cos(k_0nt) \sin(k_0t + \phi) - \sin(k_0nt) \cos(k_0t + \phi)] - n(n^2 - 1) \sin(k_0nt) \cos(k_0nt)\}}{k_0d [n^2 \cos^2(k_0nt) + \sin^2(k_0nt)]} \quad (3)$$

and

$$I = \frac{\{(2n/T^{1/2}) [n \cos(k_0nt) \cos(k_0t + \phi) + \sin(k_0nt) \sin(k_0t + \phi)] - 2n^2 \cos^2(k_0nt) - (n^2 + 1) \sin^2(k_0nt)\}}{k_0d [n^2 \cos^2(k_0nt) + \sin^2(k_0nt)]}. \quad (4)$$

In this study,  $T$  and  $\phi$  are the measured quantities. Therefore, once  $T$  and  $\phi$  are known,  $\sigma^*$  can be calculated.

#### V. DERIVATION OF FILM PARAMETERS

##### A. Transition temperature (dc measurements), x-ray-diffraction analysis, and sample morphology analysis by scanning electron microscopy

Measurements of dc resistance  $R_{dc}$  versus temperature were performed for all the films analyzed in this study using a standard four-point probe method. The temperature at which the measured resistance fell below the resolution of the measuring instrument ( $\sim 10^{-8} \Omega \text{ cm}$ ) was defined as the dc transition temperature  $T_c^{dc}$ . The transition width ( $\Delta T$ ) was defined as the temperature interval over which the resistance varied between 10% and 90% of the normal state resistance value. The  $T_c^{dc}$  for all the films are listed in Table I. Figure 3 shows the  $R_{dc}$  vs  $T$  curves for two of the films considered in this study. Also shown is the first derivative of  $R_{dc}$  with respect to  $T$ , which more clearly indicates the beginning of the transition. For film no. 3 in Table I, shown in Fig. 3(a), the  $T_c^{dc}$  was 90.6 K, and the transition width was 0.4 K.

X-ray-diffraction analysis was performed on all samples by using a Scintag diffractometer with an energy-dispersive detector which permits minor impurity-phase determination in thin films. Most of the samples studied showed predominantly  $c$ -axis orientation. The mosaic spread of the YBa<sub>2</sub>Cu<sub>3</sub>O<sub>7- $\delta$</sub>  films was determined by using

x-ray rocking curves. Table I shows the x-ray rocking curve full width at half-maximum (FWHM) for the (005) YBa<sub>2</sub>Cu<sub>3</sub>O<sub>7- $\delta$</sub>  peak measured for the samples under consideration. Note that the FWHM of the rocking curves for the films deposited on LaAlO<sub>3</sub> are in close agreement with those corresponding to films on MgO, LaGaO<sub>3</sub>, and YSZ.

TABLE I. Material parameters of YBa<sub>2</sub>Cu<sub>3</sub>O<sub>7- $\delta$</sub>  thin films.

| Sample | Substrate          | DM <sup>a</sup> | $d$ (Å) <sup>b</sup> | $T_c^{dc}$ (K) | FWHM (DEG) <sup>c</sup> |
|--------|--------------------|-----------------|----------------------|----------------|-------------------------|
| 1      | LaAlO <sub>3</sub> | LA              | 4900                 | 88.3           | 0.84                    |
| 2      | YSZ                | OAMS            | 800                  | 91             | 0.96                    |
| 3      | LaAlO <sub>3</sub> | LA              | 2400                 | 90.6           | 0.86                    |
| 4      | LaAlO <sub>3</sub> | LA              | 1769                 | 87.3           | 0.90                    |
| 5      | LaAlO <sub>3</sub> | LA              | 828                  | 85.2           | 0.74                    |
| 6      | LaAlO <sub>3</sub> | LA              | 1762                 | 55.5           | 0.68 <sup>d</sup>       |
| 7      | MgO                | OAMS            | 1000                 | 87.2           | 0.76                    |
| 8      | LaGaO <sub>3</sub> | LA              | 4000                 | 88.0           | 0.80                    |
| 9      | LaAlO <sub>3</sub> | LA              | 1000                 | 86.2           | 0.51                    |
| 10     | MgO                | LA              | 3500                 | 87.5           | 1.08                    |
| 11     | LaAlO <sub>3</sub> | OAMS            | 2600                 | 87.5           | 0.62                    |
| 12     | LaAlO <sub>3</sub> | LA              | 2665                 | 82             | ...                     |
| 13     | LaAlO <sub>3</sub> | LA              | 2655                 | 86.3           | ...                     |
| 14     | LaAlO <sub>3</sub> | LA              | 4000                 | 84.2           | 1.04                    |

<sup>a</sup>Deposition method. LA: laser ablated; OAMS: off-axis magnetron sputtered.

<sup>b</sup>Film thickness.

<sup>c</sup>Full width at half-maximum for the (005) x-ray-diffraction peak of YBa<sub>2</sub>Cu<sub>3</sub>O<sub>7- $\delta$</sub> .

<sup>d</sup>Using the (003) x-ray-diffraction peak.

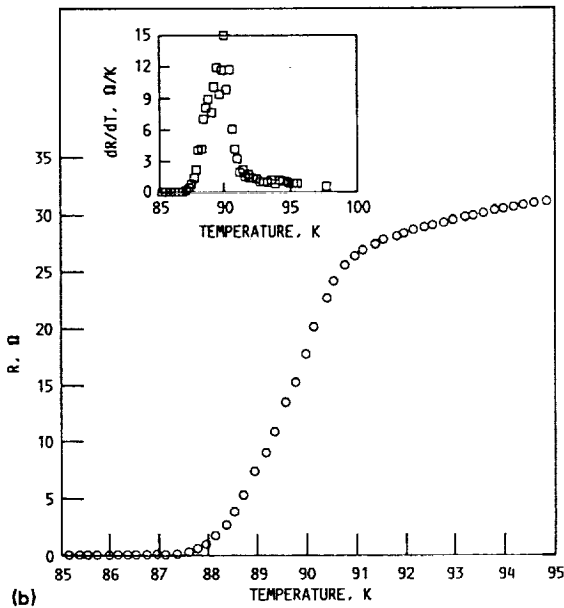
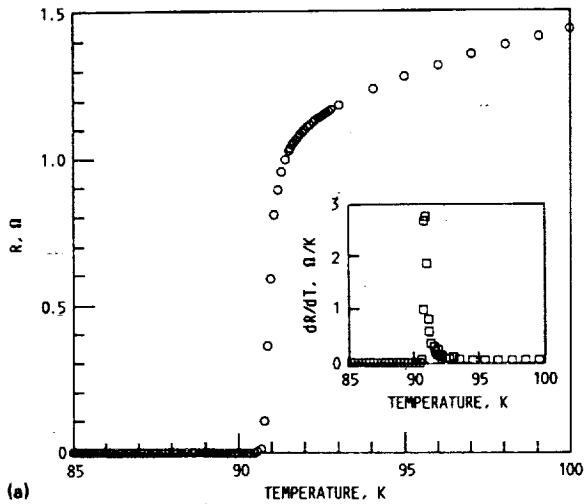


FIG. 3. dc resistance vs temperature and its first derivative ( $dR/dT$ ) for (a) laser-ablated  $\text{YBa}_2\text{Cu}_3\text{O}_{7-\delta}$  thin film (2400 Å) on  $\text{LaAlO}_3$ , (b) off-axis magnetron-sputtered  $\text{YBa}_2\text{Cu}_3\text{O}_{7-\delta}$  thin film (1000 Å) on  $\text{MgO}$ .

This indicates that the twinings of the  $\text{LaAlO}_3$  substrate, believed to broaden the rocking curve FWHM,<sup>23</sup> do not noticeably broaden the rocking curves of these samples.

The surface morphology of the films was studied by scanning electron microscopy (SEM). The laser-ablated film surfaces were generally smooth, as shown in Fig. 4(a) for a film on  $\text{LaAlO}_3$ . This is in contrast to observations by others<sup>24</sup> of grains on the surface of very high-quality laser-ablated  $\text{YBa}_2\text{Cu}_3\text{O}_{7-\delta}$  thin films. However, a view over a larger area of the film [Fig. 4(b)] shows structural inhomogeneities in the film, which may be caused by the substrate's structural defects.

Figure 5(a) shows SEM micrographs of an off-axis magnetron-sputtered film deposited on  $\text{MgO}$ . Clearly this film is not as smooth as the laser-ablated one. Superconducting grains, with sizes between 1 and 3  $\mu\text{m}$ , are uni-

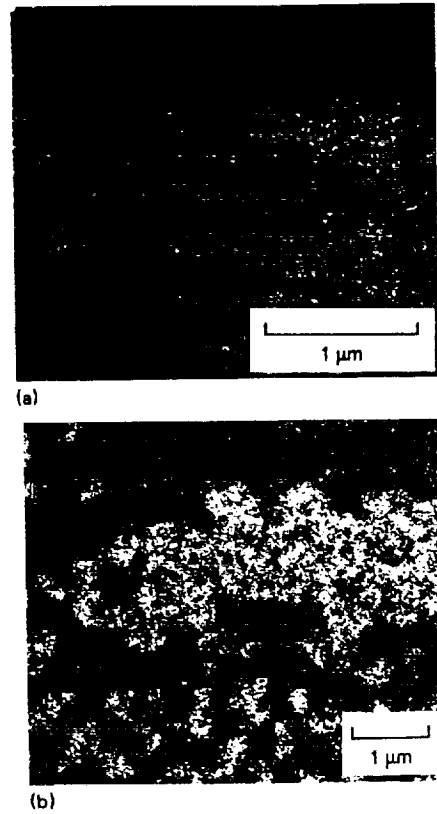


FIG. 4. Scanning electron micrographs of the surface of a laser-ablated (828 Å)  $\text{YBa}_2\text{Cu}_3\text{O}_{7-\delta}$  thin film at approximately (a) 21 000 and (b) 11 000 times.

formly distributed over a smooth surface that also shows a uniform distribution of dips [Fig. 5(b)]. These dips or voids may be caused by negative-ion (oxygen) resputtering, as previously noted by other researchers.<sup>25</sup> The effect of these grains on the microwave properties of the films is still not well understood since it has been observed that the degree of surface roughness does not always correlate with  $R_s$ .<sup>26,27</sup>

## B. Microwave measurements: Transition temperature, normal-state surface resistance, and mean free path

The transition temperature  $T_c^{\text{MW}}$  and other transport parameters of these films determined from microwave power transmission measurements are summarized in Table II. Using the microwave power transmission measurements, we defined  $T_c^{\text{MW}}$  as the temperature just above that at which  $dI/dT$  changed by more than 5% from its normal-state value. In general,  $T_c^{\text{MW}}$  agreed with the onset temperature obtained from the  $R_{\text{dc}}$  vs  $T$  measurements but was a few degrees higher than  $T_c^{\text{dc}}$ . However, we found that for some of the samples the  $T_c^{\text{dc}}$  values varied by a few degrees depending on the contact position across the film, a fact that may be explained in terms of the different paths the current can take between the current contacts. Therefore, since the whole sample can be probed by the micro-

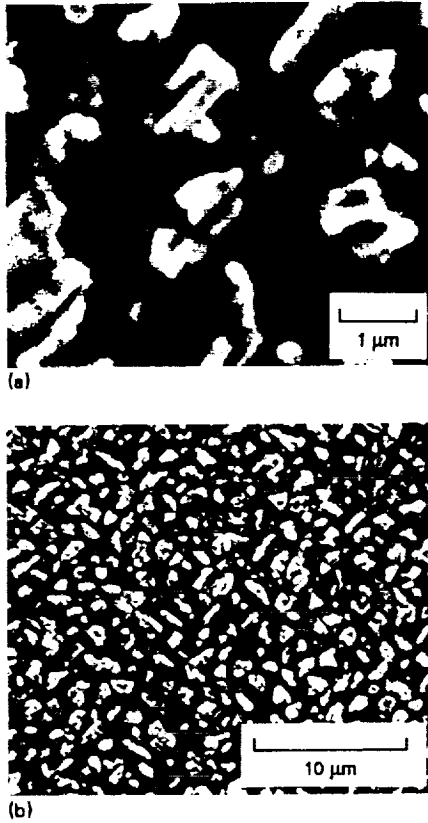


FIG. 5. Scanning electron micrographs of the surface of an off-axis magnetron-sputtered (1000 Å)  $\text{YBa}_2\text{Cu}_3\text{O}_{7-\delta}$  thin film at approximately (a) 11 000 and (b) 2 000 times.

wave technique used in this study, we consider  $T_c^{\text{MW}}$  to be more representative of the superconducting transition of the sample.

The calculation of the conductivity by microwave power transmission measurements allowed us to determine the normal-state resistivity  $\rho_N$ . Previous measurements of HTS materials have shown that the microwave and the dc conductivities are nearly equal in the normal state.<sup>14,28</sup> Therefore, we can use the microwave conductivity to obtain  $\rho_N$  from  $\rho_N = 1/\sigma_N$ . Note that the normal-state resistivities we obtained, approximately 111–400  $\mu\Omega\text{ cm}$  at  $T_c^{\text{MW}}$  for predominantly *c*-axis-oriented films (see Table II), are in close agreement with the values reported for  $\text{YBa}_2\text{Cu}_3\text{O}_{7-\delta}$  thin films by other researchers.<sup>24,29,30</sup> However, our results are large when compared with more recent values of approximately 65–90  $\mu\Omega\text{ cm}$  at temperatures around 100 K, which were obtained for very high-quality  $\text{YBa}_2\text{Cu}_3\text{O}_{7-\delta}$  thin films on  $\text{LaAlO}_3$  and  $\text{MgO}$  substrates.<sup>23</sup>

The normal-state surface resistance  $R_N$  was determined from  $\rho_N$  at  $T_c^{\text{MW}}$  by using the normal skin effect formula,<sup>13,29</sup>  $R_N = (\mu_0\omega\rho_N/2)^{1/2}$ . The values so obtained are shown in Table II. The value of  $\rho_N$  can also be used to determine the carrier mean free path  $l$  by using the free-electron expression,<sup>14,31,32</sup>

$$l\rho_N = [(2\pi e^2/h)(s^2/3\pi^2)^{1/3}]^{-1}, \quad (5)$$

where  $s$  is the density of free carriers,  $e$  is the electronic charge, and  $h$  is Planck's constant. For  $\text{YBa}_2\text{Cu}_3\text{O}_{7-\delta}$  superconductors the density of carriers (holes) is approximately  $9 \times 10^{21}\text{ cm}^{-3}$ .<sup>33</sup> Using this value in Eq. (5) gives

TABLE II. Microwave measured parameters of  $\text{YBa}_2\text{Cu}_3\text{O}_{7-\delta}$  superconducting films.<sup>a</sup>

| Sample | Substrate        | DM <sup>b</sup> | $d$ (Å) <sup>c</sup> | $T_c^{\text{MW}}$ (K) | $R_N^{\text{MW}}$ (Ω) <sup>d</sup> | $\rho_N^{\text{MW}}$ ( $\mu\Omega\text{ cm}$ ) <sup>e</sup> | $\delta_N^{\text{MW}}$ ( $\mu\text{m}$ ) <sup>f</sup> | $l$ (Å) <sup>g</sup> | $R_s$ (mΩ) <sup>h</sup> |
|--------|------------------|-----------------|----------------------|-----------------------|------------------------------------|---|---|----------------------|-------------------------|
| 1      | $\text{LaAlO}_3$ | LA              | 4900                 | 90.8                  | 0.68                               | 379   | 5.57  | 7.8                  | 29 (77)                 |
| 2      | YSZ              | OAMS            | 800                  | 92                    | 0.37                               | 111   | 3.02  | 26.5                 | 45 (77)                 |
| 3      | $\text{LaAlO}_3$ | LA              | 2400                 | 91.6                  | 0.51                               | 216   | 4.24  | 13.6                 | 3.3 (80)                |
| 4      | $\text{LaAlO}_3$ | LA              | 1769                 | 91.7                  | 0.58                               | 274   | 4.72  | 10.7                 | 32 (77)                 |
| 5      | $\text{LaAlO}_3$ | LA              | 828                  | 92.5                  | 0.61                               | 313   | 5.12  | 9.4                  | 112 (77)                |
| 6      | $\text{LaAlO}_3$ | LA              | 1762                 | 94.0                  | 0.96                               | 758   | 7.89  | 3.9                  | 566 (77)                |
| 7      | $\text{MgO}$     | OAMS            | 1000                 | 94.0                  | 0.67                               | 373   | 5.57  | 7.9                  | 15.3 (77)               |
| 8      | $\text{LaAlO}_3$ | LA              | 4000                 | 94.0                  | 0.95                               | 752   | 7.91  | 3.9                  | 13 (77)                 |
| 9      | $\text{LaAlO}_3$ | LA              | 1000                 | 88.6                  | 0.45                               | 164   | 3.66  | 17.9                 | 43 (77)                 |
| 10     | $\text{MgO}$     | LA              | 3500                 | 93.2                  | 0.70                               | 408   | 5.83  | 7.2                  | 86 (77)                 |
| 11     | $\text{LaAlO}_3$ | OAMS            | 2600                 | 93.6                  | 0.52                               | 222   | 4.26  | 13.2                 | 6.9 (77)                |
| 12     | $\text{LaAlO}_3$ | LA              | 2665                 | 88.8                  | 0.60                               | 294   | 4.97  | 10.0                 | 47 (77)                 |
| 13     | $\text{LaAlO}_3$ | LA              | 2655                 | 91.2                  | 0.70                               | 400   | 5.79  | 7.4                  | 29 (78)                 |
| 14     | $\text{LaAlO}_3$ | LA              | 4000                 | 91.4                  | 0.80                               | 524   | 6.62  | 5.6                  | 132 (77)                |

<sup>a</sup>All microwave parameters measured at 30.6 GHz.  $R_N^{\text{MW}}$ ,  $\rho_N^{\text{MW}}$ , and  $\delta_N^{\text{MW}}$  calculated at  $T_c^{\text{MW}}$ .

<sup>b</sup>Deposition method. LA: laser ablated; OAMS: off-axis magnetron sputtered.

<sup>c</sup>Film thickness.

<sup>d</sup>Normal-state surface resistance.

<sup>e</sup>Normal-state resistivity.

<sup>f</sup>Skin depth.

<sup>g</sup>Mean free path.

<sup>h</sup>Superconducting-state surface resistance. Numbers in parentheses indicate temperature in K at which  $R_s$  was measured.

$$l\rho_N^{\text{MW}} = 0.294 \mu\Omega \text{ cm } \mu\text{m} \quad (6)$$

at  $T_c^{\text{MW}}$ . The resulting values of  $l$  calculated from the microwave measurements are given in Table II. Note that contrary to the observations in low- $T_c$  superconductors of the increase in  $l$  with increasing film thickness, no correlation between  $l$  and the film thickness could be observed for the  $\text{YBa}_2\text{Cu}_3\text{O}_{7-\delta}$  thin films. However, our values of  $l$  were consistent with those reported by Bardeen and co-workers<sup>32</sup> for the  $\text{YBa}_2\text{Cu}_3\text{O}_{7-\delta}$  superconductor.

## VI. SURFACE REACTANCE AND MAGNETIC PENETRATION DEPTH

The microwave power transmitted through the high- $T_c$  superconducting thin films considered in this study can be used to determine their surface reactance  $X_r$ . This parameter is directly related to the magnetic penetration depth  $\lambda$ , which is a measure of the distance a magnetic field penetrates into the superconducting material. Therefore, knowledge of  $\lambda$  is very important in determining the suitability of the new HTS materials for microwave applications.

Sridhar<sup>13</sup> was the first to use the microwave power transmitted through Sn thin films, placed at the end walls of a cylindrical copper resonant cavity, to determine the effective surface reactance  $X_{\text{eff}}$  as a function of temperature. Since we were able to measure the microwave-transmitted power directly, we have followed Sridhar's method for obtaining  $X_{\text{eff}}$ . After satisfying all the boundary conditions of the problem, the expression for  $X_{\text{eff}}$  in terms of the transmitted power is

$$X_{\text{eff}} = R_N^{\text{MW}} \cosh(d/\lambda) |P_{\text{xmitt}}^S / P_{\text{xmitt}}^V|^{1/2}, \quad (7)$$

where  $R_N^{\text{MW}}$  is the normal-state surface resistance at  $T = T_c^{\text{MW}}$ ,  $d$  is the film thickness, and  $P_{\text{xmitt}}^V$  and  $P_{\text{xmitt}}^S$  are the power transmitted in the normal and the superconducting states, respectively.

For thin films  $X_{\text{eff}}$  is given by

$$X_{\text{eff}} = X_s \coth(d/\lambda), \quad (8)$$

where  $X_s = \omega\mu_0\lambda$ ,  $\omega/2\pi = f$  is the frequency and  $\mu_0$  is the permeability of free space. Thus, to find  $\lambda$  we solved Eq. (7) for  $X_s$  by assuming an initial value of  $\lambda = 100 \text{ \AA}$ . Using the resulting value of  $X_s$  in Eq. (8), we calculated a new value of  $\lambda$ . This value was then used in Eq. (7) and the process was repeated until the value of  $\lambda$  changed by less than 0.1% between iterations. The obtained values of  $\lambda$ , corresponding to films of different thickness, are discussed in Sec. VIII.

## VII. SURFACE RESISTANCE

The surface resistance of a conductor is important because the propagation properties of transmission lines and the quality factor  $Q$  of resonant cavities and microstrip circuits are related to the losses of electromagnetic energy in these materials during signal propagation. For a good conductor the surface impedance is given by

$$Z_s = (j\mu_0\omega/\sigma)^{1/2}. \quad (9)$$

For a superconductor the conductivity is complex and therefore  $R_s$  can be expressed in terms of  $\sigma_1$  and  $\sigma_2$  as

$$R_s = R_N \left( \left[ \left( \frac{\sigma_1}{\sigma_N} \right)^2 + \left( \frac{\sigma_2}{\sigma_N} \right)^2 \right]^{1/2} - \left( \frac{\sigma_2}{\sigma_N} \right) \right) \times \left[ \left( \frac{\sigma_1}{\sigma_N} \right)^2 + \left( \frac{\sigma_2}{\sigma_N} \right)^2 \right]^{-1/2}, \quad (10)$$

where  $R_N = (\omega\mu_0/2\sigma_N)^{1/2}$  is the surface resistance of the film at  $T_c$ . In the limit  $\sigma_2 \gg \sigma_1$  (typically at low temperatures compared to  $T_c$  and for  $\hbar\omega \ll k_B T_c$ ) the surface resistance is given by

$$R_s \sim R_N (\sigma_1/\sigma_N) (\sigma_N/\sigma_2)^{1/2} = (\omega\mu_0)^{1/2} \lambda^3 \sigma_1/2. \quad (11)$$

Note that in this limit the  $R_s$  of a superconductor increases as the square of the frequency while for a normal conductor the losses increase just as the square root of the frequency. Equation (11) agrees with experimental results within 30% for low- $T_c$  superconductors (for example, within 5% for Sn) when the BCS expression for  $\sigma_1$  is used in Eq. (11).<sup>33</sup>

## VIII. RESULTS AND DISCUSSION

### A. Transmitted power

In general, the temperature dependence of  $T$  and  $\phi$  was similar for the films. However, there were differences in the microwave power transmitted through the films mainly due to variations in their material composition and quality. For a given film the microwave power transmission coefficient was measured with a repeatability of  $\pm 5\%$  over the entire temperature range. This error was estimated by measuring several films repeatedly with the film being removed and replaced between each set of measurements.

The metallic character of the films is evidenced by the positive slope of  $T$  with decreasing temperature for  $T > T_c^{\text{MW}}$  (see Fig. 6). At  $T_c^{\text{MW}}$ , the transmitted power decreased abruptly and continued decreasing with decreasing temperature, leveling off at low temperatures. We observed that the abruptness of this transition and the temperature at which the transmitted power started to level off was closely related to the film quality, as determined by the values of  $R_s$ ,  $\lambda$ , and  $\sigma_2$ . Different power levels ( $\sim 0.1, 1.0$ , and  $16 \text{ mW}$ ) were used in probing the samples. Note that although for low power levels and low temperatures the data are noisier, the transmitted-to-incident power ratio is the same for all incident powers. This indicates that the superconducting state is not altered by the incident power, at least for the different power levels and frequency range considered in this study. The absence of any appreciable shift of  $T_c^{\text{MW}}$  for most of the films, within a resolution of  $0.5 \text{ K}$ , supports this argument. This behavior was typical of all the films considered independent of thickness.

Figure 7 shows the measured relative phase shift,  $\Delta\phi = \phi_{300 \text{ K}} - \phi(T)$ , corresponding to films 1 and 2 of Table II. Note that in the normal state  $\Delta\phi$  is basically constant. Below  $T_c^{\text{MW}}$ , an abrupt negative change in  $\Delta\phi$  takes place, leveling off at temperatures below  $85 \text{ K}$  for film 2 and continuing to decrease with decreasing temperature

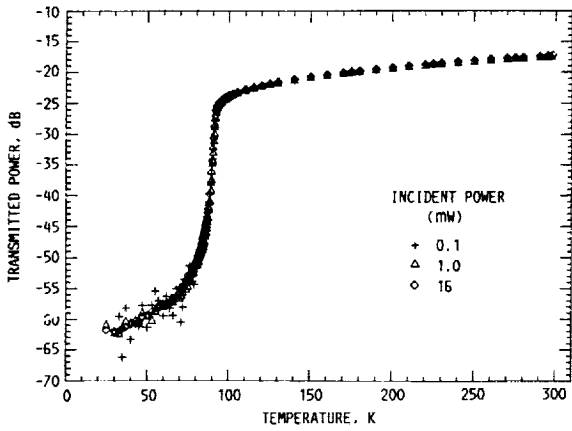


FIG. 6. Transmitted power vs temperature for a laser-ablated  $\text{YBa}_2\text{Cu}_3\text{O}_{7-\delta}$  thin film (2400 Å) on  $\text{LaAlO}_3$ .

for film 1. The observed  $\Delta\phi$  for film 2 is consistent with that expected for low- $T_c$  superconductors since its magnitude is less than the  $\pi/2$  value expected for a totally superconducting thin film ( $\sigma_2/\sigma_1 \gg 1$ ). However, for almost all the films considered in this study,  $\Delta\phi$  became larger than  $\pi/2$  at some temperature below  $T_c^{\text{MW}}$  as shown by film 1 in Fig. 7. Nichols *et al.*<sup>15</sup> also observed this effect in a transmission experiment with  $\text{YBa}_2\text{Cu}_3\text{O}_{7-\delta}$  thin films. They explained their observations in terms of leakages through the film owing to pinholes, microcracks, normal insertions, and possibly other leakage sources in the film. However, we have seen the recurrence of this effect on high-quality superconducting  $\text{YBa}_2\text{Cu}_3\text{O}_{7-\delta}$  thin films and failed to observe it in Tl- and Bi-based films probed by the same technique. Based on these observations we believe that the behavior of  $\Delta\phi$  is not exclusively the result of leakage sources but rather caused by an intrinsic, and so far not understood, mechanism present in high-quality  $\text{YBa}_2\text{Cu}_3\text{O}_{7-\delta}$  thin films. The constraints imposed by this

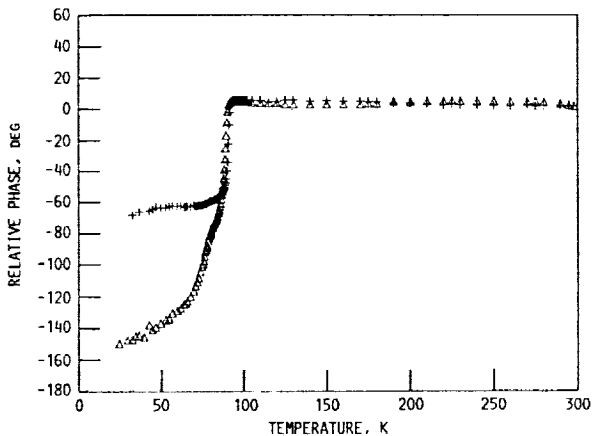


FIG. 7. Measured relative phase shift  $\Delta\phi$  for an off-axis magnetron-sputtered  $\text{YBa}_2\text{Cu}_3\text{O}_{7-\delta}$  thin film (800 Å) on YSZ (+), and for a laser-ablated  $\text{YBa}_2\text{Cu}_3\text{O}_{7-\delta}$  thin film (4900 Å) on  $\text{LaAlO}_3$  ( $\Delta$ ).

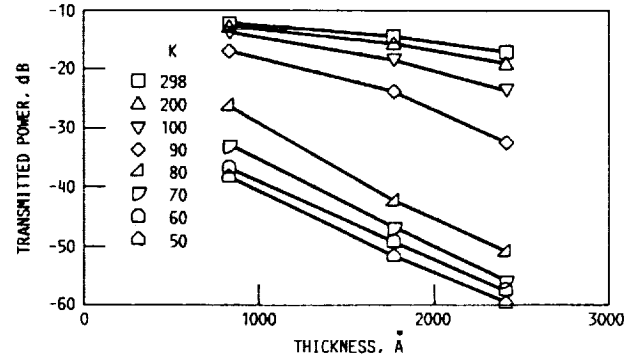


FIG. 8. Transmitted power vs thickness for laser-ablated  $\text{YBa}_2\text{Cu}_3\text{O}_{7-\delta}$  thin films.

effect on the determination of  $\sigma_1$  in the superconducting state are discussed later.

Figure 8 shows a plot of the microwave power transmitted at 33.3 GHz through three films of thickness less than 3000 Å, which were deposited by laser ablation on  $\text{LaAlO}_3$  substrates of equal thickness. As expected, the transmitted power decreases exponentially with increasing film thickness for temperatures below 70 K even though the  $T_c^{\text{dc}}$  of the films differed by approximately 5 K. The attenuation coefficient of the films varied from  $4 \times 10^5 \text{ cm}^{-1}$  at 300 K to  $1 \times 10^7 \text{ cm}^{-1}$  at temperatures below 70 K. The nonlinear behavior seen near  $T_c$  in the plot of the power vs thickness data in Fig. 8 is due to the difference in  $T_c$  values of the films. It was also noticed that for films thicker than 3000 Å the exponential dependence of the power transmitted on film thickness was not followed. This may be due to the increase in the number of  $a$ -axis-oriented grains with increasing film thickness, as has been observed by others.<sup>34</sup>

It was also observed that for the above-mentioned films the  $T_c^{\text{MW}}$  for the thinnest film was approximately 2 K higher than for the two thicker films which both have approximately the same  $T_c^{\text{MW}}$ . However, the thinnest film had a broader transition region than that exhibited by the thicker films, which may have been caused by the presence of a large number of weak links, as has been observed in similar films by others.<sup>35,36</sup> This shows that  $T_c^{\text{MW}}$  should not be the only parameter used to estimate film quality.

## B. Complex conductivity

As shown in Sec. IV, one can obtain the complex conductivity of the  $\text{YBa}_2\text{Cu}_3\text{O}_{7-\delta}$  thin films from the magnitude and phase of the microwave transmitted power, using Eqs. (3) and (4). Figure 9 shows the real and imaginary parts of the complex conductivity as a function of temperature for one of the films considered in this study (no. 1, Table II). Observe that in the normal state,  $\sigma_1$  exhibits a metallic behavior as a function of decreasing temperature (see insert in Fig. 9), whereas  $\sigma_2$  remains very close to zero as expected for a good conductor. This behavior in the normal state was typical of all the films considered in this

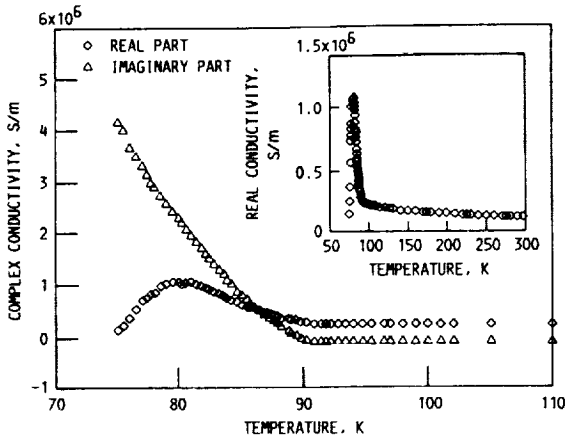


FIG. 9. Real and imaginary parts of the microwave conductivity vs temperature at 30.6 GHz for a laser-ablated  $\text{YBa}_2\text{Cu}_3\text{O}_{7-\delta}$  thin film (4900 Å) on  $\text{LaAlO}_3$ .

study. Both  $\sigma_1$  and  $\sigma_2$  increase rapidly when the films cool through the transition temperature. Observe the maximum reached by  $\sigma_1$  and its subsequent rapid decrease at temperatures not far from  $T_c^{\text{MW}}$ , while  $\sigma_2$  exhibits a monotonic increase with decreasing temperature. Similar behaviors for  $\sigma_1$  and  $\sigma_2$  just below  $T_c^{\text{MW}}$  were observed by Nichols *et al.*<sup>15</sup> in  $\text{YBa}_2\text{Cu}_3\text{O}_{7-\delta}$  thin films ( $\sim 10\,000$  Å) deposited on  $\text{Al}_2\text{O}_3$ ,  $\text{YSZ}$ , and  $\text{MgO}$  substrates, and more recently by Golosovsky *et al.*<sup>16</sup> for  $\text{YBa}_2\text{Cu}_3\text{O}_{7-\delta}$  on  $\text{MgO}$ . Nichols *et al.*<sup>15</sup> suggested that this behavior is consistent with that expected for a homogeneous superconductor which, for decreasing temperatures, exhibits both an increasing energy gap and an increasing density of quasiparticle states at the gap edge, such as a BCS superconductor.

A comparison of the measured  $\sigma_1$  with that calculated from the BCS-based Mattis–Bardeen equations<sup>3,12</sup> is shown in Fig. 10. The curve was calculated by using the measured  $T_c^{\text{MW}}$  and  $\sigma_1$  at  $T_c^{\text{MW}}$ , and assuming an isotropic energy gap. It is evident that the temperature behavior of the measured  $\sigma_1$  deviates from that expected from the BCS theory. According to the BCS theory, the increase in  $\sigma_1$  when the film cools through the transition temperature is accompanied by an increase in nuclear-spin relaxation rate ( $1/T_1$ ) above the normal-state value because of the increase of the density of quasiparticles at the gap edge. At lower temperatures both  $\sigma_1$  and  $1/T_1$  decrease exponentially to zero as the quasiparticles above the gap are frozen out.<sup>37</sup> However, Warren *et al.*<sup>38</sup> have shown that  $1/T_1$  for quasiparticles of the chain-forming  $\text{Cu}(1)$  and planar  $\text{Cu}(2)$  lattice sites decreases rapidly when the film cools through  $T_c$ . Therefore, if the observed behavior of  $\sigma_1$  is a consequence of the intrinsic superconducting state of the film, then this type of response may be due to a nonisotropic energy gap or to a superconductor that does not behave according to the BCS theory. Furthermore, if the behavior is intrinsic to the material, then one would expect the temperature dependence of  $\sigma_1$  to be the same for all the  $\text{YBa}_2\text{Cu}_3\text{O}_{7-\delta}$  HTS thin films considered, independent of

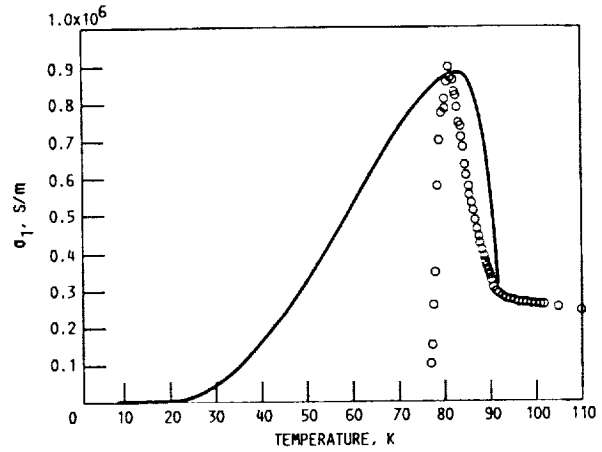


FIG. 10. Real part of the microwave conductivity for a  $\text{YBa}_2\text{Cu}_3\text{O}_{7-\delta}$  thin film (4900 Å) on  $\text{LaAlO}_3$ . The solid line represents a numerical fit using the BCS temperature dependence for  $\sigma_1$ .

the deposition technique and substrate employed in the film fabrication. Unfortunately, the data for some of the films on different substrates do not support this assertion. In these films it was observed that both  $\sigma_1$  and  $\sigma_2$  increase as the film is cooled through its transition temperature, but the rapid decrease in  $\sigma_1$  observed for most of the films analyzed in this study was not observed. Instead  $\sigma_1$  leveled off at low temperatures as shown in Fig. 11 for a laser-ablated film on  $\text{LaAlO}_3$ .

One can explain the variability of behavior of  $\sigma_1(T)$  by taking into account the granular nature of the  $\text{YBa}_2\text{Cu}_3\text{O}_{7-\delta}$  HTS thin films. Ho *et al.*<sup>14</sup> and Kobrin *et al.*<sup>28</sup> have suggested that these HTS thin films can be visualized as composed of superconducting regions embedded in a normal conducting matrix. When the grains undergo the superconducting transition as the film is cooled through  $T_c$  the microwave electric field will be excluded

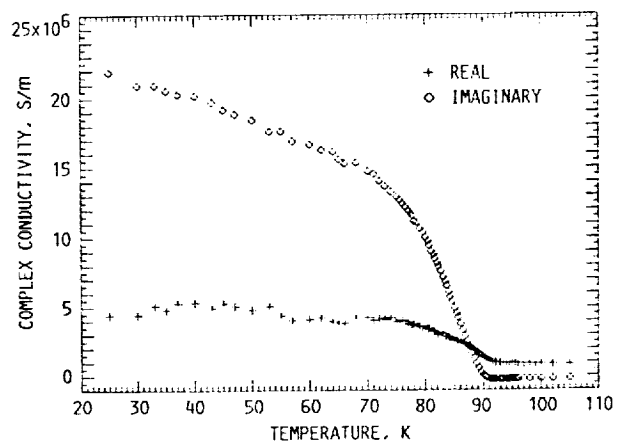


FIG. 11. Real and imaginary parts of the microwave conductivity for a laser-ablated  $\text{YBa}_2\text{Cu}_3\text{O}_{7-\delta}$  thin film (2655 Å,  $T_c^{\text{MW}} = 91.2$  K) on  $\text{LaAlO}_3$  at 35 GHz.

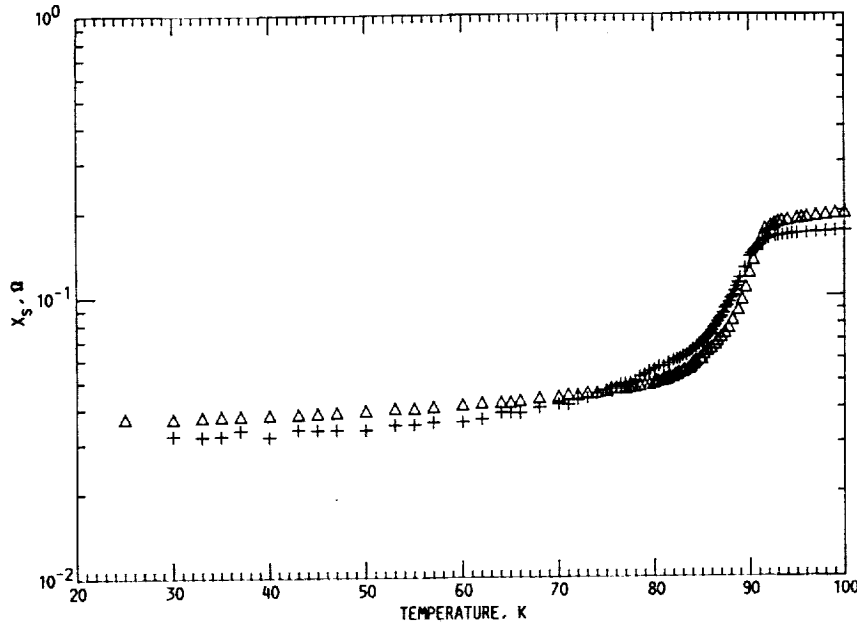


FIG. 12. Surface reactance vs temperature at 30.6 GHz for two laser-ablated films on  $\text{LaAlO}_3$  [no. 3, Table II, 2400 Å, ( $\Delta$ ); no. 4, Table II, 1769 Å (+)].

from the superconducting regions. This exclusion of the electric field from the superconducting regions will enhance the effective current density in the intergranular normal regions resulting in an increase in  $\sigma_1$  of the film. Since the distribution of nonsuperconducting inclusions varies from film to film, the temperature dependence of  $\sigma_1$  will be different for each film. In addition, the distribution of  $T_c$ 's from grain to grain may also contribute to this effect.

### C. Surface reactance and magnetic penetration depth

Figure 12 shows the surface reactance versus temperature for two of the films investigated in this study (films no. 3 and no. 4 of Table I). Observe that film no. 3 exhibits a strong shielding of the microwave field as deduced from the sharp decrease of  $X_s$  at temperatures just below  $T_c^{\text{MW}}$ , and the slow change of  $X_s$  with decreasing temperatures at temperatures below approximately 80 K. On the other hand,  $X_s$  of film no. 4 decays slower than that for film no. 3 at temperatures below  $T_c^{\text{MW}}$  and shows a much broader transition. As discussed in Sec. VI, we have used the relationship between  $X_s$  and  $\lambda$  to determine  $\lambda$  for the films analyzed in this study. Figure 13 shows a plot of  $\lambda$  versus film thickness  $d$  at 30 K for films deposited on  $\text{LaAlO}_3$ . Observe that the anisotropy of  $\lambda$  is indicated in this plot by the large value of  $\lambda$  observed in Fig. 13 for film no. 6 of Table I, which is a predominantly  $a$ -axis-oriented film as determined by x-ray-diffraction analysis. Taking the ratio between  $\lambda$  for this film and that of films no. 4 and no. 9 of Table I, which have comparable thickness, yields  $\lambda_c/\lambda_4 \approx 3.8$  and  $\lambda_c/\lambda_9 \approx 5.7$ , respectively. These ratios are consistent with the value of  $\lambda_c/\lambda_{ab} \approx 5$  reported by others for single crystals and high-purity samples of the  $\text{YBa}_2\text{Cu}_3\text{O}_{7-\delta}$  superconductor.<sup>39-41</sup> Observations by others<sup>42</sup> have shown that as the film becomes thicker it is more difficult to preserve their  $c$ -axis orientation, i.e., the

number of  $a$ -axis-oriented grains increases with increasing  $d$ . Since the shielding currents along the  $c$ -axis-oriented grains are smaller than those along the  $a$ - $b$  plane, one expects  $\lambda$  to increase with film thickness as seen in Fig. 13.

The solid line in Fig. 13 represents a fit to the data using a second-degree polynomial regression analysis. This gives a value for the penetration depth corresponding to zero film thickness of  $\lambda(d=0) = 90 \pm 30$  nm. This value of  $\lambda$  represents the smallest possible value that can be obtained for a  $c$ -axis-oriented film free from grain-boundary effects and other nonsuperconducting inhomogeneities; i.e., the intrinsic value of  $\lambda$  at low temperatures for the  $\text{YBa}_2\text{Cu}_3\text{O}_{7-\delta}$  superconductor. To our knowledge, this is the first time that this value has been estimated experimentally for any of the HTS materials.

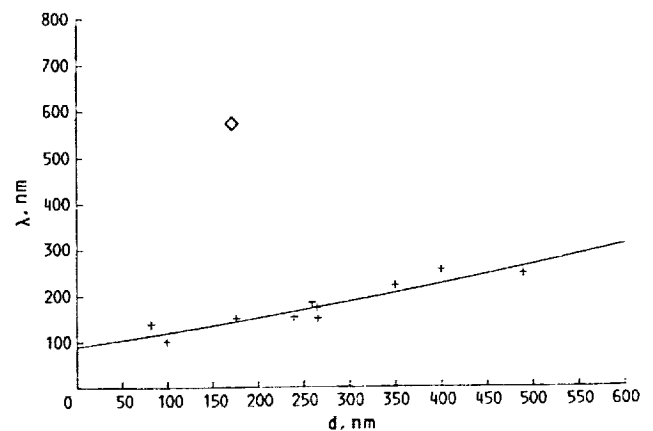


FIG. 13. Magnetic penetration depth  $\lambda$  vs film thickness  $d$  for  $\text{YBa}_2\text{Cu}_3\text{O}_{7-\delta}$  thin films.  $\diamond$  represents an  $a$ -axis-oriented film and the solid line represents a second-degree polynomial fit.

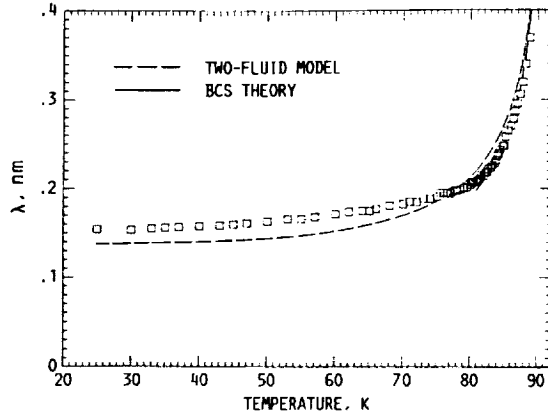


FIG. 14. Magnetic penetration depth  $\lambda$  vs temperature for a laser-ablated thin film (2400 Å) on  $\text{LaAlO}_3$ . The dashed line represents a fit to the data using the temperature dependence for  $\lambda$  according to the two-fluid model and the solid line represents a fit to the data using the temperature dependence of  $\lambda$  according to the BCS theory in the clean limit.

The temperature dependence of  $\lambda$  for a laser-ablated film on  $\text{LaAlO}_3$  (no. 3 of Table I) is shown in Fig. 14. Using the expressions for the temperature dependence of  $\lambda$  in the two-fluid model (TFM) approximation,

$$\lambda(T) = \lambda(0) [1 - (T/T_c)^4]^{-1/2}, \quad (12)$$

and according to the weak-coupling BCS theory in the clean limit,<sup>40,43</sup>

$$\lambda(T) = \lambda(0) [2(1 - T/T_c)]^{-1/2}, \quad T \rightarrow T_c, \quad (13)$$

we have estimated the zero-temperature penetration depth [ $\lambda(0)$ ], by fitting the measured  $\lambda$  to Eqs. (12) and (13) using a standard least-squares fit. All the fittings to the experimental data were carried out for  $T/T_c < 0.98$ . For the film in Fig. 14 we obtained  $\lambda_{\text{BCS}}(0) = 96 \pm 9$  nm and  $\lambda_{\text{TFM}}(0) = 138 \pm 13$  nm. These values are consistent with those reported by others for *c*-axis-oriented thin films and single crystals of  $\text{YBa}_2\text{Cu}_3\text{O}_{7-\delta}$ .<sup>39,44,45</sup> For sample no. 4, which according to the  $X_s$  plot (see Fig. 12) is not quite as good in overall quality as film no. 3, we found  $\lambda_{\text{TFM}}(0) = 145 \pm 12$  nm and  $\lambda_{\text{BCS}}(0) = 113 \pm 8$  nm, in agreement with what was expected from the  $X_s$  data. The increase of  $\lambda$  may be due to the effect of grain boundaries and other nonsuperconducting inhomogeneities as has been suggested by others.<sup>46</sup>

In summary, the power-transmission technique presented here provides a nondestructive technique for the determination of  $\lambda$  for HTS thin films, in contrast to microstrip resonator methods in which the film must be patterned. We have shown that the technique is sensitive to the intrinsic anisotropy of  $\lambda$  as well as to the overall film quality.

#### D. Surface resistance

The surface resistance of the films was calculated by using the values of  $\sigma_1$  and  $\sigma_2$  obtained from power-transmission measurements in Eq. (10). We have used  $R_N$  and

$\sigma_N$  as the surface resistance and the real conductivity, respectively, of the film in the normal state and at  $T = T_c^{\text{MW}}$ . We have already mentioned that for most of the films analyzed in this study we could not determine  $\sigma_1$  at temperatures far below  $T_c^{\text{MW}}$ . Although the values of  $\sigma_1$  obtained within this limited temperature range below  $T_c^{\text{MW}}$  allowed us to compare its behavior with that expected from the Mattis-Bardeen equations, for most of the films studied we could not determine  $R_s$  at temperatures far below  $T_c^{\text{MW}}$ .

Values of  $R_s$  calculated at temperatures around 77 K and at 30.6 GHz are given in Table II. The smallest values of  $R_s$  at 77 K were obtained for a laser-ablated thin film (2400 Å; no. 3, Table I) on  $\text{LaAlO}_3$ ,  $R_s \sim 3.3$  mΩ, and an off-axis magnetron-sputtered  $\text{YBa}_2\text{Cu}_3\text{O}_{7-\delta}$  thin film (2600 Å; no. 11, Table I) on  $\text{LaAlO}_3$ ,  $R_s \sim 6.9$  mΩ. These values are lower than those for pure copper ( $R_s \sim 16$  mΩ at 77 K and 30.6 GHz), and are also in good agreement with those reported for high-quality  $\text{YBa}_2\text{Cu}_3\text{O}_{7-\delta}$  thin films deposited by off-axis magnetron sputtering onto  $\text{LaAlO}_3$  substrates ( $\sim 500$  μΩ at 10 GHz and 77 K, which corresponds to approximately 4.7 mΩ at 30.6 GHz, assuming a quadratic frequency dependence).<sup>23</sup> However, they are still somewhat larger than the best value reported to date for a laser-ablated  $\text{YBa}_2\text{Cu}_3\text{O}_{7-\delta}$  thin film on  $\text{SrTiO}_3$ , with an  $R_s$  value of  $\sim 1$  mΩ at 30.6 GHz, again assuming a quadratic frequency dependence.<sup>24</sup>

We also observed that for films of thickness less than 1000 Å (for example, films no. 2 and no. 5 of Table II)  $R_s$  becomes larger than for most of the thicker films considered in this study. However, this effect was not directly correlated with the  $T_c$  values, i.e., a high  $R_s$  value did not necessarily imply a low value for  $T_c$  (see film no. 2 of Table II). In general, for the overall range of film thicknesses studied, no clear correlation between  $R_s$  and the thickness of the film was observed. The large value of  $R_s$  observed for film no. 6 of Table II is directly related to its *a*-axis orientation. The lack of a strong correlation between  $T_c$  and  $R_s$  for these HTS thin films is evidence of the unpredictability of the overall potential performance of these films just based on one or two measured parameters. In addition, this again indicates the tremendous problem that the differences in type, average size, and location of the impurities and lattice defects from film to film still pose for the complete and unambiguous characterization of these materials.

To date, most of the  $R_s$  measurements of  $\text{YBa}_2\text{Cu}_3\text{O}_{7-\delta}$  HTS have been performed using resonant-cavity techniques.<sup>24,47-49</sup> Although this technique provides a direct measurement of  $R_s$ , it does not provide information about other important transport parameters in the superconducting state such as  $\sigma^*$  and  $\lambda$  without assuming a model for the superconducting state. Furthermore, it has been observed that the values of  $R_s$  for  $\text{YBa}_2\text{Cu}_3\text{O}_{7-\delta}$  thin films vary by more than an order of magnitude in measurements performed at different laboratories.<sup>50</sup> In view of this, we have measured the  $R_s$  of three laser-ablated  $\text{YBa}_2\text{Cu}_3\text{O}_{7-\delta}$  thin films ( $\sim 2660$ – $4000$  Å) on  $\text{LaAlO}_3$  by microwave power transmission and resonant-cavity measurements. All three films were measured by Newman, of

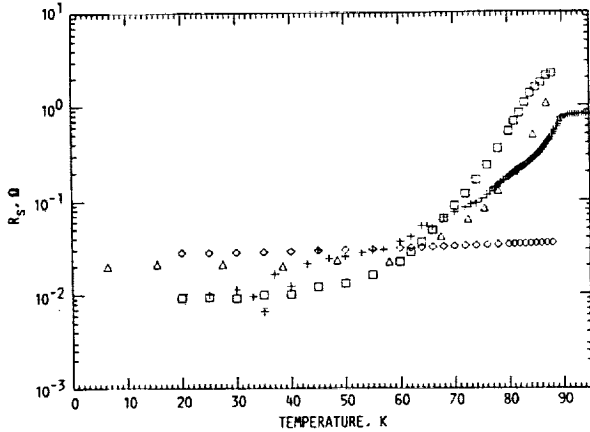


FIG. 15. Surface resistance  $R_s$  vs temperature at 36 GHz for a  $\text{YBa}_2\text{Cu}_3\text{O}_{7-\delta}$  thin film (4000 Å) on  $\text{LaAlO}_3$  as measured by a microwave power-transmission method (+) and by a cavity-wall replacement method: NRL ( $\square$ ) and FM ( $\triangle$ ). The  $R_s$  for copper ( $\diamond$ ) is also plotted for comparison.

the Naval Research Laboratory (NRL) in Washington, DC, using a  $\text{TE}_{011}$ -mode copper cavity resonant at 36 GHz. One film was also measured by Wilber, of Fort Monmouth (FM) in New Jersey, using a  $\text{TE}_{011}$ -mode copper cavity resonant at 35 GHz.

Figure 15 shows  $R_s$  versus temperature for the film ( $\sim 4000$  Å) measured by both NRL and FM. The  $R_s$  of copper is also shown for comparison purposes. This film had a  $T_c^{\text{dc}} = 84.2$  K and a  $T_c^{\text{MW}} = 90$  K.  $R_s$  values of 177 and 25 mΩ at 80 and 50 K, respectively, were obtained by using the power-transmission method. The scatter of the data below  $\sim 50$  K is due to our use of an input power of only 1 mW. Similarly,  $R_s$  values of 528 mΩ at 80 K, and 13 mΩ at 50 K, were measured at NRL. The  $R_s$  values (scaled to 36 GHz assuming an  $f^2$  dependence) measured at FM were 127 mΩ at 78 K, and 23 mΩ at 48.5 K. The uncertainty in this data is  $\pm 20\%$  below 50 K. The time elapsed between the  $R_s$  measurements shown in Fig. 15 was 1.5 months, with the NRL measurement performed first and our microwave power-transmission measurement last. Note that both techniques give an  $R_s$  that decreases rapidly when the sample is cooled through  $T_c^{\text{MW}}$  and then levels off at lower temperatures showing a residual surface resistance that changes very slowly with decreasing temperature. Although there is an appreciable discrepancy between the  $R_s$  values obtained by the two techniques at temperatures not far from  $T_c^{\text{MW}}$ , they agree within a factor of 2 at lower temperatures. A similar behavior was observed for the other two samples, and the results obtained are presented in Ref. 51. When the  $R_s$  value of the sample drops below that of copper the accuracy of copper cavities is limited and the measured value can often be considered only an upper bound to the actual  $R_s$  value. The good correspondence between the three measurements suggests that the microwave power-transmission technique can be used as an alternate technique to copper cavities for the determination of  $R_s$  in HTS thin films. Further study is necessary to

determine any lower limits on the values of  $R_s$  that may be measured by this technique.

## IX. CONCLUDING REMARKS

We have studied the microwave response of  $\text{YBa}_2\text{Cu}_3\text{O}_{7-\delta}$  superconducting thin films by measuring the microwave power transmitted through the films at frequencies within the  $Ka$  band, and at temperatures ranging from 20 to 300 K. We found that the microwave transmission properties are very weakly dependent on temperature in the normal state, but change drastically upon transition to the superconducting state. In particular, the transmission decreases and there is a negative phase shift with respect to the phase at room temperature when the sample is cooled through its transition temperature.

The magnetic penetration depth for all the films was determined from the surface reactance of the films. We were able to experimentally verify the intrinsic anisotropy of  $\lambda$  for this HTS superconductor by measuring this parameter in  $c$ -axis- and predominantly  $a$ -axis-oriented films. As expected from the anisotropy of these HTS materials, the value of  $\lambda$  for the  $a$ -axis-oriented film was larger than the values obtained for  $c$ -axis-oriented films. In fact, the ratio of  $\lambda$  for an  $a$ -axis-oriented film to that of  $c$ -axis-oriented films agrees very well with that reported by others for single crystals and very high-quality thin films of the  $\text{YBa}_2\text{Cu}_3\text{O}_{7-\delta}$  superconductor. We also observed that  $\lambda$  increased with increasing film thickness, which is consistent with the increase of the number of  $a$ -axis-oriented grains and other structural and material defects with increasing film thickness. From the thickness dependence of  $\lambda$  we were able to estimate, for the first time, the intrinsic value of  $\lambda$  for the  $\text{YBa}_2\text{Cu}_3\text{O}_{7-\delta}$  superconductor. This value is consistent with that expected from measurements of  $\lambda$  in single crystals using other techniques.

The microwave complex conductivity was determined in both the normal and the superconducting state. We observed that both  $\sigma_1$  and  $\sigma_2$  increased on transition to the superconducting state. This implies that the temperature dependence of  $\sigma_1$  deviates from the predictions of the two-fluid model. In addition, we found that the temperature dependence of  $\sigma_1$  is not consistent with that expected from the Mattis-Bardeen equations and the BCS theory.

We have calculated the surface resistance  $R_s$  for all the films, and we found that for the films of the highest quality the  $R_s$  values at 77 K were in good agreement with those reported by other researchers for similar films and were equal to or less than that for copper at the same frequencies and temperatures. Our analysis suggests that the laser-ablated and the dc off-axis magnetron-sputtered  $\text{YBa}_2\text{Cu}_3\text{O}_{7-\delta}$  thin films are promising for microwave applications. The merits of our experimental technique have been tested against widely accepted characterization techniques, such as resonant-cavity measurements. The consistency of the  $R_s$  values measured using both techniques support the validity of our method. The strength of our technique is that it allows the calculation of several transport parameters ( $\lambda$ ,  $\sigma^*$ ,  $R_s$ , etc.) from one single measurement, an attribute rarely found in other probing techniques

employed in HTS films research. The versatility of our technique rests not only in yielding values of  $\lambda$ ,  $\sigma^*$ , and  $R_s$  in good agreement with those obtained by other techniques, but also in being sensitive to the intrinsic anisotropy of these materials, as evidenced by the results of  $\lambda$  for  $\text{YBa}_2\text{Cu}_3\text{O}_{7-\delta}$  thin films.

## ACKNOWLEDGMENTS

The authors would like to thank Dr. D. E. Farrell for helpful discussions on the magnetic penetration depth. Our deepest thanks to Dr. H. Newman and Dr. W. Wilber for the  $R_s$  measurements using cavity techniques. We also thank Dr. J. Talvacchio for providing some of the films used in this study, and Ralph Garlick for the x-ray-diffraction measurements. The assistance of D. Bohmann and N. Varaljay in obtaining the SEM micrographs of the films and in measuring their thickness is deeply appreciated.

- <sup>1</sup>J. G. Bednorz and K. A. Mueller, *Z. Physics B* **64**, 189 (1986).
- <sup>2</sup>M. K. Wu, J. R. Ashburn, C. J. Torng, P. H. Hor, R. L. Meng, L. Gao, Z. J. Huang, Y. Q. Wang, and C. W. Chu, *Phys. Rev. Lett.* **58**, 908 (1987).
- <sup>3</sup>M. Tinkham, *Introduction to Superconductivity* (McGraw-Hill, New York, 1979).
- <sup>4</sup>J. H. Hinken, *Superconductor Electronics: Fundamentals and Microwave Applications* (Springer, Berlin, 1988), p. 41.
- <sup>5</sup>K. B. Bhasin, J. D. Warner, R. R. Romanofsky, V. O. Heinen, C. M. Chorey, K. S. Kong, H. Y. Lee, and T. Itoh, *IEEE MTT-S Int. Microwave Symp. Dig.* **1**, 269 (1990).
- <sup>6</sup>R. C. Hansen, *IEEE Int. Symp. Dig. Antennas Propagation*, **2**, 720 (1990).
- <sup>7</sup>Y. Yoshisato, A. Takeoka, T. Ikemachi, K. Niki, T. Yokoo, S. Nakano, and Y. Kuwano, *Jpn. J. Appl. Phys.* **29**, 1080 (1990).
- <sup>8</sup>R. E. Glover III and M. Tinkham, *Phys. Rev.* **108**, 243 (1957).
- <sup>9</sup>N. M. Rugheimer, A. Lehoczy, and C. V. Briscoe, *Phys. Rev.* **154**, 414 (1967).
- <sup>10</sup>J. Bardeen, L. N. Cooper, and J. R. Schrieffer, *Phys. Rev.* **108**, 1175 (1957).
- <sup>11</sup>S. L. Lehoczy and C. V. Briscoe, *Phys. Rev. B* **11**, 3938 (1971).
- <sup>12</sup>D. C. Mattis and J. Bardeen, *Phys. Rev.* **111**, 412 (1958).
- <sup>13</sup>S. Sridhar, *J. Appl. Phys.* **63**, 159 (1988).
- <sup>14</sup>W. Ho, P. J. Hood, W. F. Hall, P. Kobrin, A. B. Harker, and R. E. DeWames, *Phys. Rev. B* **38**, 7029 (1988).
- <sup>15</sup>C. S. Nichols, N. S. Shiren, R. B. Laibowitz, and T. G. Kazyaka, *Phys. Rev. B* **38**, 11 970 (1988).
- <sup>16</sup>M. Golosovsky, D. Davidov, C. Rettori, and A. Stern, *Phys. Rev. B* **40**, 9299 (1989).
- <sup>17</sup>S. K. Tewksbury, L. A. Hornak, and M. Hatamian, *Solid-State Electron.* **32**, 947 (1989).
- <sup>18</sup>T. Venkatesan, X. D. Wu, B. Dutta, A. Inam, M. S. Hedge, D. M. Hwang, C. C. Chang, L. Nazar, and B. Wilkens, *Appl. Phys. Lett.* **54**, 581 (1989).
- <sup>19</sup>F. A. Miranda, W. L. Gordon, V. O. Heinen, B. T. Ebihara, and K. B. Bhasin, *Advances in Cryogenic Engineering* (Plenum, New York, 1990), Vol. 35, p. 1593.
- <sup>20</sup>F. A. Miranda, W. L. Gordon, K. B. Bhasin, B. T. Ebihara, V. O. Heinen, and C. M. Chorey, *Microwave Opt. Tech. Lett.* **3**, 11 (1990).
- <sup>21</sup>J. D. Warner, J. E. Meola, and K. A. Jenkins, in *Superconductivity and Applications*, edited by H. S. Kwok, Y. H. Kao, and D. T. Shaw (Plenum, New York, 1990), p. 163.
- <sup>22</sup>J. Talvacchio, J. R. Gavaler, M. G. Forrester, and T. T. Braggins, in *Science and Technology of Thin Film Superconductors II*, edited by R. D. McConnell and R. D. Noufe (Plenum, New York, 1991), p. 57.
- <sup>23</sup>N. Newman, K. Char, S. M. Garrison, R. W. Barton, R. C. Taber, C. B. Eom, T. H. Geballe, and B. Wilkens, *Appl. Phys. Lett.* **57**, 520 (1990).
- <sup>24</sup>N. Klein, G. Muller, H. Piel, B. Roas, L. Schultz, U. Klein, and M. Peiniger, *Appl. Phys. Lett.* **54**, 757 (1989).
- <sup>25</sup>M. Migliuolo, R. M. Belan, and J. A. Brewer, *Appl. Phys. Lett.* **56**, 2572 (1990).
- <sup>26</sup>T. Venkatesan (private communication).
- <sup>27</sup>J. Talvacchio (private communication).
- <sup>28</sup>P. H. Kobrin, W. Ho, W. F. Hall, P. J. Hood, I. S. Gergis, and A. B. Harker, *Phys. Rev. B* **42**, 6259 (1990).
- <sup>29</sup>N. Klein, G. Muller, S. Orbach, H. Piel, H. Chaloupka, B. Roas, L. Schultz, U. Klein, and M. Peiniger, *Physica C* **162-164**, 1549 (1989).
- <sup>30</sup>Q. Hu and P. L. Richards, *Appl. Phys. Lett.* **55**, 2444 (1989).
- <sup>31</sup>D. C. Larson, *Phys. Thin Films* **6**, 83 (1971).
- <sup>32</sup>J. Bardeen, D. M. Ginsberg, and M. B. Salamon, in *Novel Superconductivity*, edited by S. A. Wolf and V. Kresin (Plenum, New York, 1987), p. 333.
- <sup>33</sup>J. Halbritter, *Z. Phys.* **238**, 466 (1970).
- <sup>34</sup>A. H. Carim, S. N. Basu, and R. E. Muenchausen, *Appl. Phys. Lett.* **58**, 871 (1991).
- <sup>35</sup>P. England, T. Venkatesan, X. D. Wu, A. Inam, M. S. Hedge, T. L. Cheeks, and H. G. Craighead, *Appl. Phys. Lett.* **53**, 2336 (1988).
- <sup>36</sup>M. A. Dubson, S. T. Herbert, J. J. Calabrese, D. C. Harris, B. R. Patton, and J. C. Garland, *Phys. Rev. Lett.* **60**, 1061 (1988).
- <sup>37</sup>L. C. Hebel and C. P. Slichter, *Phys. Rev.* **107**, 901 (1957); **113**, 1504 (1959).
- <sup>38</sup>W. W. Warren, R. E. Walstedt, G. F. Brennert, G. P. Espinosa, and J. P. Remeika, *Phys. Rev. Lett.* **59**, 1860 (1987).
- <sup>39</sup>D. R. Harshmann, L. F. Schneemeyer, J. V. Waszczak, G. Aeppli, R. J. Cava, B. Batlogg, L. W. Rupp, E. J. Ansaldo, and D. L. Williams, *Phys. Rev. B* **39**, 851 (1989).
- <sup>40</sup>A. Schilling, F. Hulliger, and H. R. Ott, *Physica C* **168**, 272 (1990).
- <sup>41</sup>H. Piel and G. Muller, *IEEE Trans. Magn. MAG-27*, 854 (1991).
- <sup>42</sup>S. M. Anlage, H. Sze, H. J. Snortland, S. Tahara, B. Langley, C. B. Eom, M. R. Beasley, and R. Taber, *Appl. Phys. Lett.* **54**, 2710 (1989).
- <sup>43</sup>B. Muhlschlegel, *Z. Phys.* **155**, 313 (1959).
- <sup>44</sup>L. Krusin-Elbaum, R. L. Greene, F. Holtzberg, A. P. Malozemoff, and Y. Yeshurun, *Phys. Rev. Lett.* **62**, 217 (1989).
- <sup>45</sup>N. Klein, H. Chaloupka, G. Muller, S. Orbach, H. Piel, B. Roas, L. Schultz, U. Klein, and M. Peiniger, *J. Appl. Phys.* **67**, 6940 (1990).
- <sup>46</sup>L. Drabeck, J. P. Carini, G. Gruner, T. Hylton, K. Char, and M. R. Beasley, *Phys. Rev. B* **39**, 785 (1989).
- <sup>47</sup>J. P. Carini, A. M. Awasthi, W. Beyermann, G. Gruner, T. Hylton, K. Char, M. R. Beasley, and A. Kapitulnik, *Phys. Rev. B* **37**, 9726 (1988).
- <sup>48</sup>S. Sridhar and W. Kennedy, *Rev. Sci. Instrum.* **59**, 531 (1988).
- <sup>49</sup>F. A. Miranda, W. L. Gordon, K. B. Bhasin, and J. D. Warner, *Appl. Phys. Lett.* **57**, 1058 (1990).
- <sup>50</sup>J. Talvacchio and G. R. Wagner, *SPIE Proc.* **1292**, 2 (1990).
- <sup>51</sup>K. B. Bhasin, J. D. Warner, F. A. Miranda, W. L. Gordon, and H. S. Newman, *IEEE Trans. Magn. MAG-27*, 1284 (1991).



## MAGNETIC PENETRATION DEPTH OF $\text{YBa}_2\text{Cu}_3\text{O}_{7-x}$ THIN FILMS DETERMINED BY THE POWER TRANSMISSION METHOD

Vernon O. Heinen, Félix A. Miranda and Kul B. Bhasin  
National Aeronautics and Space Administration, Lewis Research Center, Cleveland, OH 44135, U.S.A.

### ABSTRACT

A power transmission measurement technique has been used to determine the magnetic penetration depth ( $\lambda$ ) of  $\text{YBa}_2\text{Cu}_3\text{O}_{7-x}$  superconducting thin films on  $\text{LaAlO}_3$  within the 26.5 to 40.0 GHz frequency range, and at temperatures from 20 to 300 K. Values of  $\lambda$  ranging from 1100 to 2500 Å were obtained at low temperatures. The anisotropy of  $\lambda$  was determined from measurements of c-axis and a-axis oriented films. An estimate of the intrinsic value of  $\lambda$  of  $90 \pm 30$  nm was obtained from the dependence of  $\lambda$  on film thickness. The advantage of this technique is that it allows  $\lambda$  to be determined non-destructively.

**KEY WORDS:** Magnetic penetration depth,  $\text{YBa}_2\text{Cu}_3\text{O}_{7-x}$  thin films, Power transmission measurements.

### INTRODUCTION

Since the discovery of the high-transition-temperature superconductors (HTS) by Bednorz and Muller [1], and Wu et al. [2] numerous studies have been done to determine the potential of these materials for practical applications and to learn more about the nature of their superconducting state. One of the parameters of most relevance in the evaluation of the suitability of the new HTS thin films for microwave applications is the magnetic penetration depth ( $\lambda$ ). This parameter, which is a measure of the distance a magnetic field penetrates into the superconducting material, is important not only because it can provide information about the fundamental mechanisms for superconductivity in these materials but also because of its sensitivity to the quality of the superconductor near its surface. In particular, for thin films of thickness  $t$  in which  $\lambda \sim t$ ,  $\lambda$  serves as an excellent figure of merit to determine the quality of the entire film, and provides necessary information for the design of superconductor-based microwave integrated circuits [3]. To date, values of  $\lambda$  for  $\text{YBa}_2\text{Cu}_3\text{O}_{7-x}$  single crystal and ceramics have been reported using various experimental techniques, such as muon-spin-rotation and low field dc magnetization measurements [4-6]. Others have determined this parameter in HTS thin films from a variety of microwave measurements [7-10]. However, some of the most favored microwave techniques used for the determination of  $\lambda$  usually involve the alteration of the film by way of patterning it into microstrip resonators and other transmission line structures [9,10].

In this paper we present results on the determination of  $\lambda$  for  $\text{YBa}_2\text{Cu}_3\text{O}_{7-x}$  HTS thin films using a power transmission method. One of the merits of this technique is that it does not alter the film in any way so that the same film can be used for further characterizations or for the fabrication of a microwave device. Values of  $\lambda$  over a wide range of temperatures ( $T$ ) and film thickness ( $d$ ) are discussed.

### EXPERIMENTAL

The  $\text{YBa}_2\text{Cu}_3\text{O}_{7-x}$  superconducting thin films considered in this study were deposited by pulsed laser ablation on  $\text{LaAlO}_3$  substrates. The substrates were approximately  $1.0 \text{ cm}^2$ , with thickness of 10 to 20 mils and had a (100) crystallographic orientation. The thickness of the films ranged from approximately 800 to 5000 Å, as determined by using a surface profilometer over steps etched at the corner of each film with undiluted phosphoric acid ( $\text{H}_3\text{PO}_4$ ). Measurements of dc-resistance ( $R_{dc}$ ) versus temperature were performed for all the films analyzed in this study using a standard four-point probe method. The temperature at which the measured resistance fell below the resolution of the measuring instrument ( $\sim 10^{-8}$  n-cm) was defined as the dc-transition temperature ( $T_c^{dc}$ ). The transition temperature for all c-axis oriented films was between 84 and 91 K. The crystallographic orientation of the films was determined by x-ray diffraction analysis.

The main components of the experimental apparatus are an HP-8510B network analyzer and a closed-cycle helium gas refrigerator, which are both controlled by an HP 9000-216 computer. The network analyzer is

coupled to the refrigerator by Ka band (26.5 to 40.0 GHz) rectangular waveguides. The measurement technique compares the transmitted signal against the incident microwave signal to determine the transmission coefficients. The data measured in this way are then stored by the computer for subsequent analysis.

All the measurements were made under vacuum ( $<10^{-3}$  torr) in a custom-made aluminum vacuum chamber designed to fit on top of the external shield of the refrigerator and to give access to the waveguides connecting the network analyzer with the refrigerator. Mica windows were used as vacuum windows in the waveguide. The sample was oriented perpendicular to the microwave source by clamping it between two waveguide flanges thermally connected to the cold head of the refrigerator through a Au-plated Cu plate. The film side of the sample was directed toward the incident microwave signal as shown in Fig. 1. The system was calibrated before the beginning of each measurement cycle to account for the impedance of the waveguide network. The noise level for our measurements was determined to be below -60 dB. Background attenuation and phase corrections were made by subtracting the transmitted power as a function of temperature in the absence of the sample from the data obtained with the sample in place. Measurements of bare  $\text{LaAlO}_3$  substrates were used to determine any temperature dependence of their dielectric constant. The results of these measurements have been previously reported [11]. The temperature of the film was measured with two silicon diodes placed in a 1/8 inch diameter hole on top of each of the sample's supporting flanges. The accuracy of these diodes is  $\pm 1.0$  K from 1.4 to 100 K, and 1% of the actual temperature in the range from 100 to 325 K.

## ANALYSIS

The surface reactance ( $X_s$ ) of a superconductor is defined in terms of  $\lambda$ . Therefore knowledge of either one of these parameters allows the determination of the other. The surface reactance can be expressed in terms of the microwave power transmitted through them. Sridhar [12] was the first to use the microwave power transmitted through Sn thin films, placed at the end walls of a cylindrical copper resonant cavity, to determine the effective surface reactance  $X_{\text{eff}}$  as a function of temperature. Therefore, since we were able to measure the microwave transmitted power directly, we have followed Sridhar's method for obtaining  $X_{\text{eff}}$ . After satisfying the boundary conditions of the problem, the expression for  $X_{\text{eff}}$  in terms of the transmitted power is

$$X_{\text{eff}} = R_N^{\text{MW}} \cosh(d/\lambda) |P_{\text{xmitt}}^S / P_{\text{xmitt}}^N|^{\frac{1}{2}} \quad (1)$$

where  $R_N^{\text{MW}}$  is the normal state surface resistance at  $T = T_c^{\text{MW}}$ , which is the transition temperature determined from the power transmission measurements,  $d$  is the film thickness, and  $P_{\text{xmitt}}^N$  and  $P_{\text{xmitt}}^S$  are the power transmitted in the normal and the superconducting states, respectively. For thin films,  $X_{\text{eff}}$  is given by

$$X_{\text{eff}} = X_s \coth(d/\lambda) \quad (2)$$

where  $X_s = \omega \mu_0 \lambda$ ,  $\omega / 2\pi = f$  is the frequency and  $\mu_0$  is the permeability of free space. Thus, to determine  $\lambda$  we solved equation (1) for  $X_{\text{eff}}$  by assuming an initial value of  $\lambda = 100 \text{ \AA}$ . Using the resulting value of  $X_{\text{eff}}$  in (2), we calculated a new value of  $\lambda$ . This value was then used in equation (1) and the process was repeated until the value of  $\lambda$  changed by less than 0.1% between iterations. This value was taken to be the value of  $\lambda$  at the temperature under consideration.

## RESULTS AND DISCUSSION

Figure 2 shows a plot of the power transmission coefficient  $P$  versus temperature for one of the films analyzed in this study. For a given film the microwave power transmission coefficient was measured with a repeatability of  $\pm 5\%$  over the entire temperature range. This error was estimated by measuring several films repeatedly with the film being removed and replaced between each set of measurements. The metallic character of the films is evidenced by the positive slope of  $P$  for  $T > T_c^{\text{MW}}$ . At  $T_c^{\text{MW}}$ , the transmitted power decreased abruptly and continued decreasing with decreasing temperature, leveling off at low temperatures. We observed that the abruptness of this transition and the temperature at which the transmitted power started to level off was closely related to the film quality, as determined by measurements of the surface resistance ( $R_s$ ) and the complex conductivity ( $\sigma = \sigma_1 - j\sigma_2$ ). Different power levels (~0.1, 1.0, and 16 mW) were used in probing the samples. Note that although for low power levels and low temperatures the data are noisier, the transmitted-to-incident power ratio is the same for all incident powers. This indicates that the superconducting state is not altered by the incident power, at least for the different power levels and frequency range considered in this study. The absence of any appreciable shift of  $T_c^{\text{MW}}$  for most of the films, within a resolution of 0.5 K supports this argument. This behavior was typical of all the films considered independent of thickness.

As discussed in the last section we have used eqs. (1) and (2) to determine  $\lambda$  for the HTS thin films. Figure 3 shows a plot of  $\lambda$  versus film thickness ( $d$ ) at 30 K. The anisotropy of  $\lambda$  is indicated in this plot by the large value of  $\lambda$  for the film represented by the  $\diamond$  symbol which is a predominantly a-axis oriented film. Taking the ratio between  $\lambda$  for this film and c-axis oriented films of comparable thickness, yields  $\lambda_c/\lambda_{ab} \sim 3.8$  and  $\lambda_c/\lambda_{ab} \sim 5.7$ , respectively. These ratios are consistent with the value of  $\lambda_c/\lambda_{ab} \sim 5$  reported by others for single crystals and high purity samples of the  $\text{YBa}_2\text{Cu}_3\text{O}_{7-x}$  superconductor [4,14-15]. Observations by others [7] have shown that as the film thickness increases it is more difficult to preserve their c-axis orientation, i.e., the number of a-axis oriented grains increases with increasing  $d$ . Since the shielding currents along the c-axis oriented grains are smaller than those along the a-b plane, one expects  $\lambda$  to increase with film thickness as seen in Fig. 3.

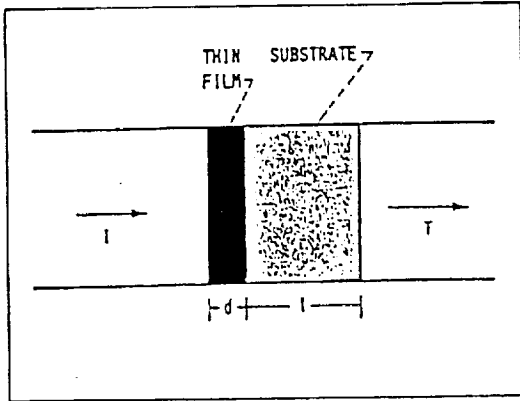


Fig. 1 Schematic of rectangular waveguide propagating the  $\text{TE}_{01}$  mode with its entire cross section covered by a high- $T_c$  superconducting thin film of thickness  $d$  deposited on a dielectric substrate of thickness  $t$  and index of refraction  $n$ .

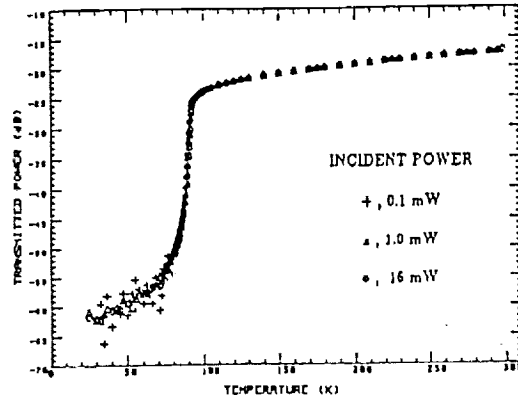


Fig. 2 Power transmission coefficient versus temperature for a laser ablated  $\text{YBa}_2\text{Cu}_3\text{O}_{7-x}$  thin film (2400 Å) on  $\text{LaAlO}_3$  (20 mils).

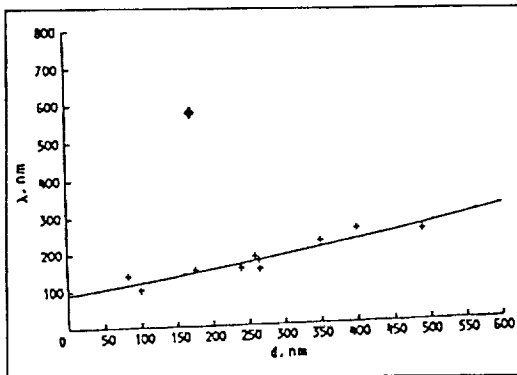


Fig. 3 Magnetic penetration depth ( $\lambda$ ) versus film thickness ( $d$ ) for  $\text{YBa}_2\text{Cu}_3\text{O}_{7-x}$  thin films on  $\text{LaAlO}_3$  (20 mils). The  $\diamond$  symbol represents an a-axis oriented film and the solid line represents a second degree polynomial fit.

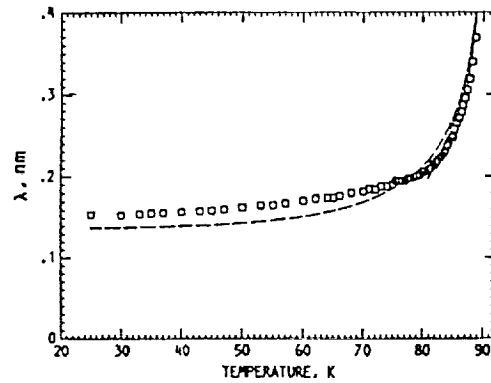


Fig. 4 Magnetic penetration depth ( $\lambda$ ) versus temperature for a  $\text{YBa}_2\text{Cu}_3\text{O}_{7-x}$  thin film on  $\text{LaAlO}_3$  (20 mils). The dashed (solid) line represents a fit to the data using the temperature dependence for  $\lambda$  according to the two-fluid model (weak coupling BCS theory in the clean limit).

The solid line in Fig. 3 represents a fit to the data using a second degree polynomial regression analysis. This gives a value for the penetration depth corresponding to zero film thickness of  $\lambda(d=0) = 90 \pm 30$  nm. This value of  $\lambda$  represents the smallest possible value that can be obtained for a c-axis oriented film free from grain boundary effects and other non-superconducting inhomogeneities; i.e., the intrinsic value of  $\lambda$  at low temperatures for the  $\text{YBa}_2\text{Cu}_3\text{O}_{7-x}$  superconductor. To our knowledge, this is the first time that this value has been estimated experimentally for any of the HTS materials.

The temperature dependence of  $\lambda$  for a film ( $d=2400$  Å) is shown in Fig. 4. Using the expressions for the temperature dependence of  $\lambda$  in the two-fluid model (TFM) approximation,

$$\lambda(T) = \lambda(0)[1 - (T/T_c)^4]^{-1/2} \quad (3)$$

and according to the weak-coupling BCS theory in the clean limit [14,16],

$$\lambda(T) = \lambda(0)[2(1 - T/T_c)]^n, \quad T \rightarrow T_c \quad (4)$$

we have estimated the zero-temperature penetration depth ( $\lambda(0)$ ), by fitting the measured  $\lambda$  to equations (3) and (4) using a standard least-squares fit. For the film in Fig. 4 we obtained  $\lambda_{\text{BCS}}(0) = 96 \pm 9$  nm and  $\lambda_{\text{TFM}}(0) = 138 \pm 13$  nm. For another film of  $d = 1769$  Å film we found  $\lambda_{\text{TFM}}(0) = 145 \pm 12$  nm and  $\lambda_{\text{BCS}}(0) = 113 \pm 8$  nm. These values are consistent with those reported by others for c-axis oriented thin films and single crystals of  $\text{YBa}_2\text{Cu}_3\text{O}_{7-x}$  [4,17,18].

## CONCLUSIONS

The magnetic penetration depth of  $\text{YBa}_2\text{Cu}_3\text{O}_{7-x}$  HTS thin films on  $\text{LaAlO}_3$  was determined using a power transmission method. We were able to experimentally verify the intrinsic anisotropy of  $\lambda$  for this HTS superconductor by measuring this parameter in c-axis and predominantly a-axis oriented films. As expected from the anisotropy of these HTS materials, the value of  $\lambda$  for the a-axis oriented film was larger than the values obtained for c-axis oriented films. In fact, the ratio of  $\lambda$  for an a-axis oriented film to that of c-axis oriented films agrees very well with that reported by others for single crystals and very high quality thin films of the  $\text{YBa}_2\text{Cu}_3\text{O}_{7-x}$  superconductor. We also observed that  $\lambda$  increased with increasing film thickness which is consistent with the increase of the number of a-axis oriented grains and other structural and material defects with increasing film thickness. From the thickness dependence of  $\lambda$  we were able to estimate, for the first time, the intrinsic value of  $\lambda$  for the  $\text{YBa}_2\text{Cu}_3\text{O}_{7-x}$  superconductor. Finally, the power transmission technique presented here provides a non-destructive technique for the determination of  $\lambda$  for HTS thin films, in contrast to microstrip resonator methods in which the film must be patterned.

## REFERENCES

1. Bednorz JG, Mueller KA (1986) Z. Physics B. 64: 189
2. Wu MK, Ashburn JR, Torng CJ, Hor PH, Meng RL, Gao L, Huang ZJ, Wang YQ, Chu CW (1987) Phys. Rev. Lett. 58: 908
3. Bhasin KB, Warner JD, Romanofsky RR, Heinen VO, Chorey CM, Kong KS, Lee HY, Itoh T (1990) IEEE MTT-S Int. Microwave Symp. Dig. 1: 269
4. Harshmann DR, Schneemeyer LF, Waszczak JV, Aeppli G, Cava RJ, Batlogg B, Rupp LW, Ansaldo EJ, Williams DL (1989) Phys. Rev. B 39: 851
5. Drabek L, Carini JP, Gruner G, Hylton T, Char K, Beasley MR (1989) Phys. Rev. B 39: 785
6. Chi H, Nagi AD (1989) Phys. Rev. B 40: 7361
7. Anlage SM, Sze H, Snortland HJ, Tahara S, Langley B, Eom CB, Beasley MR (1989) Appl. Phys. Lett. 54: 2710
8. Klein N, Muller G, Orbach S, Piel H, Chaloupka H, Roas B, Schultz L, Klein U, Peiniger M (1989) Physica C 162-164: 1549
9. Anlage SM, Langley BW, Snortland HJ, Eom CB, Geballe TH, Beasley MR (1990) J. of Supercond. 3: 311
10. Chorey CM, Kong KS, Bhasin KB, Warner JD, Itoh T (1991) IEEE Trans. Microwave Theory Tech. 39: 1480
11. Miranda FA, Gordon WL, Bhasin KB, Ebihara BT, Heinen VO, Chorey CM (1990) Microwave and Opt. Tech. Lett. 3: 11
12. Sridhar S (1988) J. Appl. Phys. 63: 159
13. Miranda FA, Gordon WL, Bhasin KB, Heinen VO, Warner JD (1991) J. Appl. Phys. 70: to be published
14. Schilling A, Hulliger F, Ott HR (1990) Physica C 168: 272
15. Piel H, Muller G (1991) IEEE Trans. on Magn. 27: 854
16. Muhlschlegel B (1959) Z. Phys. 155: 313
17. Krusin-Elbaum L, Greene RL, Holtzberg F, Malozemoff AP, Yeslurun Y (1989) Phys. Rev. Lett. 62: 217
18. Klein N, Chaloupka H, Muller G, Orbach S, Piel H, Roas B, Schultz L, Klein U, Peiniger M (1990) J. Appl. Phys. 67: 6940

# Magnetic flux relaxation in $\text{YBa}_2\text{Cu}_3\text{O}_{7-x}$ thin film: thermal or athermal

Satish Vitta,\* M. A. Stan,† J. D. Warner and S. A. Alterovitz

NASA Lewis Research Center, Cleveland, OH 44135 (U.S.A.)

## Abstract

The magnetic flux relaxation behavior of  $\text{YBa}_2\text{Cu}_3\text{O}_{7-x}$  thin film on  $\text{LaAlO}_3$  for  $H \parallel c$  was studied in the range 4.2–40 K and 0.2–1.0 T. Both the normalized flux relaxation rate  $S$  and the net flux pinning energy  $U$  increase continuously from  $1.3 \times 10^{-2}$  to  $3.0 \times 10^{-2}$  and from 70 to 240 meV respectively, as the temperature  $T$  increases from 10 to 40 K. This behavior is consistent with the thermally activated flux motion model. At low temperatures, however,  $S$  is found to decrease much more slowly as compared with  $kT$ , in contradiction to the thermal activation model. This behavior is discussed in terms of the athermal quantum tunneling of flux lines. The magnetic field dependence of  $U$ , however, is not completely understood.

## 1. Introduction

In type II superconductors the pinning of magnetic flux lines is responsible for the lack of dissipation during the flow of high current densities. The pinning is caused by various types of defects, *i.e.* grain boundaries, twins, point defects and inhomogeneities. The observation of a high degree of mobility of these flux lines in the oxide superconductors [1–3] has stimulated many theoretical studies and has led to the proposal of several models. According to the conventional thermal flux motion model [4] the magnetization relaxes logarithmically with time  $t$  for  $t < t_{cr}$  where  $t_{cr}$  is a cross-over time given by  $t_{cr} = t_{hop} \exp[U(H, T)/kT]$ ,  $t_{hop}$  is the flux line hopping time ( $10^{-6}$ – $10^{-12}$  s),  $U(H, T)$  the net flux pinning energy,  $k$  the Boltzmann constant and  $T$  the temperature. At  $t > t_{cr}$  or for high  $T$ , the motion of flux lines attains a steady state and the magnetization relaxes exponentially with  $t$  [5]. However, the observation of logarithmic decay even at large  $T$  and the non-linear behavior of the relaxation rate has led to many alternative models for the nature of the pinning energy  $U$  [6–8].

In the present work, the relaxation of screening-current-induced magnetization in a  $\text{YBa}_2\text{Cu}_3\text{O}_{7-x}$  thin film has been studied as a function of temperature  $T$  and external field  $H$ . The magnetization is found to relax logarithmically up to  $10^4$  s for  $T$  as high as  $0.45T_c$  where  $T_c$  is the superconducting transition temperature. The normalized relaxation rate  $S$  increases non-linearly

with  $T$  and is discussed in terms of the thermally activated flux motion model, but with a modified pinning energy  $U$ . The low temperature behavior, however, cannot be explained by this model and is discussed in terms of “quantum tunneling” or “athermal flux motion” model [9]. The magnetic field dependence of  $U$ , however, is not completely understood.

## 2. Experimental methods

The  $\text{YBa}_2\text{Cu}_3\text{O}_{7-x}$  thin film about  $0.3 \mu\text{m}$  thick was deposited by a pulsed laser ablation technique onto a heated  $\text{LaAlO}_3(100)$  substrate. The film texture was determined by the standard  $\Theta$ – $2\Theta$  scan and rocking curve and shows that the grains are preferentially aligned with their  $c$  axis along the plane normal. The film has a smooth surface and the average grain size, determined by scanning electron microscopy, is about  $0.25 \mu\text{m}$ . The superconducting transition temperature  $T_c(0)$  determined by the standard four-probe d.c. technique is 88.5 K with a transition width of about 1.0 K.

The magnetization and magnetic flux relaxation were studied using a commercial superconducting quantum interference device magnetometer. The data collection procedure is described in detail in ref. 3. The diamagnetic transition temperature determined from the field-cooled magnetization at 2 mT applied along the  $c$  axis was found to be 88.5 K and is the same as that determined by the electrical transport method.

## 3. Results

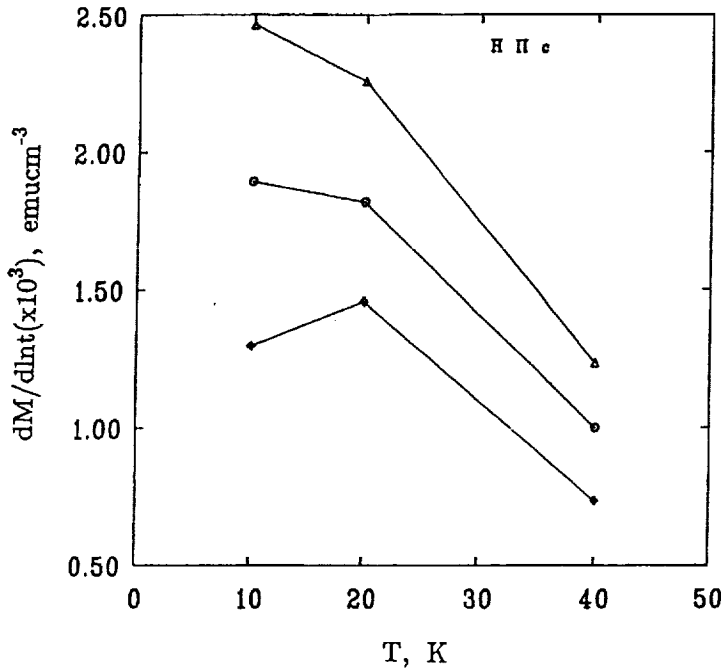
The relaxation of the screening-current-induced magnetization at  $H = 0.2$  T, 0.4 T and 1.0 T applied

\*Present address: Department of Metallurgy, Indian Institute of Technology, Powai, Bombay 400076, India.

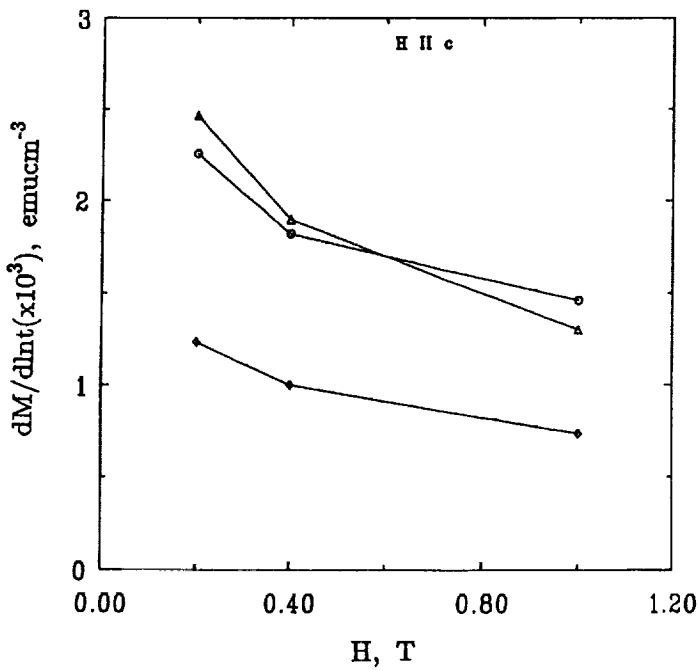
†Department of Physics, Kent State University, Kent, OH 44242, U.S.A.

perpendicular to the orthorhombic  $a$ - $b$  plane of the crystals was studied in the temperature range  $0.05T_c < T < 0.45T_c$ . The magnetization was found to relax logarithmically with  $t$  up to  $10^4$  s at all the temperatures and fields studied. The relaxation rate  $dM(H, T)/d \ln t$

is shown in Figs. 1(a) and 1(b) as a function of  $T$  and  $H$  respectively. The rate decreases continuously as  $H$  increases from 0.2 T to 0.4 T at all temperatures. At 1.0 T, however, it exhibits a peak at about 20 K. The relaxation rate  $dM(H, T)/d \ln t$  normalized by the

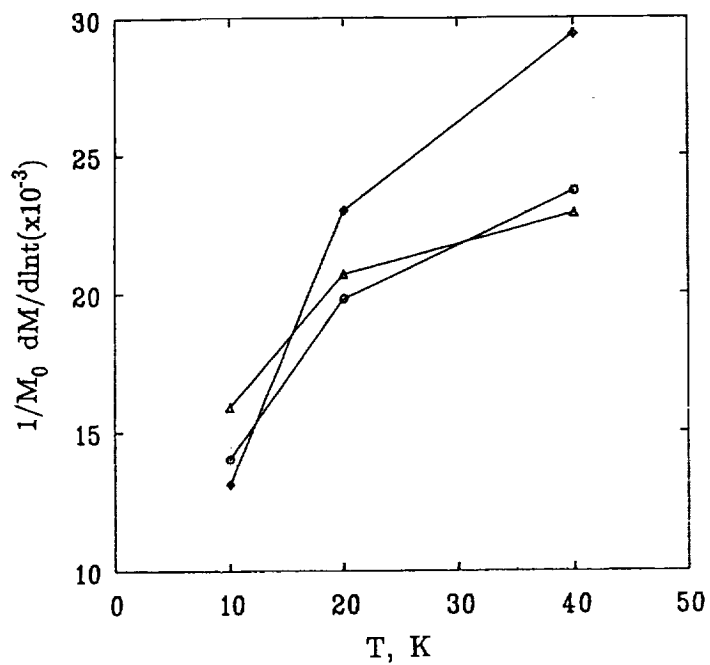


(a)

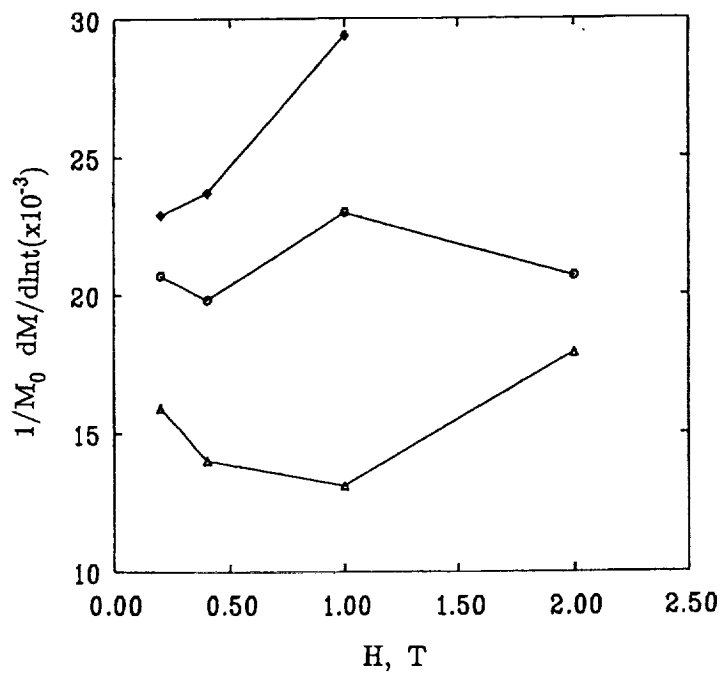


(b)

Fig. 1. The logarithmic relaxation rate  $dM/d \ln t$  of the screening-current-induced magnetization: (a) as a function of temperature  $T$  ( $\Delta$ , 0.2 T;  $\circ$ , 0.4 T;  $\diamond$ , 1.0 T); (b) as a function of external field  $H$  ( $\Delta$ , 10 K;  $\circ$ , 20 K;  $\diamond$ , 40 K). (The lines connecting the data points are aids to the eye.)



(a)



(b)

Fig. 2. The relaxation rate normalized by the initial magnetization  $M_0$ : (a) as a function of temperature  $T$ ; (b) as a function of external field  $H$ . (See caption of Fig. 1 for the meanings of the symbols.)

initial magnetization  $M_0$  at  $t_0$  eliminates the uncertainties associated with the determination of the demagnetization factor and allows the possible determination of the net pinning energy  $U$ . In analyzing the results of the present work,  $t_0$  is taken as  $10^3$  s so that the relaxation is in the logarithmic regime. Figures 2(a) and 2(b) show the normalized relaxation rate  $(1/M_0) dM(H, T)/d \ln t \equiv S$  as a function of  $T$  and  $H$  respectively.

#### 4. Discussion

In a typical relaxation measurement, the net flux pinning energy  $U(H, T, t)$  is zero at  $t = 0$  and increases rapidly with  $t$ . The driving force for the motion of these flux lines is a combination of flux line interaction, thermal activation and the flux line gradient (Lorentz force or current density  $J$ ). In the conventional thermally activated flux motion model,  $U(H, T, t)$  is assumed to be a linear function of  $J$  and independent of  $T$ . This leads to the classical relation [4, 6, 10]

$$M(H, T, t) = M_0(H, T)[1 - kT/U(H, T) \ln(t/t_{\text{hop}})] \quad (1)$$

The relaxation rate normalized by the initial magnetization can be obtained from the above relation and is given as

$$\begin{aligned} [1/M_0(H, T)] dM(H, T)/d \ln t &\equiv S \\ &= -kT/[U(H, T) - kT \ln(t_0/t_{\text{hop}})] \end{aligned} \quad (2)$$

According to the above relation  $S$  is a linear function of  $T$  only when  $U(H, T) \gg kT \ln(t_0/t_{\text{hop}})$ . Since  $U$  has to go to zero as  $T \rightarrow T_c$  it also predicts a divergence or an upward curvature for the  $S$  curve as  $T$  increases. In the present work, however, it can be clearly seen from Fig. 2(a) that neither is  $S$  a linear function of  $T$  nor does it curve upwards as  $T$  increases. This type of behavior has been observed before in magnetization studies on single crystal, aligned powder and thin film [1–3].

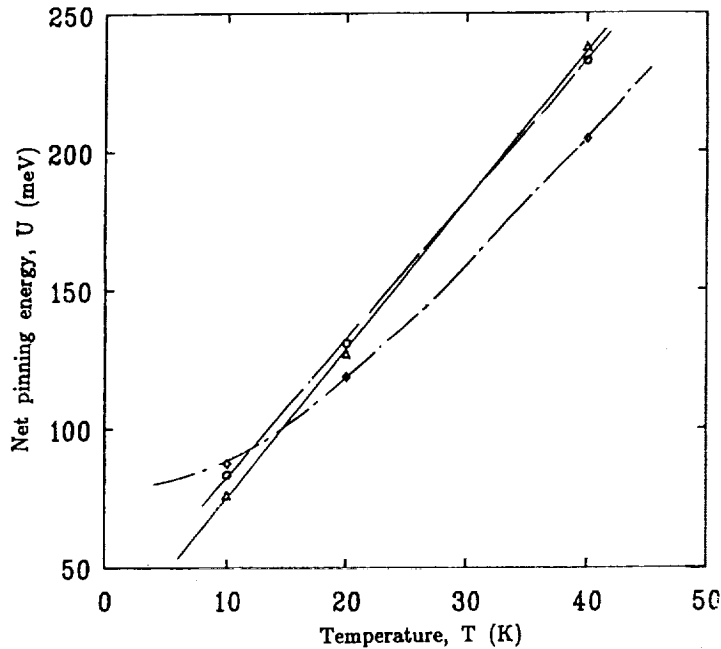
The net flux pinning energy  $U$  obtained from eqn. (2) by considering  $t_{\text{hop}}$  to be typically  $10^{-8}$  s is shown in Fig. 3. At low fields, 0.2 T and 0.4 T,  $U$  increases linearly with  $T$  in the range 10–40 K and does not exhibit divergence at large  $T$ . However, at 1.0 T,  $U$  increases non-linearly with  $T$  and has an upward curvature. To understand this behavior of  $U$  or conversely  $S$ , different forms for the shape and depth of the flux line potential well have been proposed. On the basis of a single potential well Beasley *et al.* [6] and Welch [7] have proposed that  $U = U_0(H) (1 - J/J_0)^n$  where  $J_0$  is the current density in the absence of flux relaxation and  $3/2 < n < 2$  is a constant depending on the shape of the potential well. According to this model  $U$  does not diverge as  $J \rightarrow 0$  or  $T \rightarrow T_{\text{irr}}$  where  $T_{\text{irr}}$  is the irreversibility temperature, but converges to the intrinsic pinning

potential  $U_0(H)$ . The observed  $T$  dependence of  $U$  at 0.2 T and 0.4 T indicates a qualitative agreement with this model in the temperature range studied.

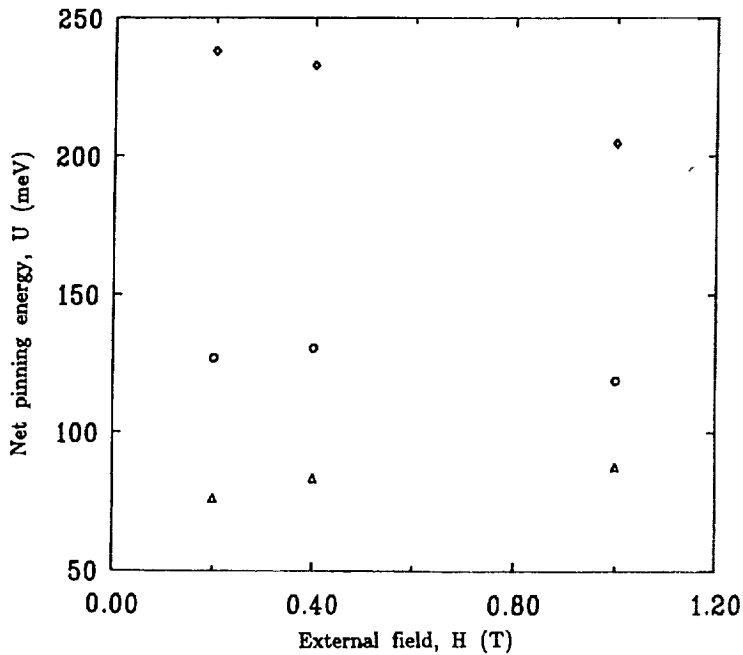
The collective flux creep model [11] and the vortex glass model [12] predict an inverse  $J$  dependence for  $U$  of the form  $U = U_0(H) [(J_0/J)^\mu - 1]$  where  $\mu$  is a variable in the collective flux creep model but a universal constant in the vortex glass model. Zeldov *et al.* [8], in contrast, proposed that  $U = U_0(H) \ln(J_0/J)$ , on the basis of a single potential well approximation. All these models predict an upward curvature for  $U$  as  $J \rightarrow 0$ , which is observed at 1.0 T. The vortex glass model also predicts that  $S$  attains a universal constant value in the range  $\approx 0.2 T_c < T < \approx 0.65 T_c$ . This behavior, however, is clearly not observed in the present work (Fig. 2(a)). The validity of the other models will be discussed in detail elsewhere [13].

Recently, substantial magnetic relaxation has been reported at temperatures as low as 0.1 K in  $\text{YBa}_2\text{Cu}_3\text{O}_7$  single crystal [14] and grain-aligned powder [15] and at 1.6 K in  $c$  axis aligned thin film [16] for  $H$  applied along the  $c$  axis. In the present work, however, 4.2 K was the lowest  $T$  at which the relaxation behavior was studied. Figure 4 shows  $S$  and  $U$  at 4.2 K for increasing  $H$ . At 0.2 T,  $S$  decreases by less than 40% compared with that at 10 K and the reduction becomes negligible as  $H$  increases. This shows that the  $T$  at which  $S$  saturates at low temperatures increases as  $H$  increases. On the contrary, the thermal activation  $kT$  is reduced by 58%. This behavior is contrary to the classical thermal activation model [4] and has also been observed in molybdenum disulfides for  $T < 0.2T_c$  by Mitin [9]. He has proposed that the observed relaxation results from quantum tunneling or hopping of the flux line segments across the potential barrier separating two pinning centers and is athermal in nature. The hopping time for this process was estimated to be about  $10^{-12}$  s, which is comparable with  $t_{\text{hop}}$  used in the present analysis. This phenomenon is similar in principle to the electron transport mechanism in disordered semiconductors [17]: quantum tunneling crossing over to thermal activation as  $T$  increases and domination of the highest rate process at any given  $T$ . At present there is no single model incorporating both of these processes.

The magnetic field  $H$  dependence of  $U$  is shown in Fig. 3(b) and also in Fig. 4. As can be seen from these two figures, the  $H$  dependence of  $U$  changes continuously as  $T$  is increased. At 4.2 K and 40 K,  $U$  decreases as  $H$  increases while at 10 K it increases as  $H$  increases. At 20 K, however,  $U$  increases to 131 meV at 0.4 T before decreasing at high fields. Keller *et al.* [18] found that  $U$  increases steadily as  $H$  increases to 5.0 T in the range 10–40 K. At 77 K, however,  $U$  decreased with increasing  $H$ . In the case of  $\text{YBa}_2\text{Cu}_3\text{O}_{7-\delta}$  single crystals Daeumling *et al.* [19] have reported an anomalous



(a)



(b)

Fig. 3. The net flux pinning energy  $U$  obtained using eqn. (2) is shown as a function of (a) temperature and (b) external field.

## 5. Conclusions

The temperature and magnetic field dependence of the flux pinning energy in a  $c$  axis oriented  $\text{YBa}_2\text{Cu}_3\text{O}_{7-x}$  thin film have been investigated. It is found that the temperature dependence can be understood

magnetization behavior and hence flux pinning as  $T$  changes. This has been attributed to the variation in pinning strength, creation of field-induced pinning centers and granularity. This clearly shows that the  $H$  dependence of  $U$  is also not completely understood at present.

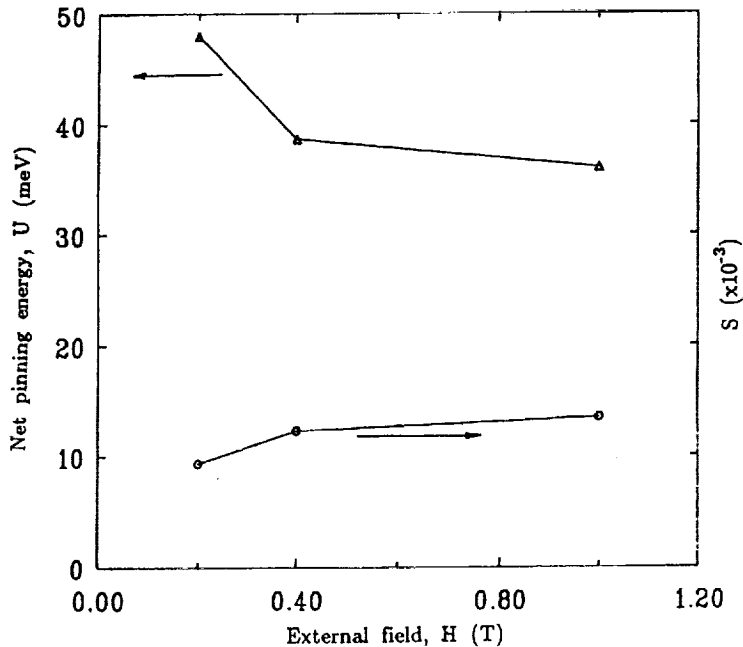


Fig. 4. The normalized relaxation rate  $S$  (○) and the net flux pinning potential  $U$  (Δ) at 4.2 K are shown as a function of external field  $H$ .

qualitatively in terms of the thermal activation model only by incorporating modified potential functions. The low temperature behavior, however, cannot be understood in terms of this model and can only be understood by considering an athermal flux line tunneling mechanism for motion. The magnetic field dependence is found to be anomalous in nature and cannot be explained by the existing models [1].

All the models proposed so far concentrate only on modifying or altering the form of the pinning potential function so as to explain the observed results. However, an attempt to relate these functions to the actual pinning centers in the material, various types of defects, is as yet lacking. The present work clearly demonstrates that the response of the flux lines to the pinning centers is not the same for temperature variations and field variations.

#### Acknowledgments

S. V. wishes to acknowledge the U.S. National Research Council for the Associateship at NASA Lewis Research Center and M.A.S. acknowledges NASA for the support through Grant NAG-440751.

#### References

1 Y. Yeshurun and A. P. Malozemoff, *Phys. Rev. Lett.*, **60** (1988) 2202.

2 Y. Xu, M. Suenaga, A. R. Moodenbaugh and D. O. Welch, *Phys. Rev. B*, **40** (1989) 10882.  
 3 S. Vitta, M. A. Stan and S. A. Alterovitz, *IEEE Trans. Magn.*, (March 1991), in the press.  
 4 P. W. Anderson and Y. B. Kim, *Rev. Mod. Phys.*, **36** (1964) 39.  
 5 P. H. Kes, J. Aarts, J. van den Berg, C. J. van der Beek and J. A. Mydosh, *Supercond. Sci. Technol.*, **1** (1989) 242.  
 6 M. R. Beasley, R. Labusch and W. W. Webb, *Phys. Rev.*, **181** (1969) 682.  
 7 D. O. Welch, *IEEE Trans. Magn.*, (March 1991), in the press.  
 8 E. Zeldov, N. M. Amer, G. Koren, A. Gupta, M. W. McElfresh and R. J. Gambino, *Appl. Phys. Lett.*, **56** (1990) 680.  
 9 A. V. Mitin, *Sov. Phys. JETP*, **66** (1987) 335.  
 10 R. Griessen, J. G. Lensink, T. A. M. Schroder and B. Dam, *Cryogenics*, **30** (1990) 563.  
 11 M. V. Fiegl'man, V. B. Geshkenbein, A. I. Larkin and V. M. Vinokur, *Phys. Rev. Lett.*, **63** (1989) 2303.  
 12 A. P. Malozemoff and M. P. A. Fisher, *Phys. Rev. B*, **42** (1990) 6784.  
 13 S. Vitta, M. A. Stan and S. A. Alterovitz, in preparation.  
 14 L. Fruchter, A. P. Malozemoff, I. A. Campbell, J. Sanchez, M. Konczykowski, R. Griessen and F. Holtzberg, submitted to *Phys. Rev. Lett.*  
 15 A. Hamzic, L. Fruchter and I. A. Campbell, *Nature (London)*, **345** (1990) 515.  
 16 R. Griessen, *J. Less-Common Met.*, **151** (1989) 39.  
 17 N. F. Mott, *Electronic Processes in Non-Crystalline Materials*, Clarendon, Oxford, 1979, p. 7.  
 18 C. Keller, H. Kupfer, A. Gurevich, R. Meier-Hirmer, T. Wolf, R. Flukiger, V. Selvamanickam and K. Salama, *J. Appl. Phys.*, **68** (1990) 3498.  
 19 M. Daeumling, J. M. Seuntjens and D. C. Larbalestier, *Nature (London)*, **346** (1990) 332.

# ***BIOGRAPHIES***



**Samuel A. Alterovitz** received his Ph.D. degree in Solid State Physics in 1971 from Tel Aviv University. After a 2-year postdoctoral appointment at the University of Illinois, he joined the staff of the Physics Department at Tel Aviv University. His work at these two universities focused on properties of superconducting materials, emphasizing critical currents and critical fields. In 1981, he accepted an appointment as senior engineering research scientist in the Electrical Engineering Department of the University of Nebraska. In 1983 he transferred to NASA Lewis Research Center as a senior research scientist in the Solid State Technology Branch. Dr. Alterovitz has played a key role in developing new materials (e.g., InGaAs) for high-speed, low-noise, high-efficiency electronic devices. He also developed ellipsometry for novel and multilayer structures, specializing in insulators, superconductors, and semiconductor materials. Dr. Alterovitz is now working on epitaxial lift-off technique development materials and devices for cryogenic electronics applications, and furthering applications of the ellipsometric technique. Dr. Alterovitz has authored more than 100 papers in referred journals and more than 100 meeting presentations, and has edited 2 books. He is an active postdoctoral advisor for the National Research Council. Dr. Alterovitz is a member of the American Physical Society, the Materials and Research Society, and the American Vacuum Society.



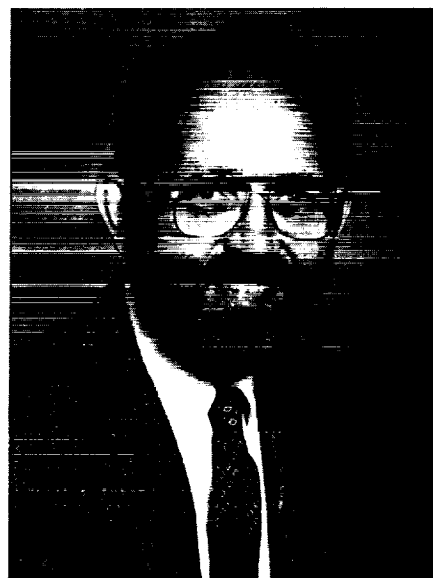
**Christopher M. Chorey** received his B.S. degree in Electrical Engineering in 1984 and his M.S. degree in Materials Science in 1987 from Case Western Reserve University. With the support of NASA Lewis Research Center, he performed 2 years of additional graduate work at Case Western Reserve University from 1987 to 1988, focusing on fabrication and testing of AlGaAs-based, high-frequency, electro-optic modulators. Mr. Chorey is currently studying microwave properties of high-temperature superconductors.



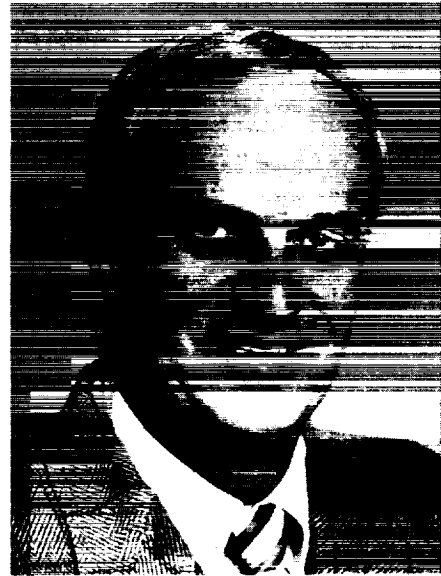
**Alan N. Downey** joined NASA Lewis Research Center in 1977 as a co-op student. He received his B.S.E.E. degree from Cleveland State University in 1979, and his M.S.E.E. degree from the University of Toledo in 1983. In 1979 he joined the Space Communications Division of Lewis. From 1979 to 1985 he was engaged in microwave measurements and solid-state technology research, followed by a 3-year hiatus in the Communications Projects Branch as Experiments Manager for the Applications Technology Satellites Program. Mr. Downey returned to the Solid State Technology Branch in July 1989. His current research interests include the RF characterization of novel High Electron Mobility Transistor (HEMT) structures at cryogenic temperatures, Monolithic Microwave Integrated Circuits (MMIC) applications, and micromachined passive electronic components for submillimeter wave radiometry.



**Edward J. Haugland** received his B.S. degree in Physics from the University of Minnesota, and M.S. and Ph.D. degrees in Solid State Physics from Case Western Reserve University. He joined NASA Lewis Research Center in 1980 as a member of the Solid State Technology Branch. Since that time, he has been involved with experimental research on electrical properties of III-V semiconductor materials, heterostructures, and SiC. Dr. Haugland was responsible for contracts concerning development of high-power Impact Ionization Avalanche Transit Time (IMPATT) diodes and MMIC power amplifiers. Dr. Haugland is a member of the American Physical Society.



**Thomas J. Kascak** received his B.S.E.E. degree from Case Western Reserve University in 1959 and joined Union Carbide Corporation where he worked with performance and reliability aspects of dry cell and alkaline batteries. Mr. Kascak received his M.S. degree in Physics in 1965 from John Carroll University and joined NASA Lewis Research Center in 1966. He has been involved in several work areas ranging from research on thermionic heat to electric power conversion devices. In 1980, he transferred to the Launch Vehicles Division where he had contract management responsibilities dealing with guidance equipment for the NASA Atlas/Centaur launch vehicle systems. He was also responsible for formulating and managing several NASA-sponsored contractual efforts involving MMIC development programs. One of these efforts, a 20-GHz MMIC Transmit Module, resulted in the R&D Magazine IR-100 award. For the last few years, he has been responsible for the set-up of the division's in-house solid-state facilities. Mr. Kascak has authored papers on thermionic direct energy conversion devices, 20- and 30-GHz MMIC devices, and MMIC-based phased array antennas. Mr. Kascak is a member of the American Vacuum Society.



**Regis F. Leonard** received his Ph.D. degree in Physics from the Carnegie Institute of Technology in 1963 and came to NASA Lewis Research Center that same year. Since that time he has completed 10 years of basic research concerning the physics of nuclear structures. For 6 years, Dr. Leonard worked towards the development of a unique Lewis facility that uses neutron radiation to treat cancer patients. For the last 11 years, he has helped develop technology in support of NASA's communications programs. This assignment includes work on the ACTS proof-of-concept (POC) technology program and, as head of the RF Systems Section, the development of an in-house communications system test capability for the ACTS POC hardware. For the last 6 years he has served as Chief of the Solid State Technology Branch. Dr. Leonard is responsible for NASA's MMIC technology development program—an active, in-house, solid state, research program—and a sizeable university grant program which supports basic research as applicable to solid-state electronics.



**Rafael A. Mena** received his B.S. degree in Electrical Engineering in 1988 from the University of Texas at El Paso and an M.S. degree in Solid State Physics in 1990 from Arizona State University. While at Arizona State University, he made theoretical calculations on the effect of a magnetic field on the optical properties of semiconductor alloys. In 1990, he joined the Solid State Technology Branch at NASA Lewis Research Center as a full-time employee. His current interests lie in both the theoretical and experimental investigation of the electrical properties of novel semiconductor materials.

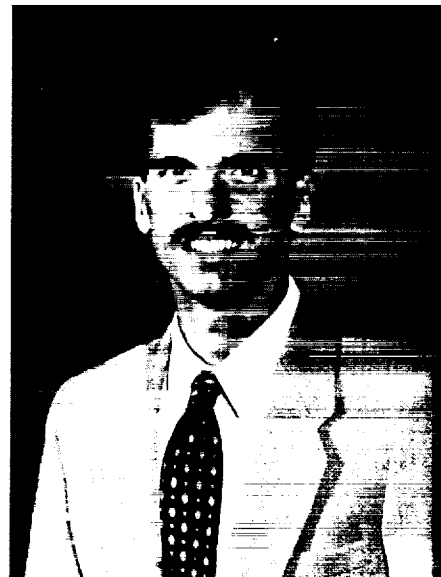


**Felix A. Miranda** received his B.S. degree in Physics from the University of Puerto Rico in 1983, an M.S. degree in Physics from the Rensselaer Polytechnic Institute in 1986, and Ph.D. degree in Physics from Case Western Reserve University in 1991. He joined NASA Lewis Research Center in March 1991 as a member of the Solid State Technology Branch. Since then he has been involved with experimental research on millimeter and microwave properties of High Transition Temperature Superconducting (HTS) thin films and HTS-based passive microwave devices. Dr. Miranda is a member of the American Physical Society and the Institute of Electrical and Electronics Engineers.

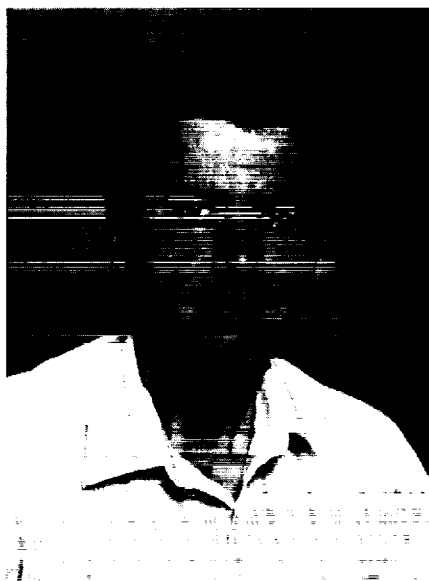
**Carlos R. Morrison** received his B.S. degree (Honorary) in Physics in 1986 from Hofstra University where he was elected to the Sigma Pi Sigma National Physics Honor Society, the Kappa Mu Epsilon National Mathematics Honor Society, and the Society of Physics Students. He received his M.S. degree in Physics in 1989 from the Polytechnic Institute of New York. He joined NASA Lewis Research Center in September of 1989. For a short time he worked in Reliability and Quality Assurance, then transferred to the Solid State Technology Branch in January of 1990. In September 1992 he was awarded a U.S. patent for the "Morrison's Temporal Device," a type of headband for use in relieving headaches. Currently Mr. Morrison is involved with plasma deposition and ellipsometry.



**George E. Ponchak** received his B.S.E.E. from Cleveland State University in 1983, and his M.S.E.E. from Case Western Reserve University in 1987. He joined the Space Electronics Division at NASA Lewis Research Center in July 1983. Since joining NASA, he has been responsible for research of microwave and millimeter wave transmission line and passive elements. Mr. Ponchak has developed many coplanar waveguide (CPW) circuit elements, including several novel CPW's for rectangular waveguide transmissions, CPW pin-diode switches, and CPW discontinuity equivalent circuit models. Mr. Ponchak has coauthored 22 papers on these topics. He is currently interested in the development of dielectric wave guides and micromachined waveguides for millimeter/submillimeter wave circuits. In addition, Mr. Ponchak has been responsible for the management of several MMIC development contracts and is currently the technical manager for the W-band MMIC Receiver Development Contract with TRW. Mr. Ponchak is currently pursuing his Ph.D. degree in Electrical Engineering at the University of Michigan.



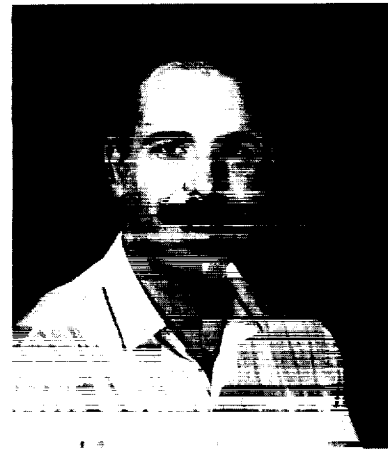
**John J. Pouch** received his Ph.D. degree in Solid State Physics from Wayne State University in 1981. His research activities at NASA Lewis Research Center include surface analysis of thin films for microelectronic applications, plasma and reactive ion etching, and plasma deposition.



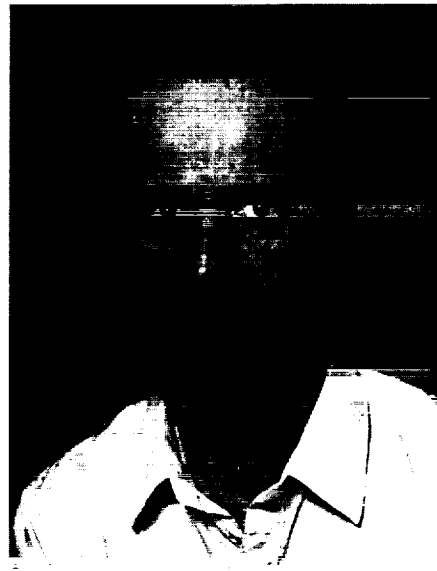
**Robert R. Romanofsky** received his B.S. degree in Electrical Engineering from Pennsylvania State University and his M.S. degree in Electrical Engineering from the University of Toledo. Mr. Romanofsky has been employed in the Space Electronics Division of NASA Lewis Research Center since 1983. He spent 1 year at NASA Headquarters in Washington, D.C., as the acting program manager for superconductivity and RF communications. His work has involved microwave transmission line research and device characterization and modeling. Recently, he has been investigating microwave applications of high-temperature superconductivity.



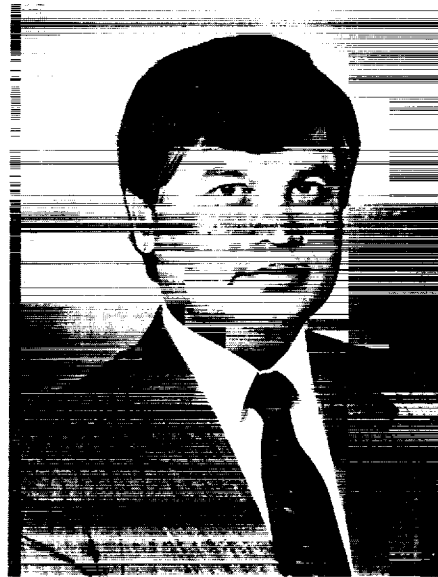
**David Rosenfeld** received his B.S., M.S., and Ph.D. degrees in Electrical Engineering from the Technion—Israel Institute of Technology in 1983, 1985, and 1989 respectively. In 1989 he joined Kidron Microelectronics Research Center at the Technion where he researched the properties of low band-gap materials used for infrared imaging systems, focusing on the connections between the material parameters, the device properties, and the performance of the complete imaging system. Currently, Dr. Rosenfeld holds a National Research Council Fellowship and is researching the properties of SiGe heterostructures.



**Samuel E. Schacham** received his B.S. degree in Mathematics and Physics with honors in 1971, and an M.S. degree in Physics in 1973 from Bar Ilan University, Israel. He performed research work on nonlinear optical effects in liquid crystals at the Weitzmann Institute and Bar Ilan University. He received a Ph.D. degree in Biomedical Engineering in 1978 from Northwestern University working on applications of lasers to microendoscopy. From 1978 to 1981, he was the manager of the optic group at Fibronics Ltd., Haifa, Israel. From there he joined the Department of Electrical Engineering at the Technion in Haifa. In 1988 he was a visiting scientist at MCNC Research, Triangle Park, NC, working on optical interconnects as part of the packaging group. Presently, he is with NASA Lewis Research Center as a National Research Council Senior Research Associate. His present research interests are in the physical properties of quantum structures and narrow band-gap semiconductors. His list of publications includes 54 papers in international scientific journals and referred conferences.



**Ajit K. Sil** received his B.S. degree from Calcutta University, India, and emigrated to the United States where he was employed by Oakwood Downriver Medical Center. He received his second B.S. degree in Electronic Engineering Technology in 1988 from Wayne State University. He joined NASA Lewis Research Center in July of 1989 as a member of the Solid State Technology Branch. Mr. Sil works with microwave integrated circuits and solid-state devices. He is currently working toward his M.S.E.E. degree at Cleveland State University.



**Rainee N. Simons** received his B.S. degree in Electronics and Communications Engineering from Mysore University, India, in 1972 and an M. Tech degree in Electronics and Communications Engineering from the Indian Institute of Technology in 1974. In 1983 he received a Ph.D. degree in Electrical Engineering from the Indian Institute of Technology. He started his career in 1979 as a Senior Scientific Officer at the Indian Institute of Technology. From 1985 to the present he has been with the Solid State Technology Branch of NASA Lewis Research Center as a National Research Council Research Associate from 1985 to 1987, as a Case Western Reserve University Research Associate from 1987 to 1990 and as a Senior Research Engineer for Sverdrup Technology, Inc., from 1990 to the present. At NASA, Dr. Simons' research has included microwave and millimeter wave semiconductor devices, circuits and antennas, space terahertz technology, optical control of semiconductor devices, and superconductivity. Dr. Simons is the author of a book entitled "Optical Control of Microwave Devices." He has received the distinguished alumni award from his alma mater and several NASA Tech Brief and Group Achievement awards. Dr. Simons is a senior member of IEEE.



**Mark A. Stan** received his B.S.E.E. degree in 1978 from the University of Akron. He was employed by the Allen-Bradley Company as a digital circuit design engineer until 1980 when he returned to graduate school at Case Western Reserve University to study the physics of melting in two-dimensional systems, completing work for his M.S. degree in 1982 and a Ph.D. degree in 1988. In 1987 Dr. Stan began research work at NASA Lewis Research Center in the areas of characterization and growth of high-temperature superconductors. Currently Dr. Stan is a Resident Research Associate. He is a member of the American Physical Society, the Materials Research Society, and the Institute of Electrical and Electronic Engineers.



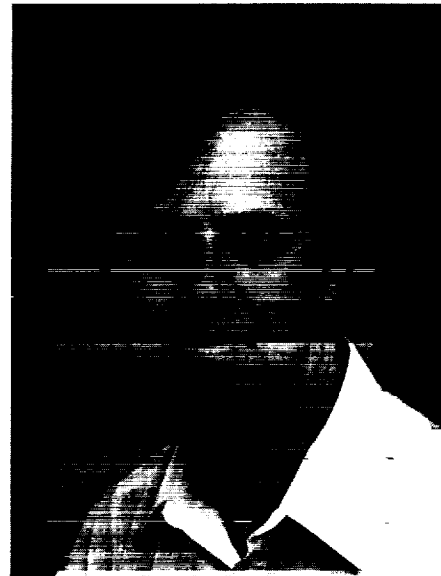
**Stephan Stecura** received his M.S. degree in Physical Chemistry in 1957 from Western Reserve University and a Ph.D. degree in Solid-State Reaction Kinetics-Thermodynamics in 1965 from Georgetown University. From 1958 to 1965 at College Park Metallurgy Center, he studied the kinetics of crystallographic transformation and the high-temperature properties of oxides by high-temperature, x-ray diffraction techniques. He designed and built high-temperature, x-ray diffraction equipment and was invited to present the high-temperature, x-ray diffraction, arc-image furnace (capable of reaching 3000 °C in air) at the International Crystallographic Society meeting. Since 1965 he has been with NASA Lewis Research Center. Dr. Stecura's work here on heat pipes led him to determine the corrosion mechanism and the true solubilities of containment metals and alloys in alkali metals. He developed thermal barrier systems for the protection of alloy components at very high temperatures, up to 1600 °C, on air-cooled components. Currently, he is studying the properties of superconducting materials and trying to identify substrate materials for superconducting films. Dr. Stecura is recognized as an authority on the thermal barrier system technology that he developed. For his work in this field, he has received two IR-100 awards, one major Space Act award, and three major patents. He has written more than 30 original publications and is a member of the American Ceramic Society.



**Susan R. Taub** received her B.S. degree in Electrical Engineering Technology in 1988, and an M.S. degree in Electrical Engineering in 1990 from Temple University. In 1988 and 1989 she worked for AT&T Bell Laboratories developing PSPICE compatible models for power Metaloxide Semiconductor Field Effect Transistor (MOSFET's). She joined the Solid State Technology Branch of NASA Lewis Research Center in 1990 and is currently involved in the design and characterization of MMIC's and the investigation of HEMT performance at cryogenic temperatures. Ms. Taub is a member of IEEE.



**Joseph D. Warner** received his M.S. degree in Physics from Carnegie-Mellon University in 1977. From 1977 to 1981, he performed research on magnetic phase transition at low temperature. Since that time, he has been with NASA Lewis Research Center where he characterized various insulators on GaAs and was among the first to demonstrate growth of GaAs by laser-assisted Organo-Metallic Chemical Vapor Deposition (OMCVD) at temperatures below 500 °C. Presently, he has set up a laser ablation experiment to grow high-temperature superconducting thin films. In 1989 he received a NASA Achievement Award for his part in establishing a high-temperature superconductor program at NASA Lewis. Mr. Warner has authored papers on magnetic phase transitions, electrical properties of insulation films on III-V compounds, laser-assisted growth of GaAs and AlGaAs, and properties and growth of high-temperature superconductors. Mr. Warner is a member of the American Physical Society, the American Vacuum Society, and the Materials Research Society.



**Paul G. Young** received his Ph.D. degree in Electrical Engineering in 1992 from the University of Toledo, an M.S. degree in Electrical Engineering from University of Cincinnati in 1987, and a B.S.E.E. degree from the University of Toledo in 1985. From 1987 to 1990, Mr. Young was employed by Harris/RCA in the Solid-State Division as a technical staff member. He has been active in the areas of III-V compound semiconductor process development, with an emphasis on InP self-gate-aligned MOSFET structures and GaAs MODFET structures. Presently, Mr. Young's research interests are in epitaxial lift-off MODFET devices and circuits, SiGe n-MODFET structures, and cryogenic on-wafer measurement of devices.



## SOLID STATE TECHNOLOGY BRANCH MEMBERS

**Address:** NASA Lewis Research Center  
21000 Brookpark Road  
Cleveland, Ohio 44135  
(FAX: (216) 433-8705)

| NAME                       | PHONE          | Mail Stop |
|----------------------------|----------------|-----------|
| *Leonard, Regis F., Dr.    | (216) 433-3500 | 54-5      |
| Alterovitz, Samuel A., Dr. | (216) 433-3517 | 54-5      |
| Bhasin, Kul B., Dr.        | (216) 433-3676 | 77-5      |
| Chorey, Chris              | (216) 433-3379 | 77-5      |
| Cubbage, Crystal D.        | (216) 433-3644 | 77-5      |
| Downey, Alan N.            | (216) 433-3508 | 54-5      |
| Haugland, Edward J., Dr.   | (216) 433-3516 | 54-5      |
| Kascak, Thomas J.          | (216) 433-3505 | 54-5      |
| Mena, Rafael A.            | (216) 433-5641 | 54-5      |
| Miranda, Felix A., Dr.     | (216) 433-6589 | 77-5      |
| Morrison, Carlos R.        | (216) 433-8447 | 54-5      |
| Ponchak, George E.         | (216) 433-3504 | 54-5      |
| Pouch, John J., Dr.        | (216) 433-3523 | 54-5      |
| Romanofsky, Robert R.      | (216) 433-3507 | 54-5      |
| Sil, Ajit K.               | (216) 433-8610 | 54-5      |
| Simons, Rainee N., Dr.     | (216) 433-3462 | 54-5      |
| Stan, Mark A., Dr.         | (216) 433-8369 | 54-5      |
| Stecura, Stephan, Dr.      | (216) 433-3264 | 54-5      |
| Taub, Susan R.             | (216) 433-6571 | 54-5      |
| Warner, Joseph D.          | (216) 433-3677 | 77-5      |

### Branch Secretary:

|                   |                |      |
|-------------------|----------------|------|
| Kimberly J. McKee | (216) 433-3514 | 54-5 |
|-------------------|----------------|------|

\*Chief, Solid State Technology Branch



# REPORT DOCUMENTATION PAGE

Form Approved  
OMB No. 0704-0188

Public reporting burden for this collection of information is estimated to average 1 hour per response, including the time for reviewing instructions, searching existing data sources, gathering and maintaining the data needed, and completing and reviewing the collection of information. Send comments regarding this burden estimate or any other aspect of this collection of information, including suggestions for reducing this burden, to Washington Headquarters Services, Directorate for Information Operations and Reports, 1215 Jefferson Davis Highway, Suite 1204, Arlington, VA 22202-4302, and to the Office of Management and Budget, Paperwork Reduction Project (0704-0188), Washington, DC 20503.

|  |   |   |                                   |
|--|---|---|-----------------------------------|
| <b>1. AGENCY USE ONLY (Leave blank)</b>  | <b>2. REPORT DATE</b><br>August 1992                            | <b>3. REPORT TYPE AND DATES COVERED</b><br>Technical Memorandum   |                                   |
| <b>4. TITLE AND SUBTITLE</b><br>Solid State Technology Branch of NASA Lewis Research Center<br>Fourth Annual Digest<br>June 1991-June 1992   |   | <b>5. FUNDING NUMBERS</b><br><br>WU-506-72-1B   |                                   |
| <b>6. AUTHOR(S)</b>  |   | <b>7. PERFORMING ORGANIZATION NAME(S) AND ADDRESS(ES)</b><br><br>National Aeronautics and Space Administration<br>Lewis Research Center<br>Cleveland, Ohio 44135-3191 |                                   |
| <b>9. SPONSORING/MONITORING AGENCY NAMES(S) AND ADDRESS(ES)</b><br><br>National Aeronautics and Space Administration<br>Washington, D.C. 20546-0001  |   | <b>8. PERFORMING ORGANIZATION REPORT NUMBER</b><br><br>E-7160   |                                   |
| <b>11. SUPPLEMENTARY NOTES</b><br><br>Responsible person, Kimberly J. McKee (216) 433-3514.  |   | <b>10. SPONSORING/MONITORING AGENCY REPORT NUMBER</b><br><br>NASA TM-105752   |                                   |
| <b>12a. DISTRIBUTION/AVAILABILITY STATEMENT</b><br><br>Unclassified - Unlimited<br>Subject Category 32   |   | <b>12b. DISTRIBUTION CODE</b>   |                                   |
| <b>13. ABSTRACT (Maximum 200 words)</b><br><br>The digest is a collection of papers written by the members of the Solid State Technology Branch of NASA Lewis Research Center from June 1991-June 1992. The papers cover a range of topics relating to superconductivity, MMIC's, coplanar waveguide, and material characterization. |   |   |                                   |
| <b>14. SUBJECT TERMS</b><br><br>Microwave integrated circuits; Microwave; Transmission lines; Antennas; Transistors  |   |   | <b>15. NUMBER OF PAGES</b><br>231 |
| <b>17. SECURITY CLASSIFICATION OF REPORT</b><br>Unclassified   |   |   | <b>16. PRICE CODE</b><br>A11      |
| <b>17. SECURITY CLASSIFICATION OF REPORT</b><br>Unclassified   | <b>18. SECURITY CLASSIFICATION OF THIS PAGE</b><br>Unclassified | <b>19. SECURITY CLASSIFICATION OF ABSTRACT</b><br>Unclassified  | <b>20. LIMITATION OF ABSTRACT</b> |